Transactions of the ASME, Journal of Heat Transfer (ISSN 0022-1481) is published monthly by The American Society of Mechanical Engineers, Three Park Avenue, New York, NY 10016. Periodicals postage paid at New York, NY and additional mailing offices. POSTMASTER: Send address changes to Transactions of the ASME, Journal of Heat Transfer, c/o THE AMERICAN SOCIETY OF MECHANICAL ENGINEERS, 22 Law Drive, Box 2300, Fairfield, NJ 07007-2300. **CHANGES OF ADDRESS** must be received at Society headquarters seven weeks before they are to be effective. Please send old label and new address. **STATEMENT from By-Laws.** The Society shall not be responsible for statements or opinions advanced in papers or ... printed in its publications (B7.1, Para. 3).

Journal of Heat Transfer

Published Monthly by ASME

VOLUME 129 • NUMBER 11 • NOVEMBER 2007(pp.1465-1615)

RESEARCH PAPERS

(Contents continued on inside back cover)

This journal is printed on acid-free paper, which exceeds the ANSI Z39.48-1992 specification for permanence of paper and library materials. ♾™
♻ 85% recycled content, including 10% post-consumer fibers.

Journal of Heat Transfer **Volume 129, Number 11** **NOVEMBER 2007**

TECHNICAL BRIEFS

The ASME Journal of Heat Transfer is abstracted and indexed in the following:

Applied Science and Technology Index, Chemical Abstracts, Chemical Engineering and Biotechnology Abstracts (Electronic equivalent of Process and Chemical Engineering), Civil Engineering Abstracts, Compendex (The electronic equivalent of Engineering Index), Corrosion Abstracts, Current Contents, E & P Health, Safety, and Environment, Ei EncompassLit, Engineered Materials Abstracts, Engineering Index, Enviroline (The electronic equivalent of Environment Abstracts), Environment Abstracts, Environmental Engineering Abstracts, Environmental Science and Pollution Management, Fluidex, Fuel and Energy Abstracts, Index to Scientific Reviews, INSPEC, International Building Services Abstracts, Mechanical & Transportation Engineering Abstracts, Mechanical Engineering Abstracts, METADEX (The electronic equivalent of Metals Abstracts and Alloys Index), Petroleum Abstracts, Process and Chemical Engineering, Referativnyi Zhurnal, Science Citation Index, SciSearch (The electronic equivalent of Science Citation Index), Theoretical Chemical Engineering

Parametric Study of Pool Boiling on Horizontal Highly Conductive Microporous Coated Surfaces

Chen Li
Assistant Professor
Mem. ASME
e-mail: lichen.cu@colorado.edu

G. P. Peterson
Professor and Chancellor
Fellow ASME
e-mail: bud.peterson@colorado.edu

Department of Mechanical Engineering,
University of Colorado at Boulder,
Boulder, CO 80309-0427

To better understand the mechanisms that govern the behavior of pool boiling on horizontal highly conductive microporous coated surfaces, a series of experimental investigations were designed to systematically examine the effects of the geometric dimensions (i.e., coating thickness, volumetric porosity, and pore size, as well as the surface conditions of the porous coatings) on the pool-boiling performance and characteristics. The study was conducted using saturated distilled water at atmospheric pressure (101 kPa) *and porous surfaces fabricated from sintered isotropic copper wire screens. For nucleate boiling on the microporous coated surfaces, two vapor ventilation modes were observed to exist: (i) upward and (ii) mainly from sideways leakage to the unsealed sides and partially from the center of porous surfaces. The ratio of the heater size to the coating thickness, the friction factor of the two-phase flow to single-phase flow inside the porous coatings, as well as the input heat flux all govern the vapor ventilation mode that occurs. In this investigation, the ratio of heater size to coating thickness varies from 3.5 to 38 in order to identify the effect of heater size on the boiling characteristics. The experimental results indicate that the boiling performance and characteristics are also strongly dependent on the volumetric porosity and mesh size, as well as the surface conditions when the heater size is given. Descriptions and discussion of the typical boiling characteristics; the progressive boiling process, from pool nucleate boiling to film boiling; and the boiling performance curves on conductive microporous coated surfaces are all systematically presented.* [DOI: 10.1115/1.2759969]

Keywords: parametric study, microporous surface, boiling characteristics, boiling performance

1 Introduction

The practice of using rough or microstructured surfaces to enhance the boiling performance and increase the CHF has been of considerable interest since it was first observed and reported by Jakob in 1931 [1]. Since that time, considerable effort has been devoted to the development of artificial surfaces and structures in order to improve nucleate boiling as well as increase the critical heat flux (CHF) for long-term operation and applications. Until 1954, however, enhanced surfaces were thought to be unusable in industrial applications, due to the decay of the enhancement caused by the little-understood "aging effect." This situation changed dramatically with the development of several patents [2–4] that were successfully employed in industry in the mid-1960s. The critical development was the work of Milton [2–4], who achieved high nucleate boiling performance through the sintering of porous coatings on tube surfaces.

Generally speaking, there are three types of enhanced or microstructured surfaces employed in nucleate boiling applications: "pore-and-tunnel" surfaces or reentrant cavities, finned surfaces, and porous media coated surfaces. The latter of these, porous coated surfaces, has been one of the most attractive techniques for enhancing the boiling heat transfer coefficient as well as the CHF for many years. Although the information available in the literature is quite extensive, there is still considerable confusion about the impact of these coatings on the heat transfer and boiling enhancement. As a result, the information presented here is restricted to porous coated surfaces and is intended to clarify the fundamental phenomena that affect the behavior and performance of these surfaces.

In addition to the specific thermophysical properties of the material, porous coated surfaces are most frequently categorized based on their thickness and structure. Experimental and numerical studies [5–18] have consistently demonstrated that nucleate boiling performance can be significantly enhanced, and boiling incipience superheat dramatically reduced, through the use of porous coatings. Investigations have revealed the physical processes and specific characteristics of boiling in porous media coated surfaces that are important, such as the location of the evaporation and nucleate boiling sites, the behavior of the liquid and vapor phases, the existence of a vapor film near the heating wall, etc. Moss and Kelly [13] performed neutron radiography of evaporation on a 6.3 mm thick sintered stainless steel wire mesh in which the sides of the porous media were open. A static, time-invariant vapor blanket was observed near the heating wall that appeared to increase in thickness with increasing heat flux. The capillary pressure across the internal liquid vapor interface also increased with increasing heat flux. In this investigation, Moss and Kelly [13] concluded that the phenomenon of vapor escaping from the sides of the wick presented a more realistic interpretation of the results than a model based on evaporation from the surface, and small vapor patches formed inside the wick would not "choke" the liquid supply, but instead, the presence of the porous structure in a boiling fluid would effectively "smooth out the formation" of individual nucleate bubbles and eliminate the sudden transition from nucleate boiling to film boiling.

Cornwell et al. [14] observed the simultaneous and continuous existence of vapor and liquid regions in a 6 mm thick polyurethane foam wick and found that these regions extended through the wick thickness and that the boundaries between the regions

Contributed by the Heat Transfer Division of ASME for publication in the JOURNAL OF HEAT TRANSFER. Manuscript received January 2, 2006; final manuscript received April 10, 2007. Review conducted by Ramendra P. Roy.

were stable. In this investigation, contact between the porous coating and the heated wall was maintained by a rod and perforated plate. The heat flux was observed to increase proportionally with the ratio of the vapor-covered area to the total heating area, A_v/A, and the frictional pressure drop of the vapor flow through the liquid saturated porous wick was found to be much higher than through a dry wick of similar dimensions.

Nakayama et al. [15] believed that boiling in porous media with reentrant grooves, was a highly dynamic process and that three "routes" for the heat transfer from the surface to the ambient liquid existed: convective heat transfer agitated by bubble formation, vaporization of the liquid near the outer surface into the growing bubbles, and vaporization in the tunnel formed by the reentrant grooves. Bergles and Chyu [16] conducted an experimental investigation of boiling on a brazed metal powder, 0.38 mm thick and with volumetric porosities ranging from 50% to 65%. The results of this investigation indicated that nucleate boiling occurs within the porous media from the reentrant cavities, and vaporization occurred within the porous media, forcing the vapor bubbles out. The low boiling incipience superheat was thought to be due to the large internal surface area, with vapor-liquid counterflow occurring during the boiling process. The vapor did not spread evenly over the surface to activate other adjacent sites, due to the internal generation of vapor, instead the random distribution of active sites resulted in what was referred to as "patch boiling."

Polezhaev and Kovalev [17] successfully modeled boiling heat transfer on 1 mm thick porous structures, numerically. In the investigation, Polezhaev and Kovalev [17] assumed that the evaporation occurred inside the porous coatings. Heat was transferred from the heating wall, through the shell of the porous structure, to the meniscus of the liquid, where vaporization occurred. Polezhaev and Kovalev [17] also found that higher effective thermal conductivities could enhance boiling performance and that the maximum evaporation occurs at the bottom of the porous coating at low heat fluxes and then decreases with increasing heat flux, causing the evaporation position to move toward the surface of the porous coating. Malyshenko [10], and Borzenko and Malyshenko [12] conducted a series of experimental and visual studies of boiling on nonconductive porous coatings, and illustrated that the porous coating thickness plays a determining role in the boiling characteristics and that there exists a drying zone, during the boiling process. In this approach, the drying zone corresponds to the thickness and there is a critical drying zone area, which does not change in size until the input heat flux exceeds the CHF. Malyshenko [10] and co-workers observed a vapor film formed near the heating wall for thick porous coatings and found that the thickness of the vapor film was approximately half the thickness of the porous coating. Based on these observations and comparisons to other data, O'Connor et al. [7] hypothesized that the improvement in the heat transfer performance from porous coated surfaces was primarily due to the increase in the number of active nucleation sites.

Based on a review of the literature presented above, and more recent work on boiling in microporous coated surfaces [19,20], it is clear that significant improvements in nucleate boiling heat transfer and reductions in the boiling incipience superheat can be achieved for both conductive and nonconductive materials. In addition, several generalizations regarding pool boiling in porous coatings can be made as follows:

- Nucleate boiling and evaporation, both occur "inside" of the porous media [13,14,16,17].
- Stable internal vapor and liquid counterflow patterns are formed in thick porous coatings during the boiling process [7,9–14,17].
- A thin vapor film is often formed near the heating wall on thick coatings, depending on the magnitude of the heat flux [10–13].
- The frictional pressure drop for vapor flow through a saturated porous media is much higher than through a dry porous media and as a result, the vapor will try to escape from the sides of the porous coating [14].
- Boiling performance increases in porous media may be due to the strong convection caused by the agitation of the vapor bubbles inside of the porous coatings and by the increase in the number of nucleate sites [7,9,15].
- The formation of individual nucleate bubbles is limited in porous media compared to plain surfaces, retarding the formation of film boiling and resulting, instead, in stable "patch boiling." This feature could eliminate the sudden transition from nucleate boiling to film boiling [13,16].
- Boiling performance and characteristics are strongly dependent on the geometric parameters, the thermal properties of the porous media, and the contact conditions between the porous coatings and the heated wall [10–13,15,17].

Although informative, because the conditions for each of these studies varied, these conclusions alone do not provide a sufficiently comprehensive or conclusive description of the boiling in porous coatings and as a result, show only limited guidance as to how to optimize the effect of the various parameters that govern these phenomena. For this reason, a systematic investigation was conducted to examine the effects of the geometric dimensions, i.e., coating thickness, volumetric porosity, and mesh size of microporous surfaces on boiling incipience and nucleation. The ratio of heater size to coating thickness is varied from 3.5 to 38 to investigate the vapor ventilation modes. This parametric study successfully verifies some of the conclusions in previous numerical simulations and has led to further understanding of the boiling characteristics and mechanisms that govern the boiling heat transfer on porous coated surfaces.

2 Experimental Test Facility and Procedure

2.1 Test Articles Structure and Fabrication. In the current investigation, a series of experimental tests were conducted using saturated distilled water at atmospheric pressure, in contact with a horizontal, 8 mm $\times$ 8 mm conductive porous coating. The key geometric parameters of the porous coating, such as the coating thickness, volumetric porosity, and pore size, were varied to determine the effects on the boiling performance and the boiling characteristics. Sintered pure isotropic copper wire screens, similar to those illustrated in Figs. 1(*a*) and 1(*b*) [19], were employed as the conductive microporous media. All sintered copper wire screens are in staggered structure in this experimental study.

The structure of the test articles, which are similar to samples in [19] except for the wing structures, is illustrated in Fig. 2. It consists of three parts: an 8 mm $\times$ 8 mm square, multilayered sintered isotropic copper mesh section; a 0.03 mm thick copper foil; and an 8 mm $\times$ 8 mm square copper heating block with a 7.8 mm threaded cylindrical portion. Three thermocouples, i.e., TC1, TC2, and TC3, are located at the center of the copper bar at 10 mm intervals, from which the steady-state 1D axial heat flux of the copper heating block could be determined by the linear temperature distribution and estimated accurately coupling with the known thermal conductivity of the pure copper. The temperature of the interface between the heating block and wick structure is derived from TC1, which is located at 0.5 mm below the interface. The detailed data reduction process is shown in Sec. 2.3.

An optimal sintering process developed by Li et al. [19] was employed to fabricate the test articles. Test data [19] illustrated that this sintering process could achieve nearly perfect contact conditions. Sintered isotropic copper wire screen was directly sintered to the heating block to avoid the contact thermal resistance at the interface between the porous material and the heating block. The fabrication procedure and sintering process are detailed in [19]. The finished surface is illustrated in Fig. 3.

A total of ten different test articles were evaluated experimentally to determine the effects of the geometric parameters of the

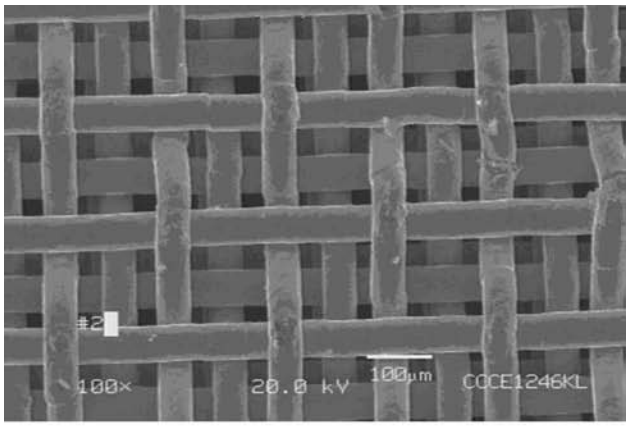

(*a*)

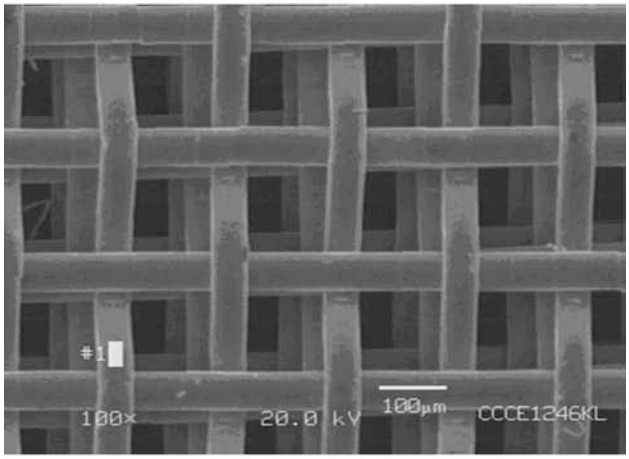

(*b*)

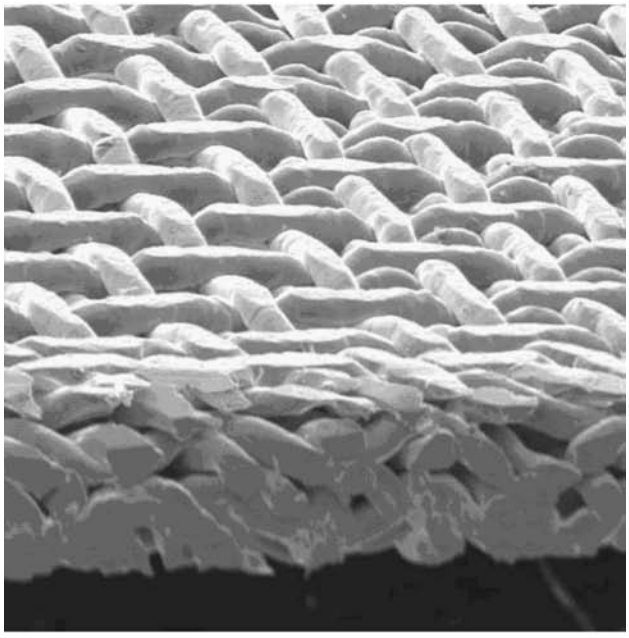

(*c*)

Fig. 1 Scanning Electron Microscope (SEM) images of sintered isotropic copper mesh with 1509 m^{-1} (145 $in.^{-1}$), 56 μm (0.0022 in.) wire diameter, fabricated at a sintering temperature of 1030°C with gas mixture protection (75% N_2 and 25% H_2) for 2 h [19]: (*a*) Top view of staggered sintered isotropic copper mesh [19], (*b*) top view of inline stacked sintered isotropic copper mesh [19], and (*c*) side view of compact sintered isotropic copper mesh [20]

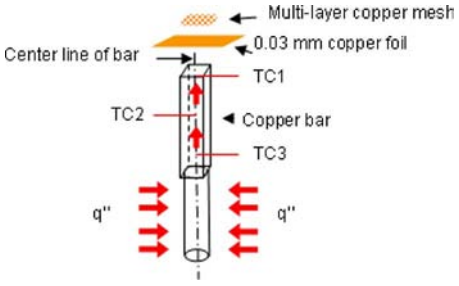

Fig. 2 Schematic of the test article

microporous surfaces on the pool boiling heat transfer performance and characteristics. The specifications of the ten test articles are listed in Table 1, where the variables are highlighted. The test article designations, which describe the specific characteristics for each, are identified. The nomenclature represents the type of boiling, followed by the number of layers and mesh number of the screen, for example, PB145-2 denotes a pool boiling test sample, which is fabricated from two layers of 5709 m^{-1} (145 $in.^{-1}$) copper wire screen.

2.2 Test Facility and Procedure. The experimental test facility is shown in Fig. 4 and has been described in detail in [19]. This test rig consists of an aluminum chamber with two guard heaters, a reservoir for the distilled water supply, a heating system, and a data acquisition system. Compared to the test facility in the film evaporation tests [19], the samples are totally immersed in saturated liquid in the present test.

Nucleate boiling on a plain surface was used to calibrate the experimental test facility [19]. Prior to the recording of any test data, all dissolved gases were removed from the distilled water by boiling for at least 2 h. Three K-type thermocouples (TC4, TC5, and TC6) are used to monitor the water temperature at different positions. The test facility was allowed to reach steady state, defined as the point at which the temperature reading for any thermocouple varied by <0.1°C over a period of 10 min. Then, the steady-state experimental data were averaged over a period of 5 min and recorded at each power level. The power was then incremented and the process repeated, until the CHF had been achieved.

2.3 Data Reduction and Experimental Uncertainties. The processes of data reduction and experimental uncertainties are identical to that described in [19]. The test data were categorized to obtain three key parameters, computed from Eqs. (1)–(3), respectively: the super heat, $T_W - T_{sat}$; the heat flux q'' (including the CHF); and the evaporation/boiling heat transfer coefficient h_{eff}.

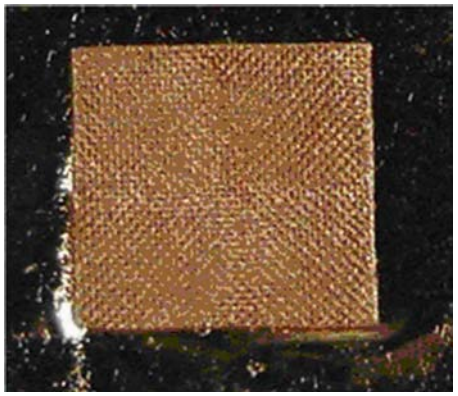

Fig. 3 Image of the completed sintered wire screen surface before the test and after dryout

Table 1 Specifications of the test samples

Grouped by varying	Sample No.	Thickness (mm)	Porosity	Wire diameter (μm)	Pore size (μm)
Thickness	PB145-2	0.21	0.737	56	119.2
	PB145-4	0.37	0.693	56	119.2
	PB145-6	0.57	0.701	56	119.2
	PB145-8	0.74	0.698	56	119.2
	PB145-16	1.38	0.69	56	119.2
	PB145-32	2.30	0.64	56	119.2
Volumetric porosity	PB145-4	0.37	0.693	56	119.2
	PB145-6c	0.36	0.56	56	119.2
	PB145-7c	0.37	0.409	56	119.2
Mesh size (mesh number and wire diameter)	PB145-4	0.37	0.693	56	119.2
	PB100-2	0.36	0.632	114	140
	PB60-1	0.38	0.67	191	232.2

$$T_W - T_{sat} = T_{TC1} - \frac{T_{TC4} + T_{TC5} + T_{TC6}}{3} - \frac{q'' t_{STC1}}{K_{Cu}} \quad (1)$$

$$q'' = \frac{K_{Cu}[(T_{TC3} - T_{TC2}) + (T_{TC2} - T_{TC1})]}{2t_{hole}} \quad (2)$$

$$h_{eff} = \frac{q''}{T_W - T_{sat}} \quad (3)$$

In Eq. (1), $T_{sat}=(T_{TC4}+T_{TC5}+T_{TC6})/3$ and $T_W=T_{TC1}-q''t_{STC1}/K_{Cu}$. Here, the terms T_{TC1}, T_{TC2}, and T_{TC3} represent the temperature for the three K-type thermocouples used to monitor the axial temperature distribution in the copper heater at 10 mm intervals. Thermocouples T_{TC4}, T_{TC5}, and T_{TC6} were used to measure the water temperature in the test chamber. Using this measured temperature, T_{TC1}, and the known thermal conductivity K_{Cu}, the temperature at the bottom of the capillary wick structure T_W was derived; then, using T_{TC1}, T_{TC2}, and T_{TC3}, the heat flux q''dissipated through evaporation/boiling under steady-state conditions could be determined. With these two values, the effective heat transfer coefficient can be estimated from Eq. (3).

The uncertainty of the temperature measurements, the length (or width), and the mass are ±0.5°C, 0.01 mm, and 0.1 mg, respectively. A Monte Carlo error of propagation simulation indicated the following 95% confidence level for the computed results: the heat flux was less than ±5.5 W/cm^2; the heat transfer coefficient was less than ±20%; the superheat ($T_{wall}-T_{sat}$) was less than ±1.3°C, and the volumetric porosity ε was less than ±1.5%.

3 Results and Discussion

The objectives of this investigation are to (i) examine the effects of thickness, volumetric porosity, and mesh size of the porous coatings on the boiling performance, characteristics, and the CHF, and (ii) identify the heat transfer and liquid/vapor phase regimes. All test results are summarized from Figs. 5–9. The heat transfer and the two-phase behavior regimes are presented in Fig. 10. The discussion begins from the general characteristics of nucleate boiling, and then proceeds to the effects of several key geometric dimensions, such as the coating thickness, the volumetric porosity and the mesh size.

3.1 Characteristics of Nucleate Boiling on Microporous Coated Surfaces

3.1.1 Two-Phase Flow Patterns at High Heat Flux. Previous investigations have demonstrated the existence of vapor film and the vapor-liquid countercurrent flow inside porous coatings during boiling [7,9–14,17]. There is also a vapor-liquid separating flow in

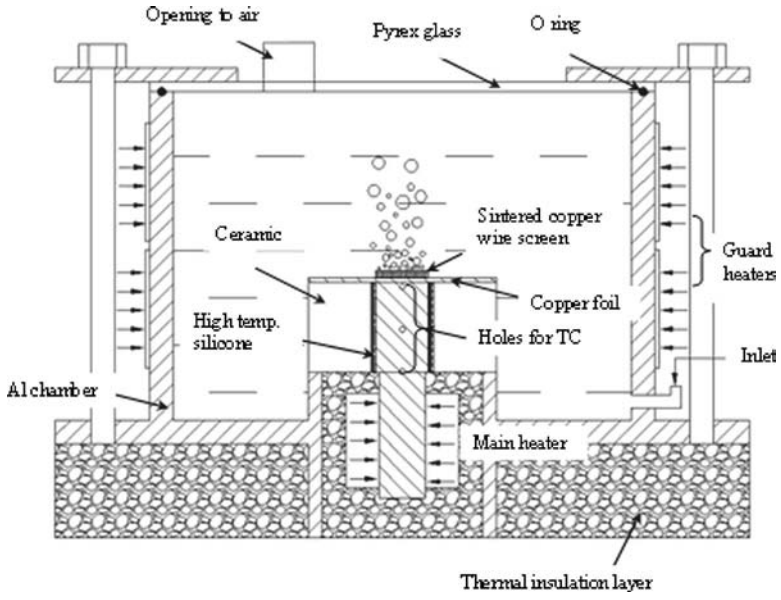

Fig. 4 Schematic of the test facility

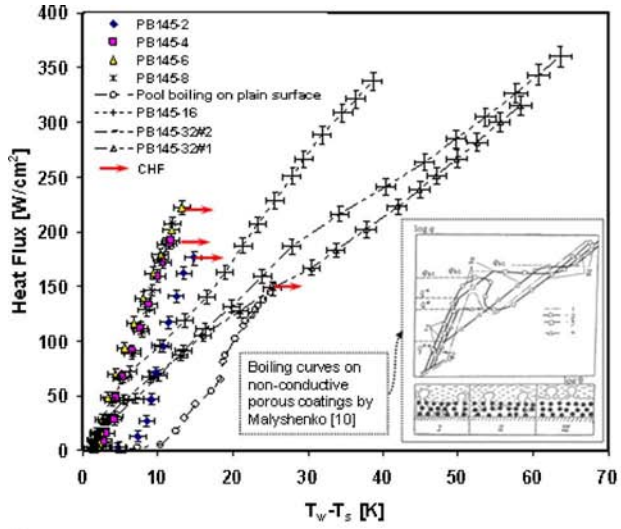

(a)

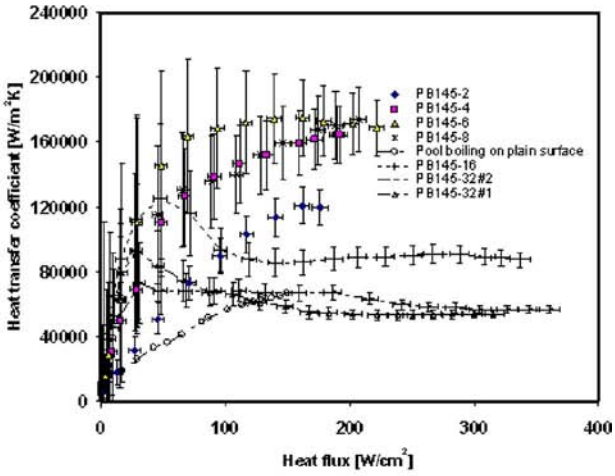

(c)

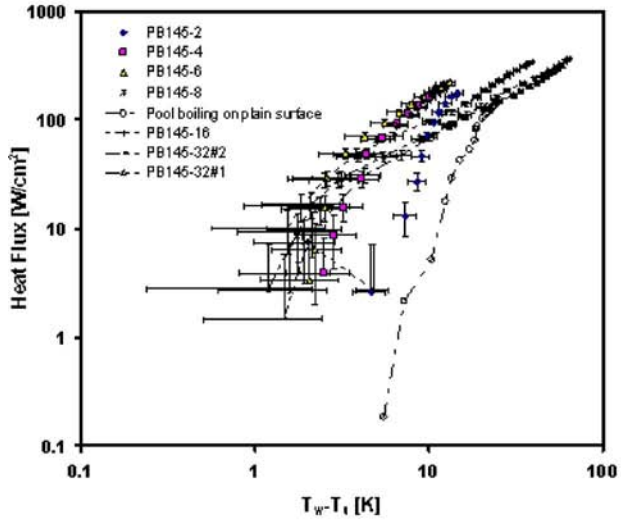

(b)

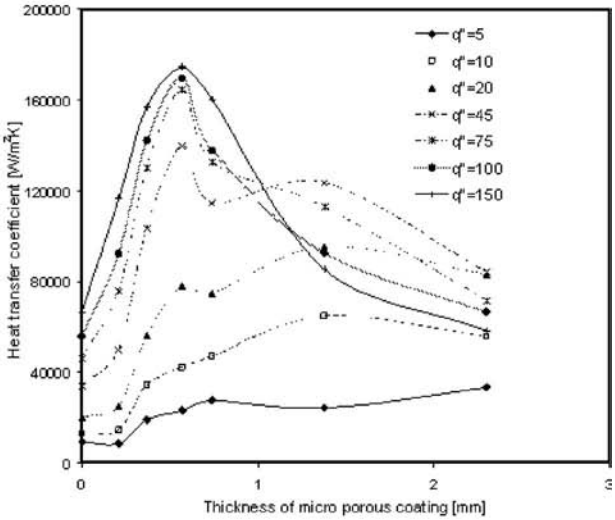

(d)

Fig. 5 (*a*) **Relationship between the heat flux and wall superheat based on the heater area as a function of thickness,** (*b*) **logarithmic relationship between the heat flux based on the heater area and wall superheat as a function of thickness,** (*c*) **relationship between the heat transfer coefficient and heat flux curve, based on the heater area as a function of thickness, and** (*d*) **relationship between boiling heat transfer performance and porous coating thickness**

this experimental study. As indicated in Figs. 5(*a*) and 5(*b*) the boiling curves of PB145-16 and PB145-32 are initially close to these test articles (i.e., PB145-4 through B145-8); however, after the heat flux exceeds a certain value, the two groups of curves begin to separate into two fairly distinct trends. This significant high wall superheat is believed to be caused by the formation of a very low conductive vapor film near the heated wall inside the porous coatings.

Assuming the vapor escapes from the top surface, the average vapor film thickness can be estimated from the test data of PB145-16 and PB145-32 using the known heat flux, thermal conductivity of vapor, and the extra temperature drop, which is the temperature difference between thin and thick wick groups at the same heat flux. The average film thicknesses for PB145-16 and PB145-32 are shown as a function of the heat flux in Fig. 6. For comparison, the thicknesses of these two porous coatings are also presented. As illustrated, the average thickness of the vapor film initially increases with increases in the heat flux, then remains relatively constant at a thickness approximately equal to, or slightly greater than, the thickness of the porous coating, which

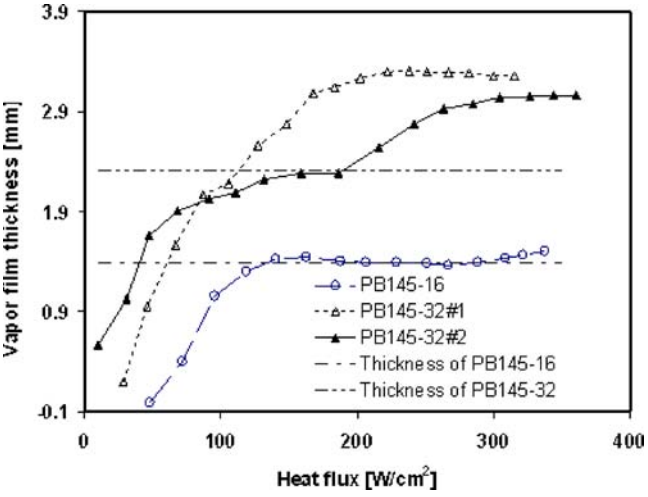

Fig. 6 Vapor film thickness as a function of heat flux at the heated wall

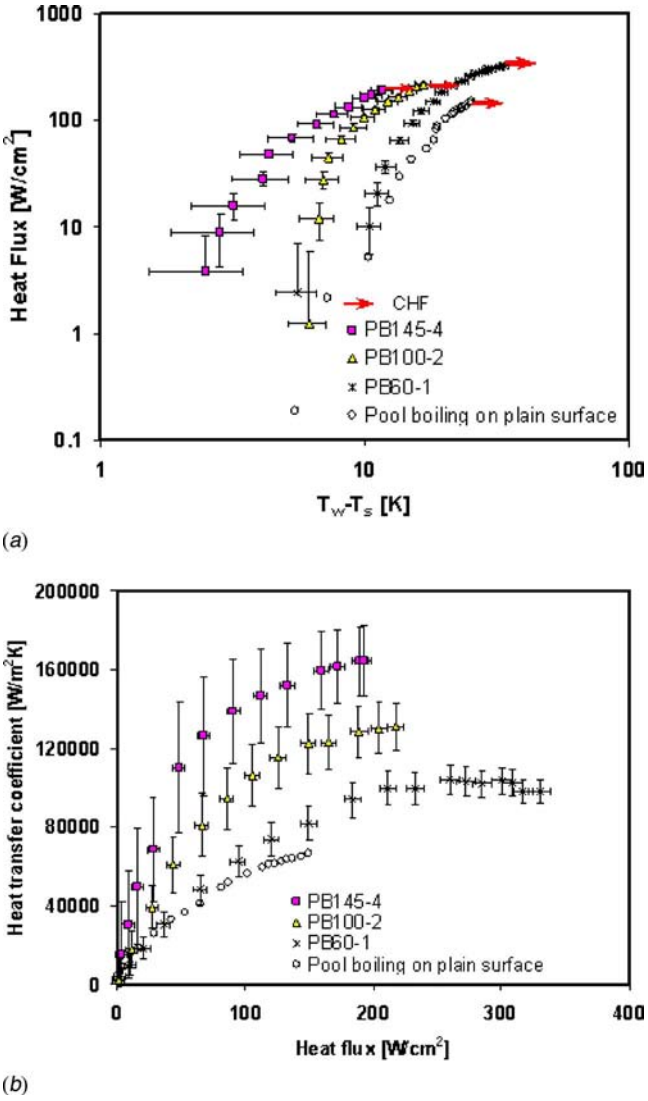

Fig. 7 (*a*) Logarithmic relationship between the heat flux based on the heater area and the wall superheat as a function of mesh size and (*b*) relationship between the heat transfer coefficient and heat flux based on the heater area as a function of mesh size

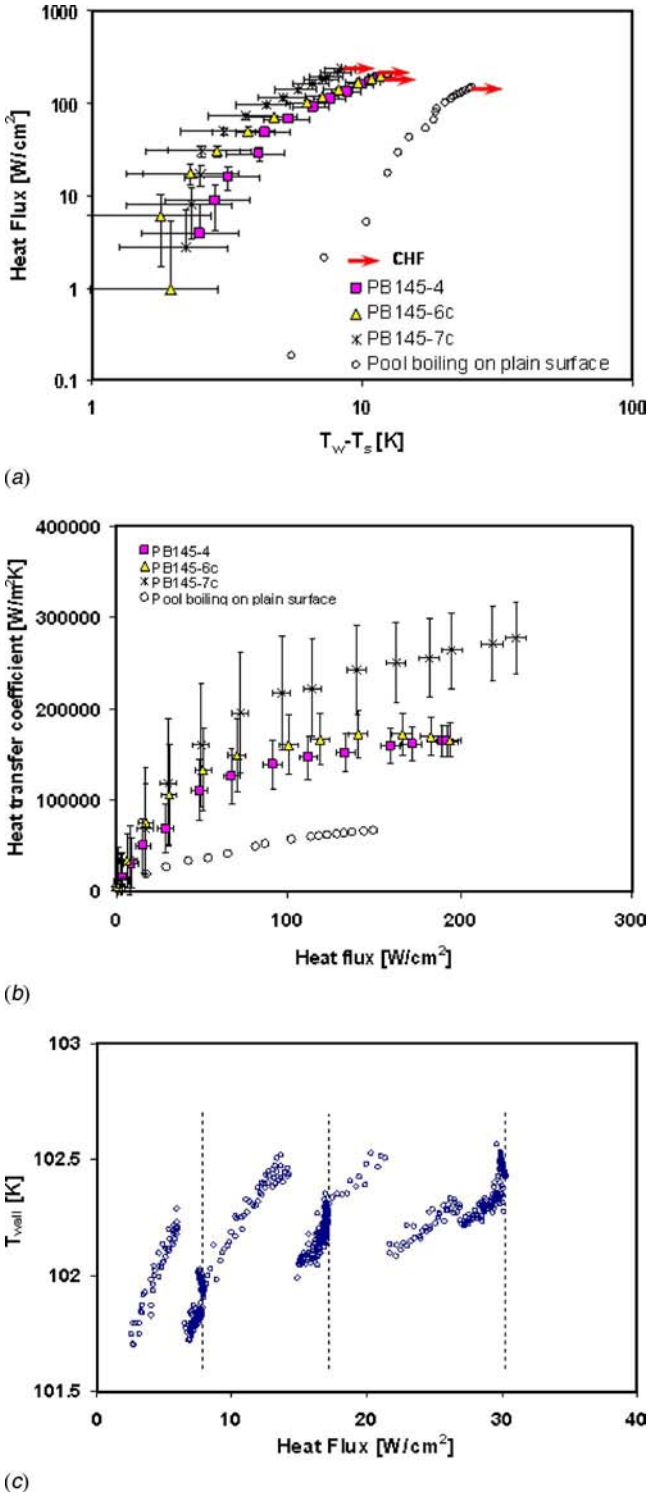

Fig. 8 (*a*) Logarithmic relationship between the heat flux based on the heater area and wall superheat as a function of volumetric porosity, (*b*) relationship between the heat transfer coefficient and heat flux curve based on the heater area as a function of mesh size, and (*c*) multiple boiling incipience phenomenon inside a porous media with low volumetric porosity

surprisingly does not trigger a sharp growth in the wall temperature, in other words, drying out. On the contrary, from Fig. 5(*c*) the boiling performance actually stops decreasing and remains relatively constant over a large range of heat fluxes. This phenomenon is hard to explain physically, until it is recognized that one of the assumptions, i.e., that the vapor is all vented through the top surface, may not be correct. The majority of the vapor actually escapes from the unsealed sides of thick porous coatings in most cases, which was consistent with what Moss and Kelly [13] concluded in their neutron radiography visualization and numerical modeling.

The vapor ventilation modes indicate two types of two-phase flow patterns: (i) liquid-vapor countercurrent flow, where the vapor escapes upward and the liquid flow is in the opposite direction driven by the gravity with partial assistance of capillary pressure, and (ii) liquid-vapor separating flow, where the major vapor vents through the vapor channel formed near the heater wall to the unsealed sides and the liquid enters the porous coatings from the top. The significant differences between these two flow patterns result from the vapor ventilation modes, which are mainly governed by the vapor flow resistance and the input heat flux. A theoretical analysis of the vapor flow resistance is given below to identify these parameters that govern the two-phase flow patterns.

The internal flow pressure drop is generally defined as in Eq. (4), with three assumptions: (i) vapors are generated inside porous

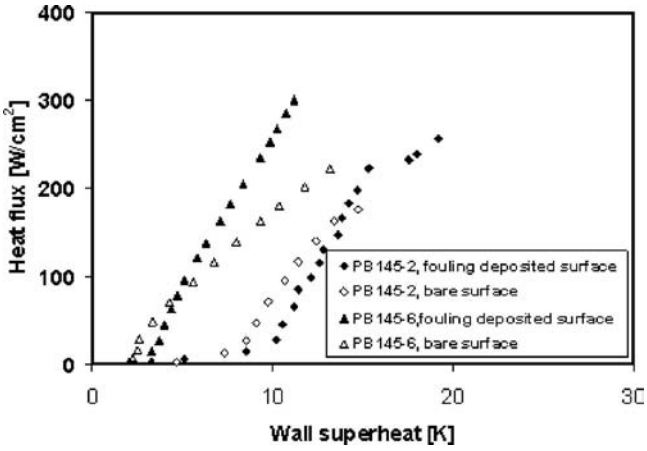

Fig. 9 Effects of surface conditions on boiling performance and characteristics for pool boiling in porous coated surfaces

media, (ii) vapor density is constant, and (iii) $f_{2\phi}$ increases with the void fraction, which also increases with input heat flux, in this case, and is generally larger than $f_{1\phi}$ at the same Re number. The vapor flow pressure equations for two phase and single phase, shown in Eq. (5), would present a theoretical analysis and be of help to explain the vapor ventilation modes.

Assuming the vapor flow resistance reaches the critical point, at which the vapor flow resistance through saturated porous media ($\Delta P_{2\phi}$) is equal to the vapor flow resistance ($\Delta P_{1\phi}$) through dry porous media, this balance can be described in Eq. (5)

$$\Delta P = \frac{1}{2} f \rho V^2 \frac{L}{D} = \frac{1}{2} f \frac{G^2}{\rho A_c^2} \frac{L}{D} \tag{4}$$

$$\Delta P_{2\phi} = \frac{f_{2\phi}(\mathrm{Re}) G_{v,2\phi}^2}{2\rho_v W_{\mathrm{heater}}^4} \frac{(t - t_{v,\mathrm{film}})}{W_{\mathrm{heater}}} = \Delta P_{1\phi}$$
$$= \frac{f_{1\phi}(\mathrm{Re}) G_{v,1\phi}^2}{2\rho_v (W_{\mathrm{heater}} t_{v,\mathrm{film}})^2} \frac{W_{\mathrm{heater}}}{\frac{4[W_{\mathrm{heater}} t_{v,\mathrm{film}}]}{2[W_{\mathrm{heater}} + t_{v,\mathrm{film}}]}} \tag{5}$$

$$G_v = \frac{q'' A_{\mathrm{heater}}}{h_{fg}} \tag{6}$$

$$\mathrm{Re}(q'') = \frac{G_v D_h}{\mu} = \frac{q'' A_{\mathrm{hetar}} D_h}{\mu h_{fg}} \tag{7}$$

where $f_{2\phi}$ and $f_{1\phi}$ are the friction factors of two-phase flow and single phase flow through wick structure, respectively; t is the wick thickness; W_{heater} is the heater characteristic size; and $G_{v,2\varphi}$ and $G_{v,1\varphi}$ are the average vapor mass flow rate through the liquid saturated (2φ) and dry porous media (1φ), respectively. They are defined in Eq. (6) and are equal. The Reynolds number is a function of input heat flux. Simplifying Eq. (5), the minimum stable vapor film thickness can be described as indicated in

$$\left(\frac{t_{v,\mathrm{film}}}{t}\right)^4 - \left(\frac{t_{v,\mathrm{film}}}{t}\right)^3 + \frac{f_{1\phi}(q'')}{2 f_{2\phi}(q'')} \left(\frac{W_{\mathrm{heatar}}}{t}\right)^3 \frac{t_{v,\mathrm{film}}}{t}$$
$$+ \frac{f_{1\phi}(q'')}{2 f_{2\phi}(q'')} \left(\frac{W_{\mathrm{heater}}}{t}\right)^4 = 0 \tag{8}$$

From this expression it is clear that the vapor film thickness is a function of $f_{2\phi}/f_{1\phi}, W_{\mathrm{heater}}/t$, and q''.

In the vapor ventilation scenario, there are two cases:

I. Vapor primarily escapes at two conditions as follows:

- When the input heat flux is small, and the $t_{v,\mathrm{film}}$ is very small; at the same time, the void fraction is also small;

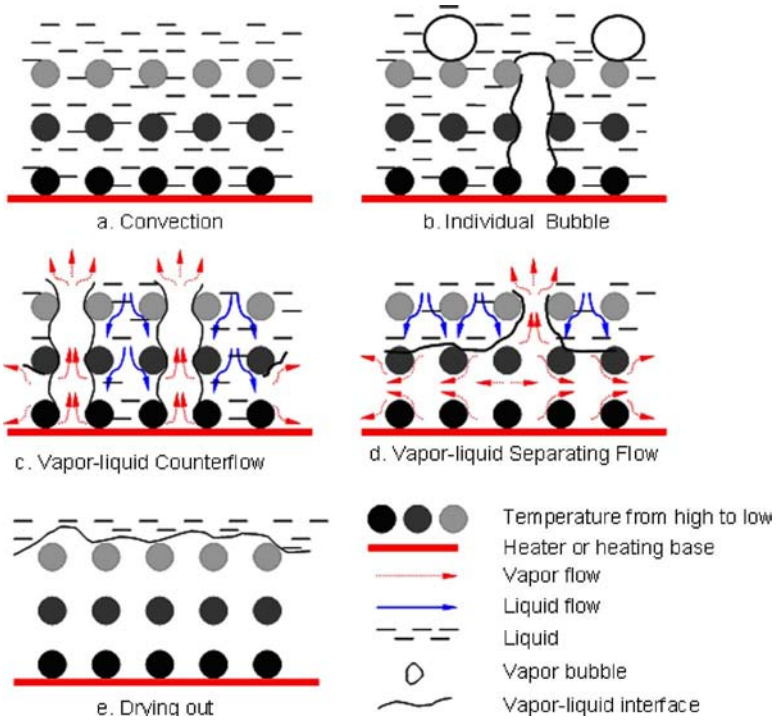

Fig. 10 Boiling and flow regimes in microconductive porous coated surfaces

thus, $f_{2\phi}$ and $f_{1\phi}$ do not vary much. From Eq. (5), $\Delta P_{2\phi}$ would be less than $\Delta P_{1\phi}$, and hence, the vapor would escape upward.

- Or the W_{heater} is much larger than the wick thickness t, which would make the vapor flow path in a single-phase channel much longer than through the liquid saturated porous media. The critical ratio of W_{heater}/t is primarily determined by the $f_{2\phi}/f_{1\phi}$.

II. Vapor primarily escapes from the unsealed sides when the W_{heater}/t is less than the critical ratio and the porous coating thickness t is larger than the minimum vapor film thickness (otherwise the surface dries out directly).

3.1.2 Heat Transfer Features. For a given heater size, there is a critical thickness t_{crit} which is equal to the minimum vapor film thickness. When the porous coating is thinner than the critical thickness t_{crit}, the boiling curve presents characteristics similar to those observed for smooth plain surfaces. Alternatively, when the porous coating is thicker than the critical thickness, the boiling curve demonstrates significantly different behaviors than those observed for smooth plain surfaces. In this latter situation, there does not appear to exist a boiling mode between nucleate boiling and film boiling, i.e., no transition boiling region, which is the case for boiling on plain surfaces. Malyshenko [10] referred to this region as "II nucleate boiling," or bubble interconnected nucleate boiling and presented similar boiling curves, as shown inside Fig. 5(*a*), based on a series of experiments on nonconductive porous coated surfaces. The observations in the current investigation are consistent with those observed by Malyshenko [10], but provided considerably more insight as to the causes and ramifications of the observed phenomena. The principal characteristics observed in this boiling region with vapor ventilation from unsealed sides can be summarized as follows:

- The heat flux does not decrease with wall superheat, but rather increases linearly with wall superheat.
- There does not exist a minimum heat flux, as in pool boiling from a plain surface during the transition from nucleate boiling to film boiling.
- The onset of film boiling is significantly delayed.
- When the vapor-liquid separating flow is formed, the CHF can be dramatically enhanced.
- The definition of the CHF for plain or thin porous coated surfaces does not appear to apply to these relatively thick porous coated surfaces.

3.2 Effect of Thickness of Microporous Coated Surfaces. In this set of experiments, the volumetric porosity and mesh size of the capillary wick were held constant, while the coating thickness was varied from 0.21 mm to 2.30 mm, to evaluate the effect of this variation on the boiling characteristics and performance. The heat flux q'' is shown as a function of the wall superheat, $T_w - T_s$, in Fig. 5(*a*), and the logarithmic relationship between these two parameters is presented in Fig. 5(*b*). The heat transfer coefficient is shown as a function of the heat flux at steady state in Fig. 5(*c*). For comparison, the boiling curve on a plain surface is also shown in Figs. 5(*a*)–5(*c*). The relationship between the boiling performance, heat flux, and thickness of the porous coatings are all illustrated in Fig. 5(*d*).

3.2.1 Effects of Thickness of Microporous Coated Surfaces on Boiling Performance. For a given heater size, previous analysis indicates that the boiling performance for conductive porous coatings is strongly dependant on the thickness. The heat transfer coefficient curve for each sample presents somewhat different characteristics. For PB145-2, the thinnest coating in this investigation, the heat transfer coefficient curve shows small improvements in the performance at low heat fluxes and significant improvements at higher heat fluxes (>28 W/cm^2) when compared to the results obtained for a smooth, plain surface. This improvement, however, is much smaller than that observed for samples PB145-4, 6, and 8. The reason for this difference is due to the combination of the reduction in the wetting area and, hence, the nucleate site density, as well as the extent of the interaction between the active nucleate sites induced by the porous coating. For samples PB145-4, 6, and 8, the performance is enhanced three to four times that of the plain surface over the entire heat flux range. This improvement is believed to be due to a combination of enhancements resulting from increases in the wetting surface area or the number of nucleation sites, the intensification of bubble interactions, and, more importantly, the introduction of the effects of the capillary and thin-film evaporation [8–12,15,16,19,20]. Furthermore, the performance of samples PB145-4, 6, and 8 do not show significant differences, which indicates that the wetting area does not always impact the boiling performance and that the principal evaporation and nucleate boiling may occur solely inside the porous coatings in the vicinity of the heating wall when the effective thermal conductivity is not sufficiently high, which was strongly supported by the phenomena observed from the sample PB145-7c in Sec. 3.4. On the sample PB145-7c, which has the highest thermal conductivity in this experimental investigation, the evaporation position is found to move upward with the heat flux increase on the highly conductive porous coatings. This observed effect of the wetting area on boiling performance also implies that heat is conducted through the solid structure of the porous media to the saturated working fluid. Thus, the boiling performance can be enhanced by augmenting the effective thermal conductivity of porous coatings. This principle was illustrated by Polezhaev and Kovalev [17] in their numerical simulations.

Because of the existence of a thin vapor film, the boiling curves for PB145-16 and PB145-32 indicate significant differences when compared to the thinner samples. As shown in Fig. 5(*a*), the performance of PB145-16 is superior to that of PB145-32 over the entire range of heat fluxes evaluated. From these two test articles, the heat transfer coefficient on both of them increased with increasing heat flux and decreased after the heat fluxes exceed a specific value, ultimately converging to a constant value. For PB145-16, the inflection point was ~ 48 W/cm^2, and for PB145-32, the value was ~ 30 W/cm^2. This inflection point seems to decrease with an increase in coating thickness. Malyshenko [10] hypothesized that this was due to the heating surface being blocked by a thin stable vapor film, established within the body of the porous coatings. Nakayama et al. [15] found that porous structures with heat fluxes of >15 W/cm^2, the boiling curves of the porous structures converged towards the boiling curve of a plain surface. This decrease in performance was attributed to the "dried-up" mode of boiling. In addition, it was hypothesized by Nakayama et al. [15] that the structure would revert toward plain surface behavior once the tunnel space was filled with vapor.

Combining the observations of the current investigation with those of other researchers as described in the Introduction, it is evident that the formation of a vapor film is responsible for this significant change in the boiling performance. As indicated in the previous analysis, the specific causes that led to the formation of the vapor film, may be due to the high flow resistance of the vapor, as it attempts to escape through the saturated porous media [10,13,14]. It is important to note that the boiling heat transfer is not terminated by the presence of the vapor film; on the contrary, stable boiling accompanied by high wall superheat has been observed in both the current investigation and in those of other researchers [10–12,15] for both conductive and nonconductive thick porous coatings.

The effect of variations in the heat flux on the boiling heat transfer coefficient is illustrated in Fig. 5(*d*) as a function of the porous coating thickness, in order to demonstrate the relationship between the boiling performance, the microporous surface thickness, and the heat flux. As shown, the boiling heat transfer coefficient is strongly dependent on the wick thickness and the heat flux when the heater size is given. When the heat flux is lower

than ~20 W/cm^2, the boiling performance was found to increase with increases in the porous coating thickness. For highly conductive porous coatings in the present investigation, the solid portion of the porous structure effectively conducts the heat for low to moderate input power levels and reduces the effective heat flux. However, at higher input power levels, the heat transfer is greater than what can be readily transferred. For example, when the heat flux is >20 W/cm^2, the boiling performance increases with increasing thickness for coating thicknesses of <0.57 mm and then decreases with additional increases in the thickness beyond that value. The observed differences between the current investigation and the results of Malyshenko [10] are believed to be due to the very different thermal conductivities of the porous coating materials, i.e., highly conductive porous media in the present study and relatively nonconductive porous media in the investigation of Malyshenko [10].

3.2.2 Boiling Incipience Superheat. Figure 5(*b*) clearly illustrates that nucleate incipience superheat for most samples is dramatically reduced through the application of a porous coating. This is consistent with the findings of other researchers that have experimented with enhanced structures and surfaces [5–20]. Virtually all of these investigations have indicated that "rough surfaces" are an effective mechanism for reducing the boiling incipience superheat. This is due to the combination of artificial cavities with large pore sizes within the porous coating [16] and the thermocapillary convection that occurs in the liquid film on the walls of the coating materials, all of which result in a reduction in the boiling incipience superheat in conductive porous coated surfaces [10–12]. As illustrated in Fig. 5(*b*), the boiling incipience superheat for relatively thin, i.e., for test article PB145-2, is not reduced significantly, even though the geometric characteristics of the heated wall are identical to other thicker porous layers. These observations indicate that thickness is one of the factors that affect the boiling incipience superheat on surfaces coated with a conductive porous media.

3.3 Effects of Mesh Size of Microporous Surfaces on Performance and Characteristics. Another series of experiments was conducted in which the thickness and volumetric porosity of the porous coatings were both maintained at approximately the same value while the mesh size was varied from 2362 m^{-1} (60 in.$^{-1}$) to 5709 m^{-1} (145 in.$^{-1}$) and with the variation of the wire diameters. All these geometric parameters are listed in Table 1. This allowed the evaluation of the effect of pore size on the boiling performance and characteristics. Test data from this series of tests are presented in Figs. 7(*a*) and 7(*b*). The boiling curve for a plain surface is added to these Figs. 7(*a*) and 7(*b*) for comparison.

As illustrated in Fig. 7(*a*), the boiling incipience superheat for this set of experiments shows a fairly large variation when the mesh size varies. The boiling incipience superheat of test article PB145-4 is significantly smaller than those of PB100-2 and PB60-1, which are almost identical with that obtained for a plain surface. For the sintered copper mesh used in the present work, the pore size in the horizontal direction increases as the mesh size decreases, which implies that only the pore size in a specific range will affect the boiling incipience superheat. When the pore size is too small or too large, the boiling incipience superheat is determined by the surface condition of the heated wall or wire surfaces, rather than the pore size of the porous coating.

Figure 7(*b*) illustrates the effects of the mesh size on the boiling performance. As indicated, the performance decreases with increasing mesh size. This phenomenon is believed to be due to the decrease in the wetting area and/or number of nucleation sites available as the mesh size increases. In a previous investigation, Li and Peterson [21] showed that the effective thermal conductivity of porous surfaces fabricated from mesh screens increases with the product of the mesh number and wire diameter. This factor may also contribute to this performance decrease since the effective thermal conductivity would decrease with increasing mesh size [17]. The boiling performance of test article PB60-1, which was fabricated from a relatively coarse mesh, is very close to that of a plain surface when the heat flux is <50 W/cm^2. Because of the beginning of the film evaporation on the upper part of the coatings, the performance is only slightly better than that of a plain surface when the heat flux exceeds 50 W/cm^2. This observation indicates that boiling initially occurs on the heated wall and then progresses through the solid structure for the porous coating once the superheat reaches a level that is directly related to the heat flux.

3.4 Effects of Volumetric Porosity of Microporous Coated Surfaces on Boiling Performance and Characteristics. The effects of volumetric porosity on boiling performance and characteristics were also examined while holding the thickness and mesh size constant. The volumetric porosity investigated here ranged from 0.409 to 0.693 and was achieved by reducing the distance between the layers in the vertical direction (i.e., normal to the heater surface direction), while the pore size does not change in the horizontal direction. The experimental test data are illustrated in Figs. 8(*a*)–8(*c*). As was the case for the previous results, the boiling curve for a plain surface is also illustrated for comparison.

As shown, the boiling incipience superheats for test articles PB145-4, PB145-6c, and PB145-7c are approximately identical and much smaller than those of a plain surface. The pore size in the horizontal direction and the thicknesses of the three samples was held constant, with only the pore size in the vertical direction varied to change the volumetric porosity. The results indicate that the boiling incipience superheat is nearly independent of pore size in the vertical direction, and as a result, the pore size in the horizontal direction and the thickness of the porous coating seems to show a significantly greater effect in determining boiling incipience superheat for a given working fluid and pressure.

A significant enhancement in the boiling performance is demonstrated in Fig. 8(*b*) and increases with a decrease in the volumetric porosity. It is interesting to note that the effective thermal conductivity of the porous coating changes with variations in the volumetric porosity. Generally, for a given porous structure, the effective thermal conductivity of the porous media would increase with decreases in the volumetric porosity. This increase in the effective thermal conductivity contributes to the boiling performance increase for test article PB145-7c. An additional phenomenon, shown in Fig. 8(*c*), can be observed for test article PB145-7c, which has the lowest volumetric porosity and, hence, the highest effective thermal conductivity of all the test articles. As illustrated in Fig. 8(*c*), for test article PB145-7c the wall temperature increases initially with the heat flux and then drops several degrees due to the higher heat transfer mode. This same phenomenon was observed in three separate tests conducted to ensure the results were repeatable and indicates that multiple boiling modes, i.e., the nucleate boiling position spread from the bottom to the top of the porous coating, could occur simultaneously in these types of porous coatings when the effective thermal conductivity is high enough, which is what was observed previously for finned surfaces [22] and predicted in the numerical simulation by Polezhaev and Kovalev [17]. Initially, nucleate boiling occurs near the heated wall and then moves through the porous coating as the heat flux is increased. This multiple boiling incipience phenomenon results in a much higher boiling performance for test article PB145-7c than for PB145-6c and provides strong evidence from which to support the conclusions presented in Sec. 3.2.1, i.e., the heat is conducted through the skeleton of the porous media and is then dissipated to the liquid through the surface of the porous coating.

3.5 Effects of Microporous Coated Surfaces on Wall Superheat. As shown in Figs. 5(*b*), 7(*a*), and 8(*a*), with the exception of test articles PB145-16, PB145-32, and PB60-1, the wall superheat at the CHF, ~12°C, is much less than that obtained for

a plain surface at 25 °C. This implies that the boiling heat transfer in porous coatings is more stable in terms of the wall temperature than for plain surfaces and as a result, provides a superior temperature control method for thermal management.

3.6 Effects of the Surface Condition of the Wires. The effects of surface conditions on boiling performance were also investigated as part of this study. To accomplish this, the surface of the porous coatings were initially saturated with water and heated to 300–400 °C to generate a thin oxide film on the individual wires in the mesh. These surfaces were then carefully cleaned using a solution of DuracleanTM 1075 to form a thin porous structure on the surfaces of the wires prior to the tests. This thin porous structure was similar to the type of surface often found on fouled heat exchanger tubes. Figure 9 presents and compares the results of tests conducted on both oxide-coated and uncoated samples. As illustrated, from a boiling perspective the bare surfaces performed better than those with the oxide layer when the heat flux was low for test article PB145-2 and low to moderate for test article PB145-6; however, as the heat flux increased to a level of 75 W/cm^2 and 175 W/cm^2 for PB145-2 and PB145-6, respectively, the performance of the oxide-coated surfaces quickly exceeded that of the bare wires. This phenomenon can be attributed to the existence of the extra thermal resistance resulting from the deposited layer, which approximates the fouling of the surfaces. When the heat flux is relatively small, the superheat on bare surfaces is higher than on the oxide-coated surface, which means there are more active nucleation sites on the bare surface than on the oxide layers, which can easily trigger nucleate boiling. These observations are consistent with the findings of Fukada et al. [23].

4 Boiling Regimes and Two-Phase Flow Pattern on Conductive Porous Coated Surfaces

Based on a review of the literature, the experimental investigations form both the current investigation and the theoretical analysis, a new set of boiling regimes have been developed as shown in Fig. 10. Summarily, when the ratio W_{heater}/t is larger than a critical ratio, which is mainly governed by the $f_{2\phi}/f_{1\phi}$ ratio, the heat transfer typically consists of four regimes: (a) convection, (b) boiling with individual bubble, (c) vapor-liquid counterflow and boiling, and (d) drying out. While the ratio W_{heater}/t is relatively small and, hence, vapor may vent from unsealed sides at high heat flux, there is one more heat transfer regime remaining after the vapor-liquid counterflow, i.e., the so-called two-phase separating flow and boiling (regime e).

As shown, the pool boiling on highly conductive porous coated surfaces starts from a regime best described as convection (i.e., regime a). With an increase in the heat flux, many individual bubbles are generated in the sharp corner regions between the individual wires, and between the heated wall and the wire surfaces, all of which result in the onset of boiling. Bubbles rising through the porous coating strengthen the convection in the upper part of the porous coated surfaces, regime b, which essentially serves as a transition regime for boiling on conductive porous coated surfaces. Single bubbles then coalesce to form a bubble stem, or slug, with further increases in the heat flux, in regime c. In this process, the bubble population above the porous surface is fairly stable and is further supported by the nearly linear relationship between the heat flux and the wall superheat [24]. Kim et al. [25] attributed this to the constant nucleation site density in the porous coated surfaces. Another important feature in this regime is that a strong liquid vapor counterflow pattern is established. This two-phase counterflow enhances the heat transfer, but also makes it more difficult for the liquid to reach the bottom of the porous coated surfaces.

When the CHF is reached for the relatively thin highly conductive porous coated surfaces, the vapor velocity is sufficiently high to retard or prevent this liquid resupply due to the flow resistance through the porous media and the shear stress generated by the high vapor velocities. Bubbles above the porous coated surface in violent motion, block the top surface of the porous coated surfaces, causing film boiling to occur, i.e., regime e. This begins in a manner identical to that of a smooth surface, with the difference being that the mushroom bubbles are further from the heated wall, due to the vapor jets from the porous coated surfaces. This enhances the heat transfer and CHF from the porous coated surfaces when compared to a plain surface.

For boiling on the relatively thick porous coated surfaces with small areas, open sides, and a sufficiently high heat flux, the vapor flow is quite fast, making it difficult for the vapor to escape through the thick saturated porous media. As a result, the vapor takes the path of least resistance through the thin vapor film layer near the heated wall [14,20]. The thickness of this vapor film increases with increasing heat flux and, when it reaches the same thickness as the porous coating, the CHF occurs. In regime d, boiling still occurs in the upper portion of the porous coated surface, but the majority of the heat is dissipated through evaporation at the vapor liquid interface close to the heated wall. The overall heat transfer in regime d is low because of the high thermal resistance caused by the stable vapor film between the heated wall and the liquid vapor interface.

5 Conclusions

The effects of the key geometric parameters of conductive microporous surfaces have been systematically investigated using saturated distilled water on horizontal surfaces. The test results demonstrated that the boiling characteristics and overall boiling performance are strongly dependent on the geometric parameters of the porous coatings, i.e., thickness, volumetric porosity, and mesh size, when the heater size and the pressure are held constant. More importantly, the enhanced understanding of the specific characteristics of boiling in and on conductive microporous coated surfaces is revealed and discussed.

The normal heat transport route in pool boiling from a porous coated surface was found to be the result of heat conducted to the skeleton of the porous structure and then transferred to the liquid through convection and, finally, dissipated through boiling or evaporation on the surface of the porous coatings. In addition, two types of liquid-vapor flow patterns are identified at a high heat flux, i.e., vapor liquid counterflow and liquid-vapor separating flow. A theoretical analysis indicates that the liquid-vapor flow patterns are generally governed by the ratio W_{heater}/t, $f_{2\phi}/f_{1\phi}$, and the input heat flux q''.

In general, the boiling characteristics from porous coated surfaces are generally superior to that of pool boiling on plain surfaces. The mechanisms of improvement are mainly due to the augmentation of the wetted area, the number of nucleation sites, the intensified interaction among bubbles, as well as film and capillary evaporation induced through the use of porous coatings. Porous coatings with higher thermal conductivity were found to perform better than those with lower thermal conductivities, especially at low heat fluxes.

The boiling incipience superheat can be significantly reduced through the use of porous coatings and the boiling incipience superheat can be controlled by varying either the pore size or the thickness of the porous coating. The experimental results demonstrated that boiling on thin porous coatings could occur over a larger range heat flux, i.e., from 0 to 210 W/cm^2, and at the same time, within a much narrower wall superheat, i.e., <12 °C, than for plain surfaces. This indicates that the boiling heat transfer on thin porous coatings is more stable in terms of temperature and, hence, may be more suitable for applications where precise temperature control is required.

Acknowledgment

The authors would like to acknowledge the support of the National Science Foundation under Grant No. CTS-0312848.

Nomenclature

A_c = cross area (m^2)
D = diameter (mm)
D_h = hydraulic diameter (mm)
F = friction factor
G = mass flow rate (kg/s)
H = heat transfer coefficient ($W/m^2 K$)
h_{fg} = latent heat (kJ/kg)
K = thermal conductivity (W/mK)
ΔP = pressure drop (Pa)
q'' = heat flux (W/cm^2)
Re = Reynolds number
L = length (mm)
t = distance or thickness (mm)
T = temperature (K)
TC = thermocouple
V = speed (m/s)
W = width (mm)

Greek Symbols

σ = surface tension (N/m)
ρ = density (kg/m^3)
ε = volumetric porosity
1ϕ = single-phase
2ϕ = two-phase

Subscripts

crit = critical parameter
gap = gap between the vapor zones or columns
heater = dimensions of heater
l = liquid phase
v = vapor phase
v, film = dimensions of vapor film
w = wall
sat = saturation condition
eff = effective parameter
Cu = copper
hole = holes in the heater to hold the thermocouples
STC1 = top surface of copper block to TC1

References

[1] Jakob, M., 1949, *Heat Transfer*, Wiley, New York, pp. 636–638.
[2] Milton, R. M., 1968, "Heat Exchange System," U.S. Patent No. 3384154.
[3] Milton, R. M., 1970, "Heat Exchange System," U.S. Patent No. 3523577.
[4] Milton, R. M., 1971, "Heat Exchange System with Porous Boiling Layer," U.S. Patent No. 3587730.
[5] You, S. M., Simon, T. W., and Bar-Cohen, A., 1992, "A Technique for Enhancing Boiling Heat Transfer With Application to Cooling of Electronic Equipment," IEEE Trans. Compon., Hybrids, Manuf. Technol., **15**(5), pp. 823–831.
[6] O'Connor, J. P., and You, S. M., 1995, "A Painting Technique to Enhance Pool Boiling Heat Transfer in Saturated FC-72," ASME J. Heat Transfer, **117**(2), pp. 387–393.
[7] O'Connor, J. P., You, S. M., and Price, D. C., 1995, "A Dielectric Surface Coating Technique to Enhance Boiling Heat Transfer from High Power Microelectronics," IEEE Trans. Compon., Packag. Manuf. Technol., Part A, **18**(3), pp. 656–663.
[8] Chang, J. Y., and You, S. M., 1997, "Boiling Heat Transfer Phenomena From Micro Porous and Porous Surfaces in Saturated FC-72," Int. J. Heat Mass Transfer, **40**(18), pp. 4437–4447.
[9] Liter, S. G., and Kaviany, M., 2001, "Pool-Boiling CHF Enhancement by Modulated Porous-Layer Coating: Theory and Experiment," Int. J. Heat Mass Transfer, **44**, pp. 4287–4311.
[10] Malyshenko, S. P., 1991, "Characteristics of Heat Transfer With Boiling on Surfaces With Porous Coatings," Therm. Eng., **38**(2), pp. 81–88.
[11] Borzenko, V. I., and Malyshenko, S. P. "Experimental Research of Heat Transfer Enhancement and Thermal Stability at Pool Boiling in Porous Surfaces," Heat Transfer Science and Technology, Beijing, pp. 492–502.
[12] Borzenko, V. I., and Malyshenko, S. P., 2001, "Mechanisms of Phase Exchange Under Conditions of Boiling on Surfaces With Porous Coating," High Temp., **39**(5), pp. 769–776.
[13] Moss, R. A., and Kelly, A. J., 1970, "Neutron Radiographic Study of Limiting Plannar Heat Pipe Performance," Int. J. Heat Mass Transfer, **13**, pp. 491–502.
[14] Cornwell, K., Nair, B. G., and Patten, T. D., 1976, "Observation of Boiling in Porous Media," Int. J. Heat Mass Transfer, **19**, pp. 236–238.
[15] Nakayama, W., Daikoku, T., Kuwahara, H., and Nakajima, T., 1980, "Dynamic Model of Enhanced Boiling Heat Transfer in Porous Surfaces—Part I: Experimental Investigation," ASME J. Heat Transfer, **102**, pp. 445–450.
[16] Bergles, A. E., and Chyu, M. C., 1982, "Characteristics of Nucleate Pool Boiling From Porous Metallic Coatings," ASME J. Heat Transfer, **104**, pp. 279–285.
[17] Polezhaev, Y. V., and Kovalev, S. A., 1990, "Modeling Heat Transfer With Boiling in Porous Structures," Therm. Eng., **37**(12), pp. 617–620.
[18] Vemuri, S., and Kim, K. J., 2005, "Pool Boiling of Saturated FC-72 on Nano-Porous Surface," Int. Commun. Heat Mass Transfer, **32**, pp. 27–31.
[19] Li, C., Peterson, G. P., and Wang, Y., 2006, "Evaporation/Boiling on Thin Capillary Wick (I)—Wick Thickness Effects," ASME J. Heat Transfer, **128**. pp. 1312–1319.
[20] Li, C., and Peterson, G. P., 2006, "Evaporation/Boiling on Thin Capillary Wick (I)—Effects of Volumetric Porosity and Mesh Size," ASME J. Heat Transfer, **128**. pp. 1320–1328.
[21] Li, C., and Peterson, G. P., 2006, "The Effective Thermal Conductivity of Wire Mesh," Int. J. Heat Mass Transfer, **49**, pp. 4095–4105.
[22] Haley, K. W., and Westwater, J. W., 1966, "Boiling Heat Transfer from a Single Fin," *Proceedings of the ASME/AIChE National Heat Transfer*, Chicago, IL, Vol. 3, pp. 245–253.
[23] Fukada, Y., Haze, I., and Osakabe, M., 2004, "The Effects of Fouling on Nucleate Pool Boiling of Small Wires," Heat Transfer Asian Res., **33**(5), pp. 316–329.
[24] Bejan, A., and Kraus, A. D., 2003, *Heat Transfer Hand Book*, Wiley, New York, pp. 704–705.
[25] Kim, J. H., Rainey, K. N., You, S. M., and Pak, J. Y., 2002, "Mechanism of Nucleate Boiling Heat Transfer Enhancement From Microporous Surface in Saturated FC-72," ASME J. Heat Transfer, **124**(3), pp. 500–506.

Experimental Evaluation of Marangoni Shear in the Contact Line Region of an Evaporating 99+% Pure Octane Meniscus

Sashidhar S. Panchamgam
Micron Technology, Inc.,
Boise, ID 83707

Joel L. Plawsky

Peter C. Wayner, Jr.[1]
e-mail: wayner@rpi.edu

The Isermann Department of Chemical and
Biological Engineering,
Rensselaer Polytechnic Institute,
Troy, NY 12180

Image analyzing interferometry was used to study the spreading characteristics of an evaporating octane meniscus (purity: 99+%) on a quartz surface. The thickness, slope, and curvature profiles in the contact line region of the meniscus were obtained using a microscopic data analysis procedure. The results obtained for the octane were compared to that of pure pentane (purity: >99.8%) under similar operating conditions. Isothermal experimental conditions of the menisci were used for the in situ estimation of the retarded dispersion constant. The experimental results for the pure pentane demonstrate that the disjoining pressure (the intermolecular interactions) in the thin-film region controls the fluid flow. Also, an imbalance between the disjoining pressure in the thin-film region and the capillary pressure in the thicker meniscus region resulted in a creeping evaporating pentane meniscus, which spreads over the solid (quartz) surface. On the contrary, for less pure octane, the intermolecular interactions between octane and quartz had a significantly different contribution for fluid flow, and hence, the octane meniscus of lower purity did not creep over the quartz surface. As a result, we had a stationary, evaporating octane meniscus. Using the experimental data and a simple model for the velocity distribution, we evaluated the Marangoni shear in a portion of the stationary, evaporating octane meniscus. An extremely small change in the concentration due to distillation had a significant effect on fluid flow and microscale heat transfer. Also, it was found that nonidealities in small interfacial systems, i.e., the presence of impurities in the working fluid, can have a significant effect on the thickness of the adsorbed film, the heat flux, the spreading characteristics of an almost pure fluid, and, therefore, the assumptions in modeling. [DOI: 10.1115/1.2759970]

Keywords: contact line, disjoining pressure, evaporating meniscus, Marangoni stresses, nanoparticles, retarded dispersion constant

Introduction

The understanding of the details of interfacial phenomena in the extended contact line region (thickness, $\delta < 3$ μm) of an evaporating completely wetting meniscus on a solid surface is used extensively for modeling fluid flow and evaporative heat transfer in thin films. In general, to optimize the design and use of microscale systems, experimental data on the microscopic details of phase change heat transfer, fluid flow, and stability in an extended meniscus are needed. Panchamgam et al. have used a high spatial resolution imaging technique to measure film thickness profiles of completely wetting liquids from nanometer to micron scale, and emphasized the significance of disjoining pressure (or intermolecular interactions between the liquid and the underlying solid surface) and capillarity in equilibrium and phase change processes [1,2]. Herein, we compare an almost pure system (octane: purity $>99+\%$) with a purer system (pentane: purity $>99.8\%$). The experimental results will have a significant effect on the assumptions used in modeling.

The fluid flow in the thin-film region of an extended meniscus and, hence, the phase change at the liquid-vapor interface near the thin-film region depends mainly on the variation of the following three factors, which are a function of the temperature and the meniscus length: the disjoining pressure or intermolecular interactions between the liquid and the underlying solid, the surface tension of the liquid, and the curvature profile of the liquid-vapor interface. These parameters depend on the working fluid, the nature of the underlying solid, the purity of the liquid (i.e., concentration, presence of liquid/solid impurities, and dissolved gases in the liquid), surface structure and chemistry (for example, smooth and rough surfaces, porous substrates, etc.), and the operating conditions (pressure and temperature). Various researchers, both experimentally and theoretically, studied a variety of systems to understand the details of interfacial phenomena by studying the roles of the disjoining pressure [1–12] and surface tension and its gradient [13–18] on the wetting and spreading phenomena [19,20], instabilities [21–25], fluid flow, and microscale phase-change phenomena [1–18] in extended menisci and drops during phase change and equilibrium processes.

To save space, the extensive literature review given in Ref. [1] will not be repeated here. However, for some continuity, the following few references are mentioned. Derjaguin and Zorin [4] and Derjaguin et al. [5], using the disjoining pressure concept, measured and modeled the stability and equilibrium thickness of adsorbed ultrathin films as a function of an interfacial temperature jump and demonstrated theoretically that thin-film transport is capable of accelerating the evaporation rate from capillaries. The disjoining pressure in the adsorbed flat thin-film region was the boundary condition at the leading edge of an evaporating meniscus. For a completely wetting, pure, isothermal fluid, the sum of the disjoining pressure and capillary pressure can be extremely

[1]Corresponding author.

Contributed by the Heat Transfer Division of ASME for publication in the JOURNAL OF HEAT TRANSFER. Manuscript received July 7, 2006; final manuscript received March 18, 2007. Review conducted by Satish G. Kandlikar.

large and lead to fluid flow and phase change in the direction of a decrease in film thickness [1–19]. The Kelvin–Clapeyron model has been used frequently to theoretically describe liquid-vapor phase-change processes, contact line motion and stability in heat transfer (e.g., [11]). We note that, since the disjoining pressure scales with thickness as δ^{-n} ($n=3$ for $\delta<20$ nm and $n=4$ for $\delta>20$ nm) with a potential limit of a monolayer, the interfacial pressure jump can be enormous. We note that the transition thickness is gradual not sharp. However, in our case, since we expect a retardation effect for the thicknesses observed during the isothermal and nonisothermal states of the two working fluids (pentane and octane) at the heat fluxes studied, we believe that δ^{-4} best describes the retardation effect. Herein, by studying almost pure systems with relatively low heat fluxes and modest pressure jumps, we demonstrate the effect of the contact line thickness and concentration on the relative importance of the disjoining pressure and the surface shear stress.

The experimental work discussed above is usually limited by the resolution of the optical techniques used. In addition, experimental data incorporating the purity of the working fluid, and its influence on the spreading characteristics and microscale heat transfer is sparse. Herein, using high spatial resolution experimental data, which incorporates nonidealities, such as impurities, in the working liquid, we compare the experimental results of an evaporating extended meniscus of 99+% pure octane to that of pentane of a higher purity on a quartz surface in a constrained vapor bubble heat exchanger. Using an image analyzing technique [e.g., [1]], we compared the adsorbed film thickness, apparent contact angle, and pressure fields of the highly pure pentane and relatively less pure octane menisci upon evaporation. It was found that for the two systems the disjoining pressure has a different role in the spreading characteristics of the fluids. Using the high-resolution experimental data and a simple velocity distribution model, we evaluated the Marangoni shear stress in the thin-film region of the relatively less pure octane meniscus and demonstrated that it is more important than the disjoining pressure at the heat flux studied. An emphasis on the effect of impurities on the spreading characteristics of the working fluid is made.

Experimental Setup

To avoid added contaminants, the simple clean cuvette made of fused silica, (square cross section, inside dimensions 3 mm $\times$3 mm, outside dimensions 5.5 mm$\times$5.5 mm, length 43 mm) in Fig. 1 was used, which eliminated the complications associated with the previously used [1] pressure transducer and vacuum inside the cuvette. The cuvette was filled partially with a working fluid inside a glove bag under an ultrafine nitrogen environment. A thermoelectric heater was attached at the top end of the cuvette ($x=-1$ mm). The cuvette was closed using a Teflon® stopper at the bottom of the cuvette. Therefore, the working fluid was in contact with a mixture of its vapor and noncondensable gases at atmospheric pressure forming a constrained vapor bubble. We believe that the presence of noncondensables would not affect the local comparison of the two systems. A series of thermocouples, to measure the axial temperature profile, were attached along the length of the quartz cuvette. The entire cuvette assembly was attached to a precision, three-way translation stage on an air-buffered vibration control bench. The translation stage allowed us to focus the microscope at any desired position along the extended meniscus formed in the corners of the cuvette.

Experimental Procedure

In the experimental system, liquid from the pool at the bottom of the cuvette rises along the corners of the cuvette due to capillary and disjoining pressure forces and thereby forms a continuous extended meniscus in the corners of the cuvette (see Figs. 1(a) and 1(b)). To study the fluid flow and evaporation, we changed the heater power from isothermal (reference) state to $Q_{in}=0.076$ W.

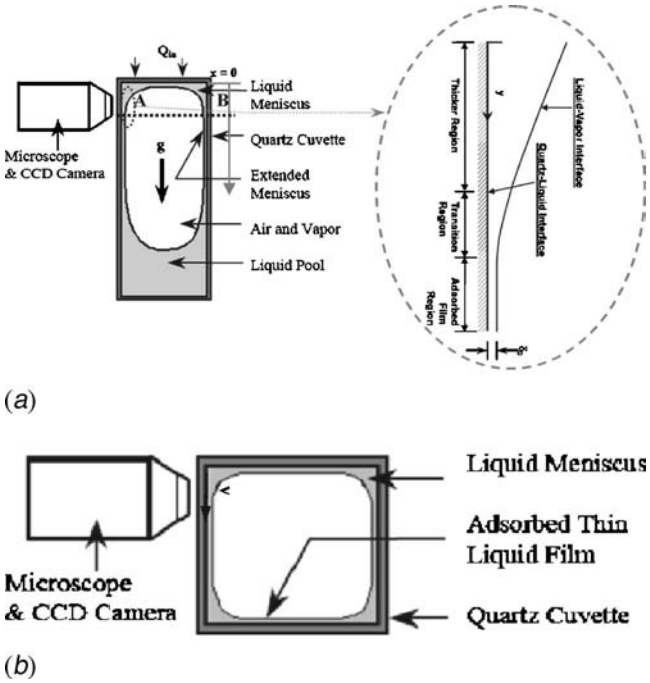

Fig. 1 (*a*) Schematic of the experimental system (inside dimensions 3 mm$\times$3 mm$\times$43 mm), (*b*) cross-sectional view (line AB in (*a*)) of the quartz cuvette. Gravity *g* is acting perpendicular to the square cross section.

The resulting movement of the meniscus due to evaporation was captured at the top end of the cuvette ($x\approx 0$) and analyzed.

Monochromatic light ($\lambda=546$ nm) from a mercury light source was used to illuminate the cuvette through the objective of the microscope. Naturally occurring interference fringes appeared (see Fig. 2), which were due to the reflection of light from the liquid-vapor and the liquid-solid interfaces. Note that the variation in the reflectivity is continuous. A charge-coupled device (CCD) camera with a maximum frame rate of 30 frames per second was used to capture the reflectivity images of the receding and advancing menisci. The captured images were digitized using a data acquisition card (DT3155- MACH Series Frame Grabber) to give the thickness profiles as described in [1].

Observations

Two types of fluids, a highly pure pentane (purity$>$99.8%) and a relatively less pure octane (purity$>$99%), were used as the working fluids in the experimental system. We believe the impurity present in the "as-received" octane to be an alkane of higher chain length. The vendor does not provide the details of the impurity (or impurities), and hence, the authors cannot furnish the exact composition details of the as-received octane. A comparison of the physical properties between the two fluids is given in Table 1. For both the working fluids, a stationary isothermal meniscus was considered as the reference state (Figs. 2(a) and 2(c) and I I′ in Fig. 3). The thermoelectric heater at the top end of the cuvette was turned on at time, $t=3.26$ s with a power input of $Q_{in}=0.076$ W. The reader should note that by applying a constant heat flux at the top end of the cuvette, we neither have a constant temperature nor a constant heat flux boundary conditions at the liquid-solid interface, and the evaluation of the exact boundary condition using complex numerical models is beyond the scope of the paper. However, a numerical modeling paper is in preparation that uses our data and gives the temperature and heat flux profiles at the liquid-vapor interface. These numerical results give a temperature profile with a dip and a heat flux spike at the liquid-solid interface, which are similar to the experimental temperature pro-

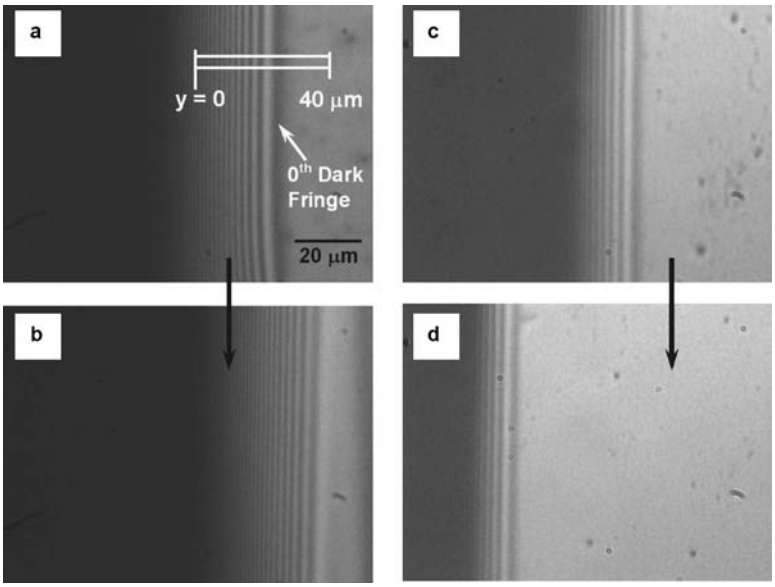

Fig. 2 Reflectivity images illustrating the movement of the pentane and octane menisci due to change in the heater power: (*a*) isothermal pentane meniscus (*t*=2.86 s), (*b*) nonisothermal (pseudosteady state) pentane meniscus (*t*=500 s), (*c*) isothermal octane meniscus (*t*=1.21 s), and (*d*) nonisothermal (pseudosteady state) octane meniscus (*t*=234.4 s). Reflectivity images were captured at an axial location of *x*≈0 (near the heater).

file presented by Sodtke et al. [12]. Figures 2(*a*) and 2(*b*) and Figs. 2(*c*) and 2(*d*), respectively, show the reflectivity images of the pentane and octane menisci during isothermal and nonisothermal (pseudosteady) states captured at an axial location, $x \approx 0$. The movement in the meniscus due to evaporation, starting from the isothermal reference state to a new steady state, was monitored by observing the distance traveled ($\Psi_{0.1\ \mu m}$) by the zeroth dark fringe

Table 1 Physical properties of pentane and octane [27,28]

Properties at 25°C	Pentane	Octane
Purity (%)	>99.8	>99
Boiling point, °C	36	126
n (refractive index)	1.358	1.398
ρ (density), kg/m^3	621	699
σ (surface tension), N/m	0.0155	0.0211
k_1 (thermal conductivity), W/mK	0.113	0.128
ν (kinematic viscosity), m^2/s	3.61×10^{-7}	7.28×10^{-7}

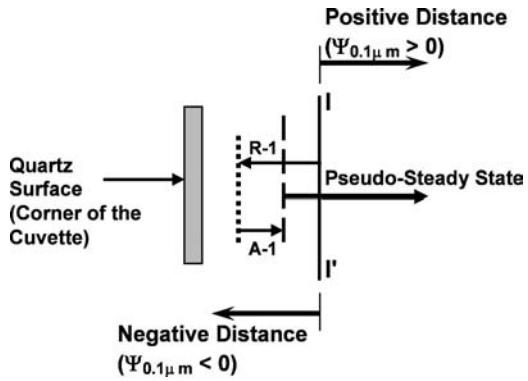

Fig. 3 Illustration of the zeroth dark fringe movement due to change in the heater power. *II′*: Isothermal reference state, R-1: receding cycle, and A-1: advancing cycle.

(thickness, δ=0.1 μm, see Fig. 2(*a*)) with respect to its position in the isothermal reference state. The sign convention for the distance traveled is shown in Fig. 3, where a negative distance implies the 0th dark fringe is in a region "behind" the reference state (between I I′ and the cuvette corner) and a positive distance implies the 0th dark fringe is in a region in "front" (ahead) of the reference state (region on right side of I I′). The velocity of the interference fringe at δ=0.1 μm of the meniscus (U_i) was calculated from the change in the measured distance ($\Psi_{0.1\ \mu m}$) between times t_{i-1} to t_i by

$$U_i = \frac{\Psi_{0.1\ \mu m}|_i - \Psi_{0.1\ \mu m}|_{i-1}}{t_i - t_{i-1}} \tag{1}$$

The maximum relative error associated with U_i is estimated to be ±2.6% and that with $\Psi_{0.1\ \mu m}$ is ±1.8%. Figure 4 shows the comparison of the profiles of the distance traveled by the pentane and the octane menisci as a function of time, and Fig. 5 shows the comparison of U_i as a function of time. Based on the $\Psi_{0.1\ \mu m}$ and U_i, the meniscus movement for both the working fluids can be classified into different regimes. A detailed explanation on the different regimes of the pentane meniscus movement due to evaporation is given in Ref. [2]. The results presented here are mainly a comparison between highly pure pentane and relatively less pure octane, and is an extension of research presented in Ref. [2]. A brief overview and comparison of the pentane and octane menisci movements is given below. The reader should note that the phenomenon is completely reproducible. However, the timing data presented below is a strong function of the room temperature and, hence, the authors could not provide error bars on the time instances.

1. Isothermal state, $0 < t < 3.26$ s (*segment A_1B_1 in Figs.* 4(*a*) and 5(*a*) *for the pentane meniscus and segment AB in Figs.* 4(*b*) and 5(*b*) *for the octane meniscus*). During this period, the pentane and the octane menisci were stationary ($\Psi_{0.1\ \mu m}$=0) and at isothermal conditions (Q_{in}=0). Hence, the velocity was zero (U_i =0). Figures 2(*a*) and 2(*c*) represent the reflectivity images of the pentane and octane menisci during the isothermal state.

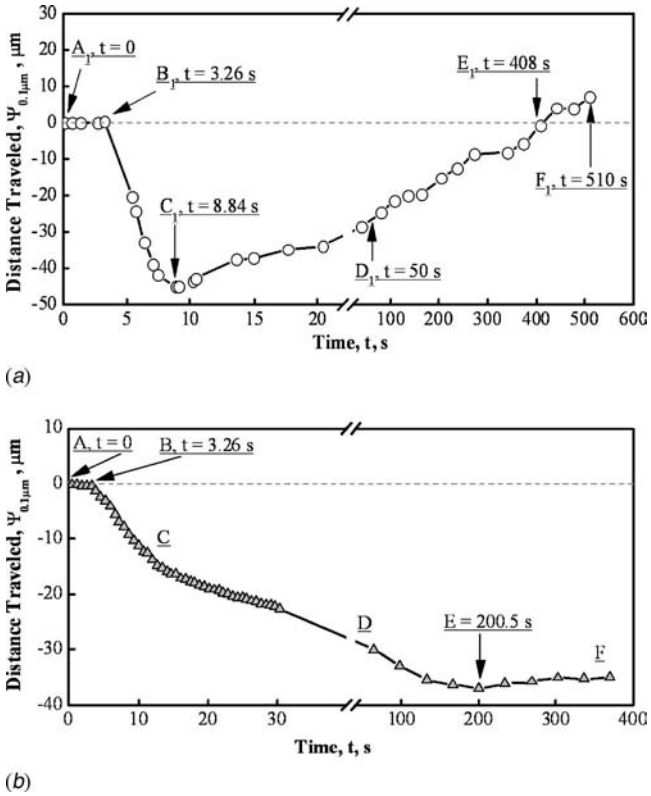

Fig. 4 Comparison of profiles of the distance traveled as a function of time by (*a*) the pentane meniscus and (*b*) the octane meniscus

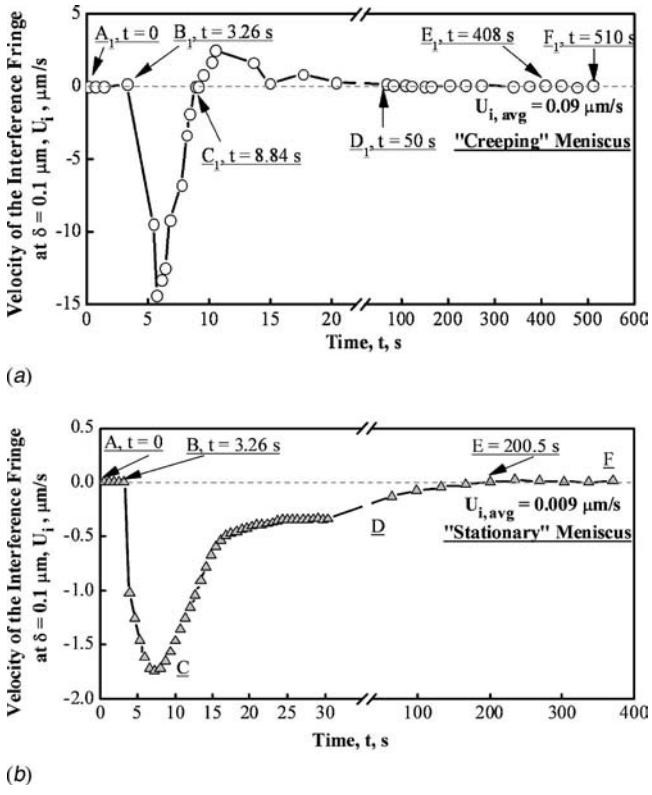

Fig. 5 Comparison of profiles of the velocity of the interference fringe at σ=0.1 μm as a function of time of (*a*) the pentane meniscus and (*b*) the octane meniscus

2. Receding cycle (*segment B_1C_1 in Figs.* 4(*a*) and 5(*a*) *for the pentane meniscus and segment BCDE in Figs.* 4(*b*) and 5(*b*) *for the octane meniscus*). At t=3.26 s, the heater power was changed from Q_{in}=0–0.076 W. Because of the heat flux entering the system, and subsequent evaporation, the pentane and the octane menisci receded toward the corner of the quartz cuvette, as shown in Fig. 4. The pentane meniscus attained maximum recession at t =8.84 s, whereas the octane meniscus attained maximum recession at t=200.5 s (point E in Fig. 4(*b*)). The difference in the time instants is due to higher volatility, purity and strong adhesion of pentane with the underlying quartz surface as compared to that of octane. Also, for $t>200.5$ s, the octane meniscus remained "stationary" with negligible velocity (0.009 μm/s), whereas the pentane meniscus "advanced." For pentane (Fig. 5(*a*)), in the time interval $3.26<t<5.71$ s, the meniscus accelerated toward the corner and in the time interval $5.71<t<8.84$ s, the meniscus decelerated towards the corner. For octane (Fig. 5(*b*)), in the time interval $3.26<t<7.33$ s, the meniscus accelerated toward the corner and in the time interval $7.33<t<200.5$ s, the meniscus decelerated toward the corner.

3. Advancing cycle (*segment C_1D_1 in Figs.* 4(*a*) and 5(*a*)). For pentane, at t=8.84 s, the meniscus stopped receding. The reader should note that the heater power is still on at 0.076 W and the meniscus is still being evaporated. During this cycle, the meniscus advanced (or moved away from the corner of the cuvette). The interfacial velocities during this cycle indicate that in the time interval $8.84<t<10.47$ s, the meniscus accelerated and in the time interval $10.47<t<50$ s, the meniscus decelerated in the direction away from the cuvette corner. However, for octane, we did not observe an advancing cycle.

4. Pseudosteady state, (*segment D_1F_1 in Figs.* 4(*a*) and 5(*a*) *for the pentane meniscus and segment EF in Figs.* 4(*b*) and 5(*b*) *for the octane meniscus*). For pentane, during time, $t>50$ s, the 0th dark fringe in the meniscus slowly advanced with negligible velocity (average velocity of the pentane meniscus was 0.09 μm/s). For $t>408$ s, the location of the 0th dark fringe in the pentane meniscus surpassed the isothermal reference state, i.e., ($\Psi_{0.1\ \mu m}$ =0) (see Fig. 4(*a*) point E_1). For pentane, the pseudosteady state regime is due to an imbalance in the capillary pressure in the thicker region and the disjoining pressure in the thinner region, which results in a net force acting toward the adsorbed film region. Hence during the pseudosteady state, the meniscus advanced slowly with an average velocity, $U_{i,avg}$=0.09 μm/s, and as a result, we have a "creeping" evaporating pentane meniscus. Figure 2(*b*) represents the reflectivity image of the creeping evaporating pentane meniscus at t=500 s.

For octane, during $t>200.5$ s, the meniscus remained almost stationary ($U_{i,avg}$=0.09 μm/s), and hence, during the pseudosteady state we have a "stationary" evaporating octane meniscus. In this case, the pseudosteady state regime is due to weaker interactions between octane and quartz (discussed below) and the Marangoni flow near the adsorbed film region. Figure 2(*d*) represents the reflectivity image of the "stationary" evaporating octane meniscus at t=234.4 s.

The reader should note that the pseudosteady state behavior of both the menisci, which is the main focus of this paper, is independent of the capacitance of the underlying solid and any drift in the saturation temperature of the working fluid. The meniscus movement of the working fluid at large time scale mainly depends on the wettability of the fluid with the quartz surface and also on the magnitude of the adsorbed film thickness.

Data Analysis

A detailed description of the determination of the meniscus thickness from the meniscus reflectivity image is given in Refs. [1,2]. Figure 6 shows the comparison of thickness profiles of the

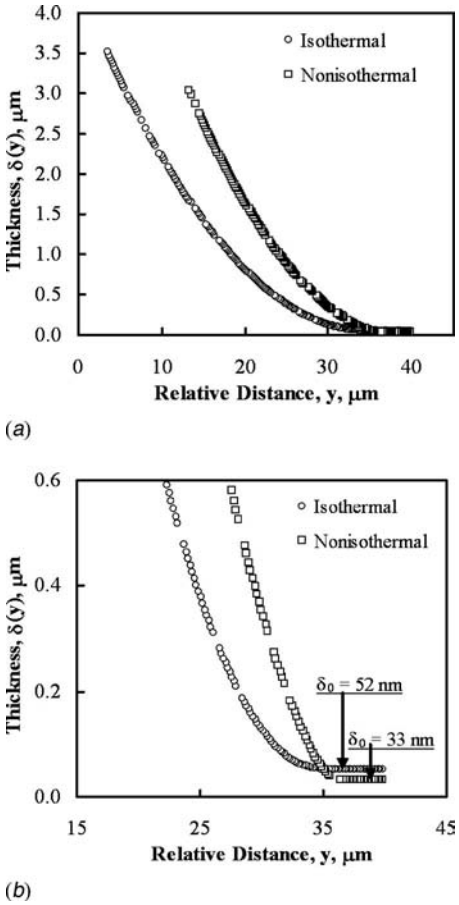

Fig. 6 (*a*) Comparison of thickness profiles of the pentane meniscus at (i) isothermal state (t=2.86 s), (ii) nonisothermal (pseudosteady) state (t=163.2 s), and (*b*) expanded scale in the contact line region

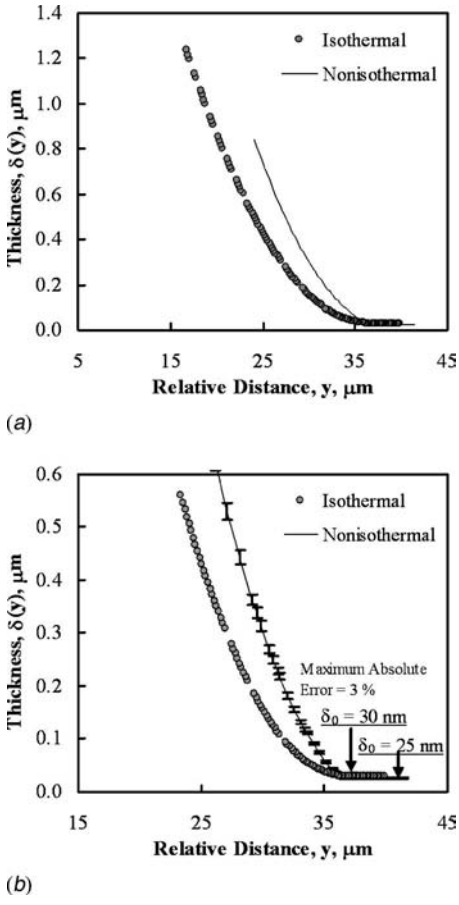

Fig. 7 (*a*) Comparison of thickness profiles of the octane meniscus at (i) isothermal state (t=1.21 s), (ii) nonisothermal (pseudosteady) state (t=234.4 s) and (*b*) expanded scale in the contact line region

pentane meniscus at the isothermal state (t=2.86 s) and nonisothermal (pseudosteady) state (t=163.2 s). Figure 7 shows the comparison of thickness profiles of the octane meniscus at the isothermal state (t=1.21 s) and nonisothermal (pseudosteady) state (t=234.4 s). The horizontal resolution of each pixel used to measure the continuous variation in the reflectivity is 0.177 μm.

To calculate the pressure gradient and the Marangoni stresses existing along the length of an evaporating meniscus, we need to determine the first (δ'), second (δ''), third (δ''') and fourth (δ'''') derivatives of the thickness profiles ($\delta(y)$). The thickness profile obtained from the technique described in Ref. [1] contains noise. Therefore, a smoothing spline function with tolerance (tol) given by, tol=$a\delta^4$, was used to remove noise in the thickness profile and derive its successive derivatives with respect to y. The value of a is determined such that the absolute error in the curve fitting is within 3% (as shown in Fig. 7(*b*)) and δ'', δ''' are piecewise continuous. To check the sensitivity to accuracy ratio, we observed that for 1% change in the relative error in the thin-film region, the δ'' changed by 2.5%.

The curvature profiles for the thickness profiles presented in Figs. 6 and 7 are shown in terms of capillary pressure, σK (where σ is the surface tension and K is the curvature of the meniscus) in Fig. 8, where Fig. 8(*a*) compares the capillary pressure profiles of the pentane and octane menisci during isothermal state and Fig. 8(*b*) compares the capillary pressure profiles of the pentane and the octane meniscus during the nonisothermal (pseudosteady) state. In Fig. 8, we see that the curvature is zero in the adsorbed thin-film region (large relative distance). For the isothermal state, the curvature increased to a constant maximum value (K_T) as the thickness increased (or as the relative distance decreased). Using the values of σK_T and adsorbed film thickness (δ_0), we characterized the surface with respect to the working fluid by estimating the retarded dispersion constant of the quartz-liquid-air/vapor system. The reader should note that a significant discrepancy in the values of the experimental or actual retarded dispersion constant due to the presence of impurities and solid particles in the working fluid and due to nonidealities in the experimental system exist compared to the ideal dispersion constant. A brief discussion on the experimental evaluation of the deviation between the ideal and actual retarded dispersion constants follows.

The value of the ideal dispersion constant is a function of the bulk refractive indices and the dielectric constants of the three phases. The average value of the ideal dispersion constant for the as-received octane-air-quartz system obtained from the Lifshitz theory is -1.42×10^{-29} Jm. Since our experimental system is not ideal, we evaluate the dispersion constant using the experimental data, as explained in Ref. [1]. Using the experimental values of the adsorbed film thickness (δ_0) and the curvature in the thicker part of the meniscus (K_T) for the as-received octane experimental system at isothermal conditions, the average dispersion constant (B_{avg}) was found to be equal to -9.07×10^{-29} Jm over the thickness range studied. We observe that the experimentally obtained retarded dispersion constant is fairly close to its ideal value. The observed deviation can be attributed to the impurities in the as-received octane, which has a purity >99% and very small suspended particles.

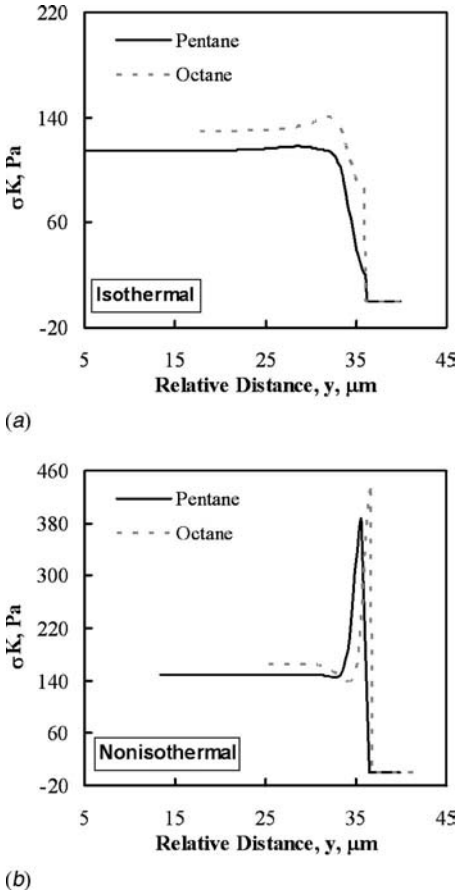

Fig. 8 Comparison of capillary pressure profiles of the pentane and octane menisci during (*a*) isothermal and (*b*) nonisothermal states

To evaluate the influence on the dispersion constant due to the presence of solid particles in the fluid and on the surface, we did an additional experimental study by adding platinum nanoparticles (average diameter of ~50 nm) to the as-received octane. A comparison of the reflectivity images of the isothermal as-received octane and as-received octane containing platinum nanoparticles with a diameter of ~50 nm is shown in Fig. 9(*a*) and Fig. 9(*b*), respectively. Clearly, we see the capillary action of octane around the platinum nanoparticles due to increase in the surface area because of nanoparticles. The capillary action disappeared on complete dry out (see Fig. 9(*c*)), which confirmed that the particles present on the quartz surface are platinum and of size ~50 nm. Liquid thickness profiles, especially the adsorbed film thickness in the later case, is now a function of local concentration of the particles adhered to the solid wall. Hence, we choose an area of interest (shown by the dotted rectangles in Fig. 9) and performed the data analysis procedure to obtain the thickness profiles. A comparison of thickness profiles in the extended region is shown in Fig. 9(*d*) [26]. Clearly, we see an increase in the adsorbed film thickness due to the presence of platinum nanoparticles on the solid surface and within the liquid. Based on the increase in the adsorbed film thickness, the experimentally measured retarded dispersion constant of the octane meniscus changed from -9.07×10^{-29} Jm to -3.81×10^{-28} Jm with the ideal retarded dispersion constant of pure octane at -1.42×10^{-29} Jm. We note that the ability to see small particles is a strong function of the size of the particles and the thickness of the thin liquid film.

In the case of pentane, we observed significant deviation from the ideal value due to the presence of finer particles and enhanced capillary action around these particles (as pentane wets more than

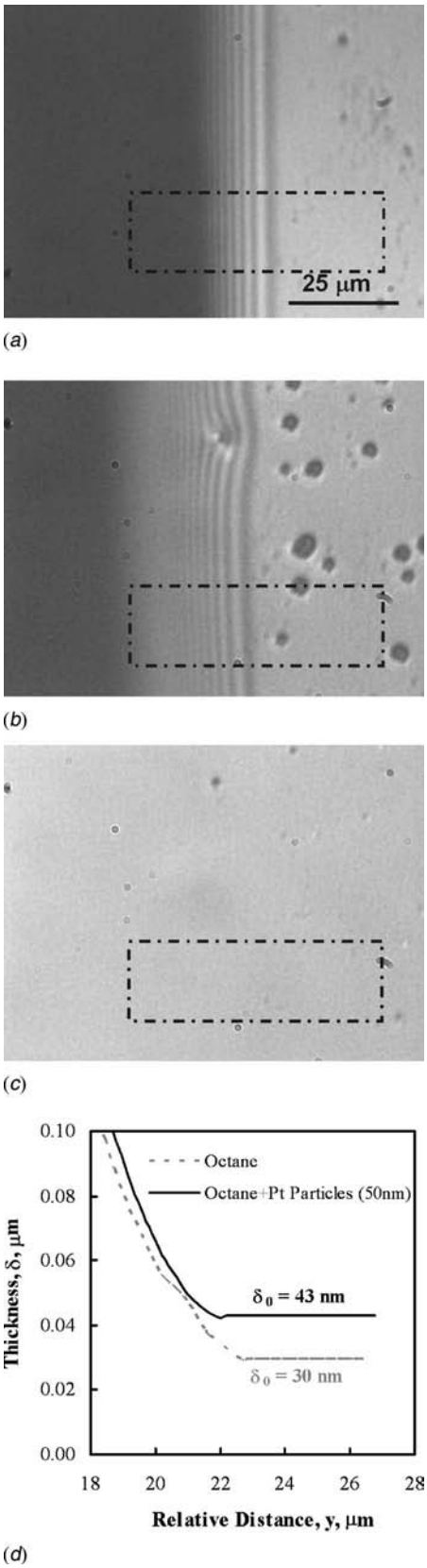

Fig. 9 (*a*) Isothermal octane meniscus on the quartz surface, (*b*) isothermal octane meniscus containing *Pt* nanoparticles (~50 nm) on the quartz surface, (*c*) reflectivity image of quartz surface containing *Pt* nanoparticles (~50 nm) after complete dryout, and (*d*) comparison of thickness profiles of the octane meniscus and octane meniscus containing *Pt* nanoparticles during isothermal state in the contact line region [26]

octane), which resulted in higher values of the adsorbed film thickness. We also note that an error in the measured adsorbed film thickness due to interfacial temperature jumps could result in a larger than expected value of the dispersion constant. As described in our previous studies Ref. [1], a possible uncontrollable interfacial temperature jump of the order of 10^{-4} K could cause an error in thickness of δ_0 of 100% and a large error in the retarded dispersion constant. However, this temperature effect is negligible for the as-received octane due to its higher boiling point and, hence, we obtained a closer match in the ideal and actual retarded dispersion constant for as-received octane. The average experimental retarded dispersion constant of the system with pentane as the working fluid is -8.71×10^{-28} Jm ($B_{\text{avg,pentane}}$) and its ideal dispersion constant from Lifshitz theory is -2.825×10^{-29} Jm. Although further detailed studies are needed to quantify these deviations and hence achieve a better understanding of the value of the dispersion constant, we emphasize that an error incorporated in the value of the dispersion constant does not effect the conclusions obtained, which depend on the change of Π from the isothermal reference state. The in situ experimental values of the retarded dispersion constant obtained for both systems are useful in estimating the disjoining pressure contribution to the pressure jump across the interface during the isothermal and nonisothermal states of the meniscus movements, as shown later.

Results and Discussion

Adsorbed Film Thickness, δ_0. Plots of the variation of the adsorbed film thickness with time for both the pentane (from Ref. [2]) and the octane menisci are shown in Figs. 10(*a*) and 10(*b*), respectively. For pentane, during the isothermal state, the adsorbed film thickness was constant at 52 nm (see Fig. 10(*a*)). During recession, the adsorbed film thickness decreased due to the heat flux entering the system. During advancement, the adsorbed film thickness decreased further to a minimum value of 17 nm at $t=10.2$ s. As the meniscus advanced further, $10.2<t<50$ s, the adsorbed film thickness increased. During the pseudosteady state, $t>50$ s, the adsorbed film thickness remained nearly constant at 34 nm, which is less than the isothermal value ($\delta_{0,\text{iso}}=52$ nm). This shows that the disjoining pressure ($-B_{\text{avg,pentane}}/\delta_0^4$) in the adsorbed film region during the pseudosteady state was significantly higher than that during the isothermal state. Since the capillary pressures in the thicker regions increase a small amount and an equal amount for the isothermal and the pseudosteady states (see Figs. 8(*a*) and 8(*b*)), there is an imbalance between the disjoining pressure in the thin-film region and capillary pressure in the thicker region that causes fluid flow and the pentane meniscus to advance during evaporation and, hence, results in the pseudosteady state for the highly pure pentane meniscus.

For relatively less pure octane, during the isothermal state, the adsorbed film thickness was constant at 30 nm (see Fig. 10(*b*)). During recession, the adsorbed film thickness decreased until it reached a minimum of 21 nm at $t=65.13$ s. For time, $65.13<t<200.5$ s, the adsorbed film thickness increased. During the pseudosteady state, $t>200.5$ s, the adsorbed film thickness remained nearly constant at 26 nm, which is only slightly lower than the value obtained for the isothermal state. This implies that the disjoining pressure ($-B_{\text{avg,octane}}/\delta_0^4$) in the adsorbed film region during the pseudosteady state was slightly higher than that during the isothermal state. Also, the contribution of disjoining pressure for fluid flow in the evaporating, stationary octane meniscus is less compared to the evaporating, creeping pentane meniscus as shown later.

Slope Angle at $\delta=0.1$ μm, $\theta_{0.1}$ μm. For a completely wetting corner meniscus, slope angles or apparent contact angles are quite often measured at a thickness of 0.1 μm (or the zeroth dark fringe in the interference pattern). A zero slope angle of a liquid on a solid surface ($\theta_{0.1\ \mu\text{m}}=0$) implies the liquid completely wets the underlying solid surface. However, in the current experimental system, the shape of the corner meniscus gives a finite value to the apparent contact angle at $\delta=0.1$ μm for a completely wetting system. Plots of the variation of slope angle profiles of the pentane and the octane menisci with the evaporation cycles are shown in Figs. 11(*a*) and 11(*b*), respectively. For pentane and octane, the average slope angles during the pseudosteady state are both higher due to the small increase in curvature than that during the isothermal state. Hence, the curvature characteristics of the pentane and octane menisci during the nonisothermal (pseudosteady) state are similar.

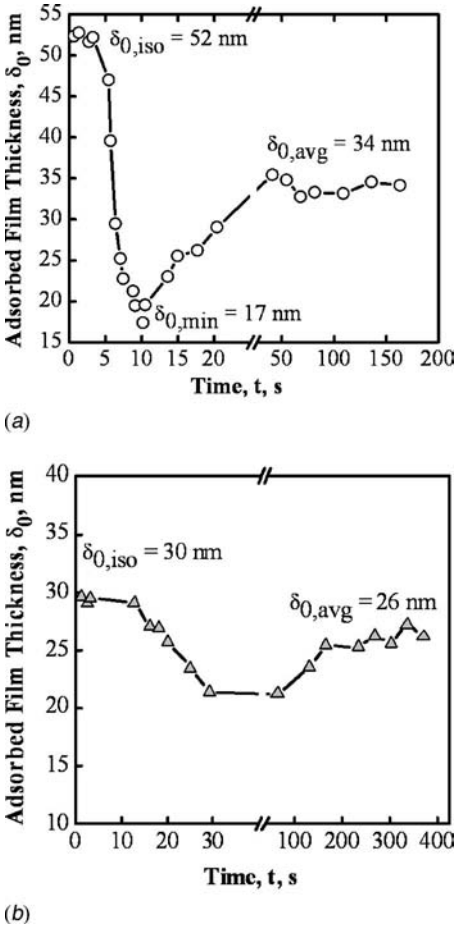

Fig. 10 Comparison of adsorbed film thickness profiles as a function of time of (*a*) the pentane meniscus and (*b*) the octane meniscus

Liquid Pressure, P_l. The liquid pressure P_l in the pentane and octane menisci during the nonisothermal state can be obtained from the augmented Young–Laplace equation given by

$$P_l = P_v - \sigma K - \Pi \tag{2}$$

where P_v is the total pressure in the vapor space, σK is the capillary pressure, and Π is the disjoining pressure equal to $-B_{\text{avg}}/\delta_0^4$. Figure 12 shows the comparison of the disjoining pressure profiles of pentane and octane menisci during isothermal and nonisothermal states. From Figs. 8(*a*) and 12(*a*), we see that both the disjoining pressure and capillary pressure profiles of the isothermal pentane meniscus are comparable to that of the octane meniscus. However, during evaporation (nonisothermal state), the disjoining pressure profiles (see Fig. 12(*b*)) changed significantly for highly pure pentane compared to relatively less pure octane, whereas the capillary pressure profiles (see Fig. 8(*b*)) still remained comparable to each other. Hence, the disjoining pressure (or the inter-

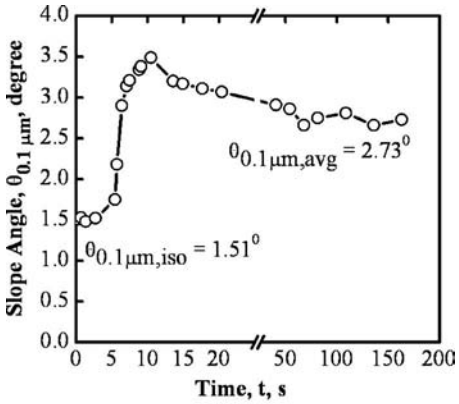

(*a*)

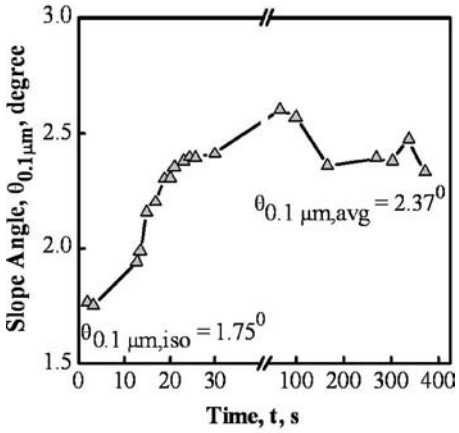

(*b*)

Fig. 11 Comparison of profiles of the slope angle at δ =0.1 μm as a function of time of (*a*) the pentane meniscus and (*b*) the octane meniscus

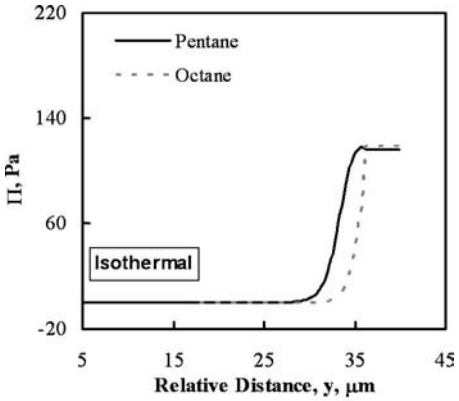

(*a*)

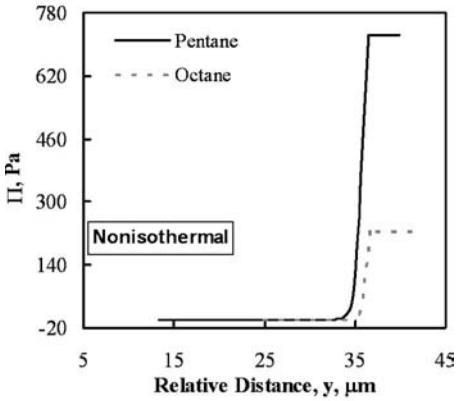

(*b*)

Fig. 12 Comparison of disjoining pressure profiles of the pentane and octane menisci during (*a*) isothermal and (*b*) nonisothermal states

molecular interactions between pentane and quartz) in the adsorbed film region was stronger for the creeping, evaporating pentane meniscus than for the stationary, evaporating octane meniscus.

Figure 13 compares the liquid pressure profiles of the pentane and octane menisci during nonisothermal states. P_v was obtained by adding the vapor pressure of the working fluid (at a temperature measured using the thermocouple at the top of the cuvette) to the atmospheric pressure. From Fig. 13, we see that, for pentane, there is a net liquid flow toward the adsorbed film region (or large relative distance) and, hence, the evaporating meniscus advanced away form the corner of the cuvette due to an imbalance in the disjoining pressure in the adsorbed film region and the capillary pressure in the thicker meniscus region. This resulted in a creeping, evaporating pentane meniscus as described earlier. However, for octane, there is a pressure barrier for liquid flow toward the adsorbed film region, shown by segment BC in Fig. 13. The reason for segment BC for octane is due to weaker intermolecular interactions between the octane and the underlying quartz surface, as shown by small increase in δ_0, and is given by the disjoining pressure profile in Fig. 12(*b*). This resulted in a stationary, evaporating octane meniscus.

Marangoni Shear Stress and Concentration Profiles. Using the experimentally obtained thickness profiles and a simple model for velocity distribution, we can evaluate the surface tension gradient along the length of the stationary, evaporating, less-pure octane meniscus.

Neglecting inertia terms and the z component (perpendicular to y) velocity, the Navier–Stokes equation for the velocity in the y direction (u) is given by

$$\mu \frac{d^2u}{dz^2} = \frac{dP_l}{dy} \tag{3}$$

where μ is the dynamic viscosity of the octane meniscus and P_l is the liquid pressure given by Eq. (2). Equation (3) was solved using the following boundary conditions:

At $z = 0$, $u = 0$ (zero slip at the solid-liquid interface)

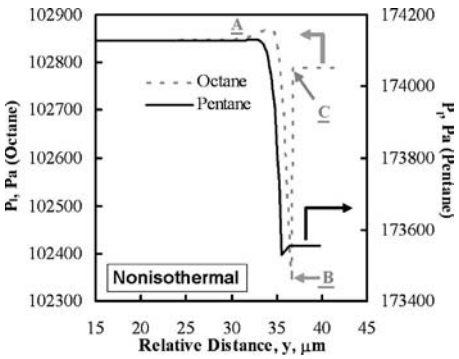

Fig. 13 Comparison of liquid pressure profiles of the pentane and octane menisci during nonisothermal state

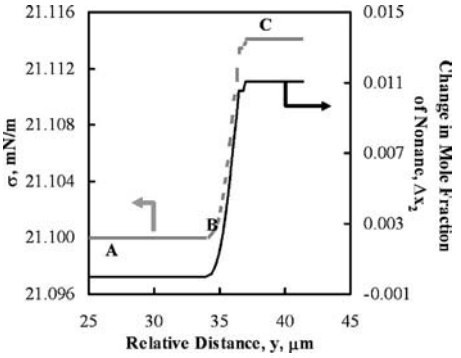

Fig. 14 Variation in the surface tension (σ) and the change in mole fraction of nonane (Δx_2) with the length of the octane meniscus during nonisothermal (pseudosteady) state for the stationary meniscus condition

$$z = \delta(y), \quad \tau_{zy} = \frac{d\sigma}{dy} \tag{4}$$

The second boundary condition implies that the shear at the interface is due to the surface tension gradient at the liquid-vapor interface, which describes the concentration driven Marangoni stresses. As the as-received octane was less pure (purity $>99\%$, Sigma Aldrich®) than pentane (purity $>99.8\%$), we have Marangoni stresses in the stationary, evaporating octane meniscus due to the presence of impurities and distillation. Solving Eq. (3) along with Eqs. (2) and (4), we have

$$u = \frac{1}{\mu}\frac{dP_1}{dy}\left[\frac{z^2}{2} - z\delta\right] + \frac{z}{\mu}\sigma' \tag{5}$$

Equation (5) can be averaged over the thickness δ, as given by

$$u_{\text{avg}} = \frac{1}{\mu\delta}\int_0^\delta \left[\frac{dP_1}{dy}\left(\frac{z^2}{2} - z\delta\right) + z\sigma'\right]dz \tag{6}$$

For the apparently stationary evaporating octane meniscus with Marangoni stresses, we postulate that u_{avg} could be equal to zero due to recirculation in a region near the adsorbed film region (segment BC in Fig. 13). For $u_{\text{avg}}=0$ in Eq. (6), we have

$$\sigma' = \frac{2\delta}{3}\frac{dP_1}{dy} \quad \text{or} \quad \sigma(y) = \int \frac{2\delta}{3}\frac{dP_1}{dy}dy + C_1 \tag{7}$$

where C_1 is a constant of integration. As a numerical example, for the region left of point B in Fig. 13, we assume a constant surface tension region, and for the region right of point B, we have a variation in surface tension given by Eq. (7). A zero average velocity in segment BC can be imagined as the sum of two flows: (i) flow from C to B due to pressure gradient (Fig. 13), and (ii) flow from B to C due to surface tension gradient such that the net flow is zero. As $dP_l/dy>0$, near the adsorbed film region (segment BC), we can assume the impurity to be a higher-order alkane, for example nonane. A plot of the variation of surface tension as a function of the meniscus length is given in Fig. 14, from we observe that the adsorbed film region is not entirely pure and contains impurities in very small quantities. We can obtain the concentration profile of the meniscus in terms of mole fraction of nonane (x_2) using the mixture rule,

$$\sigma = (1 - x_2)\sigma_1 + (x_2)\sigma_2 \tag{8}$$

where subscripts 1 and 2 in Eq. (8) refer to octane and nonane, respectively ($\sigma_1=21.1$ mN/m and $\sigma_2=22.38$ mN/m). Based on the results presented in Refs. [14–18], the experimental observations and our own in-progress modeling, the authors believe that the concentration-induced Marangoni effect is more significant compared to the temperature-induced Marangoni effect. A detailed modeling is required for the estimation of the temperature gradient along the length of the interface. However, by not considering the contribution of the temperature portion of the Marangoni effect from the temperature gradient (which decreases the surface tension gradient), we are demonstrating the effect of a concentration variation in a liquid-vapor interface due to evaporation. The concentration profile obtained herein provides an example of a level of impurity that can exist along the length of the interface at the heat flux studied in an apparently pure octane meniscus without the need of a detailed modeling. A plot of the change in mole fraction of nonane (Δx_2) with reference to its bulk concentration as a function of meniscus length is given in Fig. 14, where we see the presence of high boiling impurities in the adsorbed film region (beyond point C in Fig. 14). Hence, the presence of impurities in the working fluid affects the composition and thickness (increase) of the adsorbed film region and thus can have a significant effect on the spreading characteristics of an apparently pure octane meniscus.

Although we cannot accurately estimate the flow due to σ' at this time (using Eq. (6)), assuming $\sigma'=0$, we can estimate the local evaporative heat flux (q'') from Eq. (9) and the measured thickness profile. For the studied octane and pentane systems, the average values of q'' evaluated at $\delta=0.84$ μm were 2.15×10^4 W/m^2 and 1.87×10^5 W/m^2, respectively. This would be enhanced by $\sigma'>0$

$$q'' = h_{fg}\frac{d}{dy}(\rho\delta u_{\text{avg}}) \tag{9}$$

Further modeling, including the temperature and concentration effects on the interfacial surface tension, is essential for the understanding of the underlying phenomena and is currently in progress. The main purpose of this paper is to demonstrate, experimentally, the large effect that a small amount of a second component has on the relative effects of disjoining pressure and σ'.

Conclusions

1. Using image analyzing interferometry, the thickness profile, in the range of δ_0 (adsorbed thickness) $<\delta<3$ μm, at the leading edge of an evaporating meniscus with phase change, was measured for a 99+% pure octane and compared to that of pentane of higher purity ($>99.8\%$). Significant differences between the two systems were observed. The pentane meniscus initially receded and eventually advanced beyond the isothermal location, whereas the octane meniscus receded and remained stationary behind the isothermal location.
2. The measured pressure field for the isothermal and nonisothermal pentane and octane menisci gives insight into the spreading characteristics of both the systems studied.
3. The differences in the meniscus behavior of the two systems are attributed to Marangoni stresses in the lower purity octane and significant disjoining pressure level in the pure pentane.
4. The disjoining pressure at the leading edge controlled the creeping, evaporating, highly pure pentane system, whereas its effect on the "stationary," evaporating, less pure octane was small for the fluxes studied.
5. For relatively less pure octane, flow was controlled by Marangoni shear stresses.
6. Using the experimental data and a simple model for the velocity distribution near the adsorbed film region, we were able to evaluate the effect of a surface tension gradient and a maximum impurity level of 1.1% for the octane meniscus.
7. The impurity levels at the contact line region observed in the octane meniscus are a function of the heat flux and arise due to evaporative distillation of the relatively less pure octane meniscus.

Acknowledgment

This material is based on the work supported by the National Aeronautics and Space Administration under Grant No. NNC05GA27G.

Nomenclature

B_{avg} = average retarded dispersion constant, Jm
C_1 = constant of integration in Eq. (7)
Δx_2 = change in mole fraction of nonane
g = acceleration due to gravity, m/s^2
K = curvature, m^{-1}
K_T = constant curvature in the thicker meniscus region, m^{-1}
P = pressure, Pa
t = time, s
Q_{in} = heater power input, W
U_i = velocity of the interference fringe at δ=0.1 μm, μm/s
x = axial location, mm
y = relative distance perpendicular to the contact line, μm

Greek Symbols

δ = film thickness, μm
δ_0 = adsorbed film thickness, nm
μ = dynamic viscosity, kg/m s
Π = disjoining pressure, N/m^2
$\Psi_{0.1\ \mu m}$ = distance traveled by the meniscus, μm
σ = surface tension of the liquid, N/m
$\theta_{0.1\ \mu m}$ = slope angle at δ=0.1 μm, deg
τ = shear stress at the liquid-vapor interface, N/m^2

Subscripts

1 = octane
2 = nonane
avg = average
i = ith time instant
l = liquid
min = minimum
v = vapor/air
0 = reference state (adsorbed film region)
0.1 μm = parameters taken at δ=0.1 μm

References

[1] Panchamgam, S. S., Gokhale, S. J., Plawsky, J. L., DasGupta, S., and Wayner, Jr., P. C., 2005. "Experimental Determination of the Effect of Disjoining Pressure on Shear in the Contact Line Region of a Moving Evaporating Thin Film," ASME J. Heat Transfer, **127**, pp. 231–243.
[2] Panchamgam, S. S., Plawsky, J. L., and Wayner, Jr., P. C., 2006. "Microscale Heat Transfer in an Evaporating Moving Extended Meniscus," Exp. Therm. Fluid Sci., **30**, pp. 745–754.
[3] Potash, Jr., M., and Wayner, Jr., P. C., 1972. "Evaporation From a Two-dimensional Extended Meniscus," Int. J. Heat Mass Transfer, **15**, pp. 1851–1863.
[4] Derjaguin, B. V., and Zorin, A. M., 1957. "Optical Study of the Adsorption and Surface Condensation of Vapors in the Vicinity of Saturation on a Smooth Surface," *Proc. of 2nd Int. Congress Surface Activity (London)*, Vol. 2, pp. 145–152.
[5] Derjaguin, B. V., Nerpin, S. V., and Churaev, N. V., 1965. "Effect of Film Transfer Upon Evaporation of Liquids From Capillaries," Bull. Rilem, **29**, pp. 93–98.
[6] Holm, F. W., and Goplen, S. P., 1979. "Heat Transfer in the Meniscus Thin Film Region," ASME J. Heat Transfer, **101**, pp. 543–547.
[7] Moosman, S., and Homsy, S. M., 1980. "Evaporating Menisci of Wetting Fluids," J. Colloid Interface Sci., **73**, pp. 212–223.
[8] Wayner, Jr., P. C., 1991. "The Effect of Interfacial Mass Transport on Flow in Thin Liquid Films," Colloids Surf., **53**, pp. 71–84.
[9] Stephan, P., and Busse, C. A., 1992. "Analysis of the Heat Transfer Coefficient of Grooved Heat Pipe Evaporator Walls," Int. J. Heat Mass Transfer, **35**, pp. 383–391.
[10] Swanson, L. W., and Peterson, G. P., 1995. "The Interfacial Thermodynamics of Micro Heat Pipes," ASME J. Heat Transfer, **115**, pp. 195–201.
[11] Wayner, Jr., P. C., 1999. "Intermolecular Forces in Phase-Change Heat Transfer: 1998 Kern Award Review," AIChE J., **45**, pp. 2055–2067.
[12] Sodtke, C., Kern, J., Schweizer, N., and Stephan, P., 2006. "High Resolution Measurements of Wall Temperature Distribution Underneath a Single Vapor Bubble Under Low Gravity Conditions," Int. J. Heat Mass Transfer, **49**, pp. 1100–1106.
[13] Wayner, Jr., P. C., Tung, C. Y., Tirumala, M., and Yang, J. H., 1985. "Experimental Study of Evaporation in the Contact Line Region of a Thin Film of Hexane," ASME J. Heat Transfer, **107**, pp. 182–189.
[14] Parks, C. J., and Wayner, Jr., P. C., 1987. "Surface Shear Near the Contact Line of a Binary Evaporating Curved Thin Film," AIChE J., **33**, pp. 1–10.
[15] Kern, J., and Stephan, P., 2003. "Theoretical Model for Nucleate Boiling Heat and Mass Transfer of Binary Mixtures," ASME J. Heat Transfer, **125**, pp. 1106–1115.
[16] Pratt, D. M., and Kihm, K. D., 2003. "Binary Fluid Mixture and Thermocapillary Effects on the Wetting Characteristics of a Heated Curved Meniscus," ASME J. Heat Transfer, **125**, pp. 867–874.
[17] Wee, S.-K., Kihm, K. D., Pratt, D. M., and Allen, J. S., 2006. "Microscale Heat and Mass Transport of Evaporating Thin Film of Binary Mixture," J. Thermophys. Heat Transfer, **20**(2) pp. 320–326.
[18] Panchamgam, S. S., Plawsky, J.L., and Wayner, Jr., P. C., 2006. "Spreading Characteristics and Microscale Evaporative Heat Transfer in an Ultrathin Film Containing a Binary Mixture," ASME J. Heat Transfer, **128**(12) pp. 1266–1275.
[19] Wayner, Jr., P. C., 1994. "Mechanical and Thermal Effects in the Forced Spreading of a Liquid Film With a Finite Contact Angle," Colloids Surf., A, **89** pp. 89–95.
[20] Pesach, D., and Marmur, A., 1987. "Marangoni Effects in the Spreading of Liquid Mixtures on a Solid," Langmuir, **3**, pp. 519–524.
[21] Kavehpour, P., Ovryn, B., and McKinley, G., H., 2002, "Evaporatively-Driven Marangoni Instabilities of Volatile Liquid Films Spreading on Thermally Conductive Substrates," Colloids Surf., A, **206**, pp. 409–423.
[22] Bankoff, S., G., 1990, "Dynamics and Stability of Thin Heated Liquid Films," ASME J. Heat Transfer, **112**, pp. 538–546.
[23] Cazabat, A., M., Heslot, F., Carles, P., and Troian, S., M., 1992, "Hydrodynamic Fingering Instability of Driven Wetting Films," Adv. Colloid Interface Sci., **39**, pp. 61–75.
[24] Sharma, A., 1998, "Equilibrium and Dynamics of Evaporating or Condensing Thin Fluid Domains: Thin Film Stability and Heterogeneous Nucleation," Langmuir, **14**, pp. 4915–4928.
[25] Hosoi, A. E., and Bush, J. W., M., 2001, "Evaporative Instabilities in Climbing Films," J. Fluid Mech., **442**, pp. 217–239.
[26] Panchamgam, S. S., 2006, "Interfacial Phenomena and Microscale Transport Processes in Evaporating Ultrathin Menisci," Ph.D. thesis, Rensselaer Polytechnic Institute, Troy, NY, pp. 221–227.
[27] 2003, *CRC Handbook of Chemistry and Physics*, 84 ed., CRC Press, Boca Raton.
[28] 1997, *Perry's Chemical Engineers' Handbook*, 7th ed., McGraw-Hill, New York.

Effect of Vapor Velocity on Condensation of Low-Pressure Steam on Integral-Fin Tubes

Satesh Namasivayam

Adrian Briggs[1]
e-mail: a.briggs@qmul.ac.uk

Department of Engineering,
Queen Mary, University of London,
Mile End Road,
London E1 4NS, United Kingdom

Experimental data are presented for forced-convection condensation of low-pressure steam on a set of single, integral-fin tubes. The five tubes had fin-root diameter of 12.7 mm *and identical fin geometry except for fin spacing, which was varied from* 0.25 mm to 2 mm*. The range of vapor velocity was* 14.7–62.3 m/s *at an absolute pressure of* 14 kPa*. Heat-transfer enhancement was a strong function of both vapor velocity and fin spacing, and the interrelationship of the two parameters led to complex trends in the data. Observations of the extent of condensate flooding (i.e., condensate trapped between the fins at the bottom of the tube) indicated that the effect of vapor shear on flooding was a significant controlling factor in the heat-transfer process, and this factor explained, at least quantitatively, the trends observed.* [DOI: 10.1115/1.2764085]

Keywords: condensation, heat transfer, fin tubes, vapor velocity

Introduction

When quiescent vapor condenses on an integral-fin tube, two mechanisms influence the flow of condensate on, and hence the heat transfer to, the tube. Surface tension induced pressure gradients drain condensate from the tips and flanks of the fins, thinning the film and enhancing the local heat transfer. Additionally, condensate retention in the interfin spaces at the bottom of the tube leads to a thickening of the condensate film on this part of the tube causing a decrease in the heat transfer. When significant vapor velocity is present, vapor shear at the condensate interface will further effect the condensate flow. The combined effects of vapor shear and surface tension on the heat transfer to integral-fin tubes have received some attention in the literature but as yet their interaction is not fully understood.

Michael et al. [1] presented data for condensation of R-113 and steam on three integral-fin tubes and a plain tube. Vapor velocities ranged from 0.4 m/s to 1.9 m/s for R-113 at atmospheric pressure and 4.8–31.5 m/s for steam at approximately 12 kPa.[2] For both fluids, the relative increase in heat-transfer coefficient due to vapor velocity was smaller for the finned tubes than for the plain tube. Cavallini and co-workers [2,3] observed the same trend when condensing R-113 and R-11 at approximately 1 and 2 atm, respectively, on three finned tubes and at vapor velocities up to 10 m/s.

Namasivayam and Briggs [4–6] presented experimental data for forced-convection condensation of steam at atmospheric pressure and ethylene glycol at 15 kPa, respectively, on a total of nine single, integral-fin tubes. Vapor velocities up to 10 m/s were obtained for steam and up to 22 m/s for glycol. The tube geometry was the same in all cases except for fin spacing, which was varied from 0.25 mm to 2 mm, and fin height, which was varied from 0.5 to 1.6 mm. In almost all cases, it was found that the vapor-side enhancement ratio (defined as the vapor-side, heat-transfer coefficient for a finned tube based on the fin-root diameter, divided by that for a plain tube with diameter equal to the fin-root diameter of the finned tubes, at the same vapor-side temperature difference and vapor velocity) decreased with increasing vapor velocity. For ethylene glycol condensing on two tubes with the highest fin densities, however, the extent of condensate flooding was reduced with increasing vapor velocity and this was accompanied by an increase in enhancement ratio.

In Ref. [7], Cavallini and co-workers correlated their own data from [2,3] using an approach which incorporated the zero vapor velocity model of Briggs and Rose [8] at low vapor velocity and an empirical relation involving the film and vapor Reynolds numbers at high vapor velocity. The model predicted their own data to within 15%, but was less successful at predicting the steam data of Michael et al. [1], presumably because the empirical constants in the model were obtained from their own data for refrigerants.

In the present paper, new experimental data will be presented for condensation of steam on five integral-fin tubes with varying fin spacing. Vapor velocities, up to 60 m/s, are higher than previously reported for finned tubes in the open literature. By extending the range of data, it is hoped that an insight can be gained into the fundamental process governing condensation on integral-fin tubes with high vapor shear. The velocities and pressures used are also similar to those found in industrial steam condensers.

Apparatus

The closed-loop, stainless steel test rig is shown in Fig. 1. Vapor was generated in electrically heated boilers (maximum power 60 kW) and directed vertically downward through a calming section, before flowing over the horizontal test condenser tube. The internal diameter of the test section, and hence the length of tube exposed to the vapor, was 70 mm. Excess vapor passed to an auxiliary condenser from which the condensate returned to the boiler by gravity. Pressure in the apparatus was controlled by a vacuum pump attached to the auxiliary condenser. The required pressure in the test section (approximately 14 kPa) was maintained by alternately pumping down, or bleeding small amounts of air into, the auxiliary condenser well down stream of the test section to lower or raise the pressure as required. The mass fraction of air present in the vapor in the test section was continually checked to ensure that no air was entering the test section from the auxiliary condenser (or from any leaks in the apparatus). This was done by comparing the measured temperature and pressure and assuming saturated conditions and the Gibbs–Dalton ideal gas mixture equation.

The test condenser tube was mounted horizontally in the test

[1]Corresponding author.

[2]Throughout this paper, all vapor velocities are based on the cross-sectional area of the test section *upstream* of the test tube and all pressures are *absolute*.

Contributed by the Heat Transfer Division of ASME for publication in the JOURNAL OF HEAT TRANSFER. Manuscript received September 3, 2006; final manuscript received March 8, 2007. Review conducted by Raj M. Manglik.

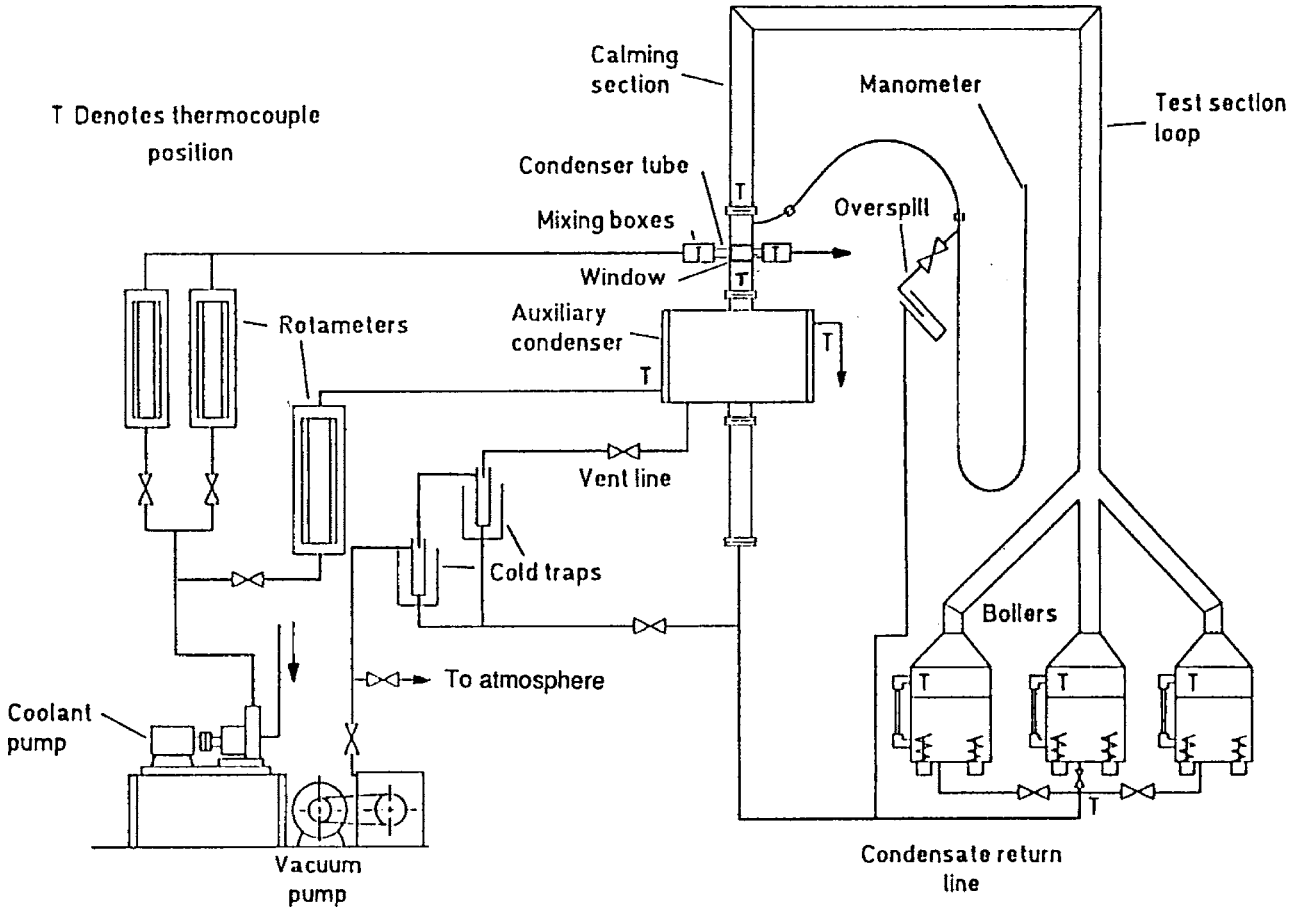

Fig. 1 Apparatus

section using PTFE ("Teflon") bushes, which also served to insulate the tube from the body of the test section. The tube was cooled internally by water. PTFE inserts were used to insulate the inside of the test tubes at entry to and exit from the test section, so that the inside and outside surface areas available to heat transfer were of equal length. A glass window in the test section allowed observation of the test condenser tube. Five copper tubes with rectangular cross-section, integral fins were tested. All the tubes had an inside diameter of 9.4 mm, a diameter at the fin root of 12.7 mm, and fin height and thickness of 1.6 mm and 0.25 mm, respectively. Fin spacings were 0.25, 0.5, 1.0, 1.5, and 2.0 mm. A plain copper tube with inside diameter of 9.4 mm and outside diameter of 12.7 mm was also tested.

The vapor velocity at approach to the test section was found from the measured power input to the boilers. A small predetermined correction for the heat loss from the well-insulated apparatus was included in the calculation. The vapor temperature was measured using K-type thermocouples inserted in stainless steel tubes in the test section and calibrated to better than ±0.1 K. The coolant-flow rate through the test tubes, which was varied in the range of 10–40 l/min, was measured using variable-aperture, float-type flow meters with an uncertainty of ±0.5 l/min. The cooling water temperature rise, from which the heat-transfer rate to the test tube was calculated, was measured using a ten-junction thermopile, with adequate isothermal immersion of the junctions and special coolant mixing arrangements. A predetermined small correction for the dissipative temperature rise of the cooling water was incorporated in the calculation of the heat-transfer rate. The estimated accuracy of the measurement of the coolant temperature rise was better than ±0.01 K, while the coolant temperature rise was in the range of 0.4–1.2 K.

The vapor-side, heat-transfer coefficient was found by subtracting the coolant and wall resistances from the measured overall thermal resistance. To obtain a correlation for the coolant-side, heat-transfer coefficient, a "modified Wilson plot" technique was applied to the data for the plain tube. This involved selecting expressions, containing unknown constants, for the vapor-side and coolant-side, heat-transfer coefficients. The unknown constants were found by minimizing the sum of squares of residuals (measured minus calculated values) of the vapor-to-coolant temperature difference. For the coolant side, an expression based on Sieder and Tate [9] for turbulent flow inside tubes was adopted.

$$\mathrm{Nu}_c = a\,\mathrm{Re}_c^{0.8}\,\mathrm{Pr}_c^{1/3}\left(\frac{\mu_c}{\mu_{\mathrm{wi}}}\right)^{0.14} \tag{1}$$

where a is a constant to be found. For the vapor side, an equation based on Shekriladze and Gomelauri [10] as presented in Ref. [11] was used.

$$\frac{\mathrm{Nu}}{\mathrm{Re}_{\mathrm{tp}}^{1/2}} = b\left[\frac{0.9 + 0.728F^{1/2}}{(1 + 3.44F^{1/2} + F)^{1/4}}\right] \tag{2}$$

where b is a constant to be found. The modified Wilson plot was applied to the data for the plain tube (52 data points), for which Eq. (2) would be applicable. For these data, the values of a and b were found to be 0.033 and 1.08, respectively. The value of a is the same as obtained by Ref. [4] using data for atmospheric steam and is slightly higher than the often quoted value of 0.027 for the original work of Sieder and Tate [9] due to the short test tubes used in the present investigation. Equation (1), with a=0.033, was used to analyze all of the data for both plain and finned tubes and at all vapor velocities by subtracting the coolant-side and wall

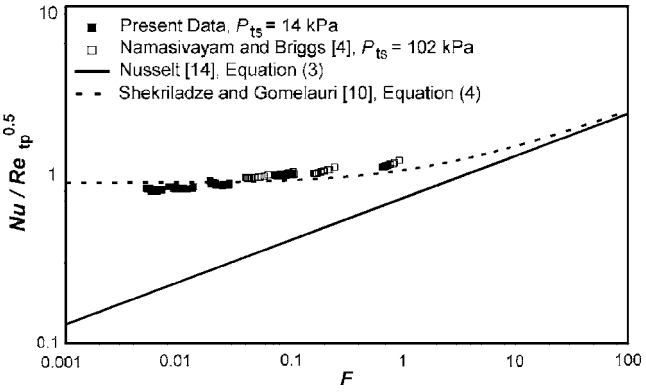

Fig. 2 Plain tube results

resistances from the measured overall resistance as described above. (Note that the finned tubes were manufactured with identical internal geometry to the plain tube, including inlet and exit arrangements, so that the coolant-side correlation found from the plain tube would be directly applicable to the finned tubes.)

An uncertainty analysis was carried out on the results using the method of Kline and McClintock [12]. This method uses the estimated uncertainties in the experimental measurements (e.g., in coolant flow rate, coolant temperature rise, etc.) and calculates the propagation of these uncertainties in the reported results (e.g., heat flux, vapor-side temperature difference, etc.). Using this method and the uncertainties in the measured parameters given above, the calculated uncertainty in the heat flux was never greater than 4%. The uncertainty in the vapor-side, temperature difference arose mainly from the use of Eq. (1) to calculate the coolant-side, thermal resistance. An uncertainty of 5% was estimated for this value, based on comparisons made in Ref. [13] between coolant-side correlations obtained by the modified Wilson plot method, as used in the present case, and direct measurement of the tube wall temperature using instrumented tubes with thermocouples embedded in the walls. When the coolant-side thermal resistance dominates the overall resistance, i.e., for highly enhanced tubes and at low coolant flow rates, this relatively small uncertainty in the coolant-side coefficient translates into large uncertainties in the calculated vapor-side coefficient. For this reason, some of the low coolant flow rate data for the most highly enhanced tubes were discarded. No vapor-side data are reported where the uncertainty in the vapor-side temperature difference is greater than ±20% and in most cases it was considerably smaller than this.

Results

All tests were carried out at an absolute pressure of 14 kPa and tests were repeated on separate days. Data were obtained for nominal vapor velocities (based on the total cross-sectional area of the test section) of 14.7, 30.5, 45.9, and 62.3 m/s for all six tubes. Data were also obtained for additional, intermediate, vapor velocities for some of the tubes where interesting trends in the data were identified.

Figure 2 shows the data for the plain tube, along with those of Namasivayam and Briggs [4] who condensed atmospheric pressure steam on the same plain tube as that used in the present investigation. Also shown in Fig. 2 are the theoretical lines of Nusselt [14] for free convection and Shekriladze and Gomelauri [10], who used the asymptotic, infinite condensation rate approximation to model the vapor shear at the liquid-vapor interface. The Nusselt result can be written as

$$\frac{\mathrm{Nu}}{\mathrm{Re}_{\mathrm{tp}}^{1/2}} = 0.728F^{1/4} \tag{3}$$

while the result of Shekriladze and Gomelauri can be written (see Ref. [11]) as

$$\frac{\mathrm{Nu}}{\mathrm{Re}_{\mathrm{tp}}^{1/2}} = \frac{0.9 + 0.728F^{1/2}}{(1 + 3.44F^{1/2} + F)^{1/4}} \tag{4}$$

Note that Eq. (4) tends to Eq. (3) for large F (low vapor velocity) and to $\mathrm{Nu}/\mathrm{Re}_{\mathrm{tp}}^{1/2}=0.9$ for small F (high vapor velocity). Both sets of data are in broad agreement with Eq. (4) and with each other, with the present results covering the lower values of F than the previous data due to the higher vapor velocities obtained at low pressure.

Figure 3 shows the plots of heat flux, based on the surface area of a plain tube with fin-root diameter, against vapor-side temperature difference for each of the five finned tubes tested. Also shown on each plot are the plain tube data for comparison and the theoretical result of Nusselt [14]. The lines on the plots are curve fits to the data, which will be used later to evaluate heat-transfer enhancement ratios. The data show good repeatability, with points from separate days but under the same conditions being indistinguishable. As noted above, the range of vapor-side temperature differences reported for high vapor velocity was limited due to uncertainties in the data at low vapor-side temperature difference.

All five tubes show enhancements in heat flux over the plain tube at the same vapor velocity and vapor-side temperature difference. All the tubes, both finned and plain, show an increase in heat flux at the same vapor-side temperature difference with increasing vapor velocity. This is due to the enhancing effect of vapor shear, which acts to thin the condensate film and hence decrease the vapor-side thermal resistance. For the same reason, the plain tube data lie above the theoretical result of Nusselt [14] for condensation of stationary vapor.

Figure 4 shows the plots of all the tubes for the four main vapor velocities tested and reveals that the best performing tube differs depending on vapor velocity. At the lowest vapor velocity of 14.7 m/s, the best performing tube was that with a fin spacing of 0.25 mm, in line with the findings of Namasivayam and Briggs [4] who condensed atmospheric pressure steam on the same set of five tubes used in the present investigation. At a velocity of 30.5 m/s, fin spacings of 1 and 1.5 mm gave the best performance. At 45.9 m/s, the best performing tubes are those with fin spacings of 0.5 and 1 mm. Finally, at 62.3 m/s the tube with 0.5 mm fin spacing is clearly the best.

Enhancement Ratios

A better understanding of the interrelated effects of vapor velocity and fin spacing can be gained by quantifying the performance of each fin spacing and at each vapor velocity by means of a heat-transfer enhancement ratio. The data for all tubes and at all vapor velocities were reasonably well fitted by equations of the form

$$q = A\Delta T^n \tag{5}$$

where A and n are constants found for each tube and vapor velocity combination. For all tubes and vapor velocities, n was found to be close to 1. This is in line with laminar theory for forced-convection condensation on horizontal plain tubes. While better fits could be obtained if the index was allowed to vary, fixing it at 1 for all cases has the advantage that it allows an enhancement ratio to be calculated, defined as the vapor-side, heat-transfer coefficient for the finned tube based on the fin-root diameter, divided by that for the plain tube, at the same vapor-side, temperature difference, and vapor velocity, which is independent of vapor-side, temperature difference. Thus,

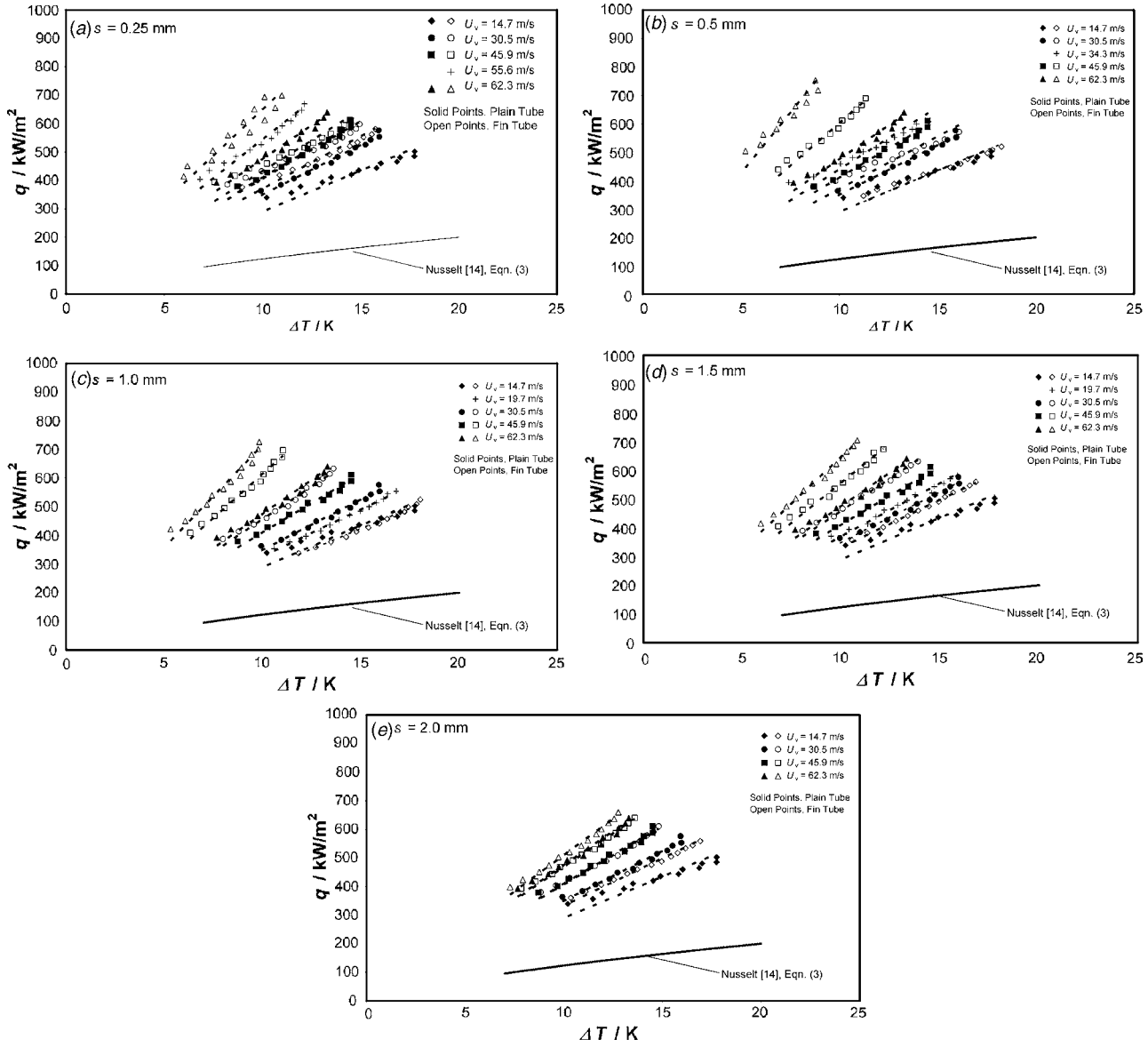

Fig. 3 Variation of heat flux with vapor-side temperature difference—effect of vapour velocity

$$\varepsilon = \left(\frac{\alpha_{\text{finned}}}{\alpha_{\text{plain}}}\right)_{\text{same } \Delta T \text{ and } U_v} = \left(\frac{q_{\text{finned}}}{q_{\text{plain}}}\right)_{\text{same } \Delta T \text{ and } U_v} = \left[\frac{A(n=1)_{\text{finned}}}{A(n=1)_{\text{plain}}}\right]_{\text{same } U_v} \quad (6)$$

Figure 3 shows the best fit lines with $n=1$. Enhancement ratios were calculated on the above basis for each of the finned tubes and at each of the vapor velocities tested. Table 1 lists the values obtained for the five tubes tested. Values for A_{plain} for vapor velocities at which the plain tube was not tested were interpolated from available values using a formula based on Eq. (4). The actual values of n for all tubes and vapor velocities varied from 0.66 to 1.02 and this variation introduces an additional uncertainty in the calculated enhancement ratios. This uncertainty will be greatest not when n varies most from unity but when the values of n for the plain and fin tubes differ the most. This occurred for the tube with a spacing of 0.5 mm and a vapor velocity of 30 m/s. By comparing the enhancement ratios at specific vapor-side temperature differences over the range of the data to the average value calculated using $n=1$, it was found that the additional uncertainty in the enhancement ratio due to this variation was less than 4% for this worst case.

Figure 5(*a*) shows the variation in enhancement ratio with fin spacing for the lowest vapor velocity tested (i.e., 14.7 m/s) along with data from Namasivayam and Briggs [4] for atmospheric pressure steam at vapor velocities of 2.3 and 10.2 m/s. All three data sets show the same trend, with the 0.25 mm fin spacing tube having the highest enhancement ratio. The combined data sets also confirm the conclusion of earlier investigations [1–4], showing a decrease in enhancement ratio with increasing vapor velocity. Following the same trend, all the data fall below the theoretical result of Briggs and Rose [8] for condensation of stationary vapor.[3]

Figure 5(*b*) shows the data for the other three main vapor velocities tested. At the lowest, 30.5 m/s, the data show a similar trend to those in Fig. 5(*a*), although the optimum spacing has

[3]Note that the discontinuity in the Briggs and Rose [8] model at a fin spacing of approximately 0.9 mm occurs where the fin just becomes fully flooded. For spacing below this value, the enhancement begins to rise again as more fins, and therefore more fin-tip area is added for a given tube length.

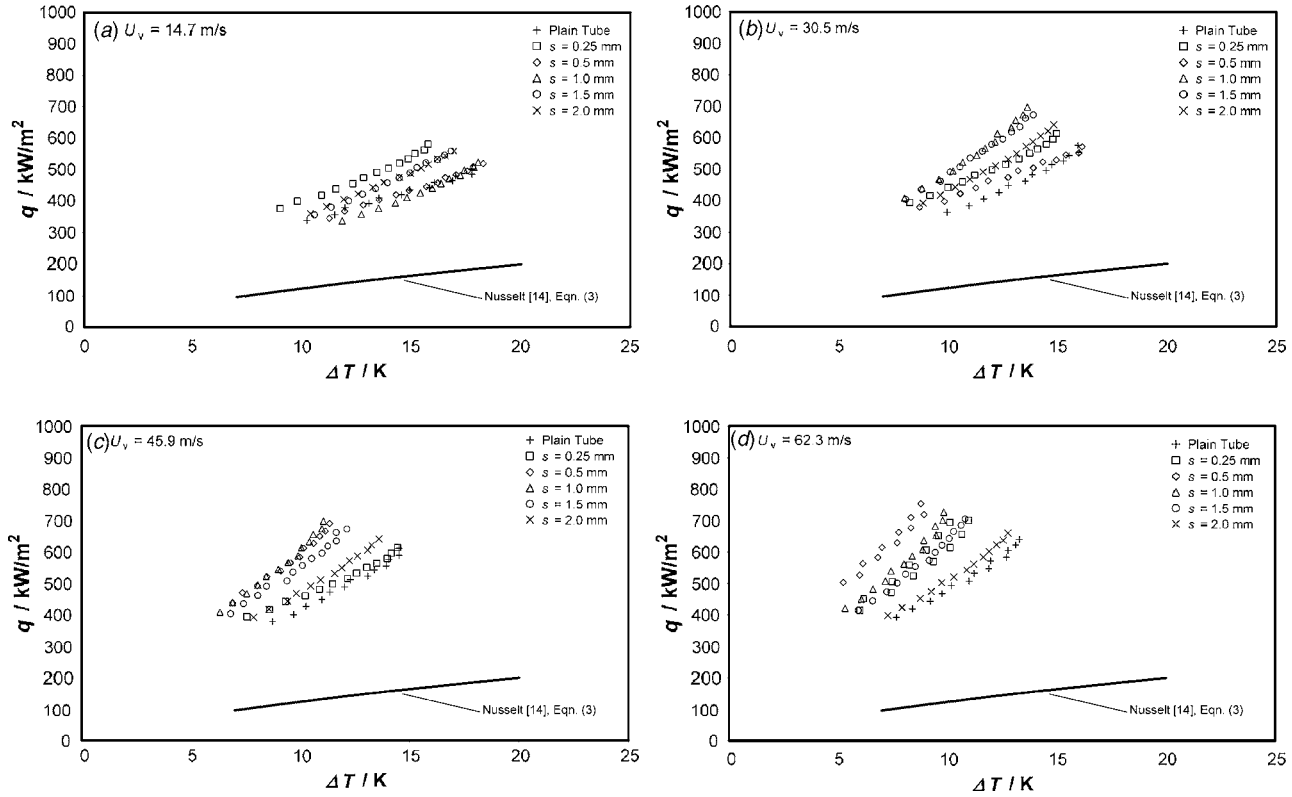

Fig. 4 Variation of heat flux with vapor-side temperature difference—effect of fin spacing

moved to between 1 and 1.5 mm. The two highest vapor velocities, however, show markedly different trends, with an optimum spacing at 0.5 mm. Figure 6 shows the plots of enhancement ratio against vapor velocity for the five finned tubes tested. The data for each of the five tubes show markedly different trends.

From all of the above, it is clear that heat-transfer enhancement is strongly effected by both vapor velocity and fin spacing, and that the interrelationship of the two parameters leads to some complex trends in the data. These trends can be explained, at least qualitatively, by examining the extent of condensate flooding on the bottom of the tubes, and how it is effected by vapor velocity. Honda et al. [15] gave the following equation for the flooding angle for condensation of quiescent vapor on a tube with rectangular cross-section fins:

$$\phi_f = \cos^{-1}\left(\frac{4\sigma}{\rho g b d_0} - 1\right) \quad \text{for } s < 2h \tag{7}$$

In the present case, the actual flooding angle was estimated visually for each tube at each of the four main vapor velocities tested. The calculated (using Eq. (7)) and observed flooding angles are listed in Table 2 and shown on Fig. 6 as a fraction of the tube circumference not covered by retained condensate. It can be seen in Fig. 6 that for all five tubes at low vapor velocity, the observed flooding is in line with Eq. (7) and where this is the case the enhancement ratio decreases with increasing vapor velocity as has been reported in earlier studies. At some critical value of vapor

Table 1 Heat-transfer enhancement ratios

s/mm	0.25	0.5	1.0	1.5	2.0
ε (U_v=14.7 m/s)	1.39	1.09	1.05	1.24	1.25
ε (U_v=19.7 m/s)	—	—	1.12	1.27	—
ε (U_v=30.5 m/s)	1.17	1.07	1.31	1.31	1.17
ε (U_v=34.3 m/s)	—	1.16	—	—	—
ε (U_v=45.9 m/s)	1.06	1.48	1.50	1.36	1.15
ε (U_v=55.6 m/s)	1.13	—	—	—	—
ε (U_v=62.3 m/s)	1.38	1.84	1.51	1.36	1.07

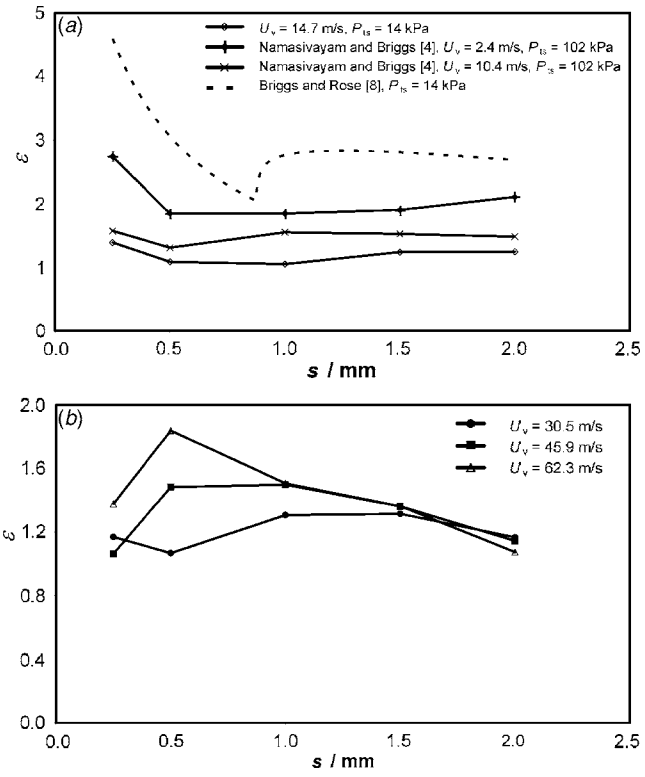

Fig. 5 Variation of enhancement ratio with fin spacing (lines through experimental data are shown to guide the eye)

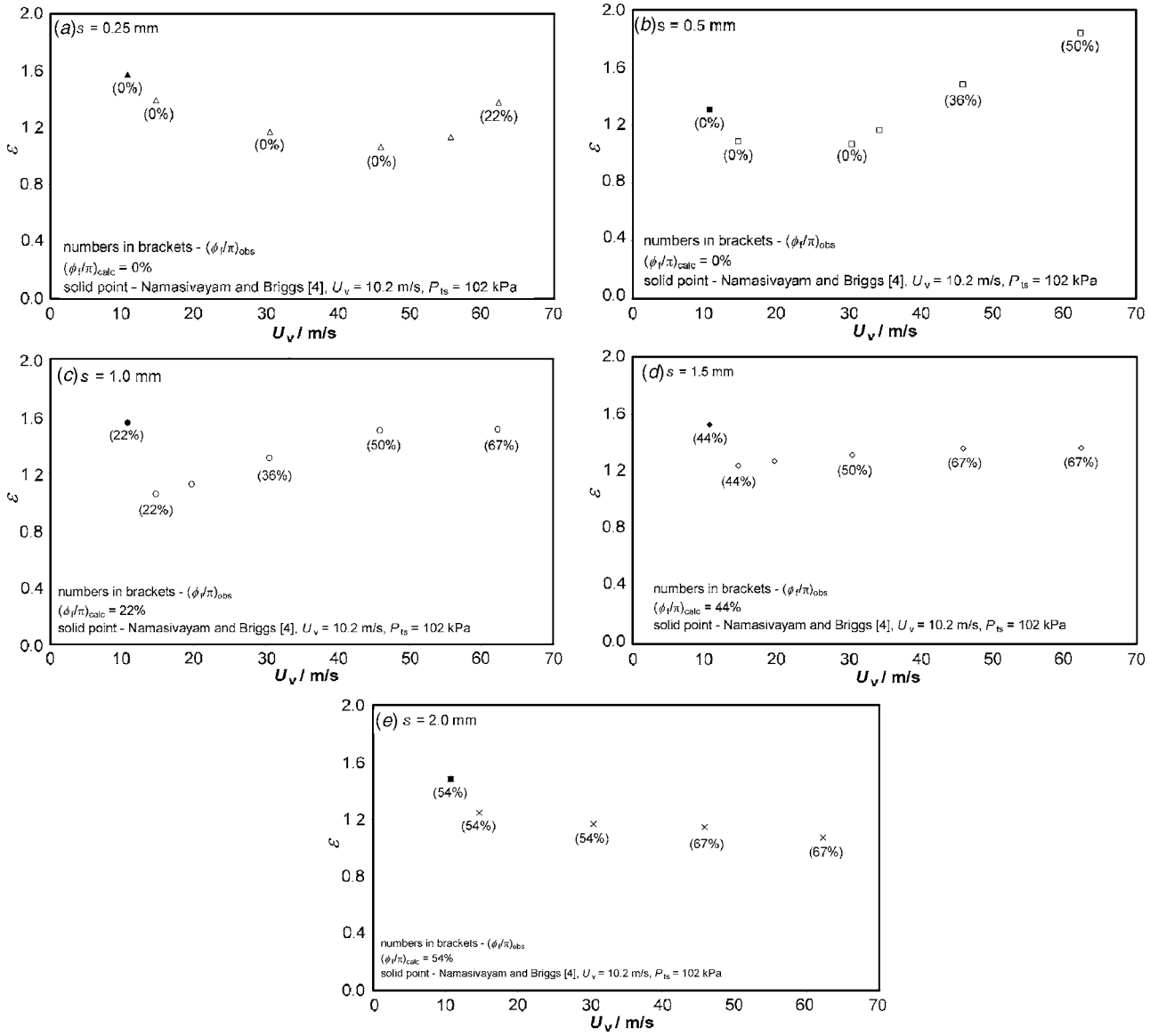

Fig. 6 Variation of enhancement ratio with vapor velocity

velocity, however (different for different fin spacings), the flooding angle begins to increase with increasing vapor velocity, and hence the proportion of the tube covered by retained condensate decreases. This is accompanied in all cases by an increase in enhancement ratio (see, in particular, the tubes with fin spacings of 0.25 and 0.5 mm). It is also interesting to note that the flooding angle never increases beyond 67% (120 deg from the top of the tube), indicating perhaps that vapor boundary layer separation occurs around this point resulting in reduced vapor shear on the bottom of the tube and consequently no further decrease in flooding. Once this point is reached, the flooding angle is unaffected by further increases in vapor velocity and enhancement ratio levels out or even begins to decrease again (see, in particular, the tubes with fin spacings of 1.5 and 2 mm).

With the flooding angle ϕ_f set to the observed value, we can obtain the active surface area enhancement ratio ξ for each tube at each vapor velocity, i.e., the total area of the fin tips plus that of the fin flank and root not covered by retained condensate, divided by the area of a plain tube. When these values are plotted against fin spacing, as in Fig. 7, the trends are similar to those for heat-transfer enhancement shown in Fig. 5. The actual values of ξ are

Table 2 Calculated (using Eq. (7)) and observed flooding angles

s/mm	0.25	0.5	1.0	1.5	2.0
$\phi_{f(\text{calc})}/\pi$	0	0	0.22	0.44	0.54
$\phi_{f(\text{obs})}/\pi$ (U_v=14.7 m/s)	0	0	0.22	0.44	0.54
$\phi_{f(\text{obs})}/\pi$ (U_v=30.5 m/s)	0	0	0.36	0.50	0.54
$\phi_{f(\text{obs})}/\pi$ (U_v=45.9 m/s)	0	0.36	0.50	0.67	0.67
$\phi_{f(\text{obs})}/\pi$ (U_v=62.3 m/s)	0.22	0.50	0.67	0.67	0.67

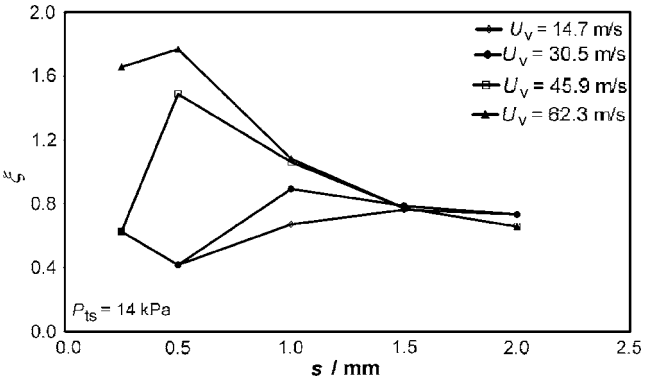

Fig. 7 Variation of active area enhancement with fin spacing

somewhat lower than the equivalent values of ε; however, reflecting the fact that heat-transfer enhancement on the unflooded part of the tubes involves significant surface-tension induced drainage on the unflooded part of the tube and is not simply a result of increased surface area.

Concluding Remarks

New experimental data are presented for forced-convection condensation of low-pressure steam on a set of five single, integral-fin tubes. The geometry of the tubes was the same except for fin spacing, which was varied from 0.25 mm to 2 mm. Vapor velocities between 15 and 62 m/s are reported. The enhancement in the vapor-side, heat-transfer coefficient, compared to a plain tube at the same vapor-side temperature difference and vapor velocity, was found to be strongly influenced by both fin spacing and vapor velocity. At relatively low velocities, the enhancement ratio decreased with increasing vapor velocity in line with results of previous investigations. At some critical vapor velocity, however, which was different for different fin spacings, vapor shear on the condensate film began to reduce the extent of condensate retention between the fins at the bottom of the tube and this was accompanied in all cases by an increase in the enhancement ratio. This dependence of flooding angle on vapor velocity will need to be incorporated in any future model if such a model is to predict the complex trends in the data reported in this work.

Nomenclature

A = constant in Eq. (5)
a = constant in Eq. (1)
b = constant in Eq. (2)
c_p = specific isobaric heat capacity
d = diameter of plain tube or fin-root diameter of finned tube
d_i = inside diameter of tube
d_o = fin-tip diameter of finned tube
F = dimensionless parameter, $\mu g d h_{fg}/kU_v^2\Delta T$
g = specific force of gravity
h = fin height
h_{fg} = specific enthalpy of evaporation
k = thermal conductivity
Nu = vapor-side Nusselt number, $\alpha d/k$
Nu_c = coolant-side Nusselt number, $\alpha_c d_i/k_c$
n = constant in Eq. (5)
q = heat flux based on surface area of plain tube with diameter equal to fin-root diameter
q_i = heat flux based on inside surface area of tube
P_{ts} = test section pressure
Pr_c = coolant Prandtl number, $\mu_c c_{pc}/k_c$
Re_c = coolant Reynolds number, $\rho_c U_c d_i/\mu_c$
Re_{tp} = two-phase Reynolds number, $\rho U_v d/\mu$
s = fin spacing
T_{cool} = mean (inlet to outlet) coolant temperature
T_v = vapor temperature
T_w = mean outside tube wall temperature (at fin root for finned tube)
T_{wi} = mean inside tube wall temperature
U_v = vapor velocity upstream of test tube
U_c = mean coolant velocity

Greek Symbols

α = vapor-side, heat-transfer coefficient, $q/(T_v - T_w)$
α_c = coolant-side, heat-transfer coefficient based on inside surface area of tube, $q_i/(T_{wi} - T_{cool})$
ΔT = vapor-side temperature difference (vapor saturation temperature minus mean outside wall temperature at fin root)
ρ = density
ε = heat-transfer enhancement ratio (vapor-side, heat-transfer coefficient for the finned tube based on fin-root diameter, divided by that for the plain tube with fin-root diameter, at same vapor-side temperature difference and vapor velocity)
μ = viscosity
ξ = active area enhancement ratio
σ = surface tension of condensate
ϕ_f = retention angle (position at which fin space becomes fully flooded with condensate) measured from top of tube

Subscripts (No Subscript Pertains to Condensate)

c = evaluated at mean coolant temperature
calc = calculated from Eq. (7)
finned = pertaining to finned tube
obs = observed
plain = pertaining to plain tube
wi = evaluated at tube inside wall temperature

References

[1] Michael, A. G., Marto, P. J., Wanniarachchi, A. S., and Rose, J. W., 1989, "Effect of Vapour Velocity During Condensation on Horizontal Smooth and Finned Tubes," *Proceedings of ASME Winter Annual Meeting*, San Francisco, HTD-Vol. 114, 1–10.
[2] Bella, A., Cavallini, A., Longo, G. A., and Rossetto, L., 1993, "Pure Vapour Condensation of Refrigerants 11 and 113 on a Horizontal Integral-Fin Tube at High Vapour Velocity," J. Enhanced Heat Transfer, **1**, pp. 77–86.
[3] Cavallini, A., Doretti, L., Longo, G. A., and Rossetto, L., 1994, "Experimental Investigation of Condensate Flow Patterns on Enhanced Surfaces," *Proceedings of CFC's, The Day After, IIR International Conference*, Padua, pp. 627–634.
[4] Namasivayam, S., and Briggs, A., 2004, "Effect of Vapour Velocity on Condensation of Atmospheric Pressure Steam on Integral-Fin Tubes," Appl. Therm. Eng., **24**, pp. 1353–1364.
[5] Namasivayam, S., and Briggs, A., 2005, "Condensation of Ethylene Glycol on Integral-Fin Tubes—Effect of Fin Geometry and Vapor Velocity," Trans. ASME, Ser. C: J. Heat Transfer, **127**, pp. 1197–1206.
[6] Namasivayam, S., and Briggs, A., 2006, "Condensation of Atmospheric Pressure Steam on Integral-Fin Tubes—Effect of Fin Height and Vapour Velocity," *Proceedings of 13th International Heat Transfer Conference*, Sydney.
[7] Cavallini, A., Doretti, L., Longo, G. A., and Rossetto, L., 1996, "A New Model for Forced-Convection Condensation on Integral-Fin Tubes," ASME J. Eng. Gas Turbines Power, **118**, pp. 689–693.
[8] Briggs, A., and Rose, J. W., 1994, "Effect of Fin Efficiency on a Model for Condensation Heat Transfer on a Horizontal, Integral-Fin Tube," Int. J. Heat Mass Transfer, **37**(1), pp. 457–463.
[9] Sieder, E. N., and Tate, G. E., 1936, "Heat Transfer and Pressure Drop of Liquids in Tubes," Ind. Eng. Chem., **28**, pp. 1429–1435.
[10] Shekriladze, I. G., and Gomelauri, V. I., 1966, "Theoretical Study of Laminar

Film Condensation of Flowing Vapor," Int. J. Heat Mass Transfer, **9**, pp. 581–591.
[11] Rose, J. W., 1984, "Effect of Pressure Gradient in Forced-Convection Film Condensation on a Horizontal Tube," Int. J. Heat Mass Transfer, **27**, pp. 39–47.
[12] Kline, S. J., and McClintock, F. A., 1953, "Describing Uncertainties in Single-Sample Experiments," Mech. Eng. (Am. Soc. Mech. Eng.), **75**, pp. 3–8.
[13] Briggs, A., 1991, "Forced-Convection Condensation on Horizontal, Integral-Fin Tubes," Ph.D Thesis, University of London.
[14] Nusselt, W., 1916, "Die Oblerflachenkondensation des Wasserdampfes," Z. Vereines Deutsch. Ing., **60**, pp. 541–546 and 569–575.
[15] Honda, H., Nozu, S., and Mitsumori, K., 1983, "Augmentation of Condensation on Finned Tubes by Attaching a Porous Drainage Plate," *Proceedings of ASME-JSME Thermal Engineering Joint Conference*, Vol. 3, pp. 289–295.

A Convection Heat Transfer Correlation for a Binary Air-Helium Mixture at Low Reynolds Number

Arindam Banerjee
Post Doctoral Research Associate
Los Alamos National Laboratory,
Los Alamos, NM 87545

Malcolm J. Andrews[1]
National Security Fellow
Los Alamos National Laboratory,
P.O. Box 1663, Mail Stop D413,
Los Alamos, NM 87545
and
Department of Mechanical Engineering,
Texas A&M University,
College Station, TX 77840
e-mail: mandrews@lanl.gov

The results of experiments investigating heat transfer from a hot wire in a binary mixture of air and helium are reported. The measurements were made with a constant temperature anemometer at low Reynolds numbers $(0.25 < \mathrm{Re} < 1.2)$ *and correlated by treating the data in terms of a suitably defined Reynolds and Nusselt numbers based on the wire diameter. The correlation was obtained by taking into account the temperature dependency of gas properties, properties of binary gas mixtures, and the fluid slip at the probe surfaces as well as gas accommodation effects. The correlation has been used to measure velocity and velocity-density statistics across a buoyancy driven Rayleigh–Taylor mixing layer with a hot wire. The measured values obtained with the correlation agree well with measurements obtained with a more rigorous and extensive calibration technique (at two different overheat ratios). The reported correlation technique can be used as a faster and less expensive method for calibrating hot wires in binary gas mixtures.*
[DOI: 10.1115/1.2764086]

Keywords: convection heat transfer, hot-wire correlation, air-helium mixture

1 Introduction

The validation of predictive turbulent transport models for inhomogeneous, anisotropic, and variable-density flows requires a priori knowledge of various velocity, density, and velocity-density statistics. However, the measurement of these quantities in a variable-density turbulent flow of gas mixtures is challenging and has been of much interest over the last 50 years [1]. A commonly used measurement technique employs a hot wire at different overheat ratios to simultaneously measure time-averaged velocity and density statistics [2–5]. Alternatively, a combination of Rayleigh light scattering for density measurement and hot-wire anemometry for velocity measurement has been used [1,6]. However, in either case, it is necessary to carefully calibrate the hot-wire response as a function of velocity and density. The usual method [7] is to develop empirical laws from calibration data that allow prediction of wire response in various gas mixtures. This paper describes the behavior of hot wires in a binary air-helium mixture and describes a heat transfer correlation for use in place of more elaborate calibration techniques [3–5].

The choice of air and helium as the two gases in this study is because of their use as the two fluids in our high Atwood number Rayleigh–Taylor experiment [8]. The experimental facility uses two gas streams, one containing-air and the other containing a helium-air mixture, that flow parallel to each other and separated by a thin splitter plate (see Fig. 1(*a*)). The streams meet at the end of a splitter plate leading to the formation of an unstable interface and a buoyancy driven mixing downstream of the splitter plate as shown in Fig. 1(*b*) [2,8]. The facility was designed for high Atwood number studies $(0 \leqslant \mathrm{At} \leqslant 0.75)$, where the Atwood number, At denotes the governing nondimensional density difference of the flow defined by $\mathrm{At} \equiv (\rho_h - \rho_l)/(\rho_h + \rho_l)$, where ρ_h and ρ_l are the densities of air (heavy fluid) and the air-helium mixture (light fluid).

Our main application of interest is the implosion phase of an inertial confinement fusion (ICF) capsule where RT mixing is formed at high Atwood numbers [9]. Our incompressible, adjustable Atwood experiment captures the same inertial dynamics associated with the fluid motion. However, since the present experimental setup can be used over a wide range of Atwood numbers $(0 \leqslant \mathrm{At} \leqslant 0.75)$, it mimics a variety of other applications, such as atmospheric instability associated with cold air overlaying warm air in the atmosphere [10], buoyant jets [11], and fingerlike ejecta of stellar materials present in the remnants of a young supernova [12]. Other applications using air-helium mixtures include the use of the gases in hypersonic wind tunnels to attain Mach numbers as high as 35 [13]. The use of helium in the mixture helps in attaining the high Mach number flows without heating the supply gas to avoid condensation in the test section [13].

2 Convection Correlations

The use of a hot-wire probe for measuring velocity fluctuations depends on correlations that govern convective heat transfer from a cylinder. These correlations are generally complicated and do not admit a theoretical evaluation over a Reynolds number (Re) range of 0.1–100. Furthermore, it is necessary to account for nonuniform wire temperature due to end cooling (conduction end losses), for which there has been extensive theoretical work to compute temperature distributions, and correction procedures have been devised [14–17]. However, such formulations are complicated to use [15], and experimental data are thus correlated using similarity principles [7,17,18]. A dimensional analysis of the governing equations shows that the dimensionless heat transfer coefficient (or Nusselt number, Nu) for an electrically heated hot wire in an incompressible fluid flow has the general form [19]

$$\mathrm{Nu} = \mathrm{Nu}(\mathrm{Re}, \mathrm{Gr}, \mathrm{Kn}, \mathrm{Pr}, \Theta, l_w/d_w) \tag{1}$$

This analysis takes into account the variation in the wire transfer due to buoyancy, rarefaction effects, fluid slip, and well finite

[1]Corresponding author.

Contributed by the Heat Transfer Division of ASME for publication in the JOURNAL OF HEAT TRANSFER. Manuscript received October 18, 2006; final manuscript received April 7, 2007. Review conducted by Anthony M. Jacobi.

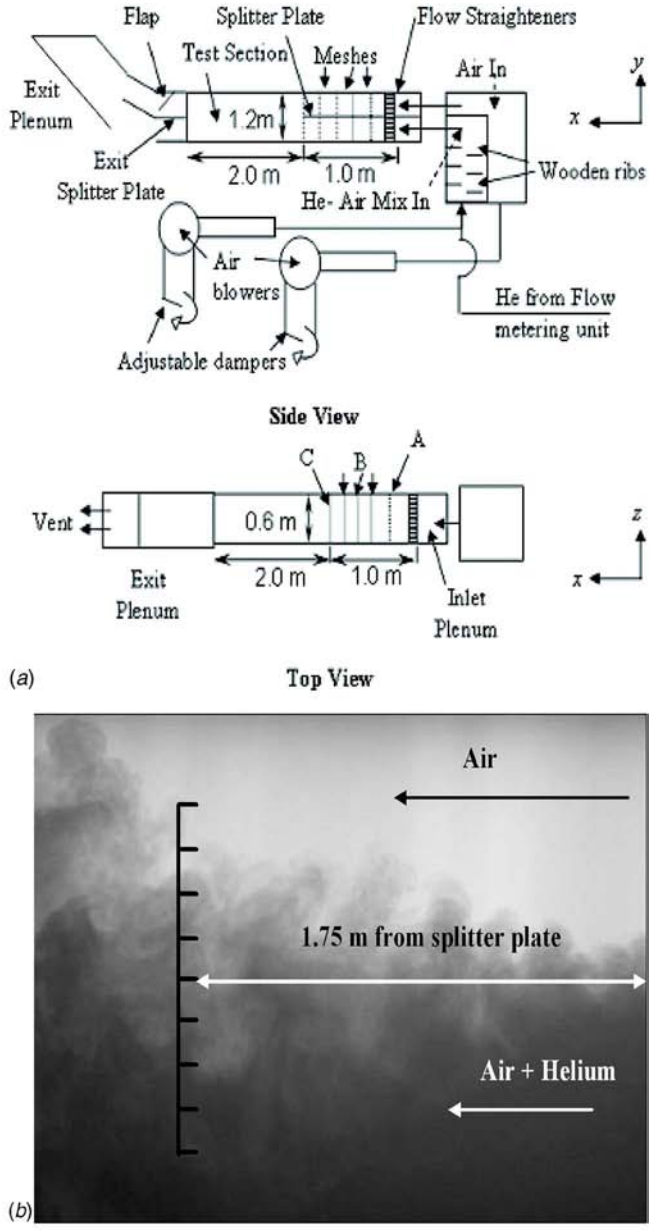

Fig. 1 (*a*) Schematic of gas channel facility. (*b*) Photograph of the mixing layer at an Atwood number of 0.04 with the location of hot wires in relation to the splitter plate.

aspect ratio of hot wires. Details about these effects are provided later. For the present study, the hot wire used is 5 μm in diameter and 1.25 mm long. For the velocity range in our air-helium RT experiments ($0.2\ \text{m/s} < \bar{U} < 3.0\ \text{m/s}$), the wire Reynolds number lies in the range of $0.06 < \text{Re} < 1.0$, and thus our literature review is restricted to low Reynolds number (low velocity) convection correlations for hot wires.

2.1 Forced Convection Correlations. King [14] performed a rigorous theoretical treatment and a detailed experimental investigation about the heat loss from platinum anemometer wires. He used a whirling arm in air and showed that the Nusselt number (Nu) could be expressed as

$$\text{Nu} = A + B\,\text{Re}'' \tag{2}$$

where A and B are constants that depend on the temperature and dimensions of the wire, with fluid properties evaluated at the free stream temperature (T_{fluid}). King assigned a value of $n=0.5$ to fit his experimental data. An analytical solution was also obtained by assuming a potential flow across the cylinder. However, the experiments were subject to interference from draughts, both natural and induced, and the results had significant systematic errors [4]. McAdams [20] formulated forced convection results for a wide range of Reynolds number ($0.1 < \text{Re} < 1000$), and his measured data were correlated as follows:

$$\text{Nu} = 0.32 + 0.43\,\text{Re}^{0.52} \tag{3}$$

A major difference between his work and the work of King [14] was that the thermal conductivity (k) and absolute (dynamic) viscosity (μ) was evaluated at the mean film temperature (T_{film}) and the density (ρ) was evaluated at the free stream temperature (T_{fluid}). Collis and Williams [7] analyzed all the available data and proposed a correlation for the range of $0.02 < \text{Re} < 140$. All properties were evaluated at T_{film}. They observed vortex shedding from the hot wire at a Re of approximately 44, and the measured data were correlated as follows:

$$\text{Nu}\left(\frac{T_{\text{film}}}{T_{\text{fluid}}}\right)^{-0.17} = 0.24 + 0.56\,\text{Re}^{0.45} \quad \text{for } 0.02 \leqslant \text{Re} < 44$$

$$= 0.48\,\text{Re}^{0.51} \quad \text{for } 44 < \text{Re} < 140 \tag{4}$$

For experiments done with hot wires, the wire diameter is sufficiently small for molecular effects that take the form of a jump in temperatures between the surface of the wire and the fluid adjacent to it [7]. The fluid slips or moves over the wire surface with a finite velocity. In rarefied gas dynamics, the ratio of the mean free path to the wire diameter, the Knudsen number (Kn), is used to characterize molecular effects. Collis and Williams [7] showed that molecular effects reduce the heat transfer from very fine wires by an amount that can be estimated by assuming that the temperature difference was reduced by a temperature jump that can be predetermined from the kinetic theory, and to account for this temperature jump, a temperature ratio in Eq. (4) was used. Collis and Williams [7] also showed that the major effect of the end cooling in the measured value of Nu was to alter the constants A and B in Eq. (2) but not the power of Re.

2.2 Free and Mixed Convection Correlations. Considerable work has been reported on free convection from cylinders [15,20,21]. The correlation takes the form of

$$\text{Nu} = \text{Nu}(\text{Gr}, \text{Pr}, \Theta) \tag{5}$$

A theoretically derived expression for Eq. (5) was provided by McAdams [20] based on a boundary layer approximation. Van der Hegge Zijnen [21] reviewed all available data and proposed a correlation (see Table 1), and the physical properties were evaluated at T_{film}. Few studies have been made to analyze the combined effects of free and forced convection. However, Van der Hegge Zijnen [21] suggested combining the two types of heat transfer vectorially. Subsequently, using a more fundamental analysis of the problem [22–24], it was found that the two effects were nonadditive, and the transition from one effect to an other was a gradual one guided by the parameter Gr/Re^2. However, due to a gradual shift from one convection mode to an other, it was difficult to predict the value of Gr/Re^2 that determines which convection mode would dominate. Also the parameter Gr/Re^2 does not take into account viscous effects and is less accurate for $\text{Pr} > 1$. Collis and Williams [7] chose the transition point as the regime, where Nu for mixed convection equals that for pure convection at the same Gr. Collis and Williams concluded that buoyancy effects were negligible for $\text{Re} > \text{Gr}^{1/3}$. In the present work, the ratio of $\text{Re}/\text{Gr}^{1/3} \sim 100$, and thus free convection effects have been neglected in the analysis. Table 1 provides a list of convection heat transfer correlations for a heated wire in free, mixed, and forced convection regimes. Parameters such as overheat ratio, l/d ratio,

Table 1 Convection heat transfer correlations for flow over a heated cylinder

Author	*Mode of convection*	Correlation equation	Θ	l_w/d_w	Kn	Re
King [14]	Forced	$Nu=0.318+0.69\,Re^{0.50}$	0.5–3.5	>1000	<0.01	0.055–55
Hilpert [45]	Forced	$Nu=0.891+[Re(T_w/T_{amb})^{0.25}]^{0.33}$	0.14–3.47	~100–500	<0.005	1–4
McAdams [20]	Forced	$Nu=0.32+0.43\,Re^{0.52}$				$0.1-10^3$
Van der Hegge Zijnen [21]	Forced	$Nu=0.38\,Pr^{0.2}+(0.56\,Re^{0.50}+0.001\,Re)Pr^{0.33}$	0.34	553	≪0.01	$0.01-10^4$
	Free	$Nu=0.35+0.25(Gr\times Pr)^{1/8}+0.45(Gr\times Pr)^{1/4}$				
Collis and Williams [7]	Forced	$Nu(T_m/T_{amb})^{-0.17}=0.24+0.56\,Re^{0.45}$	0.1–1.0	~2000–8000	0.001–0.03	0.02–44
		$=0.48\,Re^{0.51}$				44–140
Churchill et al. [46]	Forced	$Nu=0.535\,Re^{0.50}(T_w/T_{amb})^{0.12}$				300–2300
Davies and Fisher [47]	Combined	$Nu=(2.6/\gamma\pi)Re^{0.33}$	~1	400–1200	<0.01	0–50
Parnas [48]	Forced	$Nu=0.823\,Re^{0.50}(T_w/T_{amb})^{0.085}$	0.2–2.5	1000	0.0015	10–60
Andrews et al. [17]	Combined	$Nu_c=0.34+0.65\,Re^{0.45}$	0.05–2.5	~24–1300	0.003–0.12	0.015–20
Present work	Forced	$Nu_c=0.2719+0.3763\,Re^{0.5}$	1.7	250	~0.01	0.25–1.2

Kn, and Re, which are relevant for our air-helium RT experiment, are given in Table 1.

2.3 Measurements in Gas Mixtures. The present work formulates a correlation to predict the heat transfer from a hot wire (cylinder) for a binary gas mixture of air and helium over the entire mixture fraction range. Our correlation takes into account effects of thermal slip and nonlinear variation of the mixture properties as we incorporate measured calibration data into the correlation by taking into account adjustments arising from these effects. Previous work to investigate the response of a hot wire to various gas mixtures includes helium-air and argon-air mixtures [25–27], an air and carbon dioxide mixture [4,28], as well as nitrogen-helium and nitrogen-neon mixtures [29]. The present work fits air-helium calibration data to King's law as earlier work [25–29] used a similar approach to fitting their data. Corrisin [4] attempted to predict the velocity of a gas mixture by performing calibration in only one of the pure components, which led to a systematic error in the velocity measurements. Wasan and Baid [28] performed calibration in both pure components and then used linear interpolation to estimate the velocities for a binary air-carbon-dioxide mixture. However, the properties of gas mixtures suggest that if the two pure components have significantly different molecular weights, then properties such as the viscosity and thermal conductivity of binary mixtures cannot be approximated by a linear combination of the values of the two components [30,31]. The properties of the binary gas mixture are thus calculated based on ideal gas laws and with a detailed discussion in Sec. 4 below.

Calculating Nu for hot-wire probes is challenging as it depends on fluid properties ρ, μ, and k, which vary with temperature. Furthermore, the heat transfer relationship corresponds to a voltage drop across the wire, E_w, and details of the Wheatstone-bridge constant temperature anemometry (CTA) circuit as well as the wire electrical properties must be known accurately (see Table 2 for wire properties). Since the electrical energy supplied to the hot wire is dissipated by convection and conduction to the prongs, for Nu to be determined, the heat loss by conduction from the wire must be known. An accurate estimate of conduction heat loss requires knowledge of the temperature gradient of the wire at the support, which is difficult to obtain. For calibration/correlation purposes, there is a need to formulate a correlation that will hold under experimental conditions.

3 Effect of Temperature Jump on the Heat Transfer Coefficient

The use of small diameter wires ($d_w \leqslant 5\ \mu$m) in thermal anemometry means that noncontinuum effects cannot be ignored at a pressure of 1 atm [7]. There is a discontinuity in the temperature distribution at the wall when heat transfer (by conduction) takes place between a rarefied gas and the heated wire. Assuming T_{wire} as the wall temperature and T_s as the gas temperature, if the temperature gradient remained unchanged up to the surface, the discontinuity or temperature jump at the interface is given by

$$T_{wire} - T_s = -\xi\frac{\partial T}{\partial r} \tag{6}$$

where ξ is the temperature jump distance [32]. For most gases, ξ is of the order of the mean free path of the gas molecules (λ). Kennard [32] derives an expression for ξ in terms of the properties of the gas and the surface as

$$\xi = \frac{2-\chi}{\chi}\frac{2\gamma}{\gamma+1}\frac{\lambda}{\mathrm{Pr}} \tag{7}$$

The accommodation coefficient (χ) quantifies the fraction of energy transfer between an incident gas molecule and the solid surface in a gas-surface interaction. A slip parameter β [33,34] is defined by

$$\beta = \frac{\xi}{d} = \frac{2-\chi}{\chi}\frac{2\gamma}{\gamma+1}\frac{\mathrm{Kn}}{\mathrm{Pr}} \tag{8}$$

Equation (8) is a first order approximation that is valid if the velocity and temperature profiles are linear over a distance equal to the mean free path of the gas molecules [34]. However, at high values of Kn, the profiles are significantly nonlinear and this assumption is no longer valid [17]. However, for the present work, the values of Kn ~0.01 are small, and the use of a linear approximation is justified. The heat flux q'' from the wire is

Table 2 Wire properties at overheat ratios of 1.9, 1.7, and 1.6

Probe specific parameters			
Sensor resistance R_{20} (Ω)		3.38	
Sensor lead resist R_L (Ω)		0.9	
Support resistance R_s (Ω)		0.44	
Cable resistance R_c (Ω)		0.2	
Sensor TCR, α_{20} (/K)		0.0036	
Wire operating parameters			
Overheat ratio ($=R_w/R_{amb}$)	1.9	1.7	1.6
$\Delta T=T_w-T_{amb}$ (°C)	257.14	190	171.43
Operating resistance R_w (Ω)	6.51	5.75	5.47
Total resistance R_T (Ω)	7.99	7.29	6.98
Decade resistance R_D (Ω)	159.83	145.9	139.55
Bridge ratio M		1:20	

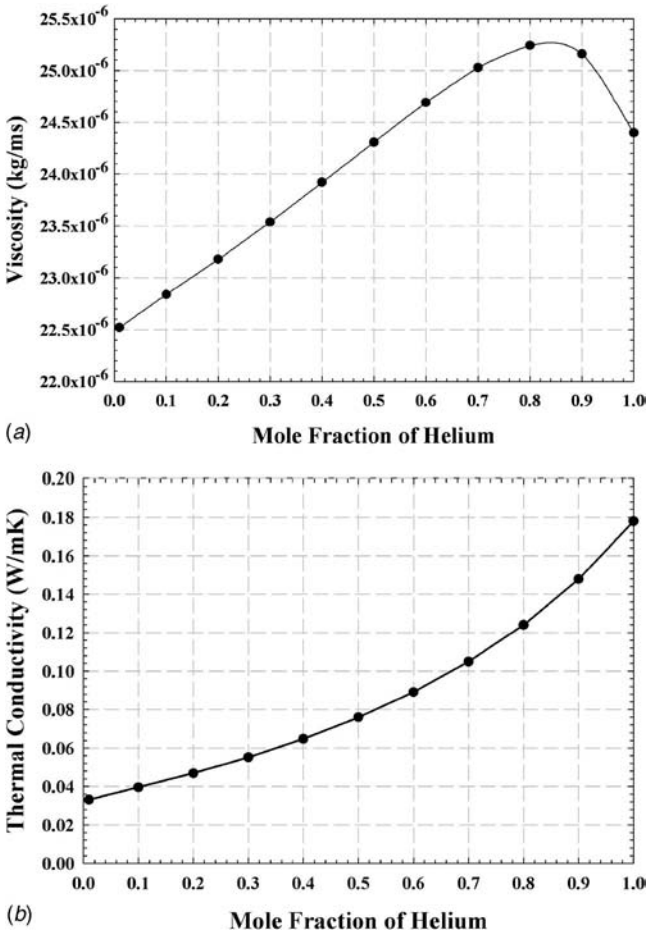

Fig. 2 Absolute viscosity and thermal conductivity of an air-helium mixture. The properties of the pure gases are evaluated at $T_{film}=(T_{wire}+T_{fluid})/2$. The properties are obtained using formulations from Wilke [30] and Mason and Saxena [31].

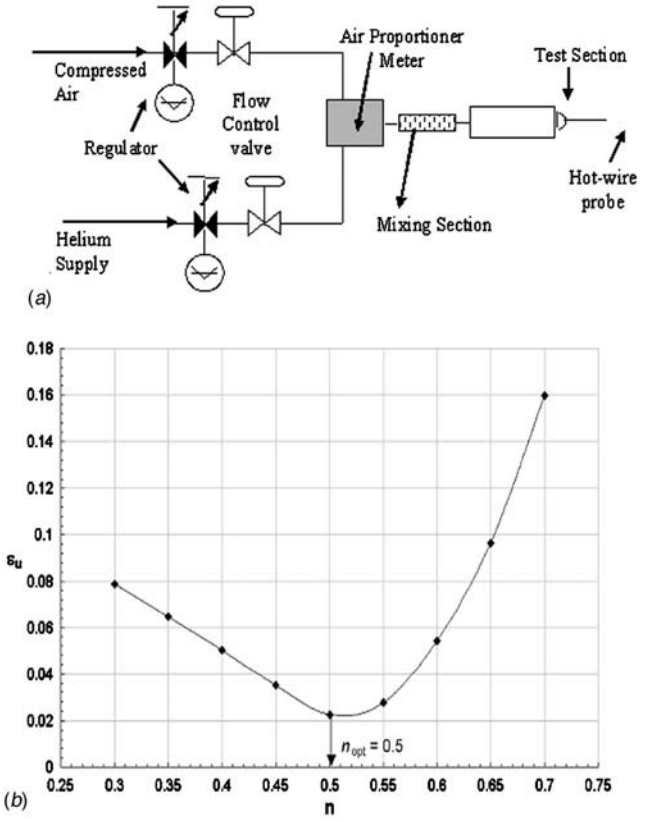

Fig. 3 (*a*) Schematic of the setup used for hot-wire calibration. (*b*) Plot of ε_u (normalized standard deviation, See Sec. 6) as a function of the exponent *n* in King's law (Eq. (2)). ε_u is based on the calibration data in air at an overheat ratio of 1.7 over a velocity range of 0.2–3 m/s.

$$q'' = h_s(T_s - T_{\text{fluid}}) = h_w(T_{\text{wire}} - T_{\text{fluid}}) \tag{9a}$$

and Eq. (9*a*) can be rewritten as

$$h_s = h_w\left(1 + \frac{T_{\text{wire}} - T_s}{T_s - T_{\text{fluid}}}\right) \tag{9b}$$

Formulations incorporating axial heat loss to the prongs and nonuniform temperature distribution are complex [15], and we have it calibrated directly with the experimental condition. Considering heat loss by conduction from the wire, $q'' = -k(\partial T/\partial r)|_{T=T_s}$, and combining with Eqs. (6) and (9*a*) gives

$$\frac{T_{\text{wire}} - T_s}{T_s - T_{\text{fluid}}} = \frac{\xi_{T_s} h_s}{k_{T_s}} \tag{10}$$

For the wire, the continuum Nusselt number Nu_c is defined as $\text{Nu}_c = h_s d_w / k_{T_{\text{film}}}$, while the Nusselt number Nu is defined as $\text{Nu} = h_w d_w / k_{T_{\text{film}}}$. Combining Eqs. (9*b*) and (10) gives the relation [7]

$$\text{Nu}_c = \frac{\text{Nu}}{1 - \text{Nu}\dfrac{\xi_{T_s} k_{T_{\text{film}}}}{k_{T_s} d_w}} \tag{11}$$

For a perfect gas at a constant pressure, it is known that $\text{Kn} \propto T^{0.5+g}$, $\mu \propto T^g$, and $k \propto T^f$ [17]. The values of g and f were chosen as 0.68 and 0.8, respectively [25]. Then, Eq. (11) can be written as

$$\text{Nu}_c = \frac{\text{Nu}}{1 - \sigma\,\text{Kn} \times \text{Nu}} \tag{12}$$

where Kn is evaluated at T_{film} and σ is given by

$$\sigma = \frac{2-\chi}{\chi}\frac{2\gamma}{\gamma+1}\frac{1}{\text{Pr}}\bigg|_{T_s}\left(\frac{T_s}{T_{\text{film}}}\right)^{0.5+g-f} \tag{13}$$

Thus, if all the properties are known, Nu_c can be calculated. One problem with using Eq. (13) was the determination of the thermal accommodation coefficient χ. A number of reviews indicate that there is a no agreement of the values of χ for a given combination of a gas on a metal surface. The value of χ is a strong function of the properties of the wire surface. It varied by a factor of 10 between a clean surface and one that was contaminated [35]. Andrews et al. [17] listed a comparison of accommodation coefficients of different gas-metal combinations. The hot-wire probes used in the present study were made of platinum plated tungsten (Dantec Dynamics). Accommodation coefficients of 0.02 for the He–Pt/W interface and 0.90 for the air-Pt/W interface were used based on the values available in Ref. 17. For intermediate gas mixtures, the accommodation coefficient was assumed to be a linear combination of the mole fraction of the two components.

4 Properties of Binary Gas Mixtures

The mix density (ρ_{mix}) is used to calculate the Reynolds number ($\text{Re}=\rho_{\text{mix}}\bar{U}d_{\text{wire}}/\mu_{\text{mix}}$) of the flow. For our binary gas mixtures of air and helium, the mix density was determined from ideal gas laws as a linear combination of the mole fraction of the components (1: air; 2: helium).

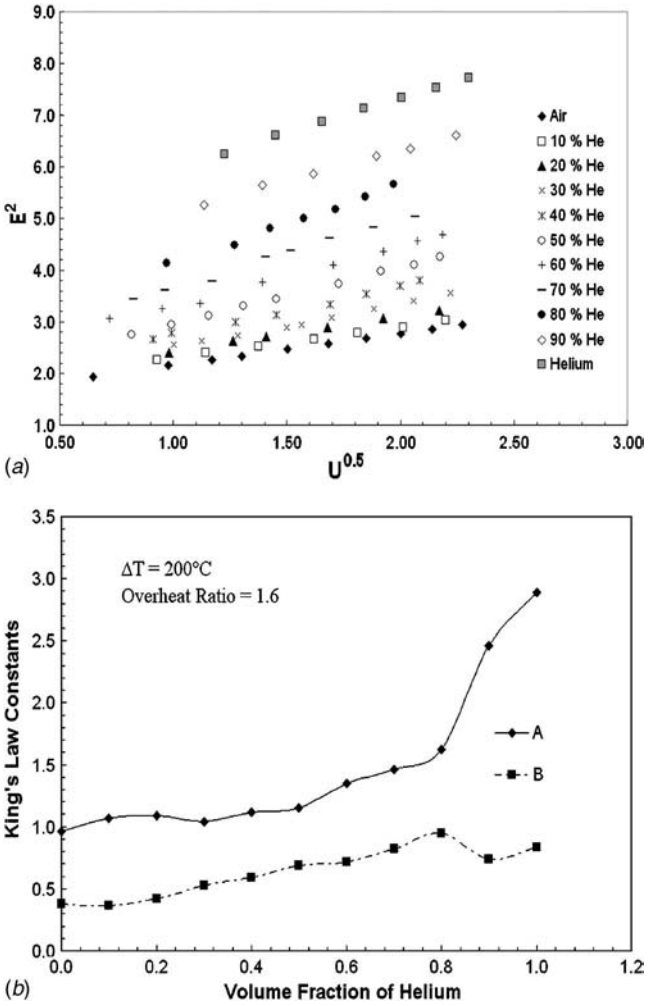

Fig. 4 (*a*) Hot-wire calibrations at different mole fractions of helium in a binary air-helium mixture. The uncertainty in voltage (*E*) measurements was 0.5%. (*b*) Variation in King's law (Eq. (2)) constants for different volume (mole) fractions of helium.

$$\rho_{\text{mix}} = \rho_1 x_1 + \rho_2 x_2 \tag{14}$$

where x_1 and x_2 are the mole fractions of the individual components in the mixture. The viscosity of the mixture (μ_{mix}) was determined from an accurate method by Wilke [30],

$$\mu_{\text{mix}} = \mu_1\left(1 + \frac{x_2}{x_1}\Phi_{12}\right)^{-1} + \mu_2\left(1 + \frac{x_1}{x_2}\Phi_{21}\right)^{-1}$$

where

$$\Phi_{ij} = \left[1 + \left(\frac{\mu_i}{\mu_j}\right)^{1/2}\left(\frac{M_j}{M_i}\right)^{1/4}\right]^2\left[8\left(1 + \frac{M_i}{M_j}\right)\right]^{1/2} \quad i \neq j \tag{15}$$

and M_1 and M_2 are the molecular weights of the pure gases. The thermal conductivity of the gas mixture (k_{mix}) is used to evaluate the continuum Nusselt number (Nu_c) and is obtained by using a kinetic theory based formula from Mason and Saxena [31],

$$k_{\text{mix}} = k_1\left(1 + \frac{x_2}{x_1}\Phi'_{12}\right)^{-1} + k_2\left(1 + \frac{x_1}{x_2}\Phi'_{21}\right)^{-1}$$

where

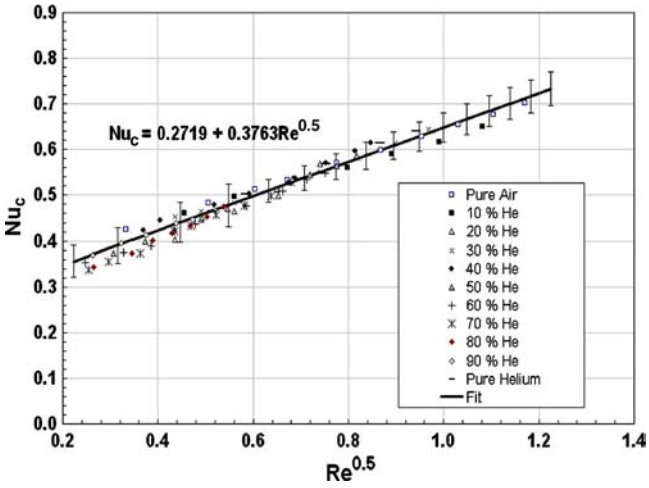

Fig. 5 Nusselt number correlation for a binary gas mixture of air and helium

$$\Phi'_{ij} = 1.065\left[1 + \left(\frac{k_i P_j}{k_j P_i}\right)^{1/2}\left(\frac{M_j}{M_i}\right)^{1/4}\right]^2\left[8\left(1 + \frac{M_i}{M_j}\right)\right]^{-1/2} \quad i \neq j \tag{16}$$

and

$$P_i = 0.115 + 0.354(c_{pi}/R_i)$$

Figure 2 shows the variation in viscosity and thermal conductivity for different mole fractions of helium.

The specific heat at a constant volume (C_v) and the specific heat at a constant pressure (C_p) were determined from ideal gas laws and is expressed as linear combinations of their mole fraction of the components (1: air; 2: helium)

$$C_{v,\text{mix}} = C_{v1}x_1 + C_{v2}x_2 \tag{17}$$

$$C_{p,\text{mix}} = C_{p1}m_1 + C_{p2}m_2 \tag{18}$$

All properties for the pure gases were obtained from thermodynamic tables [36] that were derived from an equation of state.

5 Calibration Facility and Electronics

A calibration was performed to establish the relation between CTA output and flow velocity by exposing the probe to a set of known velocities, $\bar{U}$, and then recording the voltages, E_w. A curve fit through the points $(E_w, \bar{U})$ gave the transfer function for converting data records from voltages into velocities. The hot-wire calibration needs to be verified to incorporate the individual features of each probe to include variations in anemometer circuits and settings as well as variations in the flow temperature. As a check before an experiment, a reference voltage reading was recorded by placing the probe in a known flow velocity. The temperature of the flow as well as the ambient room temperature was logged. This procedure was done to ensure that a reference point (voltage reading) during the experiment matched with the calibration. Later, during the experiment, if the mean temperature of the flow (T_{fluid}) varied from the temperature during calibration, the CTA records were corrected for temperature variations using [37],

$$E_{\text{corr}} = \left(\frac{T_{\text{wire}} - T_{\text{fluid}}}{T_{\text{wire}} - T_{\text{calib}}}\right)^{0.5} E_w \tag{19}$$

Typically, a calibration is either carried out in a dedicated probe calibrator or in a wind tunnel with a pitot-static tube giving the velocity reference [38–40] and the velocity evaluated from a difference in the pressure reading, ΔP, across the pitot static tube or a calibration nozzle. However, at low speeds ($\leqslant$3 m/s), the value

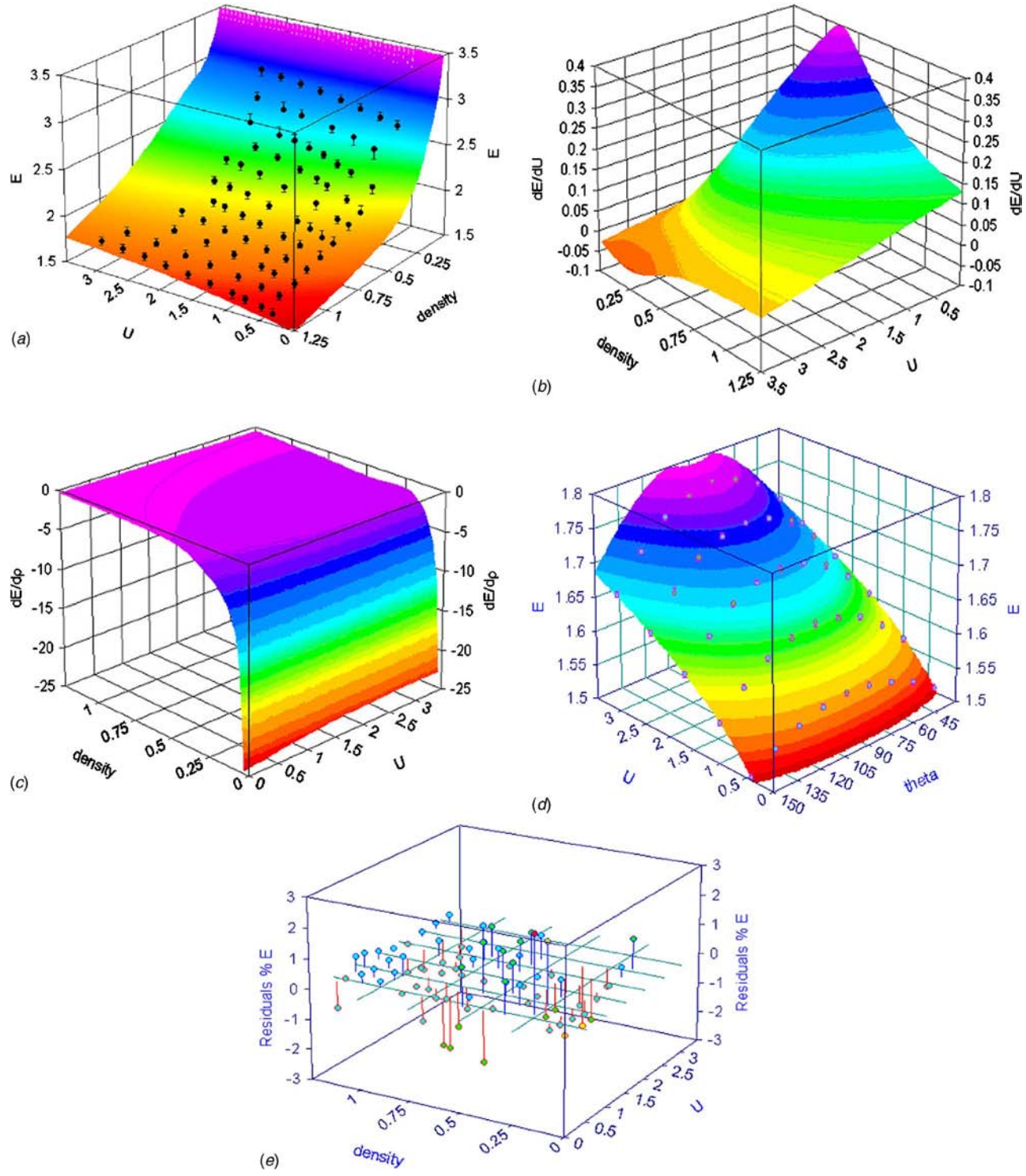

Fig. 6 (*a*) **Calibration data, wire sensitivities** (*b*) ***dE/dU*** **and** (*c*) ***dE/dρ***, (*d*) **directional calibration, and** (*e*) **errors in curve fit at an overheat ratio of 1.9 using a detailed calibration technique**

of ΔP in air becomes small (<1 mm of water), and it is difficult to obtain accurate estimates of velocities by this method. For the present study, a separate jet-flow calibration was used, as shown in Fig. 3(*a*). Similar methods have been used by a number of investigations [41–44]. A pressure regulator controlled the supply from the compressed air line ($\sim$100 psi gauge), and the air supply was fed to a proportioner meter (model No. P21A1-BA2, Aalborg Corp.) to give air flow rates up to 60 l/min. The two streams of air and helium were metered to obtain various fractions of the air-helium mixture and to give a calibration over a velocity range of 0.2–3.0 m/s. To facilitate mixing of the two gas streams, a small chamber was made by interconnecting a polyvinyl chloride (PVC) pipe and a coupling (both $\frac{1}{2}$ in. diameter$\times$1 in. long and $\frac{1}{2}$ in. diameter). The PVC pipe was added after the mixing section to create a jet of the air-helium mixture. The hot wire was inserted

Table 3 Density-velocity calibration curve fit constants $\{E=[a'+b'U+c'\ \ln\rho+d'(\ln\rho)^2+e'(\ln\rho)^3]/[1+f'U+g'U^2+h'\ln\rho+i'(\ln\rho)^2]\}$ for the three SN hot wires at overheat ratios 1.9 and 1.6

Wire No.	Overheat ratio	a'	b'	c'	d'	e'	f'	g'	h'	i'	R^2	Std. error
1	1.9	1.5976	0.1463	1.3361	0.2830	−0.3407	−0.0130	0.0108	1.1226	0.5621	0.9977	0.020
	1.6	1.3724	0.1134	1.1518	0.2654	−0.2841	−0.0225	0.0118	1.1169	0.5595	0.9975	0.018
2	1.9	1.6011	−0.0301	0.7095	0.6301	−0.3269	−0.1125	0.0140	0.7324	0.5883	0.9949	0.030
	1.6	1.3512	−0.1685	0.1663	0.8276	−0.2509	−0.2266	0.0228	0.3712	0.6022	0.9900	0.036
3	1.9	1.6654	−0.0097	0.6075	0.6085	−0.3125	−0.1173	0.0177	0.6509	0.5326	0.9991	0.014
	1.6	1.4410	0.0406	0.7200	0.3601	−0.2715	−0.0809	0.0151	0.7900	0.5038	0.9992	0.010

downstream at the end of the PVC pipe so that it was well within the fully developed velocity profile.

In summary, the complete measuring system used in the present study consisted of (a) a single normal hot-wire probe (SN probe: 55P16) with support and a 4 m BNC-BNC probe cable, (b) a mini-CTA anemometer (54T30) with a built-in signal conditioner and a power adapter, and (c) a SC 2040 sample and hold board (National Instruments) connected to a PCI-MIO-16E-4 analog-digital (A/D) board (National Instruments) mounted in a Pentium 4 computer. The NI-DAQ driver software and LABVIEW DAQ software were used for data collection at desired frequencies. A 55P16 SN probe was used for all the single wire measurements. Various parameters given in Table 2 correspond to specifications for the SN probe (Dantec Dynamics), in which the overheat ratio determines the working temperature (T_{wire}) of the sensor. An overheat adjustment is based on the measured wire resistance at the ambient fluid temperature.

6 Results

6.1 Low Velocity Calibration and Correlation for the Binary Air-Helium Mixture. The velocity range in our RT experiments are low ($0.2\ \text{m/s} < \bar{U} < 3.0\ \text{m/s}$). Consequently, the wire Reynolds number lies in the range of $0.06 < \text{Re} < 1.0$. As a first measure, the value of the exponent n in King's law (Eq. (2)) was determined based on calibration data in air. A voltage-velocity calibration in air was fitted to various exponents from $n=0.3$ to 0.7, and a normalized standard deviation $\varepsilon_u=[1/N\Sigma_{i=1}^{N}(1-\bar{U}/\bar{U}_{\text{calib}})^2]^{1/2}$ was evaluated over the range. n_{opt} was chosen based on the exponent that returned the lowest value of ε_u. The results are plotted in Fig. 3(*b*) and shows the value of $n_{\text{opt}} \approx 0.5$, which is similar to the one used by King [14]. Figure 4(*a*) plots the square of voltages as a function of $U^{0.5}$ for different mole fractions (x_{He}) of helium from pure air ($x_{\text{He}}=0$) to pure helium ($x_{\text{He}}=1.0$) in steps of 0.1 (for an overheat ratio of 1.7). At each mole fraction, the flow velocity was varied over the operational range for the experiment ($0.2\ \text{m/s} < \bar{U} < 3.0\ \text{m/s}$). Figure 4(*a*) plots the calibration data for different mole fractions, which are observed to be linear over the entire range. The R^2 values for these fits range from 0.9930 to 0.9993. Figure 4(*b*) plots the King's law constants A and B as a function of the mole fraction of helium, and it can be seen that slope B increases gradually up to a mole fraction value of 0.9. However, the value of A increases by a factor of 3 over the same range. This indicates the need to perform calibration at volume fraction steps of 0.1 as the trend is not linear, and so extrapolation by calibrating at the two pure components would give poor results.

A correlation was obtained between the Reynolds number ($\text{Re}=\rho_{\text{mix}}\bar{U}d_{\text{wire}}/\mu_{\text{mix}}$) and the continuum Nusselt number from the calibration data. From the viewpoint of obtaining Nu_c, the correlation should be given in terms of wire properties and the properties of the gas mixture. The heat loss for flow over a cylinder was evaluated based on the electrical properties of the CTA circuit and the hot wire (see Table 2), and the Nusselt number was calculated as follows:

$$q'' = h(T_{\text{wire}} - T_{\text{fluid}}) = \frac{E_w^2}{\pi l_w d_w R_w} = \frac{k}{d_w}\text{Nu}(T_{\text{wire}} - T_{\text{fluid}}) \quad (20)$$

Nu_c was then calculated based on Eq. (12). The results of the calibration are correlated below in a form similar to Eq. (2) and are plotted in Fig. 5. It is seen that all the helium-air calibration data points collapse within a narrow band that can be approximated by a straight line ($R^2=0.979$),

$$\text{Nu}_c = 0.2719 + 0.3763\ \text{Re}^{0.5} \quad (21)$$

The data points in the lower Reynolds number range (which also includes the higher mix fraction range) tend to show a high degree of scatter, and this is attributed to significant buoyancy forces as the proportion of helium in the mixture increases. However, although the calibration was performed at an overheat ratio of 1.7 ($\Delta T=200\,^\circ\text{C}$), Eq. (21) is nondimensional, and voltage-velocity calibration data for a different overheat ratio can be extrapolated if the wire and CTA electrical properties are accurately known. The correlation of Eq. (21) can thus be used as a faster and less expensive method of hot-wire calibration in binary gas mixtures. The correlation in Eq. (21) is specific for the given l_w/d_w ratio (=250) for the hot wire used. Earlier work by Andrews et al. [17] have demonstrated that the slope B of the correlation line fit (see Eq. (2)) is independent of the l_w/d_w ratio. However, intercept A changes with a change in the l_w/d_w ratio, and needs to be calibrated if a hot wire with a different l_w/d_w ratio is used.

6.2 Validation of the Correlation Method. The validation was based on two distinct sets of calibration data. The first set was obtained by separate density and velocity calibrations of the wire at overheat ratios of 1.6 ($\Delta T=171.43\,^\circ\text{C}$) and 1.9 ($\Delta T=257.14\,^\circ\text{C}$). The second set was formulated at an overheat ratio of 1.7 ($\Delta T=200\,^\circ\text{C}$) and was based on the heat transfer correlation for the binary air-helium mixture. A velocity-voltage relationship for overheat ratios of 1.6 and 1.9 was extrapolated from Eq. (21). Both the calibration sets were used to decompose the voltage traces obtained in the buoyancy driven RT mixing layer [8] at an Atwood number run of 0.04. A multiposition-multioverheat (MPMO) hot-wire technique was used for measurements [2]. The important features of the MPMO technique are summarized briefly below. More details on the technique can be found in Ref. [2].

The MPMO technique uses SN wire probes operated sequentially at different overheat ratios and different orientations [2,3,5]. Since the flow in our facility is predominately one dimensional ($\bar{U},0,0$) with three-dimensional velocity fluctuations (u',v',w') [8], the response function for a SN hot-wire probe, for small fluctuations in velocity and density, can be written as [3]

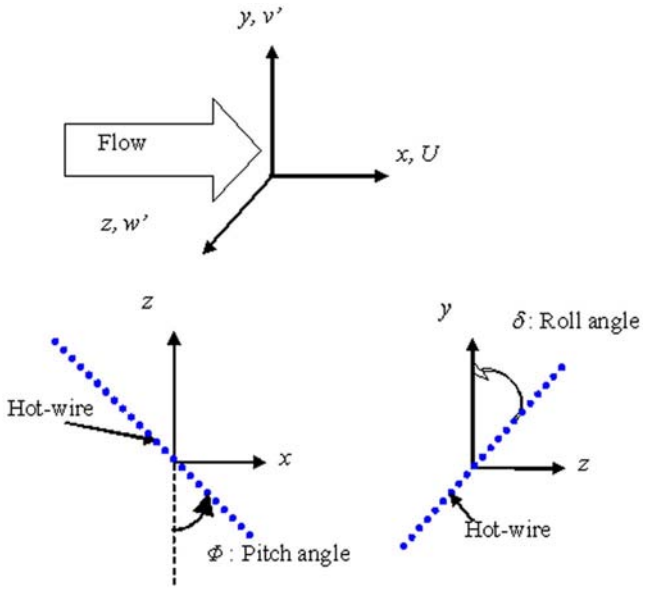

Fig. 7 Wire orientations for the MPMO technique

$$\frac{e'}{\bar{E}} = \Delta e_U \frac{u'}{\bar{U}} + \Delta e_V \frac{v'}{\bar{U}} + \Delta e_w \frac{w'}{\bar{U}} + \Delta e_\rho \frac{\rho'}{\bar{\rho}} \tag{22}$$

where Δe_U, Δe_v, and Δe_w are the velocity sensitivities and Δe_ρ is the density sensitivity of the SN wire probe. The wire sensitivities are evaluated based on the calibration of the wires and are defined as follows:

$$\begin{aligned}
\Delta e_u &= \left.\frac{\partial \ln E}{\partial \ln U}\right|_{\theta,\Delta T_w,\rho} = \left.\frac{\bar{U}}{\bar{E}}\frac{dE}{dU}\right|_{\theta,\Delta T_w,\rho} \\
\Delta e_v &= \left.\frac{\partial \ln E}{\partial \theta}\right|_{u,\Delta T_w,\rho} = \left.\frac{1}{\bar{E}}\frac{dE}{d\theta}\right|_{u,\Delta T_w,\rho} \\
\Delta e_w &= \left.\frac{\partial \ln E}{\partial \ln U}\right|_{\theta,\Delta T_w,\rho} = \left.\frac{\bar{U}}{\bar{E}}\frac{dE}{dU}\right|_{\theta,\Delta T_w,\rho} \\
\Delta e_\rho &= \left.\frac{\partial \ln E}{\partial \rho}\right|_{u,\Delta T_w,\theta=90} = \left.\frac{\bar{\rho}}{\bar{E}}\frac{dE}{d\rho}\right|_{u,\Delta T_w,\theta=90}
\end{aligned} \tag{23}$$

Squaring and taking the time average of Eq. (22) gives ten independent terms on the right hand side. Thus, ten independent measurements are needed to evaluate all these variables. However, this was simplified by using known properties of a RT mixing. In particular, because of axisymmetry of RT flows, the horizontal velocity fluctuation $\overline{u'^2}$ was verified equal to the cross-stream velocity fluctuation $\overline{w'^2}$. However, the vertical velocity fluctuation $\overline{v'^2}$, dominated by buoyancy, is significantly larger than both the horizontal and cross-stream components. Furthermore, symmetry also implies $\overline{\rho' u'}$ to be equal to $\overline{\rho' w'}$. Again, symmetry means that the cross terms in the Reynolds stress tensor are taken to be of the same order and zero, i.e., $\overline{v'w'} \sim \overline{u'w'} \sim 0$. Thus, upon simplification, we obtain [2]

$$\begin{aligned}
\overline{\left(\frac{e'}{\bar{E}}\right)^2} = &\left(\frac{2\Delta e_U^2}{\bar{U}^2}\right)\overline{u'u'} + \left(\frac{\Delta e_V^2}{\bar{U}^2}\right)\overline{v'v'} + \left(\frac{\Delta e_\rho^2}{\bar{\rho}^2}\right)\overline{\rho'\rho'} \\
&+ \left(\frac{2\Delta e_V \Delta e_\rho}{\bar{\rho}\bar{U}}\right)\overline{\rho' v'} + \left(\frac{4\Delta e_U \Delta e_\rho}{\bar{\rho}\bar{U}}\right)\overline{\rho' u'} \\
&+ \left(\frac{2\Delta e_U \Delta e_v}{\bar{U}^2}\right)\overline{u'v'}
\end{aligned} \tag{24}$$

Equation (24) has six independent terms, and thus six independent measurements are needed to estimate $\overline{u'u'}$, $\overline{v'v'}$, $\overline{\rho'\rho'}$, $\overline{\rho'v'}$, $\overline{\rho'u'}$, and $\overline{u'v'}$ for the RT flow. By using a multi(3)-position and multi(2)-overheat method, we obtained the necessary six independent traces. The wire sensitivities dE/dU, $dE/d\rho$, and $dE/d\theta$ were calculated from the calibration, during which the mole fraction (x_{He}) of the binary air-helium gas mixture was varied from pure air ($x_{\mathrm{He}}=0$) to pure helium ($x_{\mathrm{He}}=1.0$) in steps of 0.1. At each volume fraction, the flow velocity was varied over the operational range for the experiment (0.2–3 m/s). The bridge voltage ($\bar{E}$) was plotted as a function of the fluid velocity ($\bar{U}$) and the mixture density ($\bar{\rho}$) (see Fig. 6(*a*)) by using the TABLECURVE3D software (SYSTAT Inc.). Sufficient data points were taken to ensure a smooth and continuous surface over the entire operational range. The fitted curve had R^2 values of 0.9901–0.9992 (see Table 3) and was chosen so that an analytical derivative of the function could be readily taken. The resulting fitted curve is

$$E = \frac{a' + b'U + c' \ln \rho + d'(\ln \rho)^2 + e'(\ln \rho)^3}{1 + f'U + g'U^2 + h' \ln \rho + i'(\ln \rho)^2} \tag{25}$$

The velocity and density sensitivities dE/dU and $dE/d\rho$ are plotted in Figs. 6(*b*) and 6(*c*). For later experimental convenience, the analytical derivatives (dE/dU and $dE/d\rho$) of Eq. (25) were evaluated at each experiment point.

To evaluate $dE/d\theta$, a directional calibration was performed by orienting the probe at different angles to the mean flow by using a pitch/yaw calibrator (Dantec Dynamics, model No. 55H03). The coordinate system for the probe orientation is given in Fig. 7. An

Table 4 Directional calibration curve fit constants $\{E=[a''+c''\ln U+e''\theta+g''(\ln U)^2+i''\theta^2+k''\theta(\ln U)]/[1+b''\ln U+d''\theta+f''(\ln U)^2+h''\theta^2+j''\theta(\ln U)]\}$ for the three SN hot wires at overheat ratios 1.9 and 1.6

Wire No.	Overheat ratio	a''	b''	c''	d''	e''	f''	g''	h''	i''	j''	k''	R^2	Std. error
1	1.9	1.4758	−0.2843	−0.3725	−0.1264	−0.0005	0.0392	0.0565	0.0363	−0.0061	0.0049	0.0068	0.9995	0.002
	1.6	1.2551	−0.3324	−0.3779	0.0154	0.2196	0.0372	0.0416	−0.0082	−0.0743	0.0039	0.0045	0.9996	0.002
2	1.9	1.5285	−0.1413	−0.1426	−0.0859	0.0523	−0.0670	−0.1111	0.0201	−0.0278	0.0056	0.0071	0.9993	0.002
	1.6	1.3301	−0.0599	−0.0191	−0.3883	−0.4175	−0.0225	−0.0243	0.1161	0.1224	0.0075	0.0086	0.9990	0.003
3	1.9	1.6404	−0.1317	−0.1381	−0.3065	−0.3905	−0.0116	−0.0192	0.0887	0.1092	0.0079	0.0107	0.9993	0.003
	1.6	1.2176	−0.3161	−0.2995	−0.1000	0.0105	−0.0315	−0.0261	0.0005	0.0376	0.0097	0.0125	0.9984	0.003

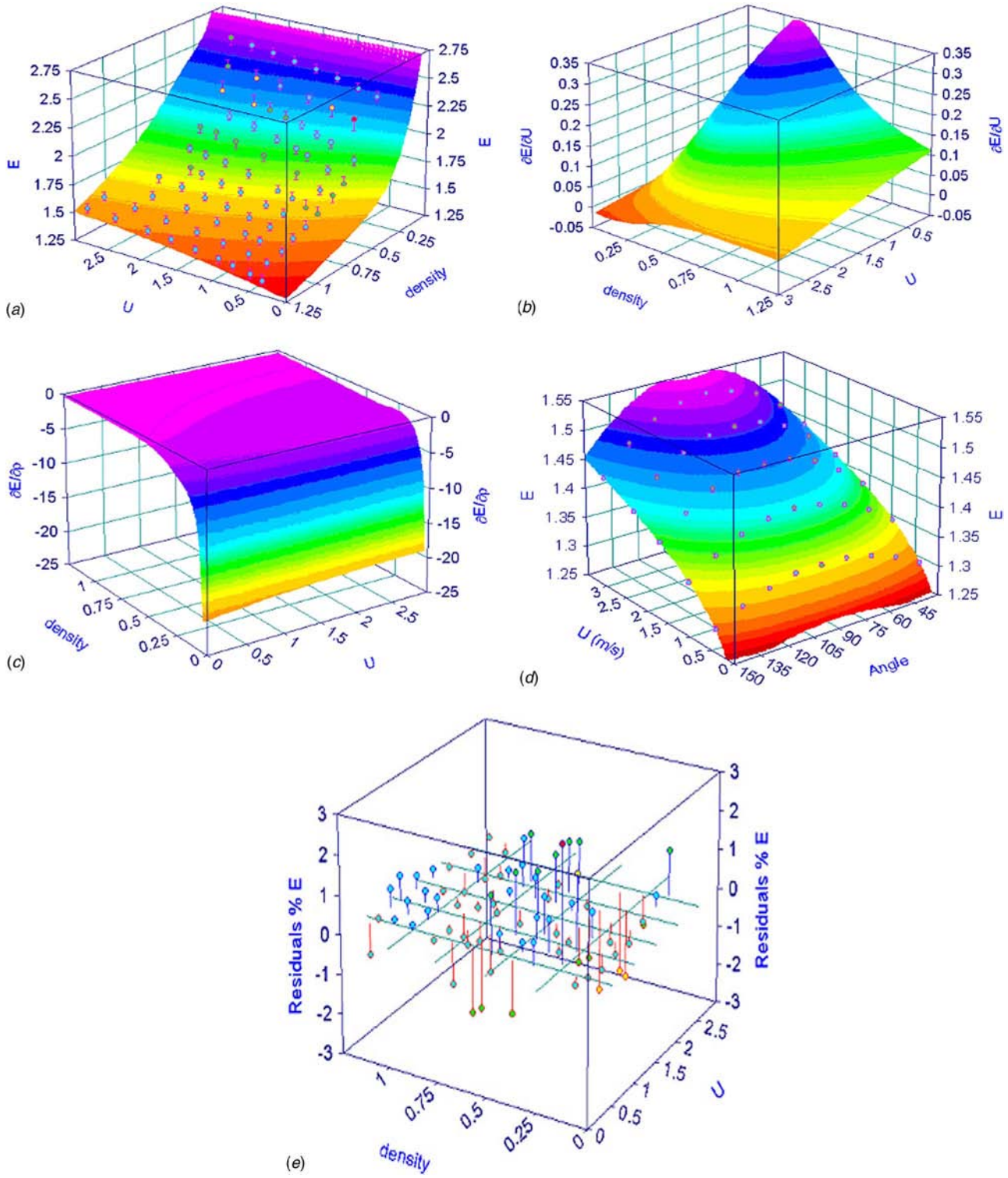

Fig. 8 (*a*) **Calibration data, wire sensitivities** (*b*) ***dE/dU*** **and** (*c*) ***dE/dρ***, (*d*) **directional calibration, and** (*e*) **errors in curve fit at an overheat ratio of 1.6 using a detailed calibration technique**

orientation of $\Phi=90$ deg corresponds to a wire normal to the flow, and an orientation of $\Phi=0$ deg corresponds to a wire parallel to the flow. Since probe interference severely affects measurements for $\Phi<30$ deg [12], values of $\Phi=90$ deg, 60 deg, and 45 deg were chosen for the directional orientations. The hot wire was calibrated by varying the angle from $\Phi=30$ deg to 150 deg in steps of 5 deg (see Fig. 6(*d*)), and the corresponding errors associated with the surface fit are plotted in Fig. 6(*e*). It is seen that the errors associated with the bridge voltage are less than ±3%. Figures 6(*a*)–6(*e*) are calibration plots at an overheat ratio of 1.9 ($\Delta T=257.14\,^{\circ}\mathrm{C}$). The fitted curve had R^2 values of 0.9984–0.9996 (see Table 4) and was chosen so that an analytical derivative of the function could be readily taken. The resulting fitted curve is

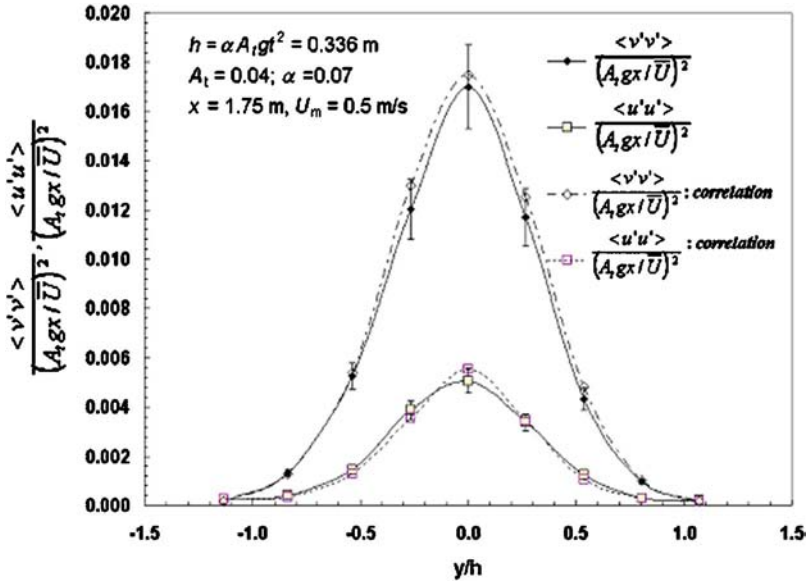

Fig. 9 Velocity correlations across the mix at x=1.75 m for At 0.04

$$E = \frac{a'' + c'' \ln U + e''\theta + g''(\ln U)^2 + i''\theta^2 + k''\theta(\ln U)}{1 + b'' \ln U + d''\theta + f''(\ln U)^2 + h''\theta^2 + j''\theta(\ln U)} \quad (26)$$

Since the MPMO technique required measurements at Mo ratios, a similar calibration was done at an overheat ratio of 1.6 (ΔT =171.43°C). Figures 8(*a*)–8(*e*) show the calibration curves and the wire sensitivities at the overheat ratio of 1.6. Tables 3 and 4 list the calibration constants, R^2 values, and the standard error for all the three wires used for the measurements at overheat ratios of 1.6 and 1.9.

Figure 9 plots the velocity correlations across the mix at x =1.75 m downstream from the splitter plate for an experimental run at an Atwood number of 0.04 with the two different calibration techniques. Since there is no shear in this experiment [2,8], $\langle v'^2 \rangle$ dominates over $\langle u'^2 \rangle$ everywhere across the mix. The velocity correlations were nondimensionalized by using a "free-fall" velocity scale: $A_t g x/\bar{U}$. It is seen that the results obtained with the wire sensitivities extrapolated from the correlation data (Eq. (22)) are in good agreement with the results obtained with the detailed and more direct calibration. The error associated with these measurements is ±5%. Figure 10 plots the values of $\langle \rho' v' \rangle$ and $\langle \rho' u' \rangle$ across the mix at the same location obtained with the two different techniques. It is seen that $\langle \rho' u' \rangle$ is negligible across the mixing layer due to the left-right symmetry of the mushroom-shaped structures, but $\langle \rho' v' \rangle$ has a peak that increases in magnitude with distance downstream. The vertical mass flux is negative because a light packet of fluid is such that $\rho' \equiv \rho - \bar{\rho} < 0$ and travels upwards with a velocity v' ($v' > 0$) and vice versa, giving a negative correlation between ρ' and v'. It is seen that the data obtained by the two calibration techniques are in good agreement for the density-velocity correlations. Thus, the Nu correlation given in Eq. (21) can be used to approximate hot-wire data over a range of velocity, density, and wire temperature (overheat ratios) and eliminates detailed calibration for each overheat ratio.

7 Conclusion

The present work formulates a heat transfer correlation (Eq. (21)) in a binary gas mixture of air and helium at low Reynolds numbers ($0.25 < \mathrm{Re} < 1.2$). The correlation takes into account the temperature dependency of gas properties, properties of binary gas mixtures, fluid slip at the probe surfaces, and gas accommo-

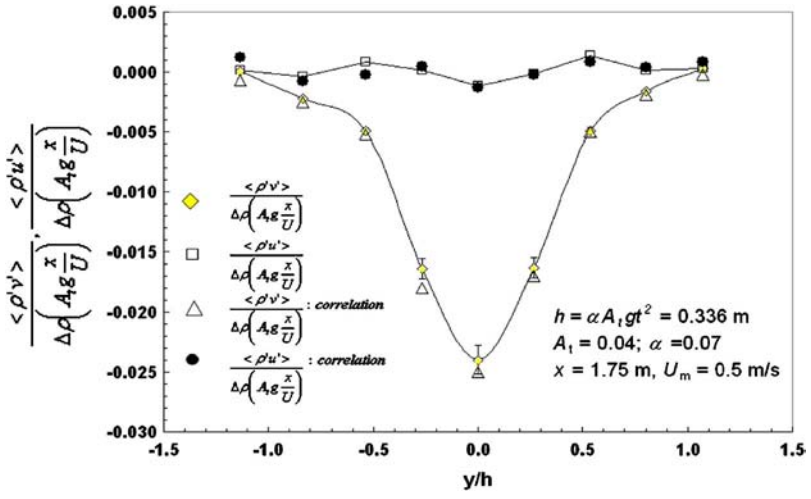

Fig. 10 Profile of $\langle \rho' v' \rangle$ and $\langle \rho' u' \rangle$ across the mix at x=1.75 m for At 0.04

dation effects. The correlation was used as a faster and less expensive method of hot-wire calibration in binary gas mixtures. The accuracy of the calibration was checked by using the correlation to measure velocity-density statistics in an air-helium buoyancy driven RT mixing layer. The measurements were then compared with results obtained by using a standard calibration procedure at different overheat ratios. It was observed that the two sets of measurements agree well to within ±5% error. The correlation can thus be used in variable-density flows, kinetic studies, and measurements in transport processes involving a binary gas mixture. In addition, there is a space for extending the calibration procedure to multicomponent mixtures. Moreover, we believe that this work serves as a basis for other applications at higher Re with the MPMO method.

Acknowledgment

This material is based on the work that is supported by the U.S. Department of Energy under Contract No. DE-FG03-02NA00060. The authors thank Wayne Kraft for his valuable suggestions regarding the calibration facility.

Nomenclature

a'-i' = calibration constants for the density-velocity calibration fit
a''–k'' = calibration constants for the directional calibration fit
At = Atwood number
$C_{p,\mathrm{mix}}$, $C_{v,\mathrm{mix}}$ = specific heats of mixture at a constant pressure and a constant volume
d_w = diameter of hot wire
e' = root mean square voltage
E_w = wire voltage
E_{corr} = corrected wire voltage (see Eq. (19))
f = power dependence of T for viscosity
g = power dependence of T for thermal conductivity
Gr = Grashof number based on wire diameter
h_s = heat transfer coefficient based on T_s
h_w = heat transfer coefficient based on T_w
Kn = Knudsen number of the fluid
l_w = length of hot wire
m_i = mass fraction of gas components (i=1: air; 2: helium)
M_i = molecular weight of gas components (i=1: air; 2: helium)
Nu = Nusselt number $=h_w d_{\mathrm{wire}}/k_{T_{\mathrm{film}}}$
Nu_c = continuum Nusselt number $=h_s d_{\mathrm{wire}}/k_{T_{\mathrm{film}}}$
P_i = see Eq. (16) (i=1: Air; 2: helium)
Pr = Prandtl number of the fluid
q'' = heat flux from wire
r = radial component
R_i = gas constant for mixture components (i=1: air; 2: helium)
Re = Reynolds number based on the wire diameter
R_w = wire resistance
T_{film} = mean film temperature $=(T_{\mathrm{wire}}+T_{\mathrm{fluid}})/2$
T_{fluid} = ambient fluid temperature far from the wire
T_s = extrapolated fluid temperature (see Eq. (6))
T_{wire} = wire temperature
$\bar{U}$ = mean velocity
$\bar{U}_{\mathrm{calib}}$ = velocity from calibration
u', v', w' = root mean square velocity
x_i = mole fraction of gas components (i=1: air; 2: helium)
x, y, z = coordinate system (see Fig. 2(a))
β = slip parameter
$\Delta e_U, \Delta e_v, \Delta e_w$ = velocity sensitivity
Δe_ρ = density sensitivity
ε_u = normalized standard deviation
γ = ratio of specific heats
k_i = thermal conductivity of gas components (i=1: air; 2: helium)
k_{mix} = thermal conductivity of the air-helium mixture
λ = mean free path of the gas molecule
μ_i = absolute (dynamic) viscosity of gas components (i=1: air; 2: helium)
μ_{mix} = absolute (dynamic) viscosity of the air-helium mixture
Φ_{ij} = intercollision parameter for viscosity
Φ'_{ij} = intercollision parameter for thermal conductivity
ρ_h = density of heavy fluid (air)
ρ_i = density of gas components (i=1: air; 2: helium)
ρ_l = density of light fluid (air-helium mixture)
ρ_{mix} = density of air-helium mixture
ρ' = root mean square density
σ = see Eq. (13)
Θ = overheat ratio of the wire $=(T_{\mathrm{wire}}-T_{\mathrm{fluid}})/T_{\mathrm{fluid}}$
ξ = temperature jump distance
χ = thermal accommodation coefficient of the wire surface

References

[1] Pitts, W. M., and McCaffrey, B. J., 1986, "Response Behavior of Hot Wires and Films to Flows of Different Gases," J. Fluid Mech., **169**, pp. 465–512.
[2] Banerjee, A., 2006, "Statistically Steady Measurements of Rayleigh-Taylor Mixing in a Gas Channel," Ph.D. thesis, Texas A&M University.
[3] Rose, W. C., 1973, "The Behavior of a Compressible Turbulent Boundary Layer in a Shock-Wave-Induced Adverse Pressure Gradient," Ph.D. thesis, University of Washington.
[4] Corrisin, S., 1949, "Extended Applications of the Hot-Wire Anemometer," Report No. NACA-TA 1864.
[5] Kovaznay, L. S. G., 1950, "The Hot-Wire Anemometer in Supersonic Flow," J. Aeronaut. Sci., **17**, pp. 565–572.
[6] Pitts, W. M., and Kashiwagi, T., 1984, "Application of Laser-Induced Rayleigh Light Scattering to the Study of Turbulent Mixing," J. Fluid Mech., **141**, pp. 391–429.
[7] Collis, D. C., and Williams, M. J., 1959, "Two Dimensional Convection From Heated Wires at Low Reynolds Numbers," J. Fluid Mech., **6**, pp. 357–384.
[8] Banerjee, A., and Andrews, M. J., 2006, "Statistically Steady Measurements of Rayleigh-Taylor Mixing in a Gas Channel," Phys. Fluids, **18**, p. 035107.
[9] Clarke, J. S., Fisher, H. N., and Mason, R. J., 1973, "Laser-Driven Implosion of Spherical DT Targets to Thermonuclear Burn Conditions," Phys. Rev. Lett., **30**, pp. 89–92.
[10] Molchanov, O. A., 2004, "On the Origin of Low- and Middle-Latitude Ionospheric Turbulence," Phys. Chem. Earth, **29**, pp. 559–567.
[11] Marmottant, P., and Villermaux, E., 2004, "On Spray Formation," J. Fluid Mech., **498**, pp. 73–111.
[12] Gull, S. F., 1975, "The X-Ray, Optical and Radio Properties of Young Supernova Remnants," Mon. Not. R. Astron. Soc., **171**, pp. 263–278.
[13] Fischer, M. C., and Wagner, R. D., 1972, "Transition and Hot-Wire Measurements in Hypersonic Helium Flow," AIAA J., **10**, pp. 1326–1332.
[14] King, L. V., 1914, "On the Convection of Heat From Small Cylinders in a Stream of Fluid: Determination of the Convection Constants of Small Platinum Wires With Applications to Hot-Wire Anemometry," Philos. Trans. R. Soc. London, Ser. A, **214**, pp. 373–432.
[15] Aihara, Y., Kassoy, D. R., and Libby, P. A., 1967, "Heat Transfer From Cylinders at Low Reynolds Numbers. II. Experimental Results and Comparison With Theory," Phys. Fluids, **10**, pp. 947–952.
[16] Preckshot, G. W., and Gorman, J. W., 1958, "Steady State Longitudinal and Radial temperature Distribution in Internally Heated Finite Wires," Ind. Eng. Chem., **50**, pp. 837–848.
[17] Andrews, G. E., Bradley, D., and Hundy, G. F., 1972, "Hot-Wire Anemometer Calibration for measurements of Small Gas Velocities," Int. J. Heat Mass Transfer, **15**, pp. 1765–1786.
[18] Baid, K. M., 1967, "Measurement of Velocity in Gas Mixtures," M.Sc. thesis, Illinois Institute of Technology.
[19] Comte-Bellot, G., 1976, "Hot-Wire Anemometry," Annu. Rev. Fluid Mech., **8**, pp. 209–231.
[20] McAdams, W. H., 1954, *Heat Transmission*, McGraw-Hill, New York.
[21] Van der Hegge Zijnen, B. G., 1956, "Modified Correlation Formulae for Heat Transfer by Natural and Forced Convection From Horizontal Cylinders," Appl. Sci. Res., Sect. A, **6**, pp. 129–140.
[22] Acrivos, A., 1966, "On the Combined Effect of Forced and Free Convection

Heat Transfer in Laminar Boundary Layer Flows," Chem. Eng. Sci., **21**, pp. 343–352.
[23] Chen, T. S., and Mucoglu, A., 1975, "Buoyancy Effects on Forced Convection Along a Vertical Cylinder," Trans. ASME, Ser. C: J. Heat Transfer, **97**, pp. 198–203.
[24] Gebhart, B., and Pera, L., 1970, "Mixed Convection From Long Horizontal Cylinders," J. Fluid Mech., **45**, pp. 1–49.
[25] Simpson, R. L., and Wyatt, W. G., 1973, "The Behaviour of Hot-Film Anemometers in Gas mixtures," J. Phys. E, **6**, pp. 981–987.
[26] Way, J., and Libby, P. A., 1970, "Hot-Wire Probes for Measuring Velocity and Concentration in Helium and Air Mixture," AIAA J., **8**, pp. 976–978.
[27] Way, J., and Libby, P. A., 1971, "Application of Hot-Wire Anemometry and Digital Techniques to Measurements in a Turbulent Helium Jet," AIAA J., **9**, pp. 1567–1573.
[28] Wasan, D. T., and Baid, K. M., 1971, "Measurement of Velocity in Gas Mixtures: Hot-Wire and Hot-Film Anemometry," AIChE J., **17**, pp. 729–731.
[29] Baccaglini, G., Kassoy, D. R., and Libby, P. A., 1969, "Heat Transfer to Cylinders in Nitrogen-Helium and Nitrogen-Neon Mixtures," Phys. Fluids, **12**, pp. 1378—1381.
[30] Wilke, C. R., 1950, "A Viscosity Equation for Gas Mixtures," J. Chem. Phys., **18**, pp. 517–519.
[31] Mason, E. A., and Saxena, S. C., 1958, "Approximate Formula for the Thermal Conductivity of Gas Mixtures," Phys. Fluids, **1**, pp. 361–369.
[32] Kennard, E. H., 1938, *Kinetic Theory of Gases*, McGraw Hill, New York.
[33] Kassoy, D. R., 1967, "Heat Transfer From Circular Cylinders at Low Reynolds Numbers. I. Theory for Variable Property Flow," Phys. Fluids, **10**, pp. 938–946.
[34] Deissler, R. G., 1964, "Analysis of Second-Order Slip Flow and Temperature Jump Boundary Conditions for Rarefied Gas," Int. J. Heat Mass Transfer, **7**, pp. 681–694.
[35] Kaminsky, M., 1965, *Atomic and Ionic Impact Phenomena on Metal Surfaces*, Springer, Berlin.
[36] McCarty, R., 1973, "Thermodynamic Properties of Helium 4 From 2 to 1500 K at Pressures up to 108 Pa," J. Phys. Chem. Ref. Data, **2**, pp. 923–1042.
[37] Kanevce, G., and Oka, S., 1973, "Correcting Hot-Wire Readings for Influence of Fluid Temperature Variations," DISA Inf. **15**, pp. 21–24.
[38] Bruun, H. H., 1996, *Hot-Wire Anemometry: Principles and Signal Analysis*, Oxford University Press, Oxford, UK.
[39] Bruun, H. H., and Tropea, C., 1985, "The Calibration of Inclined Hot-Wire Probes," J. Phys. E, **18**, pp. 405–413.
[40] Saddoughi, S. G., and Veeravalli, S. V., 1996, "Hot-Wire Anemometry Behavior at Very High Frequencies," Meas. Sci. Technol., **7**, pp. 1297–1300.
[41] Almquist, P., and Legath, E., 1965, "The Hot-Wire Anemometer at Low Air Velocities," DISA Inf. **2**, pp. 3–4.
[42] Koppius, A. M., and Trines, G. R. M., 1976, "The Dependence of Hot-Wire Calibration on Gas Temperature at Low Reynolds Numbers," Int. J. Heat Mass Transfer, **19**, pp. 967–974.
[43] Lee, T., and Budwig, R., 1991, "Two Improved Methods for Low-Speed Hot-Wire Calibration," Meas. Sci. Technol., **1**, pp. 643–646.
[44] Manca, O., Mastullo, R., and Mazzei, P., 1988, "Calibration of Hot-Wire Probes at Low Velocities in Air With Variable Temperature," DISA Inf., **6**, pp. 6–8.
[45] Hilpert, R., 1933, "Wärmeabgbae von geheizten Drähten und Rohren in Luftstrom," Forsch. Geb. Ingenieurwes., **4**, pp. 215–224.
[46] Churchill, S. W., Kruggel, R. W., and Brier, J. C., 1955, "Ignition of Solid Propellants by Forced Convection," AIChE J., **2**, pp. 568–571.
[47] Davies, P. O. A. L., and Fisher, M. J., 1964, "Heat Transfer From Electrically Heated Cylinders," Proc. R. Soc. London, Ser. A, **280**, pp. 486–527.
[48] Parnas, A. L., 1964, "Experimental Study of the Unsteady Air-Flow Effect on Heat Transfer of a Cylinder in a Transverse Flow," J. Eng. Phys., **7**, pp. 37–44.

A General Scheme for the Boundary Conditions in Convective and Diffusive Heat Transfer With Immersed Boundary Methods

Arturo Pacheco-Vega[1]
CIEP-Facultad de Ciencias Químicas,
Universidad Autónoma de San Luis Potosí,
San Luis Potosí 78210, México
e-mail: apacheco@uaslp.mx

J. Rafael Pacheco

Tamara Rodić

Mechanical and Aerospace Engineering
Department,
Arizona State University,
Tempe, AZ 85287-6106

We describe the implementation of an interpolation technique, which allows the accurate imposition of the Dirichlet, Neumann, and mixed (Robin) boundary conditions on complex geometries using the immersed-boundary technique on Cartesian grids, where the interface effects are transmitted through forcing functions. The scheme is general in that it does not involve any special treatment to handle either one of the three types of boundary conditions. The accuracy of the interpolation algorithm on the boundary is assessed using several two- and three-dimensional heat transfer problems: (1) forced convection over cylinders placed in an unbounded flow, (2) natural convection on a cylinder placed inside a cavity, (3) heat diffusion inside an annulus, and (4) forced convection around a stationary sphere. The results show that the scheme preserves the second-order accuracy of the equations solver and are in agreement with analytical and/or numerical data. [DOI: 10.1115/1.2764083]

Keywords: heat transfer, immersed boundary method, numerical simulations, forced convection, natural convection, general boundary conditions

1 Introduction

The use of the immersed-boundary (IB) technique, and of other Cartesian-grid methods, for simulating geometrically complex fluid flow problems, has increased substantially in the last three decades. The advantages provided by methodologies on Cartesian grids, such as simplicity in grid generation, savings in memory and CPU time, and straightforward parallelization, have been key factors for their expanded use in the analysis and design of engineering equipment. Numerical schemes on Cartesian grids can be broadly classified in two categories: (1) methods where the effects of the boundary are transmitted via forcing functions (IB methods) [1,2] and (2) methods where the boundary effects are embedded in the discrete spatial operators, e.g., ghost-cell and sharp-interface methods [3–6], and the immersed interface method [7–9], which have been applied to the simulation of flows around stationary and moving immersed boundaries. The present work is concerned with the implementation and application of the IB method for heat transfer analyses.

The application of most of the IB schemes reported in the literature has been directed toward the analysis of fluid flow [1,2,10,11] and has only recently been extended to simulate heat transfer phenomena [12–14]. Nevertheless, regardless of the application, the different versions of the IB technique are developed upon the same principle, i.e., to apply a "forcing term" in the discretized momentum and/or energy equations, such that the boundary conditions are satisfied on the body surface [2,10,13]. Though the technique has also drawbacks, e.g., mass conservation near the boundary where the forcing is applied, is not strictly satisfied [15], efforts to alleviate this problem have increased in recent years [10,16].

On the other hand, when using Cartesian grids, the body does not often coincide with the grid points and interpolation schemes are needed to enforce the boundary conditions on the body surface. In this context, several interpolation schemes have been developed and successfully applied to enforce Dirichlet boundary conditions [2,10,12,13]. To a lesser extent, and with less success, interpolation algorithms for enforcing the Neumann (isoflux) conditions have also been reported in the literature [12–14]. In the above mentioned investigations, not only the interpolation schemes developed for Dirichlet boundary conditions were different from those constructed for Neumann conditions owing to their differences in nature but there was no explicit assessment of the accuracy of the isoflux interpolation algorithms.

Mixed Dirichlet–Neumann (Robin) conditions arise in heat and mass diffusion processes when coupled with convection. Examples include the description of heat transfer in microvascular tissues [17], electrokinetic remediation [18], one-phase solidification and melting [19], and reaction-diffusion problems [20], among others. Thus, it would be important to have an algorithm that could handle all three possible combinations of linear boundary conditions that occur in heat transfer phenomena using fixed grid approaches.

The aim of the present article is to address this need, i.e., to develop a second-order single-interpolation scheme that can be applied to enforce either Dirichlet, Neumann, or Robin conditions on the body surface, to analyze heat transfer processes in the context of the IB method. To this end, a brief overview of the IB technique is provided first. The details of the general interpolation scheme are presented next. The accuracy of the approach is then demonstrated by applying the interpolation algorithm to several phenomenologically different two-dimensional heat transfer prob-

[1]Corresponding author.

Contributed by the Heat Transfer Division of ASME for publication in the JOURNAL OF HEAT TRANSFER. Manuscript received June 19, 2006; final manuscript received February 12, 2007. Review conducted by Louis C. Burmeister. Paper presented at the 2006 ASME International Mechanical Engineering Congress (IMECE2006), Chicago, IL, November 5–10, 2006.

lems. Finally, the capability of the scheme to handle three-dimensional problems is demonstrated by solving the forced convection around a stationary sphere.

2 Mathematical Formulation

We consider the different types of heat transfer problems namely, forced and natural convection heat transfer over heated cylinders, diffusion of heat in an annulus, and forced convection heat transfer around a stationary sphere.

2.1 Governing Equations. For heat convection, a nondimensional version of the governing equations for an unsteady, incompressible, Newtonian fluid flow with constant properties, in the Boussinesq limit, with negligible viscous dissipation, can be written as

$$\nabla \cdot \mathbf{u} = 0 \tag{1}$$

$$\partial_t \mathbf{u} + (\mathbf{u} \cdot \nabla)\mathbf{u} = -\nabla p + P_1 \nabla^2 \mathbf{u} + \mathbf{f} + P_2 \Theta \mathbf{e} \tag{2}$$

$$\partial_t \Theta + (\mathbf{u} \cdot \nabla)\Theta = P_3 \nabla^2 \Theta + h \tag{3}$$

where $\mathbf{u}$ is the Cartesian velocity vector of components u_i ($i=1,2,3$), p is the pressure, $\mathbf{e}$ and $\mathbf{f}$ are the unit vector in the vertical direction and the momentum forcing, respectively, Θ is the temperature of the fluid, and h is the energy forcing. P_1, P_2, and P_3 are defined according to the scaling of Eqs. (1)–(3) and depend on the problem under analysis. For example, for forced and mixed convection, we scale length with L_c, velocity with U, time with L_c/U, and pressure with ρU^2. We define a nondimensional temperature as $\Theta=(T-T_0)/(T_w-T_0)$, where T_w is the wall/body temperature and T_0 is a reference temperature. A Reynolds number for the flow can be defined as $\mathrm{Re}=UL_c/\nu$, where $\nu=\mu/\rho$ is the kinematic viscosity of the fluid. The Prandtl number is $\mathrm{Pr}=\nu/\alpha$, where α is the thermal diffusivity of the fluid, and the Grashof number $\mathrm{Gr}=(g\beta L_c/U^2)(T_w-T_0)(UL_c/\nu)^2$, where g is the gravitational acceleration, and β is the coefficient of thermal expansion. Therefore, $P_1=1/\mathrm{Re}$, $P_2=\mathrm{Gr}/\mathrm{Re}^2$, and $P_3=1/\mathrm{RePr}$. On the other hand, for natural convection, $P_1=\mathrm{Pr}$, $P_2=\mathrm{RaPr}$, and $P_3=1$, where we scale length with L_c, velocity with α/L_c, time with L_c^2/α, and pressure with $\rho\alpha^2/L_c^2$. The nondimensional temperature is defined as $\Theta=(T-T_0)/(T_w-T_0)$; thence, the Grashof number becomes $\mathrm{Gr}=(g\beta L_c^3/\nu^2)(T_w-T_0)$. Note that different quantities can be used in the normalization of the temperature and the definition of the Grashof number. For instance, in the case of nonhomogeneous Neumann conditions, for which there is no temperature difference characteristic of the problem, one could use a mean temperature difference $\overline{T_w-T_0}$ or a value of the temperature difference halfway along the body, as suggested by Sparrow and Gregg [21].

For the case of unsteady heat conduction within a solid surrounded by a fluid, the nondimensional governing equation with constant properties is given by

$$\partial_t \Theta_s = P_4 \nabla^2 \Theta_s + H \tag{4}$$

where Θ_s is the temperature within the solid, and H is the corresponding energy forcing. We scale length with L_c and time with a characteristic diffusion time t_c. The nondimensional temperature in the equation above is defined as $\Theta_s=(T_s-T_0)/(T_\infty-T_0)$, where T_0 is the reference temperature, T_∞ is the fluid temperature (used here as an upper-bound reference), and $P_4=\alpha_s t_c/L_c^2$, where α_s is the thermal diffusivity of the solid.

2.2 Projection Method and Time Integration. The nonstaggered-grid layout is employed in this analysis. The pressure and the Cartesian velocity components are defined at the cell center and the volume fluxes are defined at the midpoint of their corresponding faces of the control volume in the computational space. The spatial derivatives are discretized using a variation of QUICK [22], which calculates the face value from the nodal value with a quadratic interpolation scheme. The upwinding schemes are carried out by computing negative and positive volume fluxes. Using a semi-implicit time-advancement scheme with the Adams–Bashforth method for the explicit terms and the Crank–Nicholson method for the implicit terms as described in Refs. [23–26], the discretized equations corresponding to Eqs. (1)–(3) can be written as follows:

$$\frac{\mathbf{u}^* - \mathbf{u}^n}{\Delta t} = \frac{1}{2}\{-3[(\mathbf{u}\cdot\nabla)\mathbf{u}]^n + [(\mathbf{u}\cdot\nabla)\mathbf{u}]^{n-1} + P_1\nabla^2(\mathbf{u}^* + \mathbf{u}^n)\} + \mathbf{f}^{n+1/2} + P_2\Theta^{n+1}\mathbf{e} \tag{5}$$

$$\nabla^2 \phi^{n+1} = \frac{\nabla \cdot \mathbf{u}^*}{\Delta t} \tag{6}$$

$$\mathbf{u}^{n+1} = \mathbf{u}^* - \Delta t \nabla \phi^{n+1} \tag{7}$$

$$\frac{\Theta^{n+1} - \Theta^n}{\Delta t} = \frac{1}{2}\{-3[(\mathbf{u}\cdot\nabla)\Theta]^n + [(\mathbf{u}\cdot\nabla)\Theta]^{n-1} + P_3\nabla^2(\Theta^{n+1} + \Theta^n)\} + h^{n+1/2} \tag{8}$$

where $\mathbf{u}^*$ is the predicted intermediate velocity, and ϕ is often called "pseudopressure." The Poisson equation for the pressure is solved iteratively using a multigrid method [23].

In the context of the direct forcing method [27], to obtain $\mathbf{u}^*$ we need to compute the forcing function $\mathbf{f}$ in advance, such that $\mathbf{u}^{n+1}$ satisfies the boundary condition on the IB (similar argument is applied to the energy forcing h or H). One can enforce the proper boundary condition on $\mathbf{u}^*$ instead of $\mathbf{u}^{n+1}$ without compromising the temporal accuracy of the scheme [10]; thence, we replace $\mathbf{u}^*$ with $\bar{\mathbf{U}}$ in Eq. (5) and $\bar{\Theta}$ for Θ^{n+1} in Eq. (8) and solve for the forcings:

$$\mathbf{f}^{n+1/2} = \frac{\bar{\mathbf{U}} - \mathbf{u}^n}{\Delta t} + \frac{1}{2}\{3[(\mathbf{u}\cdot\nabla)\mathbf{u}]^n - [(\mathbf{u}\cdot\nabla)\mathbf{u}]^{n-1} - P_1\nabla^2(\mathbf{u}^* + \mathbf{u}^n)\} - P_2\Theta^{n+1}\mathbf{e} \tag{9}$$

$$h^{n+1/2} = \frac{\bar{\Theta} - \Theta^n}{\Delta t} + \frac{1}{2}\{3[(\mathbf{u}\cdot\nabla)\Theta]^n - [(\mathbf{u}\cdot\nabla)\Theta]^{n-1} - P_3\nabla^2(\Theta^{n+1} + \Theta^n)\} \tag{10}$$

where $\bar{\mathbf{U}}$ is the boundary condition for the velocity on the body surface or inside the body with $\mathbf{f}=0$ within the fluid. In the same context, $\bar{\Theta}$ refers to the temperature at the energy-forcing location that will ensure that the desired boundary condition is satisfied. Taking the energy-forcing in Eq. (10) as an example, when the location of h coincides with the boundary then $\bar{\Theta}=\Theta$; otherwise $\bar{\Theta}$ must be obtained by interpolation from the surrounding temperature values. The procedure just described also applies for the solution of Eq. (4) to obtain H and Θ_s, with the appropriate boundary conditions. Details of the methodology to determine $\mathbf{f}$ and h (or H), are fully described in Ref. [13] and references therein. Thence, we concentrate in the implementation of the general interpolation scheme for the Dirichlet, Neumann, and mixed boundary conditions to solve the energy equation.

3 General Interpolation Scheme

The most general linear boundary condition needed to solve the energy equations, Eqs. (3) and (4), is given as

$$a\Theta + b\nabla\Theta \cdot \mathbf{n} = c \tag{11}$$

where a, b, and c are parameters defined in accordance with the normalization that is used for the problem under analysis, and $\mathbf{n}$ is the normal unit vector.

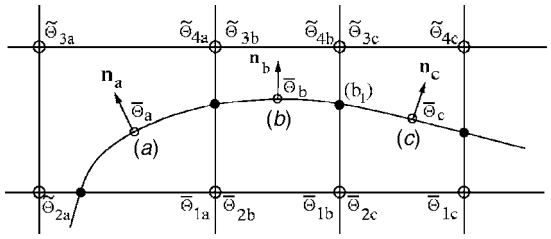

Fig. 1 Interpolation scheme at nodes (*a*), and (*b*) or (c)

To develop the interpolation scheme for the above boundary condition, we consider a two-dimensional body shown in Fig. 1. In reference to this figure, two different types of nodes are possible, e.g., nodes labeled (*a*), or nodes named either (*b*) or (*c*), where $\mathbf{n}_a$, $\mathbf{n}_b$, and $\mathbf{n}_c$ are the unit vectors defining the tangent planes at the corresponding node.

Consider first the case of the cell on the left end of Fig. 1 for point labeled (*a*). This case is shown in Fig. 2(*a*) as point (p,q). In this case, three nodal values (outside of the body) surrounding point (p,q) are known. In the following, for clarity "bars" and "tildes" are the temperature values inside and outside the body, respectively.

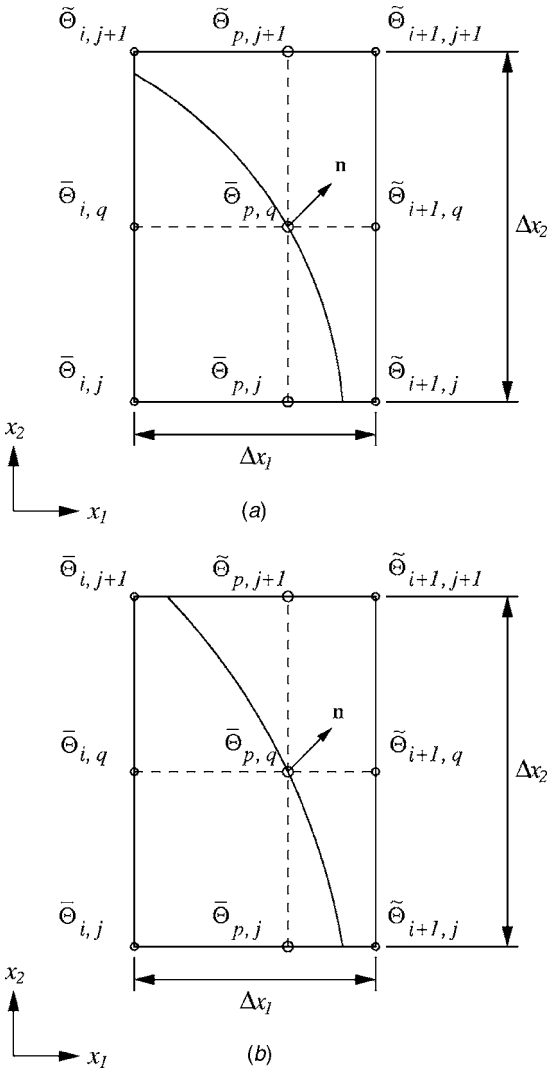

Fig. 2 General interpolation scheme for Dirichlet–Neumann boundary conditions: (*a*) three nodes outside the boundary; (*b*) two nodes outside the boundary

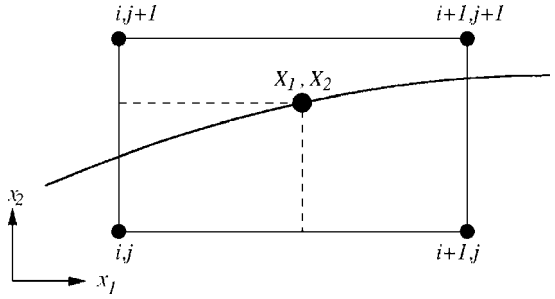

Fig. 3 Bilinear interpolation

We need to find $\bar{\Theta}_{i,j}$ to compute h in Eq. (10), such that Eq. (11) is satisfied at node (p,q) (the same applies to $\bar{\Theta}_s$ in the diffusion equation Eq. (4) to find H). Thus, we use a bilinear interpolation scheme, as shown in Fig. 3, where $\alpha=[X_1-x_{1(i,j)}]/[x_{1(i+1,j)}-x_{1(i,j)}]$, $\beta=(X_2-x_{2(i,j)})/(x_{2(i,j+1)}-x_{2(i,j)})$, and $\bar{\Theta}_{p,q}=\Theta(X_1,X_2)$ on (p,q). This is given as

$$\bar{\Theta}_{p,q}=\alpha\beta\tilde{\Theta}_{i+1,j+1}+\alpha(1-\beta)\tilde{\Theta}_{i+1,j}+(1-\alpha)\beta\tilde{\Theta}_{i,j+1}+(1-\alpha)(1-\beta)\bar{\Theta}_{i,j} \tag{12}$$

On the other hand, the values of auxiliary nodes $\bar{\Theta}_{p,j}$, $\tilde{\Theta}_{p,j+1}$, $\bar{\Theta}_{i,q}$ and $\tilde{\Theta}_{i+1,q}$, which are required to compute the derivatives for Eq. (11), can be obtained by a linear interpolation scheme, with the following expressions:

$$\bar{\Theta}_{p,j}=\alpha\tilde{\Theta}_{i+1,j}+(1-\alpha)\bar{\Theta}_{i,j} \tag{13a}$$

$$\tilde{\Theta}_{p,j+1}=\alpha\tilde{\Theta}_{i+1,j+1}+(1-\alpha)\bar{\Theta}_{i,j+1} \tag{13b}$$

$$\bar{\Theta}_{i,q}=\beta\tilde{\Theta}_{i,j+1}+(1-\beta)\bar{\Theta}_{i,j} \tag{13c}$$

$$\tilde{\Theta}_{i+1,q}=\beta\tilde{\Theta}_{i+1,j+1}+(1-\beta)\tilde{\Theta}_{i+1,j} \tag{13d}$$

On combining Eq. (11) with Eq. (12) and Eqs. (13*a*)–(13*d*), the value for $\bar{\Theta}_{i,j}$ can now be written as

$$\bar{\Theta}_{i,j}=\left\{c-\alpha\beta a\tilde{\Theta}_{i+1,j+1}-\left[\frac{\alpha b}{\Delta x_2}n_2+\alpha(1-\beta)a\right]\tilde{\Theta}_{i+1,j}-\left[\frac{\beta b}{\Delta x_1}n_1+(1-\alpha)\beta a\right]\tilde{\Theta}_{i,j+1}-\frac{b}{\Delta x_1}n_1\tilde{\Theta}_{i+1,q}-\frac{b}{\Delta x_2}n_2\tilde{\Theta}_{p,j+1}\right\}\Big/\left[\frac{(1-\beta)b}{\Delta x_1}n_1+\frac{(1-\alpha)b}{\Delta x_2}n_2+(1-\alpha)(1-\beta)a\right] \tag{14}$$

where n_1 and n_2 are the projections of $\mathbf{n}$ on the x_1 and x_2 axes, respectively. Δx_1 and Δx_2 are the corresponding spatial increments (see Fig. 2). By setting either $b=0$ or $a=0$ in Eq. (14), $\bar{\Theta}_{i,j}$ can be computed under Dirichlet or Neumann boundary conditions.

In the second case, two nodal values surrounding point (p,q) lie inside the body, as shown in Fig. 2(*b*). This case corresponds to the cell on the center of Fig. 1 for point labeled as (*b*). Apparently, there are only two known temperatures outside the boundary ($\tilde{\Theta}_{3b}$ and $\tilde{\Theta}_{4b}$) and two unknown temperatures inside the boundary ($\bar{\Theta}_{1b}$ and $\bar{\Theta}_{2b}$). However, we regard $\bar{\Theta}_{2b}$ as a known quantity, since $\bar{\Theta}_{2b}=\bar{\Theta}_{1a}$, where $\bar{\Theta}_{1a}$ was previously obtained from Eq. (14) as

Table 1 Comparison in C_D, x_c, St, and $\overline{\mathrm{Nu}}$ around a cylinder placed in an unbounded flow

Re→		40			120			150	
Study	$\overline{\mathrm{Nu}}C_D$	x_c	$\overline{\mathrm{Nu}}$	C_D	St	$\overline{\mathrm{Nu}}$	C_D	St	$\overline{\mathrm{Nu}}$
Kim and Choi [12]	—	—	3.23	—	—	5.62	—	—	—
Eckert and Soehngen [29]	—	—	3.48	—	—	5.69	—	—	6.29
Pan [30]	1.51	2.18	3.23	—	—	—	—	—	—
Lima E Silva et al. [31]	1.54	—	—	—	—	—	1.37	0.170	—
Current	1.53	2.28	3.62	1.40	0.170	5.5	1.38	0.179	6.13

explained above. Therefore, $\bar{\Theta}_{i,j}$ ($=\bar{\Theta}_{1b}$ of Fig. 1) is computed with Eq. (14) and the *known* surrounding values. Equation (14) can be used to determine the temperature values inside the body such that the desired boundary condition is satisfied. The solution procedure involves the following steps.

1. Find a nodal point where we want to satisfy the Robin boundary condition and three nodal points lie outside the body, e.g., node (a) of Fig. 1.
2. Determine temperature $\bar{\Theta}_{i,j}(=\bar{\Theta}_{1a})$ from the known surrounding values using Eq. (14).
3. Determine the corresponding node temperature of the adjacent cell, e.g., node (b) of Fig. 1, from Eq. (14) with $\bar{\Theta}_{i,j+1}$ being replaced by $\bar{\Theta}_{i,j+1}$. In this case, $\bar{\Theta}_{i,j+1}=\bar{\Theta}_{1a}$ was previously determined from a bilinear interpolation along with the adjacent nodes external to the body $\tilde{\Theta}_{2a}$, $\tilde{\Theta}_{3a}$, $\tilde{\Theta}_{4a}$, and Eq. (11) being evaluated at node (a), which are all known.
4. Repeat step 3 on the adjacent cell (right end of Fig. 1).
5. Since $\bar{\Theta}_{1b}$ must equal $\bar{\Theta}_{2c}$, this procedure must be repeated until all the nodes near the body have been exhausted, and the difference in values between consecutive iterations is negligible, e.g., $\bar{\Theta}_{1b}-\bar{\Theta}_{2c}\approx 0$.

It is to be noted that the number of iterations required to achieve zero machine accuracy, either for two- or three-dimensional simulations, is typically 10 per node.

4 Heat Transfer Simulations

In order to assess the correct implementation of the interpolation algorithm, simulations of four different heat transfer problems are carried out next.

4.1 Forced Convection Over Heated Circular Cylinders. We consider first the forced heat convection over circular cylinders placed in an unbounded uniform flow. Two different cases are analyzed in this section: (i) a single heated cylinder of nondimensional diameter $d=1$ and (ii) an arrangement of two heated cylinders, one being the *main* cylinder of nondimensional diameter $d=1$, whereas the other is a *secondary* cylinder of diameter $d_s=d/3$. Note that the characteristic length for these problems is $L_c=d$. For the two cases, the following considerations take place: The fluid is air, and thus Pr=0.71; the inflow boundary conditions are $u_1=1$, $u_2=0$, and $\Theta=0$; the outflow boundary conditions are $\partial u_i/\partial t+\overline{c_u}\partial u_i/\partial x_1=0$ and $\partial\Theta/\partial t+\overline{c_u}\partial\Theta/\partial x_1=0$ [28] (where c_u is the space-averaged velocity) for $i=1,2$; the far-field boundary conditions are $\partial u_i/\partial x_2=0$ and $\partial\Theta/\partial x_2=0$; and the value of the isothermal surface for all the cylinders is $\Theta=1$. The flow is governed by Eqs. (1)–(3) with $P_1=1/\mathrm{Re}$, $P_2=\mathrm{Gr}/\mathrm{Re}^2$ (Gr=0), and $P_3=1/\mathrm{RePr}$. The computations presented next were carried out using nonuniform grids, which are stretched away from the vicinity of the body using a hyperbolic sine function for test case (i) and a logarithmic function for test case (ii). A number of 1200 grid points inside the cylinder and 112 grid points close to the boundary were used. In all the cases analyzed here, a 400×400 mesh secured grid independence. During the computations, the time step value was changed dynamically to ensure a CFL=0.5.

In test problem (i), the cylinder was placed at the center of a computational domain of size $30d\times 30d$. The center of the cylinder has coordinates $(x_1,x_2)=(0,0)$, where $-15\leq x_1,x_2\leq 15$. The results shown next were obtained for $\mathrm{Re}=\{40,80,120,150\}$. Table 1 shows a comparison in both the hydrodynamics and the heat transfer of this flow in terms of the drag coefficient $C_D=F_D/\frac{1}{2}\rho U^2 d$, the wake bubble x_c or the Strouhal number $\mathrm{St}=fd/U$, and the averaged Nusselt number $\overline{\mathrm{Nu}}=\bar{h}d/k$. In the above expressions, F_D is the drag force on the cylinder [13], f is the shedding frequency, $\bar{h}$ is the heat transfer coefficient averaged over its half arc length, and k its thermal conductivity. As can be noted, the present results for both fluid flow and heat transfer compare quantitatively well with the published numerical and laboratory experiments [12,29–31]. As an example, for Re=40, 120, and 150, the differences in $\overline{\mathrm{Nu}}$ against the experiments of Eckert and Soehngen [29] are confined to less than 4%.

Figures 4(a) and 4(b) illustrate the streamlines and temperature contours for Re=80. From both figures, it can be seen the development of a Kárman vortex street, resembled by the alternating patterns that take place due to vortex shedding, which is typical for this value of Re [29,32]. On the other hand, Fig. 5 illustrates a comparison in the local values of the Nu number along the cylinder surface obtained from the proposed scheme and the experiments of Eckert and Soehngen [29] for Re=120. In the figure, the angle φ is measured from the leading edge of the cylinder. As can be noticed, there is a very good agreement between the present results and those of Eckert and Soehngen [29]. Also expected is a quantitative increase of the $\overline{\mathrm{Nu}}$ value from 3.62 for Re=40, to 4.70 for Re=80, and to 5.50 for Re=120. The percentage difference between the averaged Nusselt obtained here (for Re=120) and the experimental one reported by Eckert and Soehngen [29], which is 5.69, is of only 3.4%.

Test problem (ii) has been studied experimentally [32] and numerically [12] for different arrangements. Here, we consider two of them for a value of Reynolds number of Re=80. In the first arrangement, the center of the main cylinder was located at $(x_1,x_2)=(-1,0)$ with respect to a coordinate system placed at the center of a $30d\times 30d$ computational domain, whereas the secondary cylinder was centered at $(x_1,x_2)=(1,1)$.

Qualitative results for this problem are depicted in Figs. 6(a) and 6(b) in terms of the streamlines and isotherms, respectively. In contrast with the forced convection over the single cylinder, shown previously for the same Re number, the figures illustrate how the interaction between the cylinders, for this arrangement, suppresses the vortex shedding and produces a steady flow [32]. Qualitatively and quantitatively, these results are in good agreement with the data of Kim and Choi [12]. Actual values for the main and secondary cylinders are, respectively, 1.24 and 0.48 for C_D, and 4.7 and 3.0 for $\overline{\mathrm{Nu}}$.

Computations were also carried out for an arrangement where the main cylinder was centered at $(x_1,x_2)=(-1,0)$ and the secondary cylinder at $(x_1,x_2)=(1,0.5)$. As expected for this arrangement [12,32], our results showed that the flow is unsteady. Again, good agreement with Ref. [12] is found in the values of both C_D and $\overline{\mathrm{Nu}}$

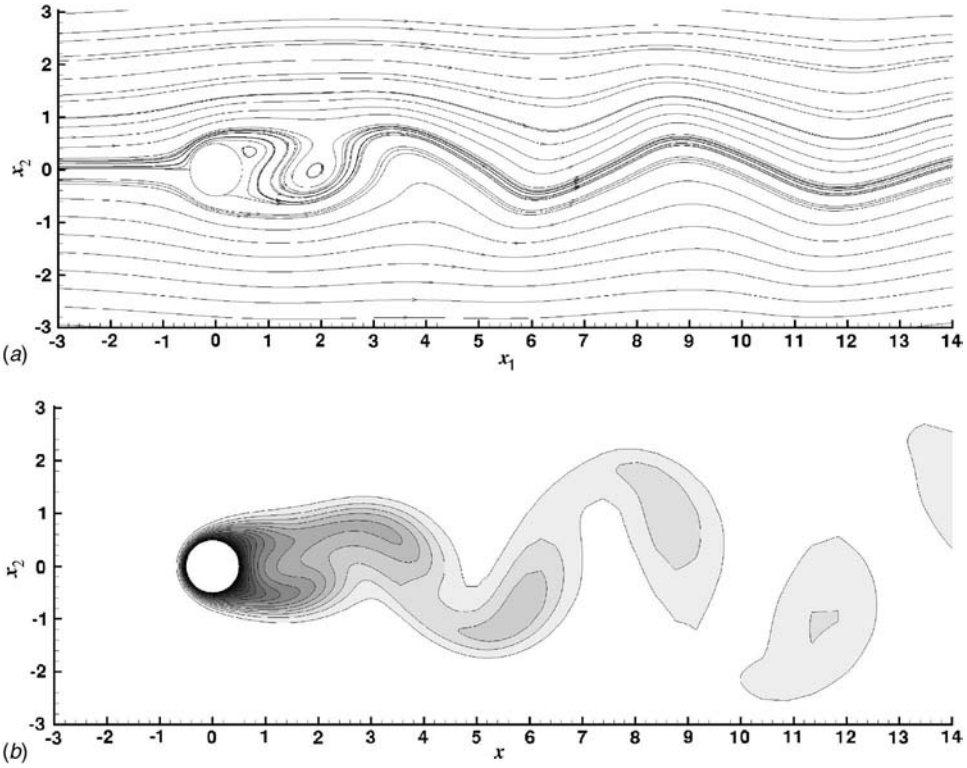

Fig. 4 Streamlines and temperature contours of flow around cylinder for Re=80: (*a*) streamlines; (*b*) isotherms

for the main and secondary cylinders. Our data for C_D are 1.22 and 0.12, and for $\overline{\mathrm{Nu}}$ 4.62 and 1.65, respectively.

4.2 Natural Convection Over a Heated Cylinder Inside a Square Cavity. The proposed algorithm is applied next to simulate the laminar natural convection from a heated cylinder placed eccentrically in a square duct of sides $L=1$. The geometry of this validation problem is shown in Fig. 7. The flow and heat transfer are governed by Eqs. (1)–(3) with $P_1=\mathrm{Pr}$, $P_2=\mathrm{RaPr}$, and $P_3=1$, where we have chosen $L_c=L$ as the characteristic length. The cylinder has a nondimensional wall temperature $\Theta=1$, whereas two different sets of thermal boundary conditions are considered for the walls of the cavity: (i) isothermal boundary conditions where all the walls are maintained at $\Theta=0$, and (ii) isothermal vertical sidewalls at $\Theta=0$ and adiabatic horizontal walls, i.e., $\nabla\Theta\cdot\mathbf{n}=0$. For the flow, in both cases, no-slip and no-penetration conditions are applied to all the surfaces.

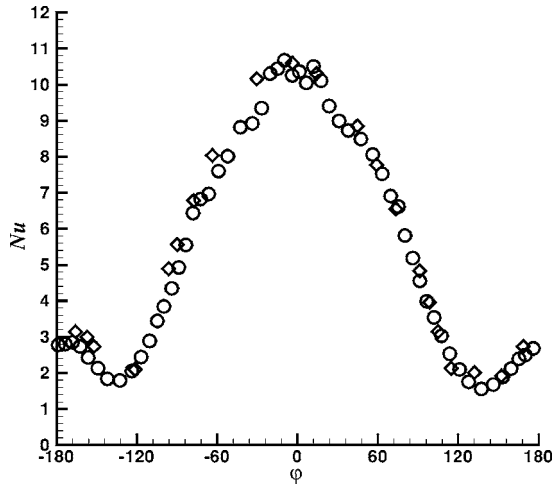

Fig. 5 Nu number along cylinder surface for Re=120. ○, present scheme; ◇, experiments by Eckert and Soehngen [29].

Test case (i) has been studied by Moukalled and Darwish [33] using a bounded skew central-difference scheme, Sadat and Couturier [34] with a meshless diffuse approximation method, and Pan [30] with an unstructured-Cartesian-mesh IB method. The cylinder has a dimensionless diameter $d=0.2$, with its center being located at $(x_1,x_2)=(-0.15,-0.15)$ as measured from the center of the duct (see Fig. 7). Our calculations were carried out until grid independence was achieved, with grid sizes ranging from 80×80 to 200×200, for values of the Rayleigh number $\mathrm{Ra}=10^4$, 10^5, and 10^6. Streamlines and temperature contours for $\mathrm{Ra}=10^4$ and $\mathrm{Ra}=10^6$ are depicted in Figs. 8 and 9, respectively. As observed, the results shown here agree qualitatively well with those presented in Refs. [30,33,34]. Figures 8(*a*) and 8(*b*) illustrate the change on the character of the flow from two well-defined rotating vortices to two distorted ones as Ra is increased from 10^4 to 10^6. In the case of the temperature contours, this change is noticed by the shift of the thermal plume now rising toward the left corner of the cavity, as illustrated in Figs. 9(*a*) and 9(*b*). Table 2 shows a quantitative comparison in the values of the average Nusselt $\overline{\mathrm{Nu}}$ number along the cylinder surface for the three values of Ra considered against published data [30,33,34]. The maximum difference between the current results and those of Pan [30], for instance, is of only 2%.

For test case (ii), in reference to Fig. 7, the cylinder has a dimensionless diameter of $d=0.4$, and its center is located at $(x_1,x_2)=(0,0.1)$ from the center of the duct. This problem has been benchmarked by Demirdžić et al. [35]. The results obtained from the current algorithm are shown in Figs. 10 and 11. Values of the Nusselt number along the cold walls, obtained with a grid size of 200×200, are compared in Fig. 10 with those of Demirdžić et al. [35], who used half of the domain and a 256×128 grid. From

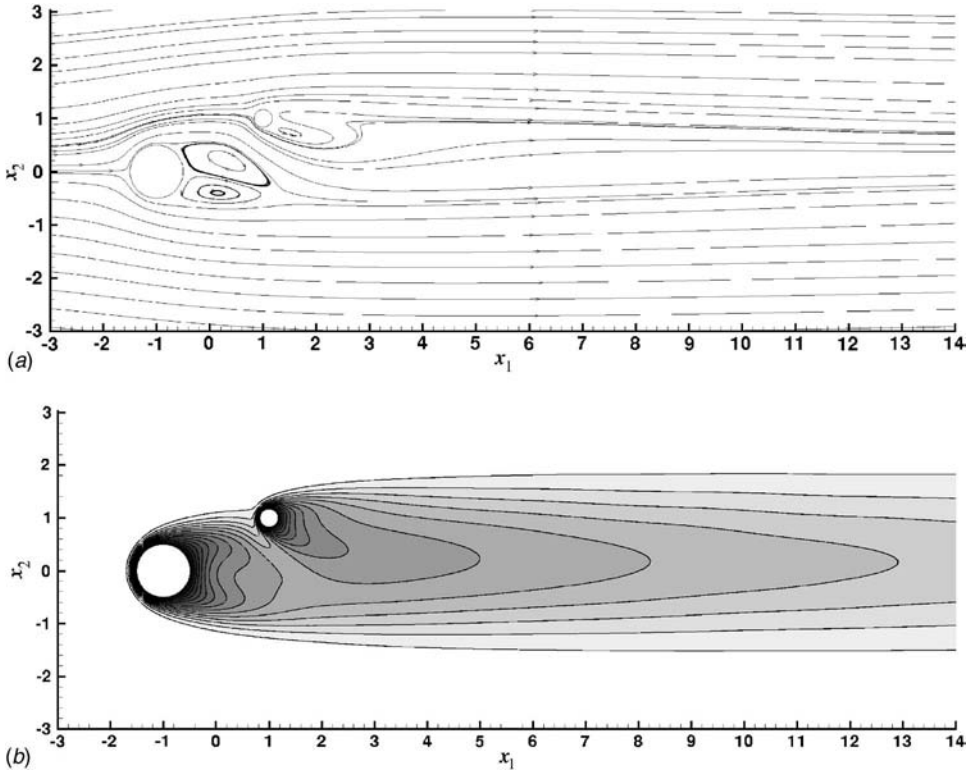

Fig. 6 Streamlines and temperature contours of flow around two cylinders for Re=80: (*a*) streamlines; (*b*) isotherms

the figure, it can be seen that the present results overlap with the "exact values" of Demirdžić et al. [35]. A comparison of the values for the Nusselt number along the cylinder surface, between the present work and that of Demirdžić et al. [35], is shown in Fig. 11. In the figure, the azimuthal angle φ is measured from top of the cylinder. As before, the agreement of the results obtained from the current scheme as compared to those of Demirdžić et al. [35] is excellent.

4.3 Heat Diffusion in an Annulus. We now carry out simulations of the steady and unsteady heat diffusion in an annulus, illustrated schematically in Fig. 12. This problem was studied by Barozzi et al. [8] using an immersed interface (II) method. The diffusion process within the annulus is governed by Eq. (4), with $P_4=1$. The annulus is initially at $\Theta_{s,0}=0$, with a uniform temperature $\Theta_{s,e}=0$ being applied to the outer surface, and Robin boundary conditions at the internal surface. The present results are compared to the solutions obtained by Barozzi et al. [8] using a nondimensional radius $r \in [1,2]$, where we have used $L_c=r_i$ as characteristic length.

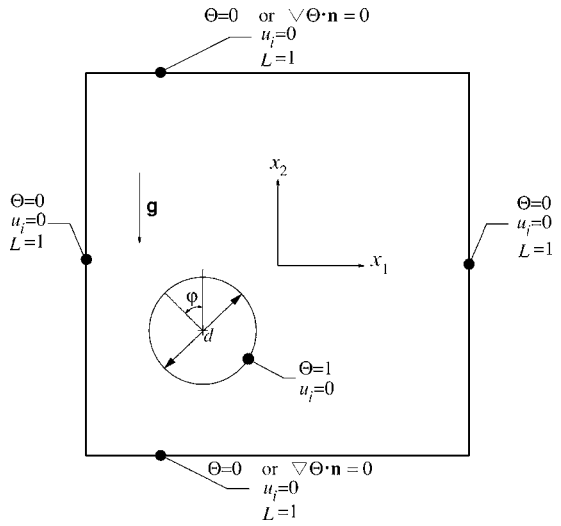

Fig. 7 Cylinder placed eccentrically in a square cavity

Three different boundary conditions were applied at the internal boundary in order to test the spatial accuracy of the present formulation. For all cases, the boundary condition at the outer radius is of the Dirichlet type ($\Theta_{s,e}=0$). The boundary conditions applied at the inner radius were (a) Dirichlet $a=1$, $b=0$, $c=1$; (b) Neumann $a=0$, $b=1$, $c=1$; and (c) mixed $a=1$, $b=1$, $c=1$. Different numbers of regular grid points, ranging from 20×20 to 120×120 in an uniform Cartesian mesh, were used. For the three boundary conditions above, accuracy of the solutions is presented in terms of the maximum $\epsilon_{\max}$- and L_2-norm distributions in Figs. 13(*a*)–13(*c*), and average values in Table 3. For comparison purposes, the results reported by Barozzi et al. [8] are also included. From the figures, and the table, it can be seen that both techniques achieve second-order accuracy, with actual numerical orders being quantitatively similar. It is to be noted that the uneven distributions of the errors in Figs. 13(*b*) and 13(*c*), as the mesh is refined, may be due to the presence of the irregular boundary whose effect is to produce a local increase in the error when the derivative is computed.

The time-dependent system, given in Eq. (4) under general conditions of the inner boundary, is analyzed next, and the results are compared with analytical solutions. Following the procedure described by Carslaw and Jaeger [36], and Özişik [37], the solution of Eq. (4) with $\Theta_{s,0}=0$, $\Theta_{s,e}=0$, and $a=b=c=1$ in Eq. (11) is given in terms of Bessel series expansions as

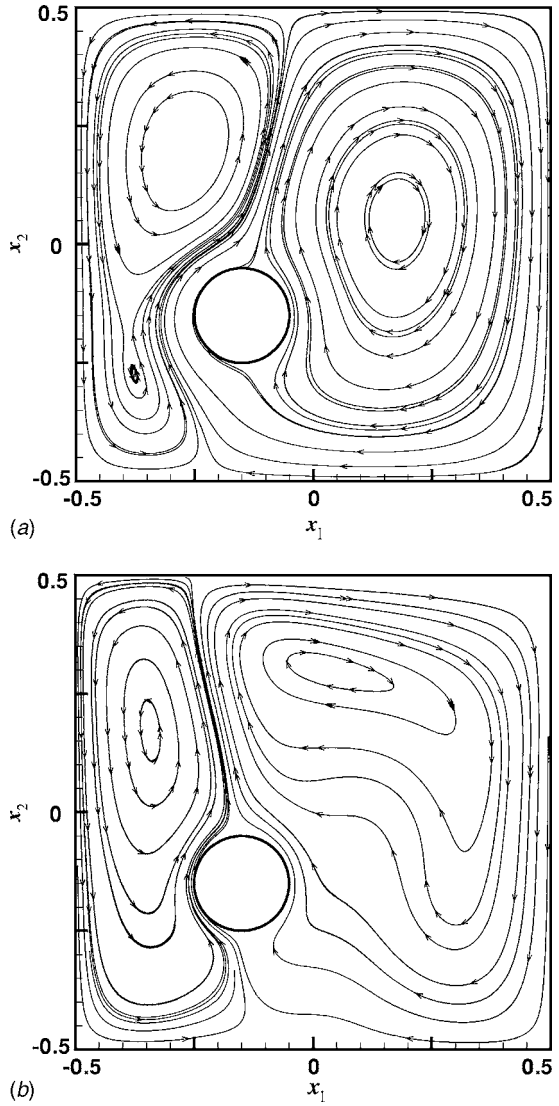

Fig. 8 Streamlines on a 200×200 grid for (*a*) Ra=10⁴ and (*b*) Ra=10⁶

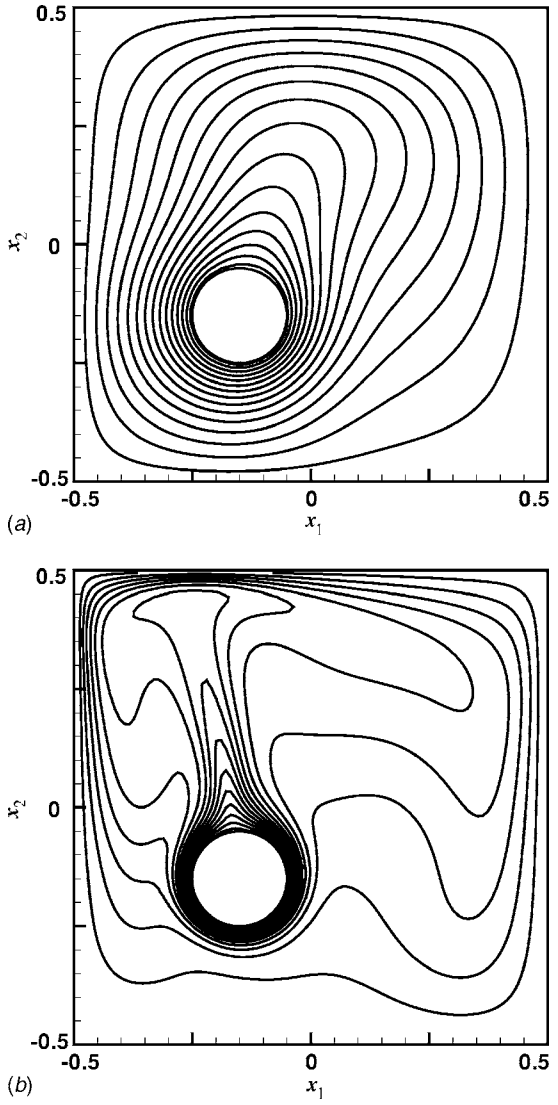

Fig. 9 Isotherms on a 200×200 grid for (*a*) Ra=10⁴ and (*b*) Ra=10⁶

$$\Theta_s(r,t) = \sum_{j=1}^{\infty} c_j \left[\frac{J_0(\lambda_j r)}{J_0(2\lambda_j)} - \frac{Y_0(\lambda_j r)}{Y_0(2\lambda_j)} \right] \exp(-P_4 \lambda_j^2 t) + \frac{\ln(r)+1}{\ln(1/2)-1} \tag{15}$$

where the eigenvalues, λ_j for $j=1,2,\ldots$, are the roots of the equation

$$\frac{\lambda_j J_1(\lambda_j) + J_0(\lambda_j)}{J_0(2\lambda_j)} - \frac{\lambda_j Y_1(\lambda_j) + Y_0(\lambda_j)}{Y_0(2\lambda_j)} = 0 \tag{16}$$

and the constants c_j for $j=1,2,\ldots$, are defined as

$$c_j = \frac{(2/\lambda_j)\{[J_1(\lambda_j)/J_0(2\lambda_j)] - [Y_1(\lambda_j)/Y_0(2\lambda_j)]\}}{4\{[J_1(2\lambda_j)/J_0(2\lambda_j)] - [Y_1(2\lambda_j)/Y_0(2\lambda_j)]\}^2 - [(1/\lambda_j^2)+1]\{[J_0(\lambda_j)/J_0(2\lambda_j)] - [Y_0(\lambda_j)/Y_0(2\lambda_j)]\}^2} \tag{17}$$

In the above equations, J_0, Y_0, J_1, and Y_1 are the Bessel functions of first and second kinds, of order 0 or 1, respectively.

The time-dependent results are shown in Fig. 14 as temperature distributions within the solid annulus at values of the nondimensional time $t=0.15$, 0.25, 0.35, and 1.40. From the figure, it can be observed an excellent agreement between the analytical solutions (symbols) with those obtained numerically (solid lines). After $t=1.40$ nondimensional units, the steady state has been reached, with a value of $\Theta_s=0.41$ at the inner boundary. The error between the two solutions is confined to less than 1%.

The temporal accuracy of the scheme is assessed next by choosing three radii locations within the annulus (see Fig. 12), corre-

Table 2 Comparison in $\overline{Nu}$ around a cylinder placed inside a cavity for Ra=10^4, 10^5, and 10^6

Study	Ra=10^4	Ra=10^5	Ra=10^6
Moukalled and Darwish [33]	4.741	7.435	12.453
Sadat and Couturier [34]	4.699	7.430	12.421
Pan [30]	4.686	7.454	12.540
Current	4.750	7.519	12.531

sponding to $r=1.03(P_A)$ close to the inner boundary, $r=1.49(P_B)$ approximately at the middle plane, and $r=1.94(P_C)$ close to the outer boundary. Note that the inner boundary condition is of the Robin type. Different time increments, i.e., $\Delta t=0.2$, 0.1, and 0.01, were used, and the results presented in Fig. 13(*d*) in terms of error distributions. From the figure, it is clear that for all the radii locations considered, the scheme is second-order accurate in time.

4.4 Three-Dimensional Forced Convection Over a Heated Sphere. The capacity of the present scheme to handle three-dimensional flows is shown next by solving the flow and heat transfer around a heated sphere. Published numerical and experimental results are used to assess the solutions obtained. Thus, let us consider a sphere of nondimensional diameter $d=1$, where $L_c=d$ is the characteristic length, placed in an unbounded flow. This flow is governed by Eqs. (1)–(3) where $P_1=1/\mathrm{Re}$, $P_2=\mathrm{Gr}/\mathrm{Re}^2$ with Gr=0, and $P_3=1/\mathrm{RePr}$ with Pr=0.71. The boundary conditions for the problem are inflow $u_1=1$, $u_2=u_3=0$, and $\Theta=0$; outflow $\partial u_i/\partial t+c_u\partial u_i/\partial x_1=0$ and $\partial\Theta/\partial t+c_u\partial\Theta/\partial x_1=0$; and far-field boundaries $\partial u_i/\partial x_2=\partial u_i/\partial x_3=0$, $\partial\Theta/\partial x_2=\partial\Theta/\partial x_3=0$, respectively, where $i=1,2,3$. The sphere is at a nondimensional temperature $\Theta=1$. The computations were carried out using a $100\times100\times100$ nonuniform grid, which stretches away from the body to the outer boundaries using a hyperbolic sine function. The sphere is located in the center $(x_1,x_2,x_3)=(0,0,0)$ of a computational cube of size $30d\times30d\times30d$. The time step value was dynamically changed to ensure a CFL=0.5. The results from the current approach were obtained for Reynolds numbers Re $=\{50,100,150,200,220,300\}$.

Figures 15(*a*)–15(*e*) illustrate the streamlines and isotherms on the symmetry plane $x_3=0$ for Re=50, 100, 150, 200, and 220, respectively. The streamlines presented in Figs. 15(*a*)–15(*d*) show that the flow is steady and separated, with an axisymmetric recirculation bubble that grows as the Reynolds number increases.

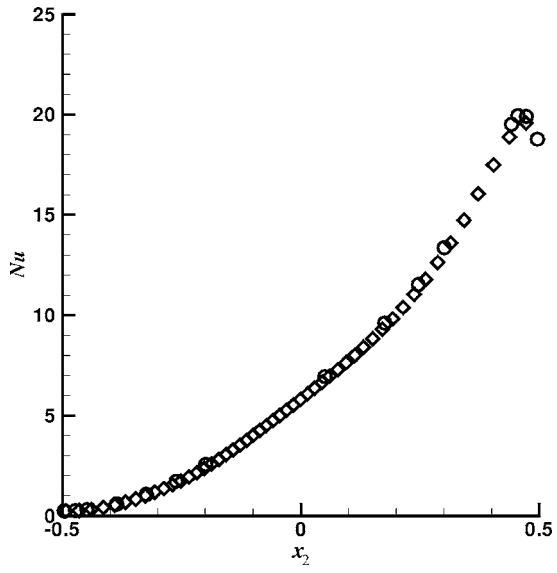

Fig. 10 Nu number along cold wall for Ra=10^6 and Pr=10. ◇, present scheme; ○, Demirdžić et al. [35].

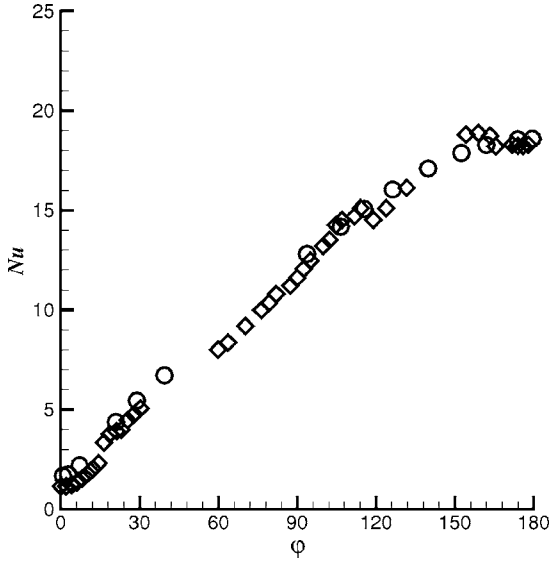

Fig. 11 Nu number along cylinder surface for Ra=10^6 and Pr =10. Angle φ is measured from top of cylinder. ◇, present scheme; ○, Demirdžić et al. [35].

Quantitatively, the present results for both drag coefficient C_D and wake bubble x_c are in good agreement with those of Marella et al. [4] and Johnson and Patel [38]. Actual values for Re=50, 100, and 150 are 1.62, 1.07, and 0.85 for C_D, and 0.42, 0.90, and 1.23 for x_c, respectively. For Re=220, Fig. 15(*e*) shows the expected axial asymmetry of the flow, which has been experimentally determined to occur in the $\mathrm{Re}\in[210,270]$ range [39].

The corresponding isotherms, shown also in Figs. 15(*a*)–15(*e*), reflect the behavior of the flow. As the Reynolds number increases, the isotherms in the wake of the sphere become more distorted due to the amount of recirculating flow. Though small values of the heat transfer coefficient are characteristics of this region, it can be seen that in the rear of the sphere (at an angle of approximately 180 deg), the heat transfer coefficient is increased locally with Re number. The computed values of the Nusselt number averaged over the surface of the sphere $\overline{\mathrm{Nu}}$ are 4.99, 7.00, 8.27, 9.19, and 9.30 for Re=50, 100, 150, 200, and 220, respectively. These results are in good agreement with the correlation developed by Feng and Michaelides [40], for the same conditions. The maximum difference between the corresponding values is less

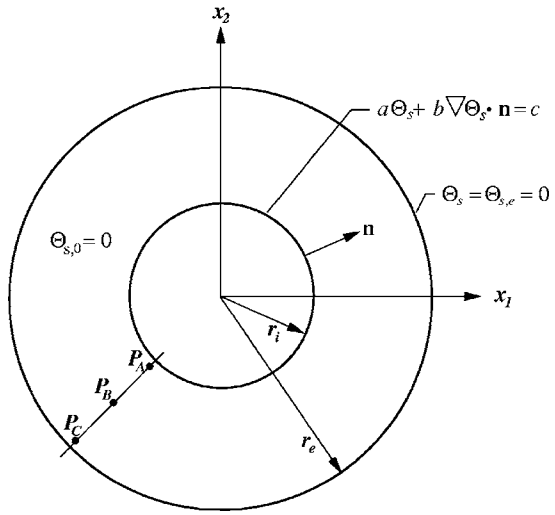

Fig. 12 Concentric cylindrical annulus

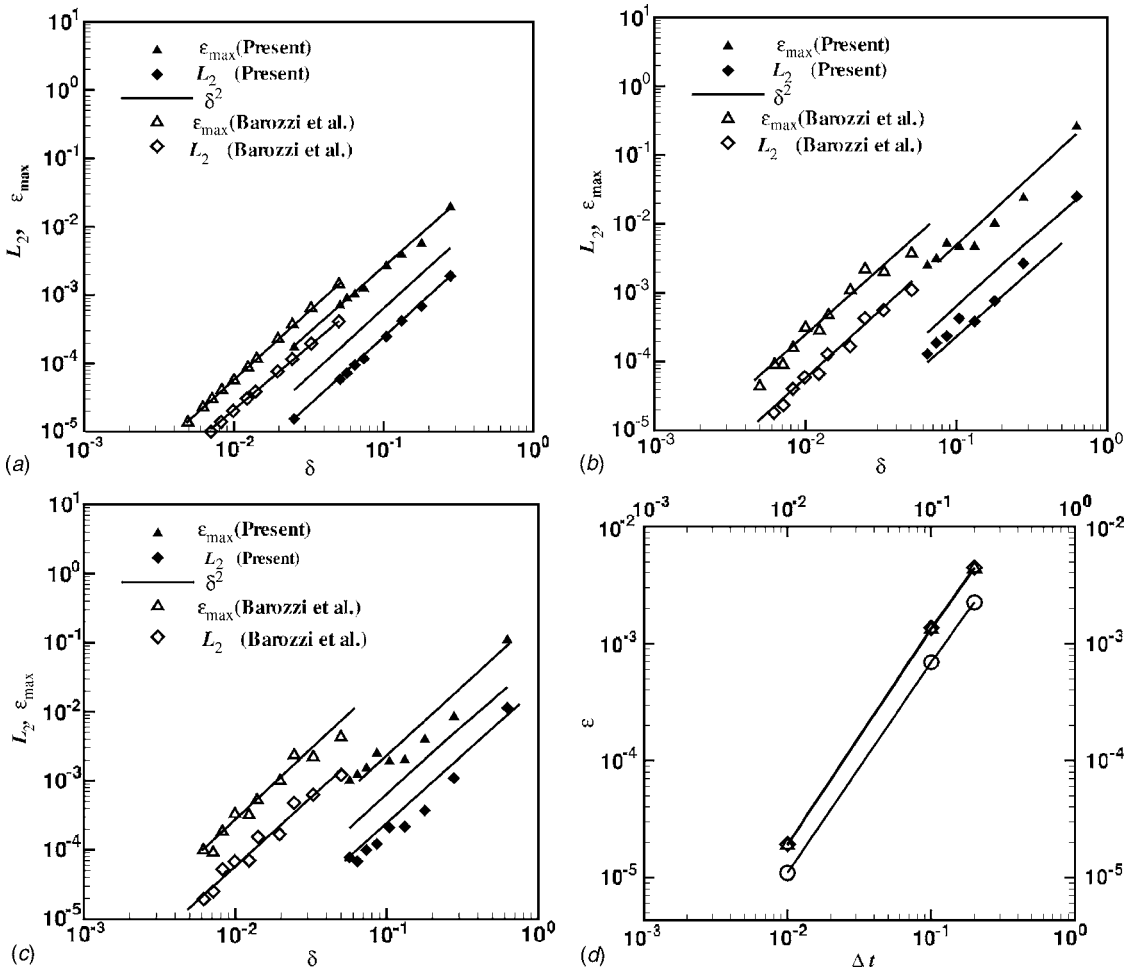

Fig. 13 ((*a*)–(*c*)) L_2 **norm and maximum norm** (ϵ_{max}) **as functions of the mesh size** δ **for different inner boundary conditions. (*d*) Error versus** Δt **for inner Robin boundary conditions. (*a*) Dirichlet (*a*=1, *b*=0, *c*=1). (*b*) Neumann (*a*=0, *b*=1, *c*=1). (*c*) Robin (*a*=1, *b*=1, *c*=1). (*d*) Radii locations: ◇, P_A; ○, P_B; △, P_C.**

than 8%.

Increasing the Reynolds number beyond 270 eventually leads to unsteady flow [38]. For Re=300, Fig. 16 illustrates the vortical structures of the flow obtained with the method proposed by Hunt et al. [41] (more in-depth details are in Refs. [42,43]). As seen in the figure, these vortical structures resemble very well the established vortex shedding. The average values of the drag coefficient C_D=0.570 and the Strouhal number St=0.133 compare well to those of Marella et al. [4] and Johnson and Patel [38]. For this value of Re number, the averaged Nusselt number Nu=10.50 deviates from that given by Feng and Michaelides [40] correlation in only 3.6%.

5 Concluding Remarks

In the current work, we have presented a novel interpolation scheme that is able to handle either Dirichlet, Neumann, or mixed boundary conditions within the context of the IB methodology. An advantage of this algorithm is that both Dirichlet and Neumann conditions can be naturally implemented by setting appropriate values to the constants in the most general linear equation. Its

Table 3 Numerical order of accuracy in terms of ϵ_{max} **and** L_2 **for the annulus problem**

	Dirichlet		Neumann		Robin	
Method / BC →	L_2	ϵ_{max}	L_2	ϵ_{max}	L_2	ϵ_{max}
Barozzi et al. [8]	1.91	1.93	2.05	1.99	2.02	1.95
Current	2.16	2.09	2.02	1.93	2.03	1.93

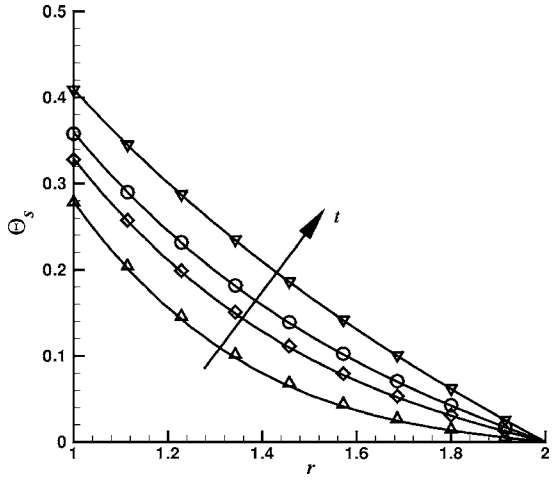

Fig. 14 Numerical (solid lines) versus analytical (symbols) time-dependent solutions. -△-, *t*=0.15; -◇-, *t*=0.25; -○-, *t*=0.35; -▽-, *t*=1.40 (steady state).

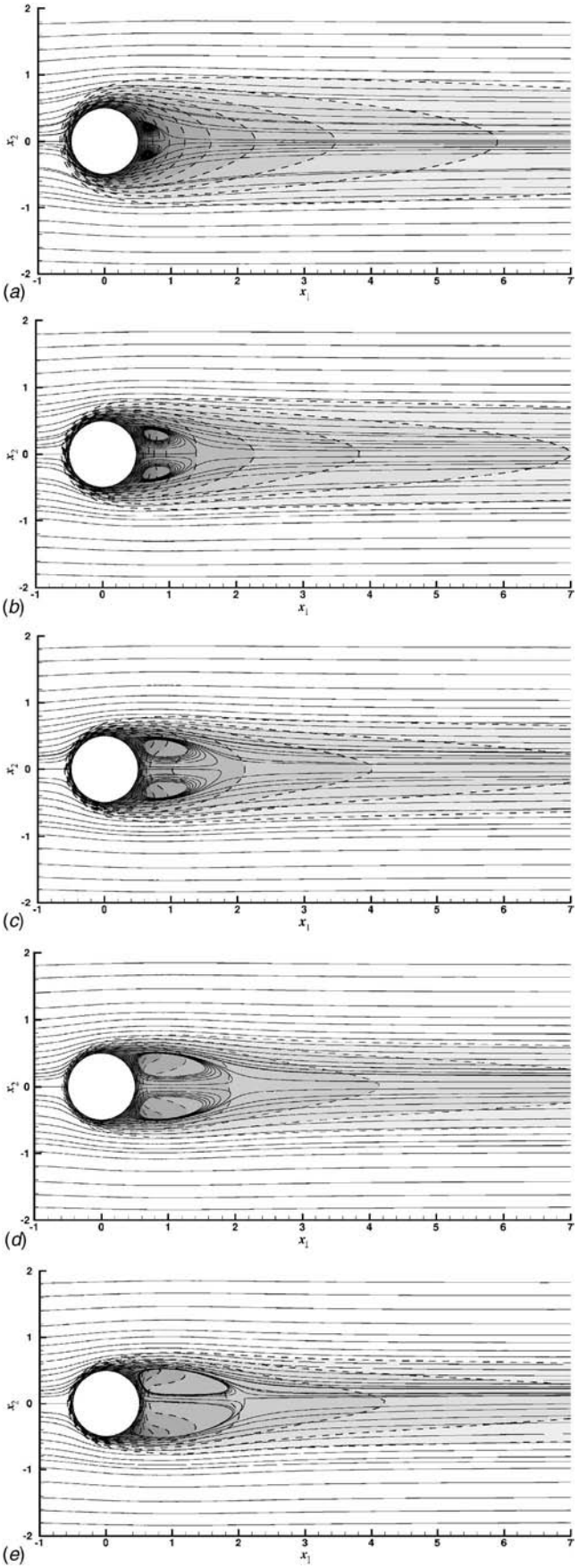

Fig. 15 Streamlines and temperature contours for flow around a sphere in the 50≤Re≤220 range. (*a*) Re=50, (*b*) Re=100, (*c*) Re=150, (*d*) Re=200, and (*e*) Re=220.

Fig. 16 Oblique view of vortical structures of flow for Re =300

validation has been assessed by favorable comparison with numerical results available in the literature and/or analytical solutions for different heat transfer problems: forced heat convection over circular cylinders, natural heat convection over a cylinder placed inside a cavity, steady and unsteady diffusion of heat inside an annulus, and three-dimensional forced convection over a sphere. The interpolation algorithm developed here provides a method that is second-order accurate in space and time and is suitable for analyzing heat transfer phenomena in single or multiple bodies with complex boundaries on two- and three-dimensional Cartesian meshes.

Acknowledgment

The authors thank Professor R.L. Street of Stanford University for providing the multigrid subroutine used in this work and to G. Constantinescu of University of Iowa for his assistance with the vortex visualization. A. P.-V. also acknowledges financial support from PROMEP, México through grants PROMEP/PTC-68 and PROMEP-CA9/FCQ-UASLP, and FAI/UASLP research fund. We are grateful for the helpful comments of the anonymous referees which improved the quality of the manuscript. Computational resources for this work were provided by the Ira A. Fulton High Performance Computing Initiative at ASU.

Nomenclature

a, b, c = constants in general boundary condition
$\underline{c_j}$ = jth constant in Eq. (15)
c_u = space-averaged velocity
$\mathbf{e}$ = unit vector in vertical direction
$\mathbf{f}$ = momentum forcing
h, H = energy forcing
L_c = characteristic length
L_2 = Euclidean norm
n_1, n_2 = projections on x_1 and x_2 axes of unit vector $\mathbf{n}$
P_1, P_2, P_3, P_4 = nondimensional parameters
P_A, P_B, P_C = radii locations
r = radius
$\mathbf{u}$ = Cartesian velocity vector
x_c = wake bubble
x_i = Cartesian coordinates
$x_{1(i,j)}, x_{2(i,j)}$ = coordinates based on node (i, j) for bilinear interpolation
X_1, X_2 = coordinates of immersed-boundary node

Greek Symbols

α = thermal diffusivity of fluid, interpolation factor
α_s = thermal diffusivity of solid
β = coefficient of thermal expansion, interpolation factor
$\Delta x_1, \Delta x_2$ = spatial increments in x_1 and x_2 directions
δ = mesh size
ϵ = error
$\epsilon_{\max}$ = maximum norm
λ_j = jth eigenvalue
∇ = Nabla operator
Θ = normalized temperature
Θ_s = normalized temperature within the solid
$\Theta_{s,0}$ = normalized initial temperature within the solid

Θ_∞ = normalized reference fluid temperature
$\bar{\Theta}$ = temperature on or inside the body
$\tilde{\Theta}$ = temperature outside the body in energy-forcing interpolation
φ = reference angle

Subscripts and Superscripts

e = outer-boundary value
i,j = indices for the Cartesian coordinates
n = index for time step

References

[1] Peskin, C. S., 1972, "Flow Patterns Around Heart Valves: A Numerical Method," J. Comput. Phys., **10**, pp. 252–271.
[2] Peskin, C. S., 2002, "The Immersed Boundary Method," Acta Numerica, **11**, pp. 479–517.
[3] Udaykumar, H. S., Mittal, R., and Rampunggoon, P., 2002, "Interface Tracking Finite Volume Method for Complex Solid-Fluid Interactions on Fixed Meshes," Commun. Numer. Methods Eng., **18**, pp. 89–97.
[4] Marella, S., Krishnan, S., Liu, H., and Udaykumar, H. S., 2005, "Sharp Interface Cartesian Grid Method I: An Easily Implemented Technique for 3D Moving Boundary Computations," J. Comput. Phys., **210**, pp. 1–31.
[5] Liu, H., Krishnan, S., Marella, S., and Udaykumar, H. S., 2005, "Sharp Interface Cartesian Grid Method II: A Technique for Simulating Droplet Impact on Surfaces of Arbitrary Shape," J. Comput. Phys., **210**, pp. 32–54.
[6] Yang, Y., and Udaykumar, H. S., 2005, "Sharp Interface Cartesian Grid Method III: Solidification of Pure Materials and Binary Solutions," J. Comput. Phys., **210**, pp. 55–74.
[7] Lee, L., Li, Z., and LeVeque, R. J., 2003, "An Immersed Interface Method for Incompressible Navier-Stokes Equations," SIAM J. Sci. Comput. (USA), **25**(3), pp. 832–856.
[8] Barozzi, G. S., Bussi, C., and Corticelli, M. A., 2004, "A Fast Cartesian Scheme for Unsteady Heat Diffusion on Irregular Domains," Numer. Heat Transfer, Part B, **46**(1), pp. 59–77.
[9] Fogelson, A. L., and Keener, J. P., 2001, "Immersed Interface Methods For Neumann and Related Problems in Two and Three Dimensions," SIAM J. Sci. Comput. (USA), **22**(5), pp. 1630–1654.
[10] Kim, J., Kim, D., and Choi, H., 2001, "An Immersed-Boundary Finite-Volume Method For Simulations Of Flow In Complex Geometries," J. Comput. Phys., **171**, pp. 132–150.
[11] Zhang, L., Gerstenberger, A., Wang, X., and Liu, W. K., 2004, "Immersed Finite Element Method," Comput. Methods Appl. Mech. Eng., **193**, pp. 2051–2067.
[12] Kim, J., and Choi, H., 2004, "An Immersed-Boundary Finite-Volume Method for Simulations of Heat Transfer in Complex Geometries," KSME Int. J., **18**(6), pp. 1026–1035.
[13] Pacheco, J. R., Pacheco-Vega, A., Rodić, T., and Peck, R. E., 2005, "Numerical Simulations of Heat Transfer and Fluid Flow Problems Using an Immersed-Boundary Finite-Volume Method on Nonstaggered Grids," Numer. Heat Transfer, Part B, **48**, pp. 1–24.
[14] Fadlun, E. A., Verzicco, R., Orlandi, P., and Mohd-Yusof, J., 2000, "Combined Immersed-Boundary Finite-Difference Methods for Three-Dimensional Complex Flow Simulations," J. Comput. Phys., **161**, pp. 35–60.
[15] Mittal, R., and Iaccarino, G., 2005, "Immersed Boundary Methods," Annu. Rev. Fluid Mech., **37**, pp. 239–261.
[16] Tyagi, M., and Acharya, S., 2005, "Large Eddy Simulation of Turbulent Flows in Complex and Moving Rigid Geometries Using the Immersed Boundary Method," Int. J. Numer. Methods Fluids, **48**, pp. 691–722.
[17] Deuflhard, P., and Hochmuth, R., 2004, "Multiscale Analysis of Thermoregulation in the Human Microvascular System," Math. Methods Appl. Sci., **27**, pp. 971–989.
[18] Oyanader, M. A., Arce, P., and Dzurik, A., 2003, "Avoiding Pitfalls in Electrokinetic Remediation: Robust Design and Operation Criteria Based on First Principles For Maximizing Performance in a Rectangular Geometry," Electrophoresis, **24**(19–20), pp. 3457–3466.
[19] DeLima-Silva, W., Jr., and Wrobel, L. C., 1995, "A Front-Tracking BEM Formulation for One-Phase Solidification/Melting Problems," Eng. Anal. Boundary Elem., **16**, pp. 171–182.
[20] Amaziane, B., and Pankratov, L., 2006, "Homogenization Of A Reaction-Diffusion Equation With Robin Interface Conditions," Appl. Math. Lett., **19**(11), pp. 1175–1179.
[21] Sparrow, E. M., and Gregg, J. L., 1958, "Similar Solutions for Free Convection From a Non-Isothermal Vertical Plate," ASME J. Heat Transfer, **80**, pp. 379–386.
[22] Leonard, B. P., 1979, "A Stable And Accurate Convective Modelling Procedure Based on Quadratic Upstream Interpolation," Comput. Methods Appl. Mech. Eng., **19**, pp. 59–98.
[23] Zang, Y., Street, R. L., and Koseff, J. F., 1994, "A Non-Staggered Grid, Fractional Step Method for Time Dependent Incompressible Navier-Stokes Equations in Curvilinear Coordinates," J. Comput. Phys., **114**, pp. 18–33.
[24] Pacheco, J. R., 1999, "On the Numerical Solution of Film and Jet Flows," Ph.D thesis, Department Mechanical and Aerospace Engineering, Arizona State University, Tempe.
[25] Pacheco, J. R., and Peck, R. E., 2000, "Non-Staggered Grid Boundary-Fitted Coordinate Method for Free Surface Flows," Numer. Heat Transfer, Part B, **37**, pp. 267–291.
[26] Pacheco, J. R., 2001, "The Solution of Viscous Incompressible Jet Flows Using Non-Staggered Boundary Fitted Coordinate Methods," Int. J. Numer. Methods Fluids, **35**, pp. 71–91.
[27] Mohd-Yusof, J., 1997, "Combined Immersed-Boundary/B-Spline Methods For Simulations of Flows in Complex Geometries," CTR Annual Research Briefs, NASA Ames/Stanford University, Stanford, CA, pp. 317–327.
[28] Orlanski, I., 1976, "A Simple Boundary Condition For Unbounded Hyperbolic Flows," J. Comput. Phys., **21**, pp. 251–269.
[29] Eckert, E. R. G., and Soehngen, E., 1952, "Distribution of Heat-Transfer Coefficients Around Circular Cylinders in Crossflow At Reynolds Numbers From 20 to 500," Trans. ASME, **75**, pp. 343–347.
[30] Pan, D., 2006, "An Immersed Boundary Method on Unstructured Cartesian Meshes for Incompressible Flows With Heat Transfer," Numer. Heat Transfer, Part B, **49**, pp. 277–297.
[31] Lima E Silva, A. L. F., Silveira-Neto, A., and Damasceno, J. J. R., 2003, "Numerical Simulation of Two-Dimensional Flows over a Circular Cylinder Using the Immersed Boundary Method," J. Comput. Phys., **189**, pp. 351–370.
[32] Strykowski, P. J., and Sreenivasan, K. R., 1990, "On the Formation and Suppression of Vortex Shedding at Low Reynolds Numbers," J. Fluid Mech., **218**, pp. 71–107.
[33] Moukalled, F., and Darwish, M., 1997, "New Bounded Skew Central Difference Scheme, Part II: Application to Natural Convection in an Eccentric Annulus," Numer. Heat Transfer, Part B, **31**, pp. 111–133.
[34] Sadat, H., and Couturier, S., 2000, "Performance and Accuracy of a Meshless Method for Laminar Natural Convection," Numer. Heat Transfer, Part B, **37**, pp. 455–467.
[35] Demirdžić, I., Lilek, Ž., and Perić, M., 1992, "Fluid Flow and Heat Transfer Test Problems for Nonorthogonal Grids: Bench-Mark Solutions," Int. J. Numer. Methods Fluids, **15**, pp. 329–354.
[36] Carslaw, H. S., and Jaeger, J. C., 1986, *Conduction of Heat in Solids*, 2nd ed., Oxford University Press, Oxford.
[37] Özisik, M. N., 1989, *Boundary Value Problems of Heat Conduction*, Dover, Mineola, NY.
[38] Johnson, T. A., and Patel, V. C., 1999, "Flow Past a Sphere up to Reynolds Number of 300," J. Fluid Mech., **378**, pp. 19–70.
[39] Magarvey, R. H., and Bishop, R. L., 1961, "Transition Ranges for Three-Dimensional Wakes," Can. J. Phys., **39**, pp. 1418–1422.
[40] Feng, Z.-G., and Michaelides, E. E., 2000, "A Numerical Study on the Transient Heat Transfer From a Sphere at High Reynolds and Peclet Numbers," Int. J. Heat Mass Transfer, **43**, pp. 219–229.
[41] Hunt, J. C. R., Wray, A. A., and Moin, P., 1988, "Eddies, Stream, and Convergence Zones in Turbulent Flows," *Proceedings of the 1988 CTR Summer Program*, NASA Ames/Stanford University, Stanford, CA, pp. 193–208.
[42] Constantinescu, S. G., and Squires, K. D., 2004, "Numerical Investigation of the Flow Over a Sphere in the Subcritical and Supercritical Regimes," Phys. Fluids, **16**(5), pp. 1449–1467.
[43] Jeong, J., and Hussain, F., 1995, "On the Identification of a Vortex," J. Fluid Mech., **285**, pp. 69–94.

Heat Transfer and Fluid Flow Characteristics of Separated Flows Encountered in a Backward-Facing Step Under the Effect of Suction and Blowing

E. Abu-Nada
e-mail: eiyad@hu.edu.jo

A. Al-Sarkhi

B. Akash

I. Al-Hinti

Department of Mechanical Engineering,
Hashemite University,
Zarqa, 13115, Jordan

Numerical investigation of heat transfer and fluid flow over a backward-facing step (BFS), under the effect of suction and blowing, is presented. Here, suction/blowing is implemented on the bottom wall (adjacent to the step). The finite volume technique is used. The distribution of the modified coefficient of friction and Nusselt number at the top and bottom walls of the BFS are obtained. On the bottom wall, and inside the primary recirculation bubble, suction increases the modified coefficient of friction and blowing reduces it. However, after the point of reattachment, mass augmentation causes an increase in the modified coefficient of friction and mass reduction causes a decrease in modified coefficient of friction. On the top wall, suction decreases the modified coefficient of friction and blowing increases it. Local Nusselt number on the bottom wall is increased by suction and is decreased by blowing, and the contrary occurs on the top wall. The maximum local Nusselt number on the bottom wall coincides with the point of reattachment. High values of average Nusselt number on the bottom wall are identified at high Reynolds numbers and high suction bleed rates. However, the low values correspond to high blowing rates. The reattachment length and the length of the top secondary recirculation bubble are computed under the effect of suction and blowing. The reattachment length is increased by increasing blowing bleed rate and is decreased by increasing suction bleed rate. The spots of high Nusselt number, and low coefficient of friction, are identified by using contour maps. [DOI: 10.1115/1.2759973]

Keywords: separated flows, heat transfer, backward-facing step, blowing, suction, porous wall

Introduction

Heat transfer and fluid flow in separated flows are frequently encountered in various engineering applications. Some examples include microelectronic circuit boards, combustors, heat exchangers, axial and centrifugal compressor blades, and gas turbines blades. The flow over a backward-facing step (BFS) has the most basic features of separated flows, such as separation, reattachment, recirculation, and development of shear layers. It is well known that heat transfer and fluid flow characteristics experience large variation within separated regions. Thus, it is very essential to understand the mechanisms of heat transfer in such regions in order to enhance heat and fluid flow.

Most of the published work on BFS has been extensively investigated for impermeable walls. For example, Armaly et al. [1] studied laminar, transition, and turbulent isothermal flows over a BFS, experimentally. In their experiments, the expansion ratio was close to 2 and the downstream aspect ratio close to 18. Also, numerical studies in the laminar regime for isothermal flows were conducted by Armaly et al. [1], Gartling [2], and Kim and Moin [3]. Thangam and Knight [4] studied the effect of step height on the separated flow past a backward-facing step. On the other hand, flow over a BFS with heat transfer was conducted [5–17]. Abu-Mulaweh [18] conducted an extensive review of research on laminar mixed convection over a BFS.

Three-dimensional studies were also conducted for flow over a BFS. A recent study by Williams and Baker [19] focused on three-dimensional numerical simulations of laminar flow over a step with sidewalls, having the same expansion ratio and aspect ratio of Armaly et al. [1]. The range of the Reynolds number studied was $100 < \mathrm{Re} < 800$. Williams and Baker [19] reported that "the interaction of a wall jet located at the step plane to the side walls with the mainstream flow causes a penetration of three-dimensional flow structure into flow near the mid plane of the channel." This penetration reduces the size of the upper secondary zone compared to two-dimensional simulation, which leads to an increase in reattachment length of the primary zone with Reynolds number. Also, they reported that the observed three-dimensionality is not caused by an inherent hydrodynamic instability of the two-dimensional base flow, but rather by the boundary conditions imposed by the sidewalls.

Moreover, Tylli et al. [20] focused on three-dimensional effects induced by the presence of sidewalls. They conducted particle image velocimetry (PIV) measurements accompanied with three-dimensional numerical simulations, for an expansion ratio of 2 and a downstream aspect ratio of 20. They showed that for $\mathrm{Re} < 400$ the sidewall effects do not affect the structure of the two-dimensional flow at the channel midplane. Also, they illustrated the existence of a wall-jet moving toward the channel midplane that causes the three-dimensionality of the flow. The wall jet intensity increases with Reynolds number for laminar flow. Moreover, they studied the effect of sidewalls on the upper secondary recirculation bubble and on the primary bubble and showed that,

Contributed by the Heat Transfer Division of ASME for publication in JOURNAL OF HEAT TRANSFER. Manuscript received August 22, 2006; final manuscript received February 1, 2007. Review conducted by Louis C. Burmeister.

for laminar flow, these effects explain the discrepancies between experimental results and two-dimensional numerical simulations.

Chiang and Sheu [21] performed three-dimensional numerical simulations for laminar flow over a BFS with the same geometry dimensions used by Armaly et al. [1]. They reported that the flow structure at the midplane, for Re=800, is similar to two-dimensional flow for channel width of up to 100 times of the step height. Further three-dimensional investigations were also conducted by Chiang and Sheu [22,23].

In terms of fundamental studies of the flow stability, Kaiktsis et al. [24] have investigated the effects of convective instabilities. Barkley et al. [25] have shown that in the absence of sidewalls the transition to three-dimensional flow structures appears at higher values of Reynolds number around 1000, via a steady bifurcation. They found that the critical eigenmode responsible for three-dimensionality is characterized by flat streamwise rolls located in the primary recirculation bubble.

Studies on BFS with permeable walls, by means of suction and blowing, have also been conducted. For example, Yang et al. [26] studied the effect of mass bleed in separated reattaching turbulent flow behind a BFS, experimentally. Batenko and Terekhov [27] conducted two-dimensional simulation for unconfined flow past a step and flow evolution in a confined channel. Kaiktsis and Monkewitz [28] studied the global destabilization of flow over a BFS by means of simultaneous suction and blowing, using numerical simulations. The extensive interest and research conducted on BFSs, in the last two decades, with the complex physics encountered in separated flow over the BFS has motivated the present investigation. The objective of the present work is to perform a detailed study on the effect of suction and blowing on the heat transfer and flow characteristics of steady flow over a BFS.

Governing Equations

The nondimensional continuity, momentum, and energy equations in Cartesian coordinates for steady flow are given as [29]

$$\frac{\partial u}{\partial x}+\frac{\partial v}{\partial y}=0 \tag{1}$$

$$u\frac{\partial u}{\partial x}+v\frac{\partial u}{\partial y}=-\frac{\partial p}{\partial x}+\frac{1}{\mathrm{Re}}\left(\frac{\partial^2 u}{\partial x^2}+\frac{\partial^2 u}{\partial y^2}\right) \tag{2}$$

$$u\frac{\partial v}{\partial x}+v\frac{\partial v}{\partial y}=-\frac{\partial p}{\partial y}+\frac{1}{\mathrm{Re}}\left(\frac{\partial^2 v}{\partial x^2}+\frac{\partial^2 v}{\partial y^2}\right) \tag{3}$$

$$u\frac{\partial \theta}{\partial x}+v\frac{\partial \theta}{\partial y}=\frac{1}{\mathrm{Re}\,\mathrm{Pr}}\left(\frac{\partial^2 \theta}{\partial x^2}+\frac{\partial^2 \theta}{\partial y^2}\right) \tag{4}$$

where

$$\mathrm{Re}=\frac{u_m D_H}{\nu}$$

$$\mathrm{Pr}=\frac{\nu}{\alpha}$$

The following dimensionless quantities are used:

$$x=\frac{\overset{*}{x}}{D_H},\quad y=\frac{\overset{*}{y}}{D_H},\quad u=\frac{\overset{*}{u}}{u_m},\quad v=\frac{\overset{*}{v}}{u_m},\quad p=\frac{\overset{*}{p}}{\rho u_m^2},\quad \text{and}$$

$$\theta=\frac{T-T_{wc}}{T_{wh}-T_{wc}}$$

where T_{wh} is the constant temperature of the hot wall and T_{wc} is the constant temperature of the cold wall.

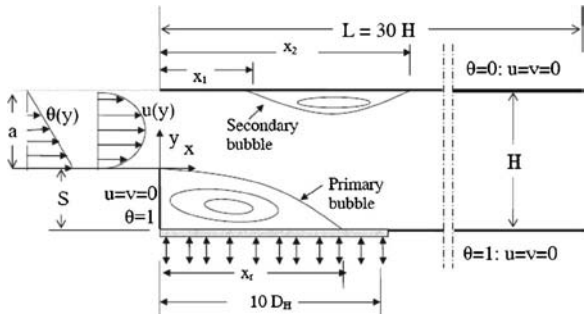

Fig. 1 Sketch of the problem geometry and boundary conditions

Problem Description

The basic flow configuration under study is shown in Fig. 1. The expansion ratio (ER=H/S) is set equal to 2.0. In the x direction, the physical domain is bounded by $0<x<(30H)$. Also, in the y direction the physical domain is bounded by $-(1/2)<y<(1/2)$. The flow is assumed two-dimensional, steady, incompressible, and having constant fluid properties.

Part of the channel's bottom wall, adjacent to the step, is considered permeable and constant uniform velocity is allowed to bleed through it (see Fig. 1). The shaded area represents the porous segment of the bottom wall. In order to study the effect of mass bleed on the entire primary recirculation bubble on the lower wall, the length of the porous segment must be at least equal to the reattachment length. It is very well documented in literature that, for Re<800, the reattachment length will not exceed a value of $10D_H$ [1–7]. Thus, this length was selected for the present study. The arrows that are shown on the porous segment represent the direction of mass bleed through the wall. Inward direction represents blowing in the domain, and outward direction represents suction flow out of the domain.

At the inlet, the flow is assumed hydrodynamically fully developed, where a dimensionless parabolic velocity distribution is given as [30]

$$u(y)=12(y-2y^2) \tag{5}$$

A no-slip velocity boundary condition is applied at the top wall of the channel and at the vertical wall of the step because these two walls are assumed impermeable. However, only the x component of velocity is set equal to zero at the bottom wall, where normal bleed velocity is imposed (for $x<10D_H$). However, for $x>10D_H$ a no-slip boundary condition is also imposed on the bottom wall.

A fully developed velocity is assumed at the channel outlet

$$\frac{\partial u}{\partial x}=\frac{\partial v}{\partial x}=0 \tag{6}$$

The dimensional y component of velocity at the porous segment is set equal to $\overset{*}{v}_w$. A nondimensional bleed coefficient is defined as [31]:

$$\sigma=\frac{\overset{*}{v}_w}{u_m} \tag{7}$$

The values of bleed coefficient used in the present work are ± (0, 0.00125, 0.0025, and 0.005), where positive values correspond to blowing and negative values correspond to suction. The case of zero value of bleed coefficient corresponds to impermeable wall. Therefore, the nondimensional velocity at the porous segment is equal to the bleed coefficient. This is expressed as

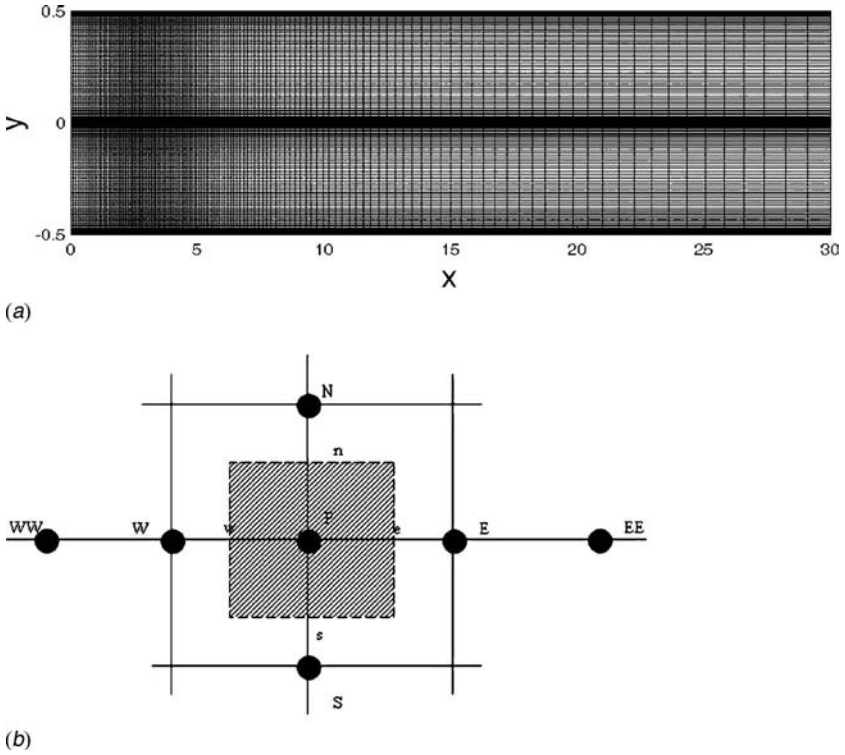

Fig. 2 (*a*) Computational mesh and (*b*) typical control volume

$$v_w = \sigma \tag{8}$$

Note that a bleed coefficient of 0.005 corresponds to a blowing volume flow rate equal to 10% of the volume flow rate at inflow.

The temperature at the inlet is assumed to be fully developed and is given as [32]

$$\theta = 1 - 2y \tag{9}$$

The temperature boundary condition at the outlet is given as

$$\frac{\partial \theta}{\partial x} = 0 \tag{10}$$

The temperature is set as a constant value ($\theta=1$) on the step vertical wall and on the bottom wall downstream of the step, including the porous segment. The temperature at the top flat wall is set to zero ($\theta=0$).

The total length of the computational domain is taken as ($L=30H$) to ensure fully developed outlet boundary condition [2,5,6,32].

Numerical Implementation

Equations (1)–(4), with corresponding boundary conditions (i.e., Eqs. (5), (6), and (8)–(10)), are solved using the finite volume approach [33,34]. The SIMPLE algorithm is used as the computational algorithm [33,34]. The diffusion term in the momentum and energy equations is approximated by second-order central difference which gives a stable solution. However, a second-order upwind differencing scheme is adopted for the convective terms. This scheme uses second-order extrapolation of two upwind neighbors to determine any transport quantity ϕ. The second-order upwind term is written in the following general form:

$$\left.\frac{\partial(u\phi)}{\partial x}\right|_P = \frac{1}{2\Delta x}(3u_P\phi_P - 4u_W\phi_W + 3u_{WW}\phi_{WW}), \quad \text{for} \quad u > 0 \tag{11}$$

$$\left.\frac{\partial(u\phi)}{\partial x}\right|_P = \frac{1}{2\Delta x}(-u_{EE}\phi_{EE} + 4u_E\phi_E - 3u_P\phi_P), \quad \text{for} \quad u < 0 \tag{12}$$

Similar expressions could be written for the y direction. Figure 2 shows the computational mesh and the control volume with the symbols used in Eqs. (11) and (12).

In the x direction, a fine grid is used in the regions near the point of reattachment to resolve the steep velocity gradients while a coarser grid is used downstream the point [35]. However, in the y direction, a fine grid is used near the top, the bottom walls, and directly at the step. Fine mesh in the x and y directions is generated by using an algebraic grid-stretching technique that results in considerable savings in terms of the grid size and in computational time.

In the x direction, the grid-stretching method is implemented by constructing uniformly distributed grid points in the x direction, and then transforming these points into a nonuniform mesh. The transformation is given as [35,36]

$$x = D_x\left\{1 + \frac{\sinh[\beta(X-A)]}{\sinh(\beta A)}\right\} \tag{13}$$

where x is the location of nonuniform stretched grid points, X is the location of the uniformly distributed grid points, and A is a constant given by [35,36]

$$A = \frac{1}{2\beta}\ln\left[\frac{1 + (e^{\beta} - 1)(D_x/L)}{1 + (e^{-\beta} - 1)(D_x/L)}\right] \tag{14}$$

The parameter β is a stretching constant, D_x is the location of grid clustering in the x direction, and L is the channel length. This grid stretching is used in the x direction. However, another transformation is used in the y direction and is given as [36]

$$y = D_H \left\{ \frac{(2D_y+\gamma)\left(\frac{\gamma+1}{\gamma-1}\right)^{(Y-D_y)/(1-D_y)} + 2D_y - \gamma}{(2D_y+1)\left[1+\left(\frac{\gamma+1}{\gamma-1}\right)^{(Y-D_y)/(1-D_y)}\right]} \right\} \quad (15)$$

where D_y represents the location of grid clustering in the y direction, γ is a stretching constant in the y direction, and Y is the location of the uniformly distributed grid points in the y direction. Figure 2(a) shows the computational nonuniform mesh used in the present work. The algebraic finite volume equations for the momentum and energy equations, in discretized form, are written into the following form:

$$-a_E\phi_E - a_W\phi_W + a_P\phi_P = a_N\phi_N + a_S\phi_S + b \quad (16)$$

where P, W, E, N, and S denote cell location, west face of the control volume, east face of the control volume, north face of the control volume, and south face of the control volume, respectively (see Fig. 2(b)) and b is a source term. The symbol ϕ in Eq. (13) holds for u, v, or T. The resulting algebraic equations are solved using the tridiagonal matrix algorithm (Thomas algorithm) with the line-by-line relaxation technique. The convergence criteria were defined by the following expression:

$$\varepsilon = \frac{\sum_{j=1}^{j=M}\sum_{i=1}^{i=N}|\text{resid}_{ij}|}{\sum_{j=1}^{j=M}\sum_{i=1}^{i=N}|\phi_{ij}|} < 10^{-5} \quad (17)$$

where ε is the tolerance and "resid" is the residual; M and N are the number of grid points in the x and the y directions, respectively.

After solving for u, v, and T, further useful quantities are obtained. For example, the Nusselt number can be expressed as:

$$\text{Nu} = \frac{h(D_H)}{k} \quad (18)$$

The heat transfer coefficient is expressed as

$$h = \frac{q_w}{T_w - T_b} \quad (19)$$

The thermal conductivity is expressed as

$$k = -\frac{q_w}{\partial T/\partial y^*} \quad (20)$$

By substituting Eqs. (19) and (20) into Eq. (18), and using the nondimensional quantities, the Nusselt number on the bottom wall is written as

$$\text{Nu} = -\left.\frac{1}{\theta_w - \theta_b}\frac{\partial\theta}{\partial y}\right|_{y=-1/2} \quad (21)$$

Similarly, the Nusselt number on the top wall is written as

$$\text{Nu} = -\left.\frac{1}{\theta_w - \theta_b}\frac{\partial\theta}{\partial y}\right|_{y=1/2} \quad (22)$$

where θ_b is bulk temperature, defined as

$$\theta_b = \frac{\int_{-1/2}^{1/2} u\theta dy}{\int_{-1/2}^{1/2} u dy}$$

The coefficient of friction is defined as [29]

$$C_f = \frac{\tau_w}{1/2\rho u_m^2} \quad (23)$$

The shear stress at the wall (τ_w) is expressed as

$$\tau_w = \mu\frac{du^*}{dy^*}$$

Using the definition of nondimensional quantities, the shear stress at the wall is expressed as

$$\tau_w = \frac{\mu u_m}{D_H}\frac{du}{dy} \quad (24)$$

Substituting Eq. (24) into Eq. (23), the coefficient of friction is written as

$$C_f = \frac{2}{\text{Re}}\frac{du}{dy} \quad (25)$$

The modified coefficient of friction is defined as

$$C_f^* = \frac{C_f\,\text{Re}}{2} \quad (26)$$

The average coefficient of friction on the top or bottom wall is defined as

$$C_{f\text{avg}} = \frac{\int_0^L \sqrt{(C_f^*(x))^2}dx}{L} \quad (27)$$

Similarly, the average Nusselt number is defined as

$$\text{Nu}_{\text{avg}} = \frac{\int_0^L \sqrt{[\text{Nu}(x)]^2}dx}{L} \quad (28)$$

Table 1 Grid independence study for σ=0, Re=800, ER=2.0: values of x_r, x_1, and x_2, as defined in Fig. 1

Grid Size	x_r	x_1	x_2
13×24	6.50	Not predicted	Not predicted
25×50	4.00	2.50	5.20
37×75	3.35	2.35	5.47
49×100	5.77	4.65	9.45
75×150	5.90	4.81	9.76
101×199	6.00	4.81	10.10
125×250	6.00	4.81	10.14
151×299	6.00	4.81	10.15

Grid Testing

Extensive mesh testing was performed to guarantee a grid-independent solution. Eight different meshes were used for Re =800 and ER=2.0 as shown in Table 1. The problem selected for the grid testing is the flow over a BFS with impermeable walls. This is a well-known benchmark problem and is accepted as a benchmark problem by the "Benchmark Solutions to Heat Transfer Problems" organized by the K-12 Committee of the ASME for code validation and assessment [4,5]. The present code was tested for grid independence by calculating the reattachment length (x_r), beginning of the top secondary bubble (x_1), and end of the upper secondary bubble (x_2); see Fig. 1. Table 1 reports the results obtained for the grid independence study. As shown in Table 1, a grid size of 125×250 (125 grid points in y and 250 grid points in x) ensures a grid-independent solution. Moreover, a grid-independence test is carried out for the permeable case for σ= −0.005 and Re=800 as shown in Table 2. It is clear that a grid size of 125×250 ensures a grid independent solution.

Table 2 Grid independence study for $\sigma=-0.005$, Re=800, ER =2.0: values of x_r, x_1, and x_2, as defined in Fig. 1

Grid Size	x_r	x_1	x_2
13×24	5.24	3.10	3.97
25×50	2.39	1.47	4.24
37×75	2.47	1.58	6.30
49×100	2.87	1.93	9.11
75×150	3.60	2.34	11.10
101×199	3.73	2.60	12.05
125×250	3.75	2.61	12.17
151×299	3.75	2.62	12.17

Code Validation

The present numerical solution is validated by comparing the present code results for the benchmark problem for Re=800 and ER=2.0 to the experiment of Armaly et al. [1] and to other numerical published data [2–6]. The problem selected for the grid testing is the flow over a BFS with impermeable walls. As shown in Table 3, the code results are very close to the previous numerical published results. However, all of the numerical published works, including the present one, underestimate the reattachment length. According to Armaly et al. [1], the flow at Re=800 has three-dimensional features. Therefore, the underestimation of x_r, by all numerical published data is due to the two-dimensional assumption embedded in the numerical solution [1,4,37]. More specifically, it is due to the sidewall-induced three-dimensional effects [19,20]. According to Williams and Baker [19], the interaction of a wall jet at the step near the sidewalls with the mainstream flow causes formation of three-dimensional flow structure in a region of essentially two-dimensional flow near the midplane of the channel. Thus, the underestimation of the reattachment length at high values of Reynolds number is due to the influence of the three-dimensional effects due to sidewalls [19,20]. Note that Barkely et al. [25] have shown that in the absence of sidewalls the transition to three-dimensional flow structures appears at higher values of Reynolds number of $\sim$1000.

Further comparisons between present code and previously published data, for ER=3, 2, and 3/2, are given in Fig. 3(*a*), which shows good agreement between the present results and the experiment of Armaly et al. [1] for $Re\leq600$. Also, it shows good agreement with all numerical published data for the whole range of Reynolds numbers and the whole range of expansion ratios. Furthermore, comparisons of temperature and x component of velocity profiles are shown in Figs. 3(*b*)–3(*d*), also showing good agreement between the present and previous investigations.

Results and Discussion

The range of Reynolds number used in the present work is $200\leq Re\leq800$. The range of bleed coefficient is taken as $-0.005\leq\sigma\leq0.005$. The Prandtl number is kept constant at 0.71.

Figure 4(*a*) shows that the reattachment length x_r distribution versus bleed coefficient. It is clear that suction decreases the value of x_r. This is due to the streamlines' attraction to the bottom wall.

Table 3 Validation tests for Re=800: values of x_r, x_1, and x_2 (defined in Fig. 1) for previous investigations and present work

Authors	Type of Work	x_r	x_1	x_2
Armaly et al. [1]	Experimental	7.20	5.30	9.40
Vradis et al. [5]	Numerical	6.13	4.95	8.82
Kim and Moin [3]	Numerical	6.00	No data	No data
Gartling [2]	Numerical	6.10	4.85	10.48
Pepper et al. [6]	Numerical	5.88	4.75	9.80
Present work	Numerical	6.00	4.81	10.15

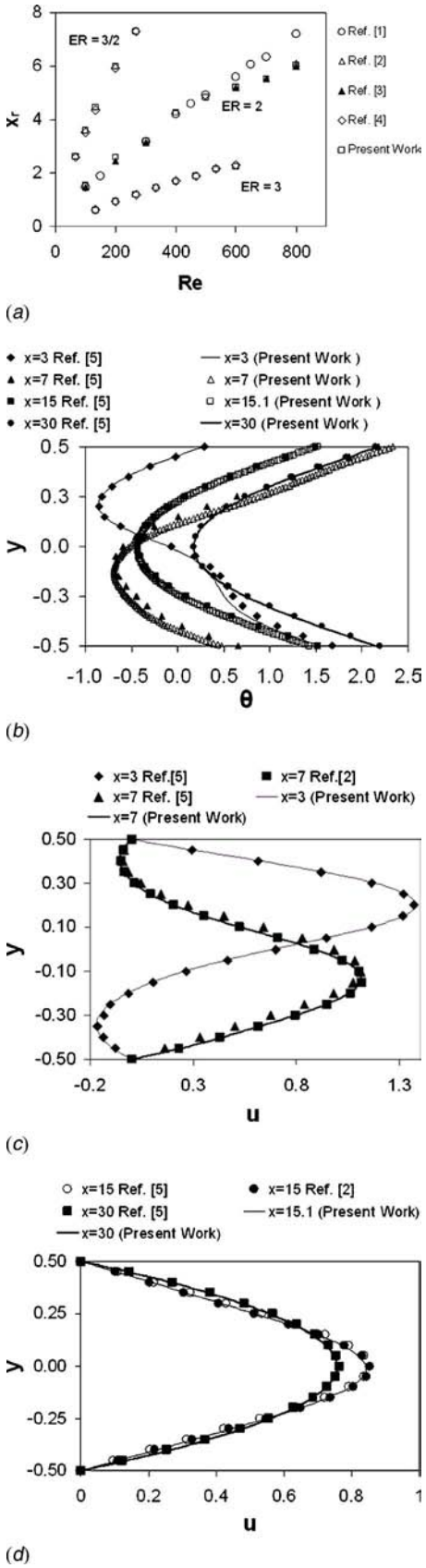

Fig. 3 Model validation: (*a*) reattachment length versus Reynolds number for various expansion ratios; (*b*) temperature profiles, Re=800; (*c*) velocity profiles, x=3 and 7, Re=800; and (*d*) velocity profiles, x=15 and 30, Re=800

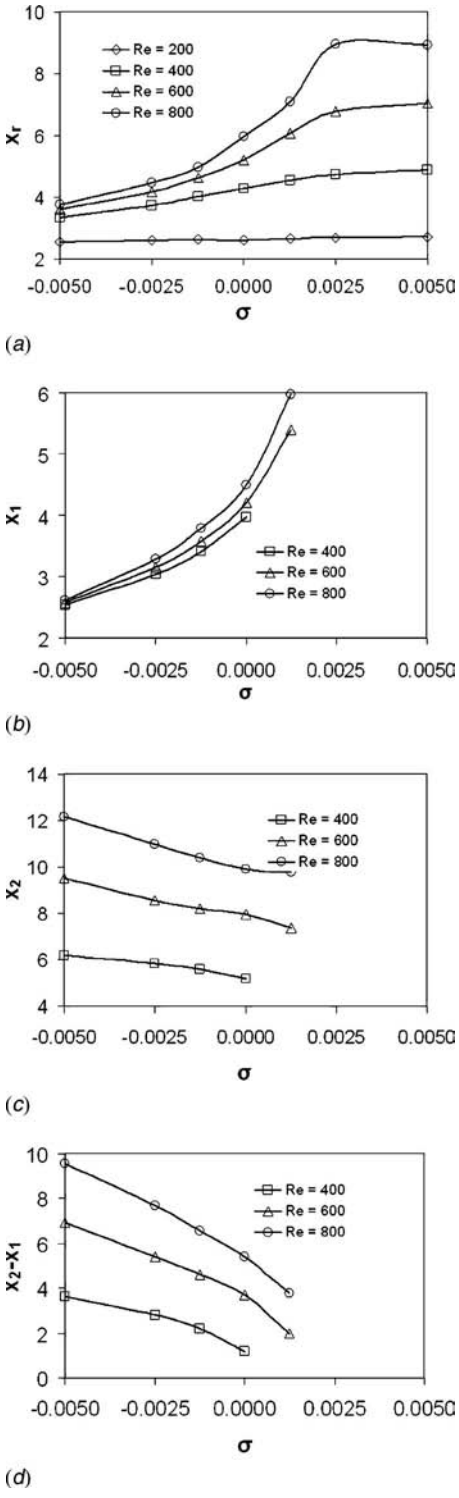

Fig. 4 (*a*) **Reattachment length,** (*b*) **beginning of secondary recirculation bubble on the top wall,** (*c*) **end of secondary recirculation bubble on the top wall, and** (*d*) **length of top-wall recirculation zone**

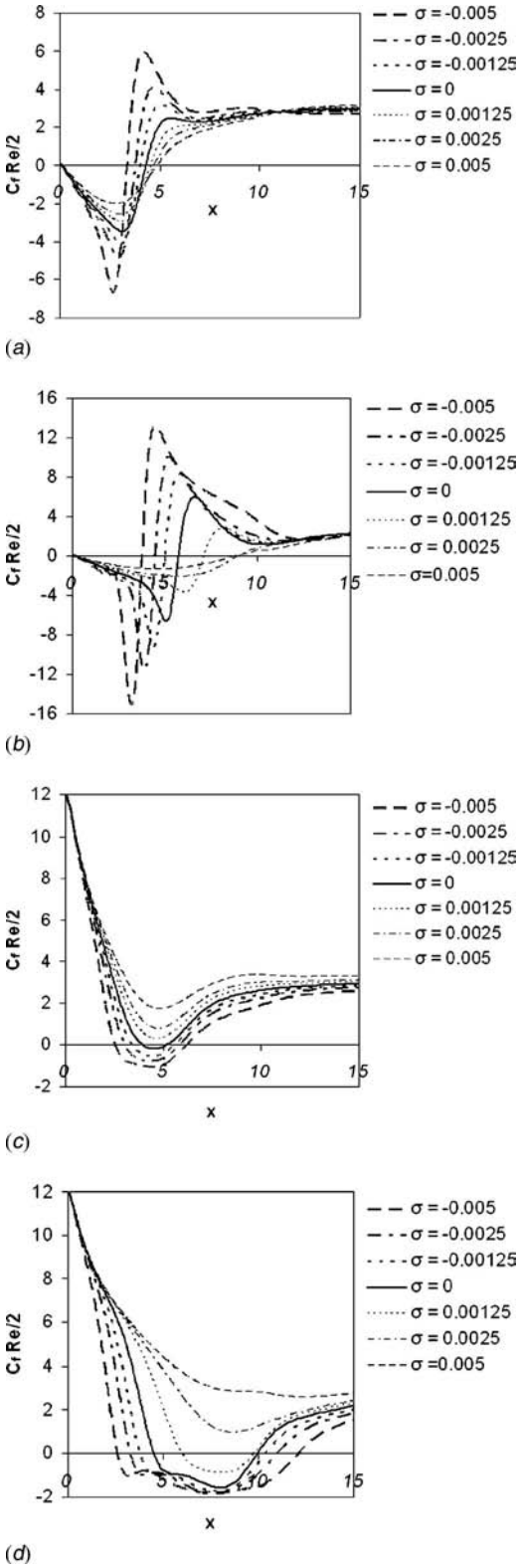

Fig. 5 Distribution of coefficient of friction: (*a*) **Bottom wall Re=400** (*b*) **bottom wall Re=800,** (*c*) **top wall Re=400, and** (*d*) **top wall Re=800**

On the other hand, for the case of blowing and for the case or Re=800, the reattachment length first increases with blowing until it reaches a maximum value, then it starts decreasing. The reason for this behavior is that, for high values of bleed coefficient, blowing forces the flow to detach. Thus, there is a specific value of blowing bleed coefficient corresponding to the maximum reattachment length. Figures 4(*b*) and 4(*c*) show the beginning and the end of the upper recirculation zone, respectively. Moreover, Fig. 4(*d*) shows the length of the secondary bubble. Also, Figs. 4(*b*)–4(*d*) show that the secondary bubble only exists for values of σ lower (or slightly higher) than 0.00125.

Figures 5(*a*) and 5(*b*) present the distribution of the modified

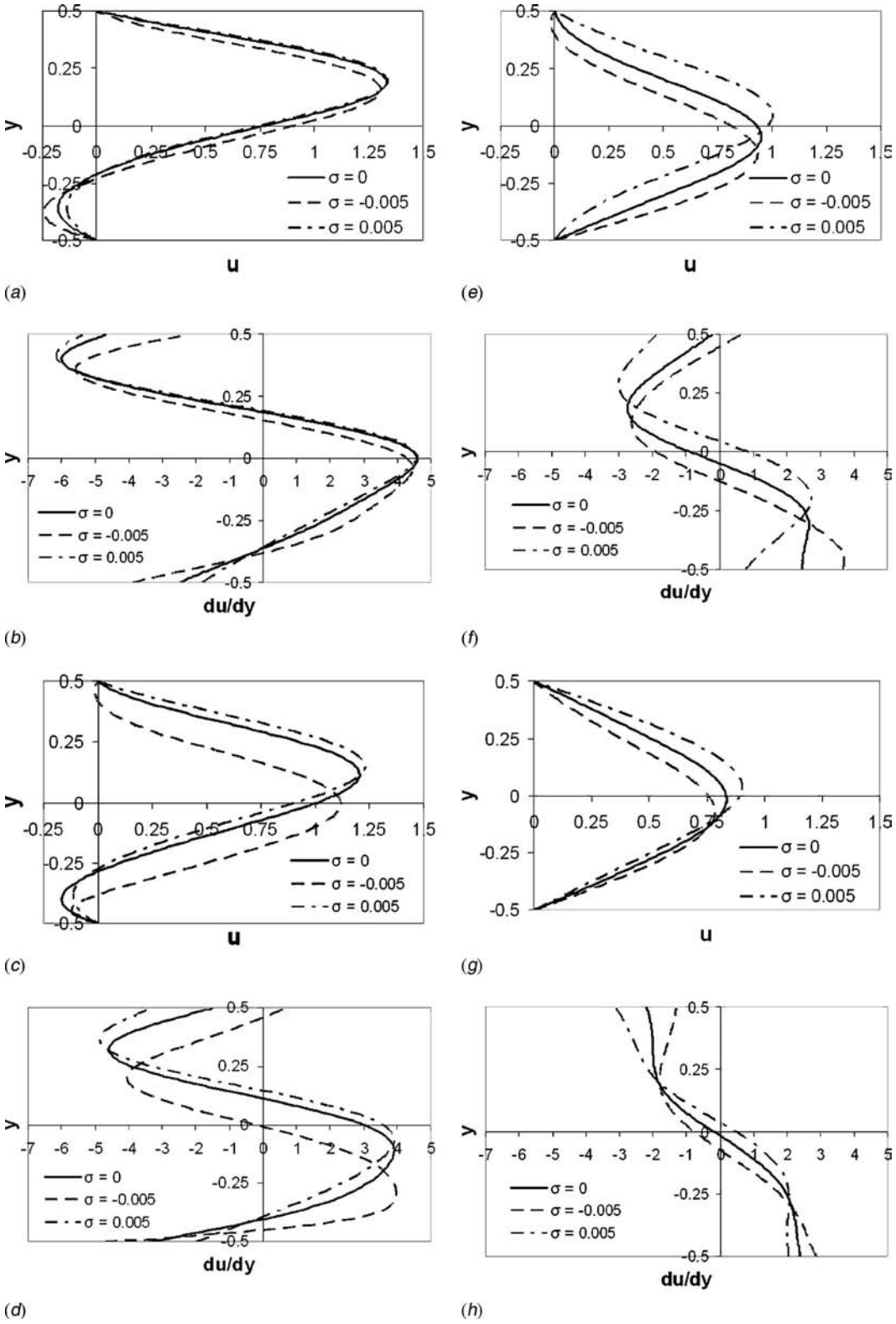

Fig. 6 ***x*** **component of velocity (*u*) and velocity gradients profiles(*du*/*dy*) for Re=400: (*a*) *u* at *x*=2.0, (*b*) *du*/*dy* at *x*=2.0, (*c*) *u* at *x*=3.0, (*d*) *du*/*dy* at *x*=3.0, (*e*) *u* at *x*=5.50, (*f*) *du*/*dy* at *x*=5.50, (*g*) *u* at *x*=8.0, and (*h*) *du*/*dy* at *x*=8.0**

coefficient of friction for various values of bleed coefficient on the bottom wall for Re=400 and 800, respectively. The modified coefficient of friction is negative inside the recirculation bubble due to the backflow. The backflow is recognized by the negative values of velocity and negative velocity gradients as shown in Figs. 6(*a*) and 6(*b*). At the point of reattachment, the coefficient of friction is zero due to the vanished velocity gradients.

By examining the effect of blowing on modified coefficient of friction, within the recirculation bubble, it is clear that blowing decreases the coefficient of friction. This is due to the repulsion of

streamlines from the bottom wall. Therefore, blowing reduces velocity gradients, as shown in Figs. 6(*a*)–6(*d*), and accordingly reduces the coefficient of friction. This behavior prevails after the point of reattachment, but a second opposing effect takes place beyond this point, which is the mass augmentation. The mass augmentation causes an increase in velocity gradients, which results in higher values of the coefficient of friction. This is clearly demonstrated in Figs. 6(*e*)–6(*h*) where the velocity gradients increase in the x direction. Thus, the reduction of coefficient of friction due to streamline repulsion is counteracted by mass augmentation effect. These two opposing factors reach a point where their net effect on modified coefficient of friction diminishes. This point is identified as the intersection of the blowing line with the impermeable wall case.

The effect of suction on the modified coefficient of friction is opposite to the effect of blowing. Before the reattachment point, suction increases the coefficient of friction due to streamlines attraction. However, after the reattachment point the mass reduction, due to suction, reduces coefficient of friction. It is important to note that for the case of suction the coefficient of friction has a peak value after the reattachment point. This peak coincides with the appearance of the secondary recirculation bubble on the top wall. The top secondary bubble narrows down the flow passage and maximizes local velocity gradients on the bottom wall.

The distribution of the coefficient of friction on the top wall is shown in Figs. 5(*c*) and 5(*d*) for Re=400 and 800, respectively. The effect of suction and blowing on the modified coefficient of friction on the top wall is opposite to that on the bottom wall. At the top wall, the flow develops as a laminar boundary layer where the maximum coefficient of friction is detected at the leading edge of the top wall, as shown in Figs. 5(*c*) and 5(*d*). The thickness of the boundary layer on the top wall is reduced by blowing, which results in an increase in the coefficient of friction. It is worth mentioning that the laminar boundary layer on the top wall is sensitive to adverse pressure gradient due to geometry expansion. By increasing the Reynolds number, the adverse pressure gradient increases, which leads to flow separation in the top-wall boundary layer. The first separation point on the top wall is identified by the beginning of the secondary recirculation bubble. The effect of suction is to widen the secondary bubble by repulsion of streamlines from the top wall. This is demonstrated in Fig. 5(*c*). However, blowing shrinks the secondary bubble by delaying boundary layer separation or eliminating it for a relatively high bleed coefficient, as shown in Figs. 5(*c*) and 5(*d*).

Figures 7(*a*)–7(*c*) present streamline patterns for Re=400, where the effect of suction and blowing on the primary recirculation bubble and the secondary recirculation bubble is clearly demonstrated. Figure 8 shows the distribution of average coefficient of friction versus bleed coefficient. On the bottom wall, the flow at Re=800 is more sensitive to bleed than that of Re=400. A comprehensive view for the distribution of the coefficient of friction on the bottom and top walls is presented in Fig. 9, where contour maps are presented for the average modified coefficient of friction on the bottom and top walls. Figure 9 is very useful in characterizing the spots of high values of coefficient of friction. For example, at the bottom wall, high values of the modified coefficient of friction correspond to the high suction bleed coefficient and high Reynolds numbers. However, low values of coefficient of friction are identified by high values of Reynolds numbers and high blowing bleed rates. On the top wall, the high values of the coefficient of friction are characterized by high blowing bleed coefficients. However, lower values correspond to high Reynolds numbers and high suction bleed rates.

Figures 10(*a*) and 10(*b*) present the variation of Nusselt number on the bottom wall and show that Nusselt number increases by suction and decreases by blowing. Suction increases the velocity gradient on the bottom wall, which leads to an increase in the temperature gradient; see Figs. 11 and 12. By studying Fig. 4(*a*), Figs. 10(*a*) and 10(*b*) simultaneously, it is clear that the maximum

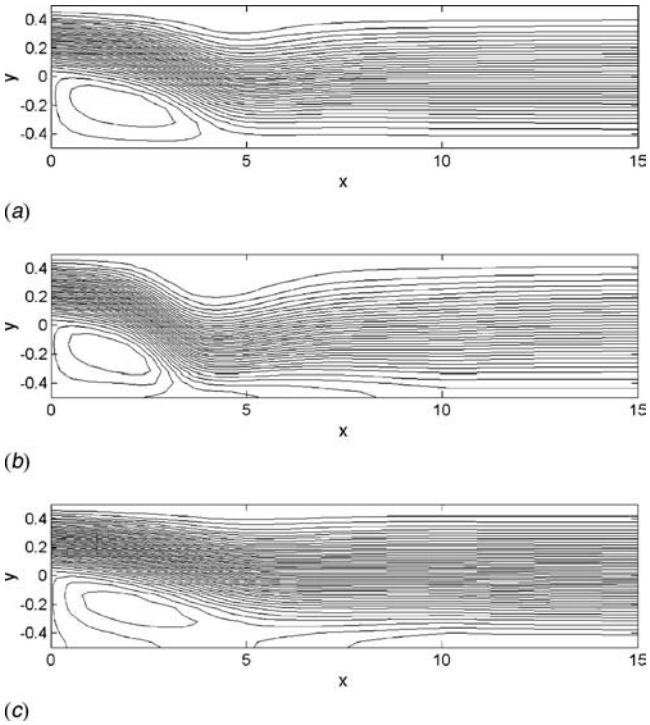

Fig. 7 Streamline patterns for Re=400: (*a*) $\sigma=0$, (*b*) $\sigma=-0.005$, (*c*) $\sigma=0.005$

value of Nusselt number on the bottom wall coincides with the point of reattachment. Besides, Fig. 10 shows that the local maximum in the Nusselt number distribution disappears for high values of the blowing bleed coefficient. The reason for this behavior is that, for high values of the blowing bleed coefficient, the flow is forced to detach. Figures 10(*c*) and 10(*d*) show the effect of the bleed coefficient on the Nusselt number for the top wall. It is clear that Nusselt number increases by blowing and decreases by suction, which is contrary to what happens on the bottom wall. The reason is that suction at the bottom wall repulses streamlines from the top wall. This leads to lower temperature gradients on the top wall and accordingly lower values of Nusselt number.

Figure 13 presents the average Nusselt number on the bottom and top walls. For the bottom wall, the average Nusselt number increases by suction and decreases by blowing. Also, it is clear that average Nusselt number on the bottom wall is more sensitive to mass bleeding than on the top wall. This is because bleed is imposed on the bottom wall. Figure 14 shows contour maps for the average Nusselt number on the bottom and top walls. The maximum values of the average Nusselt number, on the bottom wall, are identified by high values of Reynolds number and high suction bleed rates. Lower values of Nusselt number correspond

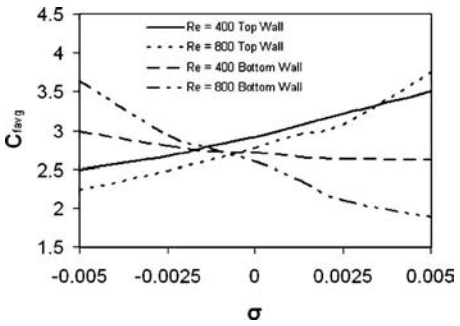

Fig. 8 Average coefficient of friction versus bleed coefficient

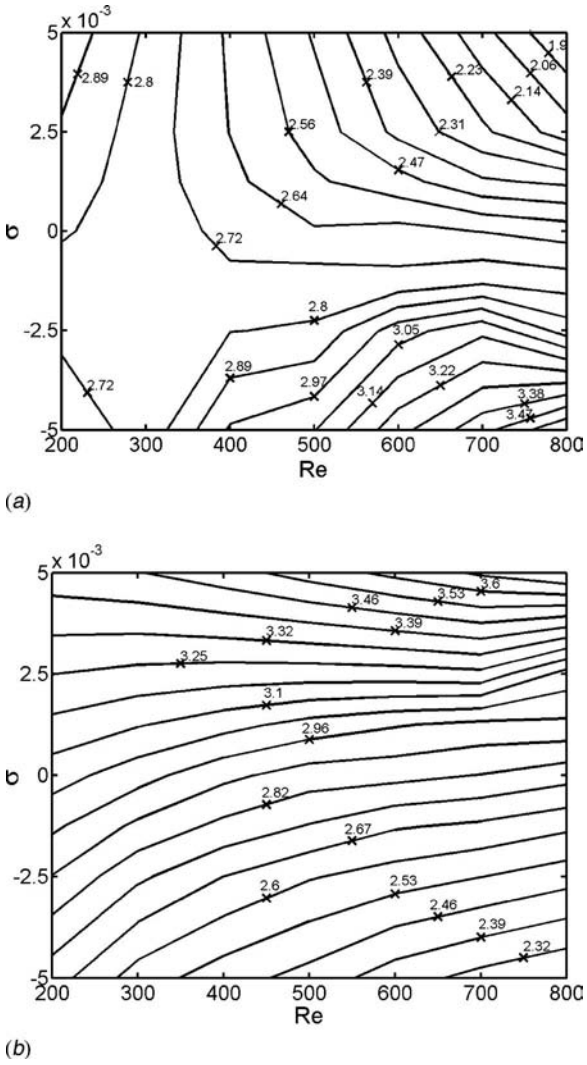

Fig. 9 Contour maps of modified coefficient of friction: (*a*) Bottom wall and (*b*) top wall

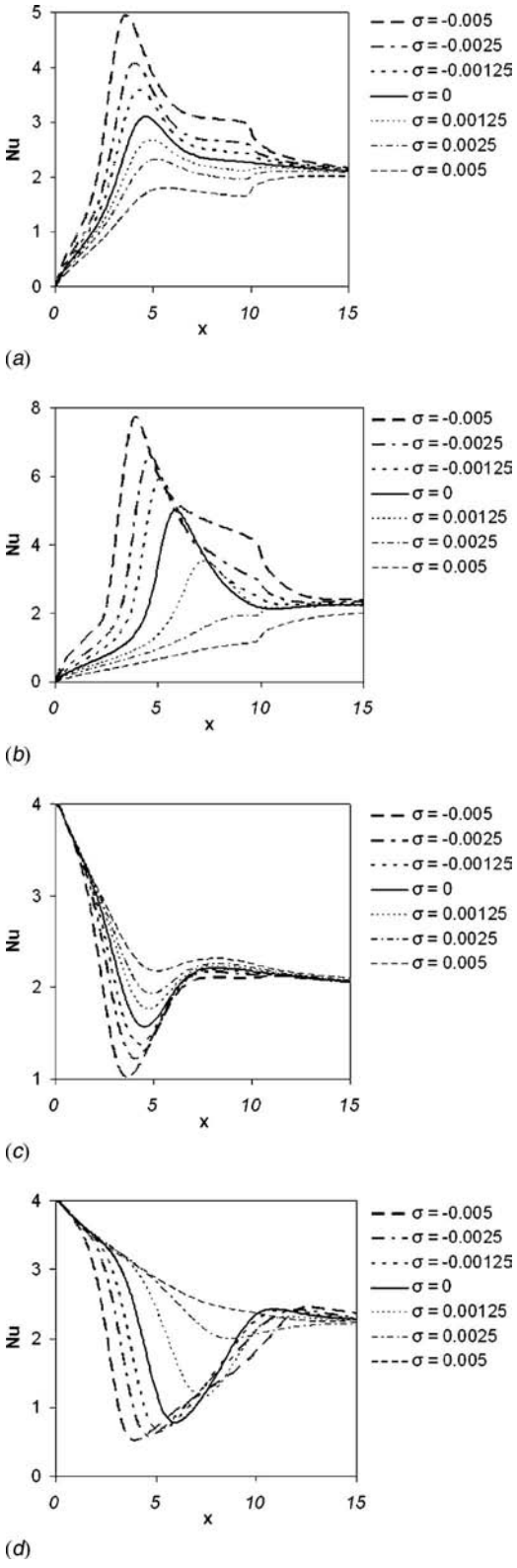

Fig. 10 Distribution of Nusselt number: (*a*) Bottom wall Re =400, (*b*) bottom wall Re=800, (*c*) top wall Re=400, and (*d*) top wall Re=800

to a high blowing bleed coefficient and high Reynolds numbers. On the other hand, for the top wall, high values of the average Nusselt numbers are found by high Reynolds numbers and high blowing bleed rates. However, lower values of Nusselt numbers are recognized by high suction bleed rates regardless of the value of the Reynolds number. Figure 14 can be used to identify the regions where high Nusselt numbers are detected and the regions of low Nusselt numbers. This could be used from an engineering viewpoint for the purpose of heat transfer enhancement.

Finally, it is interesting to comment on the effect of blowing on the flow stability and, thus, on the validity of the steady flow assumption. Blowing is expected to slightly affect backflow (equivalently, the velocity ratio values of the shear-layer-type velocity profiles after the sudden expansion) and thus have only a small effect on local absolute instability (see [38]). Given that the levels of backflow in the present problem are low (i.e., absolute instability is not strong), we expect that, in the absence of external noise, the effect of blowing on flow stability is not significant. If, on the other hand, the blowing stream is characterized by non-negligible levels of sustained noise, then the flow can exhibit unsteadiness via convective instabilities (see [24]).

Conclusions

The results of the present work show that on the bottom wall, and inside the primary recirculation bubble, suction increases the modified coefficient of friction and blowing reduces it. The reattachment length of the primary recirculation bubble is increased by increasing the blowing bleed coefficient and is decreased by increasing the suction bleed rate. Suction increases the size of the

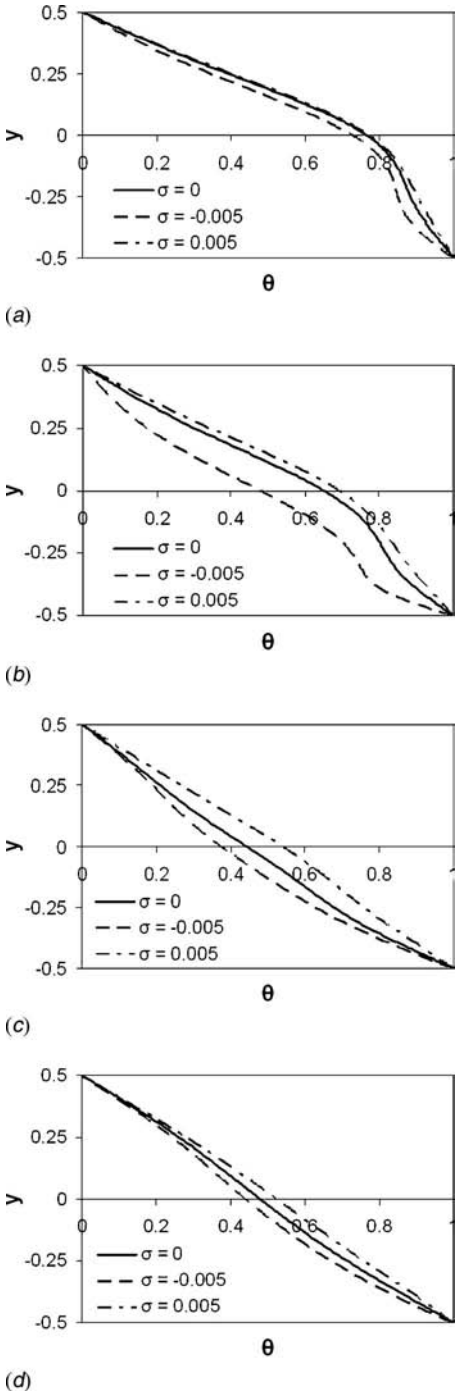

Fig. 11 Temperature profiles Re=400: (*a*) *x*=2.0, (*b*) *x*=3.0, (*c*) *x*=5.50, and (*d*) *x*=8.0

secondary bubble and blowing reduces it. The local Nusselt number on the bottom wall increases by suction and decreases by blowing, and the opposite occurs at the top wall. The maximum local Nusselt number on the bottom wall coincides with the point of reattachment. High values of average Nusselt number on the bottom wall are identified by high Reynolds numbers and high suction bleed rates. However, the low values correspond to high blowing rates. On the top wall, high Nusselt numbers are identified by high Reynolds numbers and high bleed rates.

Nomenclature

A = constant in the grid stretching equation

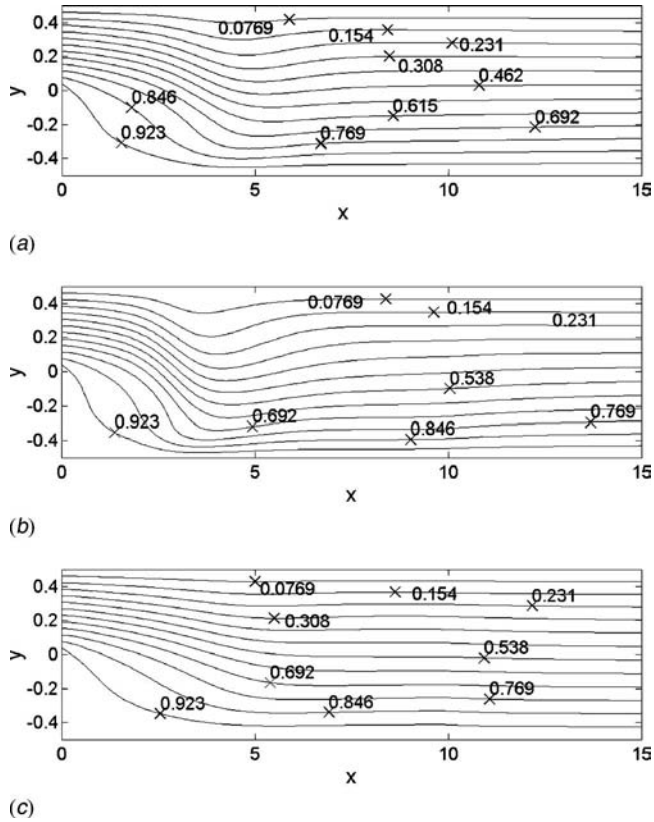

Fig. 12 Temperature isocontours for Re=400: (*a*) σ=0, (*b*) σ =−0.005, and (*c*) σ=0.005

a = upstream channel height (m)
C_f = coefficient of friction, dimensionless
C_f^* = modified coefficient of friction, dimensionless
C_{avg}^f = average coefficient of friction, dimensionless
D_x = location of grid clustering in x direction (m)
D_y = location of grid clustering in y direction (m)
D_H = hydraulic diameter at inlet (D_H=2a) (m)
ER = expansion ratio (H/S), dimensionless
H = downstream channel height (m)
h = local convection heat transfer coefficient (W m^{-2} K^{-1})
k = thermal conductivity (W m^{-1} K^{-1})
L = length of the channel (m)
M = number of points in horizontal direction
N = number of points in vertical direction
Nu = Nusselt number ($h(D_H)/k$)

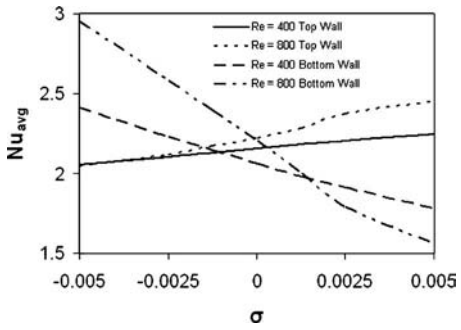

Fig. 13 Average Nusselt number distribution versus bleed coefficient for Re=800 and Re=400

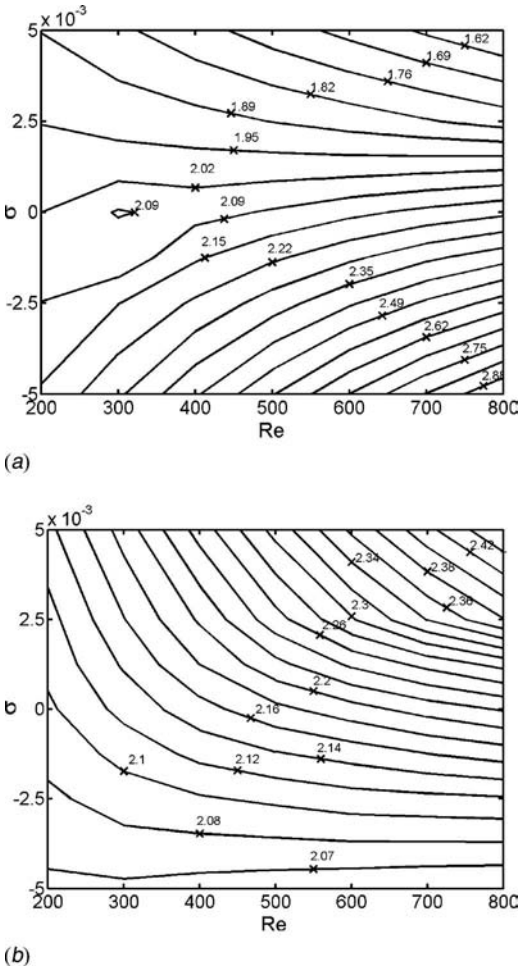

Fig. 14 Contour maps of average Nusselt number: (*a*) Bottom wall and (*b*) top wall

p = dimensionless pressure
$\overset{*}{p}$ = pressure ($N\,m^{-2}$)
Pr = Prandtl number (υ/α)
Re = Reynolds number ($u_m D_H/\upsilon$)
q_w = heat flux ($W\,m^{-2}$)
S = step height (m)
T = temperature (K)
T_w = wall temperature (K)
T_b = bulk temperature (K)
u_m = average velocity of the incoming flow at inlet (m/s)
u = dimensionless x component of velocity
$\overset{*}{u}$ = x component of velocity (m/s)
v = dimensionless y component of velocity
$\overset{*}{v}$ = y component of velocity (m/s)
v_w = dimensionless bleed velocity
$\overset{*}{v}_w$ = bleed velocity (m/s)
x = dimensionless horizontal coordinate
$\overset{*}{x}$ = horizontal distance (m)
x_1 = beginning of the secondary recirculation bubble, dimensionless
x_2 = end of the secondary recirculation bubble, dimensionless
x_r = reattachment length, dimensionless
X = location of uniformly distributed grid points
y = dimensionless vertical coordinate
$\overset{*}{y}$ = vertical distance (m)
Y = location of uniformly distributed grid points in the y direction

Greek Letters

α = thermal diffusivity (m^2/s)
β = clustering parameter in x direction
γ = clustering parameter in y direction
ε = numerical tolerance
θ = dimensionless temperature
μ = dynamic viscosity ($Ns\,m^{-2}$)
ρ = density ($kg\,m^{-3}$)
σ = bleed coefficient, $\sigma=\overset{*}{v}_w/u_m$
τ = shear stress ($N\,m^{-2}$)
ϕ = transport quantity
υ = kinematic viscosity (m^2/s)

Subscripts

avg = average
b = bulk value
LW = bottom wall
m = mean value
resid = residual
UW = top wall
w = wall
wc = cold wall
wh = hot wall

References

[1] Armaly, B. F., Durst, F., Pereira, J. C. F., and Schönung, B., 1983, "Experimental and Theoretical Investigation of Backward-Facing Step Flow," J. Fluid Mech., **127**, pp. 473–496.
[2] Gartling, D. K., 1990, "A Test Problem for Outflow Boundary Condition-Flow Over a Backward Facing Step," Int. J. Numer. Methods Fluids, **11**, pp. 953–967.
[3] Kim, J., and Moin, P., 1985, "Application of a Fractional-Step Method to Incompressible Navier-Stokes Equations," J. Comput. Phys., **59**, pp. 308–323.
[4] Thangam, S., and Knight, D., 1989, "Effect of Step Height on the Separated Flow Past a Backward Facing Step," Phys. Fluids A, **1**(3), pp. 604–606.
[5] Vradis, G. C., Outgen, V., and Sanchez, J., 1992, "Heat Transfer Over a Backward-Facing Step: Solutions to a Benchmark," *Benchmark Problems for Heat Transfer Codes ASME 1992*, ASME, New York, HTD-Vol. 222, pp. 27–34.
[6] Pepper, D. W., Burton, K. L., and Bruenckner, F. P., 1992, "Numerical Simulation of Laminar Flow With Heat Transfer Over a Backward Facing Step," *Benchmark Problems for Heat Transfer Codes ASME 1992*, ASME, New York, HTD-Vol. 222, pp. 21–26.
[7] Vradis, G., and VanNostrand, L., 1992, "Laminar Coupled Flow Downstream an Asymmetric Sudden Expansion," J. Thermophys. Heat Transfer, **6**(2), pp. 288–295.
[8] Barbosa Saldana, J. G., Anand, N. K., and Sarin, V., 2005, "Numerical Simulation of Mixed Convective Flow Over a Three-Dimensional Horizontal Backward Facing Step," ASME J. Heat Transfer, **127**, pp. 1027–1036.
[9] Nie, J. H., and Armaly, B. F., 2003, "Three-Dimensional Flow Adjacent to Backward Facing Step," ASME J. Heat Transfer, **125**, pp. 422–428.
[10] Li, A., and Armaly, B. F., 2002, "Laminar Mixed Convection Adjacent to Three-Dimensional Backward-Facing Step," ASME J. Heat Transfer, **124**, pp. 209–213.
[11] Baek, B. J., Armaly, B. F., and Chen, T. S., 1993, "Measurements in Buoyancy-Assisting Separated Flow Behind a Vertical Backward-Facing Step," ASME J. Heat Transfer, **115**, pp. 403–408.
[12] Abu-Mulaweh, H. I., Armaly, B. F., and Chen, T. S., 1995, "Laminar Natural Convection Flow Over a Vertical Backward-Facing Step," ASME J. Heat Transfer, **117**, pp. 895–901.
[13] Abu-Mulaweh, H. I., Armaly, B. F., and Chen, T. S., 1994, "Measurements in Buoyancy-Opposing Laminar Flow Over a Vertical Backward-Facing Step," ASME J. Heat Transfer, **116**, pp. 247–250.
[14] Ramachandran, N., Armaly, B. F., and Chen, T. S., 1985, "Measurements and Predictions of Laminar Mixed Convection Flow Adjacent to a Vertical Surface," ASME J. Heat Transfer, **107**, pp. 636–641.
[15] Vogel, J. C., and Eaton, J. K., 1985, "Combined Heat and Fluid Dynamics Measurements Downstream of a Backward-Facing Step," ASME J. Heat Transfer, **107**, pp. 922–929.
[16] Nie, J. H., and Armaly, B. F., 2004, "Three-Dimensional Forced Convection in Plane Symmetric Sudden Expansion," ASME J. Heat Transfer, **126**, pp. 836–839.
[17] Abu-Mulaweh, H. I., Armaly, B. F., and Chen, T. S., 1993, "Measurements of Laminar Mixed Convection Flow Over a Horizontal Forward-Facing Step," J.

Thermophys. Heat Transfer, **7**, pp. 569–573.
[18] Abu-Mulaweh, H. I., 2003, "A Review of Research on Laminar Mixed Convection Flow Over Backward and Forward-Facing Steps," Int. J. Therm. Sci., **42**, pp. 897–909.
[19] Williams, P. T., and Baker, A. J., 1997, "Numerical Simulations of Laminar Flow Over a 3D Backward Facing Step," Int. J. Numer. Methods Fluids, **24**, pp. 1159–1183.
[20] Tylli, N., Kaiktsis, L., and Ineichen, B., 2002, "Sidewall Effects in Flow Over a Backward-Facing Step: Experiments and Numerical Solutions," Phys. Fluids, **14**(11), pp. 3835–3845.
[21] Chiang, T. P., and Sheu, W. H., 1999, "A Numerical Revisit of Backward-Facing Step Flow Problem," Phys. Fluids, **11**, pp. 862–874.
[22] Chiang, T. P., and Sheu, W. H., 1999, "Time Evolution of Laminar Flow Over a Three-Dimensional Backward Facing Step," Int. J. Numer. Methods Fluids, **31**, pp. 721–745.
[23] Chiang, T. P., and Sheu, W. H., 1997, "Vortical Flow Over a 3-D Backward-Facing Step," Numer. Heat Transfer, Part A, **31**, pp. 167–192.
[24] Kaiktsis, L., Karniadakis, G. E., and Orszag, S. A., 1996, "Unsteadiness and Convective Instabilities in Two-Dimensional Flow Over a Backward-Facing Step," J. Fluid Mech., **321**, pp. 157–187.
[25] Barkley, D., Gomes, M. G. M., and Henderson, R. D., 2002, "Three-Dimensional Instability in Flow Over a Backward-Facing Step," J. Fluid Mech., **473**, pp. 167–190.
[26] Yang, J. T., Tsai, B. B., and Tsai, G. L., 1994, "Separated-Reattaching Flow Over a Back Step With Uniform Normal Mass Bleed," ASME J. Fluids Eng., **116**, pp. 29–35.
[27] Batenko, S. R., and Terekhov, V. I., 2006, "Friction and Heat Transfer in a Laminar Separated Flow Behind a Rectangular Step With Porous Injection or Suction," J. Appl. Mech. Tech. Phys., **47**(1), pp. 12–21.
[28] Kaiktsis, L., and Monkewitz, P., 2003, "Global Destabilization of Flow Over a Backward-Facing Step," Phys. Fluids, **15**(12), pp. 3647–3658.
[29] White, F. M., 1991, *Viscous Fluid Flow*, McGraw-Hill, New York.
[30] Bejan, A., 1994, *Convection Heat Transfer*, Wiley, New York.
[31] Lue, T.-S., and Ho, C.-M., 2000, "Control of Global Instability in a Non-Parallel Near Wake," J. Fluid Mech., **404**, pp. 345–378.
[32] Abu-Nada, E., 2006, "Entropy Generation Due to Heat and Fluid Flow in Backward Facing Step Flow With Various Expansion Ratios," Int. J. Exergy, **3**(4), pp. 419–435.
[33] Patankar, S. V., 1980, *Numerical Heat Transfer and Fluid Flow*, Hemisphere Taylor and Francis Group, New York.
[34] Versteeg, H. K., and Malalasekera, W., 1995, *An Introduction to Computational Fluid Dynamics: The Finite Volume Method*, Wiley, New York.
[35] Anderson, Jr., J. D., 1995, *Computational Fluid Dynamics: The Basics With Applications*, McGraw-Hill, New York.
[36] Hoffmann, K. A., 1989, *Computational Fluid Dynamics for Engineers*, The University of Texas at Austin, Texas.
[37] Abu-Nada, E., 2005, "Numerical Prediction of Entropy Generation in Separated Flows," Entropy, **7**(4), pp. 234–252.
[38] Huerre, P., and Monkewitz, P. A., 1985, "Absolute and Convective Instabilities in Free Shear Layers," J. Fluid Mech., **159**, pp. 151–168.

Heat (Mass) Transfer Distribution in a Two-Pass Trapezoidal Channel With a 180 deg Turn

S. W. Lee

H. S. Ahn

S. C. Lau[1]

Convective Heat and Mass Transfer Laboratory,
Department of Mechanical Engineering,
Texas A&M University,
College Station, TX 77843-3123

The heat transfer characteristics of airflows in serpentine cooling channels in stator vanes of gas turbines were studied. The cooling channels were modeled as a two-pass trapezoidal channel with a 180 deg *turn. Naphthalene sublimation experiments were conducted and the heat and mass transfer analogy was applied to study the local heat (mass) transfer distributions on one of the two primary walls of the channel. Results were obtained for turbulent airflow through the channel with smooth walls, and with transverse ribs on one wall and on two opposite walls, over a range of Reynolds numbers between about 10,000 and 60,000. The results showed that there was a very large variation of the local heat (mass) transfer distribution in the turn and downstream of the turn. In all of the cases studied, the regional average heat (mass) transfer was higher on the downstream half of the turn than on the upstream half of the turn and was higher in the turn with the flow entering the channel through the smaller straight section than when the flow was reversed. The shape of the local heat (mass) transfer distribution at the turn was not significantly affected by varying the air mass flow rate. In the smooth wall case, the local heat (mass) transfer was high near the end wall and the downstream outer wall in the turn and was relatively low in two regions near the upstream outer wall and the downstream edge at the tip of the divider wall in the turn. With ribs on two opposite walls, the variation of the local heat (mass) transfer was larger, especially in the turn and downstream of the turn, than in the smooth wall case. The pressure drop across the turn was higher in the case of the flow entering the channel through the larger straight section than when the flow was reversed. As expected, the ribs increased the pressure drop across the turn.* [DOI: 10.1115/1.2764084]

Keywords: forced convection, trapezoidal channel, sharp turn, naphthalene sublimation

Introduction

The high gas entry temperatures in modern gas turbines necessitate that internal components withstand temperatures higher than the melting points of the components. To protect the airfoils, the vanes and blades whose external surfaces are exposed to high temperature gases, air from the compressors is forced through internal cooling passages to remove heat from the airfoils. These shaped cooling passages often have irregular cross sections and have 180 deg turns connecting long straight sections.

A literature survey shows that there have been a large number of studies on the heat transfer in stationary and rotating, straight and multipass channels, with square and rectangular cross sections, and with rib-roughened walls, to examine the effects of the aspect ratio of the channel, the geometry of the turn, the configuration of the ribs, and rotation, on the heat transfer distribution along the channel. The results of these studies are useful in the design of serpentine cooling passages with turbulators in gas turbines. Many of these studies were discussed in two separate chapters in Han et al. [1] for stationary channels and rotating channels, respectively. In the case of turbulator-enhanced heat transfer for square and rectangular channels with no rotation, earlier studies include those by Burggraf [2], Han et al. [3], and Boyle [4], and examples of more recent studies are those of Han et al. [5], Lau et al. [6], Acharya et al. [7], Ekkad and Han [8], and Rhee et al. [9]. In the case of heat transfer in rotating channels with sharp turns and turbulators, there were earlier studies such as of Johnson et al. [10,11] and more recent studies such as of Lau and coworkers[12,13], Lee et al. [14], Cho et al. [15], Liu et al. [16], and Zhou and Acharya [17].

Ekkad and Han [8] and Ekkad et al. [18] obtained the local heat transfer distributions at a sharp 180 deg turn in a two-pass square channel with smooth walls, rib turbulators on two opposite walls, and with bleed holes on two opposite walls. Taslim et al. [19] studied the effects of bleed holes and tapered ribs on the heat transfer and pressure drop in trapezoidal channels that modeled cooling passages near the trailing edge of gas turbine airfoils. Taslim et al. [20] presented heat transfer results for 12 straight channels with square and trapezoidal cross sections, with full ribs on two opposite walls, and with and without half-length ribs on the other two walls. They found that the half-length ribs significantly enhanced the heat transfer on the two walls with full ribs. Li et al. [21] reported local heat transfer distributions for flows through wide trapezoidal channels with holes along a straight or zigzag divider wall and with ejection slots along one outer wall.

Moon et al. [22] conducted transient heat transfer experiments, using encapsulated thermochromic liquid crystals, to obtain the local distributions of the heat transfer coefficient on all of the walls at the turn of a smooth two-pass channel with a trapezoidal cross section for various rates of airflow through the channel. They found that the heat transfer was much higher on the walls in the turn and downstream of the turn than on the walls upstream of the turn. The turn caused high heat transfer in several distinct regions on the end wall, the outlet outer wall, and on the two opposite primary walls in the turn and downstream of the turn. The flow separated at the tip of the divider wall and reattached on the outlet inner wall in a region only a short distance from the turn. The heat transfer was the lowest on the inlet outer wall. Heat transfer enhancement due to the turn was the highest in the lowest

[1]Corresponding author.

Contributed by the Heat Transfer Division of ASME for publication in the JOURNAL OF HEAT TRANSFER. Manuscript received August 3, 2006; final manuscript received March 8, 2007. Review conducted by Gautam Biswas.

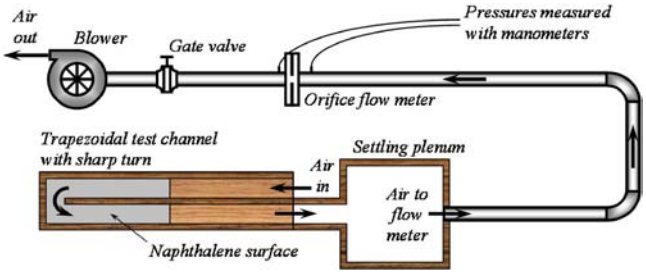

Fig. 1 Schematic of test apparatus for this study

Reynolds number case. The trends of the local heat transfer distributions on the various walls at the turn were relatively insensitive to varying the flow rate, over the range of flow rates studied.

In this study, cooling channels in turbine airfoils were modeled as a channel with two straight trapezoidal sections connected with a sharp 180 deg turn. The effect of the turn on the distribution of the local heat transfer distribution was studied in the cases of a channel with smooth walls, a channel with transverse ribs on one wall, and a channel with transverse ribs on two opposite walls. Naphthalene sublimation experiments were conducted to obtain the mass transfer distributions, and the heat and mass transfer analogy was used to convert the mass transfer distributions to heat transfer distributions. The results of this study should help gas turbine designers determine local temperature distributions in cooling passages in turbine airfoils and to identify regions with large temperature variations and high thermal stresses. The results will also enable engineers to develop numerical models to optimize these internal cooling passages to improve the thermal performance of gas turbines.

Experimental Apparatus and Procedure

A schematic of the test apparatus for this study is shown in Fig. 1. The test section consisted of a two-pass channel with two straight sections of different trapezoidal cross sections, connected with a sharp 180 deg turn. The channel was constructed of 1.91 cm thick pine wood. As shown in Fig. 2, the length of each straight section, or the distance between the channel inlet, or exit, and the end wall at the turn, was 61.0 cm, while the width of each section was 3.81 cm and the thickness of the inner or divider wall between the two sections was 1.91 cm. The width of the clearance at the turn, or the distance between the tip of the divider wall and the end wall, was also 3.81 cm. The top and bottom walls of the test channel were both flat and were at an angle of 21.8 deg with respect to each other, such that the heights of the outer and inner vertical walls of one straight section were 3.81 cm and 5.33 cm, and the heights of the inner and outer vertical walls for the other straight section were 6.10 cm and 7.62 cm, respectively. All of these dimensions were for the inside surfaces of the channel walls.

As shown in Fig. 2, a 30.9 cm long U-shaped section on the inside surface of the bottom wall was hollowed out to facilitate the installation of 16 aluminum cassettes for the determination of the streamwise variation of the mass transfer coefficient along the channel. Each of these cassettes was 0.95 cm thick and had a 0.38 cm deep cavity. During a casting process, the cavity was filled with naphthalene, exposing a smooth, flat surface that was mass transfer active. The width of the naphthalene surfaces on 14 of the cassettes was 3.81 cm, which was the same as the width of each straight section of the test channel. Two other cassettes with naphthalene surfaces that measured 3.73×4.69 cm^2 made up the portion of the bottom wall at the turn. Once these 16 cassettes were installed, the inner surface of the bottom wall was mass transfer active, except for the top of two 0.76 mm wide rims of each cassette. The other two wider rims of each cassette, with a thickness of 3.81 mm, were hidden underneath the divider wall, one of the two outer walls, or the end wall.

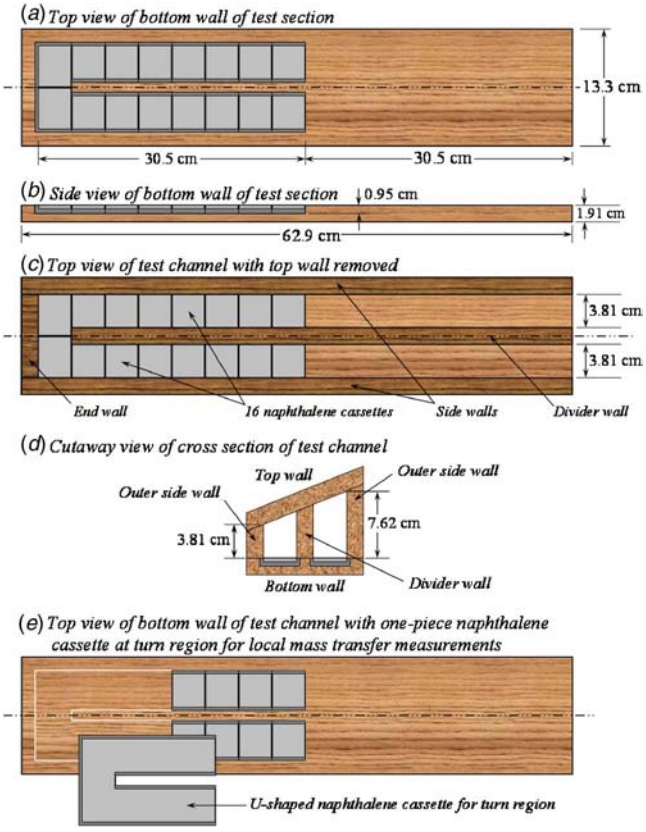

Fig. 2 Schematics of walls of trapezoidal test channel

To enable the measurement of the distribution of the local mass transfer at the turn, the eight cassettes closest to the turn were replaced with a U-shaped cassette (see Fig. 2(*e*)). Once this U-shaped cassette was installed on the bottom wall, the surface of the entire turn region of the bottom wall was mass transfer active.

For two sets of experiments, transverse ribs were attached with silicon adhesive on the bottom wall, and on both the top and bottom walls, respectively, over the entire length of the test channel, with a spacing of 3.81 cm. These ribs were 3.2×3.2 mm^2 square stripes of balsa wood. Thus, the distance between two consecutive ribs was equal to 12 times the height of the ribs. On each naphthalene cassette, the balsa wood stripe was installed on top of the thin rim along the downstream edge of the cassette.

The two-pass test channel was connected to a settling chamber and then to an open airflow loop (see Fig. 1). During an experiment, air was drawn through the flow loop from the air-conditioned laboratory and the exhaust air that contained naphthalene vapor was ducted to the outside of the laboratory through a fume hood. The air mass flow rate was controlled with a valve and was measured with an orifice flow meter along with two manometers. The temperature of the air at the entrance of the test section was measured with two thermocouples and was monitored continuously with a data acquisition system over the duration of the experiment.

To ensure that the naphthalene in all of the cassettes was in thermal equilibrium with the air in the air-conditioned laboratory, the cassettes were stored in sealed plastic bags in the laboratory for at least 12 h before an experiment. To determine the variation of the regional average mass transfer coefficient along the two-pass test channel, the naphthalene cassettes were weighed, one at a time, with an electronic balance, before and after the experiment. The difference between the weights of each cassette gave the mass transfer from the naphthalene surface of the cassette to

the airflow during the experiment. The rate of mass transfer was needed to calculate the regional average mass transfer coefficient.

To determine the local mass transfer coefficient distribution on a cassette, the elevations at a grid of predetermined points on the naphthalene surface and on the top surface of the rim of the cassette were measured with an electronic depth gauge before and after the experiment. The elevations on the top surface of the rim were needed to determine the location of the reference plane of the naphthalene surface in the calculations of the elevation changes at the grid points on the naphthalene surface. The changes of the elevations at the grid points were used to calculate the local mass transfer coefficients.

Experiments were conducted for the air entering the trapezoidal test channel through the straight section with the smaller cross section as well as entering through the straight section with the larger cross section and for four different airflow rates. Regional average and local mass transfer coefficients were obtained for airflows through the test channel with smooth walls and with transverse ribs on one wall and on two opposite walls. The analogy of heat and mass transfer was applied to convert the mass transfer coefficients to heat transfer coefficients.

To obtain the pressure drop across the turn, two pressure taps were installed on the top wall and the outer sidewall, respectively, in each of the two straight sections of the trapezoidal test channel. These pressure taps were located on the centerlines of the walls at a distance of 43.8 cm from the channel inlet and exit. The difference in the static pressures at these two pairs of taps was measured with a micromanometer or an inclined manometer, depending on the range, and was checked with a calibrated pressure transducer with a digital readout.

Additional experiments were conducted to calibrate the thermocouples and the data acquisition system with a constant temperature bath and a NIST-calibrated thermometer, to calibrate the electronic balance and the electronic depth gauge with standards provided by the respective manufacturers, and to determine the corrections to the local and average mass transfer during blower startup and shutdown, and when the naphthalene cassettes were weighed and the elevations on the surfaces of the naphthalene cassettes were determined.

To validate the experimental method, additional local and average mass transfer experiments were conducted for flow through a two-pass square channel. For these experiments, the test channel had the same bottom wall with the naphthalene cassettes from the trapezoidal channel, and the sidewalls, the divider wall, and end wall all had a height of 3.81 cm, the same as the width of each straight section of the channel. Experiments were conducted to obtain the $\mathrm{Sh}/\mathrm{Sh}_0$ distributions on the bottom wall at the turn, and the streamwise variations of $\overline{\mathrm{Sh}}/\mathrm{Sh}_0$, for four different airflow rates. The $\mathrm{Sh}/\mathrm{Sh}_0$ distributions at the turn and the variations of $\overline{\mathrm{Sh}}/\mathrm{Sh}_0$ obtained were compared with those reported by other researchers in the open literature.

Data Reduction

Once the air mass flow rate was determined using the pressure drop across the orifice in the flow meter, the Reynolds number for the flow through the test channel was calculated as

$$\mathrm{Re} = \frac{\rho \bar{V} D_h}{\mu} = \frac{4\dot{m}}{\mu P} \tag{1}$$

where D_h and P were the hydraulic diameter and the perimeter of the rectangular flow cross section between the tip of the divider wall and the end wall. For the same air mass flow rate, the two Reynolds numbers based on the hydraulic diameters of the trapezoidal cross sections of the two straight sections of the test channel were 10.5% smaller and 13.5% larger than this Reynolds number based on the hydraulic diameter of the cross section at the turn clearance.

The segmental (or regional average) mass transfer coefficient was defined as

$$\bar{h}_m = \frac{\Delta M_n / \Delta t}{A_s(\rho_{v,w} - \bar{\rho}_{v,b})} \tag{2}$$

where ΔM_n was the total mass transfer from the naphthalene surface of a cassette to the air and Δt was the duration of the experiment, over which air flowed steadily through the test channel. The vapor density of naphthalene at the wall $\rho_{v,w}$ was evaluated using the ideal gas equation of state and the vapor pressure-temperature correlation for naphthalene by Ambrose et al. [23]. The average bulk vapor density of naphthalene $\bar{\rho}_{v,b}$ was the average of the vapor densities at the upstream and downstream edges of the naphthalene surface being considered and was calculated as

$$\bar{\rho}_{v,b} = \frac{1}{2}\left[\left(\frac{\dot{M}_n}{\dot{V}}\right)_{\text{upstream}} + \left(\frac{\dot{M}_n}{\dot{V}}\right)_{\text{downstream}}\right] \tag{3}$$

where $\dot{M}_n$ was the rate of total mass transfer from the upstream naphthalene surfaces, and $\dot{V}$ was the air volumetric flow rate.

The local mass transfer coefficient was defined as

$$h_m = \frac{\dot{M}_n''}{\rho_{v,w} - \rho_{v,b}} = \frac{\rho_s \Delta z / \Delta t}{\rho_{v,w} - \rho_{v,b}} \tag{4}$$

where $\dot{M}_n''$ was the local naphthalene mass flux, ρ_s was the density of solid naphthalene, and Δz was the local change of elevation on the naphthalene surface. The local bulk vapor density $\rho_{v,b}$ in Eq. (4) was the rate of total mass transfer from naphthalene surfaces upstream of the grid point divided by the air volumetric flow rate.

The segmental and local Sherwood numbers were defined, respectively, as

$$\overline{\mathrm{Sh}} = \frac{\bar{h}_m D_h}{\sigma} \quad \text{and} \quad \mathrm{Sh} = \frac{h_m D_h}{\sigma} \tag{5}$$

where σ was the mass diffusion coefficient for naphthalene vapor in the air, which was determined with a correlation given in Goldstein and Cho [24].

According to the analogy between heat transfer and mass transfer described in Eckert [25],

$$\frac{\overline{\mathrm{Nu}}}{\mathrm{Nu}_0} = \frac{\overline{\mathrm{Sh}}}{\mathrm{Sh}_0} \quad \text{and} \quad \frac{\mathrm{Nu}}{\mathrm{Nu}_0} = \frac{\mathrm{Sh}}{\mathrm{Sh}_0} \tag{6}$$

where the reference Nusselt number and Sherwood number were based on the Dittus-Boelter correlations [26] for a fully developed turbulent flow at the same Reynolds number through a smooth channel.

A friction factor was defined as

$$f = \frac{(\Delta p / L) D_h}{\rho \bar{V}^2 / 2} = 2\rho\left(\frac{\Delta p}{L}\right)\left(\frac{A_c}{\dot{m}}\right)^2 D_h \tag{7}$$

where Δp was the pressure drop across the sharp turn, L was the streamwise distance between the locations of the pressure taps along the centerline of the test channel, and A_c was the channel flow cross-sectional area at the turn clearance. The experimental friction factor was normalized by the friction factor for fully developed turbulent flow in a smooth channel, f_0, which was given in Ref. [26].

The estimation of uncertainty values was based on a confidence level of 95% (or 20:1 odds) and the relative uncertainty analysis method of Coleman and Steele [27]. Also, in all uncertainty calculations, uncertainty values of ±1.0% for all properties of air and ±0.25 mm for all physical dimensions were used.

The uncertainty of the air mass flow rate was calculated from the uncertainties of the measured pressures at the orifice flow meter and was found to be 2.9%. The maximum uncertainty of the calculated Reynolds number was ±3.1%.

Using uncertainty values of ±1.0% for the density of solid naphthalene and the uncertainty of the measure values of Δz, the uncertainty of the local mass transfer coefficient was estimated to be ±10.9%. Similarly, using the uncertainty of the measured values of ΔM_n, the uncertainty of the average mass transfer coefficient was estimated to be ±7.7%. According to Goldstein and Cho [24], the diffusion coefficient of naphthalene vapor in air had an uncertainty of about ±2.0%. With this value, the calculated values of the relative uncertainties for the local and average Sherwood numbers were ±11.1% and ±8.0%, respectively.

Using the maximum uncertainty values of ±4.0% for the measured pressure drops and ±2.9% for the air mass flow rate, the maximum value of the relative uncertainty of the friction factor was calculated to be ±7.8%.

Presentation and Discussion of Results

In this section, the distributions of the mass transfer coefficient at the 180 deg turn and along the test channel are presented. The detailed distributions are based on the measurements of the local elevations at a grid of 3776 points on the naphthalene surface (and on the top surface of the rim) of the U-shaped cassette on the bottom wall at the turn (see Fig. 2(*e*)). The results are presented as contours of constant Sh/Sh_0 values for air entering the test channel through the smaller trapezoidal straight section and through the larger trapezoidal straight section, for the test channel with all smooth walls and with transverse ribs on two opposite walls, and for four Reynolds numbers. The variations of the regional average mass transfer coefficient along the test channel are based on the weighing of the 16 naphthalene cassettes (see Fig. 2(*c*)). The regional average results are presented as variations of $\overline{Sh}/Sh_0$ along 16 segments of the bottom wall of the test channel for air entering the test channel through the smaller straight section and through the larger straight section, for the test channel with all smooth walls and with transverse ribs on the bottom wall only and on both the top and bottom walls, and for four Reynolds numbers. According to the heat and mass transfer analogy (Eq. (6)), the local and regional average distributions give the distributions of the respective Nusselt numbers for airflows through the two-pass trapezoidal channel relative to those for fully developed turbulent flows of air through a smooth straight channel at the same Reynolds numbers.

The results of this study are reported in this section for four nominal Reynolds numbers. The actual values of the Reynolds numbers deviate from the, respectively, nominal values by a maximum of ±2.9%.

Mass Transfer Distributions for Square Channel With Smooth Walls. As mentioned earlier, local and regional average mass transfer results were obtained for airflow through a two-pass square channel to validate the experimental method. Figure 3 gives the local mass transfer distributions at the turn on the bottom wall of the square channel for four different Reynolds numbers between 10,000 and 65,000. Because the Sh/Sh_0 distributions are quite similar to one another, the shape of the local mass transfer distribution at the turn is not significantly affected by varying the air mass flow rate. The Sherwood number ratio is low and is almost constant, with a value of about 1.0, near the end of the straight section upstream of the turn, and increases along the main flow direction in the turn, with higher values near the outer walls and lower values near the tip of the divider wall in the turn. The ratio remains quite high downstream of the turn, and then it decreases further downstream along the second straight section as the flow redevelops. The mass transfer is high at the base of the upstream half of the end wall as the flow is deflected from the end wall onto the bottom wall. When the flow is pushed by centrifugal forces at the turn toward the downstream outer wall and is then deflected onto the bottom wall, the mass transfer on the bottom wall is very high along the downstream outer wall. A low mass transfer region near the upstream outer wall in the turn is the result of flow recirculation, as the flow is deflected from the end wall and turns downstream around the tip of the divider wall.

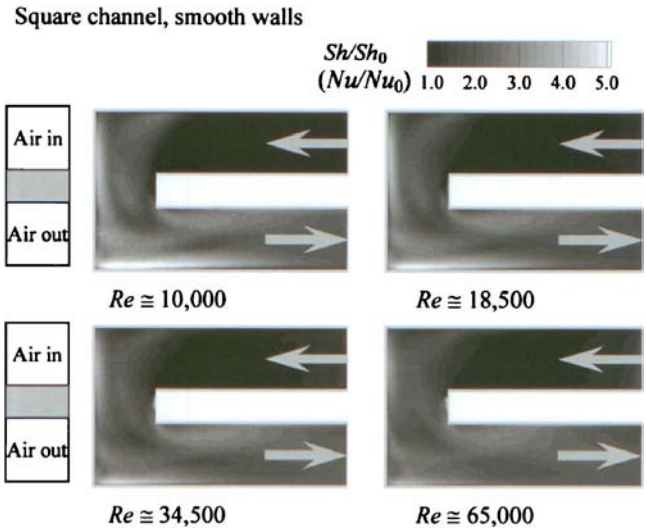

Fig. 3 Local mass transfer distributions at sharp turn in square channel with smooth walls

The vigorous mixing at the turn increases the turbulence in the flow and causes the mass transfer to be high over a large portion of the bottom wall in the turn and downstream of the turn. A distinctive relatively low mass transfer region between the downstream inner and outer edges of the turn may be caused by the interaction between the separated flow from the upstream edge of the divider wall and the deflected flow from the end wall toward the bottom wall. A third region of relatively high mass transfer is observed near a rather small region of slightly lower mass transfer just downstream of the tip of the divider wall. This mass transfer distribution along the downstream side of the divider wall may be the result of the separation of the flow at the downstream edge of the tip of the divider wall and the reattachment of the flow onto the downstream side of the divider wall and the bottom wall. Downstream of the turn, the Sh/Sh_0 value is higher near the inner and outer walls and is lower in the middle of the bottom wall. The Sh/Sh_0 distribution may suggest that there is a pair of counter-rotating vortices (of two different sizes that may change along the downstream straight section) over the bottom wall as the flow enters the downstream straight section of the channel.

The development of the flow in the upstream straight (inlet) section, the increase of the mass transfer in the turn, and the redevelopment of the flow in the downstream straight (exit) section are evident in the streamwise distributions of the segmental of regional average Sherwood number ratio given in Fig. 4. In the turn, the $\overline{Sh}/Sh_0$ values are larger on wall segment No. 9 than on wall segment No. 8, and the $\overline{Sh}/Sh_0$ values on both wall segments are larger when the Reynolds number is smaller. The Sh/Sh_0 and $\overline{Sh}/Sh_0$ distributions in Figs. 3 and 4 compare very well with and have all of the features of those at the 180 deg turns of square channels with smooth walls presented in Refs. [5,8].

Mass Transfer Distributions for Trapezoidal Channel With Smooth Walls. In Figs. 5 and 6, the local mass transfer distributions at the turn on the smooth bottom wall of the trapezoidal channel are presented for airflow entering the smaller straight section and for airflow entering the larger straight section, respectively. In each figure, the four local mass transfer distributions are for Re ≈ 9400, 16,800, 31,800, and 57,200. For either flow direction, the shape of the Sh/Sh_0 distribution at the turn is again not significantly affected by varying the air mass flow rate. Also, as in the square channel case, the Sh/Sh_0 value is low in the inlet section, is high near the end wall and the downstream outer wall in the turn, and is low in two regions near the upstream outer wall

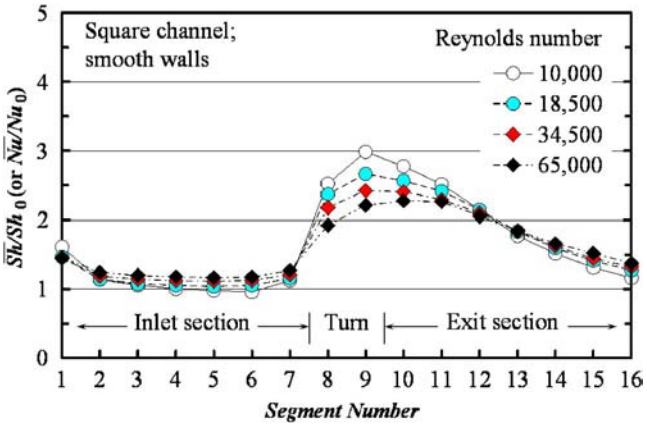

Fig. 4 Segmental mass transfer distributions along square channel with smooth walls

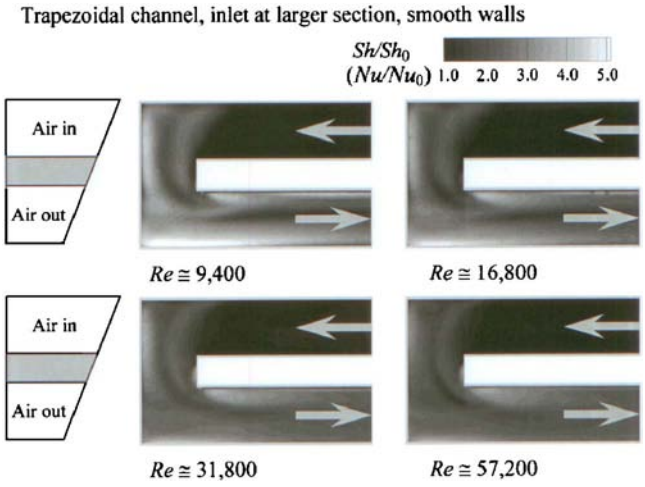

Fig. 6 Local mass transfer distributions at sharp turn in trapezoidal channel with smooth walls and a larger inlet straight section

and the downstream edge of the divider wall in the turn.

Comparing Figs. 5 and 6, it is evident that the Sh/Sh_0 value upstream of the turn is higher for airflow entering the smaller trapezoidal straight section than for airflow entering the larger trapezoidal straight section because of the higher velocities of the flow in the inlet section with the smaller flow cross-sectional area. Note that the Reynolds number is based on the hydraulic diameter at the turn clearance. The higher velocities of the flow that enters the turn from the smaller inlet section cause the mass transfer on the bottom wall to be higher along the base of almost the entire end wall, as the flow with a larger momentum impinges onto the end wall. A close examination of corresponding Sh/Sh_0 distributions for the same Reynolds numbers shows that the mass transfer is higher everywhere on the upstream half of the bottom wall in the turn in the case of airflow entering the smaller inlet section. Even as the flow cross section increases in the turn, the larger momentum of the flow from the smaller inlet section and the increase of the turbulence in the turn still cause the mass transfer to be higher on the downstream half of the bottom wall in the turn than for the accelerating flow entering the turn from the larger inlet section. The differences in the Sh/Sh_0 values, however, are smaller on the downstream half of the bottom wall than on the upstream half.

Figure 5 shows that, downstream of the turn in the larger exit section, the mass transfer remains quite high on the bottom wall,

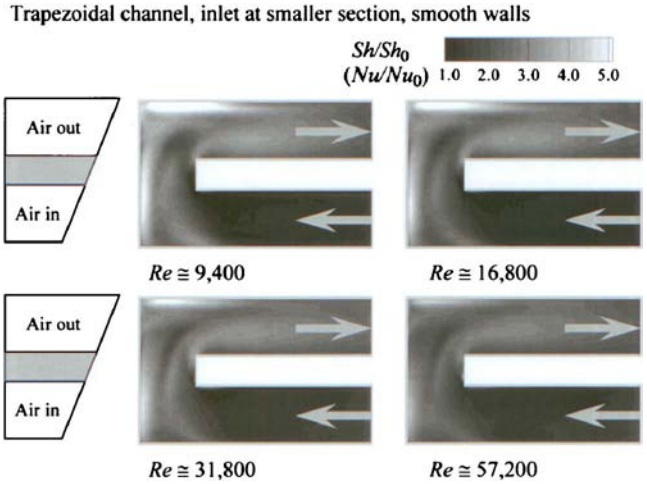

Fig. 5 Local mass transfer distributions at sharp turn in trapezoidal channel with smooth walls and a smaller inlet straight section

with the mass transfer decreasing along the outer wall and the lowest Sh/Sh_0 values along the downstream side of the divider wall. After a length of about three times the channel width downstream of the turn, the Sh/Sh_0 value decreases to about 2.0.

In the case of the flow entering the larger inlet section, the mass transfer is higher near the downstream outer wall in the turn than near the end wall. As shown in Fig. 6, the difference between the Sh/Sh_0 values in these two high mass transfer regions is larger when the Reynolds number is smaller. The flow enters the turn from the larger inlet section with relatively low velocities and accelerates around the turn as the flow cross section is reduced in the turn. Downstream of the turn in the smaller exit section, the mass transfer is lower in the middle of the bottom wall than along the outer wall and along the downstream side of the divider wall. The Sh/Sh_0 distributions downstream of the turn are similar to those for the square channel, except that the accelerating flow in the turn appears to strengthen a pair of counter-rotating vortices over the bottom wall, causing the high Sh/Sh_0 values along the two sidewalls and very low values (as low as about 1.4 for Re $\cong$9400) in the middle of the bottom wall.

Figure 7 compares the streamwise distributions of the regional average Sherwood number ratio along the trapezoidal channel for airflow entering the smaller straight section (round symbols in the figure) and those for airflow entering the larger straight section (diamond symbols). For the trapezoidal channel with smooth walls (Fig. 7(*a*)), the $\overline{Sh}/Sh_0$ distributions are higher in the smaller inlet section but are lower far downstream of the turn in the larger exit section. In the turn, the $\overline{Sh}/Sh_0$ value is higher on wall segment No. 9 than on wall segment No. 8, higher in the smaller inlet section case than in the larger inlet case, and is higher when the Reynolds number is smaller (lighter symbols for smaller Reynolds numbers and darker symbols for larger Reynolds numbers). Downstream of the turn, $\overline{Sh}/Sh_0$ decreases along the streamwise direction, with slightly higher values on wall segment Nos. 10 and 11 for airflow entering the smaller straight section, but $\overline{Sh}/Sh_0$ decreases with a steeper slope because the velocities of the flow are smaller in the larger downstream straight section. The regional average mass transfer is the highest on the downstream wall segment (segment No. 9) in the turn, except when Re$\cong$57,200, in which case $\overline{Sh}/Sh_0$ is the highest on segment No. 10, as Fig. 7(*a*) shows that the peaks of the $\overline{Sh}/Sh_0$ distributions occur at segment No. 9 or 10.

Mass Transfer Distributions for Trapezoidal Channel With Ribs on One Wall or on Two Opposite Walls. For two sets of experiments, regional average mass transfer was determined on 16

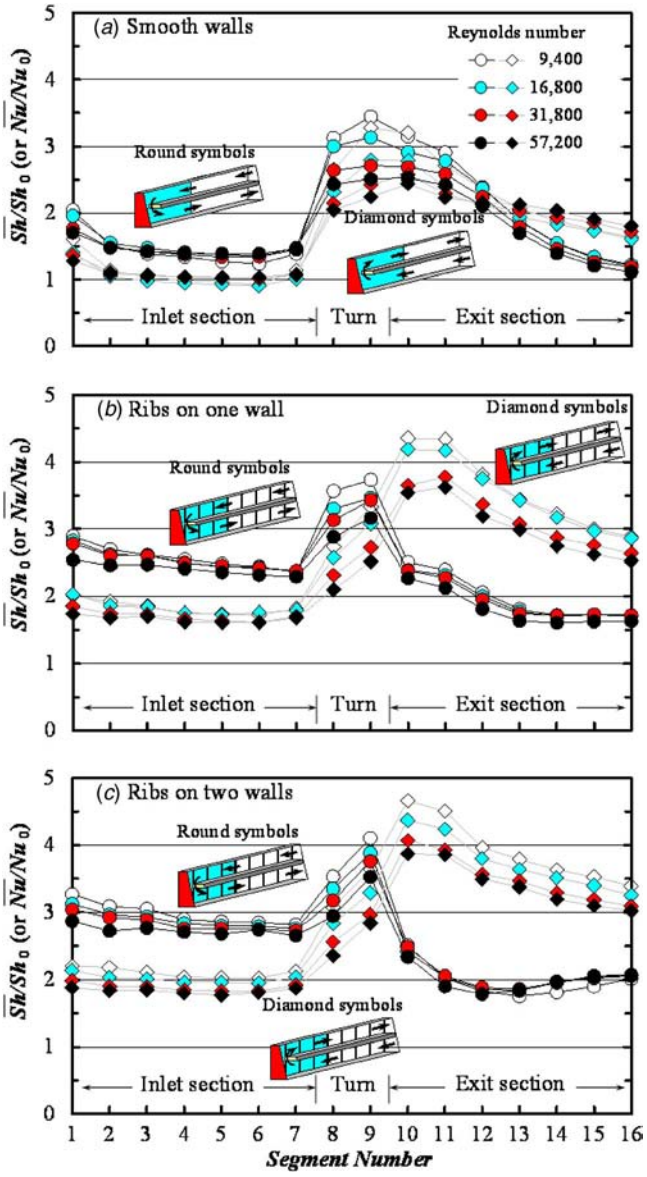

Fig. 7 Segmental mass transfer distributions along trapezoidal channel: (*a*) with smooth walls, (*b*) with ribs on one wall, and (*c*) with ribs on two opposite walls

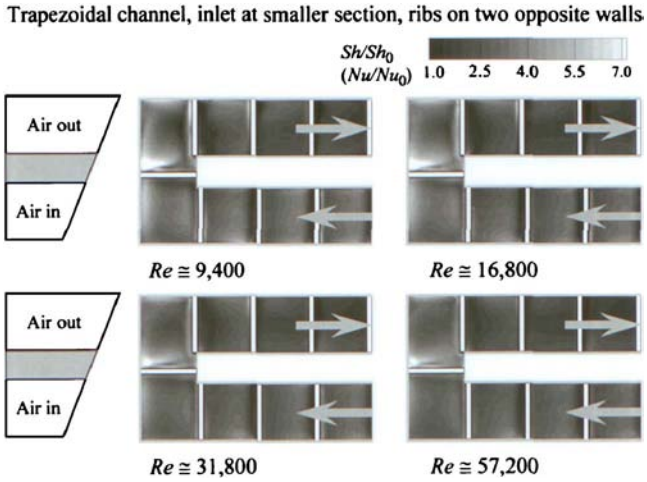

Fig. 8 Local mass transfer distributions at sharp turn in trapezoidal channel with ribs on two opposite walls and a smaller inlet straight section

segments of the bottom wall with transverse ribs on the bottom and with or without aligned transverse ribs on the top wall. As described earlier, these ribs were 3.2×3.2 mm^2 square balsa wood stripes, they were installed along the downstream edges of the 16 naphthalene cassettes, and their surfaces exposed to the airflow were mass transfer inactive. Figures 7(*b*) and 7(*c*) compare the $\overline{Sh}/Sh_0$ distributions for airflow entering the smaller straight section (round symbols) and those for airflow entering the larger straight section (diamond symbols), with ribs on the bottom wall only and with ribs on both the top and bottom walls, respectively. With the ribs periodically interrupting the boundary layers on the bottom wall, the $\overline{Sh}/Sh_0$ value is larger than 1.0 everywhere along the two straight sections of the trapezoidal channel.

In the channel with ribs on the bottom wall only, Fig. 7(*b*) shows that the $\overline{Sh}/Sh_0$ value is about 2.4 in the smaller inlet section and is about 1.7 in the larger inlet section immediately upstream of the turn. As in the channel with smooth walls, the mass transfer in the turn is higher in the smaller inlet case than in the larger inlet case. For both flow directions, the $\overline{Sh}/Sh_0$ values in the turn are again higher on the downstream wall segment (segment No. 9) than on the upstream wall segment (segment No. 8). Downstream of the turn in the larger exit section, as the flow redevelops, $\overline{Sh}/Sh_0$ decreases with an increasing (less negative) slope until it reaches a value of about 1.7, which is about the same as the $\overline{Sh}/Sh_0$ value in the larger inlet section immediately upstream of the turn. Downstream of the turn in the smaller exit section, $\overline{Sh}/Sh_0$ increases to values between 3.5 and 4.4, much higher than those in the turn, on wall segment Nos. 10 and 11, before it decreases to values between 2.5 and 2.9 at the channel exit.

The $\overline{Sh}/Sh_0$ distributions along the channel with ribs on both the top and bottom walls are similar to, but are higher than, those along the channel with ribs on the bottom wall only. Figure 7(*c*) shows that the $\overline{Sh}/Sh_0$ value is about 2.7 in the smaller inlet section and is about 2.0 in the larger inlet section immediately upstream of the turn of the channel with ribs on both the top and bottom walls. Again, the mass transfer in the turn is higher in the case of the smaller inlet section than in the case of the larger inlet section, with higher mass transfer in the downstream half of the turn than in the upstream half of the turn in both cases. Downstream of the turn in the larger exit section, $\overline{Sh}/Sh_0$ decreases abruptly to values between 1.8 and 2.0, while downstream of the turn in the smaller exit section, $\overline{Sh}/Sh_0$ increases to values as high as almost 4.7 before it decreases to values between 3.0 and 3.4 at the channel exit.

In Figs. 8 and 9, the local mass transfer distributions at the turn on the bottom wall of the trapezoidal channel with ribs on both the top and bottom walls are presented for airflow entering the smaller straight section and for airflow entering the larger straight section, respectively. These distributions are based on the local elevation measurements on the U-shaped naphthalene cassette (Fig. 2(*e*)) with balsa wood stripes attached to the naphthalene surface at the same locations where balsa wood stripes were attached to the eight individual cassettes near the turn for regional mass transfer measurements. In each of the two figures, the four Sh/Sh_0 distributions for $Re \approx 9400$, 16,800, 31,800, and 57,200 are similar, with lower values when the Reynolds number is higher. Also, the ribs cause large variations of the local mass transfer, as they periodically interrupt the boundary layers on the bottom wall. Note that the Sh/Sh_0 distributions on the ribbed wall are presented in Figs. 8 and 9 with a scale that is different from that for the distributions on the smooth bottom wall in Figs. 5 and 6.

For flows in both directions, the streamwise Sh/Sh_0 variations between consecutive ribs in the inlet section are larger than the

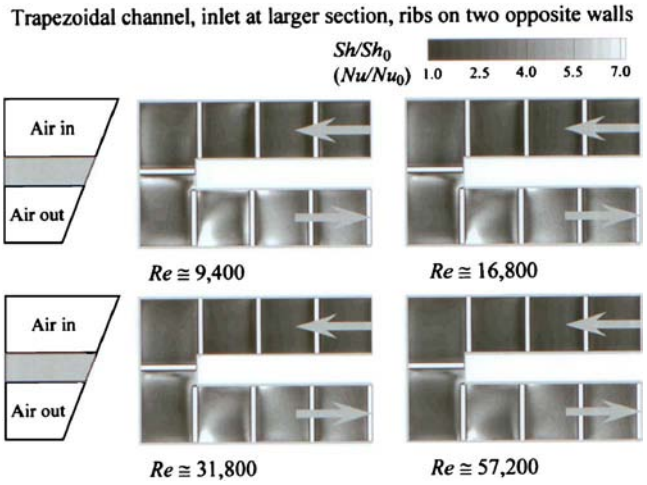

Fig. 9 Local mass transfer distributions at sharp turn in trapezoidal channel with ribs on two opposite walls and a larger inlet straight section

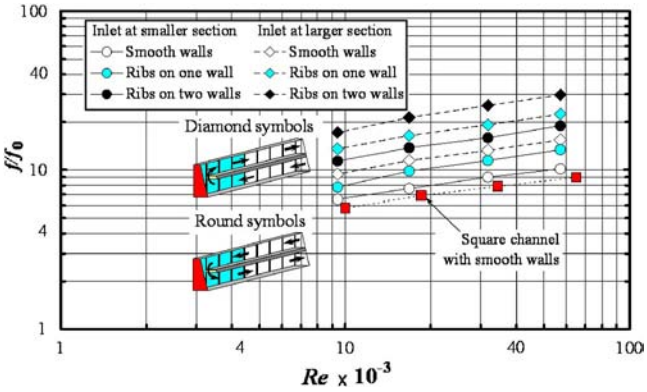

Fig. 10 Overall pressure drops across sharp turns in square and trapezoidal channels

spanwise variations. Upstream of the turn, as the flow reattaches onto the bottom wall downstream of the ribs, the Sh/Sh_0 value is higher than 3.1–3.4 over the reattachment regions in the smaller inlet section and is higher than 2.2–2.5 in the larger inlet section, depending on the Reynolds number. In the turn, there are very large mass transfer variations, with the largest Sh/Sh_0 values near the end wall just downstream of the rib in the turn and small Sh/Sh_0 values upstream of the rib in the turn and upstream of the first rib in the exit section. The local Sherwood number ratio is also large along the upstream half of the end wall and near the downstream outer wall and is small along the upstream outer wall, as in the smooth wall cases. The interactions of secondary flows in the turn with ribs on two opposite walls cause very large variations of the local mass transfer and the various individual regions of high and low mass transfer in the turn.

Comparing Figs. 8 and 9, it can be seen that the Sh/Sh_0 value upstream of the turn is higher in the smaller inlet section than in the larger inlet section because of the higher velocities of the flow in the inlet section with the smaller flow cross-sectional area. Unlike in the smooth wall case, the Sh/Sh_0 values are much lower in the larger exit section than in the turn (Fig. 8), as the air flows over the bottom wall with ribs at lower velocities in the larger exit section. In the smooth wall case, the increase of the turbulence in the flow keeps the Sh/Sh_0 values relatively high in the larger exit section (see Fig. 5). Figure 7 shows that the regional average mass transfer downstream of the turn is higher in the larger exit section with smooth walls than in the larger exit section with ribs on the top and bottom walls. The $\overline{Sh}/Sh_0$ values are between 2.1 and 3.2 in the smooth wall case and between 1.8 and 2.5 in the ribbed wall case. However, Fig. 7 also shows that $\overline{Sh}/Sh_0$ is about 2.0 further downstream in the larger ribbed exit section, while $\overline{Sh}/Sh_0$ continues to decrease along the larger smooth exit section and reaches a value of just over 1.0 at the channel exit.

For airflow entering the larger upstream straight section (Fig. 9), the mass transfer is clearly the highest downstream of the turn, as the flow that leaves the turn with very high turbulence enters the smaller exit section. Individual regions of very high Sh/Sh_0 values are evident along the outer wall and along the downstream side of the divider wall. The Sh/Sh_0 distributions between consecutive ribs in the smaller exit section are very different from the almost two-dimensional distributions resulting from the periodic separated and reattached flow over the ribs on the bottom wall in the inlet section. The local distributions in the smaller exit section with ribs given in Fig. 9 are consistent with the corresponding regional average distributions presented in Fig. 7(*c*), which shows that $\overline{Sh}/Sh_0$ is much larger on wall segment Nos. 10–12 downstream of the turn than on wall segment Nos. 8 and 9 in the turn.

Pressure Drop Across the Turn in Trapezoidal Channel. The pressure drop across the turn was defined as the difference between the static pressures at two streamwise stations near the turn in the two straight sections of the trapezoidal test channel. These stations were at a distance of 43.8 cm from the inlet and exit, respectively. The distance between the two stations (L in Eq. (7)), measured along the centerline of the test channel around the turn, was 36.2 cm. The pressure drop results are presented in this section in terms of a friction factor ratio f/f_0, which gives the average pressure gradient around the turn relative to that for fully developed turbulent flow at the same Reynolds number in a smooth straight channel with a hydraulic diameter equal to that of the cross section at the turn clearance. A minor loss coefficient for the turn may be calculated from the friction factor as $f(L/D_h)$.

In Fig. 10, the pressure drops across the turn are presented for flows at four different flow rates through a square channel with smooth walls, and trapezoidal channels with smooth walls, ribs on one wall, and ribs on two opposite walls, and with flows in opposite directions—flow entering the channel through the smaller straight section or through the larger straight section. The results show that the friction factor ratio increases with increasing Reynolds number in all of the cases studied. The turn in the trapezoidal channel with smooth walls, with airflow in either direction, causes a higher pressure drop than the turn in the square channel with smooth walls. The f/f_0 values range from 9.4 to 15.4 for the trapezoidal channel with a larger inlet section and from 6.5 to 10.2 for the trapezoidal channel with a smaller inlet section, as Reynolds number is increased from about 10,000 to 60,000. Thus, the acceleration of the flow around the turn as the flow cross section decreases appears to cause about 50% higher pressure drop than when the flow direction is reversed. As expected, ribs on one wall cause an additional pressure drop across the turn, and ribs on two walls increase the pressure drop across the turn more than ribs on one wall only. In the case of a trapezoidal channel with the airflow entering the larger straight section of the channel and ribs on two opposite walls, the pressure drop across the turn is the highest, with f/f_0 values ranging from 17.1 to 29.7, which are 50–60% higher than the corresponding values in the case with the flow direction reversed.

Summary of Results and Concluding Remarks

Naphthalene sublimation experiments were conducted and the heat and mass transfer analogy was used to study the local heat transfer distributions on one of the two primary walls of a trapezoidal channel with a 180 deg turn. Results were obtained for turbulent airflow through the channel with smooth walls, and with ribs on one wall and on two opposite walls, over a range of Rey-

nolds numbers between about 10,000 and 60,000. Based on the geometries of the test channel and the conditions of the experiments, the results may be summarized as follows.

1. There was a very large variation of the local heat (mass) transfer distribution in the turn and downstream of the turn. In all cases studied, the average heat (mass) transfer was higher on the downstream half of the turn than on the upstream half of the turn.
2. In the smooth wall case, the heat (mass) transfer was high near the end wall and the downstream outer wall in the turn and was relatively low in two regions near the upstream outer wall and the downstream edge of the divider wall in the turn.
3. With ribs on two opposite walls, the variation of the local heat (mass) transfer was larger than in the smooth wall case, especially in the turn and downstream of the turn. The regional average heat (mass) transfer was higher in the turn of the trapezoidal channel with a smaller inlet section than in the turn of the channel with a larger inlet section. Immediately downstream of the turn, the regional average heat (mass) transfer in the larger exit section decreased abruptly, while the regional average heat (mass) transfer in the smaller exit section continued to increase and reached a maximum value before it decreased as the flow redeveloped. Immediately downstream of the turn, the regional average heat (mass) transfer was lower in the larger exit section of the channel with ribs than in the exit section of the channel with smooth walls for airflow in either direction.
4. The shape of the local heat (mass) transfer distribution at the turn was not significantly affected by varying the air mass flow rate. The average heat (mass) transfer enhancement in the turn was always higher when the Reynolds number was smaller.
5. The pressure drop across the turn was higher in the case of the flow entering the channel through the larger straight section than when the flow was reversed. As expected, the ribs increased the pressure drop across the turn.

The results of this study show that there is a large variation of the local heat (mass) transfer in the turn and immediately downstream of the turn for airflow through a two-pass trapezoidal channel with smooth walls or with ribs on the walls. The large variation is caused by a very complex flow field with secondary flows, separated and reattached flows, and flow recirculation in the turn and near the ribs on the walls. To fully understand the effects of the geometries of the channel, the turn, and the ribs, or turbulence promoters, on the flow distribution in the channel, and the effect of the flow field on the local heat (mass) transfer distributions on the channel walls, parametric experimental and numerical studies must be continued to accurately measure or predict the flow fields near the turns in multipass channels of various geometries and the heat (mass) transfer distributions on the channel walls. These results are needed in the design of serpentine cooling passages in gas turbine airfoils.

Nomenclature

A_c = flow cross-sectional area at turn clearance, m^2
A_s = surface area, m^2
D_h = hydraulic diameter of flow cross section at turn clearance, m
f = friction factor
f_0 = reference friction factor for fully developed turbulent flow through smooth channel, equals to $[0.790 \ln(\mathrm{Re}) - 1.64]^{-2}$
h_m = local mass transfer coefficient, m/s
$\bar{h}_m$ = segmental or regional average mass transfer coefficient, m/s
L = streamwise distance between pressure taps, m
$\dot{m}$ = air mass flow rate, kg/s
$\dot{M}_n$ = rate of total mass transfer from upstream naphthalene surfaces, kg/s
$\dot{M}''_n$ = local naphthalene mass flux, $\mathrm{kg}/(\mathrm{m}^2\,\mathrm{s})$
$\underline{\mathrm{Nu}}$ = local Nusselt number
$\overline{\mathrm{Nu}}$ = segmental or regional average Nusselt number
Nu_0 = reference Nusselt number for fully developed turbulent flow in smooth channel, equals to $0.023\,\mathrm{Re}^{0.8}\,\mathrm{Pr}^{0.4}$
P = perimeter of flow cross section at turn clearance, m
Pr = Prandtl number
Re = Reynolds number
Sc = Schmidt number
$\underline{\mathrm{Sh}}$ = local Sherwood number
$\overline{\mathrm{Sh}}$ = segmental or regional average Sherwood number
Sh_0 = reference Sherwood number for fully developed turbulent flow through smooth channel, equals to $0.023\,\mathrm{Re}^{0.8}\,\mathrm{Sc}^{0.4}$
$\dot{V}$ = volumetric flow rate of air, m^3/s
$\bar{V}$ = average velocity, m/s

Greek Symbols

ΔM_n = total mass transfer from naphthalene surface to air, kg
Δp = pressure drop across sharp turn, N/m^2
Δt = duration of experiment, s
Δz = local change of elevation on naphthalene surface, m
μ = dynamic viscosity of air, $N\,s/m^2$
ρ = density of air, kg/m^3
$\rho_{v,b}$ = local bulk vapor density of naphthalene, kg/m^3
$\bar{\rho}_{v,b}$ = average bulk vapor density of naphthalene, kg/m^3
ρ_s = density of solid naphthalene, kg/m^3
$\rho_{v,w}$ = vapor density of naphthalene on naphthalene surface, kg/m^3
σ = mass diffusion coefficient of naphthalene vapor in air, m^2/s

References

[1] Han, J. C., Dutta, S., and Ekkad, S. V., 2000, *Gas Turbine Heat Transfer and Cooling Technology*, Taylor & Francis, New York, pp. 287–370 and 439–497.
[2] Burggraf, F., 1970, "Experimental Heat Transfer and Pressure Drop With Two Dimensional Turbulence Promoters Applied to Two Opposite Walls of a Square Tube," *Augmentation of Convective Heat and Mass Transfer*, Bergles, A. E., and Webb, R. L., eds., ASME, New York, pp. 70–79.
[3] Han, J. C., Glicksman, L. R., and Rohsenow, W. M., 1978, "An Investigation of Heat Transfer and Friction for Rib Roughened Surfaces," Int. J. Heat Mass Transfer, **21**, pp. 1143–1156.
[4] Boyle, R. J., 1984, "Heat Transfer in Serpentine Passages With Turbulence Promoters," ASME Paper No. 84-HT-24.
[5] Han, J. C., Chandra, P. R., and Lau, S. C., 1988, "Local Heat/Mass Transfer Distributions around Sharp 180° Turns in Two-Pass Smooth and Rib-Roughened Channels," ASME J. Heat Transfer, **110**, pp. 91–98.
[6] Lau, S. C., Kukreja, R. T., and McMillin, R. D., 1991, "Effects of V-Shaped Rib Arrays on Turbulent Heat Transfer and Friction of Fully Developed Flow in a Square Channel," Int. J. Heat Mass Transfer, **34**, pp. 1605–1616.
[7] Acharya, S., Dutta, S., Myrum, T. A., and Baker, R. S., 1993, "Periodically Developed Flow and Heat Transfer in a Ribbed Duct," Int. J. Heat Mass Transfer, **36**, pp. 2069–2082.
[8] Ekkad, S. V., and Han, J. C., 1997, "Detail Heat Transfer Distributions in Two-Pass Square Channels With Rib Turbulators," Int. J. Heat Mass Transfer, **40**, pp. 2525–2537.
[9] Rhee, D. H., Lee, D. H., Cho, H. H., and Moon, H. K., 2003, "Effects of Duct Aspect Ratios on Heat/Mass Transfer With Discrete V-Shaped Ribs," ASME Paper No. GT2003-38622.
[10] Johnson, B. V., Wagner, J. H., Steuber, G. D., and Yeh, F. C., 1994, "Heat Transfer in Rotating Serpentine Passages With Trips Skewed to the Flow," ASME J. Turbomach., **116**, pp. 113–123.
[11] Johnson, B. V., Wagner, J. H., Steuber, G. D., and Yeh, F. C., 1994, "Heat Transfer in Rotating Serpentine Passages With Selected Model Orientations for

Smooth or Skewed Trip Walls," ASME J. Turbomach., **116**, pp. 738–744.
[12] Park, C. W., and Lau, S. C., 1998, "Effect of Channel Orientation on Local Heat (Mass) Transfer Distributions in a Rotating Two-Pass Square Channel With Smooth Walls," ASME J. Heat Transfer, **120**, pp. 624–632.
[13] Park, C. W., Yoon, C., and Lau, S. C., 2000, "Local Heat (Mass) Transfer in a Diagonally-Oriented Rotating Two-Pass Channel With Rib-Roughened Walls," ASME J. Heat Transfer, **122**, pp. 208–211.
[14] Lee, E., Wright, L. M., and Han, J. C., 2003, "Heat Transfer in Rotating Rectangular Channel (AR=4:1) With V-Shaped and Angled Rib Turbulators With and Without Gaps," ASME Paper No. GT2003-38900.
[15] Cho, H. H., Kim, Y. Y., Kim, K. M., and Rhee, D. H., 2003, "Effects of Rib Arrangements and Rotation Speed on Heat Transfer in a Two-Pass Duct," ASME Paper No. GT2003-38609.
[16] Liu, Y. H., Wright, L. M., Fu, W. L., and Han, J. C., 2006, "Rib Spacing Effect on Heat Transfer and Pressure Loss in a Rotating Two-Pass Rectangular Channel (AR=1:2) With 45-Degree Angled Ribs," ASME Paper No. GT2006-90368.
[17] Zhou, F., and Acharya, S., 2006, "Heat Transfer at High Rotation Numbers in a Two-Pass 4:1 Aspect Ratio Rectangular Channel With 45-Degree Skewed Ribs," ASME Paper No. GT2006-90391.
[18] Ekkad, S. V., Huang, Y., and Han, J. C., 1996, "Detailed Heat Transfer Distributions in Two-Pass Smooth and Turbulated Square Channels With Bleed Holes," presented at the *1996 National Heat Transfer Conference, Houston*.
[19] Taslim, M. E., Li, T., and Spring, S. D., 1995, "Experimental Study of the Effects of Bleed Holes on Heat Transfer and Pressure Drop in Trapezoidal Passages With Tapered Turbulators," ASME J. Turbomach., **117**, pp. 281–289.
[20] Taslim, M. E., Li, T., and Spring, S. D., 1998, "Measurements of Heat Transfer Coefficients and Friction Factors in Passages Rib-Roughened on All Walls," ASME J. Turbomach., **120**, pp. 564–570.
[21] Li, L., Ding, S. T., Xu, G. Q., Tao, Z., and Deng, H. W., 2006, "Experimental Study on the Heat Transfer in the Compound Cooling Passage," ASME Paper No. GT2006-90250.
[22] Moon, S. W., Endley, S., and Lau, S. C., 2002, "Local Heat Transfer Distribution in a Two-Pass Trapezoidal Channel With a 180° Turn via the Transient Liquid Crystal Technique," J. Energy, Heat and Mass Transfer, **24**, pp. 103–121.
[23] Ambrose, D., Lawrenson, I. J., and Sprake, C. H. S., 1975, "The Vapor Pressure of Naphthalene," J. Chem. Thermodyn., **7**, pp. 1172–1176.
[24] Goldstein, R. J., and Cho, H. H., 1995, "A Review of Mass Transfer Measurements Using Naphthalene Sublimation," Exp. Therm. Fluid Sci., **10**, pp. 416–434.
[25] Eckert, E. R. G., 1976, "Analogies to Heat Transfer Processes," *Measurements in Heat Transfer*, Eckert, E. R. G., and Goldstein, R. J., eds., Hemisphere, New York, pp. 397–423.
[26] Incropera, F. P., and DeWitt, D. P., 2002, *Fundamentals of Heat and Mass Transfer*, 5th ed., Wiley, New York.
[27] Coleman, H. W., and Steele, W. G., 1989, *Experimentation and Uncertainty Analysis for Engineers*, Wiley, New York.

Detailed Heat/Mass Transfer Distributions in a Rotating Smooth Channel With Bleed Flow

Kyung Min Kim
Sang In Kim
Yun Heung Jeon
Dong Hyun Lee
Hyung Hee Cho
e-mail: hhcho@yonsei.ac.kr

Department of Mechanical Engineering,
Yonsei University,
Seoul 120-749, Korea

In this study, the effects of bleed flow on heat/mass transfer in a rotating smooth square channel were investigated. The hydraulic diameter (D_h) of the channel was 40.0 mm*, and the diameter of the bleed holes* (d) *on the leading surface was* 4.5 mm*. Tests were conducted under various bleed flow rates (0%, 10%, 20%) and rotation numbers (0, 0.2, 0.4), while the Reynolds number was fixed at 10,000. A naphthalene sublimation method was employed to determine the detailed heat transfer coefficients using a heat and mass transfer analogy. The results suggested heat/mass transfer characteristics in the internal cooling passage to be influenced by tripping flow as well as Coriolis force induced by bleed flow and channel rotation. In cases influenced by bleed flow, the heat/mass transfer on the leading surface was higher than that without bleed flow. The heat/mass transfer on the leading surface increased with the number of rotations to* Ro=0.2*, after which it decreased due to rotation effects.* [DOI: 10.1115/1.2759974]

Keywords: bleed flow, Coriolis force, naphthalene sublimation method, rotating channel

Introduction

The design of an effective cooling system has become crucial in the development of high-performance gas turbine engines. The turbine inlet temperature has been steadily increased to improve the thermal efficiency of turbine engines, but doing so has resulted in high heat loads on turbine blades. Various cooling schemes have been employed to protect blade materials from exceeding the maximum allowable temperature and being damaged. Such methods include the internal passage cooling technique for the inner surface and the film cooling technique for the outer surfaces that contact hot gases. In the film cooling technique, coolant air passes the internal passages within the turbine blades and is then ejected through holes on the blade surfaces. Many studies have considered factors such as the flow condition and the channel geometry to develop the cooling performance of an internal passage with bleed holes. Moreover, different heat transfer characteristics arise with the rotation of turbine blades due to the combination of flow structures in the passage. Therefore, it is important to understand not only the mechanism of heat transfer in a cooling channel but also how these factors affect one another for better cooling performance. To this end, heat transfer and flow patterns in internal passages have been studied extensively.

Various parameters must be investigated to ascertain an accurate depiction of heat transfer, including the effect of rib turbulators, channel geometry, and channel rotation. Through numerous investigations, it has been determined that rib conditions, such as rib height, rib angle of attack, rib-to-rib pitch, rib shape, rib arrangement, and discrete ribs, greatly affect heat transfer and friction [1–4]. The effects of channel geometry have also been of great interest to many researchers. Astarita et al. [5] measured heat transfer coefficients in rectangular channels of five different aspect ratios using an infrared scanner. Metzger and Vedula [6] investigated heat transfer characteristics in a triangular channel with various rib arrangements. Also, the effects of divider wall geometry, such as inclination angle and thickness, were reported by Hirota et al. [7].

Rotation of the cooling passage engenders complex internal flow and heat transfer characteristics. As such, many tests have been widely conducted to clarify the effects of rotation on heat transfer. Yang et al. [8] examined heat transfer performance in a four-pass serpentine passage with various Reynolds, Rossby and rotational Rayleigh numbers. Iacovides et al. [9] reported heat transfer and flow characteristics in a smooth two-pass duct, examining flow developments and local Nusselt number distributions. Dutta and Han [10] studied smooth rectangular passages with three channel orientations to understand the effects of high rotation and rib arrangement on heat transfer characteristics. Murata and Mochizuki [11] also investigated the influence of the duct aspect ratio on heat transfer and fluid flow in a rotating smooth duct.

Coolant fluid endures a centrifugal buoyancy force, and thus, temperature and flow field changes, while in a rotating passage. Based on their numerical investigation, Hwang and Lai [12] concluded that buoyancy promotes heat transfer more significantly in a radially inward-flow channel than in an outward-flow channel. Wagner et al. [13] and Bons and Kerrebrock [14] also studied the buoyancy force effect by altering the rotation number and density ratio.

To improve gas turbine performance, holes are formed on the surface of the turbine blade, and these holes significantly affect heat transfer in the cooling passage. Therefore, the investigation of bleed flow effects under various conductions is essential. However, most of the studies of bleed flow effects have been conducted in a stationary channel with various rib turbulators. Taslim et al. [15], who measured local heat transfer coefficients in trapezoidal passages with bleed holes, reported that bleed holes on the smooth surface (the sidewall) yield a more uniformly distributed spanwise heat transfer coefficient on the ribbed surface and that bleed flow resulted in a friction factor lower than that resultant without effusion. Shen et al. [16] studied the enhancements in heat transfer afforded by the combination of ribs and bleed holes, rather than just ribs. The average heat transfer was determined to be ~25% higher with the addition of bleed holes, but heat transfer was shown to decrease at high bleed ratios. Thurman and Poinastte [17] investigated how the interaction of 90 deg ribs and vari-

Contributed by the Heat Transfer Division of ASME for publication in the JOURNAL OF HEAT TRANSFER. Manuscript received November 30, 2006; final manuscript received March 10, 2007. Review conducted by Minking Chyu. Paper presented at the Proceedings of ISROMAC-11 (The 11th International Symposium on Transport Phenomena and Dynamics of Rotating Machinery), February 26–March 2, 2006, Honolulu, HI.

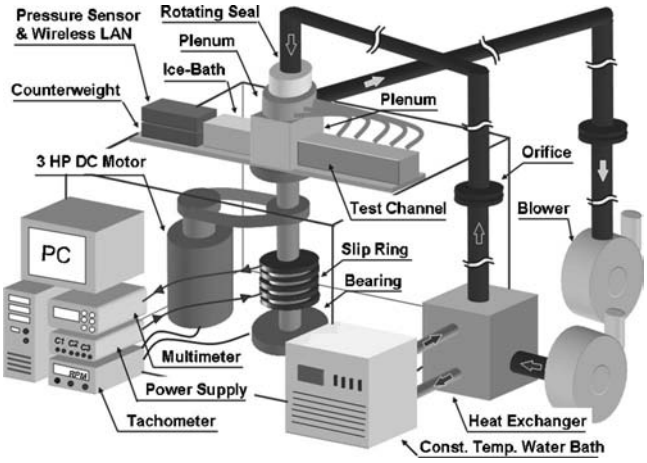

Fig. 1 Experimental apparatus

ous bleed conditions impact heat transfer. They reported that placing bleed holes after ribs widened the regions of high heat transfer by removing recirculation flow from behind the ribs. Ekkad et al. [18] performed the experiments for various rib roughened surfaces with bleed holes and reported that each rib arrangement generated similar heat transfer in the first pass. Park et al. [19] examined the effects of channel rotation and orientation in a square channel, which ejected the whole flow through the holes. They concluded that, as a result of the bleed and the channel rotation, the mean heat transfer of the leading and trailing surfaces decreases due to the main flow loss and the heat transfer discrepancy between two surfaces appears due to the Coriolis force.

Although the details of heat transfer coefficients in stationary passages with bleed holes have been widely investigated, there still exists a need for a more detailed account of the impact of various rotation numbers and bleed ratios on the heat transfer characteristics in a rotating passage. Information regarding local heat transfer augmentation via channel rotation has been particularly essential in designing internal channels that maintain low thermal stress and prevent hot spots on blade surfaces. For these reasons, previous studies [20–22] have mainly focused on the flow and local heat transfer characteristics in rotating cooling passages. Detailed local heat/mass transfer coefficients on smooth and ribbed surfaces in rotating channels with and without bleed flow have been obtained experimentally. This paper continues our efforts to attain a more complete comprehension of the effects of various rotation numbers and bleed ratios in a smooth channel with effusion holes. To validate the heat/mass transfer augmentation, numerical computations were performed using a commercial package (FLUENT 6.1). The results provide vital evidence in predicting flow structures inside a rotating passage and aid in the understanding of heat/mass transfer phenomena.

Experimental Apparatus

Rotating Facility. The experimental apparatus as shown in Fig. 1 comprised a blowing system, a suction system, rotating system, and measuring system. First, one blower (blowing system) supplied room air into the test section, the inlet of which included a bellmouth (contraction nozzle), meshes and honeycombs to make uniform profile, and high turbulence intensity of the inlet flow. Another blower (suction system) ejected the constant flow rate from each hole of the test section into the room. These blowers were controlled using frequency inverters. Air temperature was regulated during the experiment using a heat exchanger. The blowing and bleeding flow rates were measured by orifice flowmeters and then calibrated the flow rate in the channel inlet using measuring temperature difference between the duct inlet and the orifice. The Reynolds number (Re), which is based on the hydraulic diameter and the ratio of the bleed flow to the main flow (bleed ratio, (BR)) was monitored and observed to be constant (Re =10,000 and BR=0.0, 0.1, and 0.2) during the tests, where the averaged bulk velocity (u_b) of Re and Ro are based on the channel inlet flow rate. The maximum difference in the bleed flow through each bleed hole was verified to be within 1% for all cases by differential pressure tests. Leakage from the rotating part was prevented by a magnetic rotating seal and a rib seal.

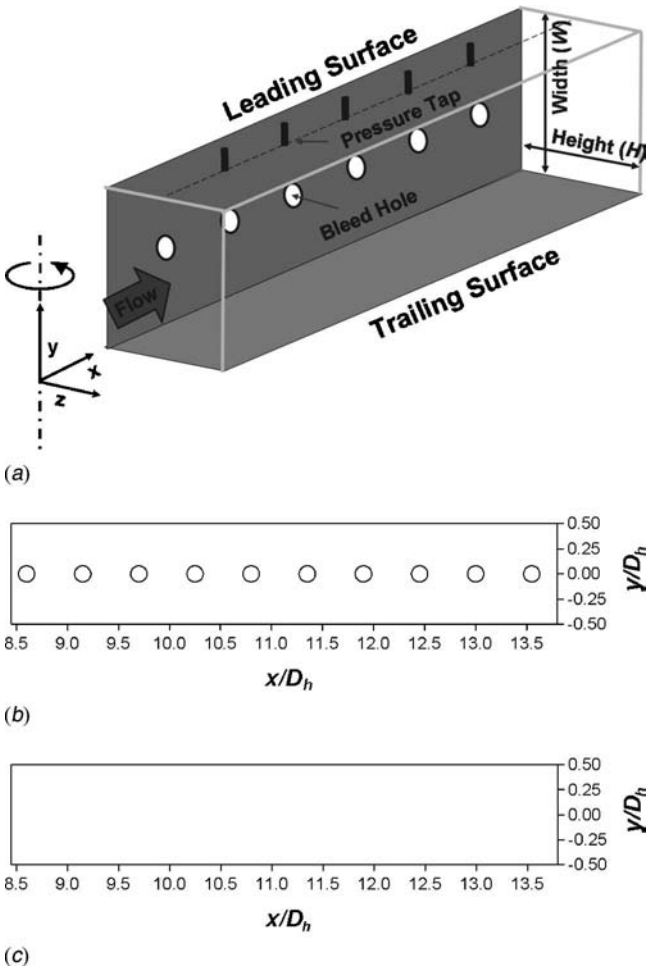

Fig. 2 Schematics of the test section: (*a*) Geometry of the channel, (*b*) coordinate system of the leading surface, and (*c*) coordinate system of the trailing surface

Next, the rotating system simulates the operating condition of gas turbine blades. A 3 HP (2.24 kW) DC motor connected to a V-belt was used to drive a rotating shaft, the rotation speed of which was measured by an optical tachometer. The rotation number was increased from 0.0 to 0.4 in increments of 0.1. The maximum rotation number (Ro=0.4) corresponds to ~400 rpm.

Lastly, electrical output signals from the test section were recorded by an Agilent data logger and a GE Druck electronic pressure sensor, which were interfaced to a computer via slip rings and a wireless LAN. As the vapor density of naphthalene is sensitive to temperature, varying ~10% per change of 1 °C, the naphthalene surface temperature was measured by J-type thermocouples embedded in the test plate. The bulk air temperature was obtained by thermocouples installed in the channel inlet and outlet. An ice bath was used as a thermocouple reference junction.

Test Section. Figure 2 presents a three-dimensional picture of the test section. As shown in Table 1, it has a hydraulic diameter (D_h) of 40.0 mm and a cross-sectional area of 40 mm(W)

Table 1 Experimental parameters and conditions

Hydraulic diameter (D_n)	40.0 mm
Passage height (H)	40.0 mm
Passage width (W)	40.0 mm
Max. rotating radius (R)	580 mm
Test section length	552 mm
Naphthalene coated length	214 mm
Bleed hole diameter (d)	4.5 mm
Rim thickness of hole	1.0 mm
Hole-to-hole pitch (p)	22.0 mm
Passage inlet averaged bulk velocity (u_b)	~4.4 m/s
Flow rate ratio of each hole to duct inlet	0%,0.5%,1.0%
Rotation number (Ro)	0.0,0.1,0.2,0.4

$\times 40$ mm(H). During the experiment, aluminum plates casting naphthalene are installed on both the leading and trailing sides of the test channel. There are total 20 holes (which are installed 10 holes in the flow-developed region and 10 holes in heat/mass transfer region) situated along the center line of the leading surface. The bleed holes have a diameter of 4.5 mm and a rim thickness of 1.0 mm. The ratio of hole spacing to hole diameter (p/d) is 4.9. The ratio of maximum rotating radius to hydraulic diameter (R/D_h) is 14.5.

The coordinate system of the test plates is depicted in Figs. 2(b) and 2(c). The streamwise, lateral, and vertical directions correspond to the x-, y-, and z-axes, respectively. The naphthalene covers the test section from $x/D_h=8.45$ (the starting point of the naphthalene surface) to $x/D_h=13.8$ (the ending point). The lateral domain ranges from $y/D_h=-0.5$ to $y/D_h=0.5$.

The pressure drop through the channel is measured through eight pressure taps with a diameter of 1.0 mm, which are drilled at $z/D_h=0.0$ on one of the sidewalls. The pressure tap spacing is 66 mm, or three times that of the hole-to-hole pitch. The pressure sensor, with a resolution of 0.01 mm H_2O, is used to measure the static pressure differences between the taps.

Experimental Data Reduction

A naphthalene sublimation method is employed to obtain detailed mass transfer coefficients using the analogy between heat and mass transfer. As reviewed by Goldstein and Cho [23], that the mass transfer results can be converted to heat transfer results even though the analogy requires that the Schmidt (Sc) and Prandtl (Pr) numbers be equal; for example, Sc for naphthalene vapor in air is 2.28 at 25°C, which is sufficiently close to Pr (e.g., Pr=0.71 in air and Pr=1–14 in water) of numerous gases and liquids that the analogy can be applied with good confidence.

The leading and trailing surfaces of the test section are cast with naphthalene to simulate a cooling channels two-sided heating condition of a gas turbine blade. When a turbine engine operates, rotor blades endure high-temperature combustion gas primarily on the leading and trailing surfaces, or the suction and pressure sides. The present surface heating condition is deduced from this observation. The naphthalene surfaces where mass transfer occurs correspond to a uniform wall-temperature boundary condition common to heat transfer experiments, while inactive surfaces maintain an adiabatic wall condition. The local naphthalene sublimation depth is measured to attain the mass transfer coefficients of each position using a liner variable differential transformer, LBB $-375TA-020$, and an automated positioning table. It is expressed as

$$h_m = \frac{\dot{m}}{\rho_{v.w} - \rho_{v.b}} = \frac{\rho_s(\Delta z/\Delta t)}{\rho_{v.w} - \rho_{v.b}} \tag{1}$$

where $\dot{m}$ is the local mass transfer rate of naphthalene per unit area, which is determined from the density of solid naphthalene ρ_s, and the sublimation rate, $\Delta z/\Delta t$. $\rho_{v.w}$ and $\rho_{v.b}$ are the vapor densities of the surface naphthalene and the bulk air, respectively. The former is calculated from the ideal gas law using the vapor pressure and the surface temperature as

$$\rho_{v.w} = \frac{P_{\text{naph}}}{R_{\text{naph}} T_w} \tag{2}$$

The naphthalene vapor pressure P_{naph} is determined from the equations suggested by Ambrose et al. [24]. The latter, or the bulk vapor density of naphthalene, is obtained from the average naphthalene sublimation depth, $\overline{z_{\text{sub}}}|_x$, measured at each position in the mainstream direction as

$$\rho_{v.b} = \frac{\rho_s W x}{\dot{Q}_{\text{air}} \Delta t} \overline{z_{\text{sub}}}|_x \tag{3}$$

From the local mass transfer coefficient, the Sherwood number is calculated as

$$Sh = \frac{h_m D_h}{D_{\text{naph}}} \tag{4}$$

where D_{naph} is the diffusion coefficient of naphthalene in air. This study employs the naphthalene properties suggested by Goldstein and Cho [23] and Ambrose et al. [24]. The Sherwood number is estimated to be accurate within ±8.0% at a 95% confidence level, based on the uncertainty estimation method of Kline and McClintock [25]. The uncertainty of the naphthalene properties, such as the mass transfer coefficient with ±7.4% error and the diffusion coefficient with ±3.0% error, are the most dominant factors in determining the uncertainty of the Sherwood number.

The Nusselt numbers can be obtained from the Sherwood numbers by the correlation $\text{Nu}/\text{Sh}=(\text{Pr}/\text{Sc})^{0.4}$, which is for turbulent flows. To effectively estimate the heat/mass transfer augmentation, the mass transfer results are presented as Sherwood number ratios, Sh/Sh_0. Sh_0, the Sherwood number for a fully developed turbulent flow in a stationary smooth circular tube, was first correlated by McAdams [26] and is converted to mass transfer parameters as

$$\text{Sh}_0 = 0.023\,\text{Re}^{0.8}\text{Sc}^{0.4} \tag{5}$$

The streamwise and the regional averaged Sherwood numbers, $\overline{\text{Sh}}_L$ and $\overline{\text{Sh}}_R$, respectively, are calculated by integrating the local Sherwood numbers weighted by constant area.

The average pressure drop is obtained from the slope calculated by a linear curve fitting of the local pressure difference data in the middle region of the channel ($\Delta P/\Delta L$), where the static pressure decreases linearly. The friction factor is calculated with the average pressure drop as

$$f = \frac{\Delta P}{4(\Delta L/D_h)(1/2)\rho u_b^2} \tag{6}$$

The uncertainty of the friction factor is within 4.4%. The friction loss results are presented as the friction factor ratios, f/f_0, where f_0 represents the friction factor for a fully developed turbulent flow in a smooth circular tube. The empirical equation that most closely fits the Kármán–Nikuradse equation proposed by Petukhov [27] is employed as $f_0=2(2.236\ln\text{Re}-4.639)^{-2}$.

The thermal performance η, obtained by considering both the heat/mass transfer augmentation and the friction loss increment, is presented based on the constant pumping power condition, which is expressed as follows:

$$\eta = \frac{\overline{\overline{\text{Sh}}}_R/\text{Sh}_0}{(f/f_0)^{1/3}} \tag{7}$$

Results and Discussion

In this study, the measured local heat/mass transfer characteristics were investigated in the internal cooling passage with bleed

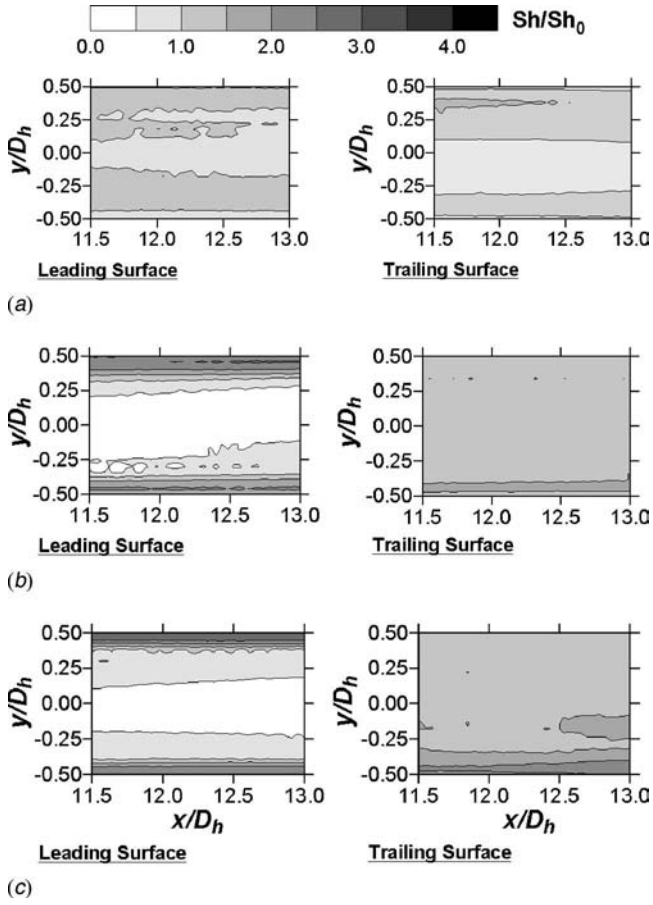

Fig. 3 Local Sh/Sh_0 distributions in the channel without bleed flow: (*a*) Ro=0.0, (*b*) Ro=0.2, and (*c*) Ro=0.4

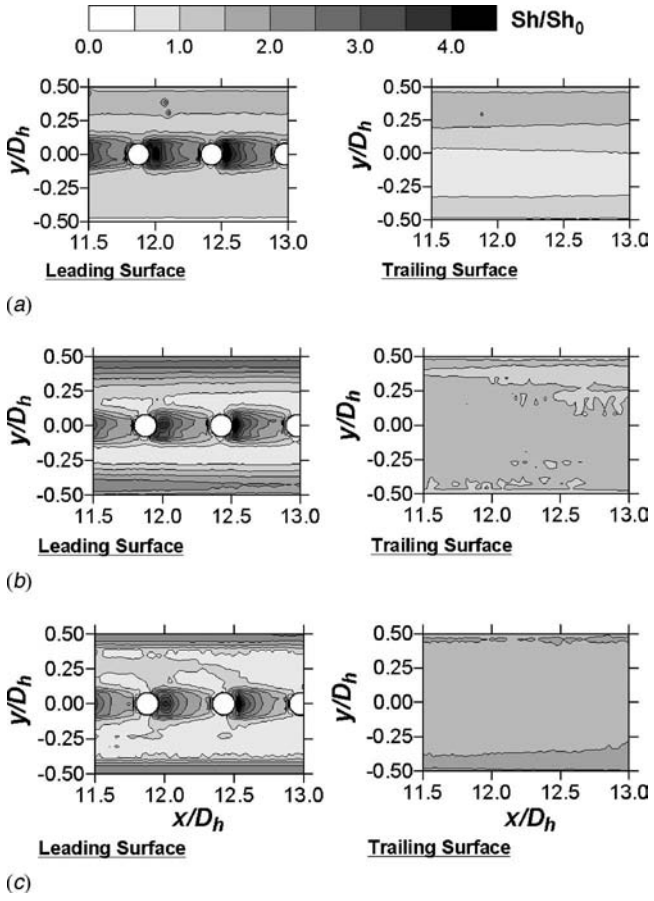

Fig. 4 Local Sh/Sh_0 distributions in the channel with bleed flow at BR=0.1: (*a*) Ro=0.0, (*b*) Ro=0.2, and (*c*) Ro=0.4

flow on the leading surface. The results were compared with the heat/mass transfer patterns, which were tested for baseline data in the smooth channel without the bleed flow.

Heat/Mass Transfer Characteristics. Figure 3 shows the measured local Sherwood number ratio distributions on the leading and trailing surfaces in the smooth passage without bleed holes at rotation numbers of 0.0, 0.2, and 0.4. In the stationary case, the contour plots of the leading and trailing surfaces were identical under the present experimental accuracy, and the Sherwood number ratios were around $Sh/Sh_0=1.0$. As the channel was rotated, a discrepancy between the heat/mass transfer of the leading and trailing surfaces was observed. The rotating effects appeared in the middle of the leading surface ($-0.25 \le y/D_h \le 0.25$). That is, the heat/mass transfer was decreased on the leading surface and augmented on the trailing surface; furthermore, the heat/mass transfer characteristics of the leading surface differed from those of the trailing surface in that the local coefficients in the outer wall regions ($-0.5 \le y/D_h \le -0.25, 0.25 \le y/D_h \le 0.5$) were higher than those in the inner region ($-0.25 \le y/D_h \le 0.25$). These results suggest that the Coriolis force generated the pair of counterrotating vortices. At the highest rotation number (Ro=0.4), the high heat/mass transfer regions became narrower than those at Ro =0.2. This is because the secondary flow by the Coriolis force was heavily augmented over the trailing surface as the rotation speed increased.

Figure 4 presents the local Sherwood number ratio distributions in the smooth channel with bleed flow at the bleed ratio of 0.1. On the leading surface, the contour plots around the bleed holes were of identical mass transfer distributions in each case. In other words, on the bleeding surface with effusion holes, the heat/mass transfer was higher than that in the other regions because the tripping flow effected stronger reattachment around the holes. It is noted that the tripping flow near the bleeding surface is entrained into the bleed holes, and then spent air, which is not expelled through the hole, collides with the region behind the hole. At the rotation number of 0.2, the lower Sherwood number ratios appeared in the leading surface regions around $y/D_h=0.25$ and behind the holes; however, in the outer wall regions of the leading surface and in the middle region of the overall trailing surface, the mass transfer coefficients increased. These regions were formed due to the tripping flow and the Corilois force. Furthermore, increases in the rotation number greatly affected the heat/mass transfer of the high and low regions.

The detailed heat/mass transfer distributions in the smooth channel at the bleed ratio of 0.2 are shown in Fig. 5. Although the bleed flow rate increased, the Sherwood number ratio distributions at BR=0.1 were similar to those at BR=0.2. However, around the bleed holes on the leading surface, the high heat/mass transfer distributions were expanded and enhanced, while the heat/mass transfer distributions on the trailing surface were decreased as the increase in bleed flow reduced the main flow rate.

Specific values of the local Sherwood number ratios among a measurement line, $x/D_h=12.14$ at various rotation numbers in nonbleeding and bleeding cases are shown in Figs. 6 and 7. The local heat/mass transfer distributions are changed greatly on the leading and trailing surfaces; thus, the corresponding domain is particularly concentrated. On the leading surface without bleed flow (Fig. 6(*a*)), local values in both the sidewall regions of stationary case are higher than those in the middle region due to the turbulent flow in the square channel; as the rotation number increases, Sh ratios in the middle region decrease, but those in both

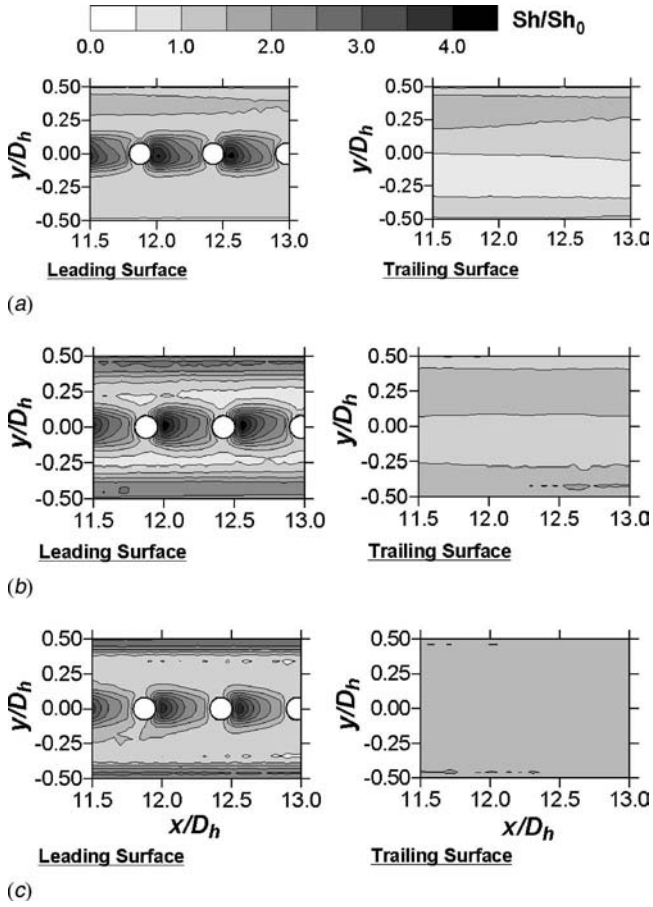

Fig. 5 Local Sh/Sh_0 distributions in the channel with bleed flow at BR=0.2: (*a*) Ro=0.0, (*b*) Ro=0.2, and (*c*) Ro=0.4

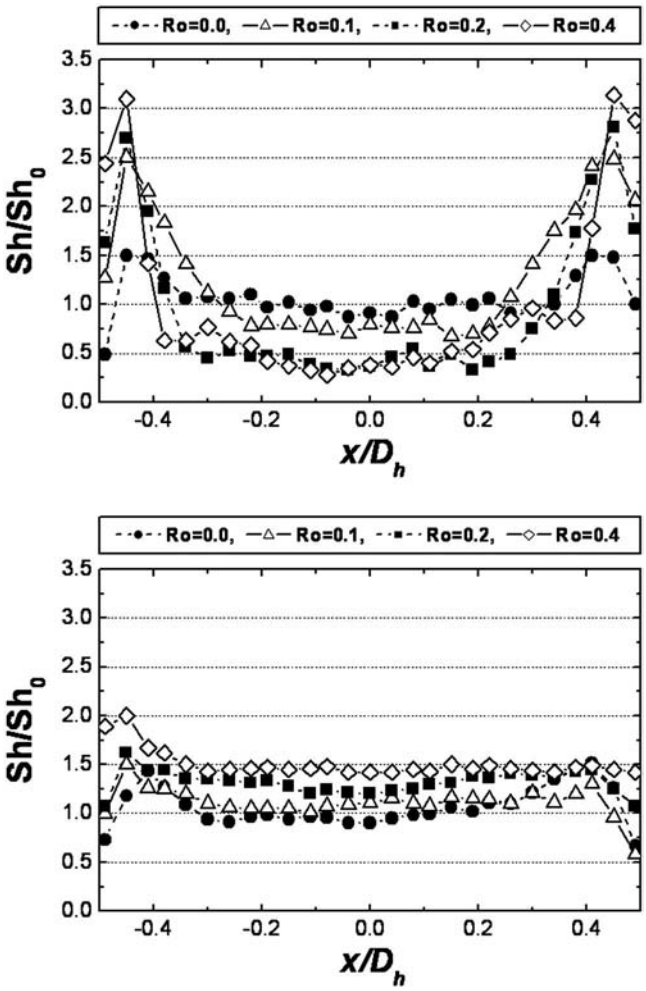

Fig. 6 Spanwise Sh ratio distributions at x/D_h=12.14 in nonbleeding case (BR=0.0): (*a*) Leading surface and (*b*) trailing surface

the sidewall regions increase because the secondary flow is generated by the Coriolis force. On the trailing surface (Fig. 6(*b*)), the similar trend of Sh ratio distributions show at all the tests; however, the values are enhanced with increment of the rotation number. In cases with bleed flow (Fig. 7), all the regions are the same trend of the case without bleed flow, although the values are higher than those without bleed flow due to impingement of the bleed flow. That is, as the rotation number increases, Sh ratios are enhanced in both the side regions on the leading surface and in all the regions on the trailing surface, but are diminished in the middle region on the leading surface.

Figure 8 shows the spanwise-averaged Sherwood number ratios on the leading surface. The effects of bleed flow or tripping flow were predominant in the stationary channel, as shown in Fig. 8(*a*). At the bleed ratio of 0.1, for instance, the regions augmented the heat/mass transfer were repeated on the leading surface among pairs of holes. However, the averaged heat/mass transfer coefficients at BR=0.2 were similar to the values at the BR=0.1. This is because the heat/mass transfer in the overall regions became lower due to the reduction of the main flow, although the heat/mass transfer around the bleed holes was shown to be greater than that of the low bleed ratio. On the leading surface in the rotating channel, the discrepancy between the heat/mass transfer of the nonbleeding and bleeding cases was enlarged by the effects of bleed flow and Coriolis force. This proves that the heat/mass transfer distributions in the outer wall regions were as high as those of the nonbleeding cases due to the secondary flow generated by the Coriolis force; additionally, the high heat/mass transfer regions around holes were identical in all cases. At Ro=0.4 (Fig. 8(*c*)), the high Sherwood number ratio distributions in the leading surface wall regions became narrower than those at Ro=0.2, and the main flow was deflected further toward the trailing surface; thus, the heat/mass transfer coefficients were decreased.

The effects of rotation and effusion become more conspicuous as the rotation number and bleed ratio increase, as shown in Fig. 9. Figure 9(*a*) presents the regional averaged Sherwood number ratios from x/D_h=10.5 to x/D_h=13.25. In the cases without bleed flow, increases in rotation number gradually enlarged the heat/mass transfer discrepancy between the leading and trailing surfaces. On the leading surface, the Sherwood number ratios are higher than the Nusselt number ratios reported by Dutta and Han [10]; however, the values on the trailing surface are lower than their data on the trailing surface. It is because the experimental method and the parameters are different. In mass transfer experiments, the measured values generally take no effects of conduction and centrifugal buoyancy force. That is, as shown in Figs. 6 and 7, the mass transfer coefficients in both side regions of the leading surface were high due to the inactive sidewall, no conduction through the sidewall, and the high turbulence intensity of the channel inlet. The discrepancy in heat transfer between the leading and trailing surfaces is small because the rotation-induced centrifugal buoyancy force is not presented in mass transfer experiment. On the leading surface in the smooth channel with bleed flow, the Sh ratio trend was reversed. That is, the heat/mass transfer increased to Ro=0.2 and then decreased due to the reduction of the main flow rate and the impinging regions of the secondary

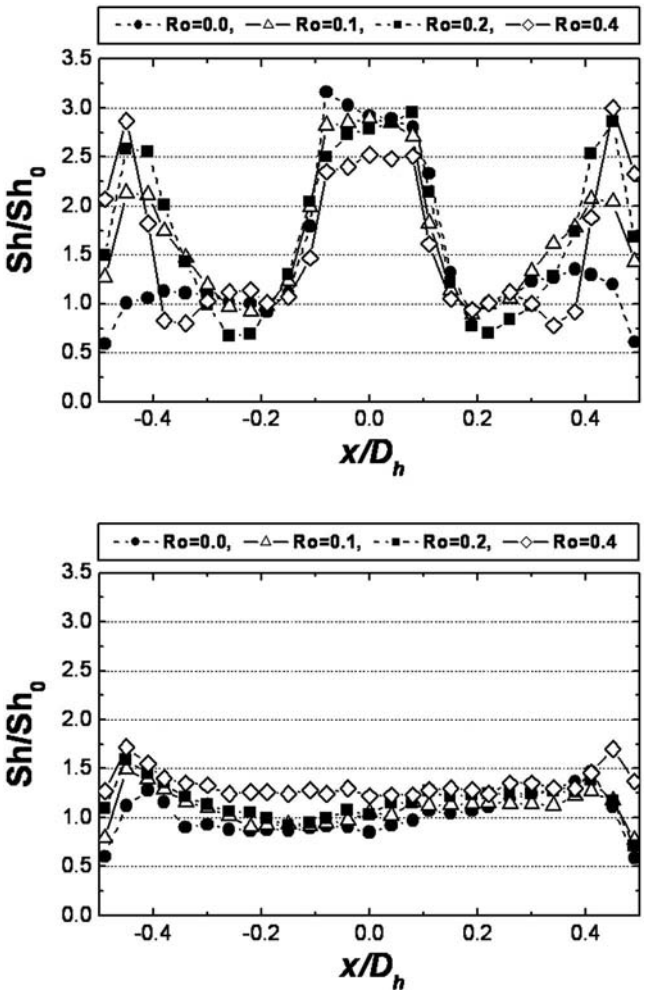

Fig. 7 Spanwise Sh ratio distributions at $x/D_h=12.14$ in bleeding case (BR=0.2): (*a*) Leading surface and (*b*) trailing surface

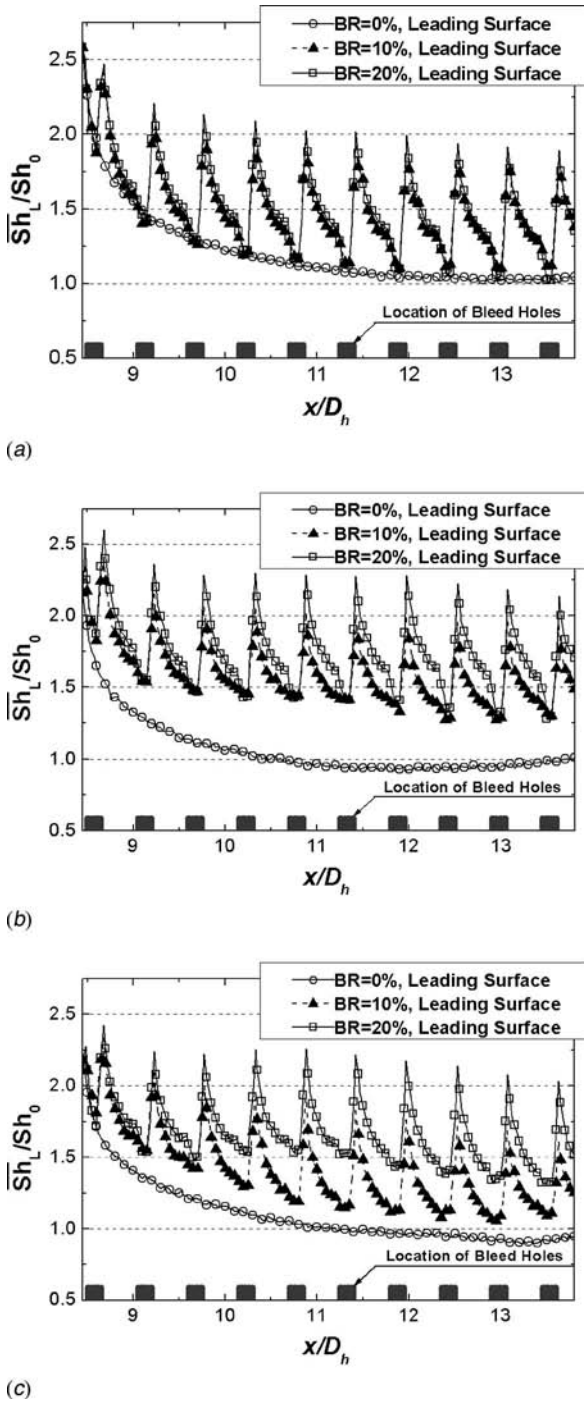

Fig. 8 Spanwise averaged Sh/Sh_0 on leading surface: (*a*) Ro =0.0, (*b*) Ro=0.2, and (*c*) Ro=0.4

flow on the leading surface. In all the cases, the values on the trailing surfaces tended to increase as the rotation number but decrease as the bleed ratio increased. As the aforementioned in the internal flow phenomena, the reason is that the rotation pushes the core flow to the trailing surface and that the increment of bleed flow yields the reduction of main flow rate. For each rotation number and bleed ratio, Fig. 9(*b*) shows the mean of the regional averaged values of both the leading and trailing surfaces in Fig. 9(*a*). The mean values increased with increasing rotation number as the secondary flow was generated by the Coriolis force; furthermore, an increase in the bleed ratio enhanced the heat/mass transfer due to the strong tripping flow.

Friction Loss and Thermal Performance. Figure 10 shows the results of the pressure drop experiments in the form of friction factor ratios. In the stationary smooth square channel without bleed flow, the friction factor ratio was ~1.2 greater than the fully developed values (f_0) for a stationary smooth circular tube. Friction losses were lower for cases with bleed flow than for the case without bleed flow for all tested rotation numbers. This resulted from the diminution of the internal flow rate due to bleed flow and the reduction in the area of bleed holes contacting the flow. Furthermore, at a high bleed ratio, the friction factor ratio was lower than that at the low bleed ratio because the main flow rate was decreased. As the rotation number increased, the friction losses increased in all cases because the turbulence intensity was strengthened to a greater extent by the rotation-induced secondary flow; however, the friction losses were nearly identical in cases with bleed flow under a rotation number of >0.2.

Figure 11 shows the thermal performance in the channel. The thermal performance with bleed flow was high for all rotation numbers due to the enhancement of the heat/mass transfer around the holes and the decrement of friction loss. Additionally, the thermal performance was enhanced as the bleed ratio was increased. As the rotation number increased, the values for all the cases were almost identical despite different heat/mass transfers and pressure drops for each case.

Although the heat transfer is enhanced by the bleed flow, a lot of coolant flow loss by the continuous bleeding elevates its

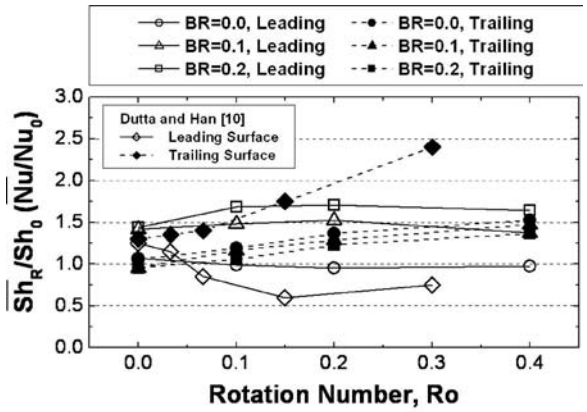

(*a*)

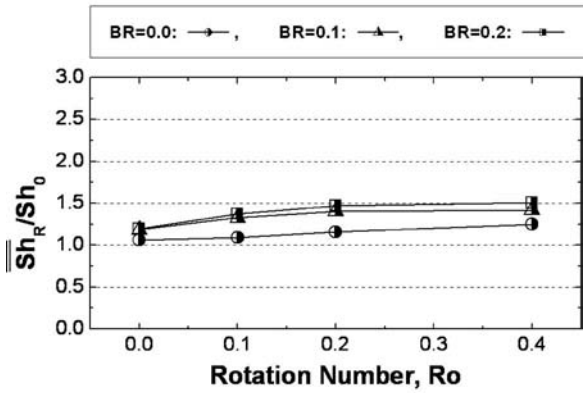

(*b*)

Fig. 9 Regional averaged heat/mass transfer coefficients ($10.5 \leq x/D_h \leq 13.25$): (*a*) Each surface and (*b*) mean values of both surfaces

streamwise temperature. Consequently, the material temperature of the actual turbine blade may be raised. Therefore, for the applications of this blade-cooling method, turbine designers should decide the bleed ratio that is suitable to maximum temperature of the coolant flow.

Conclusions

In the present study, heat/mass transfer and internal flow characteristics in a rotating smooth channel with bleed flow were experimentally and numerically investigated. The experimental characteristics were compared to those of a case without effusion. The results are summarized as follows:

1. For stationary cases, the tripping flow induced by the bleed flow was the major factor enhancing the heat/mass transfer around the holes. As increased flow was spouted through the holes, it induced a strong tripping, flow that in turn, augmented the heat/mass transfer.
2. For the rotating cases, the rotation-induced secondary flow and the tripping flow primarily influenced the heat/mass transfer in the inside wall regions of the passage. On the leading surface, the high heat/mass transfer around the holes appeared due to the tripping flow; furthermore, the impingement of the secondary flow caused the high heat/mass transfer in the outer wall regions. Although the heat/mass transfer was enhanced by the Coriolis force on the trailing surface, the decrement of the main flow rate caused the heat/mass transfer region to be lower than that of the case without bleed flow.
3. As the rotation number increased, the strong secondary flow was generated by the Coriolis force. In the cases without bleed flow, the heat/mass transfer on the leading surface decreased; however, in the cases with bleed flow, the heat/mass transfer on the leading surface increased before Ro=0.2 and then decreased after Ro=0.2. In all cases, the heat/mass transfer on the trailing surface and the mean values of both the leading and trailing surfaces increased due to increase in turbulence intensity.
4. The friction factors in the channel with bleed flow were lower than those without bleed flow at all the tested rotation numbers. With an increment of bleed ratio, the friction factor ratio was lower than that at the low bleed ratio due to reduction of the main flow. As the rotation number increased, the thermal performance of all cases became increasingly similar, despite different heat/mass transfers and pressure drops for each case.

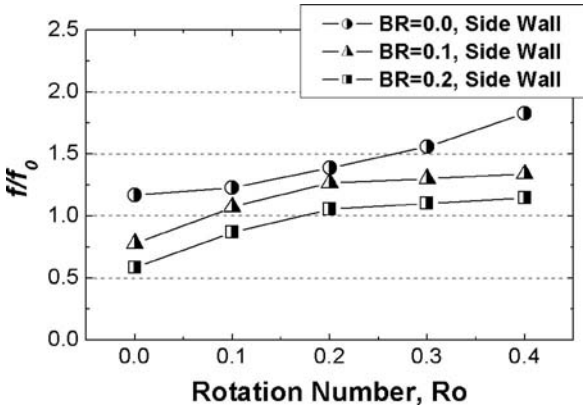

Fig. 10 Friction factor ratios at various rotation numbers

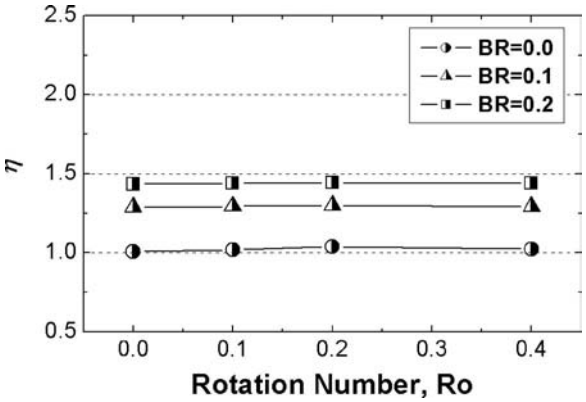

Fig. 11 Thermal performance for all tests

Acknowledgment

This work was supported partially by the Electric Power Industry Technology Evaluation and Planning.

Nomenclature

BR = ratio of bleed flow rate to main flow rate
d = bleed hole diameter
D_h = hydraulic diameter (m)
D_{naph} = mass diffusion coefficient of naphthalene vapor in air ($m^2\ s^{-1}$)
f = friction factor, Eq. (6)

f_0 = friction factor of a fully developed turbulent flow in a stationary smooth pipe
h = heat transfer coefficient ($W\,m^{-2}\,K^{-1}$)
h_m = mass transfer coefficient ($m\,s^{-1}$)
H = passage height (m)
k = turbulent kinetic energy ($m^2\,S^{-2}$)
k_c = thermal conductivity of coolant ($W\,m^{-1}\,K^{-1}$)
$\dot{m}$ = local naphthalene mass transfer rate per unit area ($kg\,m^{-2}\,s^{-1}$)
Nu = Nusselt number, hD_h/k_c
p = hole-to-hole pitch
P_{naph} = naphthalene vapor pressure ($N\,m^{-2}$)
Pr = Prandtl number, $\mu C_p/k_c$
$\dot{Q}_{\text{air}}$ = volume flow rate of air ($m^3\,s^{-1}$)
R = maximum radius of rotating arm (m)
R_{naph} = gas constant of naphthalene ($J\,mol^{-1}\,K^{-1}$)
Re = Reynolds number, $D_h u_b/\nu$
Ro = Rotation number, $D_h\Omega/u_b$
Sc = Schmidt number, ν/D_{naph}
Sh = Sherwood number, $h_m Dh/D_{\text{naph}}$
Sh_0 = Sh of a fully developed turbulent flow in a stationary smooth pipe, Eq. (5)
$\bar{\text{Sh}}_L$ = spanwise averaged Sherwood number, $\int_{-w/2}^{w/2}\text{Sh}\,dy/\int_{-w/2}^{w/2}dy$
$\bar{\text{Sh}}_R$ = regional averaged Sherwood number, $\int_{x_1}^{x_2}\int_{-w/2}^{w/2}\text{Sh}\,dydx/\int_{x_1}^{x_2}\int_{-w/2}^{w/2}dydx$
$\bar{\bar{\text{Sh}}}_R$ = mean $\bar{\text{Sh}}_R$ of both the leading and trailing surfaces
T_w = wall temperature (K)
u_b = passage inlet averaged bulk velocity ($m\,s^{-1}$)
W = width of passage (m)
x = coordinate and distance in the streamwise direction (m)
y = coordinate and distance in the lateral direction (m)
z = coordinate and distance in the vertical direction (m)
$\overline{z_{\text{sub}}}$ = average naphthalene sublimation depth (m)
β = coefficient of thermal expansion (K^{-1})
Δt = runtime (s)
Δz = sublimation depth of naphthalene surface (m)
μ = dynamic viscosity ($kg\,m^{-1}\,s^{-1}$)
ν = kinematic viscosity ($m^2\,s^{-1}$)
η = thermal performance, Eq. (7)
ρ_s = density of solid naphthalene ($kg\,m^{-3}$)
$\rho_{v,b}$ = bulk vapor density of naphthalene ($kg\,m^{-3}$)
$\rho_{v,w}$ = vapor density of naphthalene on the surface ($kg\,m^{-3}$)
Ω = angular velocity ($rad\,s^{-1}$)

References

[1] Han, J. C., Glicksman, L. R., and Rohsenow, W. M., 1978, "An Investigation of Heat Transfer and Friction for Rib-Roughened Surfaces," Int. J. Heat Mass Transfer, **21**, pp. 1143–1156.
[2] Taslim, M. E., Rahman, A., and Spring, S. D., 1991, "An Experimental Investigation of Heat Transfer Coefficients in a Spanwise Rotation Channel With Two Opposite Rib-Roughened Walls," ASME J. Turbomach., **113**, pp. 75–82.
[3] Lau, S. C., Kukreja, R. T., and McMillin, R. D., 1991, "Effects of V-Shaped Rib Array on Turbulent Heat Transfer and Friction of Fully Developed Flow in a Square Channel," Int. J. Heat Mass Transfer, **34**(7), pp. 1605–1616.
[4] Cho, H. H., Wu, S. J., and Kwon, H. J., 2000, "Local Heat/Mass Transfer Measurements in a Rectangular Duct With Discrete Ribs," ASME J. Turbomach., **122**, pp. 579–586.
[5] Astarita, T., Cardon, G., and Carlomagno, G. M., 1998, "Average Heat Transfer Measurements Near a Sharp 180 Degree Turn Channel for Different Aspect Ratios," *IMechE Conf. Trans.: In Optical Methods and Data Processing in Heat and Fluid Flow*, London, Inst. Mech. Eng., London, pp. 137–146.
[6] Metzger, D. E., and Vedula, R. P., 1987, "Heat Transfer in Triangular Channels With Angled Roughness Ribs on Two Walls," Exp. Heat Transfer, **1**(1), pp. 31–44.
[7] Hirota, M., Fujita, H., Cai, L., Nakayama, H., Yanagida, M., and Syafa'at, A., 2002, "Heat (Mass) Transfer in Rectangular Cross-sectional Two-Pass Channels With an Inclined Divider Wall," Int. J. Heat Mass Transfer, **45**, pp. 1093–1107.
[8] Yang, W.-J., Zhang, N., and Chiou, J., 1992, "Local Heat Transfer in a Rotating Serpentine Flow Passage," ASME J. Heat Transfer, **114**, pp. 354–361.
[9] Iacovides, H., Jackson, D. C., Kelemenis, G., Launder, B. E., and Yuan, Y. M., 1999, "Experiments on Local Heat Transfer in a Rotating Square-Ended U-Bend," Int. J. Heat Fluid Flow, **20**, pp. 302–310.
[10] Dutta, S., and Han, J., C., 1996, "Local Heat Transfer in Rotating Smooth and Ribbed Two-Pass Square Channels With Three Channel Orientations," ASME J. Heat Transfer, **118**, pp. 578–576.
[11] Murata, A., and Mochizuki, S., 1999, "Effect of Cross-sectional Aspect Ratio on Turbulent Heat Transfer in an Orthogonally Rotating Rectangular Smooth Duct," Int. J. Heat Mass Transfer, **42**, pp. 3803–3814.
[12] Hwang, J. J., and Lai, D., Y., 1998, "Three-Dimensional Mixed Convection in a Rotating Multiple-Pass Square Channel," Int. J. Heat Mass Transfer, **41**, pp. 979–991.
[13] Wagner, J. H., Johnson, B., V., and Hajek, T., J., 1991, "Heat Transfer in Rotating Passages With Smooth Walls and Radial Outward Flow," ASME J. Turbomach., **113**, pp. 42–51.
[14] Bons, J. P., and Kerrebrock, J. L., 1999, "Complementary Velocity and Heat Transfer Measurements in a Rotating Cooling Passage With Smooth Walls," ASME J. Turbomach., **121**, pp. 651–662.
[15] Taslim, M. E., Li, T., and Spring, S. D., 1995, "Experimental Study of the Effects of Bleed Holes on Heat Transfer and Pressure Drop in Trapezoidal Passages With Tapered Turbulators," ASME J. Turbomach., **117**, pp. 281–289.
[16] Shen, J. R., Wang, Z., Ireland, P. T., Jones, T. V., and Byerley, A. R., 1996, "Heat Transfer Enhancement Within a Turbine Blade Cooling Passage Using Ribs and Combinations of Ribs With Film Cooling Holes," ASME J. Turbomach., **118**, pp. 428–434.
[17] Thurman, D., and Poinastte, P., 2001, "Experimental Heat Transfer and Bulk Air Temperature Measurements for a Multipass Internal Cooling Model With Ribs and Bleed," ASME J. Turbomach., **123**, pp. 90–96.
[18] Ekkad, S. V., Huang, Y., and Han, J. C., 1998, "Detailed Heat Transfer Distributions in Two-Pass Square Channels With Rib Turbulators and Bleed Holes," Int. J. Heat Mass Transfer, **41**, pp. 3781–3791.
[19] Park, C. W., Yoon, C., and Lau, S. C., 1998, "Local Heat (Mass) Transfer in a Rotating Square Channel With Ejection Holes," J. Thermophys. Heat Transfer, **12**, pp. 589–595.
[20] Kim, K. M., Kim, Y. Y., Lee, D. H., Rhee, D. H., and Cho, H. H., 2006, "Local Heat/Mass Transfer Phenomena in Roating Passage, Part 1: Smooth Passage," J. Thermophys. Heat Transfer, **20**, pp. 188–198.
[21] Kim, K. M., Kim, Y. Y., Lee, D. H., Rhee, D. H., and Cho, H. H., 2006, "Local Heat/Mass Transfer Phenomena in Roating Passage, Part 2: Angled Ribbed Passage," J. Thermophys. Heat Transfer, **20**, pp. 199–210.
[22] Jeon, Y. H., Park, S. H., Kim, K. M., Lee, D. H., and Cho, H. H., 2007, Effects of Bleed Flow on Heat/Mass Transfer in a Rotating Rib-Roughened Channel," ASME J. Turbomach., **129**, pp. 636–642.
[23] Goldstein, R. J., and Cho, H. H., 1995, "A Review of Mass Transfer Measurements Using Naphthalene Sublimation," Exp. Therm. Fluid Sci., **10**, pp. 416–434.
[24] Ambrose, D., Lawrenson, I. J., and Sparke, C. H. S., 1975, "The Vapor Pressure of Naphthalene," J. Chem. Thermodyn., **7**, pp. 1173–1176.
[25] Kline, S. J., and McClintock, F. A., 1953, "Describing Uncertainty in Single-Sample Experiments," Mech. Eng. (Am. Soc. Mech. Eng.), **75**, pp. 3–8.
[26] McAdams, W. H., 1942, *Heat Transmission*, 2nd ed., McGraw-Hill, New York.
[27] Petukhov, B. S., 1970, *Advances in Heat Transfer*, Academic Press, New York, Vol. 6, pp. 503–564.

High Knudsen Number Physical Vapor Deposition: Predicting Deposition Rates and Uniformity

Chetan P. Malhotra[1]
Fellow
Tata Research Development and Design Centre, India,
54/B, Hadapsar Industrial Estate,
Pune, 411013, India
e-mail: chetan.malhotra@tcs.com

Roop L. Mahajan[2]
Department of Mechanical Engineering,
University of Colorado at Boulder,
Campus Box # 427,
Boulder, CO 80309-0427
e-mail: mahajan@spot.colorado.edu

W. S. Sampath
B120 Engineering Research Center,
Colorado State University,
Fort Collins, CO 80521
e-mail: sampath@engr.colostate.edu

*The problem of predicting deposition rates and film thickness variation is relevant to many high-vacuum physical vapor deposition (PVD) processes. Analytical methods for modeling the molecular flow fail when the geometry is more complicated than simple tubular or planar sources. Monte Carlo methods, which have traditionally been used for modeling PVD processes in more complicated geometries, being probabilistic in nature, entail long computation times, and thus render geometry optimization for deposition uniformity a difficult task. Free molecular flow is governed by the same line-of-sight considerations as thermal radiation. Though the existence of an analogy between the two was recognized by Knudsen (1909, Ann. Phys., **4**(28), pp. 75–130) during his early experiments, it has not been exploited toward mainstream analysis of deposition processes. With the availability of commercial finite element software having advanced geometry modelers and built-in cavity radiation solvers, the analysis of diffuse thermal radiation problems has become considerably simplified. Hence, it is proposed to use the geometry modeling and radiation analysis capabilities of commercial finite element software toward analyzing and optimizing high-vacuum deposition processes by applying the radiation-molecular flow analogy. In this paper, we lay down this analogy and use the commercial finite element software ABAQUS for predicting radiation flux profiles from planar as well as tube sources. These profiles are compared to corresponding deposition profiles presented in thin-film literature. In order to test the ability of the analogy in predicting absolute values of molecular flow rates, ABAQUS was also employed for calculating the radiative flux through a long tube. The predictions are compared to Knudsen's analytical formula for free molecular flow through long tubes. Finally, in order to see the efficacy of using the analogy in modeling the film thickness variation in a complex source-substrate configuration, an experiment was conducted where chromium films were deposited on an asymmetric arrangement of glass slides in a high-vacuum PVD chamber. The thickness of the deposited films was measured and the source-substrate configuration was simulated in ABAQUS. The variation of radiation fluxes from the simulation was compared to variation of the measured film thicknesses across the slides. The close agreement between the predictions and experimental data establishes the feasibility of using commercial finite element software for analyzing high vacuum deposition processes.* [DOI: 10.1115/1.2712855]

Keywords: physical vapor deposition, free molecular flow, radiation-molecular flow analogy, finite element analysis

1 Introduction

Prediction of low-pressure transport finds many applications such as determining the conductance of high-vacuum systems and calculating molecular fluxes as well as film thicknesses in a variety of low-pressure physical vapor deposition processes, including thermal evaporation, electron beam vapor deposition, and molecular beam epitaxy. Our interest in this problem stems from our work on the development of a comprehensive thermal and deposition model of the close-spaced sublimation process for fabricating inexpensive solar cells by depositing thin films of cadmium sulfide and cadmium telluride on glass panels. If the operating pressure/rate of evaporation is sufficiently low, the mean free path of the molecules is much larger than the characteristic dimension of the flow geometry and the transport is governed by line-of-sight considerations, depending mainly on the geometrical configuration of the system. Initially such processes were studied by analytical techniques and the classic papers by Knudsen [1], von Smoluchowski [2], and Clausing [3] laid the groundwork for the calculations. These analyses are predicated on the assumption of cosine reemission of molecules after collision with bounding surfaces. This assumption was initially validated by the experiments of Wood [4,5] and Knudsen [6] and has proved to be valid for most practical molecular flows. Using this assumption, many authors have developed analytical and numerical models for different source substrate configurations in various physical vapor deposition systems and verified their models experimentally. For example, Shiralagi et al. [7] calculated and experimentally verified the dependence of flux uniformity on cell orientation in molecular beam epitaxy, Curless [8] calculated and verified flux contours on planar surfaces from conical and cylindrical molecular beam epitaxy sources, Swann et al. [9] measured fluxes from magnetron sputtering sources onto off-center rotating substrates and proposed a geometrical model to verify their experimental data, and Fatima Vales Silva and Nicholls [10] proposed an empirical model using

[1]Corresponding author. Also International Centre for Science and High Technology, Trieste, Italy; University of Colorado at Boulder.

[2]Current address: Chair Professor and Director, ICTAS, Virginia Tech, Blacksburg, VA 24061.

Contributed by the Heat Transfer Division of ASME for publication in the JOURNAL OF HEAT TRANSFER. Manuscript received April 11, 2006; final manuscript received July 21, 2006. Review conducted by Ranga Pitchumani. Paper presented at the 2005 ASME International Mechanical Engineering Congress (IMECE2005), November 5–11, 2005, Orlando, FL.

powers of cosines, which successfully fit their thickness data for films deposited from two planar magnetron sputtering sources. Similar line-of-sight considerations were also applied by Cale and Raupp [11,12] and O'Sullivan et al. [13] to predict step coverage during epitaxial deposition into cylindrical vias and rectangular trenches. However, all the above studies focus on geometries which are simple enough to be amenable to analytical methods.

A popular approach for determining conductances of complex components of a vacuum system, angular distribution of molecular flux from sources or the uniformity of deposition of thin films is by using test particle Monte Carlo methods. Initially proposed by Davis [14] for finding the conductance of pipes and bends, this method has been successfully employed to many relevant vapor deposition problems and has been subject to extensive experimental verification. For example, Adamson et al. [15–17] used the test particle Monte Carlo method to verify their experimentally measured spatial distributions from gas dosers and molecular beam epitaxy sources. Lin and Cale [18] used it to calculate flux distributions from hexagonal collimator cells and Wickersham [19] used it to calculate coating uniformity from magnetron sputtering sources. However, Monte Carlo methods, being probabilistic, involve the tracking of several million particle trajectories before they converge to the desired accuracy [20]. This translates to higher computational times, especially when the geometry is complex and has to be continuously modified as in an optimization study.

An important requirement in thin-film deposition is the control of film thickness uniformity across the substrate [9,10,21], and many studies have been devoted toward meeting this goal. Wasilewski et al. [22] optimized the angle between the axis of a molecular beam epitaxy cell and the rotating substrate to achieve a film thickness variation of 0.3%, Zehe and Ramirez [23] optimized the location of molecular beam epitaxy sources and substrate to maximize the uniformity of the deposited film, and Bosch [24] presented a method to optimize the geometry of a static correction shutter to maximize the uniformity of anti-reflecting coatings on multiple lens substrates. The natural law of emission from a surface being a cosine distribution, angular dependence of flux is built into the physics of free molecular flow. Film thicknesses are inherently nonuniform unless the substrates are located on a spherical surface with the source being a plane area located on the periphery of the sphere [6]. However, most practical deposition systems are not spherical and in order to achieve uniformity, different source-substrate configurations have to be tried or one has to rely on prior experience in designing the system for desired film uniformity.

If only analytical means are employed, geometry optimization is possible only when the source is simple, as in a single capillary or a planar area focusing on an opposing flat substrate. The problem becomes intractable when the source geometry is complicated, such as the multichannel collimators used in molecular beam epitaxy sources or the multiple planar or tubular sources used in large area deposition on planar substrates. In such situations, if analytical methods are to be employed, one has to resort to oversimplification of the geometry or if numerical methods are sought, dedicated codes employing either numerical integration or Monte Carlo techniques have to be written and have to be customized every time a different geometry has to be tried. Hence, it is of value to have a means of analyzing low-pressure deposition in complex geometries, which is generic and computationally efficient so that many different configurations can be modeled and analyzed in a short time, and thus, the configuration can be optimized for maximizing the deposition uniformity.

Current commercially available finite element software codes have advanced preprocessors and parametric geometry modelers wherein complicated geometries can be easily created and parametrically modified in an optimization study. At the same time, many of these software programs incorporate cavity radiation exchange modules, which support automatic surface definition, meshing, and view factor calculation. Like free molecular flow, diffuse surface to surface radiation is a line-of-sight transport process with every trajectory being interrupted only by a wall that reemits the absorbed radiation in a diffuse manner. This analogy, though recognized by Knudsen himself during his experiments on free-molecular flow [1], has not been employed for the mainstream analysis and optimization of vapor deposition processes. If one could employ a transformation for expressing the molecular flow problem as a diffuse radiation problem, then one could make use of the modeling and radiation analysis capabilities of commercial software for analyzing complex high vacuum physical vapor deposition processes, and these systems could be readily optimized. In this paper, we present this transformation and use the radiation-molecular flow analogy to simulate deposition, initially in simple geometries, to benchmark the method with experimental data available in thin-film literature. We then show the ease of applicability of the method to real-life problems by using it to predict the film thickness variation in an actual vapor deposition experiment with a complex source-substrate configuration.

2 The Analogy

Most radiation processes can be analyzed under the diffuse-gray surface approximation [25], which assumes that the direction of emission from a surface is independent of the direction of incident radiation on the surface and that the nonideality of emission from a surface can be captured in a single parameter, namely, its emissivity, which is also assumed to be independent of the nature of incident radiation. Under such an assumption, the radiation exchange problem becomes independent of wavelength and the temperature becomes the only quantity necessary for calculating the heat flux at every surface and vice versa. The diffuse-gray surface assumption makes the problem of radiation exchange tractable for commercial software since the major expense is only in the calculation of geometrical view factors between planar facets of discretized surfaces. More importantly, diffuse surfaces obey Lambert's cosine law, which is analogous to Knudsen's assumption of cosine emission from walls in molecular flow.

The driving potential in molecular flow is the vapor pressure p_v at the surface of the evaporating material, which varies with the temperature T_s of the surface. The molecular flux Z can be related to the vapor pressure and temperature at the surface by the well-known Hertz-Knudsen equation [26],

$$Z = \frac{p_v(T_s) - p}{\sqrt{2\pi m k T_s}} \tag{1}$$

Here, p is the static pressure of the gas above the surface, m the molecular mass of the material being evaporated, and k is the Boltzmann constant. The number of molecules leaving a small surface dA_1 and intercepted by another small surface dA_2 per unit time is given by [26],

$$N_{dA_1-dA_2} = Z_{dA_1} \frac{\cos\theta_1 \cos\theta_2}{\pi r^2} dA_1 dA_2 \tag{2}$$

where θ_1 and θ_2 are the angles the line joining the centers of dA_1 and dA_2 makes with the normals to dA_1 and dA_2, respectively, and r is the distance between the centers of dA_1 and dA_2.

Similarly, the equation for net diffuse thermal radiation heat transfer from a surface A_1 to a surface A_2 is given by [25]

$$q_{1-2} = J_1 \int_{A_1} \int_{A_2} \frac{\cos\theta_1 \cos\theta_2}{\pi r^2} dA_1 dA_2 \tag{3}$$

Here, J_1 is the total radiation flux leaving surface A_1, i.e., its radiosity. The walls in free molecular flow are equivalent to reradiating surfaces in thermal radiation problems, which are characterized by zero net flux penetrating the surface. Hence, in Eq. (3), J_1 can be replaced by σT_1^4 [25] giving,

$$q_{1-2} = \sigma T_1^4 \int_{A_1} \int_{A_2} \frac{\cos\theta_1 \cos\theta_2}{\pi r^2} dA_1 dA_2 \tag{4}$$

By comparing Eqs. (2) and (4), and using Eq. (1), the analogy between thermal radiation and free molecular flow can be identified as

$$\text{Radiation heat flow } q_{1-2} \sim \text{Molecular flow } N_{1-2}$$

when the absolute temperature T in the radiation problem is specified as

$$T = \left(\frac{p_v(T_s) - p}{\sigma\sqrt{2\pi m k T_s}} \right)^{1/4} \tag{5}$$

If thermal radiation flux originating from the same area A_1 is incident on two areas A_2 and A_3, from Eq. (4), it can be seen that the ratio of the fluxes q_{1-2} and q_{1-3} is only governed by the mutual geometrical configurations of areas A_1, A_2, and A_3. These relations do not change when one considers either the radiation or the molecular flow problem. Hence, we can conclude that

$$\frac{q_{1-2}}{q_{1-3}} = \frac{N_{1-2}}{N_{1-3}} \tag{6}$$

Thus, the relative variation of molecular flux across a substrate due to a single source will be the same as that for thermal radiation flux, irrespective of the vapor pressure or temperature at the source or the target as long as these quantities have different magnitudes at the source and target and are uniform across them. This makes the analysis particularly simple when absolute values of deposition rates and molecular fluxes are not sought and only their variation along a target surface is required, such as in problems that involve maximizing the uniformity of deposition. In this case, no material properties are necessary and the problem becomes a purely geometrical one. Thus, accurate estimates of the relative variation of molecular fluxes incident on a substrate can be obtained even by assigning arbitrary temperatures to the source and the substrate in the radiation problem.

3 Numerical Simulations

The commercial radiation software ABAQUS was identified for carrying out the radiation simulations since it has a built-in solver for cavity radiation problems. It internally calculates view factors and has a preprocessor capable of creating the most complex geometries encountered while simulating real-world problems in physical vapor deposition. The preprocessor also permits the definition and discretization of exposed surfaces, which can then be directly identified as participating surfaces in the radiation problem.

The first simulation attempted was the verification of Knudsen's formula for the magnitude of free molecular flux through a long tube to establish the ability of ABAQUS to predict the absolute values of molecular flow rates in vacuum equipment and deposition geometries. The second category of simulations involved the verification of the distribution of fluxes from deposition sources rather than their absolute values. For this, flux distributions from two source geometries relevant to common PVD methods were identified. The first distribution identified for verification was the combined flux distribution from two coplanar areas onto a flat substrate. This configuration is relevant to large area deposition processes, where a planar substrate is placed directly above an array of coplanar sources and the film is deposited on its underside. The second distribution identified was the angular variation of flux from short tubes which was initially studied by Clausing [3] and has since been successfully verified experimentally by many authors [27,28]. This geometry is relevant to many deposition processes, the most studied being molecular beam epitaxy where short tubes are bundled together to form a beam collimator, which focuses the molecular flux from an effusion cell onto a small area. We note that the configurations modeled here are fairly

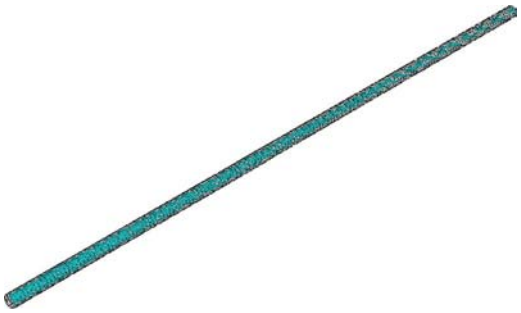

Fig. 1 Geometry for verifying Knudsen's formula for free molecular flow through a long tube

simple, but a combination of these can be used to construct more complex flow and deposition geometries.

3.1 Free Molecular Flow Through a Long Tube. The formula for free molecular flow through a long tube was first proposed by Knudsen [1] and later corrected by von Smoluchowski [2]. For a tube of radius r and length L, the free molecular flux per unit time is given by

$$N = \frac{8\pi}{3} \frac{r^3}{L} \frac{p_1 - p_2}{\sqrt{2\pi m k T}} \tag{7}$$

Knudsen experimentally verified this formula for different gases and tube diameters [29].

In order to see whether, using the analogy, we can confirm, the above formula, it was decided to simulate the flow of cesium

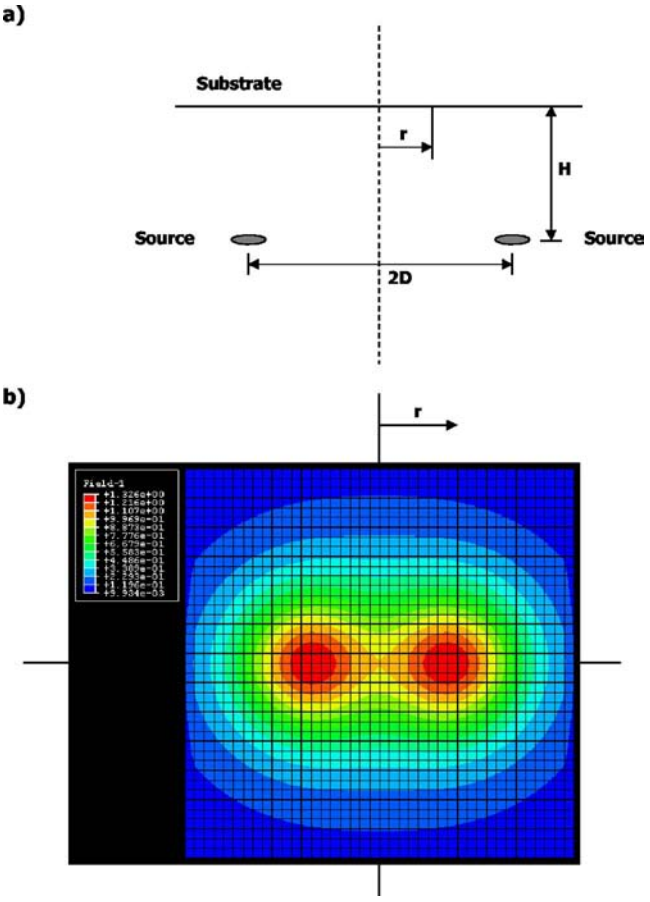

Fig. 2 (*a*) Schematic of configuration for deposition from two planar sources and (*b*) Radiation flux distribution for *D*/*H* =0.75

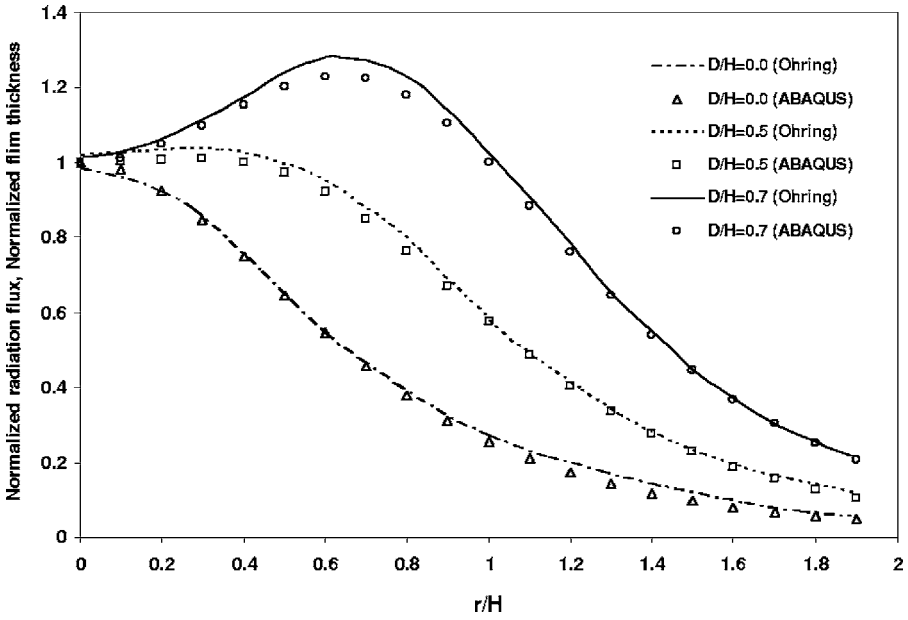

Fig. 3 Flux distribution from two coplanar sources. Continuous lines represent expected normalized film thickness variation along centerline of sources given in [30] while open markers represent results of radiation simulations in ABAQUS.

atoms through a long capillary. Cesium was chosen since its temperature-dependent vapor pressure and mean free path data are readily available in Ref. [28]. The geometry being simulated is shown in Fig. 1. One end of the tube was assumed to be a cesium source maintained at 363 K. At this temperature, the mean free path of cesium atoms is ~0.1 m. Hence, in order to simulate free molecular conditions, i.e., no collisions within the tube, the length of the tube shown in Fig. 1 was also chosen to be 0.1 m. In order to make the tube sufficiently "long," the diameter of the tube was chosen to be $1/50^{th}$ of its length at 0.002 m. The vapor pressure of cesium atoms at 363 K is 2.7×10^{-4} Torr or 3.6×10^{-2} Pa. The other end of the tube was assumed to open in a vacuum chamber evacuated to 10^{-6} Torr or 1.333×10^{-4} Pa, as was the case in the experiments of [28]. The mass of a single cesium atom is 132.905 amu or 2.207×10^{-25} kg. Using Eq. (7), the molecular flow rate through the tube was calculated to be 3.604×10^{13} mol/s.

Using Eq. (5), the temperatures in the radiation problem corresponding to the pressures in the molecular flow problem were calculated to be 9.33×10^{6} K and 0 K at the cesium source and evacuated end, respectively. However, when such large temperatures were simulated in ABAQUS, numerical instabilities were encountered, and hence, it was decided to scale down the temperatures to more real-world values. This was accomplished by scaling down the pressures by a factor of 10^{16}, which scaled down the radiation temperatures by a factor of 10^{4}. Correspondingly, the final molecular flux would have to be scaled back by multiplying the radiation flux by 10^{16}. Thus, the geometry in Fig. 1 was simulated by maintaining its two ends at 933.32 K and 0 K, respectively. The radiation flux incident on the cold end was found to be 3.39×10^{-3} W, which corresponds to a molecular flux of 3.39×10^{13} mol/s. The above simulation was also carried out using a coarser grid (by doubling the element size), which resulted in a radiative flux of 3.354×10^{-3} W, which is only 1% lower than that calculated using the finer mesh. Hence, the results were taken to be mesh independent.

The difference between the prediction of the finite-element simulation and the value calculated using Eq. (7) is 5.95% and can be attributed to the finite tube length and finite mesh size used in ABAQUS as opposed to the analytical integrals employed in calculating the factor $8r/3L$ in Eq. (7). Application of Clausing's [3]

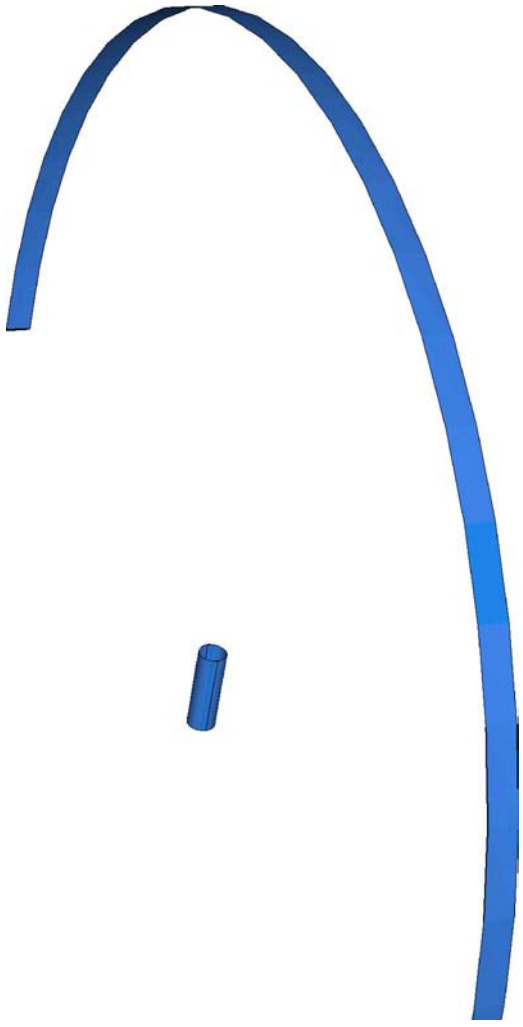

Fig. 4 Geometry for simulation of angular distribution of radiation flux from short tubes

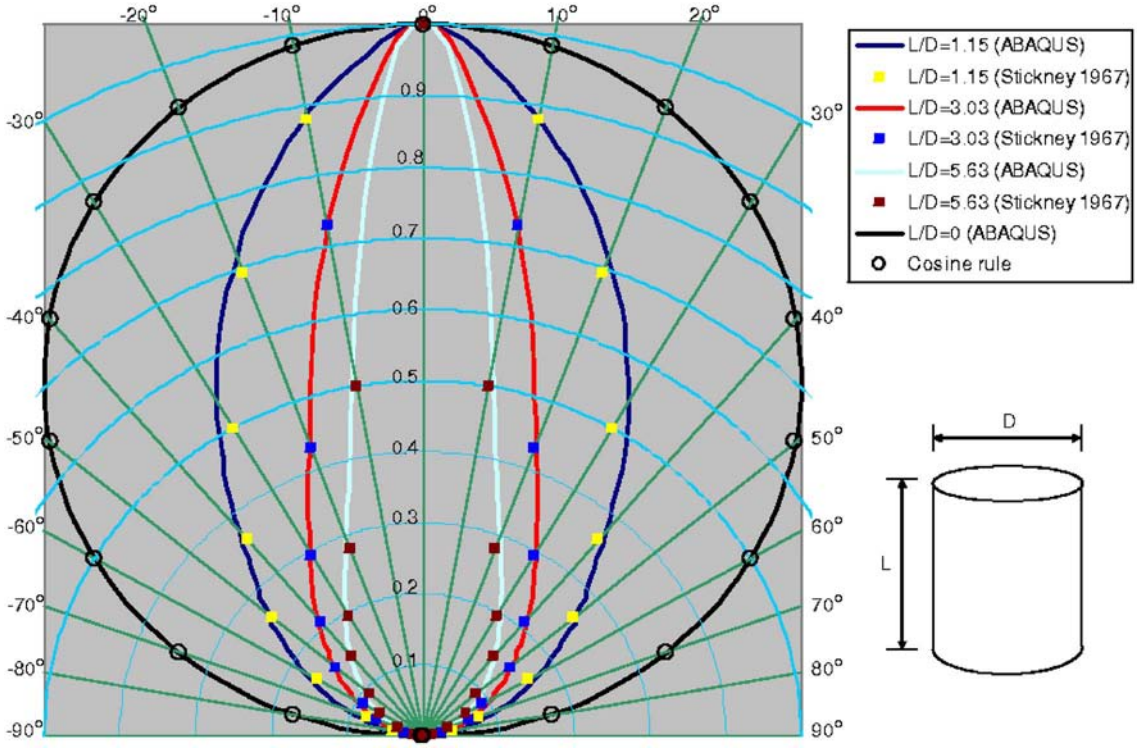

Fig. 5 Comparison of normalized angular distributions of radiation flux from short tubes with aspect ratios 1.15, 3.03, and 5.63 from ABAQUS (continuous lines) with experimental measurements of Stickney et al. [28] (solid dots). The open dots represent the cosine law which correspond to $L=0$.

correction factor to the analytical result caused negligible change in the analytical value. The error between Knudsen's formula and the ABAQUS simulation is within acceptable limits thus establishing the feasibility of ABAQUS in estimating the absolute value of molecular fluxes in low-pressure vacuum equipment.

3.2 Flux Distribution From Two Coplanar Sources. In order to simulate the flux distribution due to multiple sources on a planar substrate, the simplest case analyzed was the flux distribution on a planar target due to effusion from two small coplanar areas as a function of their mutual separation and their separation from the common target. The results are compared to values presented in [30]. Figure 2(*a*) shows the schematic of the geometry being considered. Since, only normalized distributions were sought, based on Eq. (6), arbitrary equal temperatures were assigned to the two sources and a lower arbitrary temperature was assigned to the substrate. A typical distribution ($D/H=0.75$) of the combined radiation flux from the two sources is shown in Fig. 2(*b*).

Figure 3 shows the expected variation of the film thickness, normalized with respect to that at the midpoint of the two sources, along the centerline of the sources, for different separations between the sources, as reported in [30]. Also plotted as open markers in Fig. 3, are the normalized radiation flux values from simulations in ABAQUS.

As can be seen from Fig. 3, the agreement between the literature values and those obtained from ABAQUS is very good thus establishing the utility of the cavity radiation module in ABAQUS for modeling molecular flux distributions from planar sources.

3.3 Angular Flux Distributions From Short Tubes. The final verification with literature was done for angular flux distributions from short tubes, which is relevant to molecular beam epitaxy sources. Since the original analysis by Clausing [3], this geometry has been the subject of numerous studies employing analytical [27,31,32], experimental [28,33–38] as well as Monte Carlo [15–17] methods. The geometry that was simulated in ABAQUS is shown in Fig. 4.

As seen in Fig. 4, a semi-circular arc is placed concentric with the center of the opening of the tube. The base of the tube is maintained at an arbitrary high temperature while the arc is prescribed an arbitrary lower temperature. The shell of the tube is specified to be a reradiating surface, and its temperature is estimated during the calculation. From the simulation, the radiation fluxes at locations along the arc were noted and normalized with respect to the flux at the point directly above the axis of the tube. These normalized distributions for different aspect ratios of the tube are plotted in Fig. 5. Also plotted as solid dots are measured angular distributions from the experiments of Stickney et al. [28]. The open dots represent an ideal cosine distribution, which corresponds to the limit of the tube length going to zero and the source becoming a small plane area.

The experimental distributions and the simulated distributions from ABAQUS are in excellent agreement thus reinforcing the feasibility of using ABAQUS for estimating angular distributions of molecular fluxes from planar and tubular sources. Note that although we verify the distribution from a single tube, ABAQUS could easily simulate an array of tubes, such as those used in molecular beam epitaxy sources.

4 Experiment

In order to test the applicability of the analogy in an actual physical vapor deposition setup, we conducted an experiment in an Edwards Auto 306 thermal resistance evaporation system with a FL400 deposition chamber. Figure 6 shows a schematic of the experimental setup. The material being deposited was chromium, which was in the form of a cylindrical wire with an active length

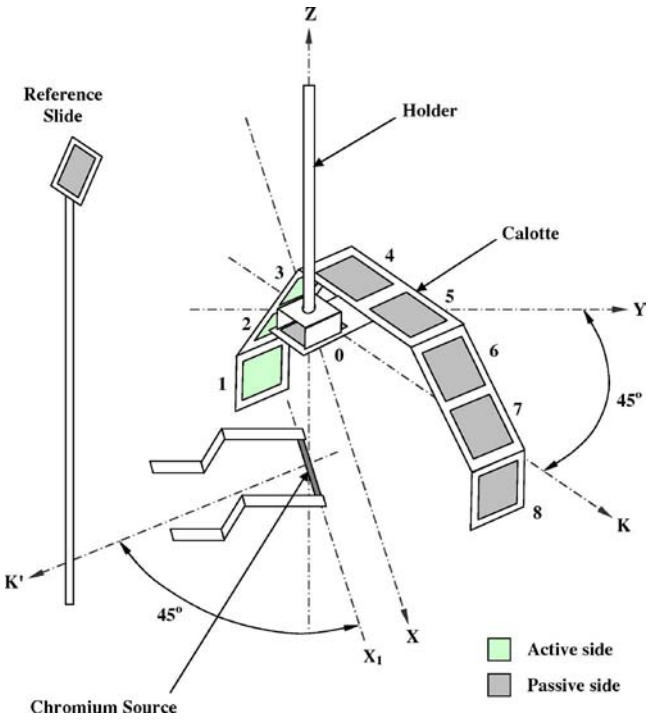

Fig. 6 Schematic of experimental setup

of 26.5 mm and diameter of 2.2 mm. The substrates were in the form of 1 mm thick 25.4 mm × 25.4 mm (1 in. × 1 in.) glass slides and were mounted in a calotte as shown in Fig. 6. The calotte was designed on purpose to give a high degree of variation in film thickness across the slides—the ratio of minimum-to-maximum film thickness was expected to be around 0.33. This was accomplished by placing the slides at different angles with respect to the source and except for the slide directly above the source, the rest of the slides were offset with respect to the axis of the source. In order to add asymmetry to the calotte as well as a further degree of complexity to the deposition geometry, the calotte was rotated by 45 deg with respect to the axis of the source after being placed in the deposition chamber as shown in Fig. 6.

Table 1 Measured and normalized film thicknesses from experiment and normalized radiation fluxes from ABAQUS. Normalization is with respect to the value at the center of slide 0.

Slide	Measured thickness (Å)	Normalized thickness	Normalized radiation flux	Percent difference (%)
Reference	32.26	0.09	0.12	3.24
0	351[a]	1.00	1.00	···
1	113.88	0.32	0.34	1.95
2	199.17	0.57	0.53	3.73
3	220.85	0.63	0.60	2.45
4	257.03	0.73	0.67	6.04
5	253.07	0.72	0.70	2.02
6	222.24	0.63	0.67	3.33
7	226.25	0.64	0.68	3.06
8	182.69	0.52	0.56	3.78

[a]Measured using Veeco Dektak 8 Profilometer instead of ellipsometer.

The slides were sandblasted on the passive side, chemically and ultrasonically cleaned, and mounted in the calotte. They were labeled with numbers 0–8, 0 being the slide directly above the source (see Fig. 6). A single slide was also mounted in a microbalance in order to monitor the film thickness during the deposition process and was denoted as the reference slide. The reference slide was used to make sure that the maximum thickness of the deposited films was lower than 300 Å in order that they would be transparent to the ellipsometer laser used to measure the thickness. The calotte was placed in the vacuum chamber and the chamber was evacuated to 1.33×10^{-4} Pa (10^{-6} Torr). At this pressure, the mean free path of the chromium molecules was expected to be ~100 m, which places the transport well into in the free-molecular flow regime. Once the vacuum was attained, current was passed through the chromium wire until it was white hot. The current was switched off when the reference slide registered a film thickness of only 30 Å. The reference slide was farthest away from the source and was thus expected to be subject to the least

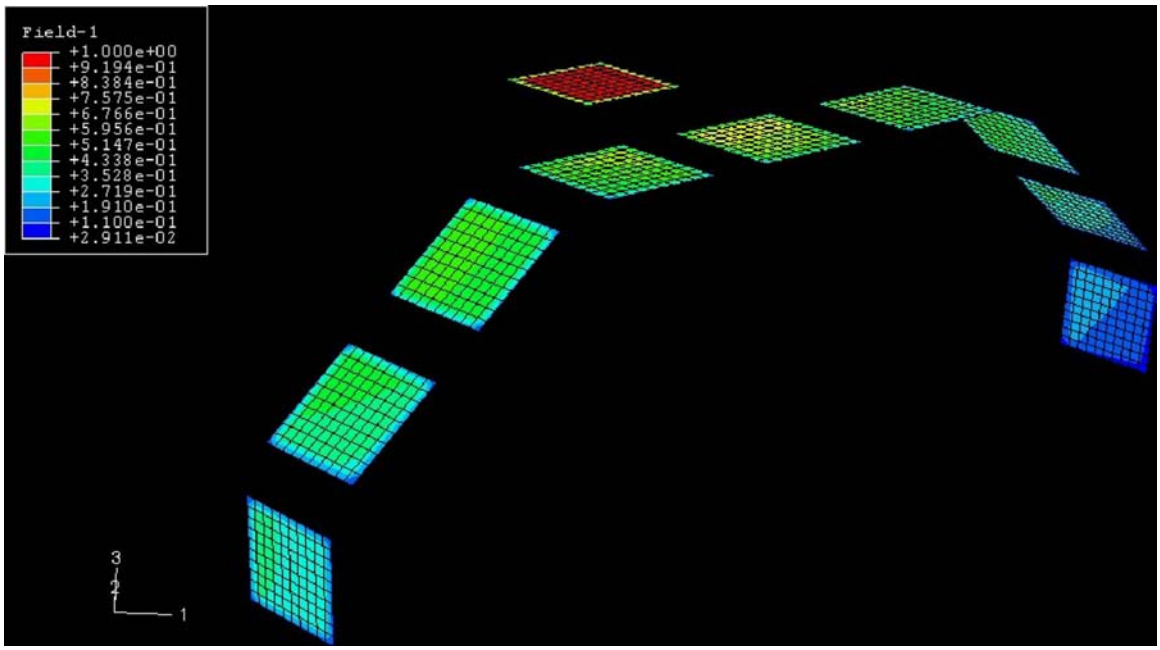

Fig. 7 Contours of normalized radiation fluxes corresponding to the experimental setup of Fig. 6 simulated using ABAQUS

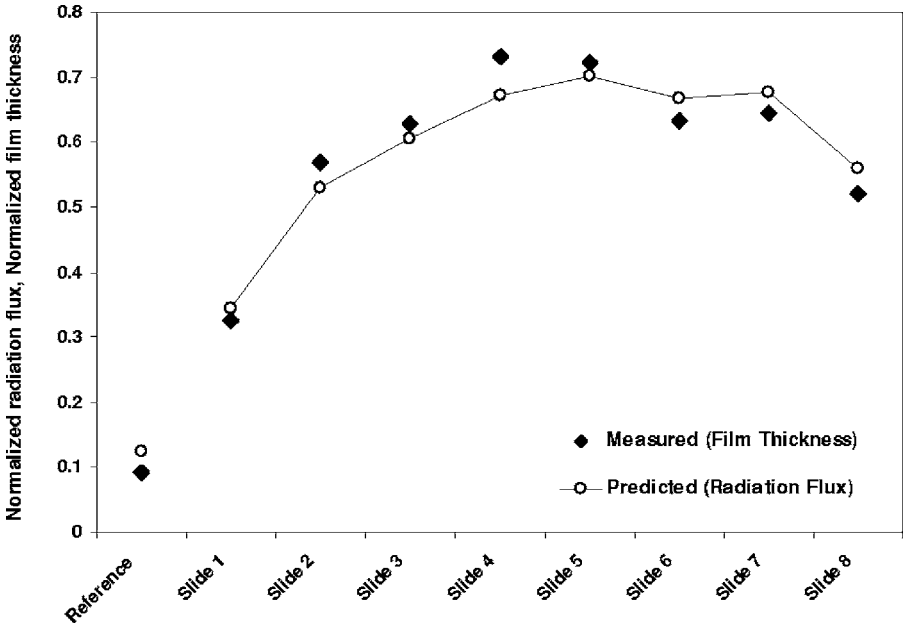

Fig. 8 Comparison of measured normalized film thickness at the center of each slide with corresponding normalized radiation fluxes from ABAQUS

incident flux. Hence, the experiment was stopped when the reference slide registered ~10% of the maximum permissible thickness.

The thickness of the films deposited on the glass slides was measured using a V-VASE spectroscopic ellipsometer. The beam of the ellipsometer was focused so as to obtain the thickness at approximately the center of each slide. Even though, the current was switched off only a few seconds after switching it on, the thickness of the film deposited on slide 0, the slide closest to the source, was slightly above the transparency limit of the ellipsometer, and hence, the ellipsometer could not be used to measure it. Instead a high-accuracy profilometer (Veeco Dektak 8 Advanced Development Profiler) was used to measure it. The measured thicknesses from the ellipsometer and profilometer are tabulated in Table 1. Since the variation in thickness rather than the absolute thickness was sought, the thicknesses measured at the center of each slide were normalized with the thickness measured at the center of slide 0. These normalized values are also presented in Table 1.

The above experiment was also simulated using the radiation solver in ABAQUS by assigning an arbitrary high temperature to the chromium source and arbitrary equal low temperatures to the slides. The radiation flux contours normalized with respect to the flux at the center of slide 0 as predicted by ABAQUS are shown in Fig. 7, and the values at the central node of each slide are also tabulated in Table 1. These values are also plotted in Fig. 8 along with the normalized measured values.

As seen from Fig. 8, the agreement between the normalized measured and predicted values is good and Table 1 indicates that the maximum difference is only 6.04%. This establishes the validity of using generic finite element software for the prediction of film thickness variation in a commercial low-pressure PVD setup. The above methodology could also be used to predict the absolute film thicknesses, but since the time for which the deposition process was carried out was uncertain, quantification of actual film thicknesses was not attempted.

5 Conclusions

Although the existence of an analogy between diffuse thermal radiation and low-pressure molecular transport is known, it has not been exploited in mainstream design of evaporation sources and vacuum equipment. With the ready availability of commercial finite element software with powerful geometry modelers and cavity radiation solvers, the analysis of diffuse radiation problems has become a straightforward process. In this paper we have made use of the analogy between radiation and free molecular flow and employed the commercial finite element software ABAQUS to corroborate experimental angular distributions of molecular flux from planar and tubular sources reported in literature. We have also confirmed the absolute value of molecular flux through a long tube, first derived and experimentally confirmed by Knudsen [1]. Finally we have conducted a PVD experiment in a laboratory scale setup, modeled it in ABAQUS, and verified the predicted relative film thicknesses with measured values from the experiment. The numerically calculated relative film thickness values, closely match the experimentally measured values, demonstrating again the feasibility of using commercial radiation software for modeling flux distributions in an actual PVD setup.

The methodology outlined in this paper is targeted at modeling low-pressure PVD processes in relatively complex geometries that cannot be analyzed by analytical means and for which Monte Carlo simulations would take long times to converge to the desired accuracy. Such geometries can easily be modeled using the above technique. The run times required for carrying out the simulations is small since the calculation is deterministic. The main application of the technique is envisaged in rapid optimization of source-substrate geometries for maximizing the uniformity of deposited films.

Acknowledgment

The authors gratefully acknowledge the partial funding extended by the International Center for Science and High Technology (ICS), Trieste, Italy.

References

[1] Knudsen, M., 1909, "Die Gesetze der Molekularströmung und der Inneren Reibungsströmung der Gase Durch Röhren," Ann. Phys., **4**(28), pp. 75–130.
[2] von Smoluchowski, M., 1910, "Zur Kinetischen Theorie der Transpiration und Diffusion Verdunnter Gase," Ann. Phys., **33**, pp. 1559–1570.
[3] Clausing, P., 1932, "Uber die Strömung Sehr Verdunnter Gase Durch Röhren von Beliebiger Lange," Ann. Phys., **5**(12), pp. 961–989.
[4] Wood, R. W., 1915, Philos. Mag., **30**, pp. 300–304.
[5] Wood, R. W., 1916, Philos. Mag., **32**, pp. 364–371.

[6] Knudsen, M., 1916, Ann. Phys., **48**, pp. 1113–1121.
[7] Shiralagi, K. T., Kriman, A. M., and Maracas, G. N., 1991, "Effusion Cell Orientation Dependence of Molecular Beam Epitaxy Flux Uniformity," J. Vac. Sci. Technol. A, **9**(1), pp. 65–70.
[8] Curless, J. A., 1985, "Molecular Beam Epitaxy Beam Flux Modeling," J. Vac. Sci. Technol. B, **3**(2), pp. 531–534.
[9] Swann, S., Collett, S. A., and Scarlett, I. R., 1990, "Film Thickness Distribution Control With Off-Axis Circular Magnetron Sources Onto Rotating Substrate Holders: Comparison of Computer Simulation With Practical Results," J. Vac. Sci. Technol. A, **8**(3), pp. 1299–1303.
[10] Fatima Vales Silva, M., and Nicholls, J. R., 2001, "A Model for Calculating the Thickness Profile of TiB_2 and Al Multilayer Coatings Produced by Planar Magnetron Sputtering," Surf. Coat. Technol., **142–144**, pp. 934–938.
[11] Cale, T. S., and Raupp, G. B., 1990, "Free Molecular Transport and Deposition in Cylindrical Features," J. Vac. Sci. Technol. B, **8**(4), pp. 649–655.
[12] Cale, T. S., and Raupp, G. B., 1990, "A Unified Line-of-Sight Model of Deposition in Rectangular Trenches," J. Vac. Sci. Technol. B, **8**(6), pp. 1242–1248.
[13] O'Sullivan, P. L., Baumann, F. H., and Gilmer, G. H., 2000, "Simulation of Physical Vapor Deposition into Trenches and Vias: Validation and Comparison With Experiment," J. Appl. Phys., **88**(7), pp. 4061–4068.
[14] Davis, D. H., 1960, "Monte Carlo Calculation of Molecular Flow Rates Through a Cylindrical Elbow and Pipes of Other Shape," J. Appl. Phys., **31**(7), pp. 1169–1176.
[15] Adamson, S., O'Carroll, C., and McGilp, J. F., 1988, "The Spatial Distribution of Flux Produced by Single Capillary Gas Dosers," Vacuum, **38**(4–5), pp. 341–344.
[16] Adamson, S., O'Carroll, C., and McGilp, J. F., 1988, "The Angular Distribution of Thermal Molecular Beams Formed by Single Capillaries in the Molecular Flow Regime," Vacuum, **38**(6), pp. 463–467.
[17] Adamson, S., O'Carroll, C., and McGilp, J. F., 1989, "Monte Carlo Calculations of the Beam Flux Distribution From Molecular Beam Epitaxy Sources," J. Vac. Sci. Technol. B, **7**(3), pp. 487–490.
[18] Lin, Z., and Cale, T. S., 1995, "Simulation of Collimated Flux Distributions During Physical Vapor Deposition," Thin Solid Films, **270**, pp. 627–631.
[19] Wickersham, C. E., 1987, "Crystallographic Target Effects in Magnetron Sputtering," J. Vac. Sci. Technol. A, **5**(4), pp. 1755–1758.
[20] Bird, G. A., 1994, *Molecular Gas Dynamics and the Direct Simulation of Gas Flows*, Oxford University Press, London.
[21] Fancey, K. S., 1995, "A Coating Thickness Uniformity Model for Physical Vapour Deposition Systems: Overview," Surf. Coat. Technol., **71**, pp. 16–29.
[22] Wasilewski, Z. R., Aers, G. C., SpringThorpe, A. J., and Miner, C. J., 1991, "Studies and Modeling of Growth Uniformity in Molecular Beam Epitaxy," J. Vac. Sci. Technol. B, **9**(1), pp. 120–131.
[23] Zehe, A., and Ramirez, A., 2000, "Homogeneity Optimized Layer Deposition on Large Substrates in the Molecular Beam Regime of Knudsen-Type Effusion Sources," Revista Superficies y Vacio, **11**, pp. 44–46.
[24] Bosch, S., 1992, "Computer-Aided Procedure for Optimization of Layer Thickness Uniformity in Thermal Evaporation Physical Vapor Deposition Chambers for Lens Coating," J. Vac. Sci. Technol. A, **10**(1), pp. 98–104.
[25] Incropera, F. P., and DeWitt, D. P., 1990, *Fundamentals of Heat and Mass Transfer*, 3rd ed., Wiley, New York.
[26] Maissel, L., and Glang, R., 1970, *Handbook of Thin Film Technology*, McGraw-Hill, New York.
[27] Grimley, R. T., Wagner, L. C., and Castle, P. M., 1975, "Angular Distributions of Molecular Species Effusing From Near-Ideal Orifices," J. Phys. Chem., **79**(4), pp. 302–308.
[28] Stickney, R. E., Keating, R. F., Yamamoto, S., and Hastings, W. J., 1967, "Angular Distribution of Flow From Orifices and Tubes at High Knudsen Numbers," J. Vac. Sci. Technol., **4**(1), pp. 10–18.
[29] Knudsen, M., 1950, *Kinetic Theory of Gases: Some Modern Aspects*, 3rd ed., Wiley, New York.
[30] Ohring, M., 1992, *The Materials Science of Thin Films*, Academic Press, New York.
[31] Giordmaine, J. A., and Wang, T. C., 1960, "Molecular Beam Formation by Long Parallel Tubes," J. Appl. Phys., **31**, pp. 463–471.
[32] Wahlbeck, P. G., and Phipps, T. E., 1968, "Effusion. II. Angular Number Distributions of Gaseous CsCl From Right-Circular Cylindrical Orifices Into Vacuum," J. Chem. Phys., **49**(4), pp. 1603–1608.
[33] Adams, J. Q., Phipps, T. E., and Wahlbeck, P. G., 1968, "Effusion III. Angular Number Distributions of Gaseous CsCl From Right-Circular Cylindrical Orifices Into Vacuum," J. Chem. Phys., **49**(4), pp. 1609–1616.
[34] Rugamas, F., Roundy, D., Mikaelian, G., Vitug, G., Rudner, M., Shih, J., Smith, D., Segura, J., and Khakoo, M. A., 2000, "Angular Profiles of Molecular Beams From Effusive Tube Sources: I. Experiment," Meas. Sci. Technol., **11**, pp. 1750–1765.
[35] Shen, L. Y. L., 1978, "Angular Distribution of Molecular Beams From Modified Knudsen Cells for Molecular-Beam Epitaxy," J. Vac. Sci. Technol., **15**(1), pp. 10–12.
[36] Buckman, S. J., Gulley, R. J., Moghbelalhossein, M., and Bennett, S. J., 1993, "Spatial Profiles of Effusive Molecular Beams and Their Dependence on Gas Species," Meas. Sci. Technol., **4**, pp. 1143–1153.
[37] Wang, K. C., and Wahlbeck, P. G., 1967, "Effusion. I. Angular Number Distributions of Gaseous CsCl From a Near-Ideal Orifice Into Vacuum," J. Chem. Phys., **47**(11), pp. 4799–4809.
[38] Krasuski, P. T., 1987, "Angular Distribution of Flux at the Exit of Cylindrical Tubes," J. Vac. Sci. Technol. A, **5**(4), pp. 2488–2492.

Experimental Investigation of the Heat Transfer Characteristics of Aluminum-Foam Heat Sinks With Restricted Flow Outlet

W. H. Shih
Research Assistant

F. C. Chou
Research Assistant

W. H. Hsieh[1]
Professor
e-mail: imewhh@ccunix.ccu.edu.tw

Department of Mechanical Engineering,
National Chung Cheng University,
Chia-Yi 621, Taiwan, Republic of China

This study investigates the heat transfer characteristics of aluminum-foam heat sinks with restricted flow outlets under impinging-jet flow conditions. An annular flow-restricting mask is used to control the height of the flow outlet of the aluminum foam sink, forcing the cooling air to reach the heat-generation surface. The enhanced heat transfer characteristics of aluminum-foam heat sinks using these flow-restricting masks are measured experimentally in this work. The effects of porosity, pore density and length of sample, air velocity, and flow outlet height on the heat transfer characteristics of aluminum-foam heat sinks are investigated. Results show that the effect of the flow outlet height is stronger than that of the pore density, porosity, or height of the aluminum heat sinks studied in this work. A general correlation between the Nusselt number and the Reynolds number based on the equivalent spherical diameter of the aluminum foam is obtained for 32 samples of aluminum-foam heat sinks with different sample heights (20–40 mm)*, pore densities* (5–40 ppi(pore/inch))*, porosities (0.87–0.96), and flow outlet heights* (5–40 mm)*. It should be noted that, based on the measured velocity profile, the increase of the Nusselt number of the aluminum-foam heat sink with the decrease in the flow outlet height is caused by the reduced convective resistance at the solid-gas interface through the increased velocity near the heat-generation surface. The reduction in flow outlet height increases the local thermal nonequilibrium condition near the heat-generation surface.* [DOI: 10.1115/1.2759972]

Keywords: porous media, metal foam, electronic cooling, heat transfer, heat sink, restricted flow outlet

Introduction

The use of porous media for dissipating the waste heat of electronic devices has attracted much attention recently due to its low weight, high heat transfer area, and enhanced cooling capacity. Previous experimental and numerical studies have shown that the cooling performance of a porous heat sink is better than that of a fin-pin array heat sink under forced convective heat transfer conditions [1–16]. In most of these heat transfer studies, the gas flow direction is parallel to the waste-heat generation surface of the heat sink.

When the direction of the cooling air is perpendicular to the waste-heat generating surface (referred to as an impinging-jet flow condition in this paper), it enhances the cooling performance of a heat sink. For example, in a study of the cooling performance of a fin-pin array heat sink, Ledezma and Bejan [17] showed an increased cooling performance of 10–20% over the parallel flow condition. Kim et al. [18] also showed that an aluminum-foam heat sink with a larger ratio of permeability (K_y/K_x) or thermal conductivity (k_y/k_x) has a better heat transfer performance under impinging-jet flow conditions. Zhou and Lee [19] installed mesh screens in front of the jet nozzle; their results indicated that the local maximum heat transfer rate was increased by ~3.92% at $z/d=4$ and that the average Nusselt number was enhanced by ~1.38% at $z/d=2$, compared to the case without a screen.

In the numerical study of the cooling performance under impinging-jet flow condition, Jeng and Tzeng [20] numerically investigated the impinging cooling of aluminum-foam heat sinks with a two-equation model. The heat transfer was found to increase as the height of the aluminum-foam heat sink decreased. The maximum heat transfer occurs at the stagnation point when the Reynolds number is low, and the heat transfer decreases when the Reynolds number increases. The thermal resistance of an aluminum-foam heat sink is 30% lower than that of a plate fin heat sink.

Hsieh et al. [21] conducted an experimental study to measure the Nusselt number and the temperature distributions of the gas and solid phases at the circumferential edge of six types of aluminum-foam heat sinks under impinging-jet flow conditions. In addition, the effects of the porosity and pore density of aluminum foam, the air velocity on Nusselt number, and the temperature distributions were investigated in that same work. The existence of a local thermal nonequilibrium condition within the aluminum-foam heat sink was discussed as well. Later on, Shih et al. [22] systematically changed the height of the aluminum-foam heat sink to maximize the cooling performance and showed that the height of the heat sink has a significant effect on the cooling performance of aluminum-foam heat sinks.

Based on the results of the above-mentioned experimental studies [21,22] under impinging-jet conditions, it is noted that a significant amount of the cooling air leaves the heat sink, radially, without reaching the waste-heat generating surface. This reduces the cooling performance of the aluminum-foam heat sink. In the present study, a flow-restricting mask, as shown in Fig. 1(*a*) is provided to control the flow outlet area and to force the cooling air to reach the heated surface. The heat-transfer characteristics of aluminum-foam heat sinks under impinging-jet conditions, com-

[1]Corresponding author.

Contributed by the Heat Transfer Division of ASME for publication in the JOURNAL OF HEAT TRANSFER. Manuscript received April 26, 2006; final manuscript received February 10, 2007. Review conducted by Jose L. Lage.

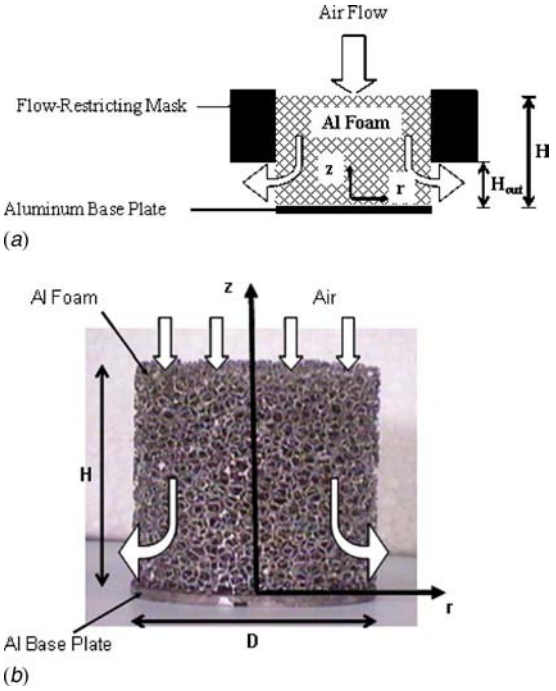

Fig. 1 (*a*) Schematic diagram of an aluminum-foam heat sink with a flow-restricting mask and (*b*) a photo of an aluminum-foam heat sink used in the study (ppi=10 and porosity=0.92)

plete with flow-restricting masks, are measured experimentally, and their cooling performances with and without flow-restricting mask are compared in this work. At the same time, the effects of the height of the flow outlet, the porosity, and the pore density of the aluminum foam, as well as the effect of the air velocity on the Nusselt number are investigated. In addition, the solid- and gas-temperature distributions at the perimeter of the heat sinks and the velocity profile in the outlet area are measured under different conditions.

Table 1 Properties of aluminum foam used in this study

Type no.	ppi (pore/inch)	Porosity	Mean pore diameter, d_p (m)	Equivalent spherical diameter, D_p (m)	k(*) (W/m K)
1	5	0.91	1.19×10^{-3}	1.59×10^{-4}	5.89
2	20	0.87	8.27×10^{-4}	1.85×10^{-4}	8.32
3	20	0.91	8.05×10^{-4}	1.21×10^{-4}	6.34
4	20	0.94	8.14×10^{-4}	8.49×10^{-5}	4.95
5	20	0.96	8.00×10^{-4}	5.26×10^{-5}	3.55
6	40	0.94	6.85×10^{-4}	7.14×10^{-5}	4.93

(*)From Calmidi and Mahajan [25].

Materials and Method

Six types of aluminum-foam heat sinks, as shown in Table 1, are used in this study. As shown in Figs. 1(*a*) and 1(*b*), each aluminum-foam heat sink is composed of a piece of aluminum foam and a base plate. The aluminum foam is attached to the base plate with a silver epoxy (Loctite Corporation, 3880, thermal conductivity=4 W/m K). The silver epoxy is cured by putting the base plate with the aluminum-foam heat sink in a furnace (Lindberg/Blue M) and going through a curing temperature cycle (heating at 8°C/min until 150°C, maintaining at 150°C for 40 min, and then cooling in the furnace). Based on the post-test examination, the thickness of the silver epoxy is observed to be $<$0.1 mm. The associated interface thermal resistance is estimated to be $\sim7.5\times10^{-3}$°C/W. The temperature measurement error based on the estimated interface thermal resistance and heat transfer across the silver epoxy interface is about 2.4×10^{-1}°C. The diameter of the aluminum foam is 65 mm. The base plate is made of 3 mm thick aluminum. In this work, the aluminum-foam heat sink was attached to the copper plate by applying a thin layer of silicone heat conductive compound (E.G-BOND, Type:EG-150, thermal conductivity=0.9 W/m K) to the copper plate and then press the heat sink against the copper plate by hand. The thickness of the silicone heat conductive compound sandwiched between the aluminum-foam heat sink and the copper plate was estimated, based on a post-test examination, to be $<$0.1 mm, and the associated thermal resistance is $<3.3\times10^{-2}$°C/W. An annulus made of balsa wood (bulk density $\leq$140 kg/m^3, thermal conductivity at 300 K$\leq$0.055 W/m K) is used as the flow-restricting mask to control the flow outlet height. The flow outlet height is controlled by adjusting the vertical position of the flow-restricting mask. The height of the aluminum-foam heat sink and the flow outlet are varied systematically in this study. As shown in Table 2, all types of aluminum-foam heat sinks, except type 2, have an identical height H of 40 mm. Type 2 has three different heights, 40 mm, 30 mm, and 20 mm. The ratio of the flow outlet height to the sample height (H_{out}/H) is systematically varied from 0.25 to 1.00. The measurement of the mean pore diameter d_p and the equivalent spherical diameter ($D_P=6/S_v$, where S_v is the surface area per unit volume of solid phase) was conducted according to the method used in Refs. [23,24]. The mean pore diameter is the mean

Table 2 Heights of aluminum-foam heat sink and flow outlet

Sample no.	Type no.	H (cm)	H_{out} (cm)	$H_n=H_{out}/H$	Sample no.	Type no.	H (cm)	H_{out} (cm)	$H_n=H_{out}/H$
1-4-4	1	4	4	1.000	3-4-4	3	4	4	1.000
1-4-2	1	4	2	0.500	3-4-2	3	4	2	0.500
1-4-1	1	4	1	0.250	3-4-1	3	4	1	0.250
1-4-0.5	1	4	0.5	0.125	3-4-0.5	3	4	0.5	0.125
2-4-4	2	4	4	1.000	4-4-4	4	4	4	1.000
2-4-3	2	4	3	0.750	4-4-2	4	4	2	0.500
2-4-2	2	4	2	0.500	4-4-1	4	4	1	0.250
2-4-1	2	4	1	0.250	4-4-0.5	4	4	0.5	0.125
2-3-3	2	3	3	1.000	5-4-4	5	4	4	1.000
2-3-2.25	2	3	2.25	0.750	5-4-2	5	4	2	0.500
2-3-1.5	2	3	1.5	0.500	5-4-1	5	4	1	0.250
2-3-0.75	2	3	0.75	0.250	5-4-0.5	5	4	0.5	0.125
2-2-2	2	2	2	1.000	6-4-4	6	4	4	1.000
2-2-1.5	2	2	1.5	0.750	6-4-2	6	4	2	0.500
2-2-1	2	2	1.0	0.500	6-4-1	6	4	1	0.250
2-2-0.5	2	2	0.5	0.250	6-4-0.5	6	4	0.5	0.125

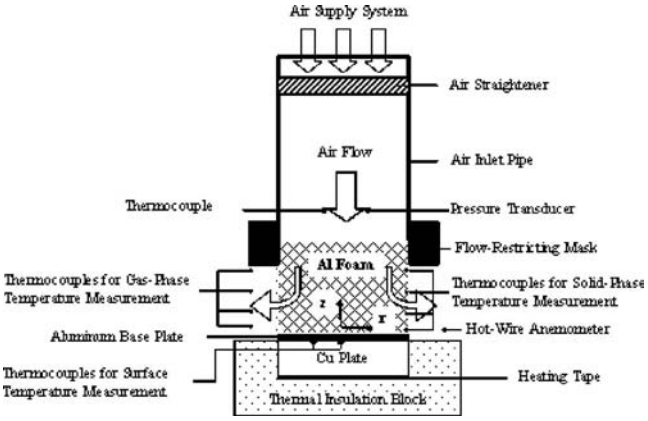

Fig. 2 Experimental apparatus for the measurements of heat transfer characteristics of aluminum-foam heat sinks

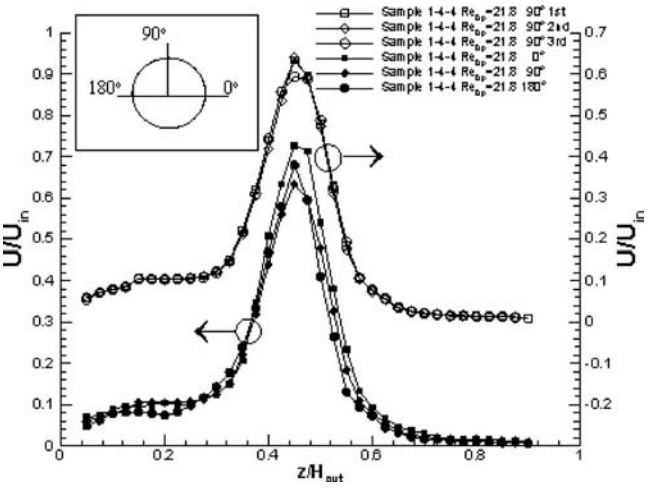

Fig. 3 Measured outlet velocity profiles from three repeated tests at three different angles (inset: top view of the heat sink showing the three different angles at which the velocity profiles are measured)

of the equivalent pore diameters, which are determined by converting each individual pore area of the aluminum foam to the diameter of an equivalent circle.

Figure 2 shows the schematic diagram of the experimental apparatus used in this study for the measurement of heat transfer characteristics of aluminum-foam heat sinks. The flow straightener (diameter=65 mm, length=50 mm) within the inlet air pipe consists of stacked foam sponges. At the inlet of the aluminum foam, the temperature and pressure of the air are measured with a T-type thermocouple and a pressure transducer (Validyne pressure transducer, 0.5% accuracy), respectively, to determine the condition of the inlet air. During the tests, the waste heat is generated by a waste heat generating block, which consists of a 20 mm thick, 65 mm dia circular copper plate and an electric heat tape, which is attached to the bottom of the copper plate as shown in Fig. 2. Three thermocouples for the measurement of the surface temperature of the copper plate (T_{Cu}) are placed in the groves at the top surface of the copper plate. Two thermocouples are installed in positions symmetrical to the center of the copper plate, and on a radius of 30 mm from the center. The third thermocouple is also installed at 30 mm distance from the center, but at 90 deg to the other two thermocouples. Because of the highly conductive nature of the copper plate, the measured temperatures from the three thermocouples are within 0.15% and, therefore, the values of the temperatures reported later in this paper are the average temperature measured from the three thermocouples. For that reason, the deduced Nusselt number based on this average number represents the overall thermal performance of the aluminum-foam heat sinks.

In measuring the solid- and gas-phase temperatures of the heat sink, five T-type thermocouples are positioned at equal spacing along a z-direction line, 1 mm away from the perimeter of the aluminum foam. These thermocouples measure the temperature profile of the air exiting the aluminum foam. Another set of six E-type thermocouples are silver glued (also at equal spacing in the z direction) at the perimeter of the solid-phase portion (aluminum portion) of the aluminum foam, for measuring the solid-phase temperature. The diameter of the insulated thermocouple wire is 1 mm. In silver gluing, the thermocouple to an aluminum-foam heat sink, the silver epoxy is applied to the contact area between the thermocouple and the aluminum-foam heat sink after they have been positioned in contact with each other on a working plate. The curing process of the silver epoxy is the same as that used in bonding the aluminum foam to the base plate. Based on the post-test examination, the thickness of the silver epoxy is observed to be <0.1 mm. The associated interface thermal resistance is estimated to be $\sim 15.9\,^{\circ}\mathrm{C/W}$. By considering the heat loss through the thermocouple wire and the insulation layer, the heat transfer across the silver-epoxy interface is about 5.39×10^{-5} W. The temperature measurement error based on the estimated interface thermal resistance and heat transfer across the silver-epoxy interface is about $8.58 \times 10^{-4}\,^{\circ}\mathrm{C}$.

During the tests, the amount of airflow is regulated by a needle valve, and the flow is straightened by the flow straightener, which is installed in the air inlet pipe prior to the air entering the test section. With the valve in the open position, the power is turned on to the heating tape, and the heat is conducted to the porous heat sink through the copper plate. The readings of the thermocouples, used to measure solid- and gas-phase temperatures, are recorded when the steady-state condition has been reached. The power to the heating tape is then turned off, and the flow rate of the air is increased so as to cool down the porous heat sink until it reaches the ambient temperature. This procedure is repeated for all samples at each flow rate. In order to examine the repeatability of the experiments, the tests are repeated three times at each flow rate for each sample. A good agreement is found in these tests at each airflow rate. The maximum difference in the measurement of the solid- and gas-phase temperature between these repeated tests for each sample is 2.6%, and for the Nusselt number it is 9.5%.

The velocity profile at the outlet of the aluminum-foam heat sink is measured by a hot-wire anemometer. During the experiments, the hot wire is positioned at four different distances, 1 mm, 5 mm, 10 mm, and 15 mm, from the perimeter of the aluminum-foam heat sink. It is worth noting that if the hot-wire anemometer is positioned at 1 mm, 5 mm, or 10 mm away from the perimeter of the aluminum-foam heat sink, the measured velocity profile becomes highly erratic between repeated tests. This is because, within this distance, the direction and magnitude of the velocity of the air exiting the aluminum foam is random, due to the blocking effect of the solid phase of the aluminum-foam heat sink. The velocity of the air downstream of the solid phase is close to zero, but downstream of a pore it is much larger. When the hot-wire anemometer is positioned 15 mm away from the perimeter of the aluminum-foam heat sink, the measured outlet velocity profiles shows good repeatability, as shown in Fig. 3. On the other hand, the measured outlet velocity profiles at three different angles also show good axisymmetry, as shown in Fig. 3. Therefore, the velocity profile reported in this paper is measured 15 mm away from the perimeter of the aluminum-foam heat sink and represents the profile of the average gas velocity at this location.

In this study, the Nusselt number defined below is measured experimentally.

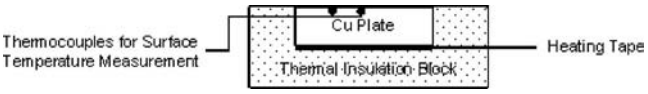

Fig. 4 Apparatus for measuring heat loss

$$\mathrm{Nu}_{D_p} = \frac{hD_p}{k} \tag{1}$$

and

$$h = \frac{q}{A(T_{\mathrm{Cu}} - T_{\mathrm{in}})} \tag{2}$$

where h is the convective heat transfer coefficient, D_p is the equivalent spherical diameter of porous media, k is the effective thermal conductivity of the aluminum foam, q is the waste-heat transfer rate in the steady-state condition, A is the base area of the aluminum-foam heat sink, T_{Cu} is the surface temperature of the waste-heat generating block (i.e., the surface temperature of the copper plate), and T_{in} is the temperature of the inlet air. The Nusselt number defined in this paper evaluates the ratio of the convective heat transfer to the conductive heat transfer (including the conduction through the air and the aluminum) of the aluminum-foam heat sink. The effective thermal conductivity used in this study is a property evaluating the ability of the aluminum foam to conduct the heat through the gas (air) and solid (aluminum) phases of the aluminum foam under a no-flow condition. Thus, following the works by Bhattacharya and Mahajan [7] and Calmidi and Mahajan [11], the effective thermal conductivity, including the contributions from the conductivity of both the air and aluminum, is used in Eq. (1) to calculate the Nusselt number. The effective thermal conductivity of the aluminum foam is calculated from the correlation developed by Calmidi and Mahajan [25]. This correlation was obtained by averaging the heat transfer through the complex structure of the aluminum foam and was verified experimentally. The aluminum foam used in this work and the foam used by Calmidi and Mahajan [25], were supplied by the same corporation. The accuracy of the correlation is 3.6%.

In determining the convective heat transfer coefficient h, Eq. (2) is used with the substitution of the measured T_{Cu}. In Eq. (2), q is the waste-heat transfer rate and is equal to the difference between the heat generated by the heating tape and the heat loss through the thermal insulation base. The heat loss through the thermal insulation base is a function of the temperature difference between the top surface of the waste-heat generating block and the ambient, obtained by the procedures reported in previous studies [21,22]. In short, Fig. 4 shows the experimental apparatus for the measurement of heat loss through the insulation block at different $(T_{\mathrm{Cu}} - T_\infty)$, where T_{Cu} is the top surface temperature of the copper plate and T_∞ is the temperature of the ambient [21,22]. The experimental apparatus is the same as the one used for the Nusselt number measurement described above, except that the aluminum-foam heat sink is removed from the apparatus. As shown in Fig. 4, the heat tape is powered by a DC power supply. A FLUKE Hydra Series II records the top-surface temperature of the copper plate T_{Cu} and the ambient temperature T_∞. The copper plate and the heat tape are placed within the thermal insulation base made of balsa wood (bulk density=140 kg/m^3, thermal conductivity at 300 K=0.055 W/m K). The temperatures of the top surface of the copper plate and the ambient are both measured under natural convection and steady-state condition. The heat loss through the insulation block at different $(T_{\mathrm{Cu}} - T_\infty)$ is calculated by the following:

$$q_{\mathrm{loss}} = q_{\mathrm{in}} - q_{\mathrm{natural}} - q_r \tag{3}$$

$$q_{\mathrm{in}} = IV \tag{4}$$

$$q_{\mathrm{natural}} = \bar{h}A(T_{\mathrm{Cu}} - T_\infty) \tag{5}$$

where q_{loss} is the heat loss through the insulation block to the ambient; q_{natural} is the heat transfer through natural convection from the top surface of the copper plate to the ambient; q_r $(=\chi\sigma A(T_{\mathrm{Cu}}^4 T_\infty^4)$, $\chi=0.072$, is the emissivity of the copper plate used in this work, $\sigma=5.6696\times10^{-8}$ W/m^2 K^4 is the Stefan–Boltzmann constant) is the radiation from the top surface of the copper plate to the ambient, $\bar{h}$ is the average natural convective heat transfer coefficient at the top surface of the copper plate [26]; A is the top surface area of the copper plate; T_{Cu} ranges from 320 K to 360 K in this study; q_{in} is the power generated by the heating tape; I and V are the input DC current and voltage, respectively. The correlation between heat loss and temperature difference of the copper plate and ambient deduced from the experimental data is

$$q_{\mathrm{loss}} = -0.019 + 0.053(T_{\mathrm{Cu}} - T_\infty) - 6.709\times10^{-5}(T_{\mathrm{Cu}} - T_\infty)^2 + 1.359\times10^{-6}(T_{\mathrm{Cu}} - T_\infty)^3 \tag{6}$$

The standard error of the estimate of the correlation [27] is $<9.5\%$. When estimating the heat loss through the heat insulation base, the measured T_{Cu} and T_∞ during an experiment of the Nu_{D_p} measurements are substituted into Eq. (6). The result shows that the heat loss is a function of the temperature difference between the top surface of the waste-heat generating block and the ambient. The heat loss is about 2.7–4.1% of the input power.

The uncertainties of the experimental apparatus used in this experiment are obtained from the apparatus suppliers. In the measurement of airflow properties, the flowmeter calibrated by the manufacturer has a volumetric flow accuracy of ±0.05%, the pressure transducer (Validyne pressure transducer) has a 0.5% accuracy, and the uncertainty of hot-wire calibration is $<2.4\%$. In supplying the waste heat, the power supply has a current uncertainty of ±0.2%. In temperature measurements, the uncertainties of the temperature reader (Fluke Hydra II) and the thermocouple calibrated with a resistance temperature detector (Omega PR-11) accuracy: ±0.35 K at 273.15–373.15 K are ±0.45 K and ±0.25%, respectively. In the measurement of sample dimensions, the dimension precision is ±0.02 mm.

In this work, the uncertainties of measured and deduced data are determined with the t-distribution under a confidence level of 0.95 [28,29]. The degree of freedom is determined by the number of test data. The uncertainties of measured pressure, air outlet velocity, inputted power, and temperature are ±4.8%, 19.9%, ±0.2%, and ±2.34–2.73%, respectively. The uncertainties for the calculated Reynolds number and heat transfer coefficient are ±3.3–15.8% and ±11.4–13.3%, respectively.

Results and Discussion

In this study, the aluminum-foam heat sinks were equipped with a flow-restricting mask to control the flow outlet area, forcing the cooling air to reach the heat-generation surface. The enhanced heat transfer characteristics of the aluminum-foam heat sinks equipped with these flow-restricting masks were then measured. The effects of the height of the flow outlet, the porosity, and the pore density of the aluminum foam, and the air velocity on the Nusselt number were investigated. In addition, the solid- and gas-temperature distributions at the perimeter of the heat sinks and the velocity profile in the outlet area were measured under different conditions.

In the impinging-jet heat transfer process of aluminum-foam heat sinks studied in this work, the flow resistance of the aluminum foam usually forces the cooling air to go radially outward, exiting from the heat sink. This reduces the percentage of the cooling air reaching the waste-heat generation surface, resulting in a reduced cooling performance. Therefore, a flow-restricting mask was provided to control the outlet area of the cooling air. The use

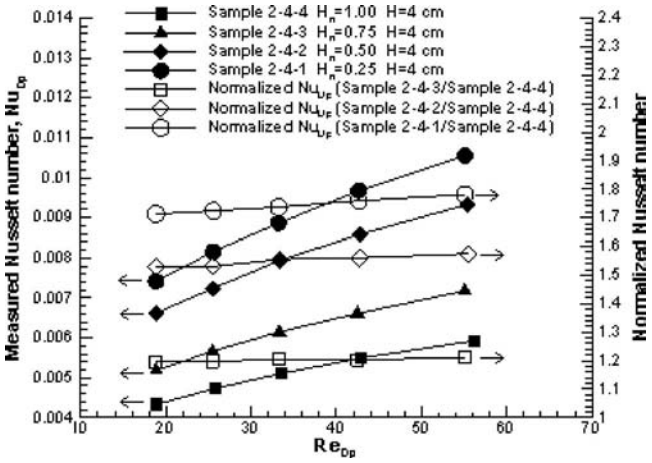

Fig. 5 Measured and normalized Nusselt numbers as functions of the Reynolds number for heat sinks with different height of flow outlet

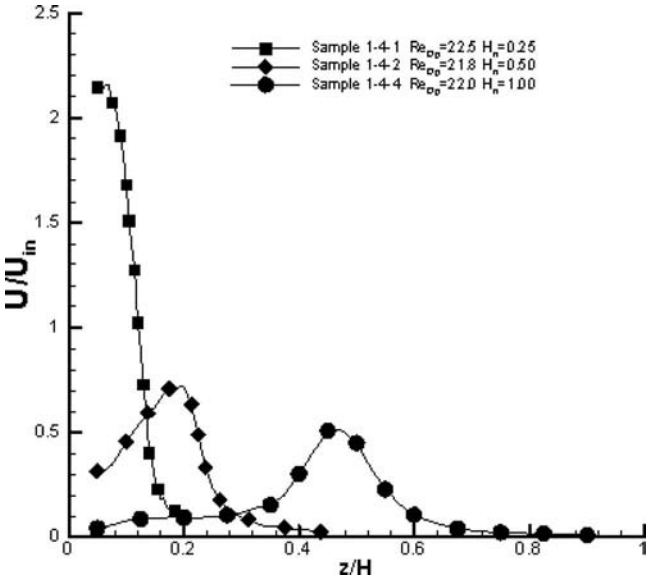

Fig. 6 Measured gas velocity as a function of the normalized flow outlet height for three samples with different flow outlet heights

of a flow-restricting mask will increase the percentage of the cooling air reaching the heated surface region thereby increasing the cooling performance of the heat sink.

The effect of the flow-restricting mask on the cooling performance of the aluminum-foam heat sink is shown in Fig. 5. In Fig. 5, the measured and normalized Nusselt numbers as functions of the Reynolds number are shown for type-2 heat sinks with different heights of the flow outlet. The measured Nusselt number is defined in Eq. (1), and the Reynolds number is defined as follows:

$$\mathrm{Re}_{D_p} = \frac{\rho U_{\mathrm{in}} D_p}{\mu} \tag{7}$$

The height of the flow outlet is controlled by adjusting the vertical position of the flow-restricting mask as shown in Fig. 1(*a*). The four samples shown in Fig. 5 have an identical heat sink height of 40 mm, but different outlet heights. The sample 2-4-4 does not use the flow restricting mask and serves as the baseline condition. The other three samples 2-4-3, 2-4-2, and 2-4-1 use the flow-restricting mask to reduce the flow outlet height to 3 cm, 2 cm, and 1 cm, respectively. The normalized Nusselt number is defined as the ratio of the measured Nusselt number of the sample with the flow-restricting mask (sample 2-4-3, 2-4-2, or 2-4-1) to that of the baseline sample without the flow-restricting mask (sample 2-4-4). The normalized Nusselt number is an indication of the enhanced cooling performance introduced by the use of the flow-restricting mask. It is evident from Fig. 5 that the measured and normalized Nusselt numbers increase with the decrease in the flow outlet height. This is caused by the fact that the cooling air is guided by the flow-restricting mask toward the heat-generation surface, and the convective coefficient is therefore enhanced through the increased velocity in the region where the highest thermal nonequilibrium exists, i.e., near the heated plate. (The measured velocity profile will be discussed in the next paragraph.) This results in a better cooling performance. It is also evident that the measured Nusselt number increases as the Reynolds number increases due to the higher mass flow rate taking away more heat.

Figure 6 shows the measured gas velocity as a function of the normalized flow outlet height for three samples with different flow outlet heights (H_n=1.0, 0.5, and 0.25). As discussed in the materials and method section, the velocity is measured at 15 mm distance from the perimeter of the aluminum-foam heat sink. It is understood that the measured velocity is not exactly the exit velocity of the cooling air from the aluminum-foam heat sink. However, under the condition of identical aluminum-foam materials and flow velocities, the measured velocity profiles can provide a reasonable indication of the velocity-profile difference between samples with different flow outlet heights. As shown in Fig. 6, the velocity profile for sample 1-4-4 (H_n=1.0) has a peak at z/H =0.48. The location of the velocity peak moves toward the heat-generated surface (z/H=0.0) as the height of the flow outlet decreases from H_n=1.0–0.25. It should be noted that the velocity at the region very close to the heat-generated surface ($z/H<0.04$) was not measured because of the difficulty in positioning the hot wire in that region.

In order to compare the relative amount of cooling air reaching the heat-generation surface for the three samples, the average velocity over the region near the heat-generation surface (z/H =0.05–0.125) is calculated from the measured velocity profile, shown in Fig. 6, based on the following equation:

$$\bar{u} = \frac{\int_a^b (U/U_{\mathrm{in}}) d(z/H)}{b-a} \tag{8}$$

where a=0.05 and b=0.125. The calculated average velocity near the heat-generation surface is shown (see Table 3) to increase with the decrease of the height of the flow outlet. Based on the increased average velocity near the heat-generation surface and the velocity profiles shown in Fig. 6, it is reasonable to state that the

Table 3 Calculated average velocity and ratio of average velocities

Type 1 H=40 mm	Average velocity (m/s) ($\bar{u}=[\int_a^b (U/U_{in})d(z/H)]/(b-a)$, where a=0.05, b=0.125)			Ratio of average velocities	
Re_{D_p}	H_n=1.00	H_n=0.50	H_n=0.25	$\frac{\bar{u}(H_n=0.50)}{\bar{u}(H_n=1.00)}$	$\frac{\bar{u}(H_n=0.25)}{\bar{u}(H_n=1.00)}$
16.2	0.081	0.44	2.068	5.4	25.5
22.0	0.142	0.875	3.904	6.16	27.5
28.8	0.211	1.685	5.734	7.98	27.2
36.7	0.269	2.842	7.755	10.6	28.8
47.5	0.367	4.409	11.29	12.0	30.8

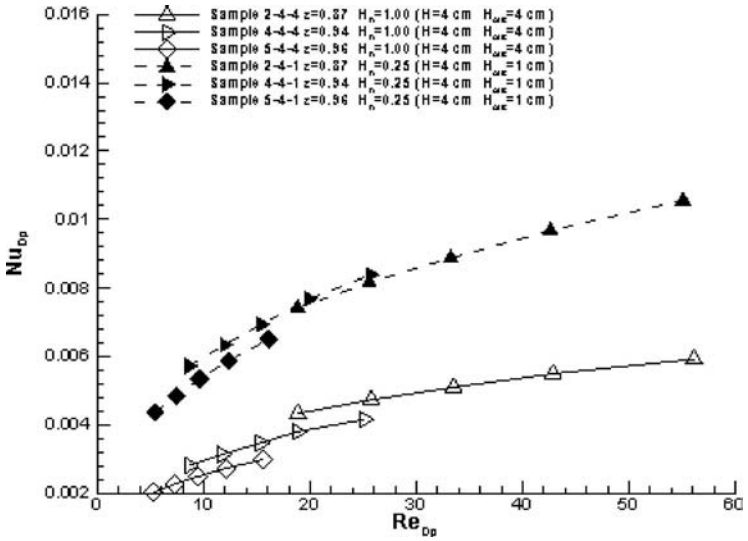

Fig. 7 Effect of porosity and flow outlet height on the Nusselt number under different Reynolds numbers

decrease in the flow outlet height increases the percentage of the cooling air reaching the heat-generation surface.

In addition to the flow outlet height, there are other parameters, such as the porosity, pore density, and length of the aluminum foam, affecting the cooling performance of the heat sink. In the following, the effects of these parameters and the comparison among them will be discussed. Figure 7 shows the effect of the porosity of the aluminum foam and the flow outlet height on the measured Nusselt number under different Reynolds numbers. In Fig. 7, the measured Nusselt numbers for six samples are given. All eight aluminum foam samples have the same pore density (20 ppi) and length (4 cm). The six samples are separated into two sets of samples based on the flow outlet height. The flow outlet height of the first set of samples (2-4-4, 4-4-4, and 5-4-4) is equal to 4 cm (H_n=1.0), and the other set of samples (2-4-1, 4-4-1, and 5-4-1) is equal to 1 cm (H_n=0.25). The porosity of these two sets of samples ranges from 0.87 to 0.96. It can be seen from Fig. 7 that the Nusselt number increases with the decrease in porosity. This is because a decrease in porosity lowers the conductive resistance in the solid phase of the aluminum foam and promotes the enhancement of heat deeper into the foam thereby making use of more of the foam for convective exchange. Figure 7 also shows that the Nusselt number increases with the decrease of the flow outlet height. The reason for this was given earlier in the discussion referring to Fig. 5. It is evident that the change in the flow outlet height has a stronger effect than that of the porosity on the measured Nusselt number.

The effect of the pore density of the aluminum foam and the flow outlet height on the measured Nusselt number is shown in Fig. 8, which also shows the measured Nusselt numbers for six samples. All six samples have similar porosity (0.92–0.94) and identical length (4 cm) of aluminum foam. The six samples can be separated into two sets of samples, depending on their flow outlet height. The flow outlet height of the first set of samples (1-4-4, 4-4-4, and 6-4-4) is 4 cm (H_n=1.0), and for the other set of samples (1-4-1, 4-4-1, and 6-4-1), it is 1 cm (H_n=0.25). The pore density of these two set of samples ranges from 10 ppi to 40 ppi.

The effect of the total height of the aluminum foam and the flow outlet height on the measured Nusselt number is shown in

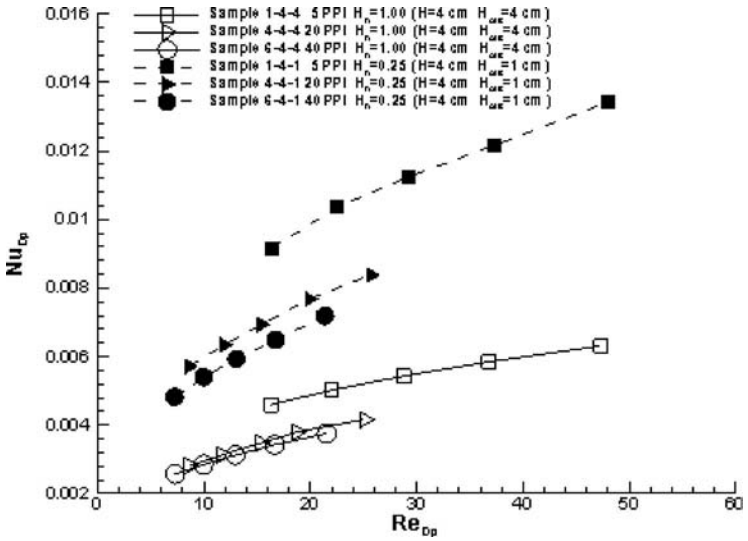

Fig. 8 Effect of pore density and flow outlet height on the Nusselt number under different Reynolds numbers

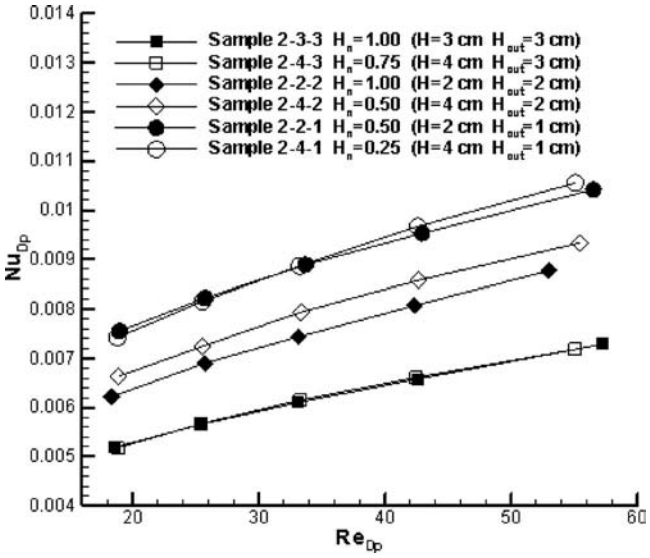

Fig. 9 Effect of length of aluminum foam and flow outlet height on the Nusselt number under different Reynolds numbers

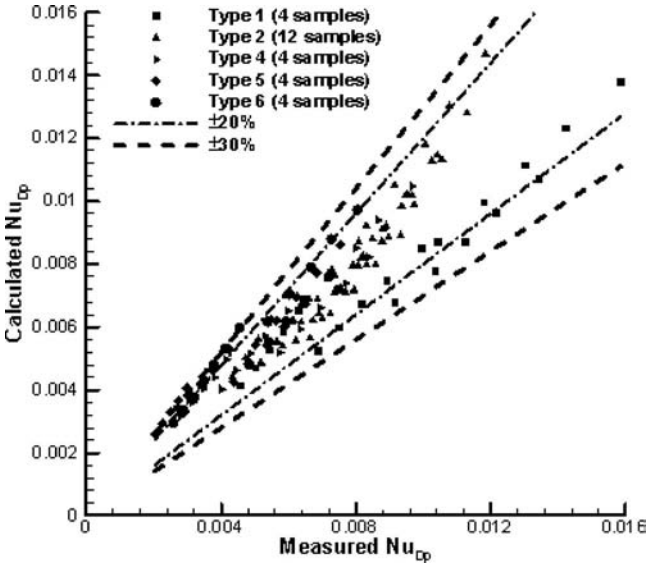

Fig. 10 Comparison between the measured and calculated Nusselt numbers

Fig. 9, which also shows the measured Nusselt numbers for the six samples. The six samples can be separated into three sets of samples, depending on the flow outlet height. The flow outlet height of the first set of samples (2-3-3 and 2-4-3) is 3 cm; for the second set of samples (2-2-2 and 2-4-2), it is 2 cm (H_n=0.25), and for the third set of samples (2-2-1 and 2-4-1), it is 1 cm. The total height of these three sets of samples ranges from 2 cm to 4 cm. In this work, the flow direction of the cooling air is mainly affected by the flow-restricting mask, as shown in Fig. 6. Under this condition, the main effect of decreasing the total height of the aluminum foam is a reduction of the total contact surface area between the aluminum foam and the cooling air. Because the heat transfer takes place mainly at the region near the heat-generation surface, the effective contact surface area between the aluminum foam and the cooling air is limited to the region near the heat-generation surface. Therefore, the reduction of the total contact area caused by the decrease of the total height of the sample does not necessarily change the effective contact surface area, as shown in Fig. 9. The decrease of the total height of the aluminum foam has little effect on the Nusselt number. On the other hand, the decrease of the flow outlet height significantly increases the Nusselt number. The effect of the flow outlet height is larger than that of the total height of the aluminum foam.

As discussed above, the flow outlet height has a significant effect on the cooling performance of the heat sink. It is therefore reasonable to include the flow outlet height in the correlation for the Nusselt number, i.e., $\mathrm{Nu}_{D_p}=f(\mathrm{Re}_{D_p},H_{\mathrm{out}}/D)$. The correlation for the Nusselt number as a function of the Reynolds number and the dimensionless height of the flow outlet is obtained by a least-squares fitting for all 28 types of samples used in this work. The correlation is given as

$$\mathrm{Nu}_{D_p}=1.032\times10^{-3}\mathrm{Re}_{D_p}^{0.436}\left(\frac{H_{\mathrm{out}}}{D}\right)^{-0.344} \tag{9}$$

The comparison between the measured and the calculated Nusselt number from Eq. (9) is shown in Fig. 10, which shows that all experimental data are within ±30% of the correlation, and that most of the data are within ±20%. The standard error of estimate representing the average error between measured data and correlation, calculated by [26], is 9.57×10^{-4}. The R^2 is 0.87.

In order to investigate the effect of the flow outlet height on the local thermal equilibrium phenomena of aluminum-foam heat sinks, the temperatures of the solid and gas phases at the perimeter of the heat sinks are measured at different Reynolds numbers for samples 3-4-4 (H_{out}=4 cm) and 3-4-2 (H_{out}=2 cm). The results are shown in Figs. 11 and 12. The dimensionless temperatures of the solid and gas phases are defined, respectively, as

$$\theta_s=\frac{T_s-T_{\mathrm{in}}}{\dot{q}H/k} \tag{10}$$

$$\theta_f=\frac{T_f-T_{\mathrm{in}}}{\dot{q}H/k} \tag{11}$$

In Fig. 11, the dimensionless solid-phase temperatures are shown to decrease with the increase of the Reynolds number and the distance away from the heat-generation surface. In addition, the reduction in the flow outlet height also decreases the dimensionless solid-phase temperature. This decrease is caused by the enhanced heat transfer between the aluminum foam and the cool-

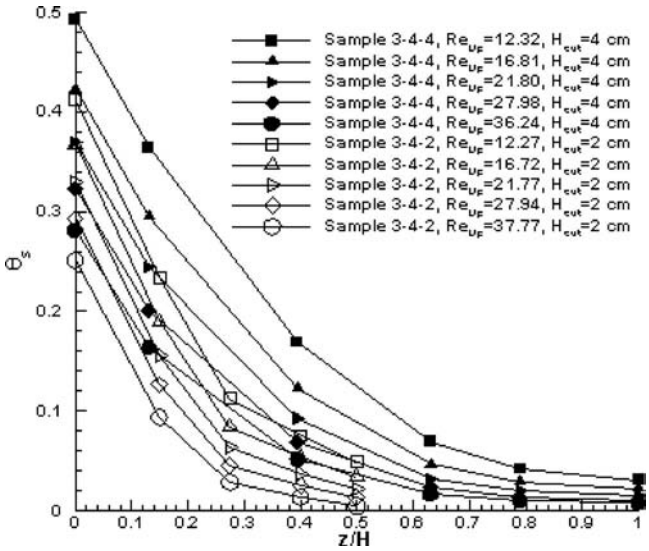

Fig. 11 Effect of the Reynolds number on the distributions of dimensionless solid-phase temperature of samples 3-4-4 and 3-4-2

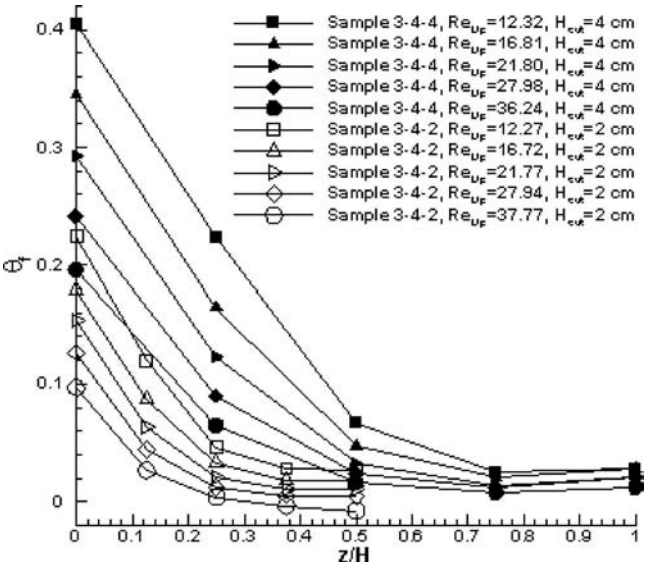

Fig. 12 Effect of the Reynolds number on the distributions of dimensionless gas-phase temperature of samples 3-4-4 and 3-4-2

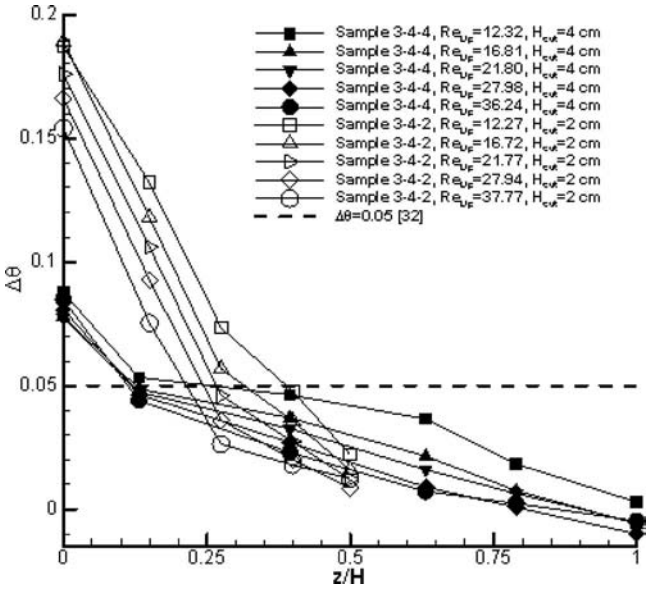

Fig. 13 Effect of the Reynolds number on the distributions of dimensionless temperature difference of samples 3-4-4 and 3-4-2

ing air at a smaller flow outlet height. Even though the increase of the Reynolds number and the decrease of the flow outlet height will both reduce the dimensionless solid-phase temperature, the effect of the Reynolds number is larger than that of the flow outlet height. Based on the data in Figs. 11 and 12, the decreases of the dimensionless temperatures of the solid and gas phases caused by the increase in the Reynolds number and the reduction of the flow outlet height are summarized in Table 4. As shown in Table 4, when the Reynolds number is increased by a factor of ~2 (from 12.8 to 28), the decrease in the dimensionless solid-phase temperature is 0.17. This reduction in the solid-phase temperature is caused by the increased heat transfer between the cooling air and the solid phase at the higher air velocity.

On the other hand, when the flow outlet height is reduced by a factor of 2, the decrease in the dimensionless solid-phase temperature is 0.08, which is much smaller than that caused by the increase of the Reynolds number. When the flow outlet height is reduced, the region where the air velocity is increased is limited to the region near the heat-generation surface; whereas when the Reynolds number is increased, the region where the air velocity is increased is throughout the aluminum-foam heat sink. This difference causes the decrease in the dimensionless solid-phase temperature introduced by the reduction of flow outlet height to be smaller than that introduced by the increase of the Reynolds number.

In Fig. 12, the dimensionless gas-phase temperatures are noted to decrease with the increase of the Reynolds number and the distance away from the heat-generation surface. The reduction in the flow outlet height also decreases the dimensionless gas-phase temperature. As the height of the flow outlet is decreased, the air is guided toward the heat-generation surface and the air velocity near the heat-generation surface increases, as discussed in Fig. 6. The increased air velocity increases both the local mass flux of the air and the convective heat-transfer coefficient between the solid phase of the aluminum foam and the air. This rate of increase of the mass flux (which is linearly proportional to the velocity) is, however, larger than that of the convective heat transfer coefficient between the solid phase of the aluminum foam and the air (which is usually proportional to the velocity raised to a power of <1). This results in a lower air temperature at a smaller flow outlet height. As shown in Table 4, this reduction in the air temperature caused by a shorter flow height is larger than that in the solid-phase temperature.

Table 4 Comparison of the effects of the Reynolds number and the flow outlet height on the decrease of dimensionless temperatures of the solid and gas phases at $Z/H \approx 0.0$

	H_{out}=4 cm			Re$_{D_p}$=12.3		
	Re$_{D_p}$ 12.3	Re$_{D_p}$ 28.0	Decrease of dimensionless temperature	H_{out} 4 cm	H_{out} 2 cm	Decrease of dimensionless temperature
θ_s	0.493	0.323	0.170	0.493	0.412	0.081
θ_f	0.405	0.242	0.163	0.405	0.225	0.180

Since the heat is conducted to the aluminum-foam heat sink from the heat-generation base plate, the local thermal nonequilibrium condition between the solid and the gas phases can be investigated by observing the temperature difference near the base plate. The effect of the flow outlet height and the Reynolds number on the distribution of the dimensionless temperature difference is shown in Fig. 13. The definition of the dimensionless temperature difference is given as

$$\Delta\theta = \theta_s - \theta_f \tag{12}$$

From Fig. 13, we can find that the temperature difference decreases with the increases of the Reynolds number, with the increase in distance from the base plate, and with the increase in the flow outlet height. In modeling the heat-transfer processes of porous materials, according to [30], the effect of a local thermal nonequilibrium between solid and gas phases should be considered when the temperature difference between the two phases exceeds 0.05 and the assumption of a local thermal equilibrium is no longer valid. According to this 0.05 temperature difference, the boundary between the local thermal equilibrium regime and the local thermal nonequilibrium regime is plotted in Fig. 13. For sample 3-4-4 (H_{out}=4 cm), the local thermal nonequilibrium regime is noted to be very close to the heat-generation base plate ($z/H<0.1$) due to the fact that most of the heat is transferred from the solid aluminum foam to the cooling air at this region. The local thermal nonequilibrium regime and the temperature difference for sample 3-4-2 (H_{out}=2 cm) are noted to be larger than sample 3-4-4 (H_{out}=4 cm). This is caused by the fact that when

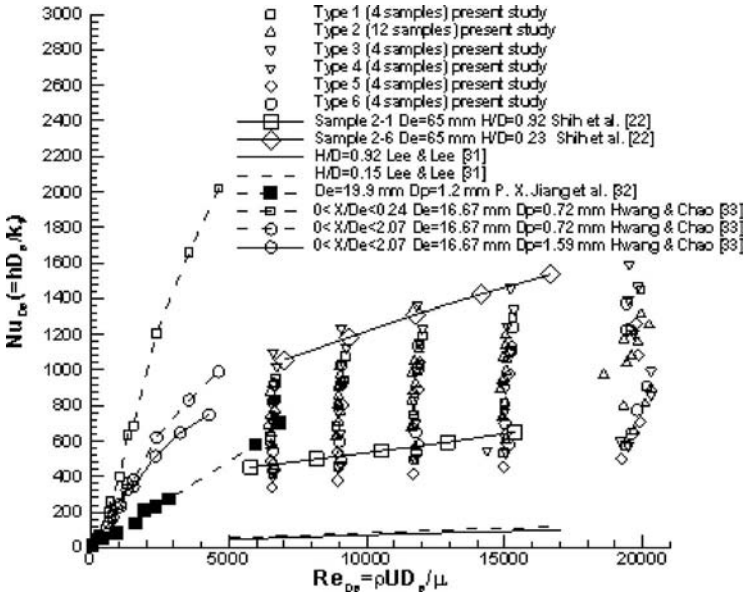

Fig. 14 Comparison of the results from this work and previous studies

the height of the flow outlet is reduced, the reduction in the gas-phase temperature is much larger than that in the solid-phase temperature, as shown in Table 4.

The comparison of the results of the present study, that of air impinging on a flat surface by Lee and Lee [31], and the forced convective heat transfer in sintered porous plate channels [32,33] and in aluminum-foam heat sinks [22] is shown in Fig. 14. Following the notation used in [25], the Nusselt and the Reynolds numbers in Fig. 14 are based on the hydraulic diameter and gas conductivity, as shown in the legend of Fig. 14.

The results in Fig. 14 show that the use of metal foam enhances the heat transfer significantly. The Nusselt number with metal foam is about 6.5–20.4 times larger than that with an impinging jet alone. The dependence of Nu_{De} on Re_{De} is similar for both studies; the Nu_{De} increases with the increase of Re_{De}, and the effect of the height is similar as well. For an impinging jet, the Nu_{De} increases monotonically with the decrease of the height of the jet. For the aluminum-foam heat sinks discussed in Fig. 14, the Nu_{De} also increases with the decrease of the height of the flow outlet.

Figure 14 also compares the results from the present study and the studies of the forced convective heat transfer in sintered porous plate channels [32,33]. As shown, although the flow pattern and materials are different, the measured Nu_{De} is in the same order of magnitude [33]. The Nu_{De} for sintered porous plate channels shows a higher Re_{De} dependence than that for the axisymmetric aluminum-foam heat sink mentioned in the present study. The results from this study are very similar to that from the study by Shih et al. [22].

Summary and Conclusions

In this work, the enhanced heat transfer characteristics of aluminum-foam heat sinks, introduced by the use of a flow-restricting mask are investigated experimentally under impinging-jet flow conditions. The heat transfer performance of the aluminum-foam heat sink could be enhanced by lowering either the conductive resistance in the solid phase or convective resistance at the gas-solid interface of the aluminum foam. The use of the flow-restricting mask guides the cooling air toward the heat-generation surface and the convective resistance is therefore reduced through the increased velocity near the heat-generation surface. This enhances the cooling performance of the heat sink and the local thermal nonequilibrium condition near the heat-generation surface. The effect of the flow outlet height on the cooling performance is found to be larger than that of the pore density, the porosity, and the length of the aluminum-foam heat sink. Because of to this strong effect, the dimensionless flow outlet height is included in the empirical correlation for the Nusselt numbers based on the measured data of 32 different types of aluminum-foam heat sinks. Based on this correlation, the Nusselt number is proportional to the Reynolds number (based on the equivalent spherical diameter of the aluminum foam) raised to a power of 0.49 and inversely proportional to the dimensionless flow outlet height raised to a power of 0.354. The Nusselt number also increases with the decrease in the pore density and the increase of the air velocity.

Acknowledgment

This paper represents part of the study results obtained by the work supported in the National Science Council of Taiwan, R.O.C. under Contract No. NSC-90-2212-E-194-038.

Nomenclature

D = pipe diameter of the air inlet pipe, m
D_p = equivalent spherical diameter of porous media, m
d_p = mean pore diameter, m
$\bar{h}$ = mean convective heat transfer coefficient, $\mathrm{W/m^2\,^\circ C}$
K_x = permeability in the direction perpendicular to the flow
K_y = permeability in the direction parallel to the flow
k_x = thermal conductivity of the porous material in the direction perpendicular to the flow
k_y = thermal conductivity of the porous material in the direction parallel to the flow
k = effective thermal conductivity, W/m K
H = height of the total test section, m
H_n = normalized height of flow outlet, $=H_{\mathrm{out}}/H$
H_{out} = height of flow outlet, m
Nu = Nusselt number
PPI = pores per inch
r = position along radius direction, m
R = thermal resistance, K/W

Re = Reynolds number
Q = flow rate, m^3/s
q = waste heat transfer rate, W
$\dot{q}$ = heat flux through the bottom of aluminum-foam heat sink
T = temperature, K
U = average velocity, m/s
$\bar{u}$ = calculated average outlet velocity in Eq. (8), m/s
z = position along axial direction, m

Greek Symbols

μ = viscosity
ε = porosity
Δ = difference

Subscripts

air = air properties
e = estimate
f = fluid
in = inlet condition
I = electric current, A
out = outlet condition
s = solid
V = voltage
W = wall
∞ = ambient condition

References

[1] Chao, C.-H., and Li, J.-M., "Foam-Metal Heat Sinks for Thermal Enhanced BGA Package Applications," *11th International Symposium on Transport Phenomena ISTP-II*, Hsinchu, Taiwan, Vol. 4, pp. 23–29.

[2] Chou, S.-F., and Yang, C.-H., 1993, "Heat Transfer Characteristics of Aluminum Foam Metal," *Proc. of Sixth International Symposium on Transport Phenomena in Thermal Engineering*, Seoul, Begell House Inc., Seoul, pp. 709–714.

[3] Lee, Y. C., Zhang, W., Xie, H., and Mahajan, R. L., 1993, "Cooling of a FCHIP Package With 100 W, 1 cm_2 Chip," *Proc. of the 1993 ASME Int. Elec. Package Conf.*, ASME, New York, Vol. 1, 419–423.

[4] Calmidi, V. V., 1998. "Transport Phenomena in High Porosity Fibrous Metal Foams," Ph.D. thesis, Department of Mechanical Engineering, Graduate School of the University of Colorado.

[5] Ould-Amer, Y., Chikh, S., Bouhadef, K., and Lauriat, G., 1998, "Forced Convection Cooling Enhancement by Use of Porous Materials," Int. J. Heat Fluid Flow, **19**, pp. 251–258.

[6] Tien, C. L., and Kuo, S. M., 1998, "Analysis of Forced Convection in Microstructures for Electronic System Cooling," *Cooling Technology for Electronic Equipment*, Win Aung, ed., Hemisphere Co., pp. 285–294.

[7] Bhattacharya, A., and Mahajan, R. L., 2002, "Finned Metal Foam Heat Sinks for Electronics Cooling in Forced Convection," ASME J. Electron. Packag., **124**, pp. 155–163.

[8] Lee, K. B., and Howell, J. R., 1991, "Media Theoretical and Experimental Heat and Mass Transfer in Highly Porous Media," Int. J. Heat Mass Transfer, **34**(8) pp. 2123–2132.

[9] Mohamad, A. A., 2003. "Heat Transfer Enhancements in Heat Exchangers Fitted With Porous Media, Part I: Constant Wall Temperature," Int. J. Therm. Sci., **42**, 385–395.

[10] Gobin, D., Goyeau, B., and Neculae, A., 2005, "Convective Heat and Solute Transfer in Partially Porous Cavities," Int. J. Heat Mass Transfer, **48**, pp. 1898–1908.

[11] Calmidi, V. V., and Mahajan, R. L., 2000, "Forced Convection in High Porosity Metal Foams," ASME J. Heat Transfer, **122**, pp. 557–565.

[12] Kim, S. Y., Paek, J. W., and Kang, B. H., 2003, "Thermal Performance of Aluminum-Foam Heat Sinks by Forced Air Cooling," IEEE Trans. Compon. Packag. Technol., **26**(1) pp. 262–267.

[13] Xu, Y., Luo, X., and Chung, D. D. L., 2000, "Sodium Silicate Based Thermal Interface Material for High Thermal Contact Conductance," ASME J. Electron. Packag., **122**, pp. 128–131.

[14] Kabus, C. J., and Wedekind, G. L., 2001, "An Experimental Investigation Into Natural Convection Heat Transfer From Horizontal Isothermal Circular Disks," Int. J. Heat Mass Transfer, **44**, pp. 3381–3384.

[15] Kim, S. Y., Kang, B. H., and Kim, J. H., 2001, "Forced Convection From Aluminum Foam Materials in An Asymmetrically Heated Channel," Int. J. Heat Mass Transfer, **44**, pp. 1451–1454.

[16] Angirasa, D., 2002, "Experimental Investigation of Forced Convection Heat Transfer Augmentation With Metallic Fibrous Materials," Int. J. Heat Mass Transfer, **45**, pp. 919–922.

[17] Ledezma, G., and Bejan, A., 1996, "Heat-Sinks With Sloped Plate Fins in Natural and Forced Convection," Int. J. Heat Mass Transfer, **39**(9), pp. 1773–1783.

[18] Kim, S. Y., Koo, J. M., and Kuznetsov, A. V., 2001, "Effect of Anisotropy in Permeability and Effective Thermal Conductivity on Thermal Performance of an Aluminum Foam Heat Sink," Numer. Heat Transfer, Part A, **40**, pp. 21–36.

[19] Zhou, D. W., and Lee, S. J., 2004, "Heat Transfer Enhancement of Impinging Jets Using Mesh Screens," Int. J. Heat Mass Transfer, **47**, pp. 2097–2108.

[20] Jeng, T. M., and Tzeng, S. C., 2005, "Numerical Study of Confined Slot Jet Impinging on Porous Metallic Foam Heat Sink," Int. J. Heat Mass Transfer, **48**, pp. 4685–4694.

[21] Hsieh, W. H., Wu, J. Y., Shih, W. H., and Chiu, W. C., 2004, "Experimental Investigation of Heat-Transfer Characteristics of Aluminum-Foam Heat Sinks," Int. J. Heat Mass Transfer, **47**, pp. 5149–5157.

[22] Shih, W. H., Chiu, W. C., and Hsieh, W. H., 2006, "Height Effect on Heat-Transfer Characteristics of Aluminum-Foam Heat Sinks," ASME J. Heat Transfer, **128**, pp. 530–537.

[23] Richardson, J. T., Peng, Y., and Remue, D., 2000, "Properties of Ceramic Foam Catalyst Supports: Pressure Drop," Appl. Catal., A, **204**, pp. 19–32.

[24] Wu, W. T., Liu, J. F., Chiu, W. C., and Hsieh, W. H., 2006, "Measurement and Correlation of Friction Characteristic of Flow Through Foam Matrixes," Exp. Therm. Fluid Sci., **30**, pp. 329–336.

[25] Calmidi, V. V., and Mahajan, R. L., 1999, "The Effective Conductivity of High Porosity Fibrous Metal Foams," ASME J. Heat Transfer, **121**, pp. 466–471.

[26] Incropera, F. P., 1996, *Introduction to Heat Transfer*, 3rd ed., Wiley, p. 462.

[27] Freund, J. E., and Simon, G. A., 1970, *Statistics—A First Course*, 6th ed., Prentice Hall, Englewood Cliffs, p. 455.

[28] Kline, S. J., and McClintock, F. A., 1953, "Describing the Uncertainties in Single Sample Experiments," Mech. Eng. (Am. Soc. Mech. Eng.), **75**, pp. 3–8.

[29] Benediet, R. P., 1984, *Fundamentals of Temperature, Pressure and Flow Measurements*, Wiley, New York.

[30] Vafai, K., and Sozen, M., 1990, "Analysis of Energy and Momentum Transport for Fluid Flow Through a Porous Bed," ASME J. Heat Transfer, **112**, pp. 690–699.

[31] Lee, J., and Lee, S.-J., 1999, "Stagnation Region Heat Transfer of A Turbulent Axisymmetric Jet Impinging," Exp. Heat Transfer, **12**, pp. 137–156.

[32] Jaing, P.-X., Li, M., Lu, Y.-J., Yu, L., and Ren, Z.-P., 2004, "Experimental Research on Convection Heat Transfer in Sintered Porous Plate Channels," Int. J. Heat Mass Transfer, **47**, pp. 2085–2096.

[33] Hwang, G. J., and Chao, C. H, 1994, "Heat Transfer Measurement and Anlaysis for Sintered Porous Channels," ASME J. Heat Transfer, **116**, pp. 456–464.

Flow, Thermal, Energy Transfer, and Entropy Generation Characteristics Inside Wavy Enclosures Filled With Microstructures

Shohel Mahmud

Roydon Andrew Fraser

Department of Mechanical Engineering,
University of Waterloo,
Waterloo, ON, N2L 3G1, Canada

Ioan Pop

Faculty of Mathematics,
University of Cluj,
R-3400 Cluj,
CP 253, Romania

Flow, thermal, energy, and irreversibility characteristics inside wavy enclosures packed with microstructures are reported in this paper. It is assumed that the entire enclosure has sufficient and interconnected void spaces; those allow fluid movement inside the cavity. The Darcy momentum equation is selected for momentum transfer modeling by considering a relatively small pore Reynolds number (Re_p). *Modeled equations are solved numerically using the finite volume method. Streamlines, isothermal lines, energy streamlines, average Nusselt number, and average entropy generation number are calculated and displayed in order to show their dependency on and variation with Rayleigh number (Ra), surface waviness* (λ), *and aspect ratio* (A_R) *of the enclosure. Depending on the wall waviness pattern, the enclosure is divided into three modes (phase-plus, phase-zero, and phase-minus modes). However, for the current calculation, wall waviness is kept symmetric with respect to the vertical and horizontal centerlines of the enclosure.*
[DOI: 10.1115/1.2759976]

Keywords: energy streamline, irreversibility, natural convection, porous media, waviness

1 Introduction

Convective flow and heat transfer inside wavy geometries (channel, duct, enclosure, etc.) are largely divided into two major groups. The first group deals with the forced convection inside channels with periodically varying cross section along the longitudinal direction. The groundbreaking works of Sobey [1,2] reported numerical and experimental results of flow patterns inside a furrowed channel. A furrowed channel is a wavy walled channel that follows the cosine function. Later, Sobey reported oscillatory flow pattern [3] and flow separation characteristics [4] inside the wavy walled channel. Several extensions of Sobey's work on separation phenomenon [4] are reported in available literature [5–7]. Forced convection heat transfer results are also reported by several researchers [8–12]. The first group problems cover a wide range of applications; for example, flow through blood vessels, food industries, large industrial heat exchangers, etc.

In contrast, the relatively new second group deals with the natural convection problem in wavy walled enclosures. This group covers a wide range of significant engineering applications, for example, microelectromechanical device, microelectronic heat transfer cooling device, double-wall thermal insulation system, underground cable system, solar collector, electric machinery, etc. Significant contributions have been made by several researchers [13–23] to model the problems of this specific group. For example, natural convection inside a vertical opposite phase cavity [13], wavy cavity with different orientations [14,15], spatially variable wall temperature [16], inphase vertical and horizontal wavy cavities [17,18], entropy generation [15,17], flow heat transfer in Darcy porous medium filled wavy enclosure [19–21], non-Darcy porous medium [22,23], etc.

A wavy cavity filled with microstructures (for example, micropinfin, microsphere, bundle of capillary tubes, stack of fissures, particles of uniform size and shape, etc.) under natural convection can be modeled by Darcy momentum and energy equations as long as the local pore Reynolds number (Re_p), based on the local volume-averaged speed ($|\mathbf{v}|$) and $K^{1/2}$, is smaller than 1. Two example cases of such geometries are shown in Figs. 1(*a*) and 1(*b*). For a given aspect ratio (A_R), the average horizontal interwall spacing (W) and cavity height (H) in all geometric modes are same. The flow, thermal, energy, and entropy characteristics inside such cavities at any phase mode of the wall are largely affected by the geometric parameters (for example, wall waviness, phase of waviness, and aspect ratio) and flow parameters (for example, Rayleigh number). This paper considers only the symmetric waviness of the cavity walls. A wide range of Rayleigh number and wall waviness are selected for a limited aspect ratio of the cavity in order to characterize the distributions of Nusselt number (Nu_{av}), entropy generation number (Ns_{av}), and Bejan number (Be_{av}). In addition, streamlines, isothermal lines, and energy streamlines are presented at some selected parameters to facilitate our understanding of such characteristic numbers (Nu_{av}, Ns_{av}, and Be_{av}).

2 Mathematical Modeling

Figure 2 shows the problem schematic, the adopted coordinate system, and boundary conditions. The wavy walls are assumed to exactly follow a cosine curve, and a is the representative parameter for the surface waviness. It is assumed that the cavity is filled with the microstructures (see Figs. 1(*a*) and 1(*b*)) with sufficient void space for the fluid to circulate. It is further assumed that the fluid and microstructures are locally in thermal equilibrium. Uneven density of fluid originating from the temperature difference of the walls yields a buoyancy force and drives convection current. In laminar natural convection flow, the velocity components are usually small in magnitude. For example, if one considers the

Contributed by the Heat Transfer Division of ASME for publication in the JOURNAL OF HEAT TRANSFER. Manuscript received July 28, 2006; final manuscript received February 24, 2007. Review conducted by Jose L. Lage.

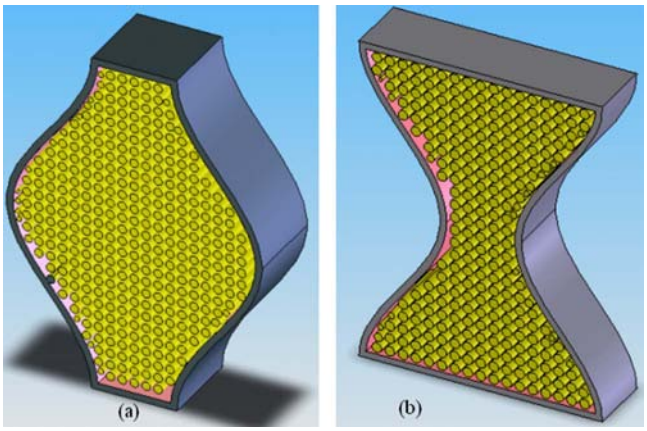

Fig. 1 Cross sections of wavy cavities packed with micropin-fins at (*a*) phase-plus mode and (*b*) phase-minus mode

maximum pore velocity, $u_p=0.1\ \mathrm{m\ s^{-1}}$; porosity (void volume/total volume), $\varphi=0.5$; kinematic viscosity of air, $\nu=1.5\times10^{-5}\ \mathrm{m^2\ s^{-1}}$; characteristic length of the microstructure or the void space, $d_p=500\ \mu\mathrm{m}$; and permeability $K=\varphi d_p^2/18(1-\varphi)$ (which roughly describes the permeability of packed sphere or circular disk in enclosures), the pore Reynolds number is approximately equal to 0.7856. Therefore, Darcy law (Eq. (1)) is suitable for modeling the momentum transfer inside the cavity

$$\mathbf{v}=\frac{K}{\mu}(-\nabla p+\rho\mathbf{g}) \tag{1}$$

Taking the curl on the both sides of Eq. (1) after using the assumptions, $\mathbf{v}=u\mathbf{i}+v\mathbf{j}$ and $\mathbf{g}=+g_y\mathbf{j}$, results in

$$\frac{\partial u}{\partial y}-\frac{\partial v}{\partial x}=-\frac{g\beta K}{\nu}\frac{\partial T}{\partial x} \tag{2}$$

where $g=g_y$. The energy equation [24] is

$$\sigma\frac{\partial T}{\partial t}+u\frac{\partial T}{\partial x}+v\frac{\partial T}{\partial y}=\alpha_m\left(\frac{\partial^2 T}{\partial x^2}+\frac{\partial^2 T}{\partial y^2}\right) \tag{3}$$

Without any external or internal source, the equation of entropy generation [24,25] is

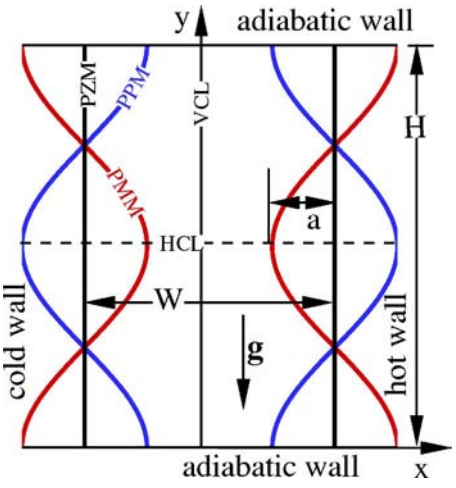

Fig. 2 Schematic of the problem under consideration with boundary conditions (PPM: phase plus mode, PZM: phase zero mode, PMM: phase minus mode, HCL: horizontal centerline, VCL: vertical centerline)

$$S'''_{\mathrm{gen}}=\frac{k}{T_0^2}\left[\left(\frac{\partial T}{\partial x}\right)^2+\left(\frac{\partial T}{\partial y}\right)^2\right]+\frac{\mu}{KT_0}(u^2+v^2) \tag{4}$$

Finally, the equation for energy flux density vector [26] is

$$\dot{\mathbf{E}}=E_x\mathbf{i}+E_y\mathbf{j}=\rho\mathbf{v}\left[\frac{1}{2}|\mathbf{v}|^2+C_p(T-T_c)\right]-k\ \mathbf{grad}(T) \tag{5}$$

Introducing the following dimensionless parameters

$$X=\frac{x}{W},\quad Y=\frac{y}{W},\quad U=\frac{u}{u_0},\quad V=\frac{v}{u_0},\quad \Theta=\frac{T-T_c}{T_h-T_c},$$
$$\tau=\frac{t}{\sigma W^2/\alpha_m},\quad u_0=\mathrm{Ra}\frac{\alpha_m}{W} \tag{6}$$

Eqs. (2)–(4) can be written, in their nondimensional forms, as

$$\frac{\partial^2\Psi}{\partial X^2}+\frac{\partial^2\Psi}{\partial Y^2}=-\frac{\partial\Theta}{\partial X} \tag{7}$$

$$\frac{\partial\Theta}{\partial\tau}+\frac{\partial\Psi}{\partial Y}\frac{\partial\Theta}{\partial X}-\frac{\partial\Psi}{\partial X}\frac{\partial\Theta}{\partial Y}=\frac{1}{\mathrm{Ra}}\left(\frac{\partial^2\Theta}{\partial X^2}+\frac{\partial^2\Theta}{\partial Y^2}\right) \tag{8}$$

and

$$Ns=\frac{S'''_{\mathrm{gen}}}{S'''_0}=\left[\left(\frac{\partial\Theta}{\partial X}\right)^2+\left(\frac{\partial\Theta}{\partial Y}\right)^2\right]+\frac{\mathrm{Ec}\times\mathrm{Pr}}{\Omega}\left[\left(\frac{\partial\Psi}{\partial X}\right)^2+\left(\frac{\partial\Psi}{\partial Y}\right)^2\right]$$
$$=Ns_{\mathrm{T}}+Ns_{\mathrm{F}} \tag{9}$$

The definitions of different parameters in Eqs. (7)–(9) are as follows:

$$\frac{\partial\Psi}{\partial Y}=U,\quad \frac{\partial\Psi}{\partial X}=-V,\quad S'''_0=\frac{k(\Delta T)^2}{W^2T_0^2},\quad \mathrm{Ra}=\frac{g\beta\Delta TWK}{\alpha_m\nu},$$
$$\mathrm{Ec}=\left(\frac{\alpha_m}{W}\right)^2\frac{C_p}{\Delta T},\quad \Omega=\frac{\Delta T}{T_0} \tag{10}$$

Equations (7) and (8) are solved numerically using the following boundary conditions:

$$\tau\geq0,\quad Y=0,\quad -\left(\frac{1}{2}-\lambda\right)\leq X\leq\left(\frac{1}{2}-\lambda\right):\Psi=0,\quad \frac{\partial\Theta}{\partial n}=0 \tag{11a}$$

$$\tau\geq0,\quad Y=A_R,\quad -\left(\frac{1}{2}-\lambda\right)\leq X\leq\left(\frac{1}{2}-\lambda\right):\Psi=0,\quad \frac{\partial\Theta}{\partial n}=0 \tag{11b}$$

$$\tau\geq0,\quad 0\leq Y\leq A_R,\quad X=-\left(\frac{1}{2}-\lambda\right)$$
$$-\lambda\left[1+\cos\left(\frac{2\pi Y}{A_R}\right)\right]:\Psi=0,\quad \Theta=0 \tag{11c}$$

$$\tau\geq0,\quad 0\leq Y\leq A_R,\quad X=\left(\frac{1}{2}-\lambda\right)$$
$$+\lambda\left[1+\cos\left(\frac{2\pi Y}{A_R}\right)\right]:\Psi=0,\quad \Theta=1 \tag{11d}$$

where $\lambda(=a/W)$ and $A_R(=H/W)$ are the dimensionless waviness and aspect ratio, respectively.

A control volume based finite volume method [27] is used to solve the governing equations. A nonstaggered and nonuniform grid system is used with a higher mesh density near the walls. The tridiagonal matrix algorithm (TDMA) solver solves discretized and linearized equation systems. For unsteady terms, the Crank–Nicolson method [27] is applied. The whole computational do-

main is subdivided by unequally spaced nonrectangular control volumes. Four grid sizes (64×64, 80×80, 100×100, and 160×160) are selected for analysis. The average Nusselt number for all four grid sizes are monitored at $\mathrm{Ra}=10^3$, $A_R=1.0$, and $\lambda=0$. The magnitude of the average Nusselt number at 160×160 grids shows very little difference with the result obtained from 100×100 grids. For the rest of the calculations in this paper, a grid size of 160×160 is selected for better accuracy. The time increment ($\Delta\tau$) is 10^{-4} in most cases; but sometimes, especially at high Ra and λ, smaller time steps are selected in order to ensure the result accuracy. The code validation test is already reported in Mahmud and Fraser [25] and is not repeated here.

3 Results and Discussion

Numerical simulation is carried out for 30 Rayleigh numbers ($1\le\mathrm{Ra}\le10^3$), 21 wall waviness ($-0.25\le\lambda\le0.25$), and 11 aspect ratios ($0.25\le A_R\le4$). For each case, calculation is started from a motionless isothermal state ($U=V=0$ and $\Theta=0.5$) of fluid and advanced in time. Results are reported only when the steady-state solution is achieved. The entropy generation rate is calculated using Eq. (9) once the steady-state values of Ψ and Θ are available. In order to calculate the energy streamfunction, a Poisson equation of type $\nabla^2\Phi=(\nabla\times\dot{\mathbf{E}})\cdot\hat{\mathbf{k}}$ is solved, where $\dot{\mathbf{E}}$ is calculated from Eq. (5) from the steady-state field data of velocity and temperature and Φ is the energy stream function.

3.1 Influence of Ra on Flow, Thermal, and Energy Fields. At some point in time ($\tau>0$), the right and left wall temperatures are instantly changed to 1 and 0, respectively. This instant temperature change introduces near-wall heat conduction close to the wavy walls. Convection is absent or negligible at this stage. If the near-wall heat conduction is limited to a distance δ from the wavy walls, then it is possible to show that $\delta\sim\sqrt{\alpha_m t/\sigma}$ by a scale analysis of the energy equation (Eq. (3)). The expression, $\delta\sim\sqrt{\alpha_m t/\sigma}$, which dictates a balance between the first and fourth term of Eq. (3), concludes that the thickness δ increases with time. However, after some time the fluid near the hot wall is heated up and near the cold wall is cooled down due to continuous near-wall conduction, and consequently, a buoyancy force develops. This buoyancy force pushes the fluid upward near the hot wall and downward near the cold wall, resulting in a circulatory motion inside the cavity. The finite fluid velocity inside the cavity facilitates to perform a second scale analysis of the momentum equation (Eq. (2)), which dictates a balance between the second and third terms of Eq. (2) and results in a scale of velocity of the form $u_0\sim Kg\beta\Delta T/\nu=\mathrm{Ra}(\alpha_m/W)$. The expression of u_0 (also the velocity scale) suggests that the buoyancy effect is stronger inside the cavity at higher Rayleigh numbers.

A stronger circulation is expected (see the value of strength of circulation, $\Psi_{\max}$, in Fig. 3) at higher Rayleigh numbers, which, in turn, affects the thermal field. For three selected values of λ, Fig. 3 shows the distribution of streamlines at three selected Rayleigh numbers. For convenience of presentation, stream-function values for each case are divided by $\Psi_{\max}$ so that the modified stream function ($\Psi^*=\Psi/\Psi_{\max}$) can vary from 0 to 1 only. The corresponding isothermal lines are presented in Fig. 4. Twenty isolines (with a difference of 0.05 between two consecutive isolines) are plotted in each of the individual parts of Figs. 3 and 4.

It is a traditional practice to use streamline and isothermal line together to describe the characteristics of flow and thermal fields in convection heat transfer problems. These isolines, however, are inappropriate in many situations for attempting to understand the energy flow mechanisms in convection problems. Combining the thermal diffusion and enthalpy flow, Kimura and Bejan [28] proposed "heatline," which is a powerful alternate way to visualize thermal energy flow. The concept of heatline is extended later for many other situations by several researchers; for example, see Costa [29,30]. The energy streamlines, which include the kinetic energy (see Eq. (5)) to the thermal energy, is a powerful visualization technique of total energy in a convection heat transfer problem. For some selected parameters, Fig. 5 shows the energy streamline distribution pattern inside the cavity. It is beneficial for discussion if one considers Figs. 3–5 together. At a very low Rayleigh number, convective motion is nearly absent inside the cavity. Therefore, conduction is the dominating mode of heat transfer. The symmetric streamline distribution exhibits very low strength at such a low Ra. For example, at $\mathrm{Ra}=1$ and $\lambda=0.25$, the strength of circulation is 68 and 276 times weaker than the flow strengths at $\mathrm{Ra}=100$ and $\mathrm{Ra}=1000$, respectively. Fluids, close to the walls, nearly follow the walls' geometry at low Rayleigh number. Without wall waviness ($\lambda=0.0$), the center region of the cavity at low Ra (see Fig. 3(*d*)) is characterized by a nearly circular streamline distribution, which becomes elliptic for nonzero λ. Isothermal lines at low Ra shows nearly symmetric conduction-type distribution (see Figs. 4(*a*), 4(*d*), and 4(*g*)).

The energy streamline distribution at small Ra is very much suitable, in an alternate way, to understanding the flow field and thermal field patterns. At vanishingly small Rayleigh number ($\mathrm{Ra}\to0$) the energy streamline simply reduces to the heat flux line ($\dot{\mathbf{E}}\approx-k\,\mathbf{grad}(T)$, from Eq. (5)). As observed in Fig. 5(*d*), the energy streamlines originate at the hot wall, remain parallel to the adiabatic wall inside the cavity, and finally intersect the cold wall. For the case of nonzero wall waviness (Figs. 5(*a*) and 5(*g*)), the energy streamlines originate at the hot wall's normal direction and follow curved paths (symmetric to the horizontal centerline of the cavity), and finally intersect the cold wall. In order to keep the heat flux constant along a particular energy streamline, the energy streamline follows a curve path inside the wavy cavity due to the variable interwall spacings along the vertical direction.

Flow inside the cavity is characterized by the stretched core region when Ra increases. The near-symmetric pattern of the streamline distribution distorts with increasing Ra. Fluid decelerates in the phase-plus mode and accelerates in the phase-minus mode near the horizontal centerline. In effect, isothermal lines are distorted and lost their symmetricity and, in turn, start turning back to the cold wall at the upper part and to the hot wall at the lower part (with respect to the horizontal centerline) of the cavity due to the strong horizontal jet. In the phase-zero mode, the concentration of isothermal lines occurs near the bottom of the hot wall and top of the cold wall and, consequently, these concentrated isothermal lines initiate the so-called thermal spot [13,15,18] in the cavity. The thermal spot high-temperature gradient causes a high heat transfer rate. The length of the thermal spot increases with increasing Ra. In the phase-minus mode, the accelerated fluid near the horizontal centerline of the cavity introduces thermal spots even earlier than the phase-zero mode. Therefore, the heat transfer rate is higher near the centerline of this mode of geometry. However, in the phase-plus mode, fluid deceleration restricts to form any thermal spot near the horizontal centerline of the cavity.

If Ra increases further, fluid in a large portion of the cavity near horizontal centerline becomes almost motionless for the phase-plus and phase-zero modes. This motionless region is small in the phase-minus mode. It is seen in Figs. 3(*c*), 3(*f*), and 3(*i*) that the concentration of streamlines (higher flow rate) is high near the vertical walls, which, in turn, introduces the thermal boundary layer as observed in Figs. 4(*c*), 4(*f*), and 4(*i*).

Some of the issues already described in the preceding paragraphs will be well understood if one considers the energy streamline distribution again. At relatively higher Ra, kinetic energy starts contributing to the total energy. The contribution of kinetic energy will be well understood if one considers the following nondimensional form of $\dot{\mathbf{E}}$:

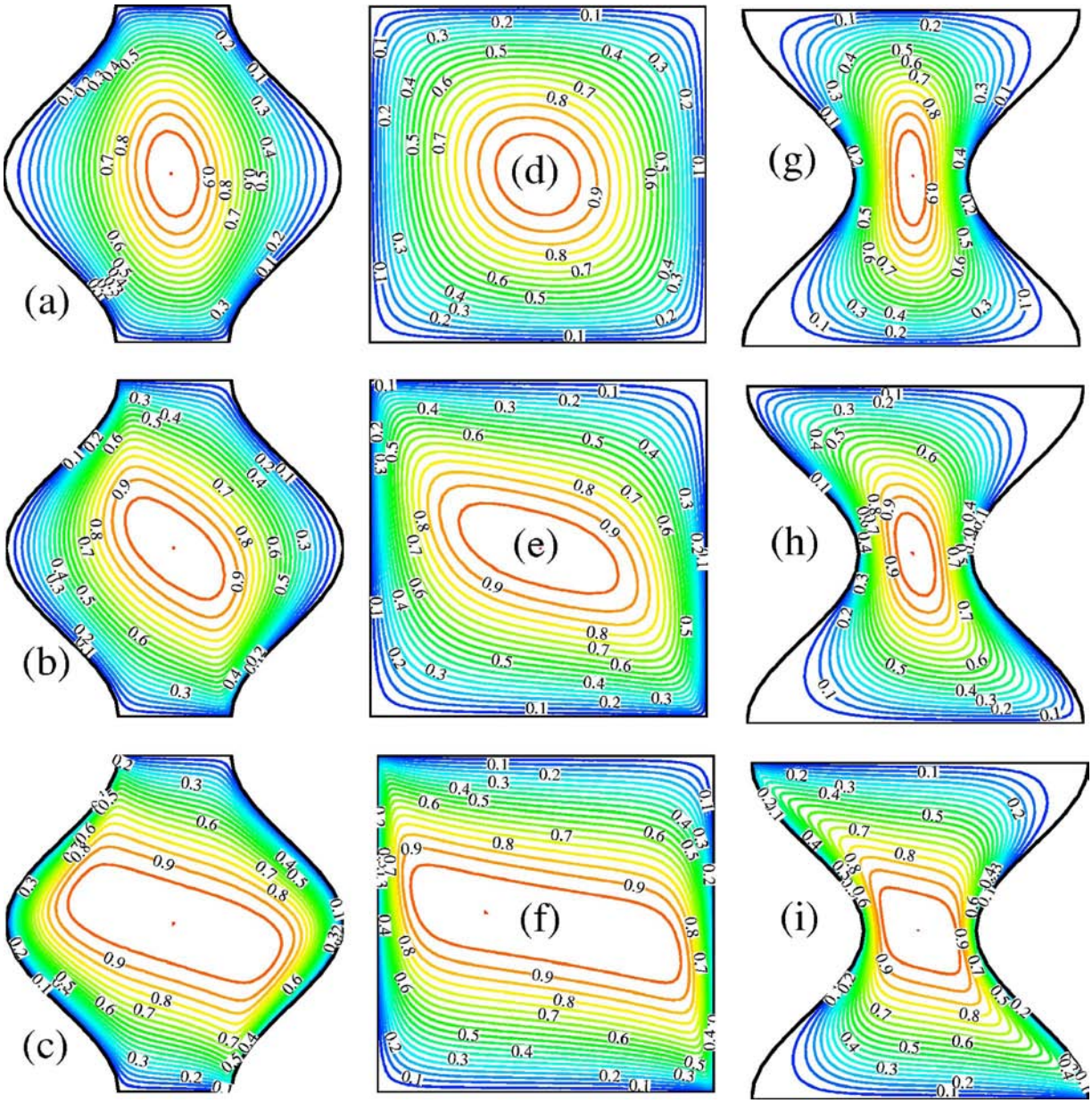

Fig. 3 Streamlines at (*a*) Ra=10, λ=0.25(Ψ_{max}=0.783); (*b*) Ra=100, λ=0.25(Ψ_{max}=5.42); (*c*) Ra=1000, λ=0.25(Ψ_{max}=21.81); (*d*) Ra=10, λ=0.0(Ψ_{max}=0.7178); (e) Ra=100, λ=0.0(Ψ_{max}=4.707); (*f*) Ra=1000, λ=0.0(Ψ_{max}=20.48); (*g*) Ra=10, λ=−0.25(Ψ_{max}=0.59); (*h*) Ra=100, −0.25(Ψ_{max}=4.259); and (*i*) Ra=1000, −0.25(Ψ_{max}=18.84). Aspect ratio A_R=1.

$$\frac{\dot{\mathbf{E}}}{\mathrm{E}_0} = \mathrm{EcRa}\left[\mathbf{V}\frac{1}{2}|\mathbf{V}|^2\right] + \mathrm{Ra}(\mathbf{V}\Theta) - \mathbf{grad}(\Theta) \tag{12}$$

where Ec is the Eckert number ($=u_0^2/C_p\Delta T$) and E_0 is the reference energy flux density ($=k\Delta T/W$). The relative magnitudes of kinetic energy (first term on the right-hand side of Eq. (12)) and convective thermal energy (second term) are compared to the conductive thermal energy (third term) because conduction is always present, whatever its magnitude. At moderate and high Ra, the convective thermal energy term is always finite and dominating. However, the kinetic energy may remain small due to the fact that the product EcRa is negligible at small and moderate Ra. At a comparatively high Ra, all three energy terms contribute to the total energy. Hot and cold walls act as a source and sink of energy, respectively. As these walls only allow thermal energy to cross as heat conduction, energy streamlines originate at the hot wall and leave through the cold wall as depicted in Fig. 5. The influence of convective thermal energy is nearly visible at Ra=10 (see Figs. 5(*b*), 5(*e*), and 5(*h*)). At high Ra, the influence of kinetic energy is also visible. For example, at Ra=100 (see Figs. 5(*c*), 5(*f*), and 5(*i*)), the closed energy streamlines indicate the dominance of kinetic energy at some regions of the cavity. The closed energy streamlines also indicate the trapped form of energy [31].

3.2 Influence of Ra on Local and Global Heat Transfer Rates. The local Nusselt number (Nu_L) calculates the local heat transfer rate and its expression is given by

$$\mathrm{Nu}_L = \frac{W}{k}h_L = \frac{W}{k}\left\{\frac{k}{\Delta T}\left(\frac{\partial T}{\partial n}\right)_{\text{hot wall}}\right\} = \left(\frac{\partial \Theta}{\partial \hat{n}}\right)_{\text{hot wall}} \tag{13}$$

where n and $\hat{n}$ represent the normal distances from the hot wall. The global or average heat transfer rate is calculated in terms of average Nusselt number (Nu_{av}) using the following integration:

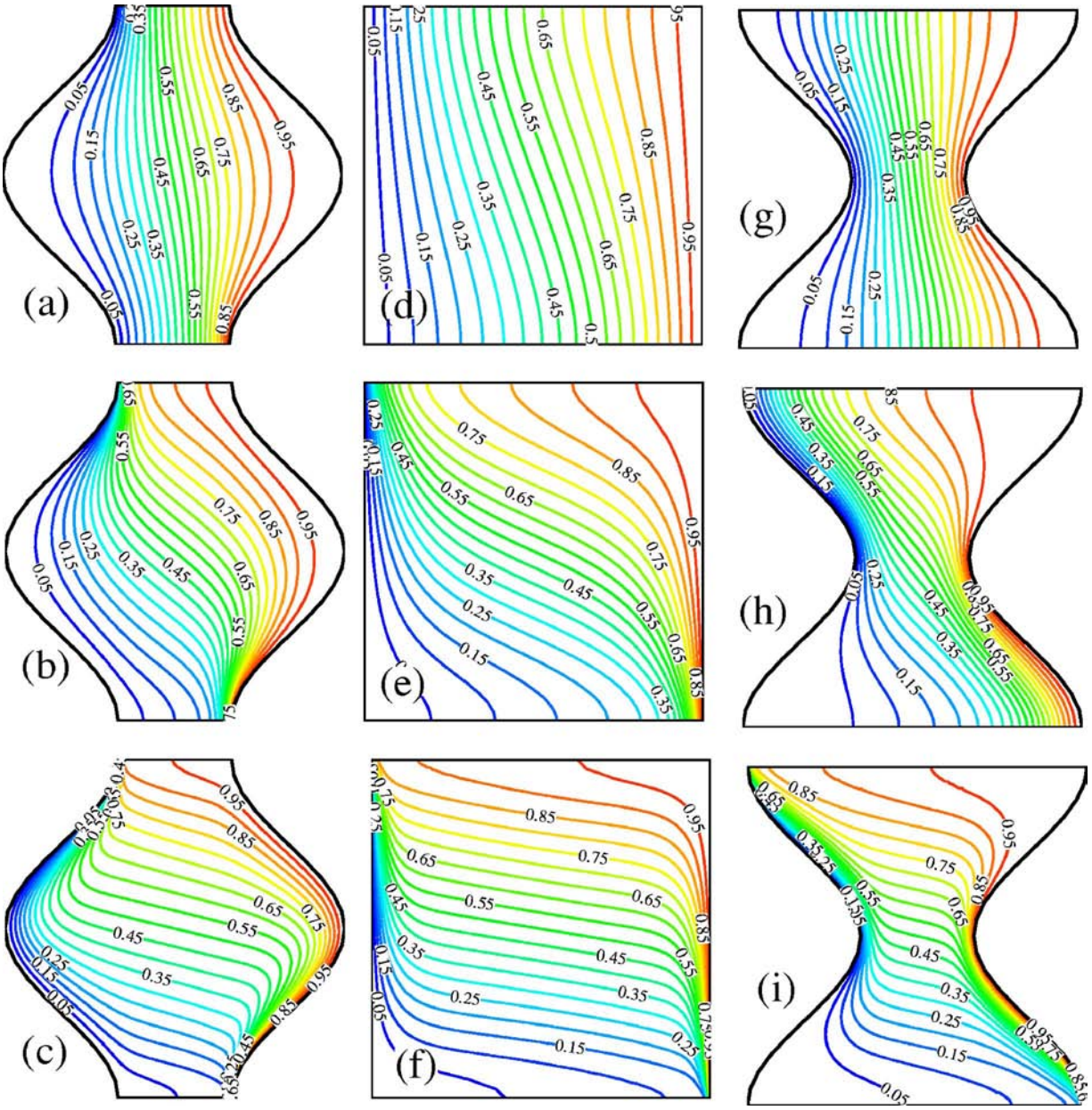

Fig. 4 Isothermal lines at (*a*) Ra=10, λ=0.25; (*b*) Ra=100, λ=0.25; (*c*) Ra=1000, λ=0.25; (*d*) Ra=10, λ=0.0; (*e*) Ra=100, λ=0.0; (*f*) Ra=1000, λ=0.0; (*g*) Ra=10, λ=−0.25; (*h*) Ra=100, λ=−0.25; (*i*) Ra=1000, λ=−0.25. Aspect ratio A_R=1.

$$\mathrm{Nu}_{av} = \frac{1}{S}\int_0^S \mathrm{Nu}_L ds, \quad \text{where} \quad S = \int_0^A \sqrt{1+\left(\frac{dX}{dY}\right)^2}\, dY = \frac{A^2 + 2\lambda^2\pi^2}{A} \tag{14}$$

where s represents the variable arc length along the hot wavy wall and S is the total arc length. For λ=−0.25, 0.0, and 0.25, Fig. 6 shows the variation in Nu_L with Y at Ra=1 and 100, respectively. In dominating conduction mode (Ra=1) of heat transfer, the distribution of Nu_L is nearly symmetric with respect to the vertical centerline of the cavity. For λ=0.0 at Ra=1, isotherms are nearly parallel to the hot wall, which results in a constant temperature gradient along the hot wall and, therefore, Nu_L is almost constant and equal to 1. For λ=0.25 at Ra=1, isotherms are close near the top and bottom parts of hot wall and symmetric about the horizontal centerline of the cavity, which results in the lowest temperature gradient at the center of the hot wall and gradually increasing temperature gradient along the hot wall toward the top and bottom adiabatic walls of the cavity. Therefore, Nu_L shows its maximum values near the intersections of hot wall with the adiabatic walls and minimum at the hot wall center. The reverse scenario is observed for λ=−0.25 at Ra=1. Nevertheless, when Nu_L is integrated over the arc length, the resulting values of Nu_{av} remain 1 due to the conduction dominating mode.

With the increase of Ra, convection starts to dominate and $\mathrm{Nu}_L - Y$ profiles lose their symmetric distribution patterns. The asymmetry in $\mathrm{Nu}_L - Y$ profiles originate from the convective distortion of isothermal lines as described in Sec. 3.1. Figure 6 shows the distribution of Nu_L at Ra=100 at three λ's. Nu_L is relatively higher in magnitude near the bottom part of the hot wall due the appearance of the thermal spot.

At the middle part of the cavity, due to the orientation of hot wall geometry and distribution of isothermal lines, Nu_L at phase-plus mode shows its minimum and, at phase-minus mode, shows its maximum value. When Nu_L is integrated over the arc length,

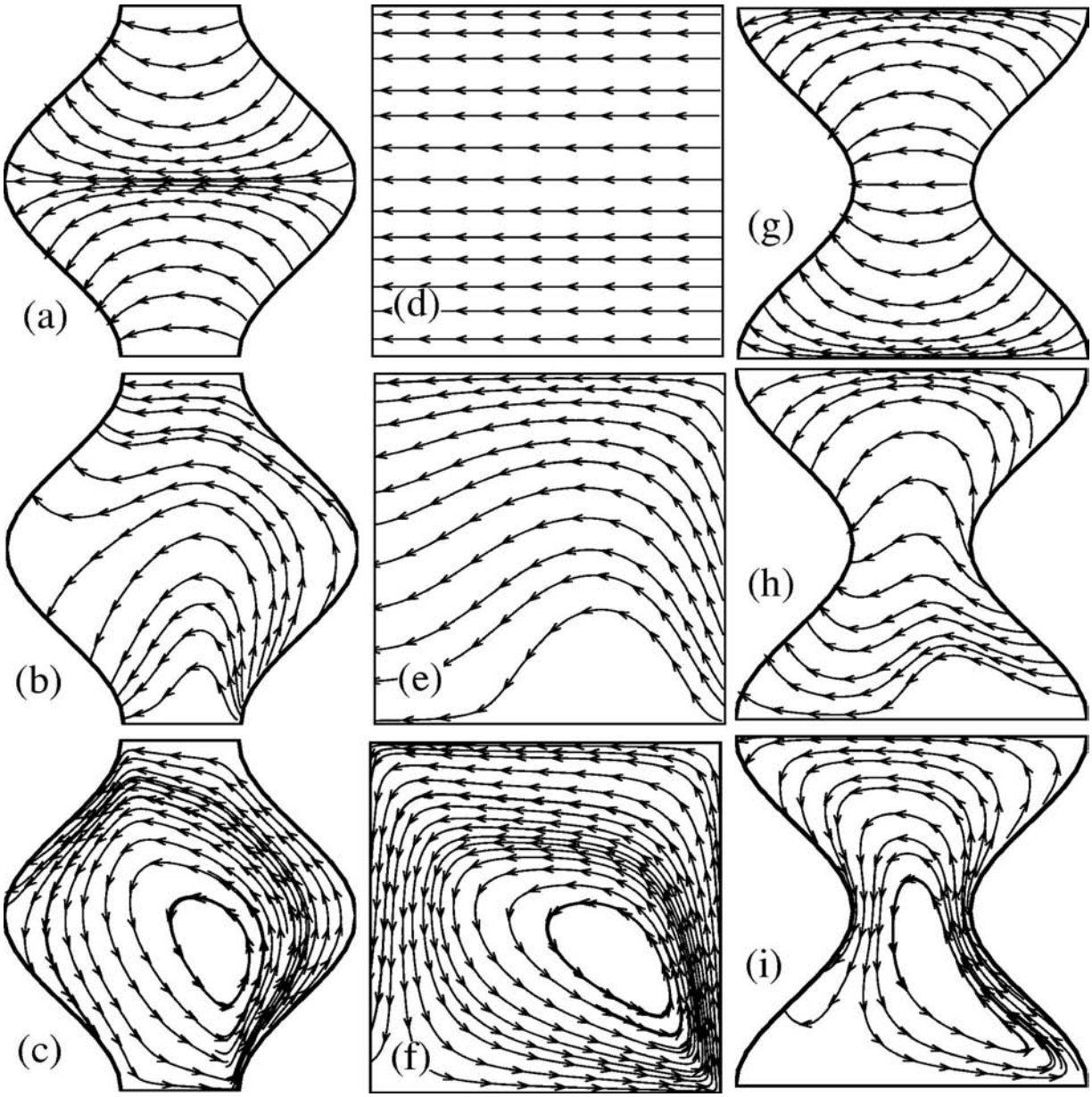

Fig. 5 Energy streamlines at (*a*) Ra=0, λ=0.25; (*b*) Ra=10, λ=0.25; (*c*) Ra=100, λ=0.25; (*d*) Ra=0, λ=0; (*e*) Ra=10, λ=0; (*f*) Ra=0, λ=0; (*g*) Ra=0, λ=−0.25; (*h*) Ra=10, λ=−0.25, and (*i*) Ra=100, λ=−0.25. Aspect ratio A_R=1.

the resulting Nu_{av} at λ=0.0 is larger than the Nu_{av} at λ=−0.25 and 0.25. This special case is also shown in Fig. 7 (see the Ra =100 line). In conduction regime (Ra≤10), Nu_{av} is unaffected by λ's variation and its magnitude is equal to 1. However, in convection regime, Nu_{av} increases with increasing Ra and, at a particular Ra, λ=0 produces the maximum Nu_{av} when compared to cases of nonzero λ. For a nonzero λ, the value of Nu_{av} is greater at phase-plus mode than the value at phase-minus mode.

The influence of λ on Nu_{av} is better understood from Fig. 8. For a particular Ra at convection regime (for example, Ra=250), Nu_{av} is minimum at the lowest value of selected λ(=−0.25). Nu_{av} increases with increasing λ and shows its maximum just after λ =0, and then decreases with further increases in λ. In the phase-minus mode, a considerable portion at the top right and bottom left corners of the cavity at moderate and high Ra shows isothermal stagnant fluid. Heat transfer across this stagnant fluid is negligible compared to the heat transfer across the fluid at other parts of the cavity. Therefore, Nu_{av} at the phase-minus mode is smaller in magnitude than the phase-plus mode provided that the value of $|\lambda|$ is fixed for both cases.

3.3 Influence of λ on Flow and Thermal Fields. In order to show the influence of λ on flow and thermal fields, Figs. 9(*a*)–9(*f*) display streamlines for six selected λ's, while Ra(=250) and A_R(=1.0) are kept constants. Corresponding isothermal lines are displayed in Figs. 10(*a*)–10(*f*). The strength of circulation (see value of Ψ_{max}) inside the cavity increases as one proceeds from Fig. 9(*a*) to Fig. 9(*f*). For this selected example case, the relative magnitude of circulation strength Ψ_0 (with respect to the strength at λ=0) and value of average kinetic energy (KE_{av}) are given in Table 1. The geometric orientation and complexity at λ=−0.25 offer the most resistance to the fluid flow for the selected λ's. This resistance is reduced, indicated by increasing KE_{av}, as the wavy walls become more straight in the phase-minus mode and ap-

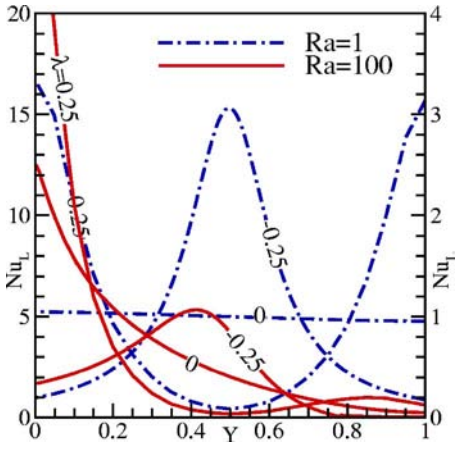

Fig. 6 Local Nusselt number distribution at Ra=1 (dashed-dotted lines) and Ra=100 (solid lines). The Nu_L labels at the right ordinate are for Ra=1 and at the left ordinate are for Ra =100.

proach the phase-zero mode. Therefore, the strength of circulation increases as the fluid gets more freedom to move inside the cavity due to the less resistance. However, in the phase-plus mode, the orientation of wall geometry assists fluid to flow with less resistance inside the cavity. Therefore, KE_{av} increases with increasing λ, which makes the circulation stronger inside the cavity.

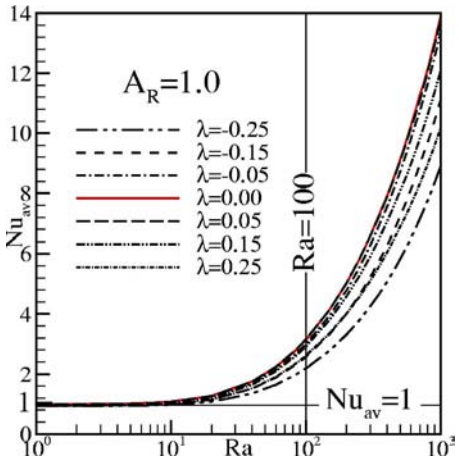

Fig. 7 Average Nusselt number as a function of Ra at different λ

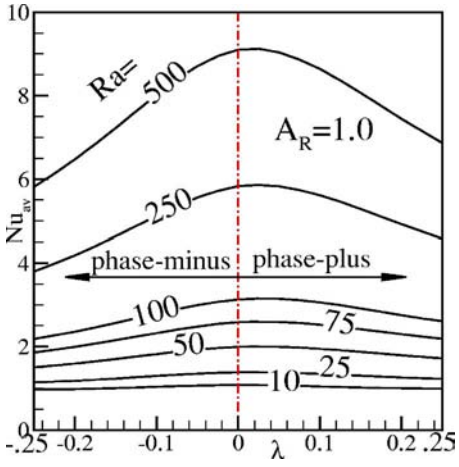

Fig. 8 Average Nusselt number as a function of λ at different Ra

Table 1 Magnitudes of relative maximum streamfunction Ψ_0 ($=\Psi_{max}/\Psi_{max,\lambda=0}$) and average kinetic energy KE_{av} ($=\forall^{-1}\int_{\forall}(u^2+v^2)d\forall$) at different λ for Ra=250 and A_R=1.

	Wall waviness, λ=								
	−0.25	−0.2	−0.15	−0.05	0.0	0.05	0.15	0.2	0.25
Ψ_0	0.909	0.922	0.938	0.965	1	1.038	1.074	1.099	1.123
KE_{av}	0.335	0.347	0.362	0.387	0.413	0.434	0.451	0.460	0.469

In the phase-minus mode, the core of counterclockwise circulation is stretched as $|\lambda|$ decreases from its maximum value (Fig. 9(*a*)) to minimum value (Fig. 9(*c*)). For the selected Ra(=250), the convective distortion of isothermal lines is clearly visible in Figs. 10(*a*)–10(*f*). Starting from the bottom right corner, the near-hot-wall fluid particles move up with acceleration due to the converging geometry of the cavity. These particles obtain their maximum velocities at the horizontal centerline and then decelerate in the diverging part of the cavity above the horizontal centerline. At the same time, the reverse situation occurs at the bottom portion of the cavity. The downward moving accelerated fluid particles near the cold wall create a horizontal jet (right to left) just below the top adiabatic wall. This horizontal jet pulls the decelerating fluid particles, moving upward near the hot wall and, consequently, creates a stagnant-isothermal fluid region at the upper right corner of the cavity. Representative patterns of velocity vectors, isothermal lines, and paths of ten particles at Ra=250 and λ=−0.25 are only shown in Fig. 11 for the magnified upper right region of the cavity.

The special cases selected for graphic illustration in Fig. 11 are intended to show several issues, namely, the magnitude of the velocity, stagnant-isothermal region, particle path, horizontal jet, and convective distortion of isothermal lines. Particles (filled circular symbols in Fig. 11) are released from an imaginary line (see Fig. 11) with equal distance between two consecutive particles. The time gap between two consecutive locations of particles in all particle paths is constant. Therefore, high concentration of circular symbols in a particle path indicates the slower moving particle, while the lower concentration indicates the faster moving particles. As discussed earlier, the velocity vectors in Fig. 11, immediately after the horizontal centerline and close to the hot wall, show high magnitudes. The faster moving particle P1 at that region becomes slower and slower as it moves up, exhibits its slowest motion when its path is very close to the stagnant-isothermal region, and passes quickly when it reach to the horizontal jet.

Similarly, the upward-moving accelerated fluid particles near the bottom part of the hot wall and downward-moving decelerated fluid particles near the bottom part of cold wall create the second stagnant-isothermal region near the lower left corner. The extent of the stagnant-isothermal fluid at the phase-minus mode (see Figs. 9(*a*)–9(*c*) and 10(*a*)–10(*c*)) decreases with decreasing $|\lambda|$ as near-wall fluid particles attain more uniformity in velocity with decreasing $|\lambda|$ in the phase-minus mode.

3.4 Influence of A_R on Heat Transfer. To observe the influence of aspect ratio mainly on the global heat transfer rate, all reported cases are resimulated by considering A_R=0.25, 0.35, 0.5, 0.65, 0.85, 2, 2.5, 3, 3.5, and 4. Results are presented only for Nu_{av} in special graphical displays of the mesh-contour plot in Figs. 12(*a*) and 12(*b*) for Ra=50 and 500. The mesh plot in Figs. 12(*a*) and 12(*b*) show the variation in Nu_{av} as functions of aspect ratio and wall waviness at constant Rayleigh number, while the contour plot represents the iso-Nu_{av} lines at different combinations of λ and A_R. The mesh plot helps one to understand the

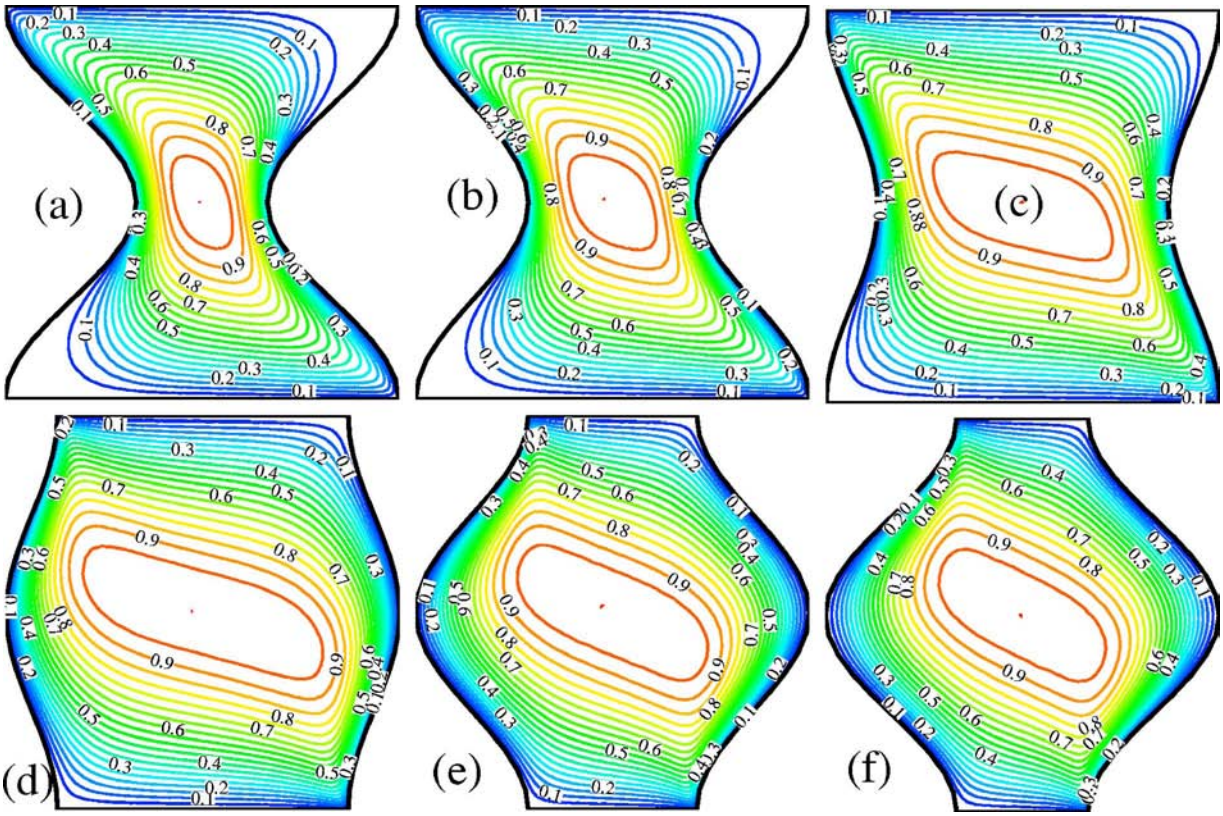

Fig. 9 Streamlines at Ra=250 for different values of λ: (*a*) λ=−0.25(Ψ_{max}=7.943), (*b*) λ=−0.2(Ψ_{max}=8.057), (*c*) λ=−0.075(Ψ_{max}=8.428), (*d*) λ=0.075(Ψ_{max}=9.0637), (*e*) λ=0.2(Ψ_{max}=9.599), and (*f*) λ=0.25(Ψ_{max}=9.81)

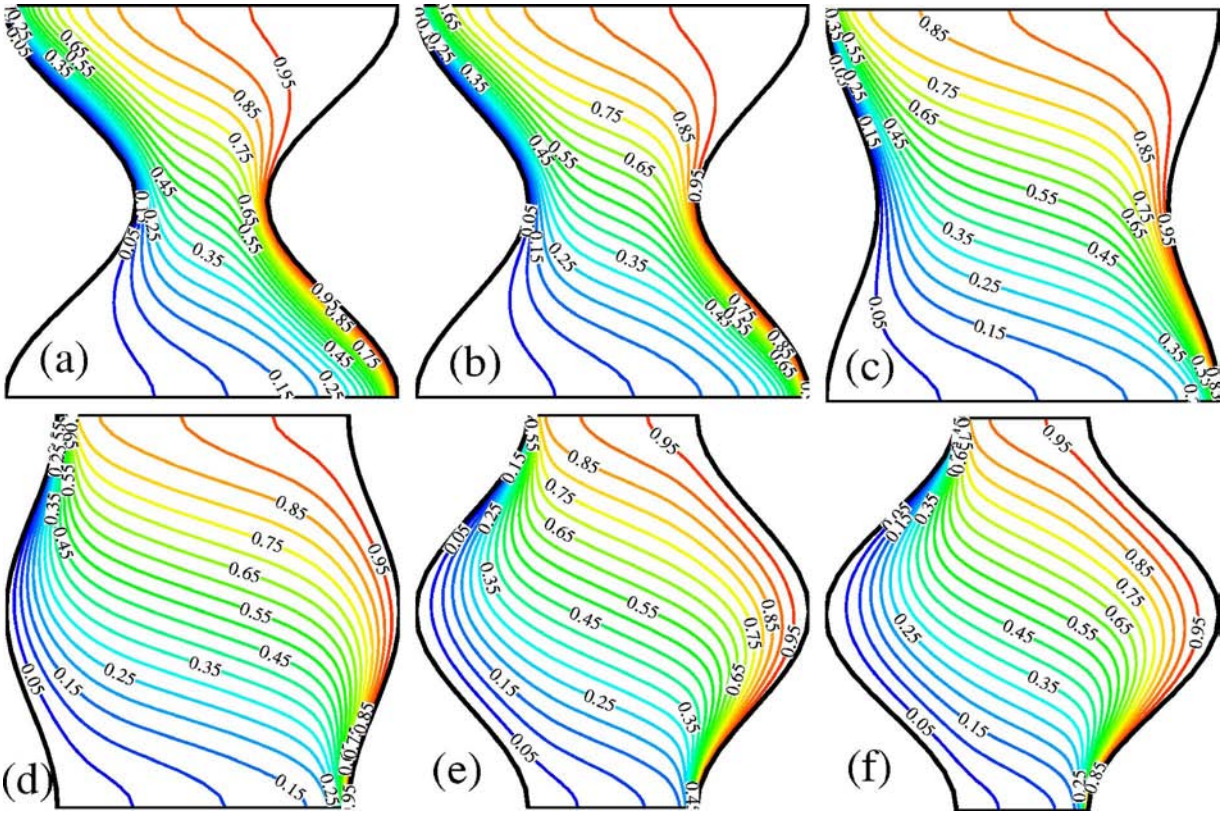

Fig. 10 Isothermal lines at Ra=250 for different values of λ: (*a*) λ=−0.25, (*b*) λ=−0.2, (*c*) λ=−0.075, (*d*) λ=0.075, (*e*) λ=0.2, and (*f*) λ=0.25

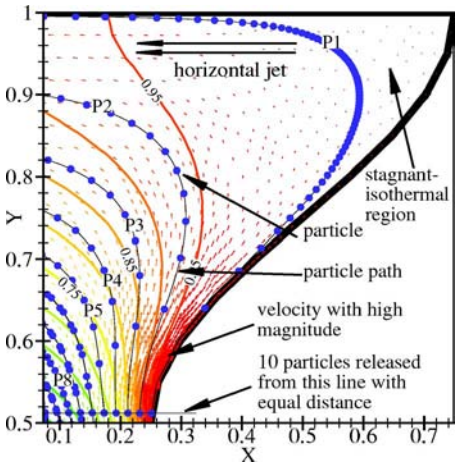

Fig. 11 Magnified view of the upper right portion of the cavity (at Ra=250 and λ=−0.25) is showing velocity vectors, isothermal lines, and paths of ten particles released from a line

variation in the magnitude of Nu_{av} with A_R and λ; the contour plot helps to select many combinations of A_R and λ for which Nu_{av} is constant.

The pattern of variation in Nu_{av} with A_R is almost similar for different λ. When $A_R < 1$, a rapid change in Nu_{av} with A_R is observed. For all Rayleigh numbers considered, the maximum Nu_{av} occurs in the phase-plus mode when λ is slightly larger than 0, while A_R, corresponding to the maximum Nusselt number, decreases with increasing Ra. In order to identify the values of A_R and λ corresponding to the maximum Nu_{av} for a fixed Ra, a cubic-spline-interpolation technique is applied using the "Spline Toolbox" of the MATLAB software [32]. The interpolated maximum Nusselt number, $(Nu_{av})_{max}$, is reported in Table 2 for six selected Rayleigh numbers. The corresponding aspect ratio $(A_R)_0$ and surface waviness λ_0 are also presented in Table 2.

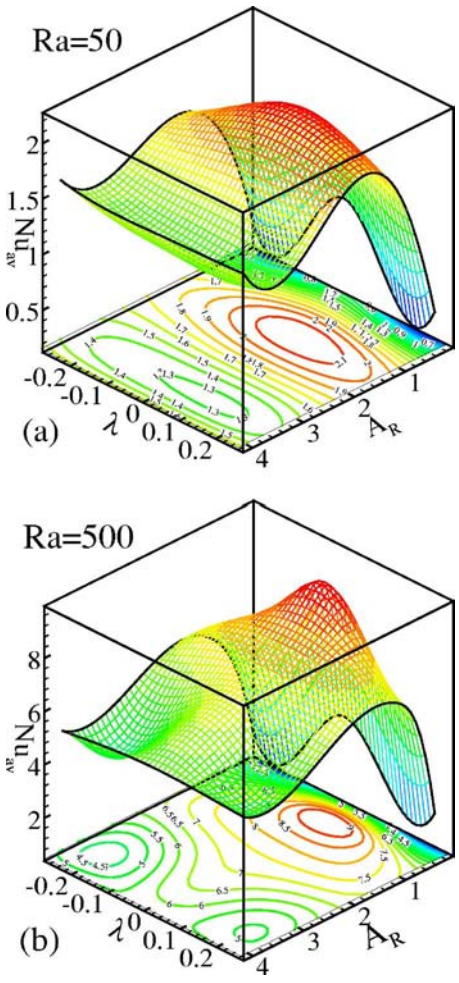

Fig. 12 Mesh-contour plot of Nu_{av} as a function of λ and A_R at (*a*) Ra=50 and (*b*) Ra=500

Table 2 Magnitude of maximum Nusselt number at a particular Rayleigh number and corresponding aspect ratio and wall waviness

	$(A_R)_0$	λ_0	$(Nu_{av})_{max}$
Ra=20	1.469	0.0375	1.339
Ra=50	1.469	0.0500	2.177
Ra=100	1.375	0.0500	3.346
Ra=250	1.000	0.0250	5.856
Ra=500	0.812	0.0125	9.528
Ra=1000	0.718	0.0125	15.430

3.5 Irreversibility Analysis. The convection process in a microstructure-filled enclosure is inherently irreversible. Nonequilibrium conditions arise due to the exchange of energy and momentum within the fluid and at the solid boundaries. This causes continuous entropy generation.

One portion of this entropy production is due to heat transfer in the direction of finite temperature gradients. Finite temperature difference heat transfer irreversibility is common in all types of thermal engineering applications. The local heat transfer irreversibility can be estimated from the first square-bracketed terms on the right-hand side of Eq. (9). Another portion of the entropy production arises due to fluid friction irreversibility. The local fluid friction irreversibility can be estimated from the second square-bracketed terms on the right-hand side of Eq. (9).

For a real system, the generated entropy is proportional to the destroyed exergy [33]. The destroyed exergy or the generated entropy is responsible for the less-than-theoretical maximum thermodynamic efficiency of a system. Through exergy accounting in smaller and smaller subsystems, one is able to draw a map of how the destruction of exergy is distributed over the engineering system of interest [33]. In this way, one is able to pinpoint the components and mechanisms (processes) that destroy the most exergy. This knowledge offers a real advantage in the search to improve system efficiency because it tells one from the start how to allocate engineering effort and resources. One attribute of an exergy-based analysis is that it makes it possible to compare, on a common basis (entropy generation platform), different interactions (inputs, outputs, work transfer, heat transfer, etc.) in a system, thus enabling a minimization of the global entropy generation rate (entropy generation minimization (EGM)).

The local entropy generation numbers (Ns, Ns_T, and Ns_F) and the Bejan number (Be) are calculated from the steady-state converged thermal-fluid field data for some selected values of Ra, λ, and A_R. These local parameters are then integrated over the entire cavity volume in order to calculate their global values; that is, global entropy generation number (Ns_{av}), global heat transfer irreversibility (GHTI), global fluid friction irreversibility (GFFI), and average Bejan number (Be_{av}). The technical definitions of these parameters are given in the nomenclature. No geometry optimization is performed in the current study; such work will be the focus of future work. Nevertheless, understanding the behavior of these irreversibility parameters is helpful to understanding the influence of factors that affects the irreversible nature of the transport phenomenon inside the wavy cavity.

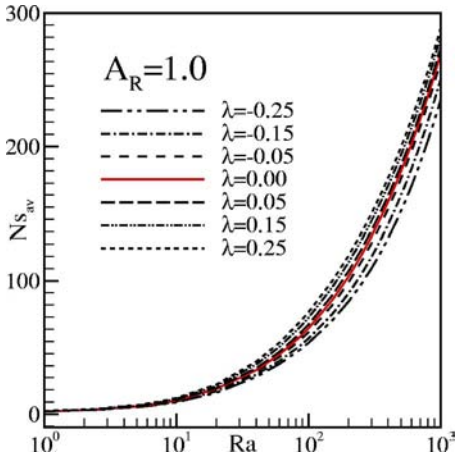

Fig. 13 Average entropy generation number as a function of Ra at different λ

For $A_R=1$, Figs. 13 and 14 show the variation in Ns_{av} and Be_{av}, respectively, as functions of Ra for different values of λ. In conduction regime, when fluid flow is nearly absent, entropy generation inside the cavity is dominated by the influence of the heat transfer irreversibility. Ns_{av} is nearly insensitive to Ra variation when $Ra<10$. Also λ shows little or no influence on Ns_{av} variation for $Ra<10$. The average Bejan number, a measure of global heat transfer irreversibility, is higher in magnitude for this range of Ra. When convection starts dominate and fluid flow becomes stronger inside the cavity at higher Rayleigh numbers, fluid friction irreversibility starts dominating the overall irreversibility. Ns_{av} increases with increasing Ra and the $Ns_{av}-Ra$ profile show the similar pattern that is previously observed in the $Nu_{av}-Ra$ profile. Be_{av} decreases with increasing Ra and asymptotes to a limiting value at high Ra. The irreversibility maps for Ra=50 and 500 are presented in Figs. 15(*a*) and 15(*b*) for $0.25\le A_R\le 4$ and $-0.25\le\lambda\le 0.25$. In each map, dotted and solid lines correspond to Ns_{av} and Be_{av}, respectively. From Figs. 15(*a*) and 15(*b*), it is observed that cavities with lower aspect ratio in the phase-plus mode exhibit high irreversibility, whereas higher aspect ratio in the phase-minus mode exhibit low irreversibility. Although the maximum heat transfer is observed for a combination of A_R close to 1 and λ close to 0 (see Fig. 13), this combination of A_R and λ, however, does not guarantee the minimum irreversibility because fluid flow does not have any role during Nu_L and Nu_{av} calculations.

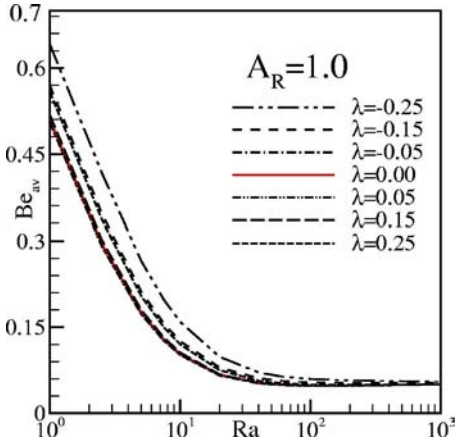

Fig. 14 Average Bejan number as a function of Ra at different λ

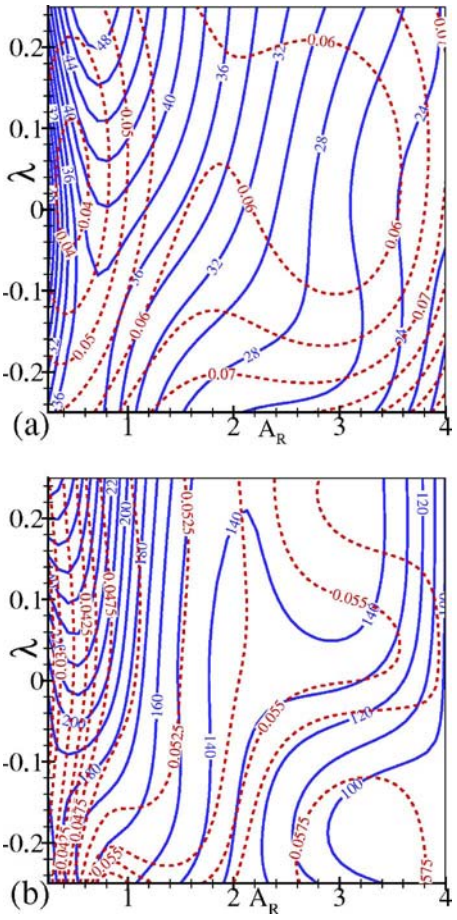

Fig. 15 Contours of Ns_{av} (dotted lines) and Be_{av} (solid lines) at (*a*) Ra=50 and (*b*) Ra=500

Conclusions

Employing the Darcy model, numerical studies of buoyancy-induced natural convection flow, heat transfer, energy transfer, and irreversibility are performed inside wavy cavities. The cavity is assumed to be filled with microstructures with sufficient void spaces for fluid flow. Convective motion is nearly absent inside the cavity at very low Rayleigh numbers ($Ra<10$) for all aspect ratios and wall waviness. The conduction-dominated thermal field results in an average Nusselt number equal to 1. Energy streamlines reduce to heat flux lines (which originate at the hot wall, which acts as an energy source) pass through the cavity without perturbation, and intersect the cold wall (which acts as a energy sink at low Rayleigh numbers). For a fixed aspect ratio and surface waviness, an increasing Rayleigh number strengthens the circulation inside the cavity and, at high Rayleigh numbers, near-wall flow intensities are high. A large portion near the middle of the cavity at the phase-zero and phase-plus modes show nearly stagnant fluid, whereas in the phase-minus mode extent of such region is small due to the geometric orientation. Two small regions near the intersections of hot wavy and top adiabatic walls and cold wavy and bottom adiabatic walls in the phase-minus mode trap isothermal-stagnant fluid that does not have any significant role in the effective heat transfer. The extents of such regions reduce with increasing wall waviness at constant Rayleigh number and aspect ratio. A gradual change in the wall waviness, starting from the maximum value at the phase-minus mode ($\lambda=-0.25$) to the maximum value at the phase-plus mode ($\lambda=0.25$) show an increasing circulation strength, which is verified by reported increasing average kinetic energy for some selected cases. Thermal spots with highly concentrated isothermal lines are a characteris-

tics feature at moderate and high Rayleigh numbers. As flow strengthens, these thermal spots elongated along the isothermal walls and heat transfer rates are high at these spots. The intensity of thermal spot (and also the local heat transfer rate), near the horizontal centerline, is high at the phase-minus mode and low at the phase-plus mode. A spline interpolation technique is applied to calculate the maximum average Nusselt number as a functions of Rayleigh number, aspect ratio, and wall waviness. The current study shows that both wall waviness and aspect ratio correspond to the maximum value of the average Nusselt-number decrease with increasing Rayleigh number. However, the combination of wall waviness and aspect ratio that exhibits the maximum average Nusselt number does not ensure minimum irreversibility.

Nomenclature

a = amplitude of the wavy wall, m
A_R = aspect ratio of the cavity, $=H/W$
A = cross-sectional area of the cavity, m^2
Be = Bejan number, $=\mathrm{GHTI}/(\mathrm{GHTI}+\mathrm{GFFI})$
Be_{av} = average Bejan number, $=\forall^{-1}\int\int\int \mathrm{Be}\, d\forall$
C_p = specific heat at constant pressure, J kg−1 K^{-1}
Ec = Eckert number, $=u_0^2 C_p/\Delta T$
g = gravitational acceleration, m s^{-2}
GFFI = global fluid friction irreversibility, $=\forall^{-1}\int\int\int Ns_F\, d\forall$
H = convective heat transfer coefficient, W m^{-2} K^{-1}
H = height of the cavity, m
GHTI = global heat transfer irreversibility, $=\forall^{-1}\int\int\int Ns_T\, d\forall$
k = thermal conductivity of the fluid, W m^{-1} K^{-1}
K = permeability of the porous media, m^2
Ns = entropy generation number, $=S'''_{gen}/S'''_0$
Ns_{av} = average entropy generation number, =GHTI +GFFI
Ns_F = local fluid friction irreversibility
Ns_T = local heat transfer irreversibility
Nu = Nusselt number, $=hL/k$
Pr = Prandtl number, $=\mu C_p/k$
Ra = Darcy-modified Rayleigh number
Re_p = Pore Reynolds number, $=|\mathbf{v}|\sqrt{K}/\nu$
S'''_0 = characteristic transfer rate, W m^{-3} K^{-1}
S'''_{gen} = local entropy generation rate, W m^{-3} K^{-1}
t = time, s
T = temperature of the fluid, °C
u = velocity component at x direction, m s^{-1}
U = dimensionless velocity component at x direction
v = velocity component at y direction, m s^{-1}
V = dimensionless velocity component at y direction
u_0 = reference velocity
W = average width of the cavity, m
x = distance along the x coordinate, m
X = distance along the dimensionless x coordinate
y = distance along the y coordinate, m
Y = distance along the dimensionless y coordinate

Greek Symbols

α = thermal diffusivity of the fluid, m^2 s^{-1}
β = volumetric coefficient of thermal expansion, K^{-1}
δ = boundary layer thickness, m
μ = dynamic viscosity of the fluid, Pa s
λ = dimensionless waviness, $=a/W$
ν = kinematic viscosity of the fluid, m^2 s^{-1}
ρ = density of the fluid, kg m^{-3}
ϕ = porosity of the porous media
ψ = stream function, m^2 s^{-1}
Ψ = dimensionless stream function, $=\psi/\alpha$
σ = an empirical constant
Θ = dimensionless temperature
τ = dimensionless time
Ω = dimensionless temperature difference, $=\Delta T/T_0$
$\forall$ = volume of the cavity, m^3
ΔT = temperature difference, °C

Subscripts and Superscripts

av = average value
C = value at the cold wall
H = value at the hot wall
m = mean value
0 = reference value

References

[1] Sobey, I. J., 1980, "On Flow Through Furrowed Channels—Part 1: Calculated Flow Patterns," J. Fluid Mech., **96**, pp. 1–26.
[2] Sobey, I. J., 1980, "On Flow Through Furrowed Channels—Part 2: Observed Flow Patterns," J. Fluid Mech., **96**, pp. 27–32.
[3] Sobey, I. J., 1982, "Oscillatory Flows at Intermediate Strouhal Number in Asymmetric Channels," J. Fluid Mech., **125**, pp. 359–373.
[4] Sobey, I. J., 1983, "The Occurrence of Separation in Oscillatory Flow," J. Fluid Mech., **134**, pp. 247–257.
[5] Leneweit, G., and Auerbach, D., 1999, "Detachment Phenomena in Low Reynolds Number Flows Through Sinusoidally Constricted Tube," J. Fluid Mech., **387**, pp. 129–150.
[6] Mahmud, S., Islam, A. K. M. S., and Mamun, M. A. H., 2002, "Separation Characteristics of Fluid Flow Inside Two Parallel Plates With Wavy Surface," Int. J. Eng. Sci., **40**, pp. 1495–1509.
[7] Mahmud, S., Islam, A. K. M. S., and Mamun, M. A. H., 2002, "Separation Characteristics of Fluid Flow in a Pipe With Wavy Surface," Appl. Mech. Eng., **7**, pp. 1255–1270.
[8] Wang, G., and Vanka, S. P., 1995, "Convective Heat Transfer in Periodic Wavy Passages," Int. J. Heat Mass Transfer, **38**, pp. 3219–3230.
[9] Russ, G., and Beer, H., 1997, "Heat Transfer and Flow Field in a Pipe With Sinusoidal Wavy Surface—I. Numerical Investigation," Int. J. Heat Mass Transfer, **40**, pp. 1061–1070.
[10] Russ, G., and Beer, H., 1997, "Heat Transfer and Flow Field in a Pipe With Sinusoidal Wavy Surface—II. Experimental Investigation," Int. J. Heat Mass Transfer, **40**, pp. 1071–1081.
[11] Mahmud, S., Islam, A. K. M. S., and Feroz, C. M., 2003, "Flow and Heat Transfer Characteristics Inside a Wavy Tube," Heat Mass Transfer, **39**, pp. 387–393.
[12] Vyas, S., Zhang, J., and Manglik, R. M., 2004, "Steady Recirculation and Laminar Forced Convection in a Sinusoidal Wavy Channel," ASME J. Heat Transfer, **126**, pp. 500–500.
[13] Mahmud, S., Das, P. K., Hyder, N., and Islam, A. K. M. S., 2002, "Free Convection in an Enclosure With Vertical Wavy Walls," Int. J. Therm. Sci., **41**, pp. 440–446.
[14] Dalal, A., and Das, M. K., 2006, "Natural Convection in a Cavity With a Wavy Wall Heated from Below and Uniformly Cooled From the Top and Both Sides," ASME J. Heat Transfer, **128**, pp. 717–725.
[15] Mahmud, S., and Islam, A. K. M. S., 2003, "Natural Convection and Entropy Generation in an Inclined Wavy Enclosure," Int. J. Therm. Sci., **42**, pp. 1003–1012.
[16] Dalal, A., and Das, M. K., 2005, "Laminar Natural Convection in an Inclined Complicated Cavity With Spatially Variable Wall Temperature," Int. J. Heat Mass Transfer, **48**, pp. 2986–3007.
[17] Mahmud, S., and Fraser, R. A., 2004, "Free Convection and Entropy Generation Inside a Vertical Inphase Wavy Cavity," Int. Commun. Heat Mass Transfer, **31**, pp. 455–466.
[18] Das, P. K., and Mahmud, S., 2003, "Numerical Investigation of Natural Convection in a Wavy Enclosure," Int. J. Therm. Sci., **42**, pp. 397–406.
[19] Kumar, B. V. R., Murthy, P. V. S. N., and Singh, P., 1998, "Free Convection Heat Transfer From a Isothermal Wavy Surface in a Porous Enclosure," Int. J. Numer. Methods Fluids, **28**, pp. 633–661.
[20] Kumar, B. V. R., 2000, "A Study of Free Convection Induced by a Vertical Wavy Surface With Heat Flux in a Porous Enclosure," Numer. Heat Transfer, Part A, **37**, pp. 493–510.
[21] Misirlioglu, A., Baytas, A. C., and Pop, I., 2005, "Free Convection in a Wavy Cavity Filled With a Porous Medium," Int. J. Heat Mass Transfer, **48**, pp. 1840–1850.
[22] Kumar, B. V. R., and Gupta, S., 2003, "Free Convection in a Non-Darcian Wavy Porous Enclosure," Int. J. Eng. Sci., **41**, pp. 1827–1848.
[23] Kumar, B. V. R., and Gupta, S., 2005, "Combined Influence of Mass and Thermal Stratification on Double-Diffusion Non-Darcian Natural Convection From a Wavy Vertical Wall to Porous Media," ASME J. Heat Transfer, **127**, pp. 637–647.
[24] Bejan, A., 1984, *Convection Heat Transfer*, Wiley, New York.
[25] Mahmud, S., and Fraser, R. A., 2004, "Magnetohydrodynamic Free Convec-

tion and Entropy Generation in a Square Porous Cavity," Int. J. Heat Mass Transfer, **47**, pp. 3245–3256.
[26] Mahmud, S., and Fraser, R. A., 2005, "Flow, Thermal, and Entropy Generation Characteristics Inside a Porous Channel With Viscous Dissipation Effect," Int. J. Therm. Sci., **44**, pp. 21–32.
[27] Ferziger, J. H., and Perić, M., 1996, *Computational Methods for Fluid Dynamics*, Springer-Verlag, New York.
[28] Kimura, S., and Bejan, A., 1983, "The 'Heatline' Visualization of Convective Heat Transfer," ASME J. Heat Transfer, **105**, pp. 916–919.
[29] Costa, V. A. F., 1999, "Unification of The Streamline, Heatline and Massline Methods for the Visualization of Two-Dimensional Transport Phenomena," Int. J. Heat Mass Transfer, **42**, pp. 27–33.
[30] Costa, V. A. F., 2003, "Unification of the Streamline, Heatline and Massline Methods for the Visualization of Two-Dimensional Heat and Mass Transfer in Anisotropic Media," Int. J. Heat Mass Transfer, **46**, pp. 1309–1320.
[31] Tasnim, S. H., and Collins, M. R., 2005, "Suppressing Natural Convection in a Differentially Heated Square Cavity With an Arc Shaped Baffle," Int. Commun. Heat Mass Transfer, **32**, pp. 94–106.
[32] MATLAB, 2004, MATLAB Release 13, The MathWorks.
[33] Bejan, A., 1996, *Entropy Generation Minimization*, CRC Press, Boca Raton.

Thermal Control Utilizing an Electrohydrodynamic Conduction Pump in a Two-Phase Loop With High Heat Flux Source

Seong-Il Jeong
Satellite Technology Research Center,
Korea Advanced Institute of Science and Technology,
373-1, Guseong-Dong, Yuseong-Gu,
Daejeon, 305-701, Republic of Korea
e-mail: jeong05@gmail.com

Jeffrey Didion
Thermal Technology Development,
NASA Goddard Space Flight Center,
Greenbelt, MD 20771
e-mail: Jeffrey.R.Didion@nasa.gov

The electric field applied in dielectric fluids causes an imbalance in the dissociation-recombination reaction generating free space charges. The generated charges are redistributed by the applied electric field, resulting in the heterocharge layers in the vicinity of the electrodes. Proper design of the electrodes generates net axial flow motion pumping the fluid. The electrohydrodynamic (EHD) conduction pump is a new device that pumps dielectric fluids utilizing heterocharge layers formed by imposition of electrostatic fields. This paper experimentally evaluates the performance of a two-phase (liquid-vapor) breadboard thermal control loop consisting of an EHD conduction pump, condenser, preheater, evaporator, transport lines, and reservoir (accumulator). This study is performed to address the feasibility of the EHD two-phase loop for thermal control of a laser equipment with high heat flux source. The generated pressure head and the maximum applicable heat flux are experimentally determined at various applied voltages and sink temperatures. Recovery from the evaporator dryout condition by increasing the applied voltage to the pump is also demonstrated. The performance of the EHD conduction pump in this study confirms that the EHD conduction pump can be used as a stand-alone system for high heat flux thermal control. [DOI: 10.1115/1.2759971]

Keywords: electrohydrodynamic, conduction pump, thermal control, high heat flux, two-phase

Introduction

Capillary pumping devices, such as heat pipes, capillary pumped loops (CPLs), and loop heat pipes (LHPs), have been used for thermal control for many years. They are two-phase heat transfer devices that transfer heat with little temperature difference. The capillary force developed by wick structure circulates the fluid. Therefore, the capillary pumping capacity is a primary limitation governing the operation of these devices. Heat pipes, in particular, have very limited pumping capability. CPLs and LHPs have relatively high pumping capability; however, they have other difficulties, such as unwarranted immediate start-up and recovery from dryout. These devices generally require a 30 W to 50 W starter heater to enhance the chances of start-up success [1]. Numerous pumping mechanisms have been proposed as alternative pumping mechanism to assist/replace the capillary pumping. Electrohydrodynamic (EHD) pumping is a promising candidate, especially in the space environment where the engineering advantages, such as simple design, nonmechanical, low acoustic noise, lightweight, rapid control of performance, and low power consumption, are most important. Furthermore, EHD pumps provide immediate start-up operation, prompt recovery from evaporator dryout, and feasibility of microscale application. Jones [2] proposed a heat pipe of radical design, which utilizes polarization EHD force effects. The basic concept was to replace the capillary wick of a conventional heat pipe with an electrode structure, which provides a net liquid pumping force to ensure the heat pipe operation, irrespective of orientation with respect to gravity. He concluded the EHD heat pipe has several advantages, such as built-in EHD heat transfer enhancement in boiling and condensation by a nonuniform electric field, reliable priming and startup, bubble ejection from axial flow structure, low liquid friction factor in comparison to that of a capillary wick, and direct voltage control of the pumping mechanism. Sato et al. [3] experimentally investigated an EHD heat pipe composed of vapor and liquid space without wick structure. The EHD pump consisted of a ring electrode and a square-shaped electrode and was used to return the condensed liquid from the condenser to the evaporator. They found that the velocity of the condensed liquid of the EHD-pumped flow increases in proportion to the applied voltage. They concluded that the EHD-pumped flow was generated by a dielectrophoretic force composed of Maxwell stress and the electrostriction force. Bryan and Seyed-Yagoobi [4] and Jeong and Seyed-Yagoobi [5] experimentally investigated the enhancement of the heat transport capacity of a monogroove heat pipe with EHD pumping. They installed an EHD pump on the liquid channel in the adiabatic section of the heat pipe. They achieved over 100% enhancement in the heat transport capacity and demonstrated immediate recovery from the evaporator dryout with the EHD pump operation using R-123 as a working fluid. In addition, Jeong and Seyed-Yagoobi [5] further clarified the EHD pumping mechanism and improved the heat transport capacity with an electrode design enhanced based on the pumping mechanism. Mo et al. [6] performed an experimental study to characterize the start-up process for an EHD-assisted capillary pumped loop (CPL) system. An EHD-assisted evaporator with 1500 W of the maximum allowable heat transport capacity was used with a spring-type electrode inserted into the liquid channel of the evaporator. Their experimental data showed that the EHD can reduce the start-up time by as much as 50% at an applied voltage of 10 kV and a power level of 10 W with R-134a as the working fluid. The start-up time reduction for 20 W and 50 W power levels were 30% and 20%, respectively.

Contributed by the Heat Transfer Division of ASME for publication in the JOURNAL OF HEAT TRANSFER. Manuscript received February 6, 2006; final manuscript received February 5, 2007. Review conducted by Ramendra P. Roy. Paper presented at the 2004 ASME International Mechanical Engineering Congress (IMECE2004), November 13–19, 2004, Anaheim, CA.

The EHD phenomena involve the interaction of electric fields and flow fields in a dielectric fluid medium. This interaction between electric fields and flow fields can induce flow motion by electric body force. The electric body force density $\vec{f}_e$ acting on the molecules can be expressed as follows [7]:

$$\vec{f}_e = c\vec{E} - \frac{1}{2}\vec{E}^2 \nabla \varepsilon + \frac{1}{2} \nabla \left[\vec{E}^2 \left(\frac{\partial \varepsilon}{\partial \rho} \right)_T \rho \right] \quad (1)$$

where c is the charge density, $\vec{E}$ is the electric field, ε is the fluid permittivity, ρ is the fluid density, and T is the fluid temperature. The first term represents the Coulomb force, which is the force acting on the free charges in an electric field. The second and third terms represent the polarization force acting on polarized charges. The second term, the so-called dielectrophoretic force, is associated to the electric permittivity gradient. It arises when the applied electric field induces a dipole due to the presence of polarizable particles or multiple phases exist in the working fluid. If the permittivity of the particle is higher than the surrounding medium, then the EHD force acts in the way that the particle moves to the high field strength region. In the converse case, the EHD force acts toward the lower electric field strength region. The third term, the electrostriction term, is relevant only for compressible fluids. Thus, EHD pumps require either free space charges or gradient in permittivity within the fluid. For the case of an isothermal and single-phase liquid, $\nabla\varepsilon$ vanishes, resulting in Coulomb force as the only force for generating a permanent EHD motion.

There are two main mechanisms for generating a space charge in an isothermal liquid. The first one is associated with the ion injection at a metal/liquid interface and the related pumping is referred to as ion-drag pumping. However, the ion-drag pumping is not desirable as the injection of ions into the working fluid can deteriorate the fluid's electrical properties. Also, ion injection requires relatively higher electric fields that can result in a hazardous operating condition. The second mechanism for generating a space charge in an isothermal liquid is associated with the process of dissociation of the neutral electrolytic species and recombination of the generated ions [8]. Under the low electric field regime, dissociation and recombination are in dynamic equilibrium,

$$A^+B^- \leftrightarrow A^+ + B^- \quad (2)$$

When an electric field exceeding a certain value ($\sim$1 kV/cm, depending on the liquid characteristics) is applied, the rate of dissociation exceeds that of the recombination, thus generating a nonequilibrium layer where the dissociation-recombination reactions are not in equilibrium [8]. The charges generated by dissociation are redistributed in the region by the applied electric field, resulting in the heterocharge layers around the electrodes. Heterocharge means that the charge has the opposite polarity from that of the adjacent electrode. The thickness of the heterocharge layer is proportional to the corresponding relaxation time (defined as the ratio of electrical permittivity and conductivity, and represents the time during which a charged particle maintains its charge in a medium) of the working fluid τ and the strength of the local electric field. The attraction between the electrode and the charges within the heterocharge layer induces a fluid motion near the electrode from the liquid side to the electrode side. This type of pumping is referred to as conduction pumping. Considering an electrode configuration as shown in Fig. 1, strong electric fields build up the heterocharge layers around the electrodes. With this electrode configuration, the net axial motion around the ring ground electrode is almost canceled due to geometric symmetry. Thus, the motion around the high voltage electrode primarily contributes to the net axial flow. Since the electric field is high near the high-voltage electrode, the thickness of the corresponding heterocharge layer and the pressure across it will be high as well. Therefore, the flow direction will be from the ground electrode to the high-voltage electrode. The current versus voltage behavior in this regime is subohmic showing only a slightly increased current with increased voltage. The details of the EHD conduction pumping mechanism can be found in Atten and Seyed-Yagoobi [9], Jeong et al. [10], and Jeong and Seyed-Yagoobi [11–13].

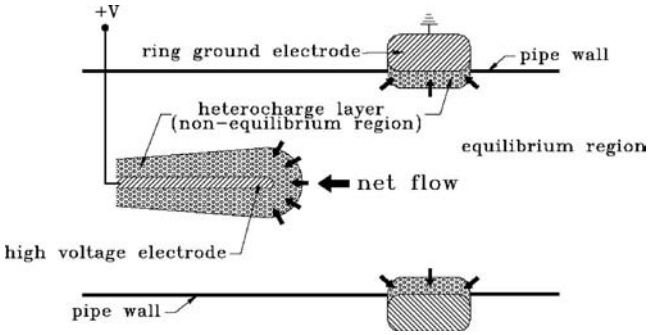

Fig. 1 Illustration of EHD conduction pumping mechanism

This paper investigates the performance of an EHD conduction pump to evaluate its feasibility for thermal control in a two-phase loop with high heat flux source. Specifically, an EHD conduction pump, consisting of six electrode pairs, was built and installed in the two-phase loop with condenser and evaporator (EV). The test matrix varies the applied voltage of the EHD pump, the sink temperature, and the heat load on the evaporator. Pressure head generated with this EHD pump, current, mass flow rate, and pressure drop across the EV are measured varying the applied voltage, the heat load, and the sink temperature. The critical heat flux is determined at 5 kV, 10 kV, and 15 kV, and the recovery from dryout condition is demonstrated. The influence of the fluid temperature and the pressure oscillation due to boiling process in the EV on EHD pump performance is also investigated. The working fluid used is degassed R-134a.

Experimental Apparatus

EHD Conduction Pump. The EHD conduction pump consists of six electrode pairs. The high-voltage electrodes are fabricated from one large-radius tube and six small-radius tubes whereas the ground electrodes are made as rings, installed against the pump inner wall. The high voltage and ground electrodes are made of stainless steel. Figure 2 presents a picture and cross section of the high-voltage electrode of the EHD conduction pump, and Fig. 3 shows the assembled EHD conduction pump. The edges of high-voltage electrode are coated with gold to remove/reduce any sharp edges. In EHD conduction pump, the electrode with less sharp points or edges is required to reduce the concurrent effects of ion injection, which act against the conduction pumping. The opening area of the high-voltage electrode is 58.3% of the pumping section, and 41.7% of the pumping section is the projected area of the high-voltage electrode. In the EHD conduction pumping, the electrode that has higher available projected area (perpendicular to axial direction) for heterocharges formation induces stronger net flow motion from the ground electrode toward the high-voltage

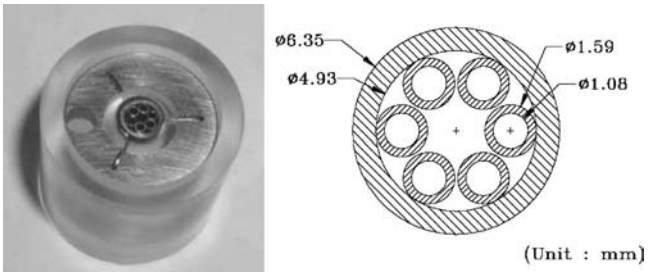

Fig. 2 Picture and cross section of the high-voltage electrode of the EHD conduction pump

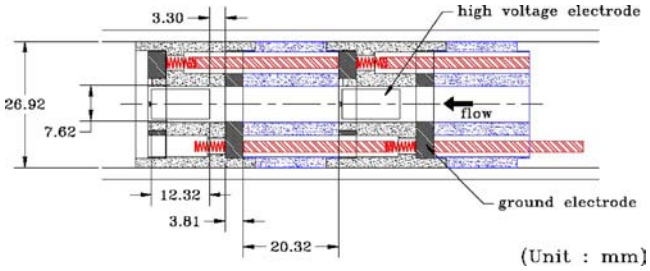

Fig. 3 Assembled EHD conduction pump (two pairs shown)

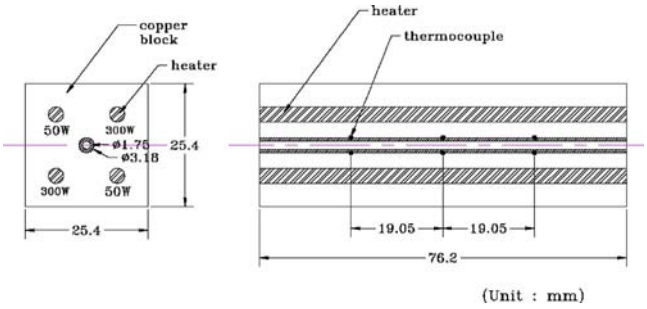

Fig. 5 Evaporator (EV)

electrode. However, at the same time, adequate percentage of the opening area and small pressure drop across the electrode should be secured in order to provide the required mass flow rate.

Two-Phase Loop. Figure 4 illustrates the experimental setup of the two-phase loop with the EHD conduction pump. The loop consists of the EHD conduction pump, condenser, preheater, evaporator (EV), reservoir, and transport lines. The total length of the loop is ~10 m. The inner diameter of the transport lines is 8.1 mm. The EHD conduction pump is installed on the liquid passage after the condenser. The EHD pump is connected to a high-voltage low-current DC power supply (EH Series from Glassman High Voltage, Inc). Positive polarity DC voltage is applied to the high-voltage electrode. The preheater and EV are installed after the EHD pump section. The EV is incorporated in the loop to simulate the high heat flux source in a laser application. The reservoir is located between the condenser and the EHD pump. The reservoir temperature controlled by a strip heater determines the saturation condition of the loop. The reservoir temperature was set to 28°C for the entire test. To minimize the heat loss to surroundings, the entire experimental apparatus is wrapped with insulation materials. Heat loads are supplied to the EV through the cartridge heaters inserted into the copper block surrounding 3.18 mm copper tubing with 1.75 mm i.d. The total heat load capacity of the EV is 700 W (two 300 W heaters and two 50 W heaters). Two multimeters are used to measure the voltage and current of the power supply for the heaters. T-type thermocouples (TC) located on the pipe surface inside the copper block (three for upper and three for lower surface) as shown in Fig. 5 measured the temperatures along the evaporator surface. These thermocouples are positioned at 19.05 mm intervals. The heat is removed at the condenser, which is connected to a recirculating chiller from FTS Systems. The temperature of the condenser is measured by T-type thermocouples located along the condenser length. The temperature at the inlet and outlet of the condenser is also measured by thermocouples. The mass flow rate of the recirculating refrigerant through the loop is measured using a flowmeter (Model: DS006S, Micro Motion, Inc.), installed before the preheater section. The absolute pressure is measured at a location between the condenser and the reservoir with a pressure transducer (Model: PX811, Omega). The differential pressures through the EHD conduction pump and the EV are also measured using the differential pressure transducer (Model: 420 DP, Sensotec). The differential pressure transducer through the EV is dedicated to the measurement of the boiling effect on the pressure drop.

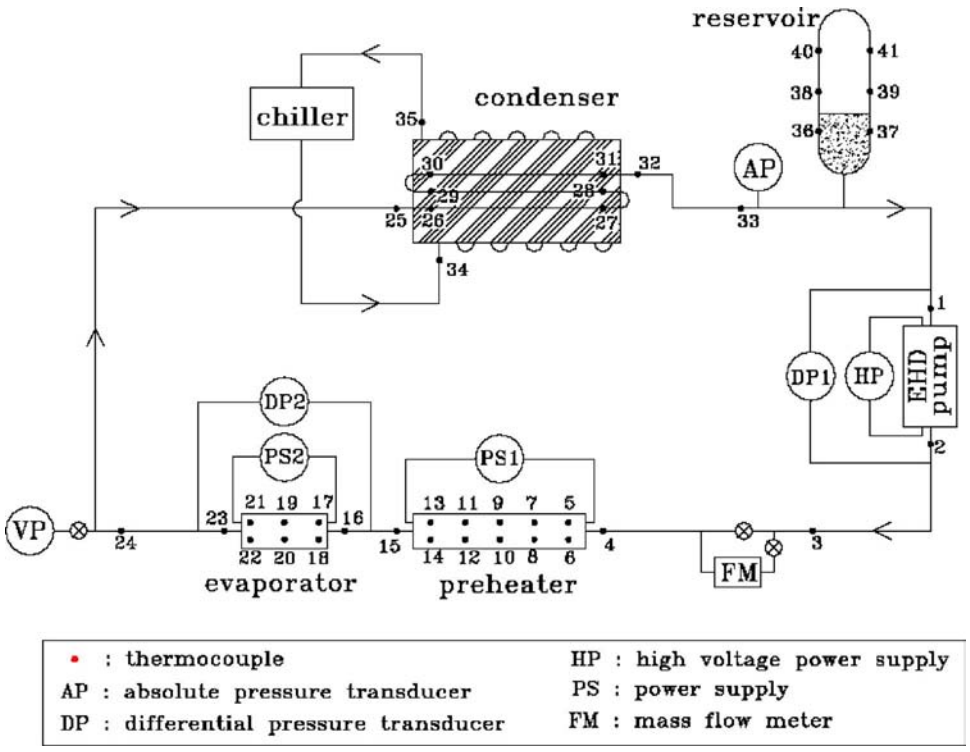

Fig. 4 Experimental setup of the test loop with the EHD conduction pump

Table 1 Bias limits and precision limits

Bias limit	
	Temperature measurement: ±0.5 K
	Voltage of high-voltage supply: 2.0%
	Current of high-voltage supply: 1.5%
	Voltage of EV heater: 2.0%
	Current of EV heater: 2.5%
	Differential pressure: 0.5%
	Mass flow rate: 1.8%
	EV inner diameter: ±15.0%
Precision limit (high-voltage supply between 5 kV and 15 kV)	
	Differential pressure: 1.1–12.0%
	Mass flow rate: 0.7–2.2%

Error Analysis

The uncertainty analysis was performed according to the ASME Policy on Reporting Uncertainties in Experimental Measurements and Results [14,15]. Table 1 shows the bias and precision limits obtained from the instrumental data, calibration, and measurement data. A high-voltage power supply provides 2.0% and 1.5% absolute accuracy in voltage and current monitoring, respectively. The accuracy of the multimeter used for the measurement of evaporator heat load is 2.0% and 2.5% for the AC voltage and AC current, respectively. The AP transducer provides ±0.1% of accuracy with ±1.5% total error of temperature effects for the range of −20–80°C.

Power consumption of the EHD pump is calculated from the applied voltage and current of the high-voltage power supply. The maximum uncertainty in power consumption is 3.8%. The total heat load of the EV is calculated from the voltage and current measured using the multimeter, and heat flux is calculated using heat load and internal surface area of EV. The uncertainty in heat load and heat flux is 4.4% and 15.7%, respectively. In the range of 5–15 kV of high-voltage supply, the uncertainty for differential pressure and mass flow rate is 1.2–12.0% and 2.9–3.5%, respectively. The uncertainty for differential pressure and mass flow rate is higher at lower applied voltage and higher sink temperature due to its smaller measurement values at that condition.

Results and Discussions

Figures 6(*a*) and 6(*b*) present the generated pressure and current as the applied voltage varies at ambient temperature without operating the heater and condenser. This test established the basic performance of the EHD pump in a single phase. TC1 and TC2 represent the EHD pump inlet and outlet temperature values. The generated pressure is approximately constant albeit the current decreases with time at a given applied voltage. This implies that the electric power consumption decreases with time. The maximum pressure head achieved with six pairs is ~9700 Pa at 16.0 kV; the maximum electric power consumption was 3.33 W. Figures 6(*a*) and 6(*b*) further show that the temperature difference across the EHD pump increases as the applied voltage increases. The maximum temperature difference across the EHD pump is ~1°C at 16 kV. The temperature increase across the EHD pump seems to be a result of Joule heating (J), where $J=\sigma\vec{E}^2$ and σ represents the electric conductivity of the working fluid, and $\vec{E}$ is the electric field. The resulting Joule heating from the applied electric field is usually negligible relative to the transported heat by EHD pumping since the electric conductivity of the working fluid is very low.

To investigate the long-term performance of the EHD pump, the generated pressure was measured over 46 h. Figure 7 presents the generated pressure and the pump inlet and outlet temperature values as a function of time at 10 kV of applied voltage. The generated pressure was maintained at a level in daily mean value within 300 Pa over a period of 24 h. The generated pressure oscillation depends on the pump inlet and outlet temperature variations, which, in this case, resulted from ambient temperature variations. In order to investigate the temperature influence on the EHD conduction pump performance, the chiller temperature set point was varied from 20°C to −20°C at a given voltage. Figure 8 shows the variation of the generated pressure and the EHD pump inlet and outlet temperature as the chiller temperature set point changes at 10 kV of applied voltage. The generated pressure increases as the temperature of the working fluid decreases. Figure 9 presents the generated pressure at 10 kV and 15 kV and the

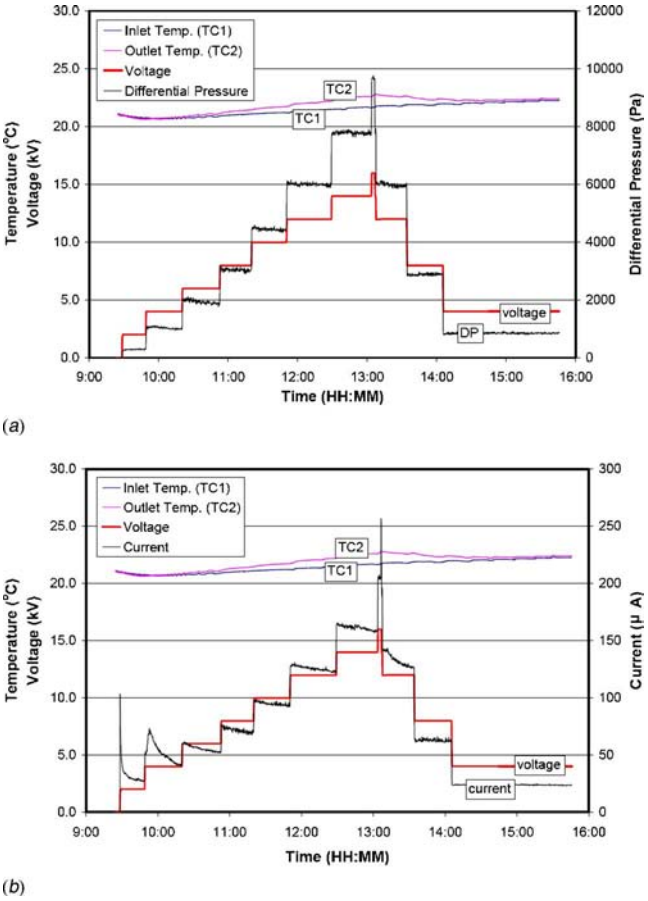

Fig. 6 (*a*) Generated pressure and (*b*) current, as the applied voltage varies (2/4/6/8/10/12/14/16/8/4 kV) at ambient temperature

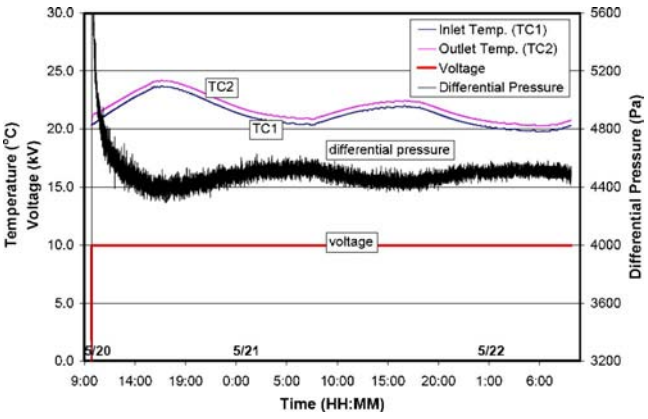

Fig. 7 Generated pressure and inlet and outlet temperature of the EHD pump at 10 kV of the applied voltage

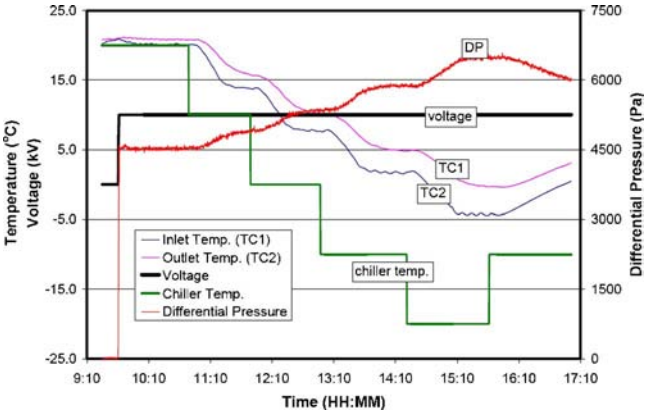

Fig. 8 Generated pressure and inlet and outlet temperature of the EHD pump at 10 kV of the applied voltage as the sink temperature varies (20/10/0/−10/−20/−10°C)

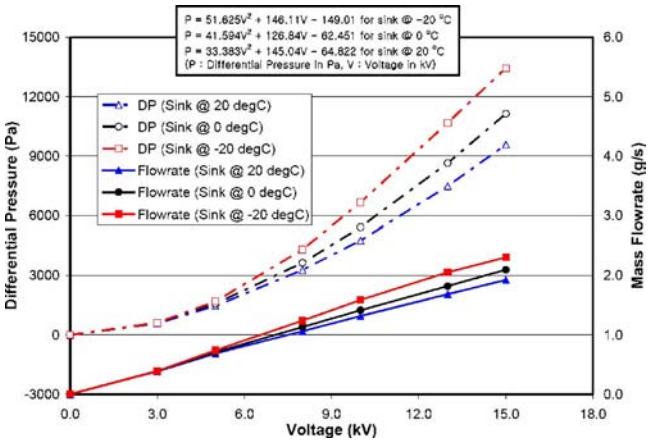

Fig. 10 Generated pressure and mass flow rate as a function of the applied voltage

relaxation time of R134a as a function of the average temperature within the EHD pump. Note that the generated pressure is closely associated with the relaxation time, which is function of the temperature. In the conduction pumping mechanism, the generated pressure increase with temperature decrease can be explained in terms of relaxation time. The increased relaxation time at lower temperature induces thicker heterocharge layers, creating more pressure head across the EHD pump. Considering the electric conductivity in Ohmic region, the relaxation time is 2.38 ms and 4.04 ms at 20°C and −5°C, respectively. The electric permittivity and conductivity of R134a, which are used for the relaxation time calculation, is 93.5 pF/m, 3.93×10^{-8} S/m at 20°C and 112.54 pF/m, 2.79×10^{-8} S/m at −5°C, respectively, and these values were obtained from Bryan [16].

Figure 10 presents the pressure generation and mass flow rate as a function of the applied voltage for the sink temperatures of 20°C, 0°C, and −20°C. The pressure generation and mass flow rate at 15 kV of the applied voltage are ~9570 Pa, 11170 Pa, 13160 Pa, and 1.92 g/s, 2.10 g/s, 2.31 g/s at 20°C, 0°C, −20°C of sink temperature, respectively. As presented in Fig. 10, the pressure generation has quadratic dependence on the applied voltage, whereas the mass flow rate has linear dependence on the applied voltage. This implies that the total pressure loss is proportional to the second power of the velocity.

We examined the loop heat transport capabilities for given operating conditions. These tests varied applied voltage on the EHD pump at a given sink temperature value. For each sink temperature value, a constant high voltage was applied on the EHD pump and the heat load to EV varied in 5 W or 10 W increments until dryout occurred. Figure 11 presents the timeline of the generated pressure of the EHD pump, the pressure drop across the EV, the temperature at the upper end section of EV (TC21), and the heat load on the EV at 10 kV of the applied voltage on the EHD pump and 0°C sink temperature. Subcooled flow, which has subcooling level from 7.4°C to 14.3°C depending on the heat load, enters to the EV and the overall EV is in the subcooled region for <30 W of heat load. The saturation temperature is controlled by a reservoir temperature set point and obtained more exactly from absolute pressure measured in the loop. The saturation temperature is 29.7°C for this experiment. The temperature at the upper end section of EV (TC21) increased to 30°C after applying 10 W of heat load; however, the boiling did not occur at this point even though the surface temperature surpassed the saturation temperature, 29.7°C. The subcooled boiling occurred at a heat load of 15 W when the upper end section temperature value (TC21) reached 35.3°C, and the temperature dropped rapidly due to the enhanced heat transfer by the boiling process. Therefore, the wall superheat required for the onset of boiling is ~5.6°C for this condition, noting that the wall superheat required for the onset of boiling depends on surface and fluid properties. The generated pressure of the EHD pump decreases with time due to temperature increase in the EHD pump section caused by increasing the heat load. Dryout occurred at 95 W of heat load from the end section of the EV moving to the front section with time. The corresponding pressure drop across the EV and the mass flow rate as a

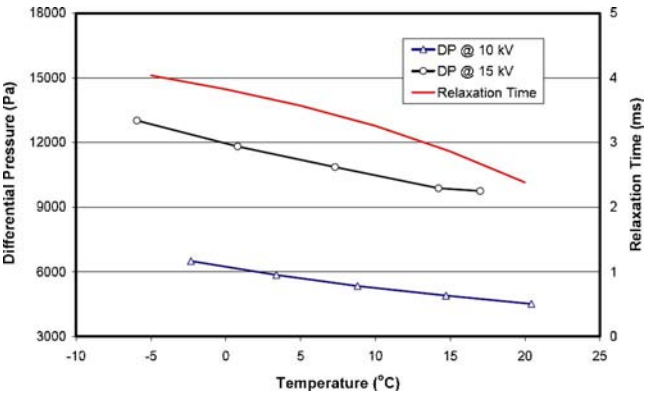

Fig. 9 Generated pressure and relaxation time as a function of temperature

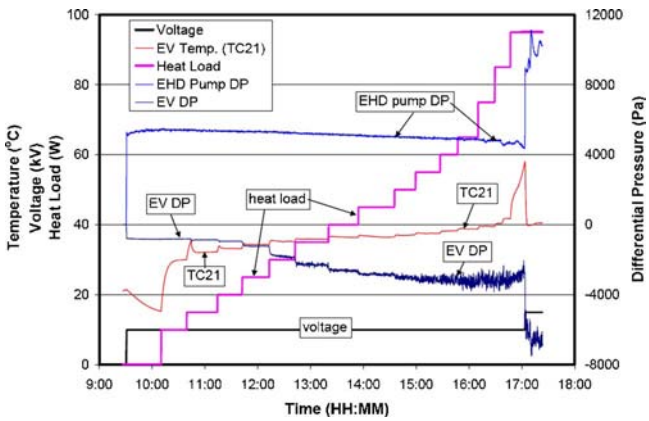

Fig. 11 Timeline of the generated pressure of the EHD pump, pressure drop across the EV, heat load on the EV, the applied voltage on the EHD pump, and the EV upper end section temperature (TC21) at 0°C sink temperature

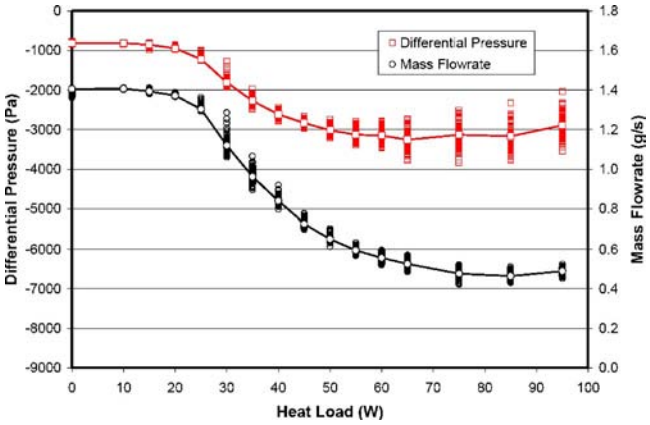

Fig. 12 Pressure drop across EV and mass flow rate as a function of heat load

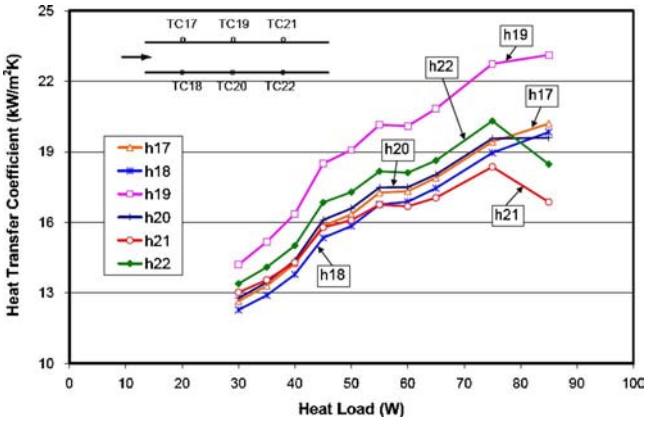

Fig. 13 Heat transfer coefficient along EV as a function of heat load

function of heat load are presented in Fig. 12. The pressure drop across the EV increased and reached a maximum of ~3260 Pa at 65 W as the heat load increased; however, it decreased beyond 65 W of heat load and reached ~2890 Pa at 95 W. On the other hand, the mass flow rate decreased and reached a minimum of ~0.46 g/s at 85 W as the heat load increased, and then increased to 0.49 g/s during the dryout point (i.e., 95 W of heat load). This inconsistency implies that pressure drop in the transport line after the EV is higher at 75 W and 85 W than that of 65 W due to the increased acceleration pressure loss in the transport line. The pressure drop decreased and the mass flow rate increased during the dryout, implying that the vapor-phase pressure drop is lower than the two-phase pressure drop. The above-mentioned trends of the pressure drop with heat load (i.e., the pressure drop increases with heat load until a certain point and decreases beyond that point) were observed in all tests with boiling phenomena in the EV. This implies that the two-phase pressure drop increases with void fraction increase until a certain value but reduces beyond that point. The data confirm that the two-phase pressure drop during boiling is a function of the flow regime. The oscillation of the pressure drop at the EV, caused by an unstable boiling process, also varies as the boiling process develops. It usually increases as the heat load increases until a certain point and was more significant with low flow rate. Table 2 shows the length of the subcooled region, X_{sat}, the local vapor quality at thermocouple locations in the EV for each heat load.

Figure 13 presents the corresponding heat transfer coefficient distributions along the EV as a function of heat load prior to dryout. The heat transfer coefficient h is calculated as $h=q/(T_w-T_{sat})$ where q is heat flux and T_w, T_{sat} is wall temperature and saturation temperature, respectively. Figure 14 presents flow pattern map based on Wojtan–Ursenbacher–Thome model [17] at $q=202864.0$ W/m^2, $G=193.1$ kg/m^{2}s, which corresponds to 85 W of heat load condition. This map is calculated according to the procedure and equations in Wojtan et al. [17]. As the vaporization process proceeds, the flow will encounter specific flow regime along the EV, depending on applied heat flux and flow mass velocity. For 85 W of heat load condition, the flow will encounter slug (S), intermittent (I), annular (A), dryout (D), and mist (M) flow regime as quality increases. Heat transfer coefficient increases with heat load until the onset of dryout peaking at annular flow regime. The heat transfer coefficient at the end section region (h21, h22) peaks at 75 W and drops at 85 W implying that dryout starts at 85 W in the region. This is in accord with the flow-pattern map presented in Fig. 14. The quality value at the location for 85 W of heat load is 0.584, and the flow is dryout flow regime. On the other hand, the heat transfer coefficient at the midsection region (h19, h20) peaks at 85 W, and the flow is intermittent flow regime in the flow-pattern map. The intermittent flow regime includes unsteady flow patterns, such as plug and slug flows. Therefore, the transition from intermittent to annular and then to dryout flow regime occurs in the region between TC19 and TC21. Transition to the dryout flow regime is usually first

Table 2 Length of the subcooled region and vapor quality at thermocouple locations in the EV for each heat load

Heat load (W)	X_{sat}[a] (mm)	Quality (x)[b] at $X=19.05$ mm	at $X=38.1$ mm	at $X=57.15$ mm
30	53.51	0.000	0.000	0.006
35	35.82	0.000	0.005	0.047
40	25.23	0.000	0.037	0.092
45	17.44	0.006	0.077	0.149
50	13.21	0.027	0.116	0.204
55	10.25	0.049	0.156	0.263
60	8.47	0.069	0.193	0.318
65	7.05	0.090	0.232	0.375
75	5.36	0.130	0.311	0.493
85	4.44	0.162	0.373	0.584

[a] $X_{sat}=\dot{m}\ C_p(T_{sat}-T_{in})/(q\cdot\pi D_i)$.

[b] $x(X)=\int_{X_{sat}}^{X} q\pi D_i dX/\dot{m}h_{lv}$, where $\dot{m}$ is the mass flow rate; D_i inner diameter; C_p, specific heat at constant pressure; T_{sat}, saturation temperature; T_{in}, evaporator inlet temperature; X, distance along the EV; and h_{lv}, latent heat of vaporization

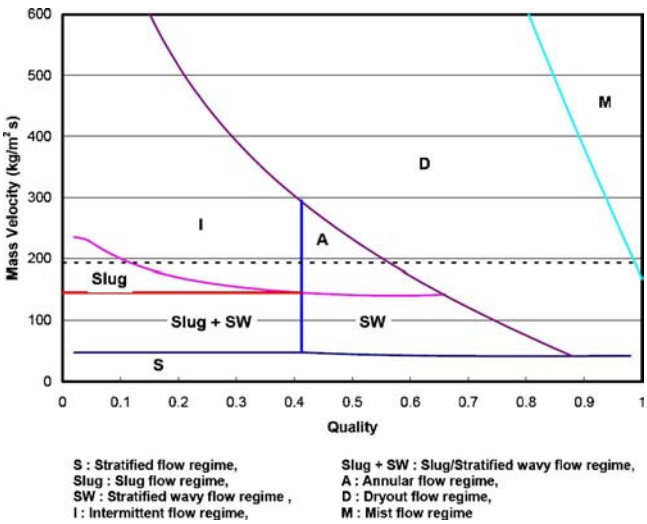

Fig. 14 Flow pattern map at 85 W of heat load ($q=202864.0$ W/m^2, $G=193.1$ kg/m^{2}s)

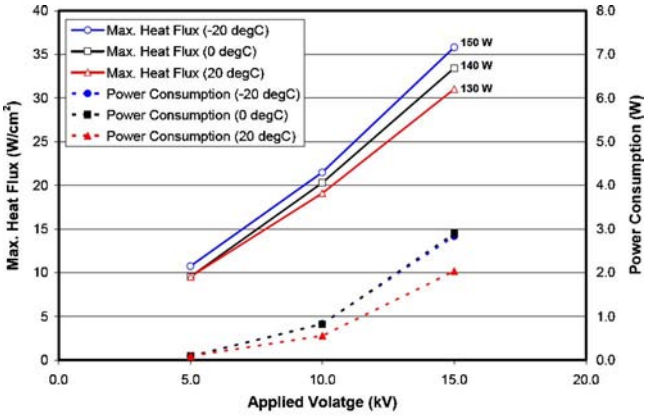

Sink (°C)	Heat Flux (W/cm²)			Power Consumption (W)		
	5 kV	10 kV	15 kV	5 kV	10 kV	15 kV
-20	10.7	21.5	35.8	0.093	0.83	2.83
0	9.5	20.3	33.4	0.10	0.83	2.89
20	9.5	19.1	31.0	0.094	0.56	2.03

Fig. 15 Critical heat flux and power consumption of the EHD pump as a function of the applied voltage at −20°C, 0°C, and 20°C of sink temperature

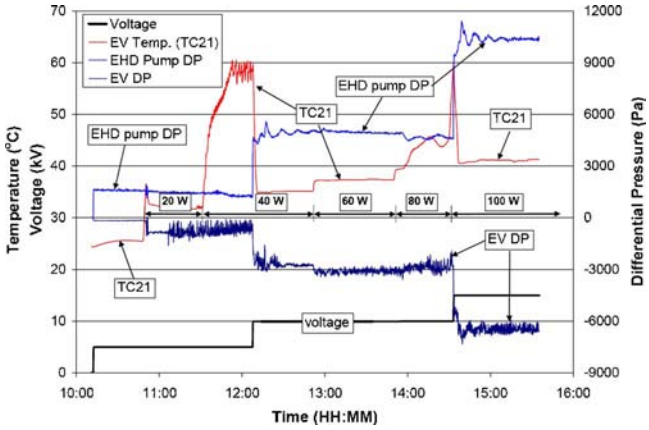

Fig. 16 Timeline of the generated pressure of the EHD pump, pressure drop across the EV, the applied voltage on the EHD pump, and the EV upper end section temperature at 0°C sink temperature

observed along the upper portion of the tube wall because of the tendency of gravity to thin the liquid film on the upper tube wall. Prior to the onset of partial dryout, heat transfer across the liquid film in annular flow regime becomes more efficient as the film becomes progressively thinner [18]. This is confirmed from that the heat transfer coefficient on the upper midsection (h19) is higher than the heat transfer coefficient on the lower midsection (h20).

Figure 15 presents the maximum heat flux and power consumption of the EHD pump as a function of the applied voltage at 20°C, 0°C, and −20°C of sink temperature, respectively. The power consumption in Fig. 15 corresponds to the value in ~8 h of operation. The power consumption decreases with time since the current usually shows the maximum value at initial operation and decreases with time approaching to a nearly constant value after long operation. The maximum heat flux increases as the sink temperature decreases. The maximum heat flux values at 15 kV for 20°C, 0°C, and −20°C correspond to 130 W, 140 W, 150 W of the EV heat load, respectively. Therefore, the maximum heat load for the test matrix (sink between −20°C and 20°C, applied voltage between 0 and 15 kV) was 150 W, providing ~1500 W m of heat transport capacity. The maximum power consumption percentage over the heat load transported is 1.56%, 2.07%, and 1.89% at 15 kV for 20°C, 0°C, and −20°C of sink temperature, respectively. Note that the pump pressure generation and the heat transport capacity could be increased simply by increasing the number of the electrode pairs at the same applied voltage. The trend of pressure generation increase with the number of electrode pairs increase can be found in [11]. The superheat required for the boiling onset was in the range between 2.6°C and 10.1°C. It did not show any specific dependency on parameters, such as mass flow rate, heat loads, sink temperature, and EV inlet temperature.

Temperature control and recovery from dryout are important operating parameters. The test procedure to demonstrate the EV dryout recovery by EHD pump operation is as follows. Initially, the chiller was turned on with a set-point temperature between −20°C and 20°C, and 5 kV was applied to the EHD pump. Once the chiller reached the steady state, the electric power to heaters was turned on. The power to heaters was maintained constant until the loop parameters, such as the temperatures at EV, pressure generation through the EHD pump, and mass flow rate, reached steady state and stepped up by 20 W to a higher level. The increase of the heat load to the EV continued until dryout occurred in the EV or the temperature reached the predetermined maximum temperature limit, 60°C. The applied voltage on the EHD pump was then stepped up by 5 kV after the dryout proceeded for a period of time. Once the dryout was recovered and the temperature of the EV reached a steady state, the heater power was again increased to a higher level. The increase in heat load to the EV continued until the dryout of the evaporator started again. Figure 16 presents the timeline of the measured pressure generation across EHD conduction pump and the pressure drop across the EV and the EV upper end section temperature (TC21) in the loop when the heat load on EV was varied from 20 W to 100 W by 20 W at 0°C chiller set temperature. Usually, the EV upper end section is the first region dryout occurs, therefore, TC21 was chosen to investigate the dryout recovery. The negative sign in differential pressure indicates the pressure drop through the EV, and the positive sign indicates the pressure generation by the EHD pump. There was 5.14 W of heat load applied to preheater before applying the heat load on the EV. The voltage on the EHD pump was initially applied with 5 kV and increased by 5 kV when dryout occurred. When 25.14 W of heater load including preheater load was applied, boiling initiated and pressure drop across the heater increased approximately from 168 Pa to 819 Pa. TC21 peaked at 36.5°C before boiling started and dropped to 31.7°C because of the enhanced heat transfer by the boiling. Dryout occurred and TC21 reached 60°C at 45.14 W of heater load but dropped rapidly to 35°C when the applied voltage on the EHD pump increased to 10 kV. At 10 kV, the EV load increased by 20–100 W and dryout occurred again and TC21 started to increase to the limit, 60°C, at 100 W of the EV load. TC21 dropped rapidly to 41°C by increasing the applied voltage to 15 kV. The pressure drop across the heater increased approximately from 2550 Pa to 6470 Pa, mainly because of the increased mass flow rate at 15 kV of the applied voltage. The same test procedure at −10°C of chiller set temperature is presented on Fig. 17. The boiling occurred at 25.14 W of total heat load when TC21 reached to 40.6°C. Similarly, the dryout occurred at 45.14 W and 105.14 W of the total heat load for 5 kV and 10 kV of the applied voltage, respectively. TC21 increased rapidly during dryout at 5 kV and 10 kV but dropped promptly when the applied voltage increased to 10 kV and 15 kV, respectively, recovering from dryout condition. The results in Figs. 16 and 17 demonstrate that the EV dryout could be easily recoverd by increasing the potential of the EHD pump.

It was observed that the pressure drop oscillation across the EV exists during boiling process and the magnitude of the oscillation varied as the boiling process developed and presented even higher

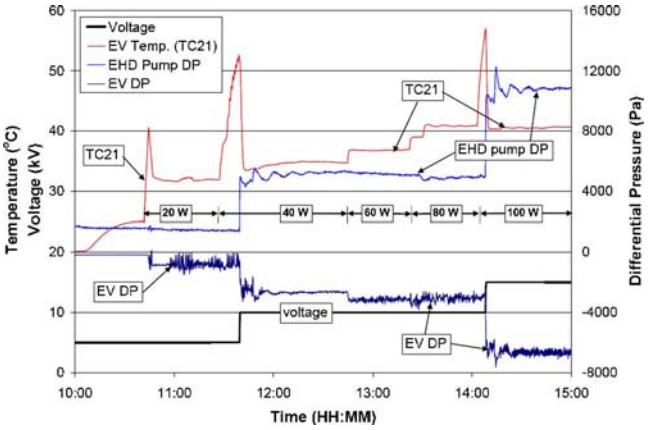

Fig. 17 Timeline of the generated pressure of the EHD pump, pressure drop across the EV, the applied voltage on the EHD pump, and the EV upper end section temperature at −10°C sink temperature

than 2000 Pa in magnitude. However, the EHD pump operated consistently without a significant perturbation or performance deterioration. This seems to be because the oscillation is damped out through the long transport lines and the condenser capacity is enough so the EHD pump always operates in single liquid phase.

Conclusion

An electrohydrodynamic (EHD) conduction pump that utilizes the heterocharge layers in the vicinity of the electrodes was built and installed in the liquid passage of a two-phase loop to investigate the heat transport capacity (maximum heat flux) the EHD pump can sustain and confirm the satisfactory operation of the EHD pump in the two-phase loop. The EHD conduction pump provided robust operation even when the loop has two-phase fluid and a significant pressure oscillation by boiling occurred in the evaporator (EV) section. Furthermore, the EHD conduction pump provided immediate recovery from dryout condition by simply increasing the applied voltage. The EHD conduction pump operated at 15 kV presented pressure head on the order of 13,000 Pa with <2.83 W of electric power at −20°C of sink temperature, providing thermal control capacity for 35.8 W/cm^2 of heat flux and 1500 W m of heat transport with R134a as the working fluid. Note that the thermal control capacity can be increased by enhancing the evaporator surface and/or simply increasing the number of the electrode pairs. It was also confirmed that the performance of the EHD conduction pump depends on the operating temperature with higher pressure generation at lower temperature of working fluid, and this phenomenon was clearly explained with the EHD conduction pumping mechanism. Most importantly, the performance of the EHD conduction pump in this study confirms that the EHD conduction pump can be used as stand-alone system for high heat flux thermal control.

Acknowledgment

This work was supported by National Research Council and NASA Goddard Space Flight Center Laser Risk Reduction Project.

Nomenclature

c = net electric charge density, C/m^3
C_p = specific heat at constant pressure, J/(kg K)
D_i = inner diameter of evaporator, m
$\vec{E}$ = electric field, V/m
$\vec{f}_e$ = electric body force density, N/m^3
G = mass velocity, kg/(m^2 s)
h = heat transfer coefficient, W/(m^2 K)
h_{lv} = latent heat of vaporization, J/kg
J = Joule heating ($=\sigma E^2$), W/m^3
$\dot{m}$ = mass flow rate, kg/s
q = heat flux, W/m^2
T = temperature, K
T_{in} = evaporator inlet temperature, K
T_{sat} = saturation temperature, K
T_w = wall temperature, K
V = voltage, V
X = distance along evaporator, m
X_{sat} = length of subcooled region in evaporator, m
x = quality

Greek Symbols

ε = electric permittivity, F/m
ρ = fluid density, kg/m^3
σ = electric conductivity, S/m
τ = charge relaxation time ($=\varepsilon/\sigma$), s

References

[1] Butler, C., Ku, J., and Swanson, T., 2002, "Loop Heat Pipes and Capillary Pumped Loops—An Applications Perspective," Space Technology and Applications International Forum (STAIF), Albuquerque, Feb. 3–7.
[2] Jones, T. B., 1974, "An Electrohydrodynamic Heat Pipe," Mech. Eng. (Am. Soc. Mech. Eng.), **96**, pp. 27–32.
[3] Sato, M., Nishida, S., and Noto, F., 1992, "Study on Electrohydrodynamical Heat Pipe," *ASME JSES KSES International Solar Engineering Conference*, Part 1 of 2, Maui, Hawaii, April 5–9, pp. 155–160.
[4] Bryan, J. E., and Seyed-Yagoobi, J., 1997, "Heat Transport Enhancement of Monogroove Heat Pipe With Electrohydrodynamic Pumping," J. Thermophys. Heat Transfer, **11**(3), pp. 454–460.
[5] Jeong, S. I., and Seyed-Yagoobi, J., 2002, "Performance Enhancement of a Monogroove Heat Pipe With Electrohydrodynamic Conduction Pumping," ASME International Mechanical Engineering Congress and Exposition (IMECE), New Orleans.
[6] Mo, B., Ohadi, M. B., Dessiatoun, M. M., and Cheung, K. H., 1999, "Startup Time Reduction in an Electrohydrodynamically Enhanced Capillary Pumped Loop," J. Thermophys. Heat Transfer, **13**(1), pp. 134–139.
[7] Melcher, J. R., 1981, *Continuum Electromechanics*, MIT Press, Cambridge, MA.
[8] Zhakin, A. I., 1998, "Conduction Models in Dielectric Liquids," *Electrohydrodynamics*, Castellanos, A., ed., Springer, New York, Chap. 6.
[9] Atten, P., and Seyed-Yagoobi, J., 2003, "Electrohydrodynamically Induced Dielectric Liquid Flow Through Pure Conduction in Point/Plane Geometry," IEEE Trans. Dielectr. Electr. Insul., **10**(1), pp. 27–36.
[10] Jeong, S. I., Seyed-Yagoobi, J., and Atten, P., 2003, "Theoretical/Numerical Study of Electrohydrodynamic Pumping Through Conduction Phenomenon," IEEE Trans. Ind. Appl., **39**(2), pp. 355–361.
[11] Jeong, S. I., and Seyed-Yagoobi, J., 2002, "Experimental Study of Electrohydrodynamic Pumping Through Conduction Phenomenon," J. Electrost., **56**, pp. 123–133.
[12] Jeong, S. I., and Seyed-Yagoobi, J., 2004, "Innovative Electrode Designs for Electrohydrodynamic Conduction Pumping," IEEE Trans. Ind. Appl., **40**(3), pp. 900–904.
[13] Jeong, S. I., and Seyed-Yagoobi, J., 2004, "Fluid Circulation in an Enclosure Generated by Electrohydrodynamic Conduction Phenomenon," IEEE Trans. Dielectr. Electr. Insul., **11**(5), pp. 899–910.
[14] Editorial Board of ASME J. Heat Transfer, 1993, "Journal of Heat Transfer Policy on Reporting Uncertainties in Experimental Measurements and Results," ASME J. Heat Transfer, **115**, pp. 5–6.
[15] Abernathy, R. B., Benedict, R. P., and Dowdell, R. B., 1985, "ASME Measurement Uncertainties," ASME J. Fluids Eng., **107**, pp. 161–164.
[16] Bryan, J. E., 1998, "Fundamental Study of Electrohydrodynamically Enhanced Convective and Nucleate Boiling Heat Transfer," Ph.D. dissertation, Department of Mechanical Engineering, Texas A&M University, College Station.
[17] Wojtan, L., Ursenbacher, T., and Thome, J. R., 2005, "Investigation of Flow Boiling in Horizontal Tubes: Part I—A New Diabatic Two-Phase Flow Pattern Map," Int. J. Heat Mass Transfer, **48**, pp. 2955–2969.
[18] Carey, V. P., 1992, "Convective Boiling in Tubes and Channels," *Liquid-Vapor Phase-Change Phenomena: An Introduction to the Thermophysics of Vaporization and Condensation Processes in Heat Transfer Equipment*, Taylor & Francis, Bristol, PA, Chap. 12.

On the Transient Analysis of a V-Shaped Microgrooved Heat Pipe

Balram Suman[1]
e-mail: suman@cems.umn.edu

Nazish Hoda

Department of Chemical Engineering and Materials Science,
University of Minnesota,
151 Amundson Hall,
421 Washington Avenue SE,
Minneapolis, MN 55455

In this paper, we present a transient mathematical model for a V-shaped microgrooved heat pipe considering the temporal variations in the fluid flow, and heat and mass transfer, and utilizing a macroscopic approach. Unlike other heat pipe models, the shear stress at the liquid-vapor interface and the disjoining pressure have been used in the momentum balance equation of the model. The sensible heat used by the substrate is also taken into account using a pseudo-lump capacity model. The coupled nonlinear partial differential equations governing the transient fluid flow, heat and mass transfer have been solved numerically. The transient and steady-state profiles for the radius of curvature, liquid and vapor velocity, liquid pressure, and substrate temperature have been obtained. The mathematical model is capable of predicting the time required for the onset of dry out at the hot end, and for a micro heat pipe to reach steady state. The time required to reach steady state is independent of heat input, heat pipe inclination, groove angle, and Q_{ss} profile. However, the time required for the onset of dry out at the hot end decreases with increasing heat input, inclination, and groove angle. The model predicted results have been successfully compared to the results from the literature. The general nature of this model and the associated study can be useful for many practical applications in the microscale heat exchange. [DOI: 10.1115/1.2759975]

Keywords: micro heat pipe, transient modeling, capillary phenomenon, interface

1 Introduction

Electronic devices have increased in computing ability and processing speed and decreased in size, and thus, the efficient removal of the heat generated in these devices has become increasingly important. Excess heat results in internal stress on the individual components, thus creating reliability problems. Fan-assisted heat sinks require electrical power and reduce battery life, and standard metallic heat sinks, while capable of dissipating the thermal load, are too large to be incorporated into the low-profile notebook packages. Two-phase heat transfer mechanism is found to be a viable option for such purposes; thus, micro heat pipes offer a highly efficient passive, compact heat transfer solution. Micro heat pipes have also been, now, used in the removal of heat from the leading edges of stator vanes in turbines, thermal conductivity enhancement in high-temperature spacecraft radiator fins, and nonsurgical treatment of cancerous tissue through hyper- or hypothermia [1,2]. Although the use of a micro heat pipe for enhanced heat transfer are becoming increasingly common, the transient operation of a V-shaped micro heat pipe and the associated capillary pumping capacity has not been investigated in detail. The transient analysis of fluid flow and heat transfer of a V-shaped micro heat pipe is also relevant for the understanding of the transfer processes and the designing of such systems. Therefore, in this paper, we discuss a transient analysis of a micro heat pipe, which will be helpful to understand the micro heat pipe operation and will also be useful for the start-up and shutdown of the micro heat pipe.

A micro heat pipe, as proposed by Cotter [3], is defined to be "so small that the mean curvature of the liquid-vapor interface is necessarily comparable in magnitude to the reciprocal of the hydraulic radius of the total flow noncircular channel." In a micro heat pipe, the capillary pressure promotes the flow of the coolant liquid from the condenser to the evaporator through the corner regions. The capillary pressure is governed by the pressure jump at the liquid-vapor interface, which is a function of the radius of curvature of the liquid meniscus, the surface tension, and the wettability of the coolant liquid and the substrate system [4,5]. In particular, the sharp corners have been shown to be necessary for an optimal heat pipe operation [6]. As the literature in this area has recently been discussed extensively elsewhere [7] and continues to evolve, we do not provide a detailed review here, but rather discuss briefly next.

Thus far, the start-up and shutdown of a V-shaped micro heat pipe have not been investigated. The unsteady-state operation of a V-shaped microgrooved heat pipe is useful in understanding the start-up and the shutdown operations, and the obtained results will also be helpful to understand the capillary phenomenon. Therefore, the mathematical modeling of the transient operation of a V-shaped is a way to start with and further, it is important for design and optimization of heat pipes. The transient behavior of heat pipes under various operating conditions has been under study for quite some time [7–18]. However, the transient operation of a micro heat pipe is rarely discussed. The experimental analysis of the transient behavior of the micro heat pipe has been performed by Wu and Peterson [8], Wu and Peterson [9], and Wu et al. [10]. Recently, Suman et al. [18] have presented a semi-transient model for a triangular micro heat pipe. They have considered temporal variation only in heat transfer, and steady state in the mass and momentum transfer processes. They have obtained the transient variation in the radius of curvature, liquid velocity, liquid pressure, and substrate temperature due to the temperature dependency of thermophysical properties of the coolant liquid. In their model, the amount of heat used to increase the sensible heat of the substrate was considered negligible compared to the heat used for the evaporation and the condensation of the coolant liquid. Because of these assumptions, the model [18] fails to capture the complete transient behavior of the micro heat pipe. For example, the model predicts that the transient liquid pressure in-

[1]Corresponding author.

Contributed by the Heat Transfer Division of ASME for publication in the JOURNAL OF HEAT TRANSFER. Manuscript received December 14, 2006; final manuscript received March 5, 2007. Review conducted by Yogesh Jaluria.

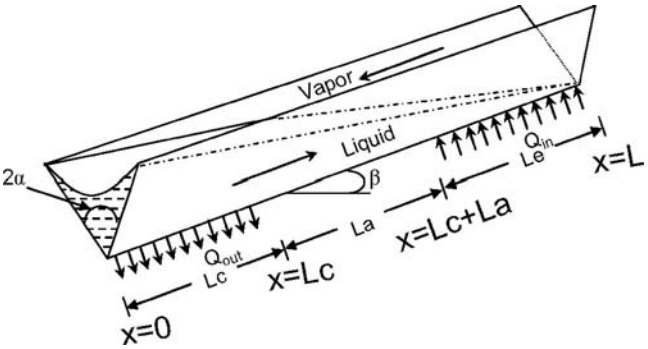

Fig. 1 A V-groove showing heat pipe dimensions and flow directions

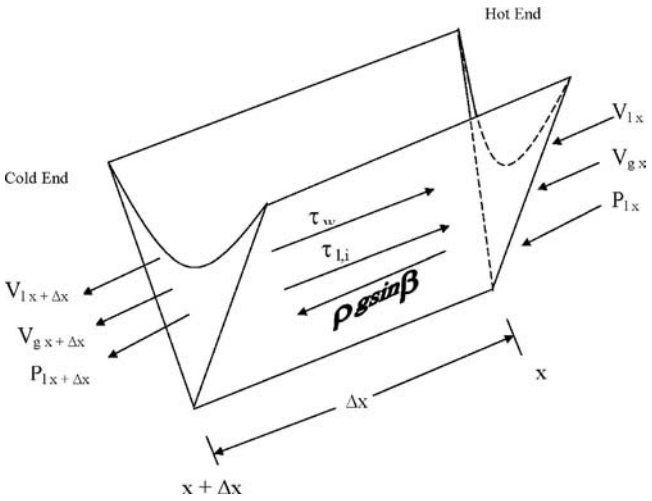

Fig. 2 Volume element of a V-shaped micro heat pipe with all forces specified

creases with time, which contradicts our physical understanding. (Details have been explained in the results and discussion section). Additionally, the variations in the radius of curvature, liquid velocity with time are found to be very small. Therefore, the transient analysis of the micro heat pipe is the subject of this work. Herein, we have first extended the previous model [18]. The extended model accounts for the shear stress, at the liquid-vapor interface, as well as disjoining pressure in the momentum balance equation, and the sensible heat in the energy balance equation. The model does not assume having same liquid and substrate temperature and also evaluates the vapor velocity. Additionally, the time to reach the onset of the dry-out has been obtained. These were not the subject of the previous study [18]. Thus, it is noteworthy to mention that this paper is significantly different from the previous paper published by Suman et al. [18]. The transient coupled nonlinear equations for the liquid flow, heat and mass transfer presented in this work have been solved using a semi-implicit scheme. The model developed is capable of handling different operating conditions, substrate and coolant liquid combinations, and grooves of different shapes and sizes, which widens the applicability of presented model in this work.

2 Model

In this study, a V-shaped microgrooved heat pipe has been considered. The schematic of a V-shaped heat pipe is shown in Fig. 1. "Hot end" and "cold end" are said to denote the farthest end of the evaporator and the condenser regions, respectively. The optimal amount of the coolant liquid is charged in a heat pipe so that at steady state, the cold end remains completely filled with the coolant liquid, such that the radius of curvature can be calculated from the groove geometry of a micro heat pipe. In an operating heat pipe, the liquid is pushed from the cold end to the hot end due to a decrease in the radius of curvature caused by the evaporation and the condensation of the coolant liquid. With a decrease in the radius of curvature, the capillary pressure difference between the hot and the cold end is generated, which gives the driving force for fluid flow. It has been shown [19] that the capillary force primarily causes the axial liquid flow. A number of micro heat pipe models [6,8,18,20,21] have neglected the shear stress at the interface arguing that the channel area for vapor flow is relatively large, and the vapor velocity is generally small at the low heat fluxes used in these studies. On the other hand, Suh et al. [16] suggested that the effect of the shear stress at the liquid-vapor interface can be obtained by appropriately correcting for the wall shear stress and derived different analytical expressions for the friction factors for two groove geometries. The general expression for the shear stress at the liquid-vapor interface has been proposed in Blangetti and Naushahi [17], which has been used in this study to account for the shear stress at the liquid-vapor interface.

2.1 Model Equations. The model equations are developed for all three regions, i.e., evaporative, adiabatic, and condenser, encompassing a heat pipe. The governing equations are derived under the following assumptions:

(i) One-dimensional unsteady incompressible flow along the length of a heat pipe since the flow along the transition region is small [19].
(ii) Negligible heat dissipation due to viscosity.
(iii) One-dimensional temperature variation along the length of a heat pipe.
(iv) Predefined steady-state heat flux distribution (Q_{ss}) with position used by the coolant liquid. The vapor pressure affects the rate of evaporation and condensation. However, a general agreement on the formulation of the dependency of heat fluxes on vapor pressure has not been done. Therefore, in this work, it has been assumed. Such an assumption has been successfully used in the literature [18,21].
(v) Convective heat loss has been neglected since the two-phase heat transfer is orders of magnitude higher than the natural convection.
(vi) Constant pressure in vapor region. The constant pressure in vapor region assumption is valid in this case because the vapor flow space in the channels is quite large, especially considering the low heat fluxes used in this study. The vapor pressure drop required for the flow has also been calculated and found to be very small.

A V-shaped microgrooved heat pipe of length Δx is taken as the control volume and shown in Fig. 2. The governing equations are similar to those presented in Suman et al. [18] and thus, discussed in brief next. The Young–Laplace equation in the differential form is given as

$$\frac{\partial P_l}{\partial x} = \frac{\sigma_l}{R^2}\frac{\partial R}{\partial x} \tag{1}$$

where $\partial P_l/\partial x$ and $\partial R/\partial x$ are the pressure and the radius of curvature gradients, respectively. The unsteady-state momentum balance has been derived considering disjoining pressure, which might be significant in the evaporative section since the liquid pool thickness is small. The differential form of unsteady-state momentum balance considering the shear stress at the liquid-vapor interface, and the disjoining pressure is given as

$$\rho_l A_l V_l \frac{\partial V_l}{\partial x} + A_l \frac{\partial P_l}{\partial x} + 2L_h \tau_w + \tau_{l,i} R_m - \rho_l g \sin\beta A_l - \frac{A' A_l}{2\pi h^4} \frac{dh}{dx} + \frac{\partial(\rho_l A_l V_l)}{\partial t} = 0 \quad (2)$$

The additional terms used in this extended model accounting for the shear stress at the interface and the disjoining pressure are fourth and sixth, respectively, where A' is the Hamaker constant and h is the liquid height. The liquid height is varying across the cross section. But the liquid height at the apex has been considered since our analysis mainly focuses on the capillary region. The substantial reduction in the liquid pool thickness is in the transition of the capillary and the thin-film regions. The expressions for R_m, liquid height h, substrate wetted length L_h, and the liquid area A_l can be obtained from the geometry [6], and are given as

$$R_m = R\phi \quad (3)$$

$$h = R\left[\frac{\cos(\alpha+\gamma)}{\tan\alpha} + \sin(\alpha+\gamma) - 1\right] \quad (4)$$

$$L_h = R\frac{\cos(\alpha+\gamma)}{\sin\alpha} \quad (5)$$

$$A_l = R^2\left[\{\cot(\alpha+\gamma) - \phi/2\} + \frac{\cot(\alpha+\gamma)\cos(\alpha+\gamma)\sin\gamma}{\sin\alpha}\right] \quad (6)$$

The differential form of the unsteady-state mass balance for the coolant liquid is given as

$$\frac{\partial(\rho_l A_l)}{\partial t} + \frac{\partial(\rho_l A_l V_l)}{\partial x} + \frac{Q_v R_m}{\lambda_l} = 0 \quad (7)$$

The differential form of the unsteady-state mass balance for the vapor is given as

$$\frac{\partial(\rho_g A_g)}{\partial t} + \frac{\partial(\rho_g A_g V_g)}{\partial x} - \frac{Q_v R_m}{\lambda_l} = 0 \quad (8)$$

The unsteady-state energy balance equation for the coolant liquid, neglecting the sensible heat of the coolant liquid, in the differential element is given as

$$Qw_b = Q_v R_m \quad (9)$$

where Q is the heat flux taken up or released by the coolant liquid from the solid substrate.

The variable Q is positive when taken up by the coolant liquid (in the evaporative section) and is negative, when released by the coolant liquid (in the condenser region) to the substrate. It is zero in the adiabatic section because no evaporation or condensation takes place in this region. The unsteady-state energy balance for the substrate is given as

$$A_{cs} K_s \frac{\partial^2 T_s}{\partial x^2} - Qw_b - \rho_s C_{ps} A_{cs} \frac{\partial T_s}{\partial t} = 0 \quad (10)$$

The heat interaction between the substrate and the coolant liquid on the heat pipe operating under steady state has been considered constant [21,24,25]. This assumption has been a compromise to make the model independent from the experiment because the heat transfer between the substrate and the coolant liquid has been obtained using an experiment in Anand et al. [26]. In this work, the variation of the heat interaction between the substrate and the coolant liquid has also been considered constant with position, but time varying, unlike a previous transient model [18], where it is constant with time as well, which is unrealistic because the heat supplied by the heater is initially conducted through the solid substrate. The supplied heat to the substrate is later taken up by the coolant liquid in the evaporative section and is transferred by two-phase heat transfer mechanism, i.e., evaporation. Similarly, the vapor is condensed in the condensing section and the released heat is being taken up by the solid substrate. No exchange of heat between the solid substrate and the coolant liquid has been considered in the adiabatic section. Thus, initially, the supplied heat by the heater is used to raise the temperature of the substrate and the heat interaction between the coolant liquid and the solid substrate is small. The heat transfer between the coolant liquid and the solid substrate increases with time since the heat used to raise the temperature of the solid substrate decreases. This phenomenon has been well approximated to the situation of the transient heat conduction problem with the external heat removal. Therefore, the heat taken up or released by the coolant liquid is approximated using a lump capacity model [27] and the exponential variation of the heat interaction between the coolant liquid and the solid substrate has been obtained as a characteristic time scale for the heat transfer in the solid substrate. Thus, the part of heat that is not to be used by the coolant liquid is considered being used in the heating of the substrate and other losses. Hence, the heat flux taken up or released by the coolant liquid is given as

$$Q = Q_{ss}\left(1 - e^{-t/\tau}\right) \quad (11)$$

where Q_{ss} is the input heat flux supplied by or taken up by the coolant liquid at steady state, Q is the heat flux used or released by the coolant liquid to the substrate at a time t, and τ is a characteristic time scale for the heat transfer in the solid substrate and defined as $\tau = \rho_s C_{ps} L^2 / K_s$.

2.2 Initial and Boundary Conditions. The boundary conditions at the cold end ($x=L$) are

$$R = R_o, \quad P_l = P_{v_o} - \frac{\sigma_l}{R_o}, \quad T_s = T_{\text{con}}, \quad V_l = 0, \quad V_g = 0, \quad \forall\ t$$

The variable R_o is the radius of curvature at the cold end and is obtained using groove geometry [24]. The temperature at the end of the condenser region, T_{con}, is taken to be 32 °C.

The boundary condition at the hot end ($x=0$) is

$$Q_{\text{heater}} = -K_s A_{cs} \left.\frac{\partial T_s}{\partial x}\right|_{x=0}$$

The initial conditions ($t=0$) are

$$T_s = T_{\text{con}}, \quad V_l = 0, \quad P_l = P_{vo} - \frac{\sigma_l}{R_o} - \rho_l g(L-x)\sin\beta$$

$$R = \frac{\sigma_l}{(P_{v_o} - P_l)}, \quad \forall\ x$$

2.3 Nondimensionalization. The following nondimensional and associated parameters have been used: friction factor (f) $= K'/N_{\text{Re}}$, Reynolds number (N_{Re}) $= D_h \rho_l V_l / \mu_l$, hydraulic diameter (D_h) $= 4A_l/2L_h$, wall shear stress (τ_w) $= \rho_l V_l^2 f/2$, shear at the liquid-vapor interface ($\tau_{l,i}$) $= [\rho_g(V_g - V_l)f/2] - \rho_g V_g(V_{g,i} - V_l)$ [23]. (Here, the velocity in the bracket is the relative velocity of the vapor), reference velocity (V_R) $= Q'/\rho_l R_o^2 \lambda_l$, reference pressure, ($P_R$) $= \sigma_l / R_o$, reference height (h_R) $= R_o[\cos(\alpha+\gamma)/\tan\alpha + \sin(\alpha + \gamma) - 1]$, reference temperature (T_R) $= T_{\text{con}}$, and time constant (τ) $= \rho_s C_{ps} L^2 / K_s$.

The dimensionless parameters are defined as follows: dimensionless radius of curvature (R^*) $= R/R_o$, dimensionless position (X^*) $= x/L$, dimensionless liquid velocity (V_l^*) $= V_l/V_R$, dimensionless vapor velocity (V_g^*) $= V_g/V_R$, dimensionless liquid pressure (P_l^*) $= P_l/P_R$, dimensionless substrate temperature (T_s^*) $= T_s/T_R$, dimensionless height (h^*) $= h/h_o = R^*$, dimensionless time (t^*) $= t/\tau$. The constant K' is used in the expression of friction factor, which is constant for a specific groove geometry. The dimensionless form of the heat and mass transfer and fluid flow equations are as follows:

$$\frac{\partial P_l^*}{\partial X^*} = \frac{1}{R^{*2}} \frac{\partial R^*}{\partial X^*} \tag{12}$$

$$\frac{\partial R^*}{\partial t^*} = -\left[\frac{\tau R^* Q_v R_m L}{2\rho_l A_l \lambda_l} + \frac{2\tau V_R V_l^*}{L R^*} \frac{\partial R^*}{\partial X^*} + \frac{\tau R^* V_R}{2L} \frac{\partial V_l^*}{\partial X^*} \right] \tag{13}$$

$$\frac{\partial V_l^*}{\partial t^*} = \frac{\tau g \sin(\beta)}{V_R} + \frac{\tau Q_v R_m V_l^*}{A_l \rho_l \lambda_l} - \frac{\tau B_2 V_l^*}{\rho_l (R_o R^*)^2} - \frac{\tau \tau_{l,i} R_m}{A_l \lambda_l} + \left[\frac{2\tau V_R V_l^{*2}}{L R^*} - \frac{\tau \sigma_l}{\rho_l V_R R_o L R^{*2}} + \frac{\tau A'}{2\pi \rho_l V_R L h_o^3 R^{*4}} \right] \frac{\partial R^*}{\partial X^*} \tag{14}$$

$$\frac{\partial V_g^*}{\partial X^*} = -\frac{Q_v R_l L}{\rho_l A_g \lambda_l V_R} + \frac{2A_l V_g^*}{A_g R^*} \frac{\partial R^*}{\partial X^*} + \frac{2A_l}{\tau \rho_l A_g V_R R^*} \frac{\partial R^*}{\partial t^*} \tag{15}$$

$$\frac{\partial T_s^*}{\partial t^*} = \frac{\partial^2 T_s^*}{\partial X^{*2}} - \frac{Q w_b L^2}{T_R A_{cs} K_s} \tag{16}$$

$$Q_V = \frac{Q w_b}{R_m} \tag{17}$$

$$Q = Q_{ss}(1 - e^{-t^*}) \tag{18}$$

The steady-state heat flux is given as

$$Q_{ss} = \frac{Q'}{f w_b L} \tag{19}$$

Here geometrical parameters A_l, w_b, R_o, and B_2 are taken from Suman and Hoda [6], taking ungrooved area to be zero and are given as

$$w_b = 2a \tag{20}$$

$$R_o = \frac{a \sin \alpha}{\cos(\alpha + \gamma)} \tag{21}$$

$$B_2 = \frac{\mu_l K' \cos^2(\alpha + \gamma)}{2 \sin^2 \alpha \left[\frac{\cot(\alpha + \gamma)\cos(\alpha + \gamma)\sin \gamma}{\sin \alpha} + \left\{ \cot(\alpha + \gamma) - \frac{2}{\phi} \right\} \right]^2} \tag{22}$$

The nondimensional boundary conditions at the cold end ($X^* = 1$) are

$$R^* = 1, \quad P_l^* = \frac{P_{vo}}{P_R} - 1, \quad T_s^* = \frac{T_{\text{con}}}{T_R}, \quad V_l^* = 0, \quad V_g^* = 0 \quad \forall \ t^*$$

The nondimensional boundary condition at the hot end ($X^* = 0$) is:

$$Q_{\text{heater}} = -\frac{K_s A_{cs} T_R}{L} \frac{\partial T_S^*}{\partial X^*}\bigg|_{X^*=0}, \quad \forall \ t^*$$

The nondimensional initial conditions ($t^* = 0$) are

$$T_S^* = \frac{T_{\text{con}}}{T_R}, \quad V_l^* = 0, \quad P_l^* = \frac{P_{vo}}{P_R} - 1 - \frac{\rho_l g L (1 - X^*) \sin(\beta)}{P_R}$$

$$R^* = \frac{P_R}{(P_{vo} - P_R P_l^*)}, \quad \forall \ X^*$$

2.4 Numerical Solution. The model inputs for governing equations (13)–(19) are heat pipe length, Q_{ss}-profile, and thermophysical properties of the coolant liquid and the substrate. The set of equations is the first- and second-order partial differential equations with different time scales. Hence, it was difficult to get a correct solution for them when solving together. Therefore, we have used a novel numerical technique, which has been described next.

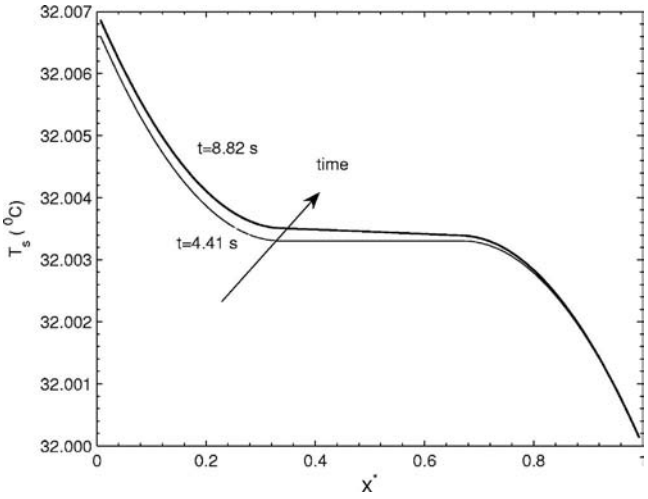

Fig. 3 Variation of the substrate temperature, T_s(°C) with the dimensionless position, X^* at different times (s)

First of all, the energy equation (Eq. (16)), being decoupled from the other three Eqs. (13)–(15) governing the radius of curvature, liquid, and vapor velocity, is solved for a given time step using Newton–Raphson method. The quantity Q_v is obtained by solving Eq. (17). Then, the set of partial differential equations (13)–(15) is converted to a system of algebraic equations using Gauss–Seidel method. The first-order spatial derivative has been estimated using forward or backward differencing method based on flow direction. The second derivatives have been estimated using a central difference method. The Neumann boundary conditions have been considered using ghost boundary nodes. The system of algebraic equations corresponding to the set of partial differential equations (13)–(15) is solved in a coupled manner using a Newton–Raphson method. Finally, the liquid pressure has been obtained using Eq. (12). Here, the semi-implicit method helps in taking a large time step without affecting the convergence.

The dimensionless step sizes for the spatial and the temporal discretizations are 0.2 and 0.1, respectively. The presented results are independent of step size. It is also observed that the quadratic convergence has been obtained for each case, and therefore, it is concluded that the Newton–Raphson method converges correctly. The reliability of the code has been verified by reproducing results of Suman et al. [18]. Using the above methodology, the transient profiles for the substrate temperature, radius of curvature, liquid velocity, etc., have been calculated.

3 Results and Discussion

For the transient analysis, 100 V-grooves of 200 μm width and spacing, and an apex angle of 60 deg have been considered. The V-groove is on the silicon substrate of 2 cm long with 10 deg inclination. Pentane is taken as a working fluid. The contact angle is considered zero. The length of the evaporative, adiabatic, and condenser regions are taken to be equal. The pressure in the vapor region is considered 101.3 kPa. For the disjoining pressure, the typical Hamaker constant ($A' = 3 \times 10^{-19}$ J) has been used. The temperature at the cold end (T_{con}) and the reference temperature (T_R) are taken as 32°C. The total heat input supplied to the heat pipe using a heater is taken as 0.5 W.

3.1 Model Predicted Results. The substrate temperature profiles as a function of axial position at different times has been presented in Fig. 3. Initially, the substrate temperature of a heat pipe is constant (32°C). This is not plotted since it is the initial condition. Because the supplied heat to the substrate taken up by

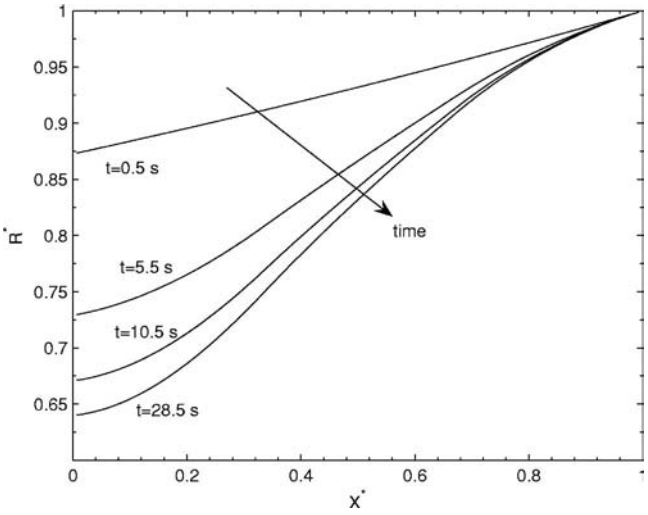

Fig. 4 Variation of the dimensionless radius of curvature, R^* with the dimensionless position, X^* at different times (s)

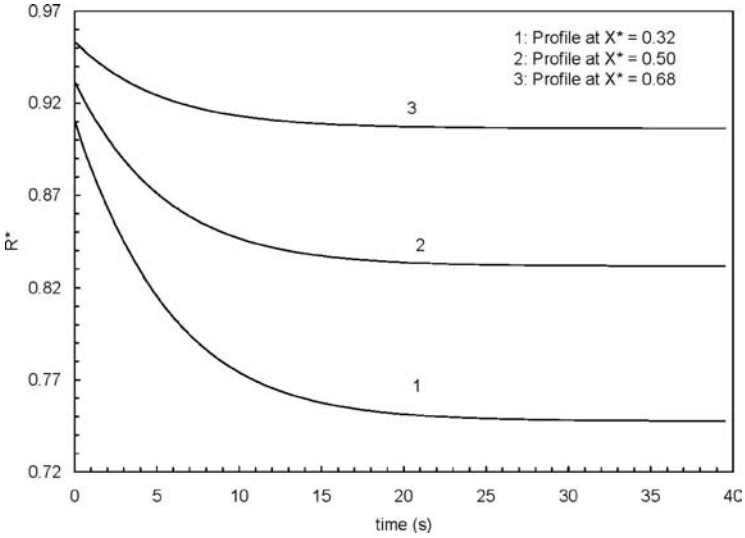

Fig. 5 Variation of the dimensionless radius of curvature, R^* with time (s) for different positions, $X^*=0.32, 0.5$, and 0.68

the coolant liquid increases, the chair-shaped temperature profile is established, flattening the adiabatic section temperature. Finally, a chair-shaped steady-state profile has been obtained. In the evaporative section, the heat is taken by the coolant liquid from the substrate and, thus, the temperature profile is concave upward and the profile is concave downward in the condensing section, where heat is taken up by the substrate from the coolant liquid. In the adiabatic section, there is no heat interaction between the coolant liquid and the substrate and, thus, the temperature is constant, which can be seen as a point of inflection. Because of the chair shape of the profile, the temperature difference between the hot and cold end is less than that in the corresponding conductive devices and, thus, a heat pipe can be used where heat has to be removed without generating a high-temperature difference.

The behavior of the radius of curvature gives the capillary pumping using the Young–Laplace equation. The capillary pumping is responsible for the fluid flow in a micro heat pipe. The profiles of the dimensionless radius of curvature along the length of a heat pipe (R^* versus X^*) at different times are presented in Fig. 4, which shows that the initial radius of curvature (referred to profile for $t=0.5$ s) is monotonically decreasing from the cold end to the hot end to balance the gravity. Once the evaporation/condensation of the coolant liquid starts, which results in decreasing a radius of curvature with time to generate enough driving force to push the coolant liquid from the cold to the hot end. Initially, the heat taken by the coolant liquid is less, and therefore, a lower driving force is required. Thus, the difference in the radius of curvature between the hot and the cold end is lower. Once the heat taken by the coolant liquid is almost constant, the amount of coolant liquid to be evaporated becomes constant and then requires a constant driving force. Therefore, at steady state, the radius of curvature is monotonically decreasing from the cold end to the hot end and remains constant with time to provide sufficient capillary pumping for the fluid flow in a heat pipe. The transient profiles of the radius of curvature at locations $X^*=0.32, 0.50$, and 0.68 have been presented in Fig. 5. One of these locations is in each evaporative, adiabatic, and condensing region. It is seen that the depression in the liquid pool is higher in the evaporative section because of evaporation to meet the requirement of the capillary pressure to sustain the fluid flow. The depression in the liquid pool in the adiabatic section is lower than that in the evaporative section as no evaporation. The liquid pool is the least depressed in the condensing region since condensation takes place. In all cases, the radius of curvature profile is monotonically decreasing with time, which is expected, as explained above in this paragraph.

The radius of curvature is decreasing as heat supplied to the coolant liquid increases with time. Thus, the difference between the vapor and the liquid pressure should increase, which results in a decrease in the liquid pressure with time. The variation of the liquid pressure with position at different times is presented in Fig. 6, and the consistent result, a decrease in the liquid pressure with time, has been obtained. Initially, a lower pressure difference is required to sustain the flow. With time, the heat supplied to the coolant liquid increases and to sustain evaporation, more liquid at the evaporative section is required, which demands a higher pressure drop between the cold end and the hot end to sustain the higher coolant liquid flow. Therefore, the pressure difference between the hot end and the cold end increases with time. The liquid pressure was found to increase with time (refer to Fig. 7(a) of Suman et al. [18]) when the temporal variation in mass and momentum transfer is neglected, where the time-varying liquid pressure is obtained due to the variations in the thermophysical properties, which fails to capture the complete transient phenomenon and produces inconsistent results. This was the motivation to consider transient in all transport processes in the present study.

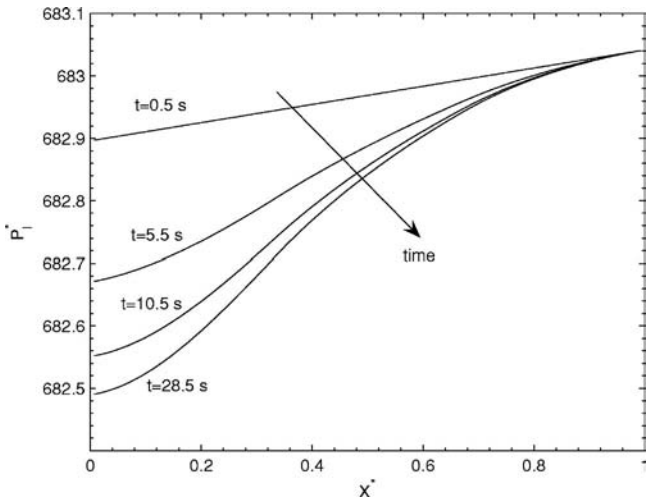

Fig. 6 Variation of the dimensionless liquid pressure, P_l^* with the dimensionless position, X^* at different times (s)

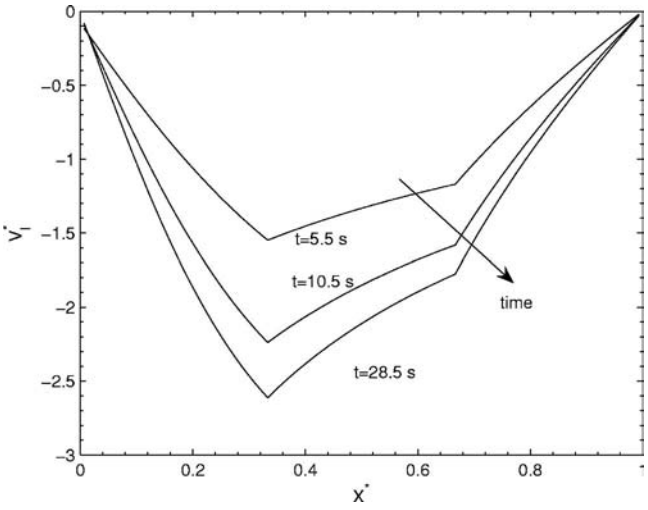

Fig. 7 Variation of the dimensionless liquid velocity, V_l^* with the dimensionless position, X^* at different times (s)

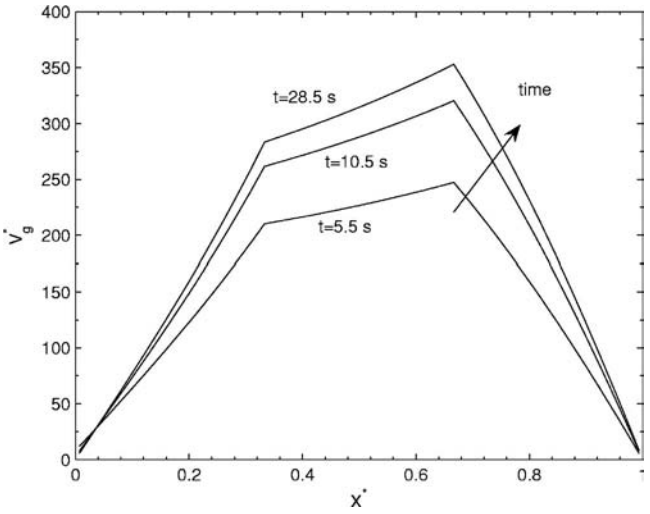

Fig. 8 Variation of the dimensionless vapor velocity, V_g^* with the dimensionless position, X^* at different times (s)

The variation of the axial liquid velocity at different times is presented in Fig. 7. The direction of the liquid velocity is from the cold end to the hot end, and thus, it is negative in Fig. 7. Initially, there is no heat supplied to the coolant liquid and, therefore, the liquid velocity is zero (initial boundary condition and has not been shown in Fig. 7). As the heat taken by the coolant liquid increases, the liquid starts flowing from the cold end to the hot end due to capillary pumping. With time, the amount of heat to be transferred increases and so does the liquid velocity. After some time, the amount of liquid to be evaporated becomes constant and requires a constant coolant liquid flow rate. Thus, the liquid velocity reaches steady state. The value of the axial liquid velocity is always zero at the hot end and increases in the evaporative region. This is due to the cumulative effect of replenishment of the amount evaporated, throughout the evaporator region. In the adiabatic region, although there is no evaporation and condensation, the liquid velocity decreases slightly. This is due to a slight increase in the radius of curvature in the adiabatic section (hence, an increase in the liquid flow area) and due to the frictional loss. In the condenser region, there is a further decrease in the liquid velocity because the condensation results in a sharper increase in the radius of curvature and, hence, the liquid flow area increases.

Equation (15) gives the vapor velocity in a heat pipe, which is important in order to check the sonic limit. It is obtained that the vapor velocity ($\sim$O(1)) is much below the sonic velocity. The vapor velocity as a function of dimensionless length at different times has been presented in Fig. 8. The direction of the vapor velocity is from the hot end to the cold end and, thus, positive. It has the similar trend as that of the magnitude of the liquid velocity in the evaporative and the condenser sections. In the adiabatic section, the radius of curvature increases and the area available for the liquid flow decreases. Therefore, a slight increase in the vapor velocity has been obtained. The magnitude of the vapor velocity is higher than that of the liquid velocity because the density of the vapor is less than that of the liquid.

The van der Waals force (disjoining pressure) is acting between the solid substrate and the vapor, and therefore, its magnitude is inversely proportional to the thickness of the liquid pool. If the force is attractive, then this force depresses the liquid-vapor interface, which results in a higher liquid velocity and, hence, a higher frictional loss and vice versa. As the radius of curvature gives the performance of a heat pipe, the effect of the disjoining pressure can be seen by plotting radius of curvature for different Hamaker constant values. In Fig. 9, the steady-state profile of the radius of curvature for different Hamaker constant values has been presented. It is seen that the effect of the disjoining pressure is not significant as both profiles for the radius of curvature coincide, as is clear from Fig. 9. Because the thickness of the liquid pool ($\sim$100 μm) is not small enough ($\sim$100 nm) in our region of interest (capillary) and, hence, it does not have a significant effect.

The micro heat pipe is a two-phase heat transfer device that transfers heat from one place to another by evaporating and condensing the circulating liquid. Thus, a micro heat pipe has liquid everywhere along the its length. When the heat input is higher than the critical heat input, a heat pipe generates a dry region near the hot end. The very first dry spot appears at the hot end, i.e., radius of curvature at the hot end is close to zero and the corresponding heat input is called the critical heat input, and then the onset of the dry out in a heat pipe is assumed. The effect of the heat input on the time required for the onset of the dry out at the hot end has been presented in Table 1. It is found that with an increase in the heat input, the time required for the onset of the dry out at the hot end decreases. As higher is the heat input, lower is the time required for evaporating the amount of coolant liquid to the onset of dry out at the hot end.

3.2 Model Validation. The mathematical model discussed in this work has been validated using experimental data and results.

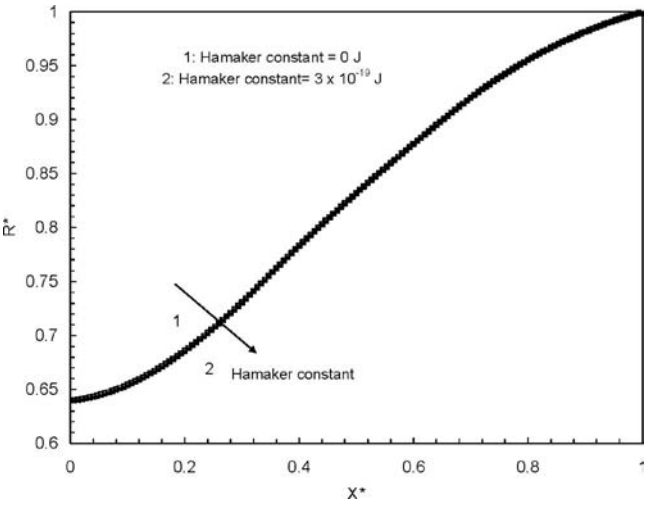

Fig. 9 Steady-state dimensionless radius of curvature (R^*) with the dimensionless position, X^* for different values of Hamaker constant

Table 1 Variation of time (s) to the onset of the dry out at the hot end with the heat input (W) for a V-shaped micro heat pipe of length 2 cm

Q' (W)	$t_{\text{dry out}}$ (s)
1.0	1.40
1.3	1.00
1.5	0.70
1.8	0.50
2.0	0.40

First, in this analysis, we have found that the time required to reach steady state is around 30 s, which is consistent with the experimental analysis conducted by Wu and Peterson [8] and Wang and Vafai [15]. It is noteworthy that the time to reach steady state is reported for a lab scale, and it will be higher for industrial applications. Additionally, Zhu and Vafai [17] also reported that the time to reach steady state is independent of the heat input, which is also verified in this study, although the substrate temperature is sensitive to the heat input due to its direct dependency. The time required to reach steady state is also found to be independent of heat pipe inclination, heat input distribution, and V-groove apex angle.

Anand et al. [26] used 33 V-grooves of 2 cm length with a groove depth of 68.82 μm, groove width of 100 μm, and a groove pitch of 200 μm. Pentane was used as a coolant liquid. The steady-state substrate temperature profile for this system is calculated for a heat input of 1.52 W for two different inclinations, 14.93 deg and 0 deg with reference temperature 32.6°C and 35.0°C, respectively. Here the evaporative length of 7 mm has been considered for the comparison because beyond that length, the temperature is almost constant, which is considered as the adiabatic section. Therefore, the profile for only the evaporative section has been presented taking dimensionless length. It is notable that in these cases, a heat pipe has a dry region. For comparison, the polynomial heat flux interaction between the substrate and the coolant liquid in the evaporative section is

$$Q_{ss} = \frac{Q'(m+1)}{w_b[L(1-f_2)]^{m+1}}(X^* - f_2)^m \tag{23}$$

and in the condensing section is

$$Q_{ss} = -\frac{Q'(m+1)}{w_b(f_1 L)^{m+1}}(f_1 - X^*)^m \tag{24}$$

where Q' is the heat input, m is the index for the heat flux interaction between the substrate and the coolant liquid polynomial, f_1 is the nondimensional coordinate of the junction of condensing and adiabatic sections, f_2 is the nondimensional coordinate of the junction of adiabatic and evaporative sections, and L is the length of a heat pipe. The values of m are 0.50 and 0.78 for 14.93 deg and 0 deg inclinations, respectively. The change in the value of m accounts for the gravity effect. The comparison of the calculated and the experimental dimensionless steady-state substrate temperature profiles is presented in Fig. 10. The substrate temperatures have been nondimensionlized using the corresponding reference temperature. The complete evaporative section has been shown, and only one point of adiabatic section has been shown because in the adiabatic section, the substrate temperature remains almost constant. Figure 10 shows a reasonable agreement between the experimental data and the theoretical predictions obtained from this transient study. The maximum discrepancy is $<5\%$. This is because of the assumption that there is no exchange of heat in the adiabatic section, which is not true in a real situation, neglecting the convective heat loss, and considering the polynomial variation of the heat flux interaction between the substrate and the coolant liquid. However, the exact variation of the heat flux interaction between the substrate and the coolant liquid with position cannot be determined without taking recourse of the experimental data [26], thereby compromising the independent nature of the developed theoretical model. It is noteworthy to mention that the temperature profile is concave upward, as it is in the evaporative section, and has a point of inflection in the adiabatic section, meaning no interaction of heat between the substrate and the coolant liquid.

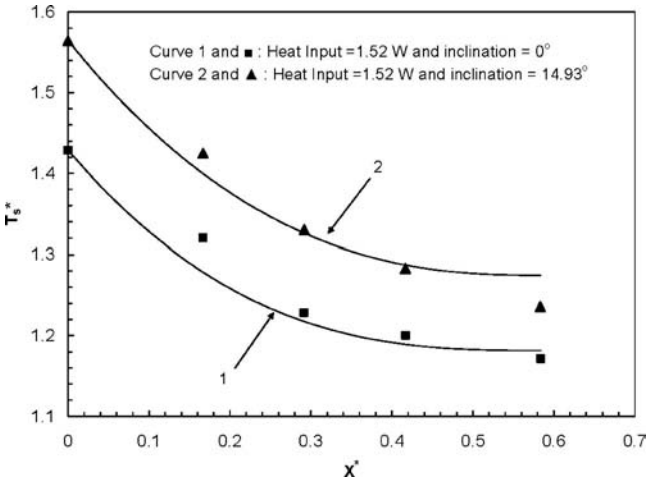

Fig. 10 Comparison of the theoretical and the experimental [23] dimensionless steady-state substrate temperature (Ts^*) with position X^*. The points are the experimental data and the solid lines are the theoretical predictions. The reference temperatures for 0 deg and 14.93 deg inclinations are 35°C and 32.6°C, respectively.

4 Summary and Conclusions

The paper presents a transient mathematical model for a V-shaped microgrooved heat pipe utilizing a macroscopic approach. The disjoining pressure, shear stress at the liquid-vapor interface, and the sensible heat have also been accounted for in the governing equations. The coupled equations for heat, mass, and momentum transfer are solved numerically to obtain the transient and steady-state profiles of various parameters, namely, substrate temperature, liquid velocity, liquid pressure, etc. This study predicts the correct trends for transient variation in the radius of curvature, the liquid velocity, the vapor velocity, and the liquid pressure. The true physical behavior, a decrease in the liquid pressure with time, is captured by the model presented in this work. The time to reach steady state is found to be independent of the heat input, heat pipe inclination, Q_{ss} variation, and groove angle. The time required to the onset of dry out at the hot end decreases with an increase in the heat input. The present study can be extended by considering two-dimensional variation in the fluid flow and heat transfer, and by eliminating the predefined heat interaction between the substrate and the coolant liquid with position.

Acknowledgment

The correspondence and discussion with Prabhat Kumar, NCSU, and the help in the manuscript preparation from Kiran Mishra are gratefully acknowledged.

Nomenclature

a = side length of a V-groove, m
A = area, m^2
A' = Hamaker constant, J
B_1 = constant in expression for A_l
B_2 = constant in expression for dV_l^*/dt^*
Cp = specific heat capacity, J/(kg °C)

D_h = hydraulic diameter, m
f = fractional length of each section in a heat pipe
f_1 = nondimensional coordinate of the junction of condensing and adiabatic sections
f_2 = nondimensional coordinate of the junction of adiabatic and evaporative sections
g = acceleration due to gravity, m/s^2
h = liquid height, m
K' = constant in expression for B_2
K = thermal conductivity, $W/(m\,^\circ C)$
L = length of a heat pipe, m
L_h = half of total wetted length, m
m = index for polynomial heat flux
N_{Re} = Reynolds number
P = pressure, N/m^2
Q = net heat flux supplied to the coolant liquid, W/m^2
Q' = net heat supplied to the coolant liquid, W
R = radius of curvature, m
R_m = meniscus surface area per unit length, m
t = time, s
T = temperature, °C
V = velocity, m/s
w_b = V-groove pitch, m
x,X = coordinate along the heat pipe, m

Greek Symbols

α = half-groove angle, rad
β = inclination of substrate with horizontal, rad
γ = contact angle, rad
ϕ = curvature, m^{-1}
λ = latent heat of vaporization, J/kg
μ = viscosity, $kg\,m^{-1}\,s^{-1}$
ρ = density, kg/m^3
σ = surface tension, N/m
τ = time constant, s, shear stress, N/m^2

Superscript

* = dimensionless variable

Subscripts

cs = cross section of substrate
con = cold end
i = interface
l = liquid
R,o = reference
s = solid
ss = steady state
v,g = vapor
w = wall

References

[1] Camarda, C. J., Rummler, D. R., and Peterson, G. P., 1991, "Multi Heat Pipe Panels," Report No. LAR-14150, NASA Technical Briefs.
[2] Badran, B., Albayyari, J. M., Gerner, F. M., Ramadas, P., Henderson, H. T., and Baker, K., 1993, "Liquid-Metal Micro Heat Pipes," *Heat Pipes and Capillary Pumped Loops*, A. Faghri, A. J. Juhasz, and T. Mahefkey, eds., ASME, New York, Vol. HTD 236, pp. 71–85.
[3] Cotter, T. P., 1984, "Principles and Prospects of Micro Heat Pipes," *Proc. of the 5th Int. Heat Pipe Conference*, Tsukuba, Japan, pp. 328–332.
[4] DasGupta, S., Schonberg, J. A., Kim, I. Y., and Wayner, P. C., Jr., 1993, "Use of Augmented Yong–Laplace Equation to Model Equilibrium and Evaporation Extended Menisci," J. Colloid Interface Sci., **157**, pp. 332–342.
[5] DasGupta, S., Schonberg, J. A., and Wayner, P. C., Jr., 1993, "Investigation of an Evaporative Extended Meniscus Based on the Augmented Yong–Laplace Equation," ASME J. Heat Transfer, **115**, pp. 201–208.
[6] Suman, B., and Hoda, N., 2005, "Effect of Variations in Thermophysical Properties and Design Parameters on the Performance of a V-Shaped Micro Grooved Heat Pipe," Int. J. Heat Mass Transfer, **48**(10), pp. 2090–2101.
[7] Suman, B., 2007, "Modeling, Experiment and Fabrication of Micro Heat Pipes: An Update," Appl. Mech. Rev., **60**, pp. 107–119.
[8] Wu, D., and Peterson, G. P., 1991, "Investigation of the Transient Characteristics of a Micro Heat Pipe," J. Thermophys. Heat Transfer, **5**, pp. 129–134.
[9] Wu, D., Peterson, G. P. and Chang, W. S., 1991, "Transient Experimental Investigation of Micro Heat Pipes," J. Thermophys. Heat Transfer, **5**, pp. 539–545.
[10] Peterson, G. P., and Mallik, A. K., 1995, "Transient Response Characteristics of Vapor Deposited Micro Heat Pipe," ASME J. Electron. Packag., **117**(1), pp. 82–87.
[11] Chang, W. S., and Colwell, G. T., 1985, "Mathematical Modeling of the Transient Operation Characteristics of a Low Temperature Heat Pipe," Numer. Heat Transfer, **8**, pp. 169–186.
[12] Colwell, G. T., and Chang, W. S., 1983, "Measurement of Transient Behavior of a Capillary Structure Under the Heavy Thermal Loading," Int. J. Heat Mass Transfer, **27**, pp. 541–551.
[13] Faghri, A., and Chen, M. M., 1989, "A Numerical Analysis of the Effects of Conjugate Heat Transfer, Vapor Compressibility, and Viscous Dissipation in Heat Pipe," Numer. Heat Transfer, Part A, **16**, pp. 389–405.
[14] Turnier, J. M., and El-Genk, M. S., 1994, "A Heat Pipe Transient Analysis Model," Int. J. Heat Mass Transfer, **37**, pp. 753–762.
[15] Wang, Y., and Vafai, K., 2000, "An Experimental Investigation of the Transient Characteristics on a Flat Plate Heat Pipe During Startup and Shutdown Operations," ASME J. Heat Transfer, **122**, p. 525.
[16] Chang, W. S., 1981, "Heat Pipe Start Up From the Supercritical State," Ph.D. desertion, School of Mechanical Engineering, Georgia Institute of Technology.
[17] Zhu, N., and Vafai, K., 1998, "Analytical Modeling of Startup Characteristics of Asymmetric Flat-Plate and Disc-Shaped Heat Pipes," Int. J. Heat Mass Transfer, **41**(17), pp. 2619–2637.
[18] Suman, B., De, S., and DasGupta, S., 2005, "Transient Modeling of a Micro Groove Heat Pipe," Int. J. Heat Mass Transfer, **48**(8), pp. 1633–1646.
[19] Ravikumar, M., and DasGupta, S., 1997, "Modeling of Evaporation From V-Shaped Microgrooves," Chem. Eng. Commun., **160**, pp. 225–248.
[20] Peterson, G. P., and Ma, H. B., 1996, "Theoretical Analysis of the Maximum Heat Transport in Triangular Grooves: A Study of Idealized Micro Heat Pipe," ASME J. Heat Transfer, **118**, pp. 731–739.
[21] Catton, I., and Stores, G. R., 2002, "A Semi-Analytical Model to Predict the Capillary Limit of Heated Inclined Triangular Capillary Grooves," ASME J. Heat Transfer **124**, pp. 162–168.
[22] Suh, J. S., Greif, R., and Grigoropouls, C., 2001, "Friction in Micro-Channel Flows of a Liquid and Vapor in Trapezoidal and Sinusoidal Grooves," Int. J. Heat Mass Transfer, **44**, pp. 3103–3109.
[23] Blangetti, F., and Naushahi, M. K., 1980, "Influence of Mass Transfer on the Momentum Transfer in Condensation and Evaporation Phenomena," Int. J. Heat Mass Transfer, **23**, pp. 1694–1695.
[24] Suman, B., De, S., and DasGupta, S., 2005, "A Model of the Capillary Limit of a Micro Grooved Heat Pipe and the Prediction of Dry Out Length," Int. J. Heat Fluid Flow, **26**(3), pp. 495–505.
[25] Ha, J. M., and Peterson, G. P., 1998, "Analytical Prediction of Axial Dry-Out Point for Evaporating Liquids in Axial Microgrooves," ASME J. Heat Transfer, **120**, pp. 452–457.
[26] Anand, S., De, S., and DasGupta, S., 2002, "Experimental and Theoretical Study of Axial Dry-Out Point for Evaporative From V-Shaped Microgrooves," Int. J. Heat Mass Transfer, **45**, pp. 1535–1543.
[27] Incropera, F. P., and DeWitt, D. P., 2000, *Fundamentals of Heat and Mass Transfer*, 4th ed., Wiley, New York.

Journal of Heat Transfer

Technical Briefs

Influence of Partition Length on Natural Convection in Partially Divided Square Enclosure

C. D. Sankhavara
V.V.P. Engineering College,
Rajkot 360 005, India
e-mail: cdsankhavara@yahoo.co.uk

H. J. Shukla
S.P.B. Patel Engineering College,
Nr. Saffrony Holiday Resort,
Mehsana 384 435, Gujarat, India
e-mail: hjshukla1@rediffmail.com

Numerical investigation is carried out for natural convection in square enclosures consisting of partitions protruding from the end walls with different thermal boundary conditions at the end walls and partitions. The vertical walls were maintained isothermal at different temperatures. The Rayleigh number varies from 10^4 *to* 10^6 *and the Prandtl number is 0.71. The thickness of the partition is fixed and is equal to one-tenth of the width of the enclosure. Their nondimensional length* (l/H) *varies from 0 (a nonpartitioned enclosure) to 0.5 (two separate enclosures). A good agreement was found between the results in the present study and those published previously. The partitions were found to significantly influence the convective heat transfer. The average Nusselt number is less in the presence of partitions, and it decreases with increasing partition length* (l/H) *from 0 to 0.5.* [DOI: 10.1115/1.2764087]

Keywords: natural convection, square, vertical, partitioned enclosures, partition length

1 Introduction

Natural convection in complex enclosures is an area of interest for several researchers. Simple cavities without baffles have been studied elaborately, but enclosures partially divided by single or multiple partitions have evoked considerable interest. This fact is amply reflected by the size of the research efforts during the past few decades dedicated to this topic. A detailed study of flow and heat transfer phenomena in partitioned enclosures is useful in understanding the processes that occur in natural convection flows in passive solar heated building, solar collector design, cooling of heat generating components in electronic packages, cryogenic storage, and nuclear industries.

An experimental study of natural convection in a square enclosure with two thick centrally located partitions at the top and bottom walls was reported by Bajorek and Lloyd [1], for comparison with numerical results of Chang [2]. Jetli et al. [3] and Zimmerman and Acharya [4] considered an enclosure with offset [3] and in-line [4] partitions fitted on horizontal surfaces with assumed perfectly conducting end walls and finitely conducting partitions. Kelkar and Patankar [5] studied two different partition geometries: one with a single partition located vertically at the center of the enclosure and another with two identical partitions located at the top and bottom walls. Ciofalo and Karayiannis [6] reported a numerical computation for a nondimensional length [l/H] of partitions from 0 to 0.5. However, in this paper, no detailed flow patterns or isotherm distributions, temperature, and velocity profiles are presented. Recently, Sankhavara and Shukla [7] reported a numerical study of natural convection in square partitioned enclosures with different thermal boundary conditions and proved that a standard adiabatic boundary condition gives the best agreement with the reported measurement by Bajorek and Lloyd [1]. Yucel and Ozdem [8] studied the effect of the number of partitions (1 or 2) and height of partitions ($l/H=0.1$ or 0.2) in a square enclosure and found that the mean Nusselt number decreases with an increase in the number of partitions; however, the decrease in the mean Nusselt number is less at lower Rayleigh numbers.

Natural convection in a completely partitioned enclosure ($l/H=0.5$) is of importance in the estimation of heat loss from solar collectors and across double-paned windows, in the design of energy-efficient buildings, and in many other applications. Anderson and Bejan [9] measured the heat transfer rates through double partitions, which are inserted in the middle of the water filled enclosure, and indicated that the heat transfer rate for double partitions is 20% smaller than that for a single partition. Nishimura et al. [10] concluded from his experimental and numerical studies for water filled high aspect ratio enclosures (AR=4 and 10) that heat transfer decreases by a factor of 0.42 for a single partition. Mamou et al. [11] studied natural convection heat transfer in a tilted fluid system consisting of multiple layers of fluid separated by solid partitions with finite thickness and conductivity. There is a lack of comprehensive study in the literature on natural convection in completely partitioned air filled cavities.

The intent of the present investigation is to numerically investigate the effect of length of partitions protruding centrally from the end walls of a square vertical enclosure on fluid flow and heat transfer rate by using the finite element method. The thickness of the partition is fixed and equal to one-tenth of the width of the enclosure [Fig. 1(*a*)]. The study is made for the range of Rayleigh numbers from 10^4 to 10^6 and for a nondimensional partition length (l/H) from 0 (a nonpartitioned enclosure) to 0.5 (completely partitioned enclosures). The influence of different thermal boundary conditions at the end walls and at the partitions was also included in the investigations.

Contributed by the Heat Transfer Division of ASME for publication in the JOURNAL OF HEAT TRANSFER. Manuscript received: November 22, 2006; final manuscript received: April 19, 2007. Review conducted by Giulio Lorenzini.

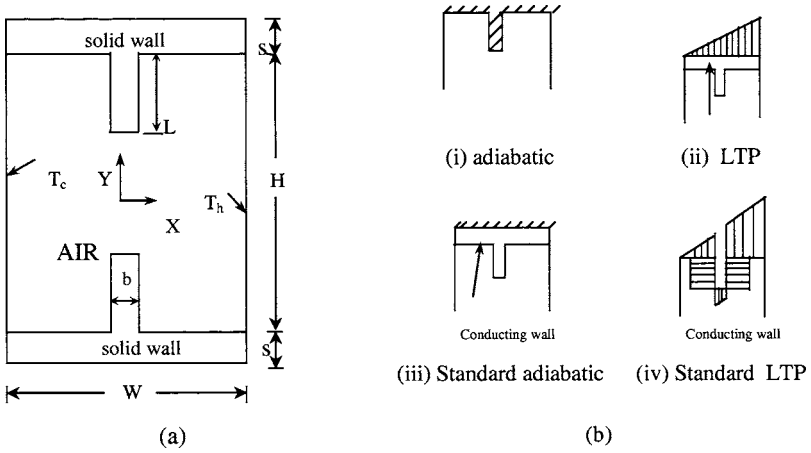

Fig. 1 (*a*) Schematic of the partitioned rectangular enclosure and (*b*) thermal boundary conditions at the end walls and partitions

2 Mathematical Modeling

A detail of the geometry relevant to the physical situation of interest area is shown in Fig. 1(*a*). The flow is assumed to be two dimensional, steady, and laminar. The density variation of the fluid follows Boussinesq's approximation and changes with temperature only. Radiation effects, which are small for moderate temperature differences, have not been included. Based on the above modeling assumptions, the nondimensional governing equations for the conservation of mass, momentum, and energy are

$$\frac{\partial U}{\partial X}+\frac{\partial V}{\partial Y}=0 \tag{1}$$

$$U\frac{\partial U}{\partial X}+V\frac{\partial U}{\partial Y}=-\frac{\partial P}{\partial X}+\Pr\left(\frac{\partial^2 U}{\partial X^2}+\frac{\partial^2 U}{\partial Y^2}\right) \tag{2}$$

$$U\frac{\partial V}{\partial X}+V\frac{\partial V}{\partial Y}=-\frac{\partial P}{\partial Y}+\Pr\left(\frac{\partial^2 V}{\partial X^2}+\frac{\partial^2 V}{\partial Y^2}\right)+\mathrm{Ra}\times\Pr(\theta-\theta_0) \tag{3}$$

$$U\frac{\partial \theta}{\partial X}+V\frac{\partial \theta}{\partial Y}=\frac{\partial^2 \theta}{\partial X^2}+\frac{\partial^2 \theta}{\partial Y^2} \tag{4}$$

In addition, there is one more energy equation for the solid conducting region (side walls),

$$\frac{\partial^2 \theta}{\partial X^2}+\frac{\partial^2 \theta}{\partial Y^2}=0 \tag{5}$$

The flow boundary conditions are $U=V=0$ on solid boundary. The thermal boundary conditions on the isothermal walls are

$\theta=0$ at $X=0$ (cold wall)

$\theta=1$ at $X=1$ (hot wall)

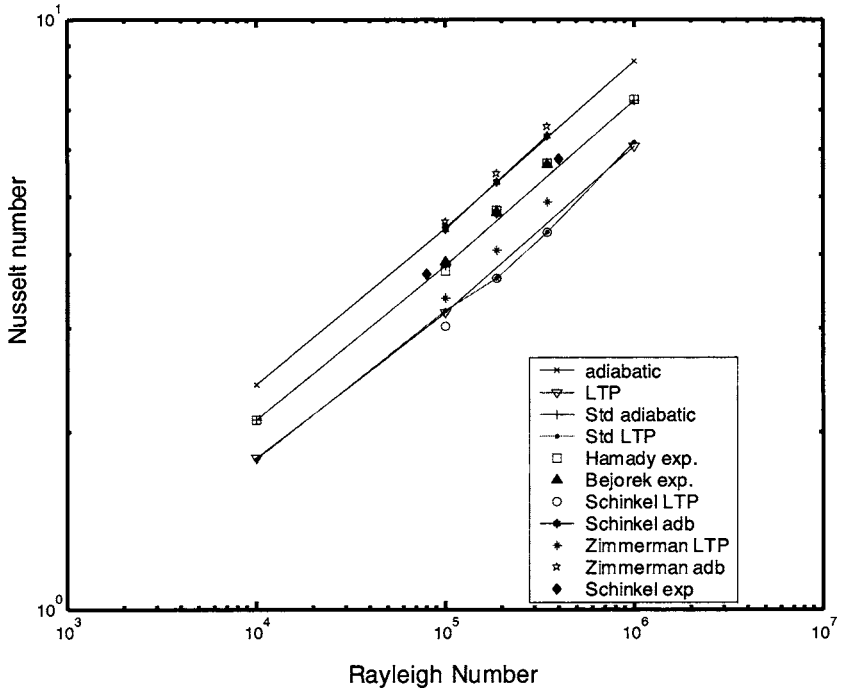

Fig. 2 Comparison of predicted results with published results for a nonpartitioned enclosure (AR=1 and φ=90 deg)

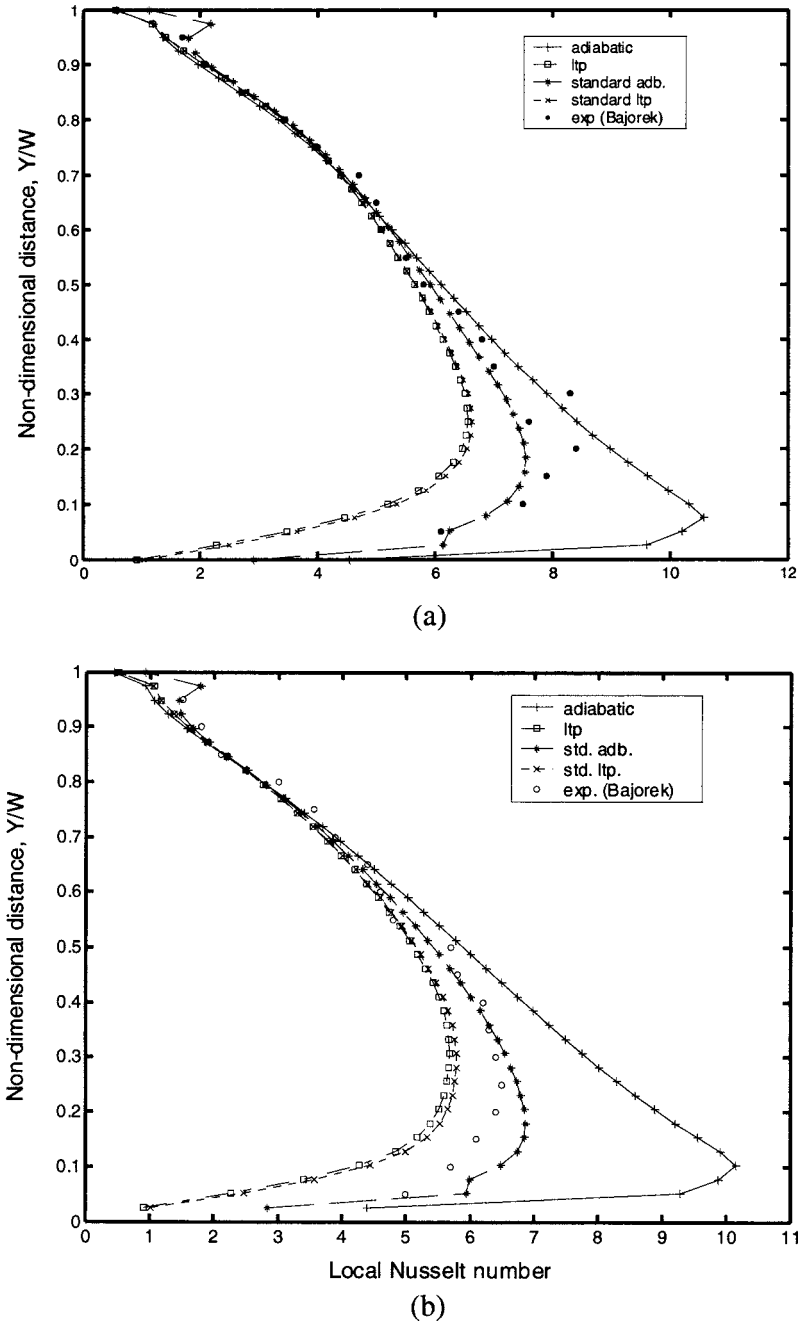

Fig. 3 Nusselt number profiles along the hot wall. (*a*) Nonpartitioned enclosure. (*b*) Partitioned enclosure at Ra=3.5×10^5 and φ=90 deg.

At the end walls and the partitions, different sets of thermal boundary conditions were considered. They are sketched in Fig. 1(*b*), which are described in detail elsewhere [7].

(i) adiabatic: $\partial\theta/\partial Y=0$
(ii) linear temperature profile (LTP): $\theta=X$
(iii) standard adiabatic: end walls of finite thickness S and conductivity k_p (thermal conductivity of end walls and partitions) with $\partial\theta/\partial Y=0$ along their outer sides
(iv) standard LTP: as in (iii) above, but with $\theta=X$ along their outer sides

When standard boundary condition (iii) or (iv) is used, the ratios S/W and k_p/k become important parameters. In all subsequent runs and in accordance with earlier work of Oosthuizen and Paul [12], the values $S/W=0.1$ and $k_p/k=25$ were chosen as representative of realistic configurations.

The conservation equations (Eqs. (1)–(5)) were solved using the computer code FLOTRAN, which is based on the Galerkin weighted residual finite element method, which has been described in detail by Rice and Schnipke [13] and Du Toit [14]. The presence of the partition in the calculation domain is accounted for by the strategy suggested by Patankar [15]. These equations after discretization were solved using the tridiagonal matrix algorithm (TDMA), which is described in detail by Patankar [15]. The convergence criterion was to stop the outer iterations when the convergence monitor fell below 10^{-5} for U, V, θ, and P. Calcula-

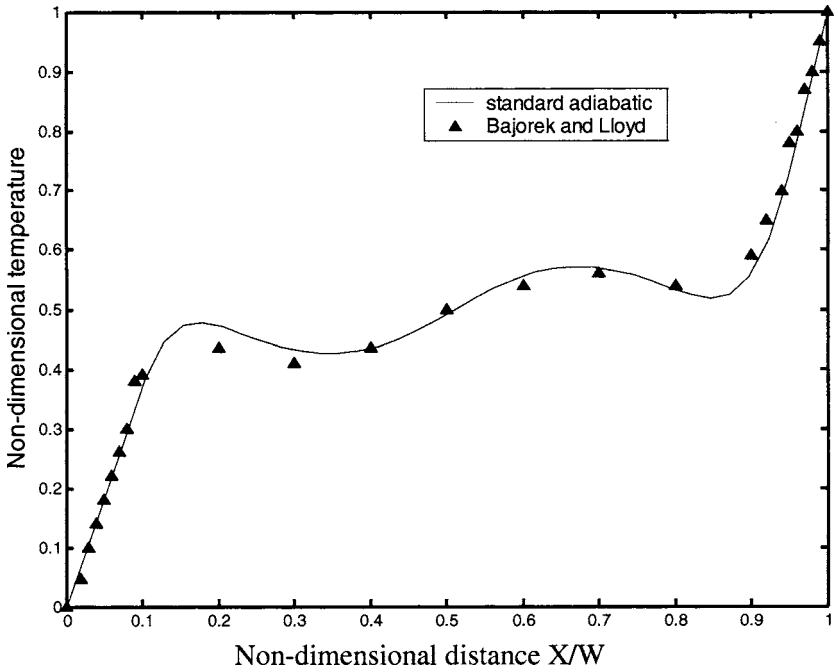

Fig. 4 Comparison of computed midheight temperature with measurement at Ra=3.5×10^5 and φ=90 deg

tions were undertaken with various grid sizes to ensure that the results presented here are essentially independent of grid size.

3 Accuracy Assessment

To check the accuracy of the computer code, the computed values of the local and average Nusselt numbers were compared with the experimental and numerical published results. In Ref. [1], the partitions were made of Plexiglas, and the dimensionless thickness b/W and length l/H were 0.1 and 0.25, respectively. In this investigation, results are obtained for the same geometrical configurations and the conductivity ratio k_r is assigned a value representative of the Plexiglas material. The results of the influence of thermal boundary conditions on heat transfer rates are summarized in Figs. 2 and 3. Figure 2 presents the Nusselt number as a function of the Rayleigh number for a nonpartitioned square enclosure under all four boundary conditions. Several experimental and numerical results by different authors are also reported for comparison. The results of the present investigation are in excellent agreement with the numerical predictions of Schinkel and Hoogendoorn [16] and Zimmerman and Acharya [4], who assumed either adiabatic or LTP end walls. The agreement with the experimental results of Bajorek and Lloyd [1], Schinkel and Hoogendoorn [16], and Hamady et al. [17] is best when the standard adiabatic condition is considered.

The local Nusselt number Nu_y along the hot wall, computed using all four boundary conditions, is compared with the experimental results of Bajorek and Lloyd [1] for a square nonpartitioned enclosure in Fig. 3(*a*) and for a partitioned enclosure in Fig. 3(*b*) at Ra=3.5×10^5. The experimental points lie closest to the "standard adiabatic" predictions. The predicted value for the average hot wall Nusselt number is 4.71, while the corresponding measured value is 4.66. The present predictions exhibit a much closer agreement with the measured values than the predictions by Zimmerman and Acharya [4] (Nu=4.3) with a LTP boundary condition and by Ciofalo and Karayiannis [6] (Nu=5.33) with "standard LTP" boundary conditions. Figure 4 presents the comparison of predicted midheight temperature profile and temperature distribution obtained by Bajorek and Lloyd [1] for a partitioned enclosure at a Rayleigh number of 3.5×10^5. The results compare excellently and a maximum discrepancy of 3.5% is found between the two profiles, which is less than 4.4% reported by Zimmerman and Acharya [4]. Thus, for both partitioned and nonpartitioned enclosures, the standard adiabatic boundary condition yields an excellent agreement with experimental results compared with other boundary conditions.

4 Results and Discussions

This section provides detailed information for an enclosure with a standard adiabatic boundary condition. The Rayleigh number Ra and partition length (l/H) are the primary parameters of interest in this study. The Rayleigh number studied in the range of 10^4–10^6 and five values of partition length l/H=0 (a nonpartitioned enclosure), 0.125, 0.250, 0.375, and 0.5 (fully partitioned enclosures) are considered.

4.1 Streamlines and Isotherms. Figures 5 and 6 presents the streamline and isotherm plots for Rayleigh numbers of 10^5 and 10^6 and dimensionless partition lengths from 0 to 0.5. In these figures, for the nonpartitioned enclosure, only one circulating cell is observed at lower Rayleigh numbers (Ra$\leqslant 10^5$), while two circulating cells are observed at a higher Rayleigh number (Ra $=10^6$), with one circulating cell near the bottom left and upper right corners inside the main circulating cell. At a Rayleigh number of 10^4, the convection currents are weak and conduction is the predominant mode of heat transfer for all the partition lengths, as reflected in the linear temperature distribution (figure not shown). As you can see in the figures, the strength of flow increases with an increase in Rayleigh number and decreases with an increase in partition length. In Fig. 5, it is observed that at l/H=0.125, there is only one circulating cell; however, at l/H=0.25 and 0.375, there is one more circulating cell near the center, both in the hot region and in the cold one. Further, with the increase of the Rayleigh number to 10^6 (Fig. 6), one circulating cell is observed at l/H=0.125, two circulating cells are observed at l/H=0.375, which are shifted near the upper end wall in the cold fluid region and near the bottom end wall in the hot one, and three circulating cells are observed at l/H=0.25, with one circulating cell behind each partition. This can be explained in the following way. The

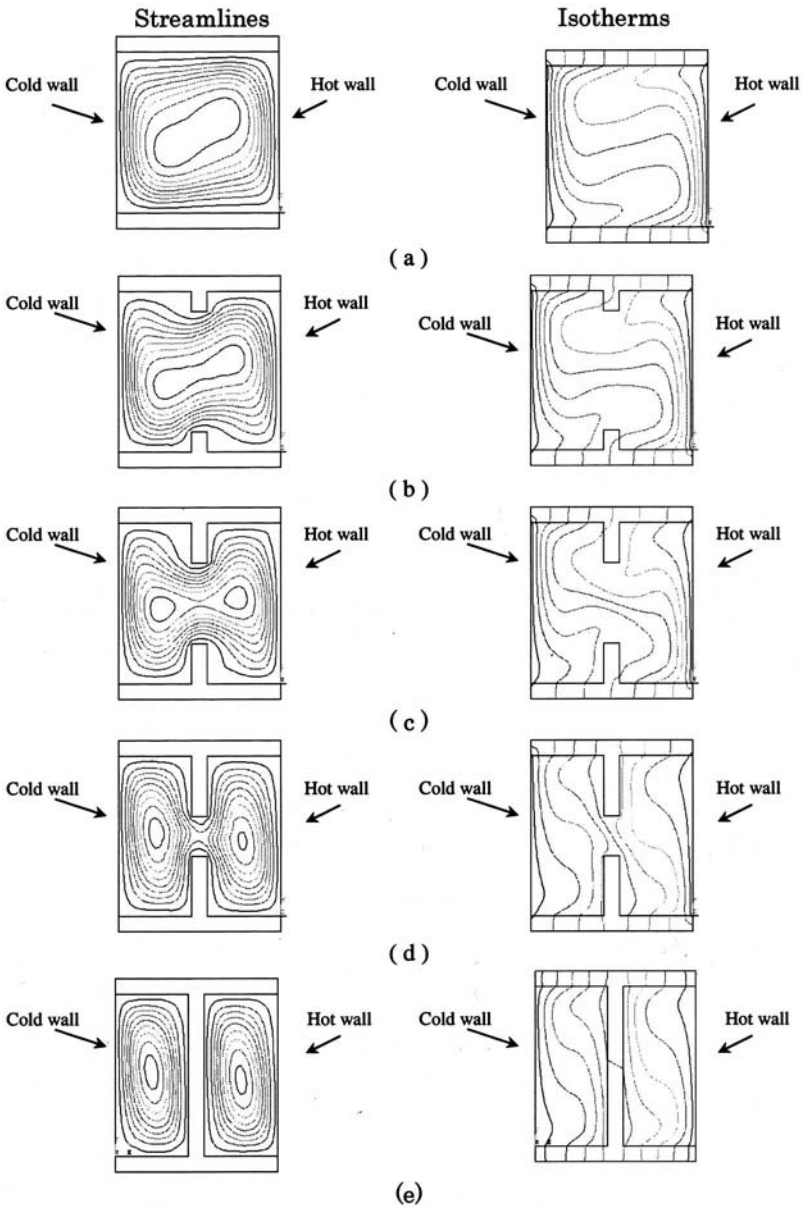

Fig. 5 Streamlines and isotherms for different partition lengths at Ra=10^5 and *b*/*W*=0.1: (*a*) *l*/*H*=0, (*b*) *l*/*H*=0.125, (*c*) *l*/*H*=0.25, (*d*) *l*/*H*=0.375, and (*e*) *l*/*H* =0.5

flow coming off the cold wall is heated by the conducting end wall and the partition. Therefore, the flow at the tip of the partition is relatively warmer, as is clearly seen by comparing the isotherm distribution in Figs. 5 and 6. At the Rayleigh number of 10^6, the warmer flow at the lower partition tip is lighter than the corresponding flow at the Rayleigh number of 10^5. The tendency of the lighter flow to move downward is less; hence, the flow is separated from the main circulating cell and forms a recirculating cell behind the partition at the Rayleigh number of 10^6. A similar explanation applies to the separation bubble behind the upper partition. At higher Rayleigh numbers, a smaller circulating cell is also observed by Zimmerman and Acharya [4] behind the partition at a higher conductivity ratio. It can also be observed that the temperature gradient next to hot and cold walls increases with an increase in Rayleigh number, while isotherms are nearly uniformly distributed in the core region at $l/H=0.125$ and 0.25, which indicates that heat transfer is dominated by conduction in the core region. At $l/H=0.5$, isotherms are almost parallel to the vertical side walls of the enclosure, indicating that most of the heat transfer is, by conduction, at lower Rayleigh numbers. As the Rayleigh number increases, the isotherms undulate remarkably, and thus the effect of convection is pronounced (Figs. 5(*e*) and 6(*e*)). At the Rayleigh number of 10^6, the density of isotherms is more severe by the side walls and the partition, but diminishes in the middle part of each cell, indicating the formation of a thermal boundary layer along the partition and side walls, and the middle part of each cell is regarded as the core region.

4.2 Nusselt Number Distribution. Figure 7 shows the variation of the mean Nusselt number with the Rayleigh number for different partition lengths (l/H), including the case of completely partitioned enclosures ($l/H=0.5$). An examination of this figure reveals that the effect of partition is much more pronounced at lower Rayleigh numbers, which is also noted by Ciofalo and Karayiannis [6]. The average Nusselt number is less in the presence of partitions and decreases with increasing partition length

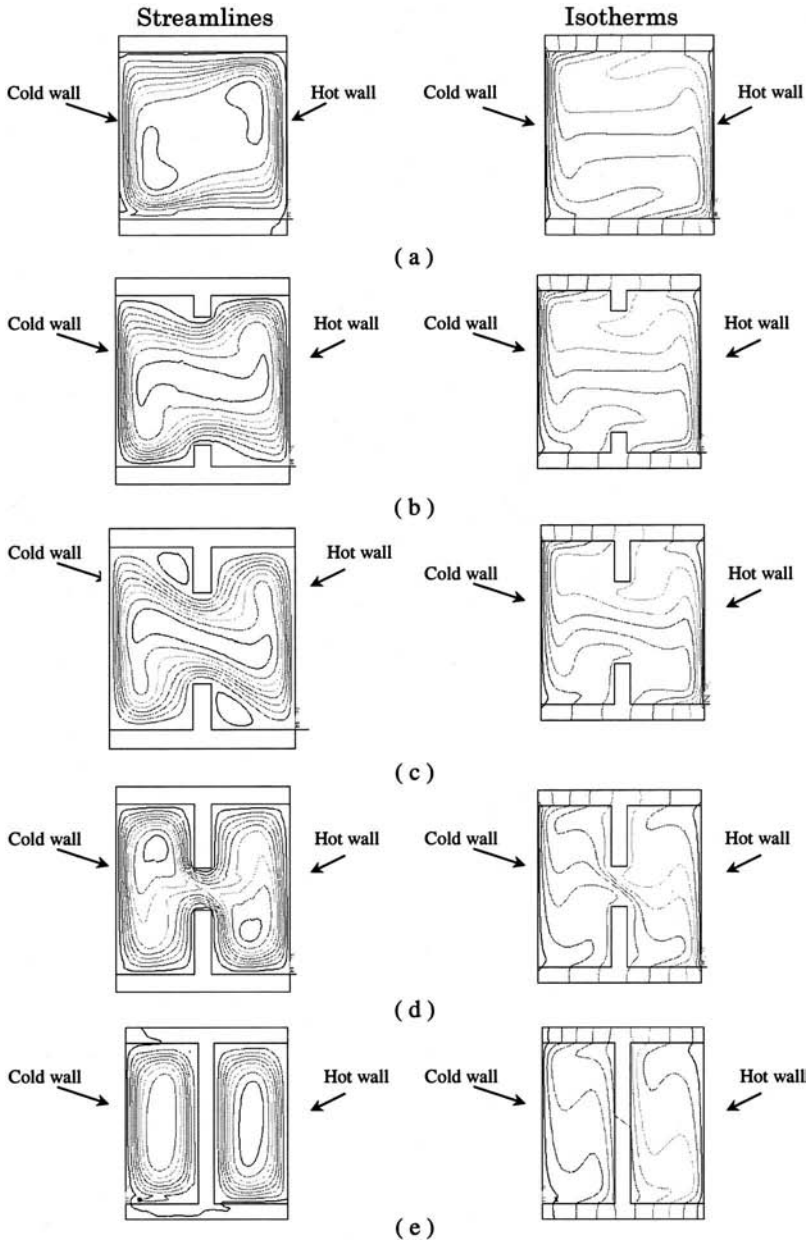

Fig. 6 Streamlines and isotherms for different partition lengths at Ra=10^6 and b/W=0.1: (*a*) l/H=0, (*b*) l/H=0.125, (*c*) l/H=0.25, (*d*) l/H=0.375, and (*e*) l/H =0.5

(l/H) from 0 to 0.5. This can be explained in the following way. The presence of a partition increases cooling near the upper partition and heating near the lower partition, which reduces local wall to fluid temperature difference. Thus, heat transfer decreases because of the reduction in the strength of the flow along the hot and cold walls. It should be noted that the 16% reduction in heat transfer for $b/W=0.1$ at the Rayleigh number of 3.5×10^5 is in excellent agreement with the computed reduction of 16% by Ciofalo and Karayiannis [6] and the measured reduction of 17% by Bajorek and Lloyd [1]. In the study of Ciofalo and Karayiannis, they observed that short partitions do not reduce the Nusselt number; in fact, they might enhance the rate of heat transfer slightly. In our computations, the Nusselt number is always smaller than the corresponding value in the nonpartitioned enclosure at all partition lengths. It can also be observed that an enclosure having a long partition, $l/H=0.375$, behaves much like a completely divided enclosure at lower Rayleigh numbers ($\mathrm{Ra}\leqslant10^5$) but much like a nonpartitioned enclosure at high Rayleigh numbers ($\mathrm{Ra}\leqslant10^6$), which is in conformity with Ciofalo and Karayiannis [6] and Bajorek and Lloyd [1]. At the Rayleigh number of 10^6, the horizontal velocity at the partition tip is maximum for $l/H=0.375$. On account of the higher velocity at the partition tip, flow separation does not occur from the primary circulating cell at the partition tip, which can also be observed from the streamline plot (Fig. 6(*d*)). Due to the interaction between hot and cold fluid regions, the average Nusselt number values increase and, hence, the partitioned enclosure behaves like a nonpartitioned enclosure at higher Rayleigh numbers.

The results of the present investigation for the completely partitioned enclosure ($l/H=0.5$) are compared to the analytical and numerical results of Mamou et al. [11] for a vertical enclosure with a single partition, as shown in Fig. 7. A small discrepancy in the results is found. This may be due to different thermal bound-

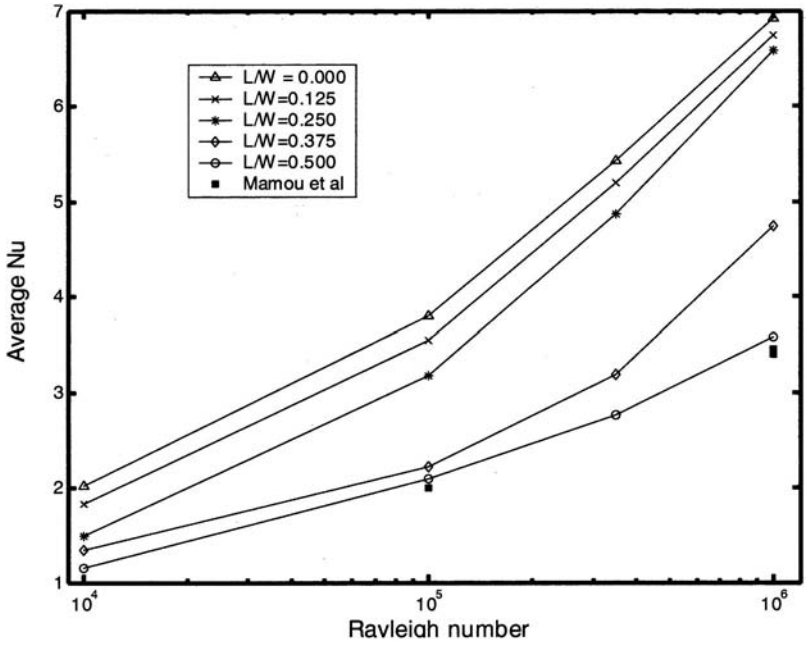

Fig. 7 Effect of the partition length and Rayleigh numbers on the mean Nusselt number for $b/W=0.1$

ary conditions considered by Mamou et al. [11]. In the present study, it is found that the single partition has an effect of reducing the heat transfer rate to the tune of 42–49% within the range of Rayleigh numbers considered. In the partially divided enclosure, the effect of partition on heat transfer rate is more up to intermediate Rayleigh numbers (maximum reduction of 45%), while at higher Rayleigh numbers, the effect of partition on heat transfer decreases (maximum reduction of 30%), but, for the completely partitioned enclosure, the effect of partition on heat transfer rate increases with an increase in Rayleigh number. The Nusselt number value decreases within the range of 42–48% with an increase in Rayleigh number from 10^4 to 10^6.

For the numerical data presented here, the correlation of the mean Nusselt number for the vertical partitioned enclosure as a function of the Rayleigh number is found to have a maximum discrepancy of 8%,

$$\mathrm{Nu} = 0.0599\mathrm{Ra}^{0.2953}(l/H)^{-0.3478}$$

$$\text{for } 0 \leqslant l/H \leqslant 0.5 \quad 10^4 \leqslant \mathrm{Ra} \leqslant 10^6 \quad b/W = 0.10 \quad k_r = 25 \quad \mathrm{AR} = 1$$

5 Conclusions

A detailed numerical study was carried out to investigate the effect of partition length (l/H) and Rayleigh number on heat transfer rate in a vertical square partitioned enclosure. A good agreement was found between the results in the present study for the partitioned enclosure and those published previously. On the basis of the results presented and discussed above, the following may be concluded.

(i) The standard adiabatic boundary condition gives an excellent conformity with the published experimental results than any other boundary conditions.

(ii) The Nusselt number value decreases with an increase in partition length (l/H) from 0 to 0.5 at all Rayleigh numbers. This can be explained as the presence of a partition reduces local wall to fluid temperature difference ΔT, which reduces the strength of the flow along the hot and cold walls. Hence, heat transfer decreases with an increase in partition length.

(iii) In the partially divided enclosure, the effect of the partition on heat transfer rate is more up to intermediate Rayleigh numbers (maximum reduction of 45%), whereas at higher Rayleigh numbers, the effect of the partition on heat transfer rate decreases (maximum reduction of 30%) because of an increase in the horizontal component of velocity at the partition tip, which increases the interaction of fluids between hot and cold regions. But for the completely partitioned enclosure, the Nusselt number value decreases within the range of 42–48% with an increase in Rayleigh number from 10^4 to 10^6.

Nomenclature

A = aspect ratio, W/H
H = height of an enclosure (m)
P = dimensionless pressure, $pW^2/\rho\alpha^2$
Pr = Prandtl number, $\mu C_p/k$
Ra = Rayleigh number, $g\beta(T_h-T_c)H^3/\nu\alpha$
S = thickness of the end walls (m)
T = dimensional temperature (K)
U = dimensionless velocity in the x direction, uW/α
V = dimensionless velocity in the y direction, vW/α
W = width of an enclosure (m)
X = dimensionless coordinate parallel to the end walls, x/W
Y = dimensionless coordinate normal to the end walls, y/W
b = thickness of the partitions (m)
g = gravitational acceleration (m/s^2)
h = local convective heat transfer coefficient (W/m^2 K)
k = thermal conductivity of air (W/m K)
l = length of partitions (m)

p = thermodynamic pressure (N/m^2)
u = velocity in the x direction (m/s)
v = velocity in the y direction (m/s)
x = dimensional coordinate parallel to the end walls
y = dimensional coordinate normal to the end walls

Greek Symbols

α = thermal diffusivity (m^2/s)
ν = kinematic viscosity (m^2/s)
θ = dimensionless temperature $(T-T_c)/(T_h-T_c)$
β = thermal expansion coefficient (K^{-1})
φ = angle of inclination (deg)
μ = absolute viscosity ($N\,s/m^2$)
ρ = density of the fluid (kg/m^3)
θ_0 = dimensionless reference temperature

Subscript

C_p = specific heat of fluid (J/kg K)
k_p = conductivity of partition (W/m K)
k_r = conductivity ratio k_p/k
Nu = average Nusselt number
Nu_y = Nusselt number along the hot wall, hW/k
T_h = hot wall temperature (K)
T_c = cold wall temperature (K)
T_0 = reference temperature, $(T_h+T_c)/2$

References

[1] Bajorek, S. M., and Lloyd, J. R., 1982, "Experimental Investigation of Natural Convection in Partitioned Enclosures," ASME J. Heat Transfer, **104**, pp. 527–532.

[2] Chang, L. C., 1981, "Finite Difference Analysis of Radiation-Convection Interactions in Two-Dimensional Enclosures," Ph.D. thesis, Department of Aerospace and Mechanical Engineering, University of Notre Dame.

[3] Jetli, R., Acharya, S., and Zimmerman, E., 1986, "Influence of Baffle Location on Natural Convection in a Partially Divided Enclosure," Numer. Heat Transfer, **10**, pp. 521–536.

[4] Zimmerman, E., and Acharya, S., 1987, "Free Convection Heat Transfer in Partially Divided Vertical Enclosure With Conducting End Walls," Int. J. Heat Mass Transfer, **30**, pp. 319–331.

[5] Kelkar, K. M., and Patankar, S. V., 1990, "Numerical Prediction of Natural Convection in Square Partitioned Enclosures," Numer. Heat Transfer, Part A, **17**, pp. 269–285.

[6] Ciofalo, M., and Karayiannis, T. G., 1991, "Natural Convection Heat Transfer in a Partially or Completely Partitioned Vertical Rectangular Enclosure," Int. J. Heat Mass Transfer, **44**, pp. 167–179.

[7] Sankhavara, C. D., and Shukla, H. J., 2003, "Natural Convection in a Partitioned Vertical Enclosure With Conducting End Walls," *Proceedings of Second BSME-ASME International Conference on Thermal Engineering*, Dhaka, Paper No. TS 59.

[8] Yucel, N., and Ozdem, A. H., 2003, "Natural Convection in Partially Divided Square Enclosures," Heat Mass Transfer, **40**, pp. 167–175.

[9] Anderson, R., and Bejan, A., 1981, "Heat Transfer Through Single and Double Vertical Walls in Natural Convection: Theory and Experiment," Int. J. Heat Mass Transfer, **24**, pp. 1611–1620.

[10] Nishimura, T., Shiraishi, M., Nagasawa, F., and Kawamura, Y., 1988, "Natural Convection Heat Transfer in Enclosures With Multiple Vertical Partitions," Int. J. Heat Mass Transfer, **31**, pp. 1679–1686.

[11] Mamou, M., Hasnaoui, M., Vasseur, P., and Bilgen, E., 1994, "Natural Convection Heat Transfer in Inclined Enclosures With Multiple Conducting Solid Partitions," Numer. Heat Transfer, Part A, **25**, pp.295–315.

[12] Oosthuizen, P. O., and Paul, J. T., 1990, "Natural Convective Flow in A Cavity With Conducting Top and Bottom Walls," *Proceedings of the Ninth International Heat Transfer Conference*, Jerusalem, Vol. 2, pp. 263–268.

[13] Rice, J. G., and Schnipke, R. J., 1986, "An Equal Order Velocity-Pressure Formulation That Does Not Exhibit Spurious Pressure Modes," Comput. Methods Appl. Mech. Eng., **58**, pp. 135–149.

[14] Du Toit, C. G., 1998, "Finite Element Solution of the Navier-Stokes Equations for Incompressible Flow Using a Segregated Algorithm," Comput. Methods Appl. Mech. Eng., **151**, pp. 131–141.

[15] Patankar, S. V., 1982, *Numerical Heat Transfer and Fluid Flow*, Hemisphere, Washington, DC.

[16] Schinkel, W. M. M., and Hoogendoorn, C. J., 1978, "An Interferometric Study of the Local Heat Transfer by Natural Convection in Inclined Air Filled Enclosures," *Proceedings of the Sixth International Heat Transfer Conference*, Vol. 6, pp. 287–292.

[17] Hamady, F. J., Lloyd, J. R., Yang, H. Q., and Yang, K. T., 1989, "Study of Local Natural Convection Heat Transfer in an Inclined Enclosure," Int. J. Heat Mass Transfer, **32**, pp. 1697–1708.

Thermomechanical Formation of Nanoscale Polymer Indents With a Heated Silicon Tip

William P. King
Woodruff School of Mechanical Engineering,
Georgia Institute of Technology,
Atlanta, GA 30332-0405
e-mail: william.king@me.gatech.edu

Kenneth E. Goodson
Department of Mechanical Engineering,
Stanford University,
Stanford, CA 94305-3030

In thermomechanical data storage, a heated atomic force microscope cantilever tip is in contact with and scans over a polymer film. Heating in the cantilever and cantilever tip induces local deformation of the polymer near the tip, with indents as small as 22 nm*. This paper reports a simple modeling approach for predicting heat and mass transfer in the cantilever tip and polymer with the goal of predicting indent formation conditions. The model accounts for subcontinuum conduction in the cantilever tip and for the time- and temperature-dependent mechanical properties of the polymer. Simulations predict steady state and transient indent formation, and the results compare well with data. For loading forces* 30–200 nN *and a tip radius of* 20 nm*, a cantilever temperature of* 200°C *is required to form an indent at steady state. For heating pulses as short as* 5 μs*, the cantilever temperature required for bit formation is as high as* 500°C*. By quantifying the conditions required for indent formation, this work may improve the operation of heated probes for thermomechanical data storage.* [DOI: 10.1115/1.2764088]

Introduction

In thermomechanical data storage [1–3], a heated atomic force microscope (AFM) cantilever tip locally melts and deforms a polymer layer to form nanometer-scale data bits. Figure 1 illustrates this technology, in which critical figures of merit are data bit density and the time and temperature required to write data bits. This paper reports a simple modeling approach to predict heat transfer in the nanoscale silicon probe tip and the polymer layer during thermomechanical indentation formation.

Thermomechanical data storage technology has a spatial resolution and writing rate that are governed by heat transfer in the cantilever tip. Past work investigated thermal conduction within the cantilever with the goal of minimizing the time required for temperature changes near the tip region [4]. Research on high-resolution thermal microscopy motivated several studies of thermal and thermoelectric transport at the contact of a probe tip and a surface [5–8]. However, no previous work considered thermal conduction in a silicon AFM cantilever tip or its interaction with a polymer layer.

Previous published work on thermomechanical data storage noted the temperature, time, and loading force required to form a data bit but did not examine the process of data bit writing in detail. Previous studies [3,9] found a minimum temperature of 350°C in the cantilever heater region required to form indents in thin layers of polymethyl methacrylate (PMMA). The temperature of the cantilever heater region can be found by measuring the electrical resistance of the cantilever, which is a function of temperature [10]. The minimum writing temperature of 350°C is higher than the glass transition temperature of PMMA, which is 100–120°C [11]. It is not well understood why the cantilever heater temperature must significantly exceed the polymer glass transition temperature in order to form an indent.

This paper considers thermal conduction along the cantilever tip in steady contact with the polymer to find the temperature distribution along the length of the cantilever and the temperature at the tip-polymer interface. The analysis also considers the melting of the polymer and motion of the tip into the polymer to predict indentation formation conditions.

Technical Approach

The most rigorous study of heat conduction in the cantilever tip would provide a detailed account for phonon dispersion, and scattering on the tip walls and other phonons [12]. Several unknown experimental parameters mitigate the practical impact of the most rigorous approach. These include the presence of native silicon oxide on the tip, uncertainty in the tip shape, tip wear, and the evolution of these parameters over long times and temperatures. The degree of thermal conductivity anisotropy in the polymer layer is not known, and the surface tension and viscoelastic properties at length scales comparable near the polymer radius of gyration have not been measured, nor do good physical models exist for their prediction. This study employs an approximate model of phonon transport in the cantilever tip. Because the uncertainties in the experimental parameters are large compared to the uncertainty in the chosen model, a more rigorous model may not yield useful insight without advancement in the related experiments.

Figure 2 shows thermal conduction resistances in the cantilever tip and polymer substrate. Heat flows from the cantilever into the substrate across the air gap and through the cantilever tip. The thermal resistance across the air gap between the cantilever and the substrate is $R_{\text{substrate}}$ and calculated from a shape factor [13]. The total thermal conduction resistance along the length of the cantilever tip is

$$R_{\text{tot}} = \int_{x=0}^{h} \frac{4x}{\pi d^2 k(x)} dx + \frac{16}{C\nu\pi d_{\text{contact}}^{\ 2}} + R_{\text{substrate}} \tag{1}$$

where the first term is R_{tip}, the thermal conduction resistance along the x direction, the second term is the thermal interface resistance $R_{\text{interface}}$ that enforces a phonon scattering site at the tip-polymer interface, and the third term is R_{spread}, the thermal resistance due to the spread of heat in the polymer layer. Note that R_{spread} is the thermal resistance to heat flow from the end of the tip, while $R_{\text{substrate}}$ is the thermal resistance to heat flow from the cantilever heater region. The interface thermal resistance is thus calculated by enforcing that all of the available phonons scatter at the tip-polymer interface [14], and $R_{\text{interface}}$ is typically 10^6–10^8 K/W. The value of R_{spread} is typically 10^8–10^9 K/W, found from solution to the heat conduction equation in the polymer layer.

The tip is modeled as a half-sphere mounted onto the end of a cone. The conduction analysis divides the tip into finite volume elements. The resistance to heat flow away from the tip is much greater than the resistance to heat flow within the tip, and thus the temperature along the tip can be analyzed as a one-dimensional problem. Thermal conduction is calculated between adjacent volume elements in the tip, conduction to the nearby air, and radiation to the nearby surfaces. The thermal conductivity in the tip is calculated using Matthiessen's rule [15,16].

Contributed by the Heat Transfer Division of ASME for publication in the JOURNAL OF HEAT TRANSFER. Manuscript received February 15, 2006; final manuscript received January 15, 2007. Review conducted by Suresh V. Garimella.

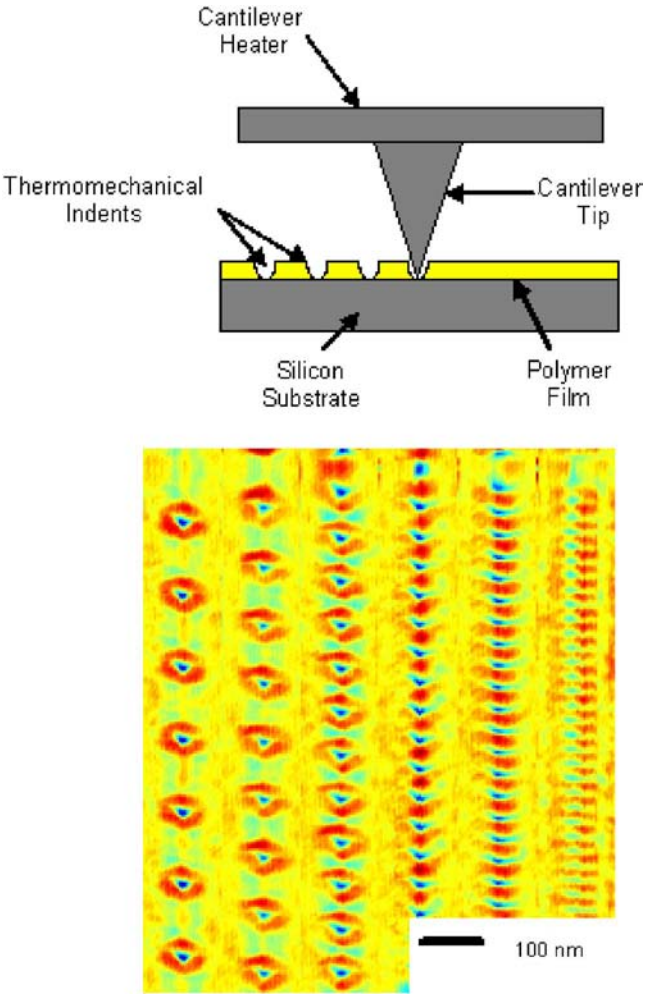

Fig. 1 Schematic of the bit-writing process and thermomechanically written indentations in polymer

$$k(x) = \frac{1}{3} Cv \left[\frac{1}{\Lambda^{-1} + d(x)^{-1}} \right] \tag{2}$$

where x is the vertical position along the tip, d is the local tip diameter, k is the local thermal conductivity of the tip, C is the volumetric heat capacity, v is the average phonon speed, and Λ is the phonon mean free path in the bulk material [15]. A value of 1.8×10^9 W/m^2 K is used for the product Cv [17]. The model assumes constant Cv, which will produce an error of not more than 15%. The temperature dependence of the bulk thermal conductivity of silicon is modeled using a fit to room temperature data for bulk samples [18], and so Λ is a function of temperature.

Typical tip loading forces are in the range of 5–300 nN [3,9] and so adhesive forces can be neglected [19]. While the PMMA polymer data layer is relatively hard with Young's modulus of 3.0×10^9 Pa [11], it is much softer than the silicon tip and elastically deforms when unheated. An exact solution [20] is available for the indentation of a half-sphere into a nonadhering elastic surface, which relates the loading force F_{load} to the contact conditions

$$F_{\text{load}} = \frac{G'}{1-\chi} \left[({r_{\text{contact}}}^2 + {r_{\text{tip}}}^2) \log\left(\frac{r_{\text{tip}} + r_{\text{contact}}}{r_{\text{tip}} - r_{\text{contact}}} \right) - r_{\text{tip}} r_{\text{contact}} \right] \tag{3}$$

where G' is the elastic modulus, r_{contact} is the radius of contact and half the value of d_{contact}, and r_{tip} is the tip radius of curvature.

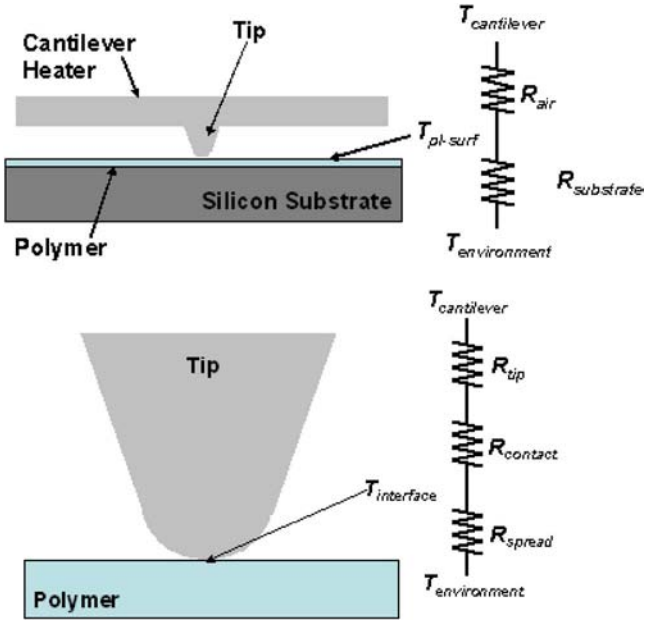

Fig. 2 Thermal resistance network showing the heat transfer modes influencing tip-sample interface temperature

Poisson's ratio is $\chi = 0.35$ for PMMA at room temperature. Once the polymer is heated above its glass transition point, it can be considered to be incompressible with $\chi = 0.5$ [11]. The thermal resistance of the portion of the tip that penetrates into the polymer is neglected, as the thermal resistance of the polymer is significantly greater than the thermal resistance of the tip.

Heat flows from the side of the tip through radiative exchange with the heater and the substrate and conduction to the surrounding air. This steady-state model assumes that conduction across the cantilever-polymer air gap produces a constant, linear temperature gradient across the gap. Typical heating times are 1–50 μs [4,21] which are much longer than the time for heat to diffuse across a typical cantilever-substrate air gap of thickness 0.3–1 μm which is approximately 100 ns. Thus, the air between the cantilever and substrate is at thermal steady state. The resistance to thermal conduction between the tip and the air depends only on the Knudsen slip resistance, which accounts for the diameter of the tip being smaller than the mean free path of the air molecules [13,22].

The tip is discretized into 1000 volume elements along its axis, and the temperature distribution is found using Gauss-Seidel iteration on the heat flow along the length of the tip. Temperature predictions are validated by an energy balance on each volume element and on the entire tip, and compare well with analytical solutions in which the thermal conductivity is held constant. The calculated value of R_{spread} compares well with a shape factor for a disk source on an infinite half-space [22]. For transient analysis, time steps of 1% of the total simulation time yield a numerical solution that agrees to within 2% of the analytical solution for constant-temperature boundary conditions in both radial and normal directions.

A comparison of the heat conduction paths along the cantilever tip and across the air gap finds that the temperature at the tip-polymer interface $T_{\text{interface}}$ is much higher than the temperature at the polymer surface away from the tip $T_{\text{pl-surf}}$. Because the temperature at the tip-polymer interface is much higher than the temperature anywhere else on the substrate surface, the cantilever might be used as a tool for highly local thermal processing or manufacturing [23,24]. Comparison of heat flow through the tip and across the air gap separating heater and polymer shows that significantly more heat travels across the cantilever-substrate air

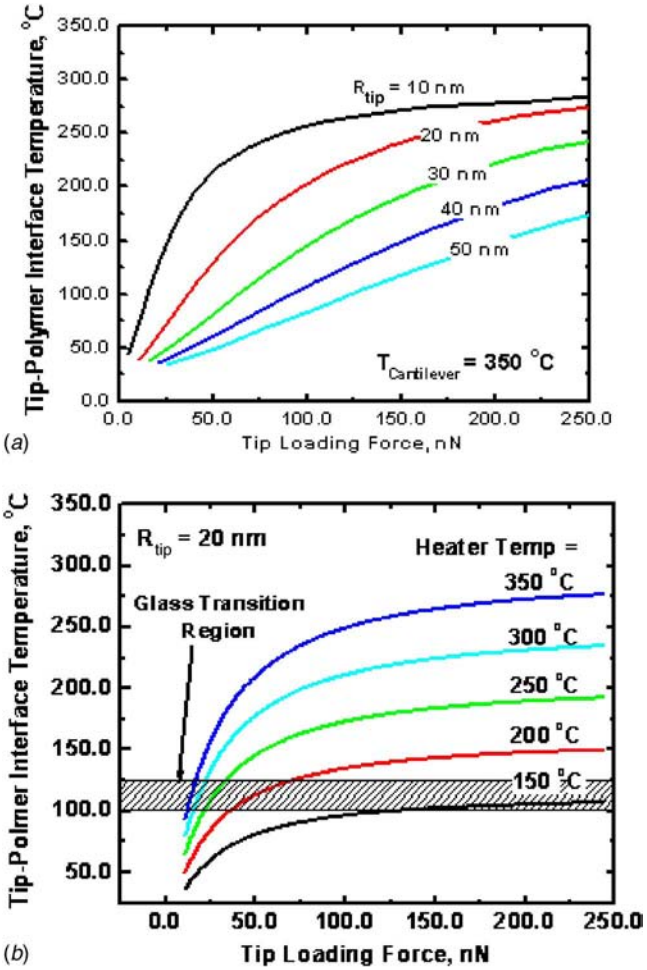

Fig. 3 Predicted steady-state tip-polymer interface temperature as a function of loading force for a range of heater temperatures and a tip radius of curvature of 20 nm. The shaded region represents the glass transition region, above which a bit will be written for long heating pulses.

gap than travels through the length of the cantilever tip. Thus, it is the thermal impedance of the cantilever-substrate air gap not the thermal impedance at the cantilever tip-polymer interface, which governs thermal data reading [13,25,26].

Figure 3 shows the effect of loading force on interface temperature. The tip loading force influences the area of tip-polymer contact, which in turn affects the interface temperature. For the smallest tip radii, the tip-polymer interface temperature is relatively close to the cantilever heater temperature. However, as the tip sharpness decreases, the tip-polymer interface temperature decreases dramatically. For indents written into PMMA films, the PMMA has a glass transition temperate in the range of 100–125°C, also shown in Fig. 3.

By coupling the mechanical and thermal analysis of bit formation, it is possible to predict the onset of data bit formation and the ultimate data bit size for a given heater temperature, heating time, and loading force. In the measurements reported on thermomechanical writing [1,3,27], the cantilever has a tip of height of 500 nm, tip radius of curvature of 20 nm, spring constant near 0.05 N/m, and a mechanical resonance frequency near 100 kHz. The polymer data substrate is a bilayer consisting of 35 nm of PMMA on 80 nm of epoxy, which resides on a silicon substrate. In the writing experiments, a cold cantilever tip is brought into contact with a cold polymer surface. After tip-polymer contact, the base of the cantilever is brought closer to the substrate such that the cantilever tip is pressed into the substrate. The cantilever tip loading force F_{load} is the product of this displacement and the cantilever spring constant k. The cantilever heats for a fixed time to a known temperature.

The temperature-dependent mechanical modulus of the polymer is calculated as a function of temperature, pressure, and time. The temperature dependence takes the form of the Williams Landel Ferry shift parameter [28], which is used to extract viscous and elastic polymer properties from tabulated values [29]. For times comparable to and longer than 10 ms, the cantilever is in thermal and mechanical equilibrium with the polymer data layer. Figure 3 shows predictions for the tip-polymer interface temperature as a function of loading force for various heater temperatures. The model predicts that the lowest heater temperature at which a bit could be written is near 200°C for a loading force above approximately 75 nN.

The cantilever motion of the cantilever tip can be described through an equation of motion

$$m_{cant}\ddot{x} + k_{cant}x = F_{load} - F_{pl} \tag{4}$$

where m_{cant} is the mass of the cantilever calculated as in previous work [3,9], x is the vertical position of the cantilever tip, and F_{pl} is the force with which the polymer resists tip motion. The force with which the polymer resists tip motion is a function of the temperature field in the polymer near the tip.

Solution of the two-dimensional transient diffusion equation within the polymer show that for all of the present calculations, the thickness of the softened polymer is thinner than the tip radius of curvature. The tip motion through the polymer can thus be modeled as a lubrication problem, where the viscoelastic polymer is squeezed between the hardened tip and the hard, cool polymer. An analytical solution for the force required to displace the lubrication layer links the tip motion to polymer relaxation. At every time step, the simulation tests whether the tip loading force is sufficient to move the tip one finite volume element thickness into the polymer layer. The force with which the polymer resists tip penetration F_{pl} can be divided into the viscous resistance [30] and the elastic resistance of the polymer [28]

$$F_{pl} = 3\pi\frac{\eta_{pl}r_{tip}^{4}}{t_{pl}^{3}}\dot{x} + 3\pi G' r_{tip}^{2}\varepsilon \tag{5}$$

where η_{pl} is the polymer viscosity, t_{pl} is the average thickness of the softened polymer near the tip, and ε is the strain in the melted polymer. If the criteria for tip motion are met, then the tip moves one element into the polymer. The new position of the tip serves as a position of the constant-temperature boundary in the solution of the heat equation. Since the tip penetration is limited by the squeeze flow of the soft polymer between the tip and the hard polymer beneath, once the polymer flows away from the tip, it exerts negligible force on the tip. The simulation stops when the tip has penetrated to a depth of 10 nm.

Figure 4 shows measurement and prediction results for writing conditions required to form an indent for tip loading forces of 30–100 nN. The measurements are from Refs. [1,27]. Predictions from the modeling of the present study are shown for both a moving tip and for steady-state thermal conditions. To within experimental error and measurement scatter, the modeling and simulation of the present work compare well with measurements.

The drop in threshold writing temperature for longer writing times is due to three factors: the inertia of the cantilever which must be overcome for tip motion, heat diffusion into the polymer, and the viscoelastic response of the polymer to tip penetration. First, the cantilever mechanical time constant prohibits a data bit from being written much faster than approximately 10 μs, so due only to the cantilever mechanical time constant, one expects an asymptotic increase in threshold writing temperature as heating times decrease to near 1 μs. The steep increase in temperature required to write a data bit for short times also corresponds to the time required for heat to diffuse into the polymer layer away from

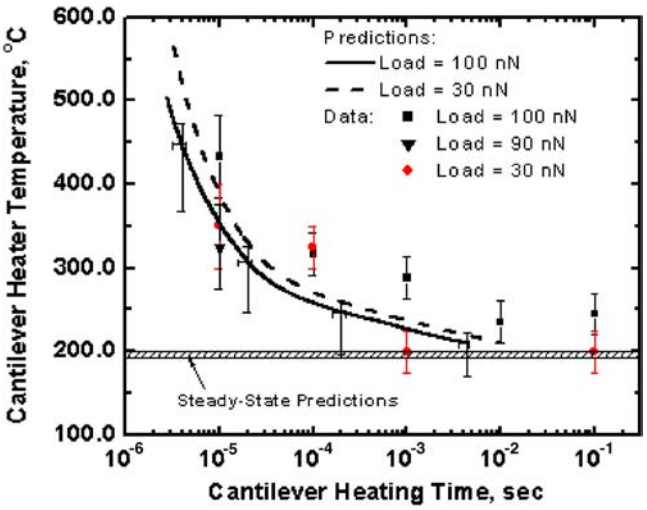

Fig. 4 Prediction of the threshold conditions of time, temperature, and tip loading force required to produce a data bit for a 20 nm tip radius of curvature. The predictions compare well with data. The gray area shows predictions for near-equilibrium conditions.

the tip, and the time- and temperature-dependences of the polymer properties away from the tip. As shown in Eq. (5), the force with which the polymer resists tip penetration has an inverse cubic dependence on the thickness of the soft polymer near the penetrating tip. The long time behavior of tip penetration, which asymptotically approaches a threshold bit-writing temperature of approximately 200°C, is a function of only the polymer temperature-dependent shear modulus.

The two loadings for which predictions are made bound the reasonable practical loading window of the present thermomechanical data storage cantilever. The large experimental scatter can be attributed to the difficulty of calibrating the cantilever heating temperature and loading force, as well as the difficulty of accurately measuring features of size near 10 nm. The predictions show a 20–50°C difference in threshold writing temperature between the 30 nN and 100 nN loading forces at a given heating time.

Figure 4 provides insight into the previously published experimental results that a threshold temperature of 350°C writes a data bit [5,14]. One possible explanation is that, as shown in Fig. 3, 350°C is the temperature at which a bit is *always* written, regardless of loading force. Another important parameter is that these reports always wrote bits at 10–20 μs, for which the predictions of Fig. 4 show that the threshold writing temperature is 300–350°C.

The shape of the cantilever tip can impact the onset writing conditions. Previous work has shown that an AFM tip can wear over time [31,32]. The limits of data density in a thermomechanical data storage system depend on the sharpness of the cantilever tip, and thus it is desirable to reduce the wear of the tip as much as possible. The tip shape affects not only the size of the ultimate bit but also the time and temperature required for bit formation.

Errors in the analysis of bit writing originate from four sources: modeling error for the thermal conductivity of the tip, differences between tabulated properties for bulk PMMA and the actual properties of PMMA in an ultrathin film, errors in modeling the value of F_{pl}, and numerical errors. The most significant errors are modeling errors, in which the simple modeling approach does not accurately capture all of the relevant physics. The phonon scattering model induces a temperature error of 15% through the assumption of constant Cv and additionally induces a temperature error of 5% in the interface resistance model. Errors in F_{pl} originate from the approximate polymer flow model and from unknown property values. The sum of these errors yields a total error of +7%/−22% in time and +6%/−23% in temperature. Figure 4 shows the overall error of the present modeling approach through error bars on the smooth prediction curves.

Conclusions

This paper describes simple modeling of the time, temperature, and force required to form a data bit indentation with a heated silicon probe tip. The predictions compare well with data for a tip radius of 20 nm, a polymer layer thickness of 35 nm, and a range of loading force, time, and heating temperature. The modeling and simulation approach and results could be used to improve writing rate and data density of thermomechanical data storage device. One possible improvement in the cantilever design would be to increase the cantilever resonance frequency while preserving the cantilever spring constant, which would allow high loading forces and improved cantilever mechanical response time. Improved experiments that carefully track the physical parameters present in thermomechanical data storage would motivate a more rigorous study of heat flow in the cantilever tip and polymer mass transport. The appropriate simulations would then consider the phonon radiation problem in the tip and the full flow field in the polymer.

Acknowledgment

The authors are grateful for extensive technical exchanges and support from the Micro/NanoMechanics Group at the IBM Zurich Research Laboratory.

Nomenclature

d = local tip diameter
$d_{contact}$ = diameter of tip-polymer contact
k = thermal conductivity of tip
k_{cant} = spring constant of cantilever
r_{tip} = tip radius of curvature
t_{pl} = thickness of melted polymer
v = average phonon velocity
x = vertical tip position
C = heat capacity of the silicon cantilever tip
F_{load} = tip loading force
F_{pl} = force with which polymer resists tip penetration
G = polymer shear modulus
$R_{contact}$ = tip-polymer thermal contact resistance
R_{spread} = thermal spreading resistance in polymer
χ = Poisson's ratio in polymer
η_{pl} = polymer viscosity
Λ = phonon mean free path

References

[1] Vettiger, P., Cross, G., Despont, M., Drechsler, U., Duerig, U., Gotsmann, B., Haberle, W., Lantz, M., Rothuizen, H., Stutz, R., and Binnig, G., 2002, "The "Millipede"-Nanotechnology Entering Data Storage," IEEE Trans. Nanotechnol., **1**, pp. 39–64.
[2] Vettiger, P., Despont, M., Drechsler, U., Durig, U., Haberle, W., Lutwyche, M. I., Rothuizen, H. E., Stutz, R., Widmer, R., and Binnig, G. K., 2000, "The "Millipede"-More Than One Thousand Tips for Future AFM Data Storage," IBM J. Res. Dev., **44**, pp. 323–340.
[3] Binnig, G., Despont, M., Drechsler, U., Häberle, W., Lutwyche, M., Vettiger, P., Mamin, H. J., Chui, B. W., and Kenny, T. W., 1999, "Ultrahigh-Density Atomic Force Microscopy Data Storage With Erase Capability," Appl. Phys. Lett., **76**, pp. 1329–1331.
[4] Chui, B. W., Stowe, T. D., Ju, Y. S., Goodson, K. E., Kenny, T. W., Mamin, H. J., Terris, B. D., and Ried, R. P., 1998, "Low-Stiffness Silicon Cantilever With Integrated Heaters and Piezoresistive Sensors for High-Density Data Storage," J. Microelectromech. Syst., **7**, pp. 69–78.
[5] Weber, L., Gmelin, E., and Queisser, H. J., 1989, "Thermal Resistance of Silicon Point Contacts," Phys. Rev. B, **40**, pp. 1244–1249.
[6] Phelan, P. E., Nakabeppu, O., Itoh, K., Hijikata, K., Ohmori, T., and Torikoshi, K., 1993, "Heat Transfer and Thermoelectric Voltage at Metallic Point Contacts," J. Heat Transfer, **155**, pp. 757–762.
[7] Shi, L. and Majumdar, A., 2002, "Thermal Transport Mechanisms at Nanos-

cale Point Contacts," J. Heat Transfer, **124**, pp. 329–337.
[8] Nakabeppu, O., Igeta, M., and Hijikata, K., 1997, "Experimental Study on Point-Contact Transport Phenomena Using the Atomic Force Microscope," Microscale Thermophys. Eng., **1**, pp. 201–213.
[9] Lutwyche, M. I., Despont, M., Drechsler, U., Durig, U., Hablerle, W., Rothuizen, H., Stutz, R., Widmer, R., Binnig, G. K., and Vettiger, P., 2000, "Highly Parallel Data Storage System Based on Scanning Probe Arrays," Appl. Phys. Lett., **77**, pp. 3299–3301.
[10] Chui, B. W., Asheghi, M., Ju, Y. S., Goodson, K. E., Kenny, T. W., and Mamin, H. J., 1999, "Intrinsic-Carrier Thermal Runaway in Silicon Microcantilevers," Microscale Thermophys. Eng., **3**, pp. 217–228.
[11] Mark, J. E., 1999, *Polymer Data Handbook*, Oxford University Press, New York.
[12] Sverdrup, P. G., Ju, Y. S., and Goodson, K. E., 2001, "Sub-Continuum Simulations of Heat Conduction in Silicon-on-Insulator Transistors," J. Heat Transfer, **123**, pp. 130–137.
[13] Masters, N., Ye, W., and King, W. P., 2005, "The Impact of Sub-Continuum Gas Conduction on the Sensitivity of Heated Atomic Force Microscope Cantilevers," Phys. Fluids, **17**, p. 100615.
[14] Schwartz, E. T., and Pohl, R. O., 1989, "Thermal Boundary Resistance," Rev. Mod. Phys., **61**, pp. 605–668.
[15] Ziman, J. M., 1960, *Electrons and Phonons*, Oxford University Press, Oxford.
[16] Casimir, H. B. G., 1938, "Note on the Conduction of Heat in Crystals," Physica (Amsterdam) **5**, pp. 495–500.
[17] Kittel, C., 1996, *Introduction to Solid State Physics*, 7th ed., Wiley, New York.
[18] Touloukian, Y. S., 1970, *Thermal Conductivity: Nonmetallic Solids*, IFI/Plenum, New York.
[19] Cappella, B., and Dietler, G., 1999, "Force-Distance Curves by Atomic Force Microscopy," Surf. Sci. Rep., **43**, pp. 1–104.
[20] Sneddon, I. N., 1965, "The Relation Between Load and Penetration in the Axisymmetric Boussinesq Problem for a Punch of Arbitrary Profile," Int. J. Eng. Sci., **3**, pp. 47–57.
[21] King, W. P., Kenny, T. W., Goodson, K. E., Cross, G. L. W., Despont, M., Durig, U. T., Rothuizen, H., Binnig, G., and Vettiger, P., 2002, "Design of Atomic Force Microscope Cantilevers for Combined Thermomechanical Writing and Thermal Reading in Array Operation," J. Microelectromech. Syst., **11**, pp. 765–774.
[22] Roshenow, W. M., and Choi, H. Y., 1961, *Heat, Mass, and Momentum Transfer*, Prentice-Hall,Englewood Cliffs, NJ.
[23] Sheehan, P. E., Whitman, L. J., King, W. P., and Nelson, B. A., 2004, "Nanoscale Deposition of Solid Inks via Thermal Dip Pen Nanolithography," Appl. Phys. Lett., **85**, pp. 1589–1591.
[24] Nelson, B. A., King, W. P., Laracuente, A., Sheehan, P. E., and Whitman, L. J., 2006, "Direct Deposition of Continuous Metal Nanostructures by Thermal Dip-Pen Nanolithography," Appl. Phys. Lett., **88**, p. 033104.
[25] King, W. P., 2005, "Design Analysis of Heated Atomic Force Microscope Cantilevers for Nanotopography Measurements," J. Micromech. Microeng., **15**, pp. 2441–2448.
[26] King, W. P., Kenny, T. W., and Goodson, K. E., 2004, "Comparison of Thermal and Piezoresistive Sensing Approaches for Atomic Force Microscopy Topography Measurements," Appl. Phys. Lett., **85**, pp. 2086–2088.
[27] Cross, G., Despont, M., Drechsler, U., Dürig, U., Vettiger, P., King, W. P., and Goodson, K. E., 2001, "Thermomechanical Formation and Thermal Sensing of Nanometer-Scale Indentations in PMMA Thin Films for Parallel and Dense AFM Data Storage," Mater. Res. Soc. Symp. Proc., **649**, pp. Q2.3.1–Q2.3.7.
[28] Ferry, J. D., 1980, *Viscoelastic Properties of Polymers*, Wiley, New York.
[29] Fuchs, K., Friedrich, C., and Weese, J., 1996, "Viscoelastic Properties of Narrow-Distribution Poly(methyl methacrylates)," Macromolecules, **29**, pp. 5893–5901.
[30] Deen, W. M., 1998, *Analysis of Transport Phenomena*, Oxford University Press, New York.
[31] Terris, B. D., Rishton, S. A., Mamin, H. J., Ried, R. P., and Rugar, D., 1998, "Atomic Force Microscope-Based Data Storage: Track Servo and Wear Study," Appl. Phys. A: Mater. Sci. Process., **66**, pp. S809–S813.
[32] Mamin, H. J., Ried, R. P., Terris, B. D., and Rugar, D., 1999, "High-Density Data Storage Based on the Atomic Force Microscope," Proc. IEEE, **87**, pp. 1014–1027.

Transition Boiling Heat Transfer of Droplet Streams and Sprays

John D. Bernardin
Space Sciences and Applications Group,
Los Alamos National Laboratory,
P.O. Box 1663, MS D466,
Los Alamos, NM 87545

Issam Mudawar
Boiling and Two-Phase Flow Laboratory,
School of Mechanical Engineering,
Purdue University,
West Lafayette, IN 47907

An experimental study was performed to characterize the transition boiling heat transfer rate from a surface to a stream of impinging water droplets and to extrapolate this information to predict the transition boiling heat transfer of a dilute spray. First, transition boiling heat transfer data were gathered for a continuous stream of monodispersed water droplets striking a polished nickel surface. From these data, empirical correlations were developed to describe the heat transfer rate and heat transfer efficiency for droplet velocities between $1.0\ \mathrm{m\,s^{-1}}$ *and* $7.1\ \mathrm{m\,s^{-1}}$*, droplet diameters ranging from* 0.250×10^{-3} m to 1.002×10^{-3} m*, and surface temperatures covering* $110-240\,^{\circ}\mathrm{C}$*. By properly accounting for the hydrodynamic differences between a spray and a single droplet stream, the empirical single droplet stream heat transfer correlations were effectively extrapolated into a model for predicting the transition boiling heat flux of dilute sprays* ($Q''\approx0.5\times10^{-3}\ \mathrm{m^3\,s^{-1}\,m^{-2}}$). [DOI: 10.1115/1.2764090]

Keywords: droplet, spray, transition boiling, heat transfer

Introduction

The transition boiling heat transfer regime plays an important role in materials processing, power generation, and electronic cooling applications. However, because of its complex and unsteady behavior, it has historically been the least studied of the various boiling regimes. Furthermore, the multifaceted aspects of spray hydrodynamics add further difficulty to the study and understanding of spray transition boiling heat transfer.

The basics of spray boiling heat transfer and the definitions of the four distinct heat transfer regimes are best described by the transient quenching curve, as shown in Fig. 1. At relatively high surface temperatures the film boiling regime exists. In this regime, liquid-solid contact is very brief as the liquid becomes separated from the surface by an insulating vapor layer, resulting in low heat fluxes and slow cooling rates. The lower temperature limit of the film boiling regime is referred to as the Leidenfrost point, which separates the film and transition boiling regimes. Within the transition boiling regime, the liquid droplets make partial and extended contact with the solid surface, as evident by the higher heat fluxes and faster cooling rates. Unique to the transition boiling regime, the heat transfer rate is inversely proportional to the surface temperature. As the surface temperature decreases in the transition boiling regime, the droplet-to-surface contact time increases along with a corresponding increase in the surface heat flux. At the lowest temperature limit of the transition boiling regime, the critical heat flux (CHF) point is encountered. At this point, the liquid droplets make efficient contact with the surface, and boiling heat fluxes as well as cooling rates are at their highest values. Below CHF, the nucleate boiling regime exists. In this regime, the liquid droplets effectively wet the surface and the heat fluxes are large, rapidly decreasing with surface temperature to the lower limit, termed the bubble incipience point. Below this limit, heat transfer occurs by single-phase convection.

Figure 1 is quite general, and the shape of the plot is highly influenced by fluid thermal and hydrodynamic properties, the heated surface characteristics, and surface orientation. Missing from Fig. 1 are the influential aspects of the droplet hydrodynamic parameters including diameter, velocity, frequency, and volumetric flux, as well as the surface properties.

Several qualitative studies have been performed to investigate the many parameters that influence the transition boiling behavior of individual impinging droplets. Chandra and Avedisian [1] used flash photography to investigate the influence of surface temperature on the droplet spreading structure for *n*-heptane droplets impinging upon a polished stainless steel surface. Inada et al. [2], Takeuchi et al. [3], and Makino and Michiyoshi [4] all used high speed photography to study the influence of various droplet and surface parameters on the transition boiling behavior of impinging water droplets. More recently, Bernardin et al. [5,6] used high speed and still photography to develop photographic libraries and droplet regime maps to identify the effects of droplet velocity, surface temperature, and surface roughness on the spreading and heat transfer characteristics of impinging water droplets. Bernardin et al. also made heat transfer measurements to estimate the CHF and Leidenfrost points, the boundaries of the transition boiling regime.

The characterization of droplet heat transfer is typically accomplished by measuring the average heat flux, average heat transfer coefficient, or droplet heat transfer efficiency, the latter of which is defined by

$$\varepsilon=\frac{Q_{\mathrm{sd}}}{Q_{\max}}=\frac{Q_{\mathrm{sd}}}{\rho_f\dfrac{\pi d_0^3}{6}h'_{fg}} \tag{1}$$

Araki et al. [7] developed an analytical model and incorporated empirical data to estimate the transition boiling heat transfer coefficient for a stream of water droplets impinging upon a heated surface. Inada et al. [2] employed transient temperature measurements and a two-dimensional (2D) analytical model to determine the transition boiling heat flux to impinging water droplets over a wide range of liquid subcooling. Takeuchi et al. [3] and Senda et al. [8] used similar transient quenching techniques of a hot surface by a stream of water droplets to measure the heat transfer rate and heat transfer efficiency over a range of surface temperatures as well as droplet velocities and frequencies.

Deb and Yao [9] used a dimensional analysis to develop the following heat transfer efficiency for a single impinging drop in the transition and film boiling regimes:

$$\varepsilon_{\mathrm{sd}}=0.0273\exp\left[\frac{0.081\sqrt{\ln(\mathrm{We}/35+1)}}{(B+S/60.5)^{1.5}}\right]+0.2109KB\exp\left(\frac{-90}{\mathrm{We}+1}\right) \tag{2}$$

where the dimensionless parameters are $\mathrm{We}=\rho_f u_o^2 d_o/\sigma$, $B=c_{p,g}(T_s-T_{\mathrm{sat}})/h_{\mathrm{fg}}$, $K=k_g/(c_{p,g}\mu_g)$, and $S=(k\rho c_p)_s^{0.5}/(k\rho c_p)_{\mathrm{steel}}^{0.5}-1$.

The droplet studies discussed here provide important qualitative and quantitative information concerning the heat transfer characteristics of individual droplets. However, they do not provide the tools to directly predict the heat transfer rate of a spray.

Contributed by the Heat Transfer Division of ASME for publication in the JOURNAL OF HEAT TRANSFER. Manuscript received June 22, 2006; final manuscript received February 12, 2007. Review conducted by Ramendra P. Roy. Paper presented at the 2005 ASME International Mechanical Engineering Congress (IMECE2005), Orlando, FL, November 5–11, 2005.

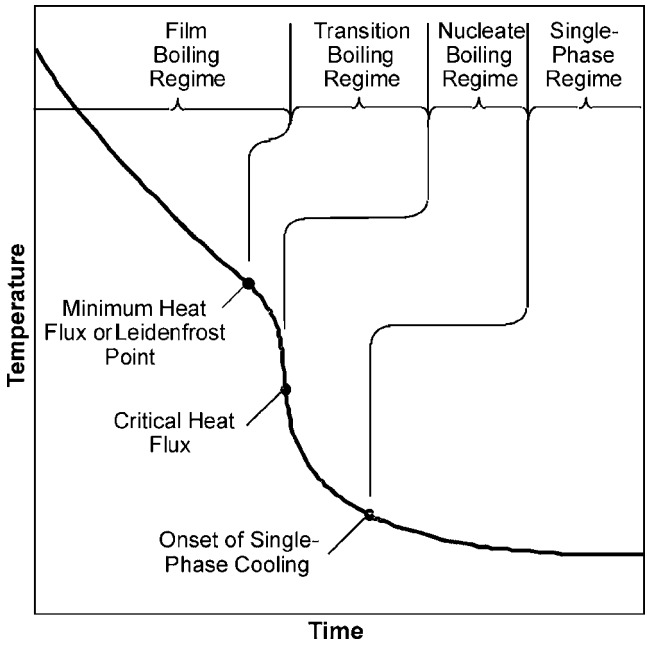

Fig. 1 Temperature-time history of a surface during spray quenching with a subcooled liquid

The primary influential parameters for a transitional boiling heat transfer rate in sprays have been reported to include surface temperature, droplet diameter, droplet velocity, and spray volumetric flux [9–13].

The droplet diameter has been reported to be of minor influence on the spray transition boiling heat flux. Mudawar and Valentine [14] as well as Klinzing et al. [10], using full cone spray nozzles, observed the heat flux to decrease slightly with an increase in droplet Sauter mean diameter over a range of 0.633×10^{-3}–1.350×10^{-3} m. Yao and Choi [13] and Deb and Yao [9], utilizing an impulse droplet atomizer to create a spray of uniform droplets, saw little or no influence of droplet diameter on the transition boiling heat flux.

The transition boiling heat flux was consistently observed to increase with droplet velocity for a variety of studies covering a wide range of spray parameters [9–13]. In all cases, the relationship between the heat flux and droplet velocity was highly nonlinear and very much dependent on the surface temperature and volumetric spray flux.

The second most dominant parameter in spray transition boiling heat transfer is the spray volumetric flux. In Refs. [9,12,13], the effects of volumetric spray flux were isolated by utilizing a monodispersed spray generator to maintain a uniform droplet diameter and velocity while adjusting the volumetric spray flux. From the data presented in those studies, the heat flux appeared to increase linearly with increasing volumetric spray flux ($0.000091 < Q'' < 0.0021$ m^3 s^{-1} m^{-2}). Klinzing et al. [10] employed a full cone spray nozzle and also found heat flux to increase with volumetric spray flux, although the relationship depended on whether the spray was dilute ($Q'' < 0.0035$ m^3 s^{-1} m^{-2}) or dense ($Q'' > 0.0035$ m^3 s^{-1} m^{-2}). It should be noted that although no quantitative categorization of dilute and dense sprays exists, studies [9,10,13,15] have reported liquid volumetric spray flux values in the range of 0.0002–0.0035 m^3 s^{-1} m^{-2} as the boundary between the two spray regimes.

Empirical spray transition boiling heat transfer correlations have been developed for water sprays [10,11,14] over a range of spray conditions. Klinzing et al. [14] presented the following correlation for the transition boiling heat flux q''_{trans}, for full cone water sprays based on local spray hydrodynamic parameters of liquid volumetric flux ($0.6 \times 10^{-3} < Q'' < 9.96 \times 10^{-3}$ m^3 s^{-1} m^{-2}), mean droplet velocity ($10.6 < u_m < 26.5$ m s^{-1}), Sauter mean drop diameter ($0.434 \times 10^{-3} < d_{32} < 2.005 \times 10^{-3}$ m), and surface temperatures up to 400°C,

$$q''_{\text{trans}} = q''_{\text{CHF}} - \frac{q''_{\text{CHF}} - q''_{\text{min}}}{(\Delta T_{\text{CHF}} - \Delta T_{\text{min}})^3}[\Delta T_{\text{CHF}}^3 - 3\Delta T_{\text{CHF}}^2 \Delta T_{\text{min}} + 6\Delta T_{\text{CHF}} \Delta T_{\text{min}} \Delta T - 3(\Delta T_{\text{CHF}} + \Delta T_{\text{min}})\Delta T^2 + 2\Delta T^3] \tag{3}$$

where

$$q''_{\text{CHF}} = 122.4 \rho_g h_{fg} Q'' \left[1 + 0.0118 \left(\frac{\rho_g}{\rho_f}\right)^{0.25} \left(\frac{\rho_f c_{pf} \Delta T_{\text{sub}}}{\rho_g h_{fg}}\right)\right] \times \left(\frac{\sigma}{\rho_f Q''^2 d_{32}}\right)^{0.198} \tag{4}$$

and

$$\Delta T_{\text{CHF}} = T_{\text{CHF}} - T_f = 18 \left[(\rho_g h_{fg} Q'') \left(\frac{\sigma}{\rho_f Q''^2 d_{32}}\right)^{0.198}\right]^{0.180} \tag{5}$$

and q''_{min} and ΔT_{min} are given in Eqs. (6) and (7) for dilute sprays ($Q'' < 3.5 \times 10^{-3}$ m^3 s^{-1} m^{-2}),

$$q''_{\text{min}} = 33.244 \times 10^5 Q''^{0.544} u_m^{0.324} \tag{6}$$

$$\Delta T_{\text{min}} = 204.895 Q''^{0.066} u_m^{0.138} d_{32}^{-0.035} \tag{7}$$

Reviews of the literature have revealed that while there have been several qualitative and quantitative studies of the transition boiling characteristics of droplets and sprays, a comprehensive model that possesses the ability to accurately model and predict the transition boiling heat transfer rate of a complex spray is still unavailable. The object of the present study is to construct a spray transition boiling heat transfer correlation based on the heat transfer characteristics of a single droplet stream and the statistical droplet distributions of sprays. To achieve this goal, quantitative assessments are made regarding the significance of droplet diameter, droplet velocity, and surface temperature on the transition boiling heat transfer rate for a single stream of impinging droplets. The empirical correlations that capture these quantitative assessments are then combined with a basic analytical spray heat transfer model to arrive at a semiempirical model for the transition boiling heat flux of a spray. Finally, the spray heat transfer model is compared to empirical spray transition boiling heat transfer correlations to demonstrate its effectiveness and limitations.

Experimental Apparatus and Procedures

Figure 2 displays the experimental apparatus used to study the transition boiling heat transfer from a heated surface to a controlled single stream of water droplets. The apparatus is comprised of a water delivery system, a droplet generator and associated electronics, a heater module with instrumentation, and a data acquisition system. Complete details for all of the experimental equipment can be found in Refs. [16,21], and thus only a brief summary is given here.

The droplet generator [16–19], developed to produce monodispersed droplets, was equipped with one of four stainless steel orifice plates possessing orifice diameters of 0.130×10^{-3} m, 0.249×10^{-3} m, 0.343×10^{-3} m, and 0.533×10^{-3} m, to produce droplets with respective diameters of 0.244×10^{-3} m, 0.468×10^{-3} m, 0.645×10^{-3} m, and 1.002×10^{-3} m [21]. The droplet generation process is achieved by forcing liquid through a narrow orifice to develop a laminar jet, which is then mechanically vibrated over a narrow frequency range and forced to disintegrate into a periodic stream of uniformly sized droplets. Rayleigh [20] demonstrated that an axisymmetric disturbance, whose wavelength is greater than the circumference of the laminar jet, would overcome surface tension forces and cause the jet to break up into

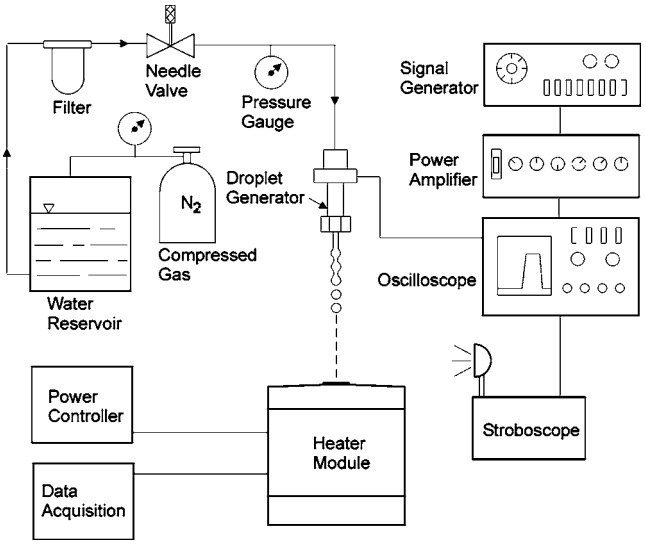

Fig. 2 Droplet heat transfer apparatus

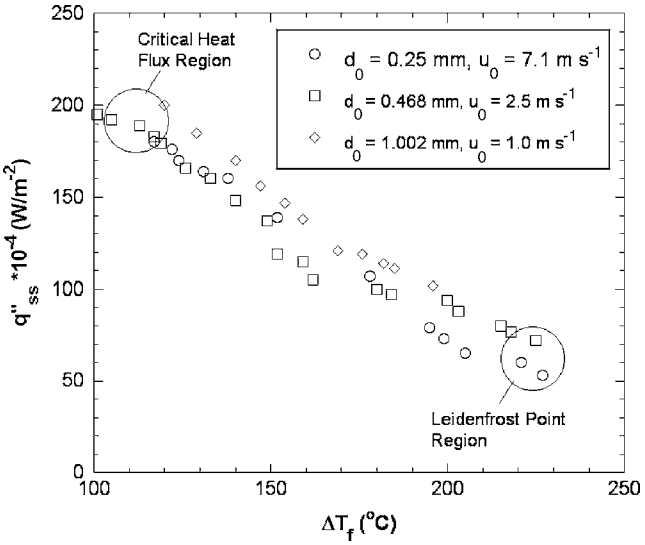

Fig. 3 Empirical data of heat flux from a heated surface to a single stream of droplets with a given diameter and velocity

a series of uniform droplets. Bernardin and Mudawar [16] showed that the optimum jet breakup frequency f_0 can be related to the droplet velocity u_0, droplet diameter d_0, most unstable wavelength λ_{opt}, or jet diameter D by

$$f_0 = \frac{u_0}{\lambda_{opt}} = \frac{u_0}{2.35 d_0} = \frac{u_0}{4.44 D} \tag{8}$$

A piezoceramic crystal, powered by a signal generator and power amplifier, was used to produce the mechanical vibrations for the droplet generator. As shown in Fig. 2, an oscilloscope was connected to the output of the power amplifier to precisely determine the electric field frequency. Furthermore, a strobe light, connected parallel to the output signal, was used to visually verify the successful breakup of the liquid jet into discrete droplets and to verify that the prescribed electrical disturbance frequency matched the droplet frequency. As discussed in Ref. [16], the droplet velocity was set by adjusting the flow rate to the generator for a given orifice diameter. This droplet generation technique created very stable and consistent droplet streams where no droplet-droplet interaction was witnessed prior to impact with the heated surface.

Table 1 summarizes the mean droplet diameters, velocities, and frequencies used in this study. Droplet diameters and velocities were measured with a Kodak Ektapro 1000 video motion analyzer in conjunction with a 200 mm zoom lens and a graduated ruler. Measured droplet diameters and velocities were within 10% and 5%, respectively, of the values listed in Table 1.

Table 1 Single droplet stream test parameters

Test number	$d_o \times 10^3$ (m)	$Q_{ss} \times 10^9$ ($m^3\ s^{-1}$)	u_o ($m\ s^{-1}$)	f (s^{-1})
1	0.250	40	3.0	5218
2	0.250	63	4.8	8311
3	0.250	78	5.8	10,162
4	0.250	94	7.1	12,327
5	0.468	74	1.5	1372
6	0.468	97	2.0	1817
7	0.468	120	2.5	2233
8	0.645	144	1.6	1032
9	0.645	177	1.9	1265
10	1.002	227	1.0	432
11	1.002	253	1.1	481

The heater module was designed to measure the heat transfer rate to a single stream of droplets impinging upon the polished nickel-plated surface. Wrapped around the circumference of the heater assembly was an electrical resistance heater (200 W at 120 V ac), which was powered by a variable ac voltage transformer. The heater assembly employed four calibrated type-K thermocouples (±0.2°C) to measure the heat conducted to the surface and dissipated by the droplet stream. The thermocouples, made from 0.076 mm (0.003 in.) diameter wires and inserted into 0.343 mm (0.135 in.) ceramic tubes, were placed at a depth of 3.99 mm (0.157 in.) and a spacing of 2.54 mm (0.10 in.). This heater configuration ensured a one-dimensional heat flow along the instrumented section [16,21]. A one-dimensional curve fit to the thermocouple readings allowed for an extrapolation of the surface temperature and heat flux. An error analysis based on uncertainties in geometry, thermocouple calibration values, copper thermal conductivity, and heat losses resulted in a maximum error of 7% in heat flux measurements [16,21].

Distilled water was used as the working fluid for all tests. To minimize the risk of contamination, the liquid was never recirculated in the flow apparatus. The clean fluid and intermittent repolishing of the test surface minimized the likelihood of changes in the heater surface conditions.

For a detailed description of the experimental test procedure, the reader is directed to Ref. [16].

Results

Experimental Measurements and Data Correlation. Figure 3 shows three data sets, typical of the experimental results obtained in this study. The plot displays the surface heat flux versus the temperature difference between the heater surface and the droplet for three different droplet stream conditions. These data sets encompass the transition boiling regime, from the CHF point to the Leidenfrost point. Additional data corresponding to the nucleate and film boiling regimes were obtained to identify the boundary points of the transition boiling regime but were omitted from Fig. 3 [16,21] for data correlation purposes.

Similar to the approach used in Ref. [16] for film boiling heat transfer, the transition boiling heat transfer rate for a single droplet stream was correlated in this study to the following form:

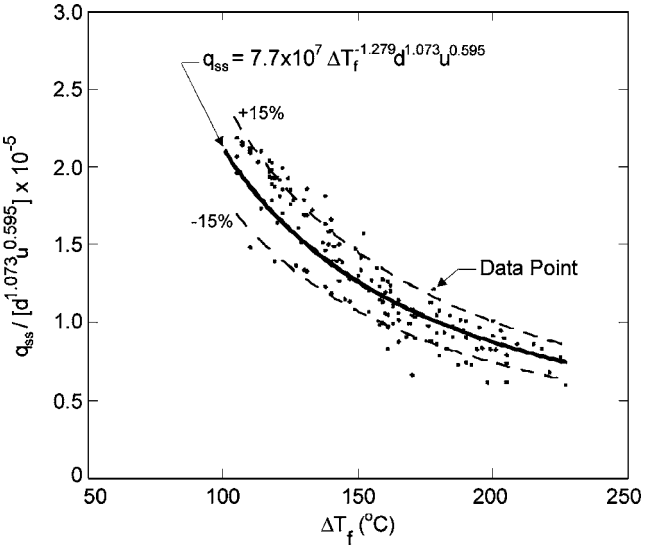

Fig. 4 Correlation of the single droplet stream transition boiling heat transfer rate data

$$q_{ss} = a_1 \Delta T_f^{a_2} d_0^{a_3} u_0^{a_4} \tag{9}$$

where a_1–a_4 are empirically determined coefficients. Using a linear least squares fitting technique, the following form of the correlation was obtained:

$$q_{ss} = 7.7 \times 10^7 \Delta T_f^{-1.279} d_0^{1.073} u_0^{0.595} \tag{10}$$

where q_{ss}, ΔT_f, d_0, and u_0 have the units of W, °C, m, and m s^{-1}, respectively. Figure 4 displays this correlation against the empirical data and indicates that the majority of the data lies within a +/−15% bracketed band about the correlation. Given this data scatter and the uncertainties in the droplet diameter, droplet velocity, and heat flux measurements, it is estimated that Eq. (10) has a mean uncertainty of 11%.

While Eq. (10) describes the transition boiling heat transfer rate to a droplet stream, it does not indicate the efficiency of the heat transfer process. Droplet heat transfer efficiency, as defined previously in Eq. (1), is the ratio of the actual to the maximum possible amount of heat transferred from a surface to a droplet. For a single droplet stream, this can be represented by

$$\varepsilon_{ss} = \frac{Q_{sd}}{Q_{max}} = \frac{q_{ss}}{f\rho_f \dfrac{\pi d_0^3}{6} h'_{fg}} \tag{11}$$

Substituting Eqs. (8) and (10) into Eq. (11) gives the transition boiling heat transfer efficiency of the single droplet streams investigated in this study,

$$\varepsilon_{ss} = \frac{3.46 \times 10^8}{\rho_f h'_{fg}} \Delta T_f^{-1.279} d_0^{-0.927} u_0^{-0.405} \tag{12}$$

Equation (12) corresponds to a closely packed or high frequency stream of droplets where a significant interference from successive drops occurs during the impact and heat transfer process on the heater surface. Consequently, the efficiency predicted by Eq. (12) will be lower than those obtained for single droplets or dilute sprays.

Equations (10) and (12) are valid for water droplet streams of uniform diameter, frequency, and velocity and for the following parametric ranges: $100 \leq \Delta T_f \leq 220$ °C, $0.250 \times 10^{-3} \leq d_0 \leq 1.002 \times 10^{-3}$ m, and $1.0 \leq u_0 \leq 7.1$ m s^{-1}

Dilute Spray Modeling and Assessment. In this section, the heat transfer correlation for a single droplet stream is incorporated into the development of a semiempirical model of the transition boiling heat flux for a dilute spray, q''_{sp}. A spray may be thought of, in a simplistic manner, as a series of droplet streams impinging upon a heated area. Furthermore, as pointed out in Ref. [16], it is reasonable to expect that the interaction between droplets in a spray will be different than in a droplet stream. Therefore, to model a spray as a series of droplet streams, a correction must be applied to account for differences in heat transfer efficiency of a spray and of a droplet stream. The entire mathematical development of this model and justification of the supporting arguments parallels that found in Ref. [16] for a similar model of spray film boiling, and thus the reader is directed to that reference for all of the supplementary information. Taking the approach outlined in Ref. [16], but employing the transition boiling expressions of Eqs. (10) and (12) of the present study, and replacing the single stream droplet diameters and velocities with, respectively, the spray Sauter mean diameter d_{32} and the spray mean droplet velocity u_m, the following transition boiling heat flux prediction for a dilute spray may be obtained:

$$q''_{sp,pred} = \rho_f h'_{fg} Q''_{sp} \varepsilon_{sd} \left(1 - \frac{Q''_{sp}}{Q''_{sp,dense}}\right) + 3.46 \times 10^8 \Delta T_f^{-1.279} d_{32}^{-0.927} u_m^{-0.405} \left(\frac{Q''^2_{sp}}{Q''_{sp,dense}}\right) \tag{13}$$

where the spray flux corresponding to a dense spray, $Q''_{sp,dense}$, was reported in Refs. [10,16] to be approximately 5×10^{-3} m^3 s^{-1} m^{-2}, as the lower limit for a fully dense spray.

The transition boiling heat transfer efficiency for a single impinging droplet, ε_{sd}, can be determined directly from Eq. (2). Another approach, which is more applicable to full cone water sprays, is to divide Eq. (3) by the maximum amount of heat transfer to a spray, $\rho f h'_{fg} Q''_{sp}$, and evaluate the result at a dilute volumetric spray flux of 0.175×10^{-3}m^3 s^{-1}m^{-2} [16]. This approach does not account for all aspects of droplet interference that could exist on a surface being exposed to a medium or dense spray. However, it is believed that these equations provide a reasonable characterization of a dilute spray.

Consequently, by knowing the single droplet heat transfer efficiency ε_{sd}, the spray parameters (d_{32}, u_m, Q''), and the excess surface temperature ΔT_f, Eq. (13) can be used to predict the local spray transition boiling heat flux. This model's predictive capability is best matched over the following parameteric ranges: $100 \leq \Delta T_f \leq 220$ °C, $0.250 \times 10^{-3} \leq d_{32} \leq 1.002 \times 10^{-3}$ m, and $1.0 \leq u_0 \leq 7.1$ m s^{-1}.

Figure 5 displays a comparison of the spray transition boiling heat flux model Eq. (13) versus two empirical spray transition boiling heat flux correlations [10,11] for a single set of spray parameters. Figure 5 allowed for the evaluation of two different methods that were used to calculate the single droplet heat transfer efficiency ε_{sd}, for Eq. (13). The first method included direct utilization of Eq. (2), which is the correlation by Deb and Yao [9]. The second method involved dividing Eq. (3) by the maximum amount of heat transfer to a spray, $\rho f h'_{fg} Q''_{sp}$, and evaluating the result at a dilute volumetric spray flux of 0.175×10^{-3} m^3 s^{-1} m^{-2}. As Fig. 5 indicates, the latter of these two methods yields a closer agreement between the spray heat flux model and the empirical correlations, and thus this approach was employed in all remaining model assessments. The disagreement between the heat flux model and the empirical correlation of Ref. [10] at low temperatures is explained in Fig. 6(*a*).

Figure 6 compares the spray transition boiling heat flux model Eq. (13) versus the empirical dilute spray heat flux correlation of Klinzing et al. [10] (Eq. (3)) for various spray fluxes, droplet diameters, and droplet velocities. Figure 6(*a*) shows an excellent agreement for the low volumetric spray flux (0.5×10^{-3} m^3 s^{-1} m^{-2}) and gradual departure in the agreement as the spray flux is increased. It appears that the model of Eq. (13) is applicable for very dilute sprays, but begins to lose its accuracy

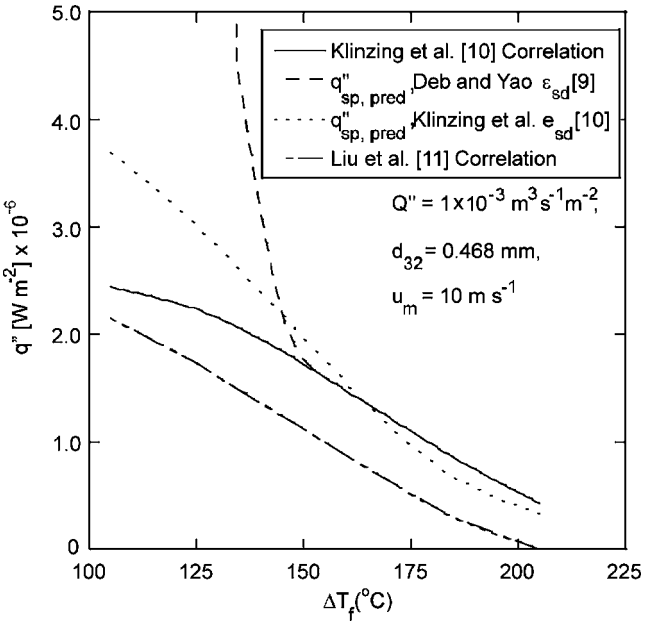

Fig. 5 Comparison of the spray transition boiling heat flux model to spray heat flux correlations

for spray fluxes greater than 1.0×10^{-3} m^3 s^{-1} m^{-2}. It is speculated that complex droplet interference and interaction effects, which occur in medium and dense sprays, can account for the limited capabilities of Eq. (13) [16]. Nevertheless, Fig. 6(*b*) and 6(*c*) indicate that the model's predictive capability is very good for droplet diameters and droplet velocities over the ranges of 0.250×10^{-3}–1.000×10^{-3} m and 5.0–15.0 m s^{-1}, respectively, for a volumetric spray flux of 0.5×10^{-3} m^3 s^{-1} m^{-2}.

Conclusions

This investigation focused on the transition boiling heat transfer rate and the heat transfer efficiency of a single stream of monodispersed water droplets. Furthermore, the study demonstrated how the complex behavior of spray transition boiling heat transfer can be modeled from fundamental observations of the controlled single droplet stream. From the experimental measurements and analytical modeling comparisons, the following key conclusions can be drawn.

1. Empirical correlations were developed for the transition boiling heat transfer rate and the heat transfer efficiency for a single stream of uniform droplets impinging upon a polished horizontal surface. The influential parameters for these correlations include droplet diameter, droplet velocity, and surface temperature.
2. By properly accounting for the hydrodynamic differences between a spray and a single droplet stream, the empirical single droplet stream heat transfer correlations were effectively extrapolated into a model for predicting the transition boiling heat flux of dilute sprays ($Q''\approx0.5\times10^{-3}$ m^3 s^{-1} m^{-2}).

Nomenclature

Symbol

c_p = specific heat (J kg^{-1} K^{-1})
D = laminar jet diameter (m)
d_o = droplet diameter (m)
d_{32} = droplet Sauter mean diameter (m)
f = frequency (s^{-1})
h_{fg} = latent heat of vaporization (J kg^{-1})

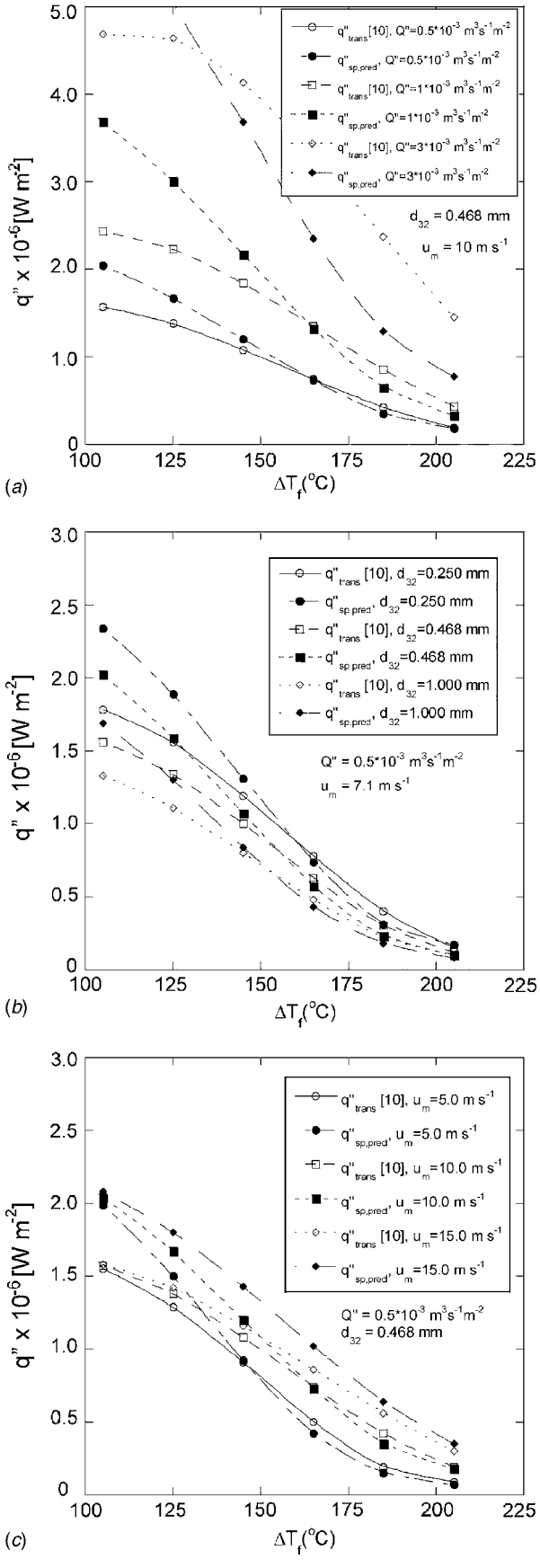

Fig. 6 Comparison of the spray transition boiling heat flux model, $q''_{sp,pred}$, to the spray heat flux correlation of Klinzing et al. [10], q''_{trans}, for various (*a*) volumetric spray fluxes, (*b*) droplet diameters, and (*c*) droplet velocities

h'_{fg} = modified latent heat of vaporization $h_{fg}+c_{p,f}(T_{sat}-T_f)$ (J kg^{-1})
k = thermal conductivity (W m^{-1} K^{-1})
Q = total heat transfer (J), volume flow rate (m^3 s^{-1})
Q'' = volumetric spray flux (m^3 s^{-1} m^{-2})
q = heat transfer rate (W)
q'' = heat flux (W m^{-2})
T = temperature (°C)
T_{CHF} = temperature at CHF (°C)
T_{min} = temperature corresponding to minimum heat flux (°C)
u_o = droplet velocity (m s^{-1})
u_m = mean drop velocity in spray (m s^{-1})
We = Weber number, $(\rho u_o^2 d_o)/\sigma$

Greek Symbol

ΔT_{CHF} = $T_{CHF}-T_f$ (°C)
ΔT_f = T_s-T_f (°C)
ΔT_{min} = $T_{min}-T_f$ (°C)
ε = drop or spray heat transfer efficiency
λ = wavelength (m)
μ = dynamic viscosity (N s m^{-2})
ρ = density (kg m^{-3})
σ = surface tension (N m^{-1})

Subscript

CHF = critical heat flux condition
dense = dense spray condition
f = property of liquid
fg = difference between liquid and vapor
g = property of vapor
max = maximum
min = minimum heat flux or Leidenfrost point
pred = predicted
s = solid, surface
sat = saturation
sd = single droplet
sp = spray
ss = single droplet stream
trans = transition boiling

References

[1] Chandra, S., and Avedisian, C. T., 1991, "On the Collision of a Droplet With a Solid Surface," Proc. R. Soc. London, Ser. A, **432**, pp. 13–41.
[2] Inada, S., Miyasaka, Y., Nishida, K., and Chandratilleke, G. R., 1983, "Transient Temperature Variation of a Hot Wall Due to an Impinging Water Drop—Effect of Subcooling of the Water Drop," *Proceedings of the ASME-JSME Thermal Engineering Joint Conference*, Honolulu, HI, ASME, New York, Vol. 1, pp. 173–182.
[3] Takeuchi, K., Senda, J., and Yamada, K., 1983, "Heat Transfer Characteristics and the Breakup Behavior of Small Droplets Impinging Upon a Hot Surface," *Proceedings of the ASME-JSME Thermal Engineering Joint Conference*, Honolulu, HI, ASME, New York, Vol. 1, pp. 165–172.
[4] Makino, K., and Michiyoshi, I., 1984, "The Behavior of a Water Droplet on Heated Surfaces," Int. J. Heat Mass Transfer, **27**, pp. 781–791.
[5] Bernardin, J. D., Stebbins, C. J., and Mudawar, I., 1997, "Mapping of Impact and Heat Transfer Regimes of Water Drops Impinging on a Polished Surface," Int. J. Heat Mass Transfer, **40**, pp. 247–267.
[6] Bernardin, J. D., Stebbins, C. J., and Mudawar, I., 1997, "Effects of Surface Roughness on Water Droplet Impact History and Heat Transfer Regimes," Int. J. Heat Mass Transfer, **40**, pp. 73–88.
[7] Araki, K., Yoshinobu, S., Nakatani, Y., and Moriyama, A., 1982, "Stationary Measurement for Heat Transfer Coefficient in Droplet-Cooling of Hot Metal," Trans. Iron Steel Inst. Jpn., **22**, pp. 952–958.
[8] Senda, J., Yamada, K., Fujimoto, H., and Miki, H., 1988, "The Heat Transfer Characteristics of a Small Droplet Impinging Upon a Hot Surface," JSME Int. J., Ser. II, **31**, pp. 105–111.
[9] Deb, S., and Yao, S. C., 1987, "Heat Transfer Analysis of Impacting Dilute Spray on Surfaces Beyond the Leidenfrost Temperature," *Proceedings of the ASME National Heat Transfer Conference*, Pittsburgh, PA, ASME, New York, Vol. 1, pp. 1–8.
[10] Klinzing, W. P., Rozzi, J. C., and Mudawar, I., 1992, "Film and Transition Boiling Correlations for Quenching of Hot Surfaces With Water Sprays," J. Heat Treating, **9**, pp. 91–103.
[11] Liu, G. W., Morsi, Y. S., and Clayton, B. R., 2000, "Characterization of the Spray Cooling Heat Transfer Involved in a High Pressure Die Casting Process," Int. J. Therm. Sci., **39**, pp. 582–591.
[12] Choi, K. J., and Yao, S. C., 1987, "Mechanisms of Film Boiling Heat Transfer of Normally Impacting Spray," Int. J. Heat Mass Transfer, **30**, pp. 311–318.
[13] Yao, S. C., and Choi, K. J., 1987, "Heat Transfer Experiments of Mono-Dispersed Vertically Impacting Sprays," Int. J. Multiphase Flow, **13**, pp. 639–648.
[14] Mudawar, I., and Valentine, W. S., 1989, "Determination of the Local Quench Curve for Spray-Cooled Metallic Surfaces," J. Heat Treating, **7**, pp. 107–121.
[15] Delcorio, B., and Choi, K. J., 1991, "Analysis of Direct Liquid-Solid Contact Heat Transfer in Monodispersed Spray Cooling," J. Thermophys. Heat Transfer, **5**, pp. 613–620.
[16] Bernardin, J. D., and Mudawar, I., 1997, "Film Boiling Heat Transfer of Droplet Streams and Sprays," Int. J. Heat Mass Transfer, **40**, pp. 2579–2593.
[17] Brenn, G., and Frohn, A., 1993, "An Experimental Method for the Investigation of Droplet Oscillations in a Gaseous Medium," Exp. Fluids, **15**, pp. 85–90.
[18] Berglund, R. N., and Liu, B. Y., 1973, "Generation of Monodispersed Aerosol Standards," Environ. Sci. Technol., **7**, pp. 147–153.
[19] Anders, K., Roth, N., and Frohn, A., 1992, "Operation Characteristics of Vibrating-Orifice Generators: The Coherence Length," Part. Part. Syst. Charact., **9**, pp. 40–43.
[20] Rayleigh, L., 1878, "On the Instability of Jets," Proc. London Math. Soc., **10**, pp. 4–13.
[21] Bernardin, J. D., 1996, "Leidenfrost Point and Film Boiling Heat Transfer of Single Dropets and Sprays," Ph.D. thesis, Purdue University, West Lafayette, IN.

Heat Transfer Enhancement for Turbulent Flow Through Blockages With Round and Elongated Holes in a Rectangular Channel

H. S. Ahn

S. W. Lee

S. C. Lau[1]

Convective Heat and Mass Transfer Laboratory,
Department of Mechanical Engineering,
Texas A&M University,
College Station, TX 77843-3123

Experiments were conducted to determine the average heat transfer coefficients on three wall segments between blockages with holes in a wide rectangular channel. Eight different configurations of the holes in the blockages—two diameters and four aspect ratios of the holes—were examined. The pressure drops across the blockages were also measured. The results showed that the elongated holes in the blockages in this study enhanced more heat transfer than the round holes, but they also caused larger pressure drops across the blockages. [DOI: 10.1115/1.2764091]

Keywords: forced convection, heat transfer enhancement, internal cooling of turbine airfoils, blockages with holes

Introduction

In a design concept for protecting airfoils from the hot combustion gases in gas turbines, engineers proposed to force cooling air through staggered holes in blockages in internal passages in the tail regions of airfoils to enhance the heat transfer to the cooling air before it exits the airfoils through the trailing edge slots. In Ref. [1], the tail region of an airfoil with these blockages was modeled as two converging rectangular channels. Air flowed through staggered elongated holes with rounded edges along the two blockages in each channel. These blockages have the same cross section as the flow cross section of the converging channel without the blockages. Downstream of the second blockage, the air left the channel through exit slots. Naphthalene sublimation experiments were conducted to determine the overall mass transfer coefficients and the distributions of the local mass transfer coefficient on the wall segments between the two blockages and between the second blockage and the exit slots, for two different entrance channels and two exit slot configurations. The analogy between heat transfer and mass transfer was used to relate the experimentally determined mass transfer enhancement to heat transfer enhancement. Lau et al. [1] also reviewed published studies on heat transfer for flows through full and partial blockages, and the references for these studies will not be repeated here. For information on published studies on internal cooling of gas turbine blades and vanes, readers are referred to publications such as Refs. [2,3].

The objective of this study was to examine, for turbulent air flow through holes in blockages, the effects of the aspect ratio (width-to-height ratio) of the holes and the total hole-to-blockage area ratio on the average heat transfer on the wall segments between consecutive blockages, and the pressure drops across the blockages. This parametric study was different from Ref. [1] in which blockages with two specific hole configurations in two converging rectangular channels with specific dimensions and entrance and exit configurations were considered.

Test Apparatus and Instrumentation

The test section for this study was a rectangular channel with a cross section of 30.5 cm (width) $\times$ 2.54 cm (height), and thus an aspect ratio of 12:1. The walls of the test section were constructed of 1.27 cm thick oak plywood. As shown in the schematic of the side view of the test section in Fig. 1, there were four blockages with staggered round or elongated holes in the test section. These blockages were constructed of acrylic. They had the same height as the channel and were 1.14 cm thick. The distance between two consecutive blockages was 5.08 cm or twice the height of the channel.

For this study, there were eight sets of four blockages with different hole configurations, and the holes had a height (or diameter, in the round hole case) of either 1.27 or 1.91 cm. Table 1 lists the widths of the holes and the center-to-center spacings between holes in the various blockages. While the aspect ratio of the holes ranged from 1.0 (round holes) to 3.4, and the total number of holes varied from 2 to 12, the ratios of the total hole-to-channel cross-sectional areas were kept constant and were equal to about 0.2 and 0.3, respectively, in the smaller and larger hole cases. Figure 2 shows two of each set of these blockages with staggered holes.

Air was the working fluid. During an experiment, it was drawn through the test section with two centrifugal blowers that were connected in series. After the air left the test section, it passed through a settling plenum, an orifice flow meter, and a gate valve and a bypass valve, before it was ducted to the outside of the laboratory.

Figure 3 shows the top views of the top and bottom walls of the test section. To determine the average heat transfer on one of the two principal walls of the test section downstream of the blockages, three copper plates were installed in three slots in the top wall of the test section. Each copper plate measured 5.08 $\times$ 30.5 cm^2 and was 1.27 cm thick. During an experiment, heat was supplied to each copper plate from a flexible electric heater that was attached with silicon rubber adhesive onto the outer surface of the copper plate. Balsa wood with a thickness of 3.2 mm was attached, also with silicon rubber adhesive, onto the four edges of each copper plate. After the copper plate was installed in one of the three slots in the top wall of the test section, the wooden rim rested on top of the two blockages and the two sidewalls, such that the balsa wood minimized the heat transfer by conduction to the acrylic blockages. Styrofoam insulation was used to minimize extraneous heat losses to the surroundings, and silicon sealant was used to prevent air leakage at the interfaces between the copper plates and the top wall.

For each experiment, after a steady state was attained, the heater voltage drops and currents were measured with two TRMS digital multimeters. The temperature of each of the three copper plates was measured with seven 36-gage T-type thermocouples, along with a computer-controlled data acquisition system. The pressure drops across the blockages were measured with 15 static pressure taps at five streamwise stations along with a calibrated pressure transducer. Figure 3 shows the locations of the 21 thermocouples in the three copper plates and the locations of the 15 static pressure taps at five streamwise stations in the bottom channel wall.

Experiments were conducted with each set of blockages to obtain the average heat transfer coefficient on the wall segments downstream of the blockages and the pressure drops across the blockages, for three air mass flow rates corresponding to Reynolds numbers of about 7000, 12,000, and 17,000. Separate experiments

[1]Corresponding author.

Contributed by the Heat Transfer Division of ASME for publication in the JOURNAL OF HEAT TRANSFER. Manuscript received June 29, 2006; final manuscript received March 8, 2007. Review conducted by A. Haji-Sheikh.

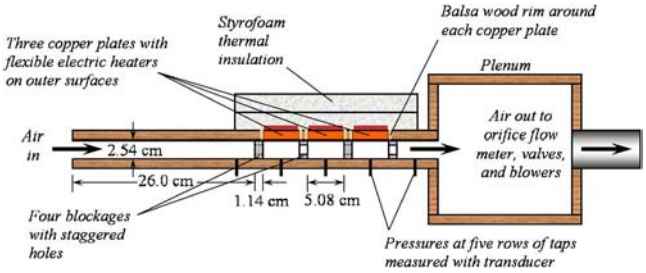

Fig. 1 Schematic of test apparatus for this study

were conducted to calibrate the instruments for measuring the air mass flow rate, the wall and air temperatures, and pressures, and to determine the extraneous heat losses to the surroundings.

Data Reduction

The average Nusselt number for each of the three wall segments between two blockages was defined as

$$\overline{\mathrm{Nu}} = \frac{\bar{h}D_h}{k} \tag{1}$$

where the average heat transfer coefficient was evaluated as

$$\bar{h} = \frac{IV - q_{\mathrm{loss}}}{A_s(\bar{T}_w - \bar{T}_m)} \tag{2}$$

The bulk temperature at the downstream edge of a wall segment was determined based on an energy balance calculation with the net rate of heat transfer from the wall segment, the air mass flow rate, and the bulk temperature at the upstream edge of the wall segment as inputs. The average bulk temperature was the average of the two bulk temperatures.

The Reynolds number for the air flow through the test channel was also defined based on the hydraulic diameter of the test channel and might be written as

$$\mathrm{Re} = \frac{4\dot{m}}{\mu P} = \frac{2\dot{m}}{\mu(W+H)} \tag{3}$$

Based on the pressure gradient across the blockages, the friction factor was determined as

$$f = \frac{(\Delta p/\Delta x)D_h}{\rho\bar{u}^2/2} = 2\rho D_h\left(\frac{\Delta p}{\Delta x}\right)\left(\frac{A_c}{\dot{m}}\right)^2 \tag{4}$$

The average Nusselt number and friction factor were normalized, respectively, with the Nusselt number and friction factor for fully developed turbulent flow through a smooth channel at the same Reynolds number given by

$$\mathrm{Nu}_0 = 0.023\,\mathrm{Re}^{0.8}\,\mathrm{Pr}^{0.4} \tag{5}$$

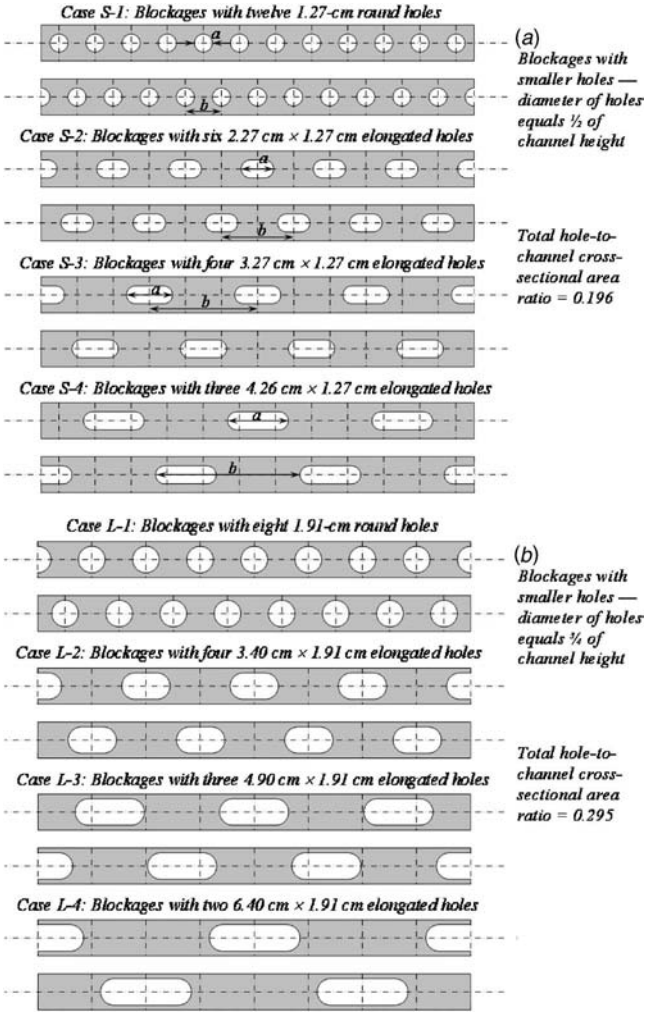

Fig. 2 Schematics of blockages with round and elongated holes for this study

$$f_0 = [0.79\ln(\mathrm{Re}) - 1.64]^{-2} \tag{6}$$

The thermal performance was defined as

$$\mathrm{TP} = (\overline{\mathrm{Nu}}/\mathrm{Nu}_0)(f/f_0)^{-1/3} \tag{7}$$

This parameter compares the heat transfer enhancement by the blockages per unit pumping power relative to the heat transfer for fully developed turbulent flow through a smooth channel.

The uncertainties of the Reynolds number, Nusselt number, and friction factor were estimated based on the uncertainty analysis method of Ref. [4] and a confidence level of 95%. With the un-

Table 1 Configurations of holes in blockages

Diameter=1.27 cm, area ratio=0.196	Case S-1	Case S-2	Case S-3	Case S-4
Number of holes in each blockage	12	6	4	3
Width of holes, a (cm)	1.27	2.27	3.27	4.26
Center-to-center spacing between holes, b (cm)	2.54	5.08	7.62	10.2
Aspect ratio of holes	1.0	1.8	2.6	3.4
Diameter=1.91 cm; area ratio=0.295	Case L-1	Case L-2	Case L-3	Case L-4
Number of holes in each blockage	8	4	3	2
Width of holes, a (cm)	1.91	3.40	4.90	6.40
Center-to-center spacing between holes, b (cm)	3.81	7.62	10.7	15.2
Aspect ratio of holes	1.0	1.8	2.6	3.4

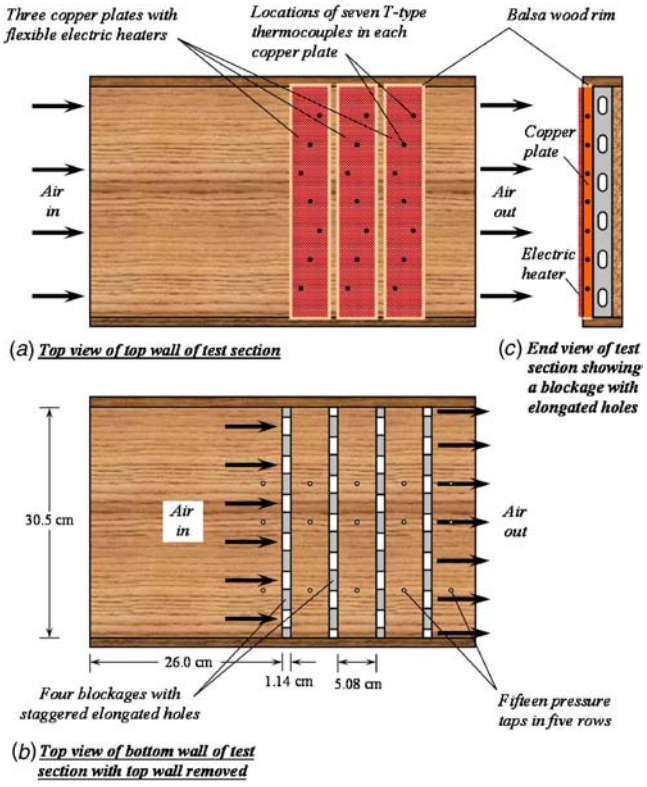

Fig. 3 Schematic of top and bottom walls of wide (12:1) rectangular channel with four blockages for this study

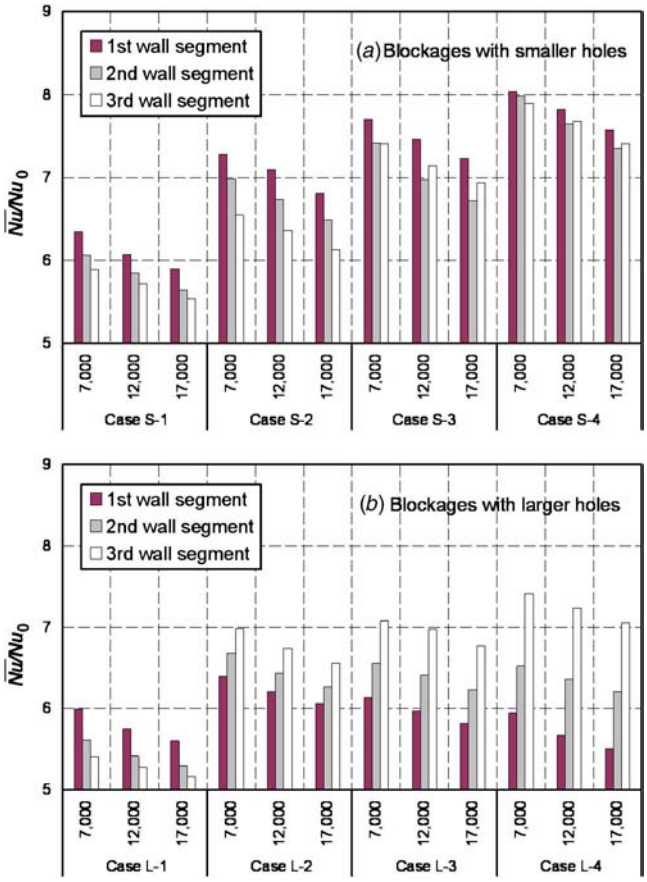

Fig. 4 Heat transfer enhancement on wall segments downstream of blockages (numbers along the abscissa are Reynolds numbers)

certainties of ±1.0% for all properties of the air and ±0.5% for all physical dimensions, the uncertainty of the mass flow rate was calculated to be ±2.2%, and the uncertainty of the Reynolds number was estimated to be ±2.5%.

The uncertainties for the heater voltage and current were found to be ±2.2% and ±1.2%, and those for the average wall and bulk temperatures were ±2.5% and ±2.6%, respectively. With these values, the uncertainty of the Nusselt number was calculated to be ±6.1%. With uncertainties of ±6.8% for the pressure drop and ±2.2% for the air mass flow rate, the uncertainty of the friction factor was estimated to be ±8.4%.

Presentation and Discussion of Results

Heat Transfer on Wall Segments. In this study, average heat transfer coefficients were determined on three wall segments between blockages with holes in a wide rectangular channel. Eight different configurations of the holes in the blockages—two diameters and four aspect ratios of the holes—were examined. Experiments were conducted at three different air flow rates. The pressure drops across the blockages were also measured. The heat transfer and pressure drop results are presented in this section in terms of a Nusselt number ratio $\overline{Nu}/Nu_0$ and a friction factor ratio f/f_0. These two ratios give, respectively, the heat transfer enhancement by the blockages and the increase in the pressure drop caused by the blockages.

Figure 4 shows the heat transfer enhancement on the three wall segments by the blockages with holes. In the figure, the $\overline{Nu}/Nu_0$ values for the three Reynolds numbers of about 7000, 12,000, and 17,000 are presented for the eight cases with different hole configurations: (a) Cases S-1–S-4 for the blockages with the smaller holes and (b) Cases L-1–L-4 for the blockages with the larger holes. The results show that the value of $\overline{Nu}/Nu_0$ ranges from 5.2 to 8.0. Thus, the heat transfer coefficients on the wall segments downstream of the blockages with holes are much higher than those for fully developed flows through an open channel without blockages at the same Reynolds numbers. The blockages with the smaller holes increase the heat transfer on the wall segments more than those with the larger holes. In all cases, the heat transfer enhancement is lower when the air flow rate is higher. Increasing the Reynolds number from about 7000 to about 17,000 decreases the $\overline{Nu}/Nu_0$ value by 6.1%, on average, with a maximum change of −9.3%.

For the blockages with the smaller holes, Fig. 4(*a*) shows that increasing the aspect ratio of the holes from 1.0 to 3.4 increases the Nusselt number ratio monotonically. The $\overline{Nu}/Nu_0$ values for the blockages with the widest holes (Case S-4) are 27–34% larger than those for the blockages with the round holes (Case S-1). The $\overline{Nu}/Nu_0$ values are larger on the first wall segment between the first two blockages than on the two downstream wall segments.

For the blockages with the larger holes, Fig. 4(*b*) shows that the $\overline{Nu}/Nu_0$ values are smaller in Case L-1 for the blockages with the round holes than in Cases L-2–L-4 for the blockages with elongated holes. In Case L-1, the $\overline{Nu}/Nu_0$ values are the largest on the first wall segment and the lowest on the third wall segments, while in Cases L-2–L-4, the trend reverses. For the blockages with the elongated holes, with an increase of the aspect ratio of the holes, $\overline{Nu}/Nu_0$ decreases on the first wall segment, remains about constant on the second wall segment, and increases on the third wall segment, with a maximum change of less than 9.1%.

Figure 4 clearly shows that there are variations of the heat transfer coefficients on the three wall segments for the eight dif-

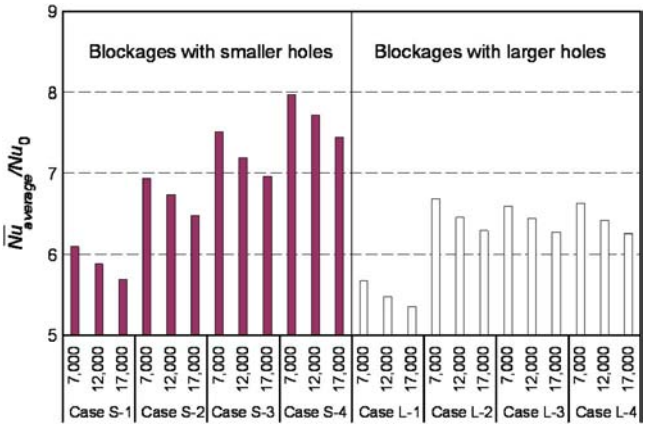

Fig. 5 Average heat transfer enhancement on wall segments downstream of blockages (numbers along the abscissa are Reynolds numbers)

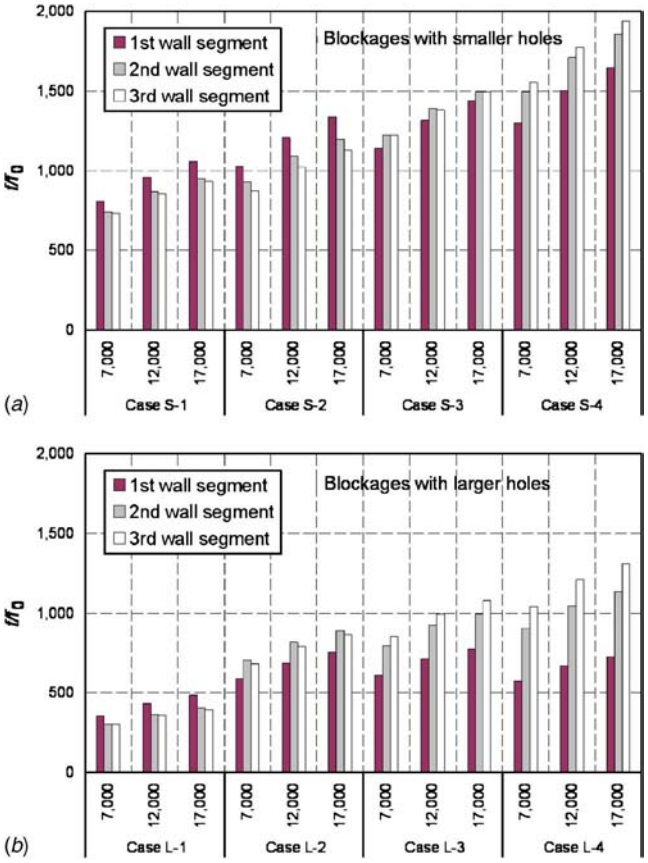

Fig. 6 Pressure drops across wall segments downstream of blockages relative to that for fully developed turbulent flow through a smooth channel without blockages (numbers along the abscissa are Reynolds numbers)

ferent configurations of the holes in the blockages in this study, and that the flows through the blockages were not periodic during the experiments. In Fig. 5, the average heat transfer results over the three wall segments are presented. From these average results, it can be readily seen that the average heat transfer enhancement on the three wall segments decreases with increasing mass flow rate and is larger in the cases of the blockage with the smaller holes. The average heat transfer enhancement increases monotonically with an increase of the aspect ratio of the smaller holes, and the $\overline{Nu}_{av}/Nu_0$ values are lower in the case of the larger round holes than similar values in the three cases with the larger elongated holes.

In Ahn Ref. [5], naphthalene sublimation experiments were conducted to obtain the average mass transfer and the local mass transfer distributions on three wall segments downstream of the same blockages considered in this study, using the test section of this study, for Re≅7000 and 17,000. By applying the heat and mass transfer analogy, the measured average and local Sherwood number ratios were converted to average and local Nusselt number ratios. The effects of the hole configuration and the mass flow rate on $\overline{Nu}/Nu_0$ based on the mass transfer measurements in Ref. [5] are found to be consistent with the effects on $\overline{Nu}/Nu_0$ that are reported here. For all eight hole configurations considered, the $\overline{Nu}/Nu_0$ values based on the mass transfer experiments (with an estimated uncertainty of ±8.2%) are slightly higher (by 4.9% on average) than those in this study, with a maximum deviation of 9.9% and a standard deivation of 2.7%. In Ref. [5], the local heat (mass) transfer distributions helped explain the effect of the hole configuration on the average heat (mass) transfer on the wall segments downstream of the blockages with holes.

Friction Factor. The friction factors were calculated with Eq. (4) using the pressure drops across the two consecutive blockages—between the pressure taps in the first and third rows, between the pressure taps in the second and fourth rows, and between those in third and fifth rows (see Fig. 3(*b*)). As expected, because the blockages with the smaller and larger holes in this study block 80% and 70%, respectively, of the flow cross section of the rectangular channel, the pressure drops are much larger across the blockages than for airflows through an open channel at the same flow rates. Figure 6 shows that the blockages with the smaller holes in Cases S-1–S-4 cause larger pressure drops than the blockages with the larger holes in Cases L-1–L-4. The friction factor ratio f/f_0 increases as the hole aspect ratio is increased, with values ranging from about 700 to about 1900 for the blockages with the smaller holes, and from about 300 to about 1300 for the blockages with the larger holes.

In all cases, f/f_0 is larger when the Reynolds number is increased. The f/f_0 values for Re≅12,000 and Re≅17,000 are about 16% and 27%, respectively, higher than the corresponding values for Re≅7000. In almost all cases, f/f_0 is larger when the hole aspect ratio is larger. For the blockages with the smaller holes, increasing the aspect ratio of the holes from 1.0 to 3.4 increases the friction factor ratio by 55% to over 100%. For the blockages with the larger holes, increasing the aspect ratio of the holes from 1.0 to 3.4 may more than triple the f/f_0 values. The wider sections of the blockages between staggered holes with a larger aspect ratio appear to increase the resistance to the air flow through the channel more than the blockages that have holes with a smaller aspect ratio and a smaller spacing between holes.

There are variations of the f/f_0 values for the three wall segments. For the blockages with the round holes, the pressure drops are the largest across the first wall segment (that is, across the first two blockages) and the smallest across the last wall segment (that is, across the last two blockages). For the blockages with the widest elongated holes, the trend reverses. Evidently, the holes with various aspect ratios in the blockages affect differently the air flows from an open channel and those through the holes in one or two upstream blockages.

Thermal Performance. The thermal performance was evaluated with Eq. (7) using the average Nusselt number over the three wall segments and the average of the friction factors for the three wall segments. Although the smaller holes in the blockages effect more heat transfer than the larger holes in the blockages, they also cause a larger increase of the pressure drop across the blockages than the larger holes. While $\overline{Nu}/Nu_0$ decreases with increasing Re, f/f_0 increases. Figure 7 compares the thermal performances of the

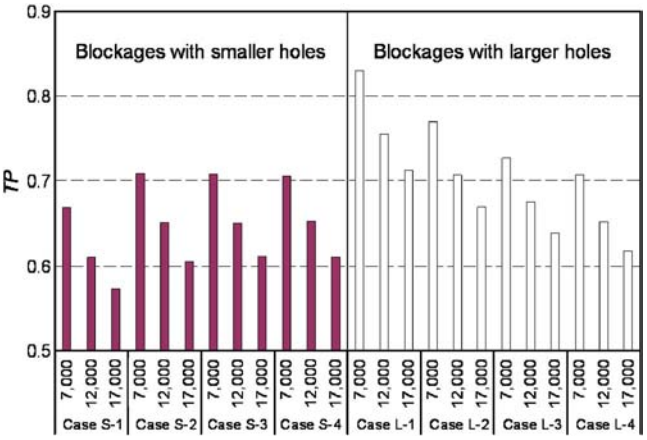

Fig. 7 Thermal performances of blockages with holes—heat transfer enhancement per unit pumping power relative to that for fully developed flow through a smooth channel (numbers along the abscissa are Reynolds numbers)

blockages with the smaller and the larger holes. In all cases, the TP value decreases with an increase of the Reynolds number. The blockages with the larger holes outperform those with the smaller holes slightly, with TP values ranging from 0.62 to 0.83 versus values from 0.57 to 0.71. For the blockages with the smaller holes, the TP values for the three elongated hole cases are about the same (within 1% for the same Re) and are about 6% higher than those for the round hole case. For the blockages with the larger holes, the thermal performance decreases with an increase of the hole aspect ratio while keeping the total hole-to-channel cross-sectional area constant.

Summary and Concluding Remarks

The results of this experimental study may be summarized as follows:

1. Blockages with holes significantly enhance the heat transfer on the channel wall segments downstream of the blockages, but they also cause substantial increases of the pressure drop, when compared with the heat transfer and pressure drops for fully developed flows at the same flow rates through a channel with the same cross section but no blockages.
2. The elongated holes in the blockages in this study enhance more heat transfer than the round holes, but they also cause larger pressure drops across the blockages.
3. The blockages with the larger holes in this study outperform the blockages with the smaller holes.

Before any design of blockages with holes may be recommended for cooling channels in gas turbine airfoils, or for heat transfer enhancement in heat exchangers in general, additional parametric studies are needed to obtain local and average heat transfer data to optimize the size and the aspect ratio of the holes in the blockages, the spacing between the holes, and the spacing between two blockages, relative to the channel height, to improve thermal performance and to minimize thermal stresses resulting from large variations of the local heat transfer. Data are also needed for heat transfer on the surfaces of the holes, and the upstream and downstream surfaces of the blockages, since a substantial amount of heat may be conducted from the walls to the blockages.

Nomenclature

A_c = flow cross-sectional area of test channel, m^2
A_s = heat transfer surface area, m^2
D_h = hydraulic diameter of test channel, m
f = friction factor
f_0 = friction factor for fully developed turbulent flow through a smooth channel
$\bar{h}$ = average heat transfer coefficient, $W/(m^2\,K)$
H = height of test channel
I = current, A
k = thermal conductivity of air, $W/(m\,K)$
$\dot{m}$ = air mass flow rate, kg/s
$\overline{Nu}$ = average Nusselt number
$\overline{Nu}_{av}$ = average Nusselt number over three wall segments downstream of blockages
Nu_0 = Nusselt number for fully developed turbulent flow through a smooth channel
p = pressure, N/m^2
P = perimeter of test channel, m
Pr = Prandtl number
q_{loss} = rate of extraneous heat losses, W
Re = Reynolds number
$\bar{T}_m$ = average bulk temperature, K
TP = thermal performance, $(\overline{Nu}/Nu_0)(f/f_0)^{-1/3}$
$\bar{T}_w$ = average surface temperature, K
$\bar{u}$ = average velocity, m/s
V = voltage, V
W = width of the test channel, m

Greek Symbols

Δp = pressure drop across two consecutive blockages, N/m^2
Δx = distance between two rows of pressure taps across two consecutive blockages, m
μ = dynamic viscosity of air, $N\,s/m^2$
ρ = density of air, kg/m^3

References

[1] Lau, S. C., Cervantes, J., Han, J. C., and Rudolph, R. J., 2006, "Internal Cooling Near Trailing Edge of a Gas Turbine Airfoil With Cooling Airflow Through Blockages With Holes," *Proceedings of ASME Turbo Expo 2006*, Barcelona, Spain, May 8–11, ASME Paper No. GT2006-91230, ASME J. Turbomach., accepted.
[2] Han, J. C., Dutta, S., and Ekkad, S. V., 2000, *Gas Turbine Heat Transfer and Cooling Technology*, Taylor & Francis, New York, pp. 251–529.
[3] Lau, S. C., 2001, "Enhanced Internal Cooling of Gas Turbine Airfoils," *Heat Transfer in Gas Turbines*, B. Sundén and M. Faghri, eds., WIT, Southampton, pp. 109–173.
[4] Coleman, H. W., and Steele, W. G., 1989, *Experimentation and Uncertainty Analysis for Engineers*, Wiley, New York.
[5] Ahn, H. S., 2006, "Heat and Mass Transfer Enhancement for Flow through Blockages With Round and Elongated Holes in a Rectangular Channel," Part I of Ph.D. thesis, Texas A&M University, College Station.